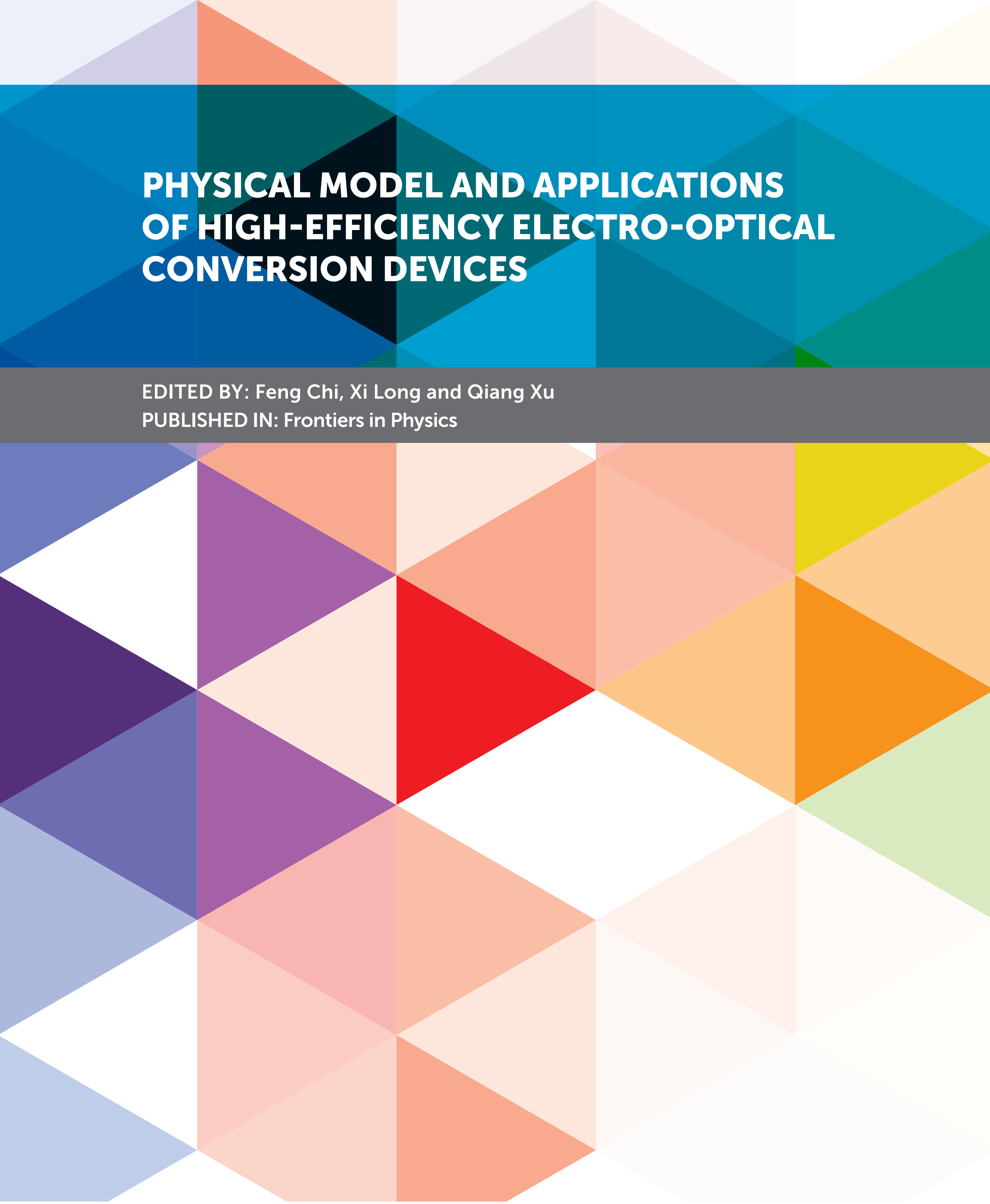

PHYSICAL MODEL AND APPLICATIONS OF HIGH-EFFICIENCY ELECTRO-OPTICAL CONVERSION DEVICES

EDITED BY: Feng Chi, Xi Long and Qiang Xu
PUBLISHED IN: Frontiers in Physics

frontiers Research Topics

About Frontiers

Frontiers is more than just an open-access publisher of scholarly articles: it is a pioneering approach to the world of academia, radically improving the way scholarly research is managed. The grand vision of Frontiers is a world where all people have an equal opportunity to seek, share and generate knowledge. Frontiers provides immediate and permanent online open access to all its publications, but this alone is not enough to realize our grand goals.

Frontiers Journal Series

The Frontiers Journal Series is a multi-tier and interdisciplinary set of open-access, online journals, promising a paradigm shift from the current review, selection and dissemination processes in academic publishing. All Frontiers journals are driven by researchers for researchers; therefore, they constitute a service to the scholarly community. At the same time, the Frontiers Journal Series operates on a revolutionary invention, the tiered publishing system, initially addressing specific communities of scholars, and gradually climbing up to broader public understanding, thus serving the interests of the lay society, too.

Dedication to Quality

Each Frontiers article is a landmark of the highest quality, thanks to genuinely collaborative interactions between authors and review editors, who include some of the world's best academicians. Research must be certified by peers before entering a stream of knowledge that may eventually reach the public - and shape society; therefore, Frontiers only applies the most rigorous and unbiased reviews.
Frontiers revolutionizes research publishing by freely delivering the most outstanding research, evaluated with no bias from both the academic and social point of view.
By applying the most advanced information technologies, Frontiers is catapulting scholarly publishing into a new generation.

What are Frontiers Research Topics?

Frontiers Research Topics are very popular trademarks of the Frontiers Journals Series: they are collections of at least ten articles, all centered on a particular subject. With their unique mix of varied contributions from Original Research to Review Articles, Frontiers Research Topics unify the most influential researchers, the latest key findings and historical advances in a hot research area! Find out more on how to host your own Frontiers Research Topic or contribute to one as an author by contacting the Frontiers Editorial Office: frontiersin.org/about/contact

ISSN 1664-8714
ISBN 978-2-88974-232-5
DOI 10.3389/978-2-88974-232-5

PHYSICAL MODEL AND APPLICATIONS OF HIGH-EFFICIENCY ELECTRO-OPTICAL CONVERSION DEVICES

Topic Editors:
Feng Chi, Zhongshan Institute, China
Xi Long, Philips Research (Netherlands), Netherlands
Qiang Xu, Nanyang Technological University, Singapore

Citation: Chi, F., Long, X., Xu, Q., eds. (2022). Physical Model and Applications of High-Efficiency Electro-Optical Conversion Devices. Lausanne: Frontiers Media SA. doi: 10.3389/978-2-88974-232-5

Table of Contents

frontiers in Physics

EDITORIAL
published: 13 December 2021
doi: 10.3389/fphy.2021.819303

Editorial: Physical Model and Applications of High-Efficiency Electro-Optical Conversion Devices

Feng Chi[1]*, **Qiang Xu**[2] **and Xi Long**[3]

[1]College of Electron and Information, Zhongshan Institute, University of Electronic Science and Technology of China, Zhongshan, China, [2]School of Physical and Mathematical Sciences, Nanyang Technological University, Singapore, Singapore, [3]Department of Electrical Engineering, Eindhoven University of Technology, Eindhoven, Netherlands

Keywords: electro-optical conversion devices, modeling, conversion efficiency, thermoelectric properties, algorithms

Editorial on the Research Topic

Physical Model and Applications of High-Efficiency Electro-Optical Conversion Devices

MODELING OF HIGH-EFFICIENCY ELECTRO-OPTICAL CONVERSION DEVICES

To improve the performances of an electro-optical conversion device, a physical model of the same is needed. In fact, once an appropriate model is built, the optimization of the device design is possible. In particular, electrochemical properties are very relevant to the efficiency of electro-optical conversion devices. It has been shown that impurity doping is an effective method of improving electrochemical performance [1–4]. An Al-doping ternary cathode material model based on first principles density functional theory is proposed to improve the electrochemical performance of the device (Gao et al.). In this model, Al doping provides the ternary cathode material with better electrical conductivity and cycling ability, therefore results in a significant improvement in the rate performance of the material. On this basis, considering that Li-rich Mn-based oxides are also commonly used cathode materials for battery modules of electro-optical conversion devices, a similar model is established to simulate the effects of changing sodium doping amounts on the electrochemical properties of the oxide (Gao et al.). The results show that the conductivity is larger when the sodium doping amount is 0.1 mol. In addition, a model is developed to prepare n^{-}-n^{+} photodiodes by growing Bi-doped MAPbCl3 epitaxial layer on MAPbCl3 single crystal substrate (Zhao et al.). Specifically, impurity doping can improve the physical and electrochemical properties of conventional materials, leading to an increase in the efficiency of electro-optical conversion devices [5, 6].

At the same time, high self-heating and low heat dissipation are the critical issues needed to be addressed during the operation of electro-optical conversion devices. Heat is generated during devices operation, resulting in higher device temperature and thermal droop. Building some specific models to reduce the thermal droop can effectively boost the efficiency of the devices and promote the energy saving [7–9]. A model based on thermal transport effects is proposed to study electron transports and transport efficiency of LEDs under high and low bias voltages. When the applied voltage is lower than the photon voltage, heat generated in the circuit is exchanged and absorbed by carriers. This allows to improve the efficiency of the whole system through energy recovery and heat collection (Lu et al.). The new model can act as the research prototype to design high-efficient LED arrays for better energy recycling and thermal control. Based on the concept of heterostructure, a model is proposed to obtain a new type of nanowire (NW) photoanode by strong enhancement of the photocurrent in solar water splitting.

Edited and reviewed by:
Lorenzo Pavesi,
University of Trento, Italy

***Correspondence:**
Feng Chi
chifeng@semi.ac.cn

Specialty section:
This article was submitted to
Optics and Photonics,
a section of the journal
Frontiers in Physics

Received: 21 November 2021
Accepted: 29 November 2021
Published: 13 December 2021

Citation:
Chi F, Xu Q and Long X (2021) Editorial:
Physical Model and Applications of
High-Efficiency Electro-Optical
Conversion Devices.
Front. Phys. 9:819303.
doi: 10.3389/fphy.2021.819303

A heterostructure with correct staggered band arrangement greatly enhances the separation and transmission of photogenerated carriers. It not only improves the efficiency of n-type photoanode, but also solves the problem of p-type doping that has a great impact on the device (Zhao et al.).

The presence of Majorana bound states (MBSs) in the circuits can greatly affect the value of the currents. Therefore, accurate detection of MBSs is one of the core issues addressed by modeling electro-optical conversion devices [10]. In the framework of the nonequilibrium Green's function, a new model is established to investigate electronic transport in a quantum dot (QD) which is coupled to a phonon bath and MBSs simultaneously (Wang et al.). With a certain bias voltage, by selecting correct parameters, heating can be suppressed even if the current is increased. This permits to eliminate the waste heat generated by the current through the low dimensional circuit. Properties of spin Seebeck effect in a quantum dot coupled to topological superconductor hosting a pair of MBSs are theoretically studied by nonequilibrium Green's function method (Sun et al.). This model may have practical applications in the detection of MBSs and be used in highly efficient spin-thermal devices. It is an ideal choice for designing energy-saving devices. Based on the characteristics of MBSs in photon-assisted tunneling (PAT) process, it is valuable to study the influence of MBSs on thermoelectric properties by using optical technology [11–14]. Considering the irradiation of photon field, conductivity and thermoelectric properties of a QD coupled to MBSs are studied (He et al.). As the coupling strength between the QD and MBSs increases, the combined action of MBSs and PAT can significantly improve the thermoelectric energy. Meanwhile, a sign change of the thermopower induced by changing either dot-MBSs coupling or temperature is analyzed. This can be used as the evidence of the existence of MBSs. In spintronic devices, a key quantity is the relative change of current called tunnel magnetoresistance (TMR). A model of double quantum dots in series is established, and the properties of electrical current and TMR in the model are studied theoretically (Tang et al.). The magnitude of currents can be changed by adjusting the sign of spin polarization and the arrangement of magnetic moments. When two spin polarizations are the same in sign, a negative TMR emerges which is useful in detection of the MBSs. This tunable current and TMR can also be used for efficient spintronic devices or information processing. The properties of local heat originated from energy exchange are studied theoretically in a quantum dot (QD) (Wang et al.). A dual negative differential of heat generation (NDHG) effect is found in the model. In addition, the simulation results show that the dual NDHG effect is robust against the variation of intradot Coulomb interaction strength, and may remedy some limitations of tunneling spectroscopy technique.

The previous physical models can determine the properties of electro-optical conversion, electrochemistry and heat generation, etc. Selecting right parameters to optimize models can lead to higher efficiency in electro-optical conversion devices. As electro-optical devices continue to shrink in size, increasing the conversion efficiency of devices will not only allow for better performance, but also expand their application in new materials and structures.

APPLICATIONS OF HIGH-EFFICIENCY ELECTRO-OPTICAL CONVERSION DEVICES

The development of new materials and structures is needed for the application of electro-optical conversion devices [15, 16]. III-V multijunction solar cells are widely used in space applications due to their super high electro-optical conversion efficiency and radiation resistance (Li et al.). The need of a tradeoff between bandgap matching and lattice matching promotes the development of new structures and materials of solar cells (Li et al.). The conversion efficiency can be effectively improved by crystalline silicon heterojunction solar cell. Furthermore, latticematched GaInP/GaAs/Ge triple junction solar cell fabrication technology is mature and can be used in large-scale production. A polychromic macromolecular dye system using azopyrazolone as chromophore is proposed (Deng et al.). The dye system is constructed with azopyrazolone dye as the chromogenic matrix. The binding effect of the bridge group in space is used to reduce the dipole moment of the entire molecule and the backflow effect of oil with external electric field. This method can effectively improve the solubility, absorption coefficient and light stability of dyes. In addition, an ultrafast modulation effect on local magnetization orientation in the GdFeCo layer is obtained when it is triggered by the femtosecond laser pulse and driven by the effective exchange field (Xie et al.). This method is conducive to the development of exchange-coupled composites.

The optimization of algorithms is of great significance to promote the application of high-efficiency electro-optical conversion devices (Liu et al.). In order to measure the actual driving distance of vehicle ahead, an improved sum of squared difference (SSD) algorithm is proposed (Lin et al.). Gaussian blur and gray conversion are used to optimize images, and then the improved SSD is used for stereo matching and disparity calculation to obtain the corresponding distance value of each point. This method can effectively improve the accuracy of stereo matching and disparity calculation, and can be applied to license plate recognition and other fields. A novel generation and transmission method of 400G signal is demonstrated with single discrete Fourier transform-spread (DFT-spread) band to avoid multi-band inter-sub-band interference (Liu et al.). The problem of increasing bandwidth brings about by the development of mobile Internet can be solved by this technology. The optimization of algorithms can also be used to improve the performance of electro-optical conversion devices, such as electrophoretic displays (EPDs) and electrowetting displays (EWDs) (Tian et al.) [17, 18]. A driving waveform based on driving process fusion and black reference gray scale is proposed to improve the performance of EPDs (Wang et al.). In this driving waveform, the DC balance rule is used to prevent the display breakdown caused by charge trapping, and the black state is used as the reference gray scale to reduce the driving time. Similarly, some driving waveforms are proposed to reduce contact angle hysteresis, response time and charge trapping, and improve the aperture ratio of EWDs (Yi et al.) [19]. A driving scheme for EWDs using alternating current (AC) voltage is proposed and the inhibitory effect of AC voltage on contact angle hysteresis is proved (Wang et al.). As for reducing response time, a driving waveform based on overdriving voltage is proposed to increase the response speed of oil (Zeng et al.). The influence of different overdriving voltages on response time is tested. The experimental results show that overdriving the voltage can effectively reduce the response time. The charge trapping of EWDs also needs to be solved. A method shows that charge trapping can be reduced by a periodic reset signal, and the oil backflow can also be reduced by the reset signal (Zhang et al.). In a previous study, it has been proven that oil splitting is one factor which can lead to the decrease of aperture ratio [20]. A driving waveform with a narrow falling ramp, low-voltage maintenance, and a rising ramp is proposed to reduce oil splitting (Lai et al.). The low voltage maintenance stage in this driving waveform can effectively suppress the oil splitting. In addition, the inhibitory effect of rising gradient voltage on oil splitting is shown in another driving scheme (Tian et al.).

The latest progress of applications of electro-optical conversion devices was discussed in this section. Study on new materials, structures and algorithms can effectively improve the electro-optical conversion efficiency and increase the various possible applications of electro-optical conversion devices, which may enable new technologies to facilitate people's lives and promote further industrialization.

CONCLUSION

The latest technology developments impose tighter requirements for the conversion efficiency of electro-optical conversion devices. In this reserch topic, new high-efficiency electro-optical conversion devices are described. At first, the impact of the latest models of electro-optical conversion devices on their performance is introduced. Then, the new materials, structures and algorithms of electro-optical conversion devices are classified and summarized, which provides reference value for increasing their performance and application scenarios. In the future, the rapid development of electro-optical conversion devices is expected to bring technological breakthroughs in the fields of solar cells and new displays.

AUTHOR CONTRIBUTIONS

All authors listed have made a substantial, direct, and intellectual contribution to the work and approved it for publication.

REFERENCES

1. Jian J, Jiang G, van de Krol R, Wei B, Wang H Recent Advances in Rational Engineering of Multinary Semiconductors for Photoelectrochemical Hydrogen Generation. *Nano Energy* (2018) 51:457–80. doi:10.1016/j.nanoen.2018.06.074
2. Cho S, Jang J-W, Lee K-H, Lee JS Research Update: Strategies for Efficient Photoelectrochemical Water Splitting Using Metal Oxide Photoanodes. *Apl Mater* (2014) 2:010703. doi:10.1063/1.4861798
3. Chi F, Liu L, Sun L Photon-mediated Spin-Polarized Current in a Quantum Dot under thermal Bias. *Chin Phys. B* (2017) 26:037304–94. doi:10.1088/1674-1056/26/3/037304
4. Chi F, Fu Z-G, Liu L, Zhang P Enhanced Spin-dependent Thermopower in a Double-Quantum-Dot Sandwiched between Two-Dimensional Electron Gases. *Chin Phys. B* (2019) 28:107305. doi:10.1088/1674-1056/ab3f98
5. Sarkar P, Srivastava A, Tripathy SK, Baishnab KL, Lenka TR, Menon PS, et al. Exploring the Effect of Ga3+ Doping on Structural, Electronic and Optical Properties of CH3NH3PbCl3 Perovskites: an Experimental Study. *J Mater Sci Mater Electron* (2020) 32:12841–55. doi:10.1007/s10854-020-04019-w
6. Xiong Y, Xu L, Wu P, Sun L, Xie G, Hu B Bismuth Doping-Induced Stable Seebeck Effect Based on MAPbI 3 Polycrystalline Thin Films. *Adv Funct Mater* (2019) 29:1900615. doi:10.1002/adfm.201900615
7. Meneghini M, De Santi C, Tibaldi A, Vallone M, Bertazzi F, Meneghesso G, et al. Thermal Droop in III-Nitride Based Light-Emitting Diodes: Physical Origin and Perspectives. *J Appl Phys* (2020) 127:211102. doi:10.1063/5.0005874
8. Lei QQ, Aierken A, Sailai M, Heini M, Shen XB, Zhao XF, et al. 150 KeV Proton Irradiation Effects on Photoluminescence of GaInAsN Bulk and Quantum Well Structures. *Opt Mater* (2019) 97:109375. doi:10.1016/j.optmat.2019.109375
9. Shen D-F, Guo J-J, Lin G-S, Lin J-Y Content-aware Specular Reflection Suppression Based on Adaptive Image Inpainting and Neural Network for Endoscopic Images. *Comput Methods Programs Biomed* (2020) 192:105414. doi:10.1016/j.cmpb.2020.105414
10. Karzig T, Knapp C, Lutchyn RM, Bonderson P, Hastings MB, Nayak C, et al. Scalable Designs for Quasiparticle-Poisoning-Protected Topological Quantum Computation with Majorana Zero Modes. *Phys Rev B* (2017) 95:235305. doi:10.1103/physrevb.95.235305
11. Li Y, Kundu A, Zhong F, Seradjeh B Tunable Floquet Majorana Fermions in Driven Coupled Quantum Dots. *Phys Rev B* (2014) 90:121401. doi:10.1103/PhysRevB.90.121401
12. Väyrynen JI, Rastelli G, Belzig W, Glazman LI Microwave Signatures of Majorana States in a Topological Josephson junction. *Phys Rev B* (2015) 92:134508. doi:10.1103/PhysRevB.92.134508
13. Chen H, Zhu K All-optical Scheme for Detecting the Possible Majorana Signature Based on QD and Nanomechanical Resonator Systems. *Sci China Phys Mech Astron* (2015) 58:1–14. doi:10.1007/s11433-014-5637-4
14. Tang H-Z, Zhang Y-T, Liu J-J Photon-assisted Tunneling through a Topological Superconductor with Majorana Bound States. *AIP Adv* (2015) 5:127129. doi:10.1063/1.4939096
15. Jin M, Shen S, Yi Z, Zhou G, Shui L Optofluid-based Reflective Displays. *Micromachines* (2018) 9:159. doi:10.3390/mi9040159
16. Yi Z-C, Chen Z-B, Peng B, Li S-X, Bai P-F, Shui L-L, et al. Vehicle Lighting Recognition System Based on Erosion Algorithm and Effective Area

Separation in 5g Vehicular Communication Networks. *IEEE Access* (2019) 7: 111074–83. doi:10.1109/access.2019.2927731

17. Yi Z, Shui L, Wang L, Jin M, Hayes RA, Zhou G A Novel Driver for Active Matrix Electrowetting Displays. *Displays* (2015) 37:86–93. doi:10.1016/j.displa.2014.09.004
18. Yi Z-c., Bai P-f., Wang L, Zhang X, Zhou G-f. An Electrophoretic Display Driving Waveform Based on Improvement of Activation Pattern. *J Cent South Univ* (2014) 21:3133–7. doi:10.1007/s11771-014-2285-9
19. Yi Z, Huang Z, Lai S, He W, Wang L, Chi F, et al. Driving Waveform Design of Electrowetting Displays Based on an Exponential Function for a Stable Grayscale and a Short Driving Time. *Micromachines* (2020) 11:313. doi:10.3390/mi11030313
20. Luo Z, Fan J, Xu J, Zhou G, Liu S A Novel Driving Scheme for Oil-Splitting Suppression in Electrowetting Display. *Opt Rev* (2020) 27:339–45. doi:10.1007/s10043-020-00601-z

Conflict of Interest: The authors declare that the research was conducted in the absence of any commercial or financial relationships that could be construed as a potential conflict of interest.

frontiers
in Physics

ORIGINAL RESEARCH
published: 18 January 2021
doi: 10.3389/fphy.2020.616107

Electronic Transport Through Double Quantum Dot Coupled to Majorana Bound States and Ferromagnetic Leads

Li-Wen Tang and Wei-Guo Mao*

Department of Materials Engineering, Xiangtan University, Xiangtan, China

We have studied theoretically the properties of electrical current and tunnel magnetoresistance (TMR) through a serially connected double quantum dot (DQD) sandwiched between two ferromagnetic leads by using the nonequilibrium Green's function technique. We consider that each of the DQD couples to one mode of the Majorana bound states (MBSs) formed at the ends of a topological superconductor nanowire with spin-dependent coupling strength. By adjusting the sign of the spin polarization of dot–MBS coupling strength and the arrangement of magnetic moments of the two leads, the currents' magnitude can be effectively enhanced or suppressed. Under some conditions, a negative TMR emerges which is useful in detection of the MBSs, a research subject currently under extensive investigations. Moreover, the amplitude of the TMR can be adjusted in a large regime by variation of several system parameters, such as direct hybridization strength between the MBSs or the dots and the positions of the dots' energy levels. Such tunable currents and TMR may also find use in high-efficiency spintronic devices or information processes.

Keywords: double quantum dots, Majorana bound states, spin-dependent coupling strength, tunnel magnetoresistance, ferromagnetic leads

Edited by:
Qiang Xu,
Nanyang Technological University,
Singapore

Reviewed by:
Li Wang,
Zhongshan Polytechnic, China
Ji-Pei Chen,
Guangzhou University, China

****Correspondence:***
Li-Wen Tang
qdtang2020@163.com

Specialty section:
This article was submitted to
Optics and Photonics,
a section of the journal
Frontiers in Physics

Received: *11 October 2020*
Accepted: *30 October 2020*
Published: *18 January 2021*

Citation:
Tang L-W and Mao W-G (2021)
Electronic Transport Through Double
Quantum Dot Coupled to Majorana
Bound States and
Ferromagnetic Leads.
Front. Phys. 8:616107.
doi: 10.3389/fphy.2020.616107

1 INTRODUCTION

Electronic transport through structures composing of quantum dots (QDs) hybridized with a topological superconductor nanowire (TSNW) hosting Majorana bound states (MBSs) [1–3] has aroused much interest in recent years. The zero-energy MBSs are exotic self-conjugate quasiparticles that have been successfully realized in encouraging experiments [4–6] during the last decade. One of the most attractive platforms [7, 8] to host and detect MBSs is a superconductor proximitized semiconductor nanowire having the spin–orbit interaction and strong Zeeman splitting. Previous theoretical work predicted that the combined effects of the spin–orbit interaction and the large enough Zeeman splitting will convert an ordinary s-wave superconductor into a p-wave one so as to realize the MBSs. Recently, quantized electrical conductance peak at zero-bias voltage [9, 10] in a TSNW device was observed, which is a significant breakthrough for the demonstration of MBSs. Unfortunately, this zero-bias abnormal conductance peak cannot solely be attributed to the existence of MBSs and then some other means, such as the fractional Josephson effect [11–13] and thermoelectric effect [14–18] in systems composing of QDs with side-coupled MBSs were proposed to detect the existence of MBSs.

Some previous theoretical and experimental work has shown that the MBSs will affect the electronic transport processes through QD-based devices in a significant way [19, 20]. For example, Baranger and his co-author proved that the value of the conductance in a single QD, which is coupled to the left and right leads, will remain at half of its quantum value $e^2/2h$, regardless of the positions of the dot's energy levels [21]. If both the spin directions of electrons on the QD are coupled to the MBSs [20, 22–24] with different hybridization amplitudes, which depend on the spin–orbit interaction length in the TSNW, they will interfere with each other through the MBSs and then will change the current significantly. For electron–hole symmetry, the zero-bias conductance is $3e^2/2h$ which is the sum of $e^2/2h$ for one spin direction and e^2/h for the opposite spin direction. In addition to the single-QD structure, impacts of MBSs in the double quantum dot (DQD) have also been investigated in recent years [25–27]. As compared to the single QD, there are richer physical contents in the DQD with more tunable system parameters, such as the interaction between the two dots, arrangement of the dots' energy levels, separate coupling between the dots and the leads, and so on.

It is known that the zero-energy MBSs exert remarkable effects on the electrical conductance and current around the zero-bias regimes. But under such a condition, the amplitude and changes of the above quantities are usually small and hard to be detected. In fact, the quantity of tunnel magnetoresistance (TMR) [28–30], which measures the relative change of the currents' amplitude, is frequently used as detection means in electronic transport. It is also a key quantity in spintronic devices. The TMR is defined as TMR = $(J_P - J_{AP})/J_{AP}$, where $J_{P(AP)}$ is the electrical current when the ferromagnetic leads' magnetic moments are arranged in parallel (antiparallel) configuration. Usually, the value of TMR is positive because J_P is contributed from transport processes when electrons tunnel between the majority–majority and minority–minority spin bands, whereas J_{AP} is from electronic transport between major–minority spin bands. The tunneling in parallel configuration is easier than in the antiparallel one, inducing a positive TMR [28–30]. In the presence of coupling between the QDs and MBSs, however, the electrical current when the leads' magnetic moments are in antiparallel can be enhanced to be larger than that of the parallel configuration. Such a change in the currents will induce a negative TMR which is promising in detection of the MBSs, as was proved in our previous work [31], in which we found two criteria that can be used for detecting the existence of MBSs. One is the peak to valley evolution of TMR when the dot's level is fixed at zero, and the other is the sign change of TMR for the nonzero QD's energy level. Moreover, we have found that the negative TMR can be significantly enhanced by the left–right asymmetry of the line-width functions. In the present DQD system, however, we study other mechanisms to reverse the sign of TMR, that is, the spin polarization of the DQD–MBS coupling strength. The most interesting result we find is that the magnitude of TMR can be either enhanced or suppressed by changing the sign of the spin polarization of the dot–MBS coupling strength. The negative TMR is unchanged by various system parameters, such as the direct overlapping between the MBSs, the difference between the dots' level, and the tunnel coupling between the two dots. Single QD has been successfully inserted in between the ferromagnetic leads [32], and abnormal sign change of the TMR may be realized in experiments. There are also investigations on the Kondo effect in a single QD coupled to ferromagnetic leads [24] and showed that the impacts of the ferromagnetism on the leads will induce more interesting result due to the presence of the MBSs [33]. As a natural extension, we study properties of the electrical current and TMR in a DQD coupled to ferromagnetic leads and MBSs (see **Figure 1**). Different from some previous work [31, 33], we consider that the case that spin-up and spin-down electrons on the QD are coupled to the MBSs with different hybridization amplitudes [20, 22–24]. Our results show that the sign and the amplitude of the TMR can be adjusted in a large regime by variation of several system parameters, especially the spin polarization of the DQD–MBS hybridization, which is useful in detection of the MBSs, as well as in the design of spintronic devices or information processes. It should be noted that except the topological superconductor nanowires, the MBSs have also be prepared in some other systems, such as electrostatic defects in topological superconductors [34], the semiconductor [7], or ferromagnetic [35] nanowires with native strong spin–orbit interaction proximitization to a conventional s-wave superconductors, and theJosephson junctions [11].

2 MODEL AND METHODS

The Hamiltonian of the studied system shown in **Figure 1**, which is composed of the DQD each of which connected to the left and right ferromagnetic leads and to one mode of the MBSs, can be written as the following form [21, 24],

$$\begin{aligned} H = &\sum_{k\alpha\sigma}\varepsilon_{k\alpha\sigma}\varepsilon^{+}_{k\alpha\sigma}\varepsilon_{k\alpha\sigma} + \sum_{i=1,2;\sigma}\varepsilon_i d^{+}_{i\sigma}d_{i\sigma} + t_c\sum_{\sigma}\left(d^{+}_{1\sigma}d_{2\sigma} + d^{+}_{2\sigma}d_{1\sigma}\right) \\ &+\sum_{ki\sigma}\left(V_{kL\sigma}d^{+}_{1\sigma}c_{kL\sigma} + V_{kR\sigma}d^{+}_{2\sigma}c_{kR\sigma} + H.c.\right) + H_{MBSs}, \end{aligned} \tag{1}$$

where the creation (annihilation) operator $c^{\dagger}_{k\alpha\sigma}\,(c_{k\alpha\sigma})$ is for electrons having wave vector k, energy $\varepsilon_{k\alpha\sigma}$, and spin $\sigma = \uparrow, \downarrow$ in the α-th ($\alpha = L/R$) ferromagnetic lead. The second term in the right side of **Eq. 1** is for electrons on the DQD with energy level ε_i. The creation (annihilation) operator of the electrons on the QD-i is $d^{\dagger}_{i\sigma}\,(d_{i\sigma})$. The third term in the right side of **Eq. 1** denotes hopping between the two dots via a tunnel barrier with strength t_c. The forth term in the right side of **Eq. 1** describes tunneling between the dots and ferromagnetic leads with amplitude $V_{k\alpha\sigma}$. In the present structure, QDs 1 and 2 are connected to the left and right ferromagnetic leads, respectively. The last term in **Eq. 1** is for the MBSs realized at opposite ends of the TSNW and their couplings to the DQD [21, 24],

$$H_{MBSs} = \sum_{\sigma}\frac{\lambda_{1\sigma}}{\sqrt{2}}\left(d_{1\sigma} - d^{+}_{1\sigma}\right)\gamma_2 + i\sum_{\sigma}\frac{\lambda_{2\sigma}}{\sqrt{2}}\left(d_{2\sigma} + d^{+}_{2\sigma}\right)\gamma_2 + i\delta_M\gamma_1\gamma_2, \tag{2}$$

in which $\lambda_{i\sigma} = \lambda_i(1 + \sigma\Delta\lambda)$ is the spin-dependent coupling strength between the QD-i and the mode-i of the MBSs, in which λ_i is the QD–MBS coupling strength independent of the

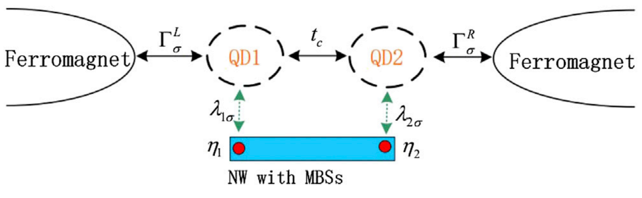

FIGURE 1 | Schematic plot of the DQD coupled to ferromagnetic leads with coupling strength $\Gamma_\sigma^{L/R}$ and to each other by t_c. The left and right dots interact individually with one mode of the MBSs at the end of topological superconductor nanowire with spin-dependent hybridization amplitude is given by $\lambda_{1(2)\sigma} = \lambda(1 + \sigma\Delta\lambda)$, in which $\Delta\lambda$ is the spin polarization of the dot–MBS coupling strength. The two modes of the MBSs overlap with each other with amplitude of δ_M.

electron spin and $\Delta\lambda$ is the spin polarization of the coupling strength. The operators of the MBSs have the properties of $\gamma_{1(2)} = \gamma_{1(2)}^\dagger$ and $\{\gamma_i, \gamma_j\} = 2\delta_{ij}$. For the convenience of calculations [21], we replace the Majorana fermion operators $\gamma_{1(2)}$ with the regular fermion operators f and $f^\dagger$ by the transformation of $\gamma_1 = \frac{1}{\sqrt{2}}(f^+ + f), \gamma_2 = \frac{i}{\sqrt{2}}(f^+ - f)$, and then **Eq. 2** is rewritten as

$$H_{MBSs} = \delta_M\left(f^+f - \frac{1}{2}\right) + \sum_\sigma\left[\frac{\lambda_{1\sigma}}{\sqrt{2}}(d_{1\sigma} - d_{1\sigma}^+)(f + f^+) + \frac{\lambda_{2\sigma}}{\sqrt{2}}(d_{2\sigma} + d_{2\sigma}^+)(f - f^+)\right], \tag{3}$$

In terms of the Hamiltonians given by **Eqs 1** and **3**, spin-dependent electrical currents J_σ can be calculated by the nonequilibrium Green's function technique as [23, 24]

$$J_\sigma = \int d\varepsilon T_\sigma(\varepsilon)[f_L(\varepsilon) - f_R(\varepsilon)] \tag{4}$$

in which the Fermi distribution function for the left and right leads are given by $f_{L/R}(\varepsilon) = [\exp[(\varepsilon - \mu_{L/R})/k_B T_e] + 1]^{-1}$, with $\mu_{L/R}$ being the chemical potential in the left/right lead held at temperature T_e. The transmission coefficient $T_\sigma(\varepsilon)$ in **Eq. 4** is calculated with the help of Green's function as [34] $T_\sigma(\varepsilon) = \Gamma_\sigma^L\Gamma_\sigma^R\left|G_{12,\sigma}^r(\varepsilon)\right|^2$, where $G_{12,\sigma}^r(\varepsilon)$ is the electron retarded Green's function and $\Gamma_\sigma^\alpha = 2\pi|V_{k\alpha\sigma}|^2\rho_{\alpha\sigma}$ is the line-width function with $\rho_{\alpha\sigma}$ being the local density of states in the lead α [28–30]. As an equivalent choice, the ferromagnetism on the leads is considered by the spin-dependent tunneling amplitude between the leads and the dot $V_{k\alpha\sigma}$. Introducing the spin polarization of the leads $p_{L(R)} = (\Gamma_\uparrow^{L(R)} - \Gamma_\downarrow^{L(R)})/(\Gamma_\uparrow^{L(R)} + \Gamma_\downarrow^{L(R)})$, we obtain $\Gamma_\uparrow^{L/R} = \Gamma(1 + p_{L(R)})$ and $\Gamma_\downarrow^{L/R} = \Gamma(1 - p_{L(R)})$, where $\Gamma = (\Gamma_\uparrow^{L/R} + \Gamma_\downarrow^{L/R})/2$. In the present article, we consider that the cases of the magnetic moments are arranged in parallel ($p_L = p_R = p$) and antiparallel ($(p_L = -p_R = p)$) configurations. We calculate Green's function in terms of the Dyson equation technique [24], that is, first, we calculate the free dots' Green's function by the equation of motion method and then the interactions between the dots and the leads, as well as with the MBSs are taken into consideration in the form of self-energies. In the absence of the Coulomb interaction between electrons, the present Dyson equation will give essentially the same Green's function as that derived by the equation of motion method [23, 36, 37]. Choosing the basis as $\Psi = \left(d_{1\uparrow}\ d_{1\uparrow}^+\ d_{1\downarrow}\ d_{1\downarrow}^+\ d_{2\uparrow}\ d_{2\uparrow}^+\ d_{2\downarrow}\ d_{2\downarrow}^+\ f\ f^+\right)$, the Dyson equation is written in a matrix form as $\widehat{G}^r = (\widehat{g}^{r-1} - \widehat{\Sigma}^r)^{-1}$, in which $\widehat{g}^r$ is the dot's retarded Green's function in the absence of all interactions and $\widehat{\Sigma}^r$ is the self-energy. The matrix form of $\widehat{g}^r$ is

$$\widehat{g}^r = \begin{pmatrix} [\widehat{g}_{11}^r(\varepsilon)]_{4\times4} & 0 & 0 \\ 0 & [\widehat{g}_{22}^r(\varepsilon)]_{4\times4} & 0 \\ 0 & 0 & [\widehat{g}_{MM}^r(\varepsilon)]_{2\times2} \end{pmatrix} \tag{5}$$

in which the diagonal matrix is

$$\widehat{g}_{11(22)}^r(\varepsilon) = \begin{pmatrix} g_{11(22),\uparrow}^r(\varepsilon) & 0 & 0 & 0 \\ 0 & \tilde{g}_{11(22),\uparrow}^r(\varepsilon) & 0 & 0 \\ 0 & 0 & g_{11(22),\downarrow}^r(\varepsilon) & 0 \\ 0 & 0 & 0 & \tilde{g}_{11(22),\downarrow}^r(\varepsilon) \end{pmatrix} \tag{6}$$

with $g_{ii,\sigma}^r(\varepsilon) = 1/(\varepsilon - \varepsilon_i)$, $\tilde{g}_{ii,\sigma}^r(\varepsilon) = 1/(\varepsilon + \varepsilon_i)$, $g_{MM}^r(\varepsilon) = 1/(\varepsilon - \delta_M)$, and $\tilde{g}_{MM}^r(\varepsilon) = 1/(\varepsilon + \delta_M)$. The matrix self-energy $\widehat{\Sigma}^r$ is composed by the line-width function (for interaction between the dots and the leads) Γ_σ^α and the dot–MBS coupling strength $\lambda_{1(2)\sigma}$; its expression is

$$\Sigma^r = \begin{pmatrix} \left[\widehat{\Sigma}^{L,r}\right]_{4\times4} & \left[\widehat{T}_c\right]_{4\times4} & \left[\widehat{K}_1\right]_{4\times2} \\ \left[\widehat{T}_c^*\right]_{4\times4} & \left[\widehat{\Sigma}^{R,r}(\varepsilon)\right]_{4\times4} & \left[\widehat{K}_2\right]_{4\times2} \\ \left[\widehat{K}_1^*\right]_{2\times4} & \left[\widehat{K}_1^*\right]_{2\times4} & [0]_{2\times2} \end{pmatrix} \tag{7}$$

in which

$$\widehat{\Sigma}^{L/R,r} = \begin{pmatrix} -i\Gamma_\uparrow^{L/R}/2 & 0 & 0 & 0 \\ 0 & -i\Gamma_\uparrow^{L/R}/2 & 0 & 0 \\ 0 & 0 & -i\Gamma_\downarrow^{L/R}/2 & 0 \\ 0 & 0 & 0 & -i\Gamma_\downarrow^{L/R}/2 \end{pmatrix} \tag{8a}$$

$$\widehat{T}_c = \begin{pmatrix} t_c & 0 & 0 & 0 \\ 0 & -t_c & 0 & 0 \\ 0 & 0 & t_c & 0 \\ 0 & 0 & 0 & -t_c \end{pmatrix} \tag{8b}$$

$$\widehat{K}_{1(2)} = \begin{pmatrix} \lambda_{1(2)\uparrow}/\sqrt{2} & \lambda_{1(2)\uparrow}/\sqrt{2} \\ -\lambda_{1(2)\uparrow}/\sqrt{2} & -\lambda_{1(2)\uparrow}/\sqrt{2} \\ \lambda_{1(2)\downarrow}/\sqrt{2} & \lambda_{1(2)\downarrow}/\sqrt{2} \\ -\lambda_{1(2)\downarrow}/\sqrt{2} & -\lambda_{1(2)\downarrow}/\sqrt{2} \end{pmatrix} \tag{8c}$$

The spin-dependent transmission is then calculated by [24] $T_{\uparrow(\downarrow)}(\varepsilon) = \Gamma_{\uparrow(\downarrow)}^L\Gamma_{\uparrow(\downarrow)}^R\left|[\widehat{G}^r]_{15(37)}\right|^2$.

3 RESULTS AND DISCUSSION

In this section, we present our numerical results for the spin-dependent currents and TMR. We choose the leads' bandwidth $D \equiv 40$ as the energy unit with fixed $\mu_L = eV$, $\mu_R = 0$, $\Gamma = 0.1$, and $T_e = 0.001$ throughout the article. **Figure 2** shows the impacts of

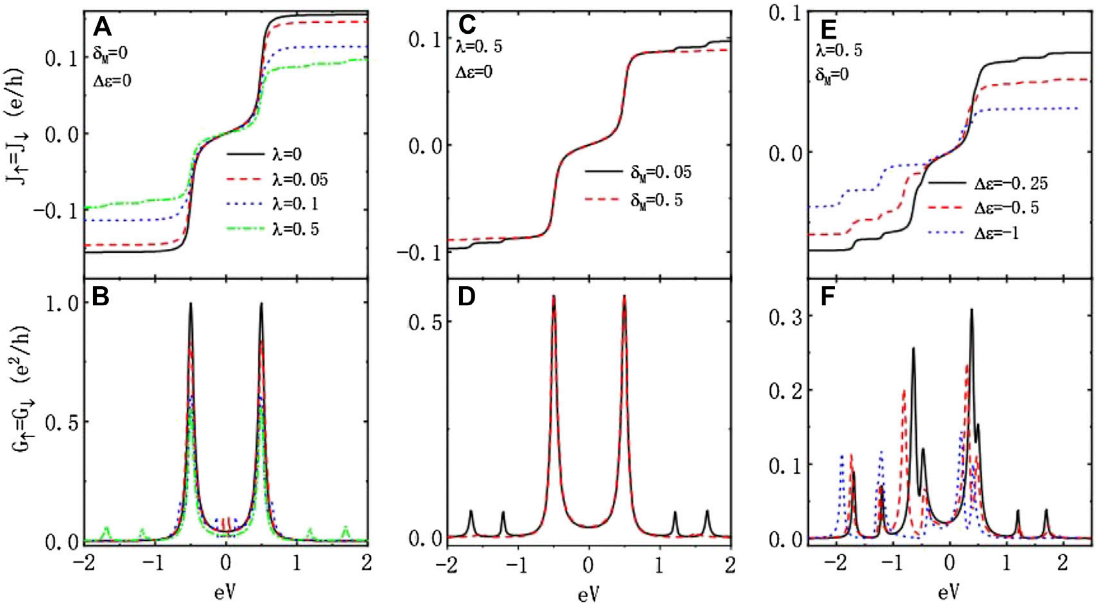

FIGURE 2 | Electronic current J_σ in A,C, and E and the associated differential conductance in B,D, and F varying with respect to the bias voltage *eV* for the case of the DQD coupled to nonmagnetic leads (p = 0). In addition to the parameters given in the figure, other ones are Γ = 0.1, T_e = 0.001, ε_1 = ε_2 = 0, t_c = 0.5, and $\Delta\lambda$ = 0. In such a system, the spin-up and spin-down currents are identical.

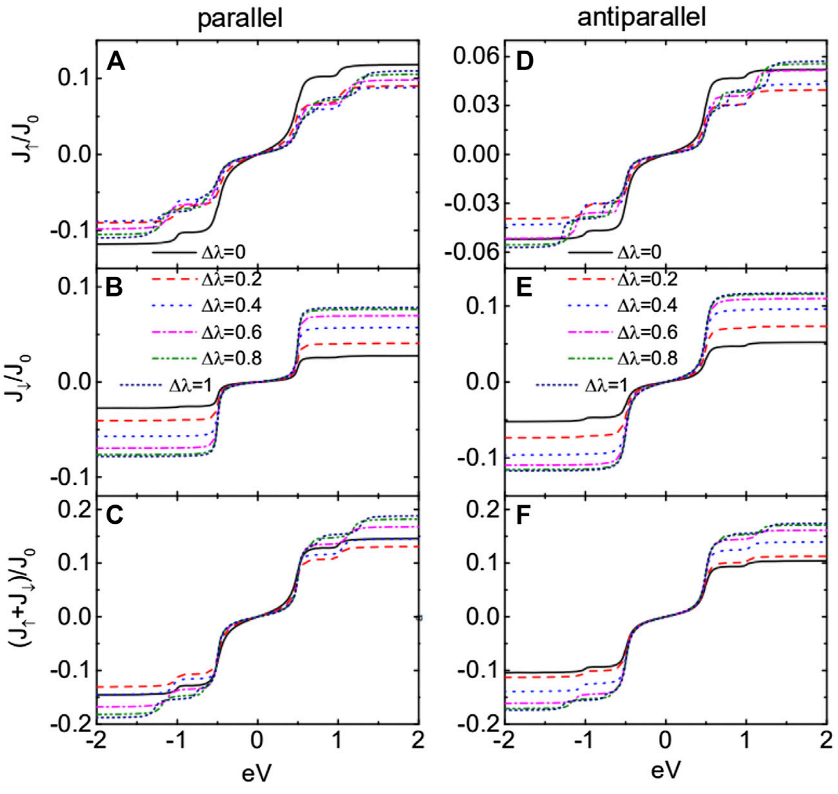

FIGURE 3 | Spin-dependent and total currents for parallel configuration in A–C, and antiparallel one in D–F with λ = 0.25, p = 0.5, and different values of $\Delta\lambda$. Other parameters are as in **Figure 2**.

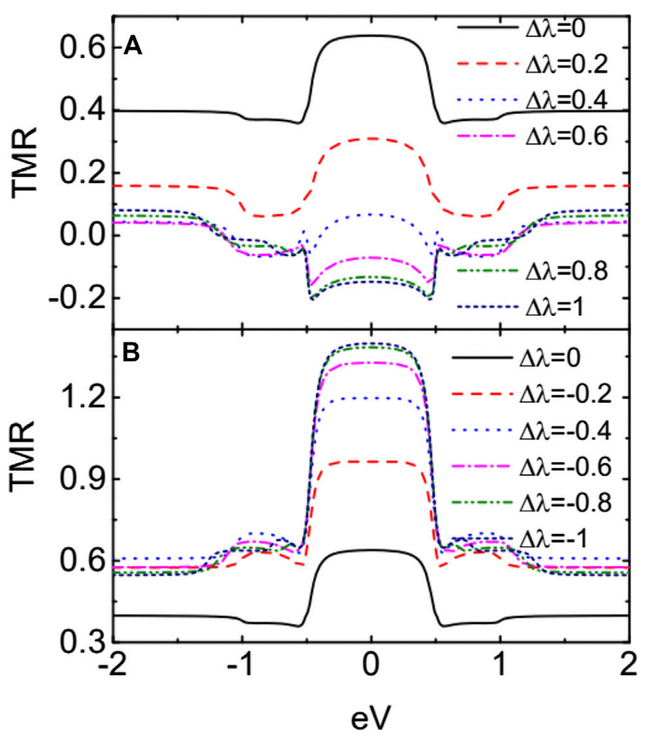

FIGURE 4 | TMR for positive $\Delta\lambda$ in A and negative $\Delta\lambda$ in B. Other parameters are as in **Figures 2**, **3**.

dot–MBS coupling strength $\lambda_1 = \lambda_2 = \lambda$, overlap amplitude between the MBSs δ_M, and difference between the dots' levels $\Delta\varepsilon = \varepsilon_1 - \varepsilon_2$ on the currents $J_\uparrow = J_\downarrow$ and differential conductance $G_\sigma = dJ_\sigma/dV$ without ferromagnetism on the leads ($p = 0$) and spin polarization of the dot–MBS coupling strength ($\Delta\lambda = 0$). In the absence of interaction between the DQD and MBSs, the molecular states of the system are positioned at $\varepsilon = (\varepsilon_1 + \varepsilon_2)/2 \pm \sqrt{(\varepsilon_1 - \varepsilon_2)^2/4 + t_c^2}$, around which the current develops a step as shown in **Figure 2A** [38]. For the chosen parameters, the molecular states in **Figure 2A** are at $\varepsilon = \pm t_c$, where the conductance arises a peak as seen from the solid black line. The reason is that when the bias voltage eV (Fermi level of the left lead μ_L) equals to each of the molecular states, electrons will tunnel into the dots from one lead and out to the other one, resulting in an increase of the current [34, 35]. Note that the current is attributed from electrons whose energy is close to the Fermi level of the leads. Therefore, the current reaches a plateau when the bias voltage is shift away from the molecular state as all the electrons have taken part in transportation (see also the conductance in **Figure 2B** which is almost zero when the bias voltage is larger or smaller than the resonant energies). In the presence of coupling between the MBSs and DQD ($\lambda \neq 0$), the states on the dots are split. For the case of $\lambda < t_c$, the states are roughly at [24, 27] $\pm\sqrt{2}\lambda$ and $\pm t_c$ and then are shifted to $\pm t_c$ and $\pm(\sqrt{2}\lambda \pm t_c)$ for $\lambda \geq t_c$, at which the conductance in **Figure 2B** develops peaks. It should be emphasized that the steps (peaks) in the current (conductance) at the molecular states $eV = \pm t_c$ are robust against the dot–MBS coupling. The peaks at $eV = \pm t_c$ are lowered by increasing λ but remain at the same positions. The stabilization of the states at $\pm t_c$ can also be seen from **Figures 2C, D**, in which the steps of the current and peaks of the conductance at $\pm t_c$ are almost unchanged by the variation of δ_M. The two molecular states (peaks in the conductance) at large bias voltage regimes disappear due to the presence of direct coupling between the MBSs δ_M, which is consistent with the previous results that the overlapping between the two modes of the MBSs will reduce their impacts on the electronic transport processes [19, 20]. One of the attractive advantages in the DQD as compared to the simple single QD is the tunable difference between dots' levels that can adjust tunneling through the system. **Figures 2E, F** present the current and conductance under different values of $\Delta\varepsilon$, respectively. As was indicated above, the difference between the dots' levels shifts the positions of the molecular states and then the positions of the steps (peaks) in the current (conductance). Moreover, the magnitudes of the currents and the conductance are weakened by increasing $\Delta\varepsilon$, as shown by the dashed and dotted lines in **Figures 2E, F**. This is because that the direct tunneling under the condition of identical dots' levels is blockaded in the presence of $\Delta\varepsilon$, and then, electronic transport can only take place through the levels mediated by the MBSs [24, 27, 34]. From **Figure 2**, one can see that the influences of the MBSs on the transport properties through the present DQD are quite different from those in the single QD system. For example, the zero-bias peaks in electrical conductance formed in the single dot structure by the presence of MBSs disappear in this DQD due to the direct tunneling between the two dots. Moreover, the value of the conductance in the single dot keeps at its half of quantum value $e^2/2h$ at sufficiently low temperatures, regardless of the dot' level [21], but in the DQD, there is no certain value in the presence of coupling between the DQD and MBSs.

With the results in **Figure 2**, we now study the currents in **Figure 3** for different values of $\Delta\lambda$ when the dots are coupled to ferromagnetic leads whose magnetic moments are arranged in either parallel or antiparallel configurations. The spin-up current $J_\uparrow$ in **Figure 3A** is suppressed with increasing $\Delta\lambda$ in a non-monotonous way due to the complex molecular states induced by dot–MBS coupling. Since both spin-up and spin-down electrons interact with the MBSs, they will interfere with each other during tunneling through the structure [20, 24]. Therefore, the transport processes in the present DQD are more interesting and complex than those in the absence of MBSs. The absolute value of $J_\uparrow$ in **Figure 3B** is monotonously enhanced with increasing $\Delta\lambda$ due to the weaker coupling strength between spin-down electrons and the MBS. The absolute value of the total current J_P in **Figure 3C** is mainly suppressed (enhanced) in the bias voltages $|eV| \leq t_c$ ($|eV| > t_c$). When the magnetic moments of the two leads are arranged in antiparallel configuration, the properties of the currents essentially resemble those in the parallel configuration. By comparing **Figure 3C** with **Figure 3F**, one can see that the total current in antiparallel J_{AP} changes more obviously than J_P. The reason can be explained as follows [30, 31, 38]: when the magnetic moments of the leads are in parallel configuration, spin-up and spin-down electrons transport through the DQD from the major–major and minor–minor

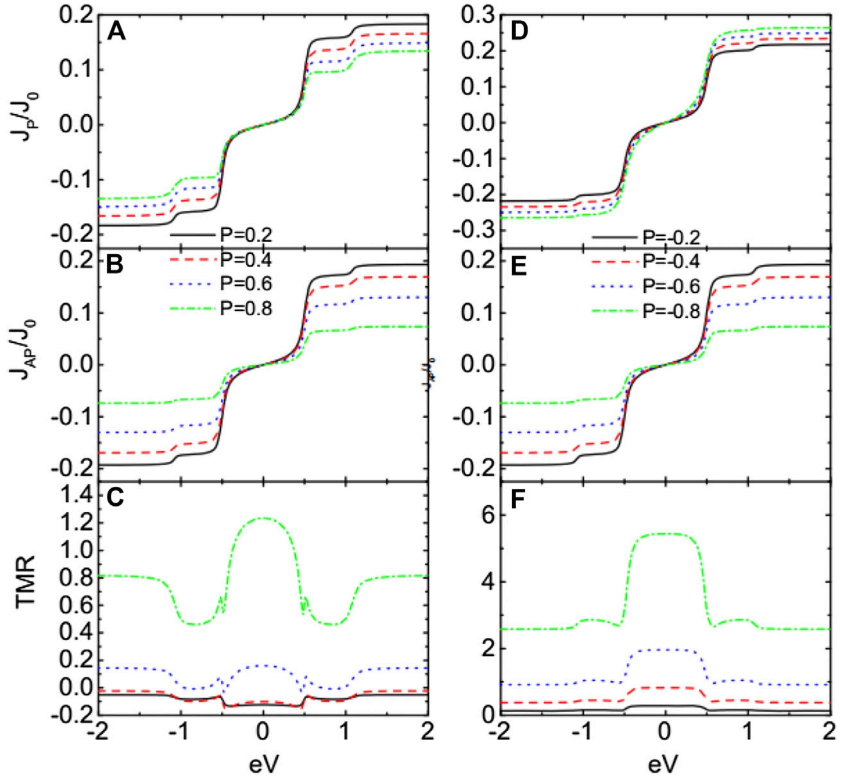

FIGURE 5 | Total currents in parallel configuration J_P and antiparallel configuration J_{AP} and TMR for positive p in A–C and negative p in D–F. Here, we set $\Delta\lambda = 0.8$, and other parameters are as in **Figures 2, 3**.

bands, respectively. Now the incoming and outgoing tunneling rates (line-width function) are the same for both spin directions. But when the leads' magnetic moments are in antiparallel configuration, both of the spin-up and spin-down electrons are transporting between major and minor bands, which means that the incoming and outgoing tunneling rates are different from each other, and then, the current's amplitude is weaker than that in the parallel configuration. In the presence of coupling between the dots and MBSs, the currents in the parallel configuration are changed more obviously than those in the antiparallel one [20, 31]. This may cause the total current in the parallel configuration to be larger than that in the antiparallel one and induce a negative TMR as will be shown later.

As is seen from **Figures 2**, **3**, the variation of the currents around the zero bias, where the MBSs play an important role, is quite nonobvious. We then present the TMR in **Figure 4** varying with respect to the bias voltage for both positive and negative $\Delta\lambda$. For $\Delta\lambda > 0$, the coupling strength $\lambda_{1(2)\uparrow}$ is larger than $\lambda_{1(2)\downarrow}$ and then the current contributed from spin-up electrons, which tunnel between major–major spin bands in the parallel configuration and are the main contribution to the total current, is suppressed [24, 34, 35]. Even the spin-down electrons in the parallel configuration is slightly enhanced; the total current near zero bias is suppressed which can be seen from **Figure 3**. When the magnetic moments are arranged in the antiparallel configuration, the change of the total current is relatively small as the electrons tunnel between major–minor spin bands. Due to the above change of the current in different configurations, the TMR is negative for sufficiently large $\Delta\lambda$ in **Figure 4A**. When the spin polarization of the dot–MBS coupling strength is negative $\Delta\lambda < 0$, the coupling between spin-up electrons becomes weaker with increasing $\Delta\lambda$, and then, the magnitude of the spin-up current is enhanced, accordingly. Since the spin-up electrons are the main contribution to the current in the parallel configuration, the total current will also increase with increasing $\Delta\lambda$. Just for the same reason, the total current in the antiparallel configuration changes much less obviously than that in the parallel configuration. These result in an enhanced positive TMR as shown in **Figure 4B**. In the bias regimes of $|eV| \le t_c$, both negative and positive TMR develop a plateau at large $\Delta\lambda$. This change from the positive peak to negative dip in the TMR is quite interesting as it is useful in either detection of the MBSs or design of spintronic devices.

Figure 5 shows the influences of the ferromagnetism of the leads on the currents and the TMR for $\Delta\lambda = 0.8$, which gives the dot–MBS coupling strength as $\lambda_{1(2)\uparrow} = 0.45$ and $\lambda_{1(2)\downarrow} = 0.05$. For the case of $p > 0$, $|J_\uparrow|$ in the parallel configuration decreases with increasing p in that more electrons are influenced by the MBSs. As for the spin-down electrons that are less influenced by the MBSs because their coupling between the leads are weakened with

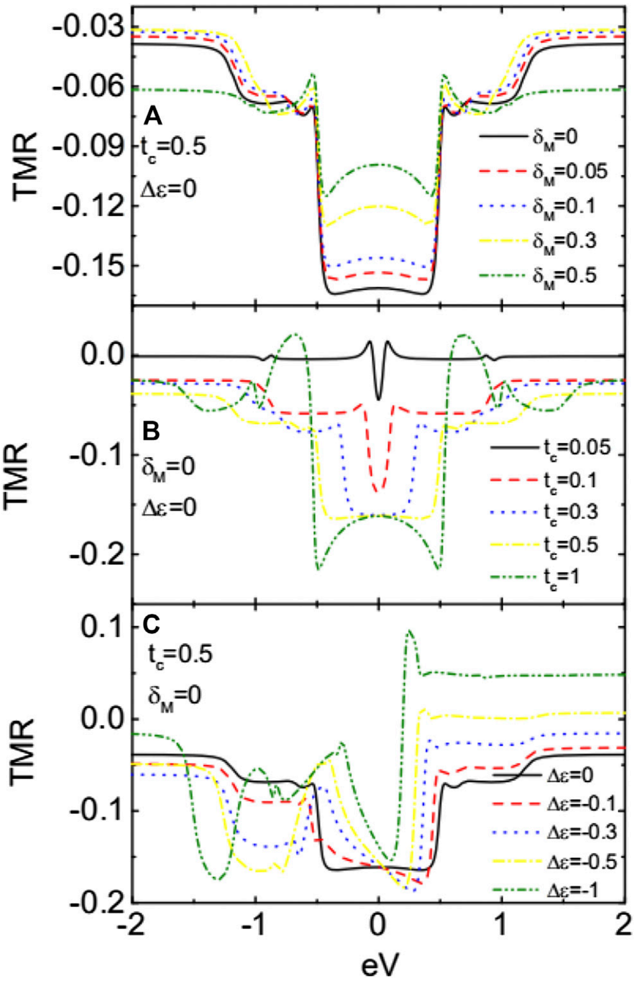

FIGURE 6 | TMR for different values of δ_M in A, different t_c in B, and different Δε in C. In addition to the parameters given in each figure, other ones are as in **Figures 2, 3**.

increasing p, the absolute current contributed from them is suppressed. The properties of the current in the antiparallel configuration can be explained in the same way. The TMR for $p > 0$ changes from the negative value to the positive one with increasing p as shown in **Figure 4C**. This is because that the negative TMR arises from the coupling between the QDs and MBSs. With increasing spin polarization of the leads, the coupling between spin-up electron and the leads is enhanced due to the increased spin-up line-width function. Therefore, the impacts of the dot–MBS coupling on the current then become relatively weak with increasing p, and then, the value of TMR is enhanced to positive. When $p < 0$, the absolute value of current in the parallel (antiparallel) configuration is enhanced (suppressed) with increasing p, which results in larger TMR shown in **Figure 5F**. The value of the TMR for $p = -0.8$ is about ten times larger than that of $p = -0.2$, a phenomenon useful in spintronics.

Figure 6 presents the impacts of δ_M, t_c, and Δε on the TMR. As is known, the direct overlapping between the two modes of the MBSs will weaken the influences of MBSs on electronic transport around zero-bias regime. This can be seen from **Figure 6A** that the negative plateau of the TMR in the bias regimes of $|eV| \le t_c$ is raised with increasing δ_M. But even for $\delta_M = 0.5$, the TMR remains negative with a relatively large value. **Figure 6B** indicates that the negative plateau becomes wider and lower with increasing t_c, which is consistent with the above discussions. For sufficiently large $t_c \ge 0.3$, the zero-bias TMR keeps at a minimum value. **Figure 6C** shows that the plateau of negative TMR is split into two dips by the presence of Δε due to the shift of the molecular states as indicated in **Figure 2**. Interestingly, the magnitude of the negative TMR remains almost unchanged even if the dots' levels are different from each other. The above three figures indicate that the phenomenon of negative TMR are rather stable in this DQD structure and may provide a reliable means to detect the existence of the MBSs. It is known that the Coulomb interaction between electrons plays an important role in transport processes. At temperatures higher than Kondo one [24], the Coulomb interaction mainly induces the so-called Coulomb blockade effect [23] in mesoscopic systems, that is, the current–voltage curve will display steps corresponding to the peaks in the electrical conductance, which arises from the blockade of additional electron transport processes when the scattering regions (such as QD) are occupied by electrons. In the present article, however, we neglect the impacts of the Coulomb blockade effect in that the MBSs affect transport processes when the dots' level is aligned to the Fermi levels in the leads. The Coulomb interaction will only induce another step in the current in higher energy levels, where the impacts of MBSs are weak.

4 SUMMARY

In summary, we have studied the spin-polarized currents and TMR in a DQD coupled to both ferromagnetic leads and MBSs formed at the ends of a topological superconductor nanowire. Our calculation results show that the currents through the system can be effectively adjusted in terms of the spin polarization of either ferromagnetic leads or coupling strength between the dots and the MBSs. When the two spin polarizations are the same in sign, the currents' amplitude in the antiparallel configuration can be larger than that in the parallel one, which results in an obvious negative TMR that can be used for detecting the existence of the MBSs. If the two spin polarizations are different in sign, however, then the TMR is positive and can be further enhanced by adjusting system's parameters. Such a result is useful in designing high-efficiency spintronic devices. The negative or positive TMR is robust against variations of the overlapping between the MBSs, the tunnel coupling between the two dots, or even the difference between the dots' energy levels.

DATA AVAILABILITY STATEMENT

The original contributions presented in the study are included in the article/Supplementary Material; further inquiries can be directed to the corresponding author.

AUTHOR CONTRIBUTIONS

W-GM and L-WT contributed the ideas equally and performed the numerical calculations. L-WT derived the formulae in the paper and wrote the original manuscript.

FUNDING

This work was supported by the National Natural Science Foundation of China (Grant Nos. 11772287 and 11572277).

REFERENCES

1. Kitaev AY. Unpaired Majorana fermions in quantum wires. *Phys Usp* (2001) 44: 131–6. doi:10.1070/1063-7869/44/10S/S29
2. Fu L, Kane CL. Superconducting proximity effect and Majorana fermions at the surface of a topological insulator. *Phys Rev Lett* (2008) 100:096407. doi:10.1103/PhysRevLett.100.096407
3. Nayak C, Simon SH, Stern A, Freedman M, Sarma SD. Non-Abelian anyons and topological quantum computation. *Rev Mod Phys* (2008) 80:1083–159. doi:10.1103/RevModPhys.80.1083
4. Mourik V, Zuo K, Frolov SM, Plissard SR, Bakkers EPAM, Kouwenhoven LP. Signatures of Majorana fermions in hybrid superconductor-semiconductor nanowire devices. *Science* (2012) 336:1003–7. doi:10.1126/science.1222360
5. Finck ADK, Van Harlingen DJ, Mohseni PK, Jung K, Li X. Anomalous modulation of a zero-bias peak in a hybrid nanowire-superconductor device. *Phys Rev Lett* (2013) 110:12–22. doi:10.1103/PhysRevLett.110.126406
6. Albrecht SM, Higginbotham AP, Madsen M, Kuemmeth F, Jespersen TS, Nygård J, et al. Exponential protection of zero modes in Majorana islands. *Nature* (2016) 531:206–9. doi:10.1038/nature17162
7. Sau JD, Lutchyn RM, Tewari S, Sarma SD. Generic new platform for topological quantum computation using semiconductor heterostructures. *Phys Rev Lett* (2010) 104:4–29. doi:10.1103/PhysRevLett.104.040502
8. Oreg Y, Refael G, Oppen F. Helical liquids and Majorana bound states in quantum wires. *Phys Rev Lett* (2010) 105:17–22. doi:10.1103/PhysRevLett.105.177002
9. Zhang H, Liu CX, Gazibegovic S, Xu D, Logan JA, Wang G, et al. Quantized Majorana conductance. *Nature* (2018) 556:74–9. doi:10.1038/nature26142
10. Gül Ö, Zhang H, Bommer JDS, Moor MWA, Car D, Plissard SR, et al. Ballistic Majorana nanowire devices. *Nat Nanotechnol* (2018) 13:192–7. doi:10.1038/s41565-017-0032-8
11. San-Jose P, Prada E, Aguado R. AC Josephson effect in finite-length nanowire junctions with Majorana modes. *Phys Rev Lett* (2012) 108:257001. doi:10.1103/PhysRevLett.108.257001
12. Xu L, Li XQ, Sun QF. Majorana dc Josephson current mediated by a quantum dot. *J Phys Condens Matter* (2017) 29:195301. doi:10.1088/1361-648X/aa6661
13. Chiu CK, Das Sarma S. Fractional Josephson effect with and without Majorana zero modes. *Phys Rev B* (2019) 99:035312. doi:10.1103/PhysRevB.99.035312
14. Leijinse M. Thermoelectric signatures of a Majorana bound state coupled to a quantum dot. *New J Phys* (2014) 16:89–97. doi:10.1088/1367-2630/16/1/015029
15. López R, Lee M, Serra L, Lim JS. Thermoelectrical detection of Majorana states. *Phys Rev B* (2014) 89:205418. doi:10.1103/physrevb.89.205418
16. Hong L, Chi F, Fu ZG, Hou YF, Wang ZG, Li KM, et al. Large enhancement of thermoelectric effect by Majorana bound states coupled to a quantum dot. *J Appl Phys* (2020) 127:124302. doi:10.1063/1.5125971
17. Chi F, Fu ZG, Liu J, Li KM, Wang ZG, Zhang P. Thermoelectric effect in a quantum dot side-coupled to Majorana bound states. *Nanoscale Res Lett* (2020) 15:79. doi:10.1186/s11671-020-03307-y
18. Niu PB, Liu LX, Su XQ, Dong LJ, Shi YL, Luo HG. Spin Seebeck effect induced by a Majorana zero mode in a nanomagnet. *Phys E* (2020) 124:114313. doi:10.1016/j.physe.2020.114313
19. Lee EJH, Jiang XC, Aguado R, Katsaros G, Lieber CM, Franceschi SD. Zero-Bias anomaly in a nanowire quantum dot coupled to superconductors. *Phys Rev Lett* (2012) 109:186802. doi:10.1103/PhysRevLett.109.186802
20. Deng MT, Vaitiekėnas S, Hansen EB, Danon J, Leijnse M, Flensberg K, et al. Majorana bound state in a coupled quantum-dot hybrid-nanowire system. *Science* (2016) 354:1557–62. doi:10.1126/science.aaf3961
21. Liu DE, Baranger HU. Detecting a Majorana-fermion zero mode using a quantum dot. *Phys Rev B* (2011) 84:1–4. doi:10.1103/PhysRevB.84.201308
22. Hoffman S, Chevallier D, Loss D, Klinovaja J. Spin-dependent coupling between quantum dots and topological quantum wirs. *Phys Rev B* (2017) 96:1–18. doi:10.1103/PhysRevB.96.045440
23. Elsa P, Ramon A, Pablo S. Measuring Majorana non-locality and spin structure with a quantum dot. *Phys Rev B* (2017) 96:1–11. doi:10.1103/PhysRevB.96.085418
24. Górski G, Kucab K. The spin-dependent coupling in the hybrid quantum dot–Majorana wire system. *Phys Status Solidi B* (2019) 256:1800492. doi:10.1002/pssb.201800492
25. Leijnse M, Flensberg K. Parity qubits and poor man's Majorana bound states in double quantum dots. *Phys Rev B* (2012) 86:134528. doi:10.1103/PhysRevB.86.134528
26. Sherman D, Yodh JS, Albrecht SM, Nygård J, Krogstrup P, Marcus CM. Normal, superconducting and topological regimes of hybrid double quantum dots. *Nat Nanotechnol* (2017) 12:212–7. doi:10.1038/nnano.2016.227
27. Ivanov TI. Coherent tunneling through a double quantum dot coupled to Majorana bound states. *Phys Rev B* (2017) 96:035417. doi:10.1103/PhysRevB.96.035417
28. Barnaś J, Martinek J, Michałek G, Bułka BR, Fert A. Spin effects in ferromagnetic single electron transistors. *Phys Rev B* (2000) 62:12363–73. doi:10.1103/PhysRevB.62.12363
29. Chi F, Zeng H, Yuan X. Flux-dependent tunnel magnetoresistance in parallel-coupled double quantum dots. *Superlattice Microst* (2009) 46:523–32. doi:10.1016/j.spmi.2009.04.002
30. Stefanski P. Tunneling magnetoresistance anomalies in a Coulomb blockaded quantum dot. *Phys Rev B* (2009) 79:085312. doi:10.1103/PhysRevB.79.085312
31. Tang LW, Wei GM. Detection of Majorana bound states by sign change of the tunnel magnetoresistance in a quantum dot coupled to ferromagnetic electrodes. *Front Phys* (2020) 8:147. doi:10.3389/fphy.2020.00147
32. Hamaya K, Kitabatake M, Shibata K, Jung M, Kawamura M, Ishida S, et al. Oscillatory changes in the tunneling magnetoresistance effect in semiconductor quantum-dot spin valves. *Phys Rev B* (2008) 77:081302. doi:10.1103/PhysRevB.77.081302
33. Yang FB. Spin-polarized transport through a hybrid Majorana quantum dot system coupled ferromagnetic leads. *Phys E* (2019) 109:164–8. doi:10.1016/j.physe.2019.01.020
34. Wimmer M, Akhmerov AR, Medvedyeva MV. Majorana bound states without vortices in topological superconductors with electrostatic defects. *Phys Rev Lett* (2010) 105:046803. doi:10.1103/PhysRevLett.105.046803
35. Choy TP, Edge JM, Akhmerov AR. Majorana fermions emerging from magnetic nanoparticles on a superconductor without spin-orbit coupling. *Phys Rev B* (2011) 84:195442. doi:10.1103/PhysRevB.84.195442
36. Deng MT, Vaitiekenas S, Prada E, San-Jose P, Nygard J, Krogstrup P, et al. Nonlocality of Majorana modes in hybrid nanowires. *Phys Rev B* (2018) 98: 085125. doi:10.1103/PhysRevB.98.085125
37. Ricco LS, de Souza M, Figueira MS. Spin-dependent zero-bias peak in a hybrid nanowire-quantum dot system: distinguishing isolated Majorana fermions from Andreev bound states. *Phys Rev B* (2019) 99:155159. doi:10.1103/PhysRevB.99.155159
38. Weymann I, Barns J. Transport through two-level quantum dots weakly coupled to ferromagnetic leads. *J Phys Condens Matter* (2007) 19:1–21. doi:10.1088/0953-8984/19/9/ 096208

Conflict of Interest: The authors declare that the research was conducted in the absence of any commercial or financial relationships that could be construed as a potential conflict of interest.

frontiers in Physics

REVIEW
published: 02 February 2021
doi: 10.3389/fphy.2020.631925

A Brief Review of High Efficiency III-V Solar Cells for Space Application

J. Li, A. Aierken*, Y. Liu*, Y. Zhuang, X. Yang, J. H. Mo, R. K. Fan, Q. Y. Chen, S. Y. Zhang, Y. M. Huang and Q. Zhang

School of Energy and Environment Science, Yunnan Normal University, Kunming, China

The demands for space solar cells are continuously increasing with the rapid development of space technologies and complex space missions. The space solar cells are facing more critical challenges than before: higher conversion efficiency and better radiation resistance. Being the main power supply in spacecrafts, III-V multijunction solar cells are the main focus for space application nowadays due to their high efficiency and super radiation resistance. In multijunction solar cell structure, the key to obtaining high crystal quality and increase cell efficiency is satisfying the lattice matching and bandgap matching conditions. New materials and new structures of high efficiency multijunction solar cell structures are continuously coming out with low-cost, lightweight, flexible, and high power-to-mass ratio features in recent years. In addition to the efficiency and other properties, radiation resistance is another sole criterion for space solar cells, therefore the radiation effects of solar cells and the radiation damage mechanism have both been widely studied fields for space solar cells over the last few decades. This review briefly summarized the research progress of III-V multijunction solar cells in recent years. Different types of cell structures, research results and radiation effects of these solar cell structures under different irradiation conditions are presented. Two main solar cell radiation damage evaluation models—the equivalent fluence method and displacement damage dose method—are introduced.

Keywords: III-V solar cells, multijunction, high efficiency, radaition resistance, degradation

Edited by:
Feng Chi,
University of Electronic Science and Technology of China, China

Reviewed by:
Changsi Peng,
Soochow University, China
Xingji Li,
Harbin Institute of Technology, China

***Correspondence:**
A. Aierken
erkin@ynnu.edu.cn
Y. Liu
542110131@qq.com

Specialty section:
This article was submitted to Optics and Photonics, a section of the journal Frontiers in Physics

Received: 21 November 2020
Accepted: 21 December 2020
Published: 02 February 2021

Citation:
Li J, Aierken A, Liu Y, Zhuang Y, Yang X, Mo J H, Fan RK, Chen QY, Zhang SY, Huang YM and Zhang Q (2021) A Brief Review of High Efficiency III-V Solar Cells for Space Application. Front. Phys. 8:631925. doi: 10.3389/fphy.2020.631925

INTRODUCTION

Space solar cells, being the most important energy supply unit, have been employed in spacecrafts and satellites for over sixty years since the first satellite was launched in 1958 [1]. It has been developed from the initial single junction low efficiency silicon solar cells [2] to the now high efficiency multi-junction III-V compound multi-junction solar cells [3]. The main objectives of space solar cell development are directed toward to improving the conversion efficiency and reducing the mass power ratio and increase the radiation hardness [4–7]. At present, the highest conversion efficiency of solar cells is 47.1% achieved by six-junction inverted metamorphic (6 J IMM) solar cells under 143 suns [8]. The high-efficiency III-V triple-junction cells are also becoming the mainstream of space solar cells. The best research-grade multi-junction space solar cell efficiency so far is 35.8% for five-junction direct bonded solar cell and 33.7% for the monolithically grown 6 J IMM multi-junction solar cell [9, 10]. Despite the high fabrication cost, they offer excellent performance and reliable stability for space missions [11–13]. GaInP/GaAs/Ge (1.82/1.42/0.67 eV) lattice-matched triple-junction cells are well established with efficiencies of over 30% and fulfilled many space applications in the past two decades. However, the current mismatch between its subcells makes it difficult to improve the conversion efficiency further [14]. New structures of current matched or lattice mismatched solar cell structures and different fabrication methods are proposed to overcome this problem, such as the metamorphic (MM) growth method [15], mechanical stack [16], wafer bonding technology [17], etc.

While improving the efficiency of space solar cells, the radiation resistance should also be considered. In-orbit solar cells suffer from irradiation damages due to high energy protons and electrons in the earth's radiation belt and cosmic rays [18, 19], and consequently, the photoelectric performance of solar cells will be degraded. The main reason of the degradation of solar cell performance is due to the radiation-induced displacement damage in the solar cell lattice, resulting in a decrease in the lifetime of the photo-generated carriers [20–22]. Therefore, the degradation mechanism and performance of solar cells under an irradiation environment must be explored, and it is necessary to apply radiation hardening methods before the space mission starts. The degradation of electrical performance in solar cells directly affects the life-time of space missions. The researchers aimed at improving the radiation resistance of solar cells by adding a certain thickness of protective cover to the solar cell to shield the damage of certain particles [23], using back-surface (BSF) [24] or distributed Bragg reflector (DBR) [25], and thinning the base layer thickness of the current-limiting subcell [26], or using the p-i-n structure and different doping methods for multi-junction solar cells [27]. The experimental observations show that annealing of the multi-junction solar cell can restore certain electrical properties after being radiated by high-energy particles [28].

In recent years, various new types of multi-junction solar cells with different combinations of materials have been developed by different research groups, and the expectations for future development are different. Solar cell conversion efficiencies are rapidly being updated, and scientists are still struggling to come up with solar cells which have high conversion efficiency and possess good radiation resistance. Although there are several reviews available which cover the manufacturing, efficiency, and application prospects of photovoltaic modules [29, 30], the new types of high efficiency space solar cells based on III-V compound materials have not been summarized yet. This review attempts to give a brief review on different types of space solar cells and emphasize the high energy particle irradiation effects of solar cells and recent results on the most promising types of solar cells, including dilute nitride, metamorphic, mechanical stack, and wafer bonding multi-junction solar cells.

DIFFERENT TYPES OF HIGH-EFFICIENCY SOLAR CELLS

With the improvement of the manufacturing process and deposition technology of materials, the solar cells industry has developed tremendously. Solar cell materials are developed from a single material (single crystal Si, single-junction GaAs, CdTe, CuInGaSe, and amorphous Si:H) to compound materials, such as III-V multi-junction solar cells, perovskite cells, dye-sensitized cells, organic cells, inorganic cells, and quantum dot cells [31–33]. The structure of solar cells also forms homogeneous junction cell to heterogeneous junction solar cell, Schottky junction solar cell, compound junction solar cell, and liquid junction solar cell. In the purpose of its usage, it has also been developed from flat cells to concentrator cells and flexible cells [34, 35].

The silicon solar cells were used as the first choice in the spacecraft since the first solar-powered satellite was launched in 1958. The Soviet Space station, MIR, was launched in 1986, was equipped with 10 kW GaAs solar cells, and the power per unit area reached 180 W/m^2 [36]. Then, the fabrication technique of GaAs-based cells experienced changes from Liquid Phase Epitaxy (LPE) to metal organic vapor phase epitaxy (MOVPE), from homogeneous epitaxy to heterogeneous epitaxy, from single junction to multi-junction structure [37–39]. Notably, their efficiency was continuously improved from the initial 16–25%, and over 100 kW industrial-scale power output per year has been reached [40]. Higher efficiency reduces the size and weight of the array, increases the payload of the spacecraft and results in lower costs for the entire satellite power system. Therefore, GaAs-based solar cells are widely used in space systems and continue to be used today [41–43]. Comparing with silicon solar cells, GaAs solar cells have the following advantages [42]:

(1) Higher photoelectric conversion efficiency.
(2) Direct-gap semiconductor materials.
(3) The band-gap tailoring by controlling the composition and doping of material.
(4) Superior radiation resistance.

However, the processes involved in GaAs solar cell fabrication are complicated, and its cost is much higher than that of silicon solar cells owing to the expensive equipment and material preparation. Therefore, GaAs solar cells cannot be widely utilized in the civil market. Nevertheless, GaAs solar cells have gradually replaced silicon solar cells in the aerospace field, where higher cell efficiency and better radiation resistance are needed.

The loss in the efficiency of solar cells can be divided into two parts: the unabsorbed loss and excessive energy loss. When the photon interacts with the semiconductor materials, where the photon energy is smaller than the bandgap width, the valence band electrons are not excited, and they do not generate an electron-hole pair to form an electrical current. However, when the photon energy is greater than the gap width, the excess energy is lost in the form of phonons or heat [44]. Fortunately, multi-junction solar cells successfully solved this problem. Semiconductor materials with different band-gaps are composed from top to bottom from large to small band-gaps, and the higher energy photons are absorbed by the top large band-gap material. The lower energy photons go through the upper large band-gap material and reach the appropriate band-gap width to generate power. Therefore, for multi-junction solar cells, finding a current matching and lattice matching cell material is the critical and general focus [14, 45]. The following sections present a brief introduction of different types of multijunction solar cells in terms of their performance.

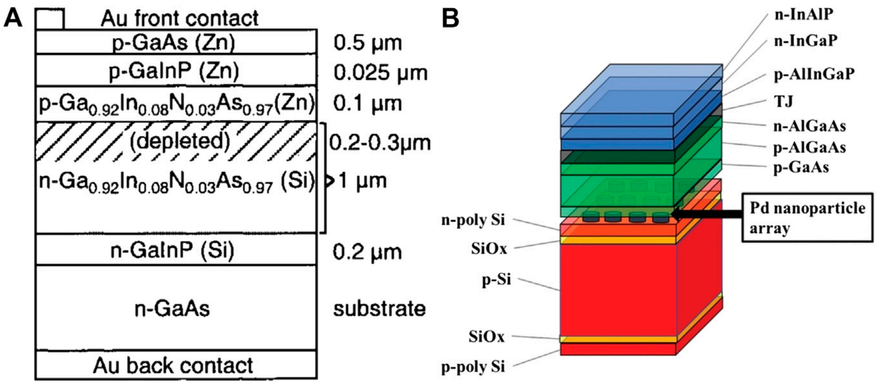

FIGURE 1 | (A) The structure of GaInNAs device grown by MOVPE with dimethylhydrazine as the nitrogen source [50]; **(B)** The structure of InGaP/AlGaAs//Si triple-junction solar cell [67].

TABLE 1 | The parameters of GaInAsN solar cell after 1 MeV electron irradiation [51].

Fluence	V_{oc} (%)	FF (%)	J_{sc} (%)	Power (%)
5×10^{14}	97.7 ± 1	98.6 ± 1	97 ± 3	93 ± 3
1×10^{15}	96.2 ± 1	97.8 ± 1	95 ± 4	89 ± 4

Lattice Matched GaInNAs Multi-Junction Solar Cell

In 1996, Kondow et al. demonstrated the epitaxial growth of 1.0 eV band gap GaInNAs material with lattice matching to GaAs substrate, and applied it to fabricating infrared laser [46]. Since then diluted nitride GaInNAs materials have been widely used in heterojunction bipolar transistors (HBTs) [47] and lasers [48], where GaInNAs HBTs base layer can reduce the open voltage and run under low working voltage. These features of diluted nitride GaInNAs materials are also useful in wireless communications and power amplifier applications. GaInAsN is a direct band-gap semiconductor material, which can change its band-gap by adjusting the component content of nitrogen and indium while keeping its lattice constant matching to conventional substrate materials such as GaAs and Ge. These advantages bring great potential for using 1.0 eV subcell in a high efficiency multijunction solar cell [49].

The $Ga_{1-x}In_xN_yAs_{1-y}$ is used as a sub-cell material for GaInP/GaAs/GaInNAs/Ge four-junction solar cell by NREL [50]. When y = 0.3x, the lattice constant of $Ga_{1-x}In_xN_yAs_{1-y}$ matches GaAs and Ge, which is an ideal material to construct a GaInP/GaAs/GaInNAs/Ge (1.88/1.42/1.05/0.67 eV) four-junction solar cell with band-gap matching. **Figure 1A** shows the representative GaInNAs devices structure grown by MOVPE. The device is grown with dimethylhydrazine (DMHy) as the nitrogen source. At the same time, the experimental results showed that the remaining factor of GalnAsN cell efficiency is 0.93 and 0.89 after 5×10^{14} and 1×10^{15} e/cm^2 electron fluence of 1 MeV electrons irradiation, respectively [51]. The specific degradation of the device parameters is summarized in **Table 1**. The results showed that this type of cell structure possesses superior radiation resistance comparing to the traditional lattice matched multi-junction solar cell.

However, difficulties in epitaxial growth of diluted nitride materials have prevented its further development. It is also found that the diffusion length of minority carriers is short, the internal quantum efficiency is low for the GaInNAs subcell, and these poor minority carrier transmission characteristics resulted in lower current and voltage. Since the current of a multi-junction solar cell is determined by the smallest sub-cell, the low current in GaInNAs subcell has a significant impact on the overall cell performance [51]. The quality of GaInNAs solar cells was improved by fabrication of p-i-n structure cells [52], annealing [53], doping Sb in GaInNAs material [54], and changing substrate epitaxial orientation [55]. Miyashita et al. demonstrated a solar cell with p-i-n (*p*-GaAs/i-GaInAsN (Sb)/n-GaAs) structure, and tested the cell under the AM1.5 spectrum. The short-circuit current density (J_{sc}) reached 21.5 mA/cm^2, the open-circuit voltage (V_{oc}) reached 0.42 V, and the filling factor (*FF*) reached 0.71 [56]. They further optimized the content of Sb and found that the content of Sb was less than 1%, which is more beneficial to improve GaInAsN crystal quality and device performance [57]. Han et al. found that GaAsN material grown by (311) B substrate epitaxy could not only improve the incorporation efficiency of nitrogen, but also effectively enhance the carrier lifetime of the material [58]. Although the theoretical conversion efficiency of GaInNAs multijunction solar cell could reach 41%, the actual growth problem still needs to be overcome, which needs to be focused on as a development goal in the future.

Mechanically Stacked Solar Cell

According to the theoretical calculation, the optimum bandgap energy for top and bottom subcell for a tandem multijunction solar cell is 1.65–1.8 eV and 1.0–1.5 eV, respectively, and the conversion efficiency of this structure reaches 32.5% under 1-sun AM0 spectrum [59]. Typically, the III-V compound material based multijunction solar cells are fabricated by MOVPE or molecular beam epitaxy (MBE) techniques, where the lattice matching and energy matching between subcells is a critical

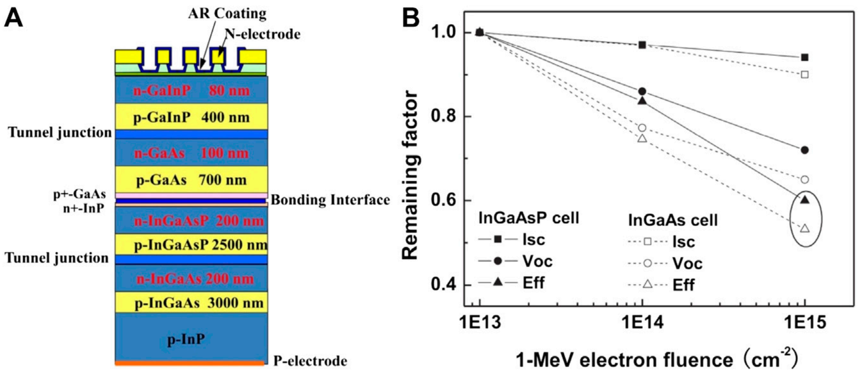

FIGURE 2 | (A) Schematic structure of wafer-bonded GaInP/GaAs//InGaAsP/InGaAs four junction solar cell; **(B)** the remaining factors of InGaAs and InGaAsP single-junction solar cells as a function of 1 MeV electron irradiation fluence **(B)** [71].

problem. The presence of mechanical stacks makes this feasible and allows to use of lattice- and current-mismatched combinations of semiconductor materials. By using the mechanical stacking method, III-V compound materials can be stacked together regardless of their bandgap energy and lattice constants. This technique can reduce the production cost significantly, and the substrate removal process greatly reduces the weight of solar cells, which is useful if used in space solar cell applications [60–62].

Still, the utilization of multiple substrates requires the removal of substrates, thereby, it makes the solar cell fabrication process complicated and affects the interface quality [63]. At the same time, a complicated design requirement becomes an obstacle for large-scale applications of mechanical stacked solar cells in space [64]. Since each subcell in a multi-junction solar cell consists of a p-n junction, if individual subcells directly stacked together in series, it will form a reverse p-n junction between subcells which block the current flow. Therefore, interconnecting individually processed solar cells keeping both electrical and optical properties still is a technical challenge need to consider with high conductivity and low transmission loss [65]. This problem can be solved by adding a tunnel junction between the subcells [66]. The 30% conversion efficiency of III-V//Si multi-junction solar cells using smart stack technology have been reported [67]. A schematic diagram of InGaP/AlGaAs//Si triple-junction solar cell is shown in **Figure 1B**. A "smart stack," "areal current matching," and "solar concentration" two-terminal GaAs/Si tandem solar cell, having potential to achieve an efficiency of approximately 30%, are proposed and the indoor experiment proves its feasibility, although the experiment result is lower than the simulation [64]. These types of mechanical stacking processes are quite flexible and allow different cells to be combined, and consequently reduces the fabrication cost and increases the cell efficiency.

Wafer Bonded Multijunction Solar Cell

In multi-junction solar cells, the lattice dislocations induced by the lattice mismatch during the epitaxial growth reduce the material quality and deteriorates the device performance. The wafer bonding technique, which refers to the physical integration of the two different materials, overcomes this issue very well and allows the formation of a monolithic multijunction solar cell structure without both electrical and optical losses, regardless of the different lattice constant of subcells [68]. As early as 1986, Lasky et al. demonstrated surface treated silicon wafer bonding at room temperature and obtained very good bonding strength through high-temperature annealing [69]. The freedom of material selection in the process of semiconductor device design is greatly improved because the bonding technology can realize the lamination structure of materials with different thermal expansion coefficient and lattice constant, and can limit the dislocation and defect to the area near the bonding interface. **Figure 2A** shows the structure of GaInP/GaAs//InGaAsP/InGaAs wafer-bonded four junction solar consists of GaInP/GaAs and InGaAsP/InGaAs dual junction cells, whereas **Figure 2B** shows the degradation of InGaAsP and InGaAs subcell electrical properties under 1 MeV electron irradiation. The result shows that the bonding interface has no effects on overall cell performance and radiation resistance, the main degradation happened in the third and fourth subcell, and InGaAsP subcell has a superior radiation resistance than InGaAs cell owing to In-P bonds [70].

At present, the wafer bonding technology has been studied extensively and widely used in the structural design and integration field of microelectronics and optoelectronics. A variety of bonding methods have been developed, however, they can be mainly divided into two categories: direct bonding and intermediate-layer bonding [71]. The direct wafer bonding process includes cleaning and activating two polished wafers and sticking them together at room temperature. Heterogeneous integration of multi-junction solar cells has to meet three stringent conditions: good mechanical strength at the bonding interface, high optical transmittance, and low resistivity. It does not work without each condition being met. Intermediate-layer bonding technology introduces a layer with good ductility and adhesion to alleviate stress and improve the bonding interface [72]. GaInP/GaAs//GaInAsP/GaInAs four-junction wafer-bonded concentrator solar cells with an efficiency of 46% at 508 suns have been reported [73]. It demonstrates that the wafer bonding is a feasible method to combine lattice mismatched

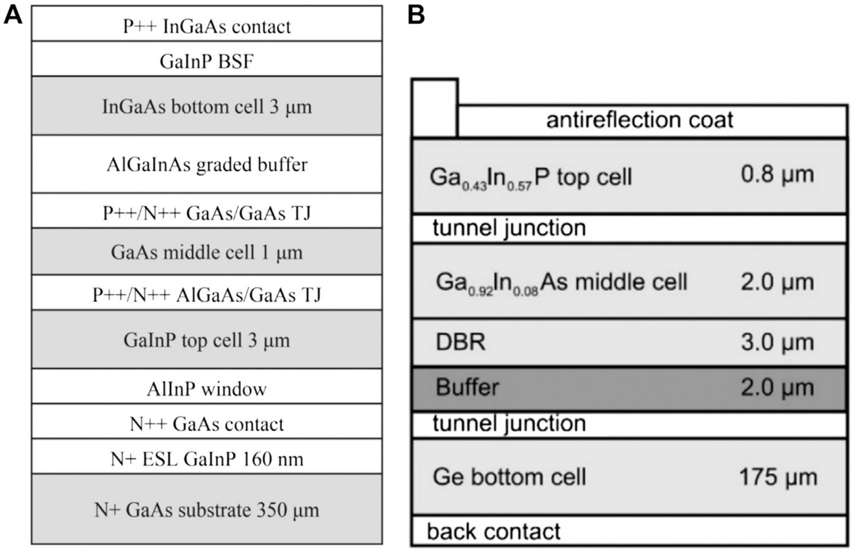

FIGURE 3 | Schematic structure of **(A)** GaInP/GaAs/InGaAs IMM solar cell, and **(B)** GaInP/InGaAs/Ge UMM solar cell [78].

different III-V compound materials and realize high efficiency multijunction solar cell structure. The main challenge of wafer bonding technology is the preparation of the bonding surface which should have a low surface roughness to ensure high electrical conductivity.

Inverted Metamorphic and Upright Metamorphic Solar Cells

Another approach of solving current matching issue in multijunction solar cell is the metamorphic growth method, which involves applying a compositionally graded buffer (CGB) layer between the lattice mismatched subcells [74]. The main purpose of using a CGB layer is to distribute the strain relaxation layers into a lattice constants gradually changed thick buffer layer instead of growing a highly lattice mismatched layer onto its under layer [75]. According to the growth method, the metamorphic growth technique can be divided into two types: IMM [76] and upright metamorphic (UMM) [77]. In the IMM method, for example GaInP/GaAs/InGaAs triple junction solar cell, a CGB layer is inserted between the GaAs and InGaAs subcells and the growth direction of solar cell epilayers is in the inverse direction, in order to delay the strain relaxation in CBG layer at the later stages of growth process. However, the IMM method requires an additional step of substrate lift-off before solar cell device fabrication processes. On the other hand, in the UMM method, the growth direction is from bottom subcell to top subcell, so it requires an even higher quality CBG layer to control the strain relaxation. **Figures 3A,B** show the general structure of IMM and UMM cells, respectively.

Comparing to traditional lattice matched (LM) solar cells, metamorphic multijunction solar cells are aiming to achieve current matching between its subcells and expected to have higher conversion efficiency. Experimentally, NREL has shown that IMM solar cells have a conversion efficiency of 40.8% for triple-junction solar cells at high concentration [15] and 47.1% efficiency for 6 J solar cells at 143 suns concentration [8]. Furthermore, IMM cell can reduce the cell weight by removing the substrate and increase the mass power ratio. IMM cells also can be utilized to develop flexible solar cells for any non-flat surfaces. These high efficiency, flexible, and lightweight properties of IMM multi-junction solar cells make them the most promising for space applications [[14, 78, 79]]. For UMM multijunction solar cell, the conversion efficiency exceeded 31% under one Sun AM0 spectrum compared to traditional lattice matched solar cell conversion efficiency is limited to 30% [80]. The critical point of increasing UMM solar cells is improving the quality of CGB layer to suppress lattice dislocation and threading dislocations induced by strain relaxation. However, the fabrication process of UMM solar cells is similar to the matured fabrication technology of LM cells, therefore, this advantage makes the UMM multi-junction solar cell utilization possible for potential applications [77].

The reported experimental efficiency, theoretical limits, and their advantages of all above mentioned solar cells in *Lattice Matched GaInNAs Multi-Junction Solar Cells, Mechanically Stacked Solar Cells, and Wafer Bonded Multijunction Solar Cells* are presented in **Table 2**. According to the Shockley-Queisser balance model, the theoretical efficiency limit of single-junction, triple-junction, and four-junction solar cells are 33.5%, 56% and 62%, respectively [85]. Along with the rapid development of new materials and high quality fabrication technologies, all these solar cells could achieve higher efficiency and better performance. Furthermore, UMM and IMM solar cell efficiencies tend to surpass LM cells even more as their manufacturing technology continues to be innovated and developed, and they are expected to become the next generation space solar cells.

TABLE 2 | Comparison of the conversion efficiency of various types of solar cells have been reported.

Classification	Experimental efficiency (%)	Theoretical limit efficiency (%)	Technical advantages
Si	26.7 ref. 81	33.5	Mature technology, rich output
GaAs	29.1 ref. 82	33.5	High temperature, better resistance, mature technology
GaInP/GaAs/GaInNAs/Ge	27.4 ref. 50	62.0	Band-gap matching, superior radiation resistance
InGaN	3.4 ref. 83	33.5	Adjustable band-gap
GaInP/GaAs/Ge (LM)	30 ref. 80	56.0	Lattice matching, mature technology
GaInP/InGaAs/Ge (UMM)	31.7 ref. 84	56.0	Band-gap matching, fabrication process is similar to LM solar cell
InGaP/GaAs/InGaAs (IMM)	33.7 ref. 9	56.0	Band-gap matching, lightweight

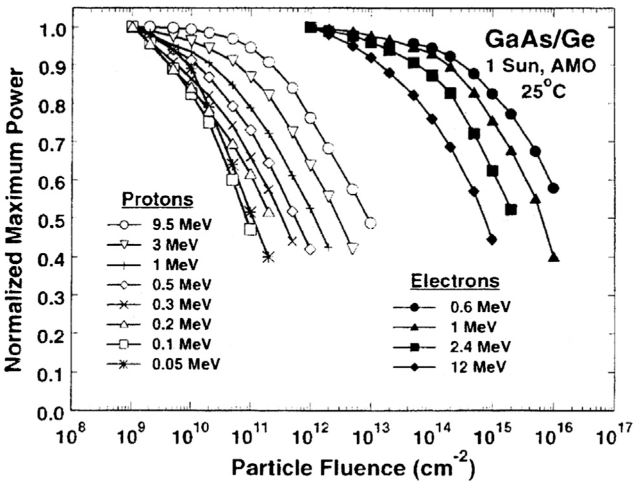

FIGURE 4 | Normalized $P_{\max}$ degradation of GaAs/Ge solar cells irradiated by electrons and protons of different energy and with different particle fluence [88].

STUDIES ON RADIATION EFFECTS OF SOLAR CELLS

The solar cell arrays in a spacecraft are exposed to a harsh space environment during its mission. Therefore, radiation resistance is also a critical index to evaluate the quality of space solar cells. The main reason for the performance deterioration of space solar cells is the irradiation of high-energy particles, that include electrons (energy up to 10 MeV) and protons (energy up to several hundred MeV) from the earth's radiation belt, as well as solar cosmic rays (energy up to GeV) [86]. When these high-energy particles collided with the cell materials, the transmitted energies cause the lattice atoms to shift their original positions and form displacement damages, and, consequently, the diffusion length of minority carriers decreases and the performance of solar cells is degraded [87]. Therefore, only solar cells with high conversion efficiency and good radiation resistance could be employed as space solar cells.

Radiation Effects of Double-Junction GaAs/Ge Solar Cell

Messenger et al. investigated the electron and proton irradiation effects of double-junction GaAs/Ge solar cell with different energies [88]. The cell performance is degraded with an increase of the particle fluence under both electron and proton irradiation, as shown in **Figure 4**. Additionally, electron irradiation with greater incident energy resulted in more severe deterioration of cell performance for the same irradiation fluence. For proton irradiation, on the other hand, low energy protons produced a bigger reduction in cell performance when the proton energy is in the range of 0.2–9.5 MeV. Proton irradiation experiments on GaInP/GaAs/Ge, GaAs/Ge solar cells with proton energy of less than 200 KeV are reported and it was found that the low energy particle irradiation caused defects in different subcells and different regions in the tandem multi-junction solar cell [23, 89].

The radiation-induced defects in the base and the emitter layers form non-radiative recombination centers and capture photo-generated electron-hole pairs before they are collected by the junction region, and eventually reduce the short circuit current. On the other hand, the radiation-induced damages in the junction region mainly cause the degradation of open circuit voltage by introducing deep energy levels into the band gap and accelerating the recombination of valence band holes and conduction band electrons [89].

The effects of 40, 100, 170 keV energy proton irradiation on GaAs/Ge cells with different fluences were discussed, the degradation of spectral response results indicated that the largest damages are caused by 170 keV protons, and the lowest by 40 keV protons, in the long wavelength range (720–900 nm). The degradation effect on the normalized maximum power ($P_{\max}$) is the largest for the 170 keV protons and lowest for 100 keV protons because irradiation with 170 keV protons produces the most severe damage in the junction region of the cells. The short circuit current decreases with increasing proton energy under the energies of 40–170 keV proton irradiation and the degradation extent of V_{oc} is the largest for 170 keV proton because they produce defects with deep energy levels in the space charge region, accelerating the recombination of electrons and holes, which is also the reason for the significant decline in $P_{\max}$ for solar cell [23].

Radiation Effects of Lattice Matched GaInP/GaAs/Ge Triple-Junction Solar Cell

Sharps et al. investigated the electron and proton radiation effects of GaInP/GaAs/Ge solar cells with different energies [91]. Same as that of GaAs/Ge double-junction solar cell, the $P_{\max}$ of solar

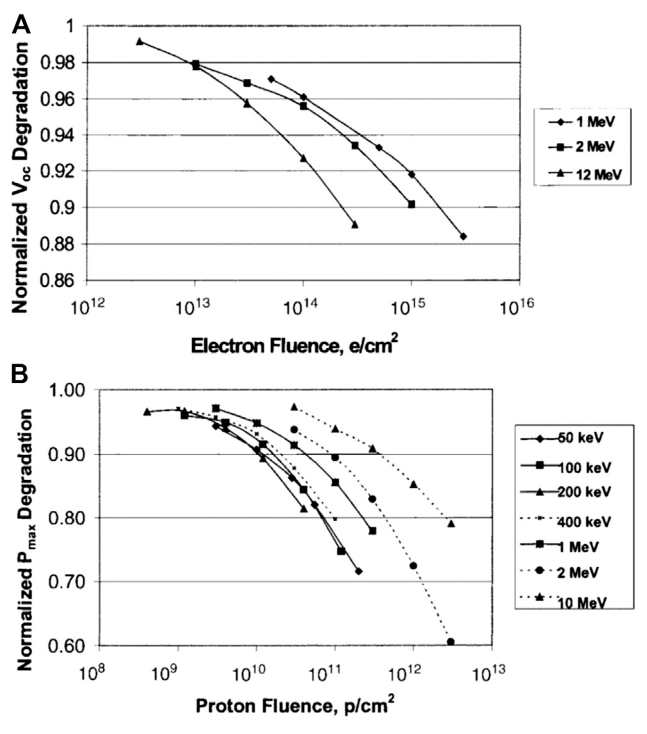

FIGURE 5 | The normalized P_{max} degradation of lattice-matched GaInP/GaAs/Ge solar cells under different **(A)** electrons and **(B)** protons irradiation with different particle fluence [91].

cells declined with the increase of the particle fluence for the same energy. For 1–12 MeV electron irradiation, the degradation of cell performance is severer for higher energy electrons for same irradiation fluence, as shown in **Figure 5A**. The degradation of P_{max} is 9 and 13% for 1 MeV electrons at fluences of 5×10^{14} and 1×10^{15} e/cm^2. However, for proton irradiation, the degradation of cell performance is bigger for lower energy protons in the energy range of 50–200 keV, as shown in **Figure 5B**. The main reason for this is that less relative damage occurs for energies below 200 keV, and lower energies would have more of an effect on the emitter as compared with the base region. At the same time, GaInP top cell and GaAs middle cell current matching point was studied in more detail by quantum efficiency measurements. It was found that the crossover from GaInP current-limited subcell to GaAs current-limited subcell occurs at 2×10^{15} e/cm^2 for the 1 MeV electrons [90]. This result indicated that advanced triple junction solar cells with current matching at end of life (EOL) can be achieved by reducing the amount of beginning of life (BOL) current mismatch, which is helpful for designing high efficiency radiation hardened space solar cells.

Wang et al. investigated the electron irradiation effects of GaInP/GaAs/Ge solar cell with 1.0–11.5 MeV energy electron beams [91]. The degradation of normalized P_{max} of GaInP/GaAs/Ge solar cell under different fluence of electron irradiation is shown in **Figure 6A**, whereas the degradation of external quantum efficiency (EQE) changes irradiated with 1.8 MeV electron beam with different fluences are shown in **Figure 6B**. The degradation effects of electron irradiation of the P_{max} and the EQE of LM solar cells increase with the increase of irradiation fluences and electron energy, as observed in GaAs/Ge double-junction cell. **Figure 6C** exhibits that the EQE of GaAs middle cell degrades more than GaInP top cell under same irradiation fluence which is indicating the radiation resistance of GaInP/GaAs/Ge triple-junction cells is dominated by the GaAs middle cell.

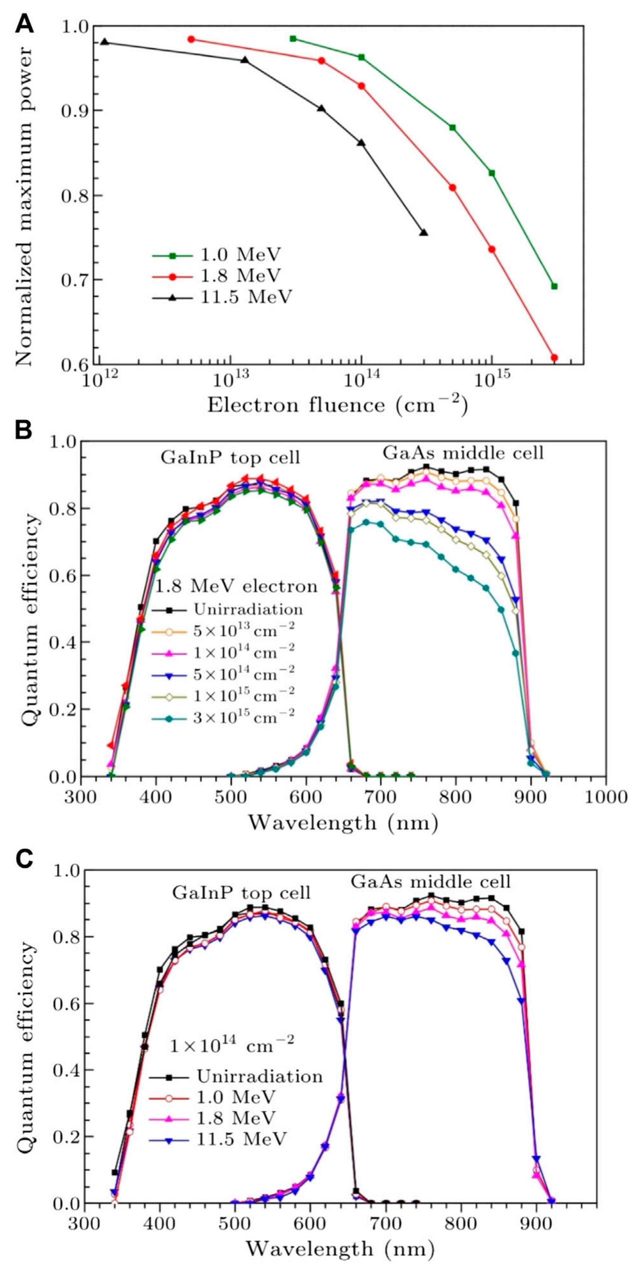

FIGURE 6 | (A) The normalized P_{max} degradation of GaInP/GaAs/Ge solar cell under different energy electron irradiation with different particle fluence; **(B)** The degradation of EQE with 1.8 MeV electron irradiation and **(C)** with different energy electrons with a particle of 1×10^{14}cm^{-2} [92].

TABLE 3 | Changes of electrical parameters of IMM GaInP/GaAs/InGaAs triple-junction solar cell under 1 MeV electron irradiation [92].

Cell type	Fluence (e/cm^2)	Voc (mV)	Jsc (mA/cm^2)	FF	Eff (%)	Remaining factor of eff (%)
GaInP/GaAs/InGaAs (higher efficiency at BOL)	0	3055.2	68.2	0.842	31.2	-
	1E15	2728.3	65.7	0.823	26.2	84.1
	3E15	2651.9	64.3	0.772	23.4	75.1
GaInP/GaAs/InGaAs (higher efficiency at EOL)	0	3058.3	67.3	0.838	30.6	-
	1E15	2709.6	66.4	0.831	26.5	86.7
	3E15	2602.8	66.3	0.794	24.3	79.5

Radiation Effects of Metamorphic GaInP/GaAs/InGaAs Triple-Junction Solar Cell

By taking advantages of bandgap tailoring in III-V compound materials and using a CGB layer, IMM multijunction solar cells can be adjusted to its output parameters suitable for BOL or EOL requirements. Takamoto et al. studied the radiation effects of these two types of IMM GaInP/GaAs/InGaAs space solar cells under 1 MeV electron irradiation, where the electrical parameters of both types solar cells declined with the increase of electron irradiation fluence [92]. In this study, the electrical parameters V_{oc}, I_{sc} (short-circuit current) and η decayed o 89.3%, 96.3%, 84.1% and 88.6%, 98.6%, and 79.5% of its original values for one group of cells have higher efficiency at BOL and another group of cells have higher efficiency at EOL, respectively, when the electron irradiation fluence reaches $1 \times 10^{15}\,\mathrm{cm}^{-2}$. These details of degradation of electrical parameters of these two types of cells are summarized in **Table 3**.

Imaizumi et al. studied the radiation response of $In_{0.5}Ga_{0.5}P$, GaAs, $In_{0.2}Ga_{0.8}As$, and $In_{0.3}Ga_{0.7}As$ single-junction solar cells, whose materials are also used as component subcells of inverted metamorphic triple-junction solar cells, and results show that the photo-generation current in the InGaAs bottom subcell of InGaP/GaAs/InGaAs IMM3J cells was severely damaged under the electron and proton radiation, which can be attributed to the stronger decrease of minority-carrier diffusion length in InGaAs compared with that in InGaP and GaAs subcells after irradiation [93]. By comparing the irradiation resistance of two InGaAs cells ($In_{0.2}Ga_{0.8}As$ and $In_{0.3}Ga_{0.7}As$ cells), GaAs and InGaP cells, it was found that radiation resistance of these two InGaAs cells is approximately equivalent to InGaP and GaAs cells from the initial material qualities. However, the InGaAs cells show lower radiation resistance especially for the I_{sc} comparing to InGaP and GaAs cells due to the bigger decrease of minority-carrier diffusion length in InGaAs materials. And the InGaP and two InGaAs cells exhibited equivalent radiation resistance of V_{oc}, but with different degradation mechanisms.

Zhang et al. investigated the 1 MeV electron radiation effects of IMM GaInP/GaAs/InGaAs solar cells by electrical properties, spectral response, and photoluminescence (PL) signal amplitude analysis [94]. The results show that the electrical parameters of IMM solar cell decrease continuously with an increase in the electron fluence same as traditional LM GaInP/GaAs/Ge solar cells. As shown in **Figure 7**, $P_{\max}$ illustrates the maximum degradation compared to V_{oc} and I_{sc}, and, V_{oc} is degraded more compared to I_{sc}. This phenomenon is explained as V_{oc} is the sum of three series sub-cell voltages, where the I_{sc} is the smallest current produced in three series sub-cells. The $In_{0.3}Ga_{0.7}As$ bottom subcell exhibited most severe damage in the irradiated IMM triple junction cells due to the drastic degradation of the effective minority carrier lifetime (τ_{eff}) of $In_{0.3}Ga_{0.7}As$ subcell than that of GaAs subcell. Therefore, the radiation hardness of IMM GaInP/GaAs/InGaAs solar cell is mainly determined by the InGaAs subcell.

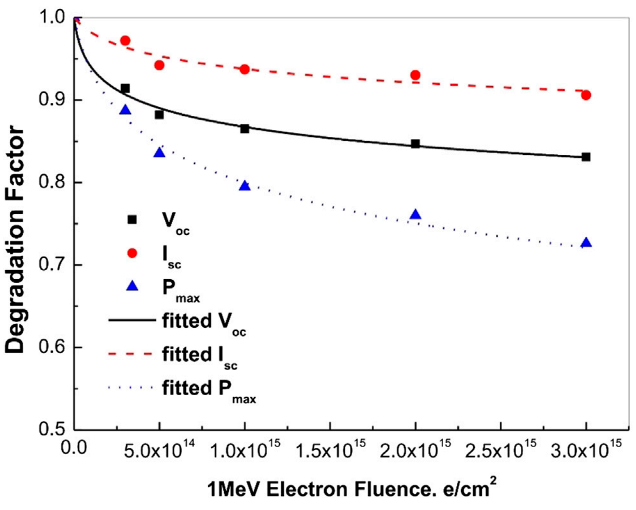

FIGURE 7 | The degradation of electrical parameters of GaInP/GaAs/InGaAs solar cell under 1 MeV electron irradiation with different particle fluence [95].

RADIATION DAMAGE EVALUATION OF SPACE SOLAR CELLS

To obtain better radiation hardened performance, it is essential to explore the radiation damage mechanism of the solar cells. The interaction of high energy charged particles in irradiation environment with the solar cell materials includes ionization and non-ionization (displacement damage) processes [95]. The displacement damage effect is the main reason for the degradation of solar cell performance. It is an effective method to explain the formation, distribution, and evolution of displacement defects after irradiation by different high-energy particles. To examine the electrical characteristics of solar cells, I-V test, spectral response test, dark characteristic test and photofluorescence intensity test are used. Whereas, to study the displacement defects of multi-junction solar cells, deep level transient spectrum, photofluorescence spectrum, electrofluorescence spectrum and spectral response are employed.

At present, for space solar cells, two assessment methods for evaluating radiation damages of solar cells are available, which are through ground irradiation simulation experiments: equivalent fluence method and equivalent displacement damage method [88]. Both methods are used to study the radiation damage effect and to reveal the degradation mechanism of solar cells. They also provide theoretical guidance and an experimental basis for scientifically predicting the on-orbit behavior of solar cells.

The Equivalent Fluence Method

The equivalent fluence method was proposed by Tada et al. from Jet Propulsion Laboratory, California Institute of Technology [96, 97]. The key point of this approach is the corresponding relative damage coefficient, which is related to the radiation damage effects caused by different types of charged particles with a different energy to relative damage coefficients.

In the first step, the critical fluence (ϕ) of electron or proton irradiation, which is corresponding to the electrical properties of the solar cell degraded to a specified level of its original value (such as 75% of I_{sc0}, V_{oc0}, $P_{\max 0}$), has to be determined according to the experimental results [98]. Then, the relative damage coefficient (RDC) of different energy electron and proton regarding 1 MeV electron and 10 MeV proton is calculated. The ratio of the critical fluence for 1 MeV electrons to the critical fluence for other electron energies is taken as a measure of the RDC of electrons, and similarly, the relative damage coefficients of different proton energies are normalized regarding the 10 MeV proton critical fluence for RDC of protons, as shown in the following equations [88]:

$$\mathrm{RDC}_{x\to 1} = \frac{\phi_e(xMeV)}{\phi_e(1MeV)} \tag{1}$$

$$\mathrm{RDC}_{x\to 10} = \frac{\phi_p(xMeV)}{\phi_p(10MeV)} \tag{2}$$

where ϕ_e and ϕ_p are the critical fluence for electrons and protons.

The next step is using the orbital environment parameters to calculate the corresponding relative damage coefficients for omnidirectional particles on bare cells from the measured values for normally incident particles. By substituting the electron and proton environment parameters under consideration into following integration equations, one can obtain the equivalent 1 MeV electron fluence for the mission in question.

$$\phi_{\mathrm{1MeV,electron,electrons}} = \int \frac{d\phi_e(E)}{dE} D_e(E)dE \tag{3}$$

$$\phi_{\mathrm{1MeV,electron,protons}} = D_{pe}\int \frac{d\phi_p(E)}{dE} D_p(E)dE \tag{4}$$

where $\phi_e(E)$ and $\phi_p(E)$ is the particle fluence of electron and proton, respectively at energy E. $D_e(E)$ and $D_p(E)$ are the relative damage coefficient of electron and proton, respectively. D_{pe} is the proton to electron damage equivalency ratio, which converts 10 MeV proton fluence to an equivalent 1 MeV electron fluence. The calculation result of **Eqs. 3, 4** are the 1 MeV electron fluence normally incident on solar cells that will cause same damage as the selected omnidirectional spectrum. The result of calculated relative damage coefficient for omnidirectional proton irradiation and electron irradiation of GaAs/Ge solar cells are shown in **Figures 8A,B**.

In the equivalent fluence method, it requires a sufficient measurement of data to calculate the RDC and generate a detailed degradation curve, as shown **Figure 4**, which shows eight proton energies (0.05, 0.1, 0.2, 0.3, 0.5, 1.3, and 9.5 MeV) and four electron energies (0.6, 2.4, and 12 MeV). Another relatively simple way of predicting the degradation of a solar cell performance regarding a given electron or proton fluence is using a semi-empirical equation [99]:

$$\frac{P_\phi}{P_0} = 1 - C\cdot\ln\left(1+\frac{\phi}{\phi_x}\right) \tag{5}$$

where P_0 and P_ϕ are the output power (also can be replaced with I_{sc} and V_{oc}) of the solar cell before and after irradiation with different irradiation fluences ϕ, respectively. C and ϕ_x are the fitting parameters for the same structure solar cell using a large amount of experimental data upon specific irradiation particles.

The Displacement Damage Dose Method

The displacement damage dose method was initiated by Naval Research Laboratory (NRL) [100]. The key point of this method is finding the non-ionizing energy loss (NIEL) values for different materials. By using the NIEL method, the radiation fluence of particles is converted into displacement damage dose (*DDD*), and the degradation curve of the electrical parameters of solar cells with the change of *DDD* can be obtained.

The NIEL values of different materials upon different particles with different energies can be calculated by using MULASSIS software [101] or the following equation [102]:

$$\mathrm{NIEL}(\mathrm{E}) = \mathrm{n}\cdot\int_{T_d}^{Q_{\max}}\left(\frac{d\sigma(\theta,E)}{d\mathrm{Q}}\right)_E(Q)\cdot G(Q)\cdot Q\cdot d\mathrm{Q} \tag{6}$$

where n is the atomic density of the target material, T_d is the threshold energy to displace atom, $Q_{\max}$ is the maximum energy that can be given to a recoil nuclei by an incident particle of a given energy E, G(Q) is the energy partition function and $(d\sigma/dQ)_E$ the differential interaction cross section. **Figure 9A** shows the calculated results of electron and proton NIEL for GaAs with the energy range from zero up to 200 MeV. The *DDD* induced by irradiation particles can be calculated by the following equation using particle fluence:

$$D_d(E) = \phi(E)\cdot\mathrm{NIEL}(E)\cdot\left[\frac{\mathrm{NIEL}(E_e)}{\mathrm{NIEL}(E_{1MeV})}\right]^{n-1} \tag{7}$$
$$(proton\ n = 1, electron\ 1 < n < 2)$$

where $D_d(E)$ is the *DDD*, $\phi(E)$ is the particle fluence, and NIEL is the non-ionizing energy loss value of the target material. When

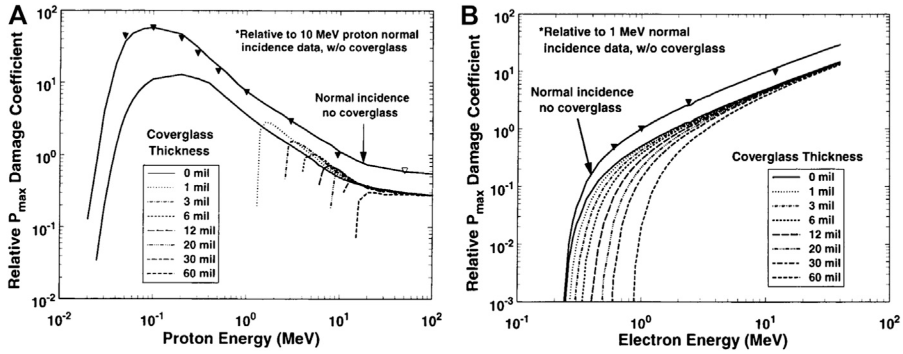

FIGURE 8 | Relative damage coefficient for omnidirectional **(A)** proton and **(B)** electron irradiation of shielded GaAs/Ge solar cells [89].

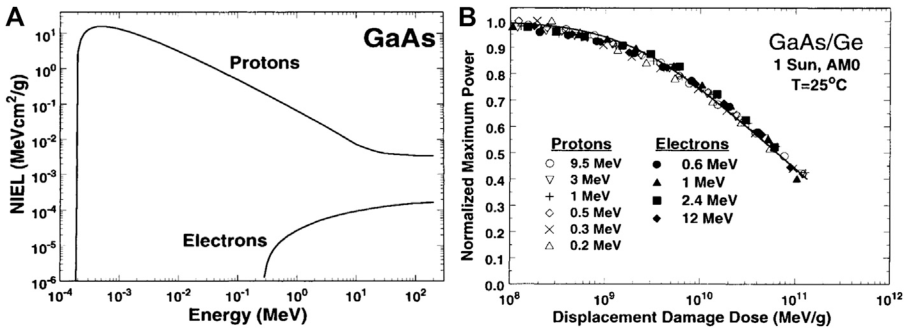

FIGURE 9 | (A) NIEL of electron and proton irradiation in GaAs; **(B)** using the electron to proton damage equivalency factor Rep to fit all of the data from **Figure 4** come a single curve [88].

calculating D_d of proton irradiation, n value is 1, and the n value of electron irradiation is in the range of 1 to 2. Using NIEL of the same particle with different energies, the relative damage coefficient for different energies of a charged particle, i.e. proton, the irradiation can be obtained from using the following equation [99]:

$$D_{x\rightarrow 10} = \frac{\mathrm{NIEL}_{(xMeV)}}{\mathrm{NIEL}_{(10MeV)}} \tag{8}$$

where $D_{x\rightarrow 10}$ is the X MeV proton to 10 MeV proton relative damage coefficient, and NIEL is the corresponding non-ionization damage energy for different energies. Electron to proton irradiation damage equivalency factor Rep can be calculated by following equation [99]:

$$\mathrm{R}_{ep} = \frac{1}{n}\sum_{n}\frac{Dj}{Di}(n = 1, 2, 3\cdots n) \tag{9}$$

where Rep is electron to proton irradiation equivalent damage coefficient, D_j is the actual DDD values by using electron irradiation and D_i is the corresponding fitting values of DDD. By considering Rep degradation curves of electrical parameters of solar cells against the irradiation fluence can be described into a single curve against the D_d. For example, **Figure 9B** shows the re-plot of **Figure 4** using NIEL method. The DDD of solar cells in complex electron and proton environment can be calculated by **Eq. 10**, and applied to evaluate the degradation curve of the electrical performance of space solar cells with the DDD.

$$D_d = \int \frac{d\phi(E_e)}{dE_p}\cdot \mathrm{NIEL}\big(E_p\big)dE_p + R_{ep}\int \frac{d\phi(E_e)}{dE_e} \cdot \mathrm{NIEL}(E_e)\left[\frac{\mathrm{NIEL}(E_e)}{\mathrm{NIEL}(1MeV)}\right]^{n-1} dE_e \tag{10}$$

Besides, predicting the degradation of a solar cell performance regarding a given electron or proton fluence can also be conducted by using the following semi-empirical equation:

$$\frac{P_{\max}}{P_0} = 1 - C\cdot \ln\left(1 + \frac{D_d}{D_x}\right) \tag{11}$$

where $P_{\max}$ and P_0 are the output power (also can be I_{sc} or V_{oc}) of solar cell before and after irradiation, D_d is the given DDD regarding to the given irradiation fluence, respectively. C and D_x are the fitting parameters obtained by on-ground experimental data. **Eq. 4** is more versatile than **Eq. 5** for different kinds of particles by using D_d as variable for given irradiation condition.

Comparing to the equivalent fluence method, the NIEL approach requires fewer experimental measurements to successfully predict the radiation damage of different particles

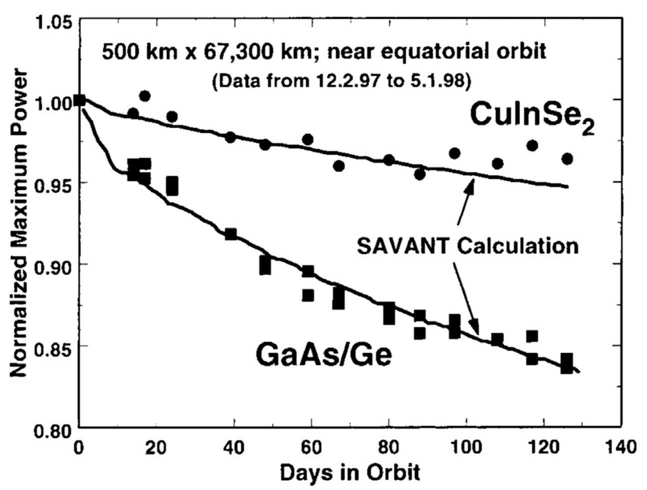

FIGURE 10 | The displacement damage does method measurements for GaAs/Ge and CIS solar cells [88].

at different energies and is easier to implement. Only taking few energies of proton and electron irradiation test data, one can obtain the degradation trends of the electrical properties a solar cell under different particles with different energies and different fluences. Messenger et al. compared the equivalent fluence method and the displacement damage dose method in details and concluded that the key of the displacement damage dose method was NIEL, while the equivalent fluence method needed a lot of experimental data [88]. The displacement damage dose method was successfully applied for predicting on-board solar cell measurements for GaAs/Ge and CIS solar cells at 500 × 67,300 km near equatorial orbit, shown in **Figure 10**.

The Development Trends of Space Solar Cells

There is no doubt that space solar cells should move toward higher efficiency, low cost and better radiation resistance. In this direction, many types of new technologies are trying to solve these problems. Currently, LM triple-junction solar cells are the main stream in space applications. In theory, the solar cell has more junction number has higher efficiency, but it is difficult to increase the number of cell junctions in real cell fabrication. The theoretical limit of N-junction (N for the infinite) solar cells conversion efficiency can reach 68.2% [3]. But the cell fabrication becomes more difficult when the number of junctions is increased, especially for more than 5–6 junctions. The efficiency of multi-junction solar cells from single-junction to six-junction is presented in **Table 4**. Besides, apart from the high cost of III-V materials, the price of GaAs is ten times than that of Si, the growth of III-V materials requires expensive equipment, and hence, the production cost of multijunction solar cells is very high and mostly used in space applications now. Therefore, in the future, the development trends of III-V multijunction solar cells are low-cost, high efficiency, high radiation resistance and simple fabrication method.

CONCLUSION

III-V multijunction solar cells are the primary power supply for space application due to its super high photoelectric conversion efficiency and better radiation resistance. Despite the high fabrication cost, it is widely used in different space applications. New types of space solar cells with new materials and new structures are continuously coming out and the performance characteristics of various space solar cells have been extensively studied. Owing to the development of the balance between the bandgap matching and lattice matching, the structure of solar cells is continuously optimized, more suitable new materials are discovered, and more mature manufacturing processes are utilized. The highest conversion efficiency of solar cells is constantly being refreshed. Comparing to conventional silicon solar cells, the conversion efficiency of III-V multijunction solar cells is significantly improved. Till now, the highest efficiency of crystalline silicon heterojunction solar cell reached 25.6%, and the world record of 47.1% conversion efficiency is achieved by six-junction inverted metamorphic solar cells under 143 suns. Furthermore, lattice-matched GaInP/GaAs/Ge triple junction solar cell fabrication technology is becoming more and more mature with large scale of mass production while keeping the conversion efficiency over 30%.

The space radiation environment is the main threat for in-orbit solar cell performance and lifetime. The high energy particles, such as electrons and protons, induce displacement damages in different regions of solar cell structure and lead to electrical and spectral performance degradation of solar cells. The main reason for the deterioration of space solar cells is that the radiation induced displacement damages forms non-radiative recombination centers and reduces the minority carrier lifetime, and, consequently, results in a reduction of solar cell electrical and spectral parameters. The equivalent fluence method and the displacement damage dose method

TABLE 4 | Comparison of the efficiency of various types of solar cells under concentrated sunlight.

Classification	Efficiency (%)	Area (cm^2)	Intensity (suns)
Si	27.6 ± 1.2 ref. 103	1.00 (aperture area)	92
GaAs	30.5 ± 1.0 ref. 104	0.10043 (designated illumination area)	258
GaInP/GaAs/Ge	40.6 ± 2.0 ref. 97	287 (aperture area)	365
InGaP/GaAs/InGaAs	44.4 ± 2.6 ref. 105	0.1652 (designated illumination area)	302
GaInP/GaAs/GaInAsP/GaInAs (4 J)	46.0 ± 2.2 ref. 73	0.09709 (designated illumination area)	508
AlGaInP/AlGaAs/GaAs/GaInAs/GaInAs/GaInAs (6 J)	47.1 ± 3.2 ref. 8	0.099 (designated illumination area)	143

are two main approaches for evaluating solar cell radiation effects and degradation of cell parameters. Especially, the displacement damage dose method is a more convenient and effective tool. Although the radiation effects of solar cells are widely studied, the radiation damage mechanism of multijunction solar cells with different materials and different structures are not fully explored yet. More experimental and theoretical studies are still needed for further investigating feasible radiation hardening methods.

DATA AVAILABILITY STATEMENT

The data that supports the findings of this study are properly cited with literature and also available from the corresponding author upon reasonable request.

AUTHOR CONTRIBUTIONS

JL, AA, and YL designed the research, conducted the literature review and wrote this manuscript. All authors contributed to the literature review, discussion of the results and edited the manuscript.

FUNDING

This work was supported by a key project of Natural Science Foundation of China (Grant number: 61534008), Basic Research Foundation of Yunnan Province (Grant number: 202001AU070090, 202001AT070086) and Doctoral Start-up Funding of Yunnan Normal University (Grant number: 2019XJLK05/01700205020503040).

REFERENCES

1. Flood DJ. Space photovoltaics - history, progress and promise. *Mod Phys Lett B* (2001) 15(17n19):561–70. doi:10.1142/S0217984901002038
2. Yukinori K, Shoichi N, Shinya T. Recent progress in Si thin film technology for solar cells. *Vacuum* (1991) 42:1035–36. doi:10.1016/0042-207X(91)91251-I
3. Razykov TM, Ferekides CS, Morel D, Stefanakos E, Ullal HS, Upadhyaya HM. Solar photovoltaic electricity: current status and future prospects. *Sol Energy* (2011) 85(8):1580–608. doi:10.1016/j.solener.2010.12.002
4. Dincer F. The analysis on photovoltaic electricity generation status, potential and policies of the leading countries in solar energy. *Renew Sustain Energy Rev* (2011) 15(1):713–20. doi:10.1016/j.rser.2010.09.026
5. Polman A, Knight M, Garnett EC, Ehrler B, Sinke WC. Photovoltaic materials: present efficiencies and future challenges. *Science* (2016) 352:aad4424. doi:10.1126/science.aad4424
6. Green MA. Third generation photovoltaics: solar cells for 2020 and beyond. *Phys E Low-dimens Syst Nanostruct* (2002) 14(1–2):65–70. doi:10.1016/S1386-9477(02)00361-2
7. Yamaguchi M, Takamoto T, Araki K, Ekins-Daukes N. Multi-junction III-V solar cells: current status and future potential. *Sol Energy* (2005) 79(1):78–85. doi:10.1016/j.solener.2004.09.018
8. Geisz JF, France RM, Schulte KL, Steiner MA, Norman AG, Guthrey HL, et al. Six-junction III–V solar cells with 47.1% conversion efficiency under 143 Suns concentration. *Nature Energy* (2020) 5(4):326–35. doi:10.1038/s41560-020-0598-5
9. Patel P, Aiken D, Chumney D, Cornfeld A, Lin Y, Mackos C, et al. Initial results of the monolithically grown six-junction inverted metamorphic multi-junction solar cell. In: IEEE 38th photovoltaic specialist conference part 2; 2012 June 3–8. Austin, TX, USA: IEEE (2012). p. 1–4.
10. Chiu PT, Law DC, Woo RL, Singer SB, Bhusari D, Hong WD, et al. 35.8% space and 38.8% terrestrial 5J direct bonded cells. In: IEEE 40th photovoltaic specialist conference; 2014 June 8–13. Denver, CO, USA: IEEE (2014). p. 11–3.
11. Cariou R, Benick J, Feldmann F, Hohn O, Hauser H, Beutel P, et al. III-V-on-silicon solar cells reaching 33% photoconversion efficiency in two-terminal configuration. *Nature Energy* (2018) 3(4):326–33. doi:10.1038/s41560-018-0125-0
12. Stan M, Aiken D, Cho B, Cornfeld A, Diaz J, Ley V, et al. Very high efficiency triple junction solar cells grown by MOVPE. *J Cryst Growth* (2008) 310(23):5204–8. doi:10.1016/j.jcrysgro.2008.07.024
13. King RR, Karam NH, Ermer JH, Haddad M, Colter P, Isshiki T, et al. Next-generation, high-efficiency III-V multijunction solar cells. In: Conference record of the twenty-eighth IEEE photovoltaic specialists conference; 2000 Sept 15–22. Anchorage, AK, USA: IEEE (2000). p. 998–1001.
14. Geisz JF, Kurtz S, Wanlass MW, Ward JS, Duda A, Friedman DJ, et al. High-efficiency GaInP/GaAs/InGaAs triple-junction solar cells grown inverted with a metamorphic bottom junction. *Appl Phys Lett* (2007) 91:023502. doi:10.1063/1.2753729
15. Geisz JF, Friedman DJ, Ward JS, Duda A, Olavarria WJ, Moriarty TE, et al. 40.8% efficient inverted triple-junction solar cell with two independently metamorphic junctions. *Appl Phys Lett* (2008) 93(12):123505. doi:10.1063/1.2988497
16. Kao YC, Chou HM, Hsu SC, Lin A, Lin CC, Shih ZH, et al. Performance comparison of III–V//Si and III–V//InGaAs multi-junction solar cells fabricated by the combination of mechanical stacking and wire bonding. *Sci Rep* (2019) 9(1):4308. doi:10.1038/s41598-019-40727-y
17. Dimroth F, Grave M, Beutel P, Fiedeler U, Karcher C, Tibbits TND, et al. Wafer bonded four-junction GaInP/GaAs//GaInAsP/GaInAs concentrator solar cells with 44.7% efficiency. *Prog Photovoltaics Res Appl* (2014) 22(3):277–82. doi:10.1002/pip.2475
18. Dharmarasu N, Khan A, Yamaguchi M. Effects of irration on n+p InGaP solar cells. *J Appl Phys* (2002) 91:3306–11. doi:10.1063/1.1445276
19. Ochoa M, Yaccuzzi E, Espinet-Gonzalez P, Barrera M, Barrigon E, Ibarra ML, et al. 10 MeV proton irradiation effects on GaInP/GaAs/Ge concentrator solar cells and their component subcells. *Sol Energy Mater Sol Cell* (2017) 159:576–82. doi:10.1016/j.solmat.2016.09.042
20. Sato S, Miyamoto H, Imaizumi M, Shimazaki K, Morioka C, Kawano K, et al. Degradation modeling of InGaP/GaAs/Ge triple-junction solar cells irradiated with various-energy protons. *Sol Energy Mater Sol Cell* (2009) 93(6–7):768–73. doi:10.1016/j.solmat.2008.09.044
21. Zhang L, Niu P, Li Y, Song M, Zhang J, Ning P, et al. Investigation on high-efficiency $Ga_{0.51}In_{0.49}P/In_{0.01}Ga_{0.99}As/Ge$ triple-junction solar cells for space applications. *AIP Adv* (2017) 7:125217. doi:10.1063/1.5006865
22. Maximenko SI, Messenger SR, Hoheisel R, Scheiman D, Gonzalez M, Lorentzen J, et al. Characterization of high fluence irradiations on advanced triple junction solar cells. In: IEEE 39th photovoltaic specialist conference; 2013 June16–21. Tampa, FL, USA: IEEE (2013). p. 2797–800.
23. Hu J, Wu Y, Xiao J, Yang D, Zhang Z. Degradation behaviors of electrical properties of GaInP/GaAs/Ge solar cells under < 200 keV proton irradiation. *Sol Energy Mater Sol Cell* (2008) 92(12):1652–6. doi:10.1016/j.solmat.2008.07.017
24. Gao H, Yang R, Zhang Y. Improving radiation resistance of GaInP/GaInAs/Ge triple-junction solar cells using GaInP back-surface field in the middle subcell. *Materials* (2020) 13(8):1958. doi:10.3390/ma13081958
25. France RM, Espinet-Gonzalez P, Ekins-Daukes NJ, Guthrey H, Steiner MA, Geisz JF. Multijunction solar cells with graded buffer Bragg reflectors. *IEEE J Photovoltaics* (2018) 8(6):1608–15. doi:10.1109/JPHOTOV.2018.2869550

26. Arzbin HR, Ghadimi A. Improving the performance of a multi-junction solar cell by optimizing BSF, base and emitter layers. *Mater Sci Eng B* (2019) 243: 108–14. doi:10.1016/j.mseb.2019.04.001
27. Das AK. Efficiency improvement of p-i-n structure over p-n structure and effect of p-Layer and i-Layer properties on electrical measurements of gallium nitride and indium nitride alloy based thin film solar cell using AMPS-1D. *IOSR J Appl Phys* (2015) 7(2):08–15. doi:10.9790/4861-07220815
28. Fang M, Fei T, Bai M, Guo Y, Lv J, Quan R, et al. Annealing effects on GaAs/Ge solar cell after 150 keV proton irradiation. *Int J Photoenergy* (2020) 2020:1–8. doi:10.1155/2020/3082835
29. Sharma S, Jain KK, Sharma A. Solar cells: in research and applications—a review. *Mater Sci Appl* (2015) 06(12):1145–55. doi:10.4236/msa.2015.612113
30. Kabir E, Kumar P, Kumar S, Adelodun AA, Kim K-H. Solar energy: potential and future prospects. *Renew Sustain Energy Rev* (2018) 82(1):894–900. doi:10.1016/j.rser.2017.09.094
31. Snaith HJ. Perovskites: the emergence of a new era for low-cost, high-efficiency solar cells. *J Phys Chem Lett* (2013) 4(21):3623–30. doi:10.1021/jz4020162
32. Hagfeldt A, Boschloo G, Sun L, Kloo L, Pettersson H. Dye-sensitized solar cells. *Chem Rev* (2010) 110(11):6595–663. doi:10.1021/cr900356p
33. Hoppe H, Sariciftci NS. Organic solar cells: an overview. *J Mater Res* (2004) 19(7):1924–7945. doi:10.1557/JMR.2004.0252
34. Kayes BM, Zhang L, Ding IK, Higashi GS. Flexible thin-film tandem solar cells with > 30% efficiency. *IEEE J Photovoltaics* (2014) 4(2):729–33. doi:10.1109/JPHOTOV.2014.2299395
35. Yamaguchi M, Takamoto T, Araki K, Ekins-Daukes N. Multi- junction III-V solar cells: current status and future potential. *Sol Energy* (2005) 79(1):78–85. doi:10.1016/j.solener.2004.09.018
36. Bouisset P, Nguyen VD, Akatov YA, Siegrist M, Parmentier N, Archangelsky VV, et al. Quality factor and does equivalent investigations aboard the soviet space station MIR. *Adv Space Res* (1992) 12(2–3):363–7. doi:10.1016/0273-1177(92)90130-P
37. Moon S, Kim K, Kim Y, Heo J, Lee J. Highly efficient single-junction GaAs thin-film solar cell on flexible substrate. *Sci Rep* (2016) 6:30107. doi:10.1038/srep30107
38. Stephen P, Steven J, Mark S, Keith A. Assessment of MOCVD- and MBE-growth GaAs for high-efficiency solar cell applications. *IEEE Trans Electron Dev* (1990) 37(2):469–77. doi:10.1109/16.46385
39. Iles PA, Yeh Y-CM, Ho FH, Chu C-L, Cheng C. High-efficiency (> 20% AMO) GaAs solar cells - grown on inactive-Ge substrates. *IEEE Electron Device Lett* (1990) 11(4):140–2. doi:10.1109/55.61775
40. Yamaguchi M, Lee KH, Araki K, Kojima N, Yamada H, Katsumata Y. Analysis for efficiency potential of high-efficiency and next-generation solar cells. *Prog Photovoltaics Res Appl* (2018) 26(8):543–52. doi:10.1002/pip.2955
41. Gaddy EM. Cost performance of multi-junction, gallium arsenide, and silicon solar cells on spacecraft. In: Conference record of the twenty fifth IEEE photovoltaic specialists conference; 1996 May 13–17. Washington, DC, USA: IEEE (1996). p. 293–6.
42. King RR, Fetzer CM, Colter PC, Edmondson KM, Ermer JH, Cotal HL, et al. High-efficiency space and terrestrial multijunction solar cells through bandgap control in cell structures. In: Conference record of the twenty-ninth IEEE photovoltaic specialists conference; 2002 May 19–24. New Orleans, LA, USA: IEEE (2002). p. 776–81.
43. Messenger SR, Burke EA, Walters RJ, Warner JH, Summers GP. Using SRIM to calculate the relative damage coefficients for solar cells. *Prog Photovoltaics Res Appl* (2005) 13(2):115–23. doi:10.1002/pip.608
44. Nishioka K, Takamoto T, Agui T, Kaneiwa M, Uraoka Y, Fuyuki T. Evaluation of InGaP/InGaAs/Ge triple-junction solar cell and optimization of solar cell's structure focusing on series resistance for high-efficiency concentrator photovoltaic systems. *Sol Energy Mater Sol Cell* (2006) 90(9):1308–21. doi:10.1016/j.solmat.2005.08.003
45. Guter W, Schoene J, Philipps SP, Steiner M, Siefer G, Wekkeli A, et al. Current-matched triple-junction solar cell reaching 41.1% conversion efficiency under concentrated sunlight. *Appl Phys Lett* (2009) 94(22):223504. doi:10.1063/1.3148341
46. Kondow M, Uomi K, Niwa A, Kitatani T, Watahiki S, Yazawa Y. GaInNAs: a novel material for long-wavelength-range laser diodes with excellent high-temperature performance. *Jpn J Appl Phys* (1996) 35(No 2s):1273. doi:10.1143/JJAP.35.1273
47. Lew K, Yoon S, Wang H, Wicaksono S, Gupta J, McAlister S, et al. GaAsNSb-base GaAs heterojunction bipolar transistor with a low turn-on voltage. *J Vac Sci Technol B* (2006) 24(3):1308. doi:10.1116/1.2200376
48. Tansu N, Kirsch NJ, Mawst LJ. Low-threshold-current-density 1300-nm dilute-nitride quantum well lasers. *Appl Phys Lett* (2002) 81(14):2523. doi:10.1063/1.1511290
49. Polojärvi V, Aho A, Tukiainen A, Raappana M, Aho M, Schramm A, et al. Influence of As/group-III flux ratio on defects formation and photovoltaic performance of GaInNAs solar cells. *Sol Energy Mater Sol Cells* (2016) 149: 213–20. doi:10.1016/j.solmat.2016.01.024
50. Friedman DJ, Kurtz SR. Breakeven criteria for the GaInNAs junction in GaInP/GaAs/GaInNAs/Ge four-junction solar cells. *Prog Photovoltaics Res Appl* (2002) 10(5):331–44. doi:10.1002/pip.430
51. Kurtz S, King RR, Edmondson KM, Friedman DJ, Karam NH. 1-MeV-electron irradiation of GaInAsN cells. In: Conference record of the twenty ninth IEEE photovoltaic specialists conference; 2002 May 19–24. New Orleans, LA, USA: IEEE (2002). p. 1006–9.
52. Miyashita N, Shimizu Y, Kobayashi N. Fabrication of GaInNAs-based solar cells for application to multi-junction tandem solar cells. In: Conference record of the 2006 IEEE 4th world conference on photovoltaic energy conversion; 2006 May 7–12. Hawaii, USA: IEEE (2006). p. 869.
53. Sailai M, Qiqi L, Aierken A, Heini M, Fan Zhao X, Ting Hao R, et al. 1 MeV electron irradiation and post-annealing effects of GaInAsN diluted nitride alloy with 1 eV bandgap energy. *Thin Solid Films* (2020) 709:138237. doi:10.1016/j.tsf.2020.138237
54. Jackrel DB, Bank SR, Yuen HB, Wistey MA, Harris JS, Ptak AJ, et al. Dilute nitride GaInNAs and GaInnAsSb solar cells by molecular beam epitaxy. *Jpn J Appl Phys* (2007) 101(11):114916. doi:10.1063/1.2744490
55. Han XX, Suzuki H, Lee JH, Kojima N, Ohshita Y, Yamaguchi M. N incorporation and optical properties of GaAsN epilayers on (311) A/B GaAs substrates. *Jpn J Appl Phys* (2011) 44(1):015402. doi:10.1088/0022-3727/44/1/015402
56. Miyashita N, Ahsan N, Islam M, Okada Y. Study on the device structure of GaInNAs (Sb) based solar cells for use in 4-junction tandem solar cells. In: Conference record of the 38th IEEE photovoltaic specialists conference; 2012 June 3–8. Austin, USA: IEEE (2012). p. 000954.
57. Miyashita N, Ahsan N, Okada Y. Effect of antimony on uniform incorporation of nitrogen atoms in GaInNAs films for solar cell application. *Sol Energy Mater Sol Cells* (2013) 111:127–32. doi:10.1016/j.solmat.2012.12.036
58. Han XX, Tanaka T, Kojima N, Ohshita Y, Yamaguchi M, Sato S. Growth orientation dependent photoluminescence of GaAsN alloys. *Appl Phys Lett* (2012) 100(3):032108. doi:10.1063/1.3679079
59. Andreev VM. IId-1-GaAs and high-efficiency space cells. *Pract Handb Photovoltaics Fundamentals Appl* (2003) 417–33. doi:10.1016/B978-185617390-2/50017-9
60. Gee JM, Virshup GF. A 31%-efficient GaAs/silicon mechanically stacked, multijunction concentrator solar cell. In: Conference record of the 20th IEEE photovoltaic specialists conference; 1988 Sept 26–30. Las Vegas, NV: IEEE (1988). p. 754–8.
61. Yazawa Y, Tamura K, Watahiki S, Kitatani T, Ohtsuka H, Warabisako T. Three-junction solar cells comprised of a thin-film GaInP/GaAs tandem cell mechanically stacked on a Si cell. In: Conference record of the 26th IEEE photovoltaic specialists conference; 1997 Sept 29–Oct 3. Anaheim, CA, USA: IEEE (1997). p. 899–902.
62. Essig S, Ward S, Steiner MA, Friedman DJ, Geisz JF, Stradins P, et al. Progress towards a 30% efficient GaInP/Si tandem solar cell. *Energy Procedia* (2015) 77: 464–9. doi:10.1016/j.egypro.2015.07.066
63. Zhao L, Flamand G, Poortmans J. Recent progress and spectral robustness study for mechanically stacked multi-junction solar cells. *AIP Conf Proc* (2010) 1277(1):284. doi:10.1063/1.3509212
64. Baba M, Makita K, Mizuno H, Takato H, Sugaya T, Yamada N. Feasibility study of two terminal tandem solar cellsintegrated with smart stack, areal current matching,and low concentration. *Prog Photovoltaics Res Appl* (2016) 25(3):255–63. doi:10.1002/pip.2856

65. Mizuno H, Makita K, Matsubara K. Electrical and optical interconnection for mechanically stacked multi-junction solar cells mediated by metal nanoparticle arrays. *Appl Phys Lett* (2012) 101(19):191111. doi:10.1063/1.4766339
66. Yoshidomi S, Furukawa J, Hasumi M, Sameshima T. Mechanical stacking multi junction solar cells using transparent conductive adhesive. *Energy Procedia* (2014) 60:116–22. doi:10.1016/j.egypro.2014.12.352
67. Makita K, Mizuno H, Tayagaki T, Aihara T, Oshima R, Shoji Y, et al. III-V//Si multijunction solar cells with 30% efficiency using smart stack technology with Pd nanoparticle array. *Prog Photovoltaics Res Appl* (2019) 28(1):16–24. doi:10.1002/pip.3200
68. Tanabe K, Fontcuberta i Morral A, Atwater HA, Aiken DJ, Wanlass MW. Direct-bonded GaAs/InGaAs tandem solar cell. *Appl Phys Lett* (2006) 89(10):102–6. doi:10.1063/1.2347280
69. Dharmarasu N, Yamaguchi M, Khan A, Yamada T, Tanabe T, Takagishi S, et al. High-radiation-resistant InGaP, InGaAsP, and InGaAs solar cells for multijuction solar cells. *Appl Phys Lett* (2001) 79(15):2399. doi:10.1063/1.1409270
70. Dai P, Ji L, Tan M, Uchida S, Wu Y, Abuduwayiti A, et al. Electron irradiation study of room-temperature wafer-bonded four-junction solar cell grown by MBE. *Sol Energy Mater Sol Cell* (2017) 171:1181–22. doi:10.1016/j.solmat.2017.06.046
71. Essig S, Benick J, Schachtner M, Wekkeli A, Hermle M, Dimroth F, et al. Wafer-bonded GaInP/GaAs//Si solar cells with 30% efficiency under concentrated sunlight. *IEEE J Photovoltaics* (2015) 5(3):977–81. doi:10.1109/JPHOTOV.2015.2400212
72. Dimroth F, Roesener T, Essig S, Weuffen C, Wekkeli A, Oliva E, et al. Comparison of direct growth and wafer bonding for the fabrication of GaInP/GaAs dual-junction solar cells on silicon. *IEEE J Photovoltaics* (2014) 4(2):620–5. doi:10.1109/JPHOTOV.2014.2299406
73. Dimroth F, Tibbits TND, Niemeyer M, Predan F, Beutel P, Karcher C, et al. Four-junction wafer-bonded concentrator solar cells. *IEEE J Photovoltaics* (2016) 6(1):343–9. doi:10.1109/JPHOTOV.2015.2501729
74. Sinharoy S, Patton MO, Valko TM, Weizer VG. Progress in the development of metamorphic multi-junction III-V space solar cells. *Prog Photovoltaics Res Appl* (2002) 10(6):427–32. doi:10.1002/pip.449
75. France RM, Geisz JF, Garcia I, Steiner MA, McMahon WE, Friedman DJ, et al. Design flexibility of ultrahigh efficiency four-junction inverted metamorphic solar cells. *IEEE J Photovoltaics* (2016) 6(2):578–83. doi:10.1109/JPHOTOV.2015.2505182
76. Long J, Xiao M, Huang X, Xing Z, Li X, Dai P, et al. High efficiency thin film GaInP/GaAs/InGaAs inverted metamorphic (IMM) solar cells based on electroplating process. *J Cryst Growth* (2019) 513:38–42. doi:10.1016/j.jcrysgro.2019.02.057
77. Aierken A, Fang L, Heini M, Zhang QM, Li ZH, Zhao XF, et al. Effects of proton irradiation on upright metamorphic GaInP/GaInAs/Ge triple junction solar cells. *Sol Energy Mater Sol Cell* (2018) 185:36–44. doi:10.1016/j.solmat.2018.04.035
78. France RM, Geisz JF, Steiner MA, Friedman DJ, Ward JS, Olson JM, et al. Pushing inverted metamorphic multijunction solar cells toward higher efficiency at realistic operating conditions. *IEEE J Photovoltaics* (2013) 3(2):893–8. doi:10.1109/JPHOTOV.2013.2239358
79. Garcia I, France RM, Geisz JF, McMahon WE, Steiner MA, Johnston S, et al. Metamorphic III–V solar cells: recent progress and potential. *IEEE J Photovoltaics* (2016) 6(1):366–73. doi:10.1109/JPHOTOV.2015.2501722
80. Guter W, Dunzer F, Ebel L, Hillerich K, Koestler W, Kubera T, et al. Space solar cells-3G30 and next generation radiation hard products. *11th Eur Space Power Conf* (2017) 16:03005. doi:10.1051/e3sconf/20171603005
81. Yoshikawa K, Kawasaki H, Yoshida W, Irie T, Konishi K, Nakano K, et al. Silicon heterojunction solar cell with interdigitated back contacts for a photoconversion efficiency over 26%. *Nature Energy* (2017) 2(5):17032. doi:10.1038/nenergy.2017.32
82. Kayes MK, Nie H, Twist R, Spruytte SG, Reinhardt F, Kizilyalli IC, et al. 27.6% conversion efficiency, a new record for single-junction solar cells under 1 sun illumination. In: 37th IEEE photovoltaic specialists conference; 2011 June 19–24. Seattle, WA, USA: IEEE (2011). p. 4–8.
83. Chen Z, Zheng X, Li Z, Wang P, Rong X, Wang T, et al. Positive temperature coefficient of photovoltaic efficiency in solar cells based on InGaN/GaN MQWs. *Appl Phys Lett* (2016) 109(6):062104. doi:10.1063/1.4960765
84. Yamaguchi M. Multi-junction solar cells and novel structures for solar cell applications. *Phys E Low Dimens Syst Nanostruct* (2002) 14(1–2):84–90. doi:10.1016/S1386-9477(02)00362-4
85. Bhuiyan AG, Sugita K, Hashimoto A, Yamamoto A. InGaN Solar Cells: present state of the art and important challenges. *IEEE J Photovoltaics* (2012) 2(3):276–93. doi:10.1109/JPHOTOV.2012.2193384
86. Hamache A, Sengouga N, Meftah A, Henini M. Modeling the effect of 1MeV electron irradiation on the performance of n+–p–p+ silicon space solar cells. *Radiat Phys Chem* (2016) 123:103–8. doi:10.1016/j.radphyschem.2016.02.025
87. Rehman AU, Lee SH, Lee SH. Silicon space solar cells: progression and radiation-resistance analysis. *J Kor Phys Soc* (2016) 68(4):593–8. doi:10.3938/jkps.68.593
88. Messenger SR, Summers GP, Burke EA, Walters RJ, Xapsos MA. Modeling solar cell degradation in space: a comparison of the NRL displacement damage dose and the JPL equivalent fluence approaches. *Prog Photovoltaics Res Appl* (2001) 9(2):103–21. doi:10.1002/pip.357
89. Hu JM, Wu Y-Y, Zhang Z, Yang DZ, He SY. A study on the degradation of GaAs/Ge solar cells irradiated by <200keV protons. *Nucl Instrum Methods Phys Res Sect B Beam Interact Mater Atoms* (2008) 266(2):267–70. doi:10.1016/j.nimb.2007.11.010
90. Sharps PR, Aiken DJ, Stan MA, Thang CH, Fatemi N. Proton and electron radiation data and analysis of GaInP2/GaAs/Ge solar cells. *Prog Photovoltaics Res Appl* (2002) 10(6):383–90. doi:10.1002/pip.444
91. Wang R, Lu M, Yi T-C, Yang K, Ji X-X. Effects of 1.0–11.5 MeV electron irradiation on GaInP/GaAs/Ge triple-junction solar cells for space applications. *Chin Phys Lett* (2014) 31(8):086103. doi:10.1088/0256-307X/31/8/086103
92. Takamoto T, Juso H, Ueda K, Washio H, Yamaguchi H. IMM triple-junction solar cells and modules optimized for space and terrestrial conditions. In: IEEE 44th photovoltaic specialist conference; 2017 June 25–30. Washington, DC, USA: IEEE (2017). p. 3506–10.
93. Imaizumi M, Nakamura T, Takamoto T, Ohshima T, Tajima M. Radiation degradation characteristics of component subcells in inverted metamorphic triple-junction solar cells irradiated with electrons and protons. *Prog Photovoltaics Res Appl* (2017) 25(2):161–74. doi:10.1002/pip.2840
94. Zhang Y, Wu Y, Zhao H, Sun C, Xiao J, Geng H, et al. Degradation behavior of electrical properties of inverted metamorphic tri-junction solar cells under 1 MeV electron irradiation. *Sol Energy Mater Sol Cell* (2016) 157:861–6. doi:10.1016/j.solmat.2016.08.006
95. Allam EE, Inguimbert C, Addarkaoui S, Meulenberg A, Jorio A, Zorkani I. NIEL calculations for estimating the displacement damage introduced in GaAs irradiated with charged particles. *IOP Conf Ser Mater Sci Eng* (2017) 186:012005. doi:10.1088/1757-899X/186/1/012005
96. Tada HY, Carter JR, Anspaugh BE. *Solar cell radiation handbook*. Pasadena, USA: Jet Propulsion Laboratory (1982).
97. Green MA, Keevers MJ, Thomas I, Lasich JB, Emery K, King RR. 40% efficient sunlight to electricity conversion. *Prog Photovoltaics Res Appl* (2015) 23(6):685–591. doi:10.1002/pip.2612
98. Anspaugh BE. *GaAs solar cell radiation handbook*. Pasadena, USA: Jet Propulsion Laboratory (1996).
99. Zhao XF, Aierken A, Heini M, Tan M, Wu YY, Lu SL, et al. Degradation characteristics of electron and proton irradiated InGaAsP/InGaAs dual junction solar cell. *Sol Energy Mater Sol Cell* (2020) 206:110339. doi:10.1016/j.solmat.2019.110339
100. Walters RJ, Summers GP. Analysis and modeling of the radiation response of multijunction space solar cells. In: Conference record of the twenty-eighth IEEE photovoltaic specialists conference; 2020 Sept 15–22. Anchorage, AK, USA: IEEE (2000). p. 1092–7.
101. Lei F, Truscott PR, Dyer CS, Quaghebeur B, Heynderickx D, Nieminen P, et al. MULASSIS: a geant4-based multilayered shielding simulation tool. *IEEE Trans Nucl Sci* (2002) 49(6):2788–93. doi:10.1109/TNS.2002.805351

102. Inguimbert C, Gigante R. NEMO: a code to compute NIEL of protons, neutrons, electrons, and heavy ions. *IEEE Trans Nucl Sci* (2006) 53(4): 1967–72. doi:10.1109/TNS.2006.880926
103. Slade A, Garboushian V. 27.6% Efficient silicon concentrator solar cells for mass production. In: Technical digest, *15th international photovoltaic science and engineering conference*; 2005 Oct 10–15. Shanghai, China: CRES (2005). p. 701.
104. Green MA, Hishikawa Y, Dunlop ED, Levi DH, Hohl-Ebinger J, Yoshita M, et al. Solar cell efficiency tables (Version 53). *Prog Photovoltaics Res Appl* (2019) 27(1):3–12. doi:10.1002/pip.3102
105. Green MA, Dunlop ED. Solar cell efficiency tables (Version 55). *Prog Photovoltaics Res Appl* (2019) 28(1):3–15. doi:10.1002/pip.3228

Conflict of Interest: The authors declare that the research was conducted in the absence of any commercial or financial relationships that could be construed as a potential conflict of interest.

frontiers in Physics

ORIGINAL RESEARCH
published: 16 February 2021
doi: 10.3389/fphy.2021.642682

Design of Driving Waveform Based on Overdriving Voltage for Shortening Response Time in Electrowetting Displays

Wenjun Zeng[1,2]*, Zichuan Yi*[1]**, Yiming Zhao*[1]*, Weibo Zeng*[1]*, Simin Ma*[1]*, Xichen Zhou*[1]*, Haoqiang Feng*[1,2]*, Liming Liu*[1]*, Lingling Shui*[1]*, Chongfu Zhang*[1]*, Jianjun Yang*[1] *and Guofu Zhou*[2]

[1]*College of Electron and Information, University of Electronic Science and Technology of China, Zhongshan Institute, Zhongshan, China,* [2]*South China Academy of Advanced Optoelectronics, South China Normal University, Guangzhou, China*

A fast response speed of a pixel is important for electrowetting displays (EWDs). However, traditional driving waveforms of EWDs have the disadvantage of long response time. So, a driving waveform, which based on overdriving voltages and charge trapping theory, was proposed in this paper to shorten the response time of EWDs. The driving waveform was composed of an overdriving stage and a driving stage. Firstly, a simplified physical model was introduced to analyze the influence of driving voltages on the response time. Then, an overdriving voltage was applied in the overdriving stage to increase the respond speed of oil, and a target voltage was applied in the driving stage to obtain a target luminance. In addition, the effect of different overdriving voltages and overdriving time values on the response time was analyzed by charge trapping theory to achieve an optimal performance. Finally, the driving waveform was imported into an EWD for performance testing. Experimental results showed that the response time of the EWD can be shortened by 29.27% compared with a PWM driving waveform.

Keywords: electrowetting displays (EWDs), overdriving voltage, response time, driving waveform, charge trapping

OPEN ACCESS

Edited by:
Qiang Xu,
Nanyang Technological University,
Singapore

Reviewed by:
Ji-Pei Chen,
Guangzhou University, China
Congcong Ma,
Nanyang Institute of Technology,
China

****Correspondence:***
Zichuan Yi
yizichuan@163.com

Specialty section:
This article was submitted to
Optics and Photonics,
a section of the journal
Frontiers in Physics

Received: *16 December 2020*
Accepted: *11 January 2021*
Published: *16 February 2021*

Citation:
Zeng W, Yi Z, Zhao Y, Zeng W, Ma S, Zhou X, Feng H, Liu L, Shui L, Zhang C, Yang J and Zhou G (2021) Design of Driving Waveform Based on Overdriving Voltage for Shortening Response Time in Electrowetting Displays.
Front. Phys. 9:642682.
doi: 10.3389/fphy.2021.642682

INTRODUCTION

Electrowetting displays (EWDs) are a new type of electronic paper with fast response speed and extremely low energy consumption [1, 2], and it can compensate for the limitations of electrophoretic displays (EPDs) effectively in the two major performances of color and video [3–8]. However, certain improvements are required for commercialization of EWDs, such as enhancement of response speed [9, 10]. In addition, driving waveforms are the voltage sequence applied to the EWD, which can control the movement of oil [11]. Therefore, it is of great significance to shorten the response time of EWDs by optimizing the driving waveform.

At present, the method for shortening the response time of EWDs, including reducing oil oscillation, suppressing charge trapping and suppressing oil backflow, has been proposed [12, 13]. In the study of reducing oil oscillation, an amplitude-frequency mixed modulation driving system was proposed, the oil was driven by a high voltage to achieve a target luminance, and then the driving voltage was decreased to stabilize the oil, this method can improve the response speed of gray scale displaying and reduce the oil oscillation [14]. In addition, the oil oscillation can be reduced by optimizing the rising stage of the driving waveform, a driving waveform with an exponential function

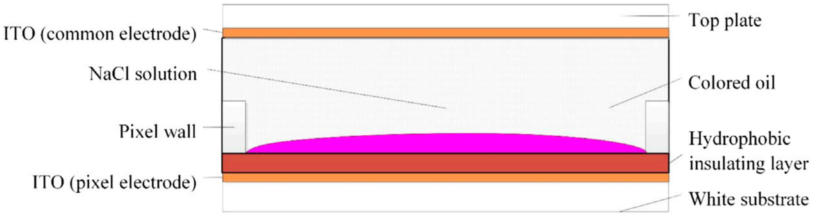

FIGURE 1 | The structure of an EWD pixel. It is in an equilibrium state, and the colored oil forms a continuous spreading film between the hydrophobic insulating layer and the conductive liquid.

rising stage was proposed to reduce the oil oscillation, and it can shorten the response time effectively [15]. But the period of the driving waveform was prolonged by using this method. In the study of suppressing charge trapping, an error diffusion algorithm based on pixel neighborhood gray information and direct current (DC) balanced driving waveform were proposed to suppress the charge trapping, and videos can be played in real-time by using this driving waveform [16]. A driving waveform with sawtooth wave was designed, a section of resetting wave was used to eliminate the influence of charge trapping [17]. The degree of charge trapping in electrowetting liquid lens driven by sinusoidal, bipolar and single pulse has been analyzed, and it was proved that the positive and negative polarities of driving voltages can cause a significant difference in the response speed [18]. However, the EWD was damaged easily by applying the negative polarities of driving voltages [19]. In the study of suppressing oil backflow, a series of sub-frames was used to drive multi-gray pixel data, the time of these sub-frames can be chosen to minimize the effect of the oil backflow in EWDs [20]. But these sub-frames would decrease the stability of oil. Besides, the research of the dynamic model of electrowetting and contact angle saturation has provided a theoretical basis for analyzing the influencing factors of response time in EWDs [21–24].

In this paper, a driving waveform which based on the principle of EWDs and charge trapping, was designed to shorten the response time in EWDs. An overdriving voltage was used to speed up the response speed of oil. Then, the optimal overdriving voltage and overdriving time were determined by the theory of charge trapping and a physical model of EWDs. So, the effect of charge trapping was reduced, and the shortest response time can be obtained.

PRINCIPLE

Principle of EWDs

The structure of EWDs is mainly composed of top plate, white substrate, indium tin oxide (ITO), hydrophobic insulating layer, pixel wall, colored oil and conductive liquid (NaCl solution). An EWD pixel is in an equilibrium state when no voltage is applied, and the colored oil forms a continuous spreading film between the hydrophobic insulating layer and the conductive liquid. So, the pixel can display the color of the colored oil [25, 26], and it is in an "off" state, as shown in **Figure 1**. Instead, the wettability of the colored oil on the hydrophobic insulating layer can be changed when a certain voltage is applied between a common electrode and a pixel electrode. Then, the colored oil can be shrunk, and the surface of the hydrophobic insulating layer can be displayed. At this time, most of light can be reflected directly through the conductive liquid, only a small part cannot be reflected because of the colored ink. So, the pixel point can display the background color of the white substrate, and it is in an "on" state. The ratio of white area to the pixel area is called aperture ratio, and its can be calculated by **Eq. 1**.

$$W_A = 1 - \left(\frac{S_{oil}}{S_{pixel}}\right) \times 100\% \tag{1}$$

Where W_A is the aperture ratio, S_{oil} is the area of the colored oil in the pixel, S_{pixel} is the area of the pixel.

Physical Model of EWDs

A simplified physical model of EWDs is proposed to analyze the influence of driving voltages on oil movement [27]. In the physical model, the pixel of EWDs can be treated as a parallel capacitor when an applied voltage is applied between the common electrode and the pixel electrode. Specifically, the pixel wall and the oil can be treated as connected in series, and then they are connected in parallel with the hydrophobic insulating layer to form a loop. However, the photoresist material of the pixel wall has a lower conductivity compared with the oil. The capacitance of the pixel wall can be neglected. Therefore, the oil and the hydrophobic insulating layer are connected in parallel in the physical model. Ohm's law can be used to calculate parameters of the physical model. So, the capacitance of the pixel C can be calculated by **Eq. 2**.

$$C = C_{oil} + C_D = \frac{1}{4\pi k}\left(\frac{\varepsilon_{oil} S_{oil}}{h} + \frac{\varepsilon_D S_{pixel}}{d}\right) \tag{2}$$

Where C_{oil} is the capacitance of the oil, C_D is the capacitance of the hydrophobic insulating layer, k is electrostatic constant, ε_{oil} is the dielectric constant of the oil, h is the thickness of the oil, ε_D is the dielectric constant of the hydrophobic insulating layer, d is the thickness of the hydrophobic insulating layer. Furthermore, the contact angle of the oil can be controlled by changing the applied voltage according to the Lippmann–Young equation, which is shown in **Eq. 3** and Ref. 28.

$$cos\theta = 1 - \frac{CV^2}{2\gamma_{OL}} \tag{3}$$

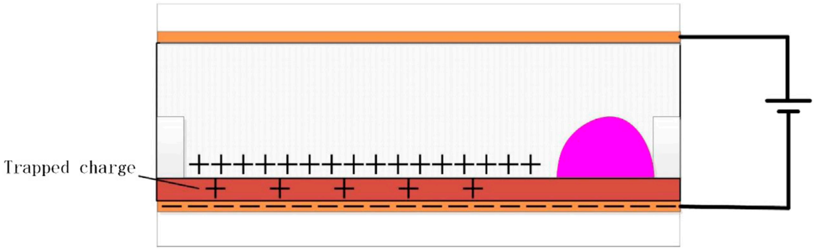

FIGURE 2 | The phenomenon of charge trapping. Charges become trapped in the hydrophobic insulating layer. At this time, the interaction between ions and the hydrophobic insulating layer is stronger than the interaction between ions and the conductive liquid.

Where θ is a oil–solid interface contact angle, V is a driving voltage applied to the pixel, and γ_{OL} is the oil–liquid interfacial tension. The contact angle is related to the aperture ratio, the greater the contact angle, the greater the aperture ratio. So, it can be seen that the aperture ratio is proportional to the driving voltage, as shown in **Eq. 3**. At the same time, the response speed is related to the driving voltage. The higher the driving voltage, the faster the response speed [9].

According to **Eq. 2** and **Eq. 3**, the relationship between the thickness of the hydrophobic insulating layer and the driving voltage can be obtained by **Eq. 4**.

$$V = \sqrt{\frac{2(1-cos\theta)\gamma_{OL}}{\frac{1}{4\pi k}\frac{\varepsilon_{oil}S_{oil}}{h} + \frac{\varepsilon_D S_{pixel}}{d}}} \sim \sqrt{d} \tag{4}$$

It can be seen that the driving voltage is proportional to the thickness of the hydrophobic insulating layer, so the thinner the hydrophobic insulating layer, the lower the driving voltage which can be applied. Excessive driving voltage cannot be applied to the EWD, otherwise the hydrophobic insulating layer would be broken down and the EWD would be damaged.

Charge Trapping of EWDs

Ions in conductive liquid would be pulled toward the hydrophobic insulating layer by electrostatic force when the driving voltage is applied to a pixel. There is a possibility that charge becomes trapped in or on the hydrophobic insulating layer when the interaction between ions and the hydrophobic insulating layer is stronger than the interaction between ions and the conductive liquid. The phenomenon of charge trapping is shown in **Figure 2**. The relationship between the contact angle of oil and driving voltage can be determined by **Eq. 5** and Ref. 29.

$$cos\theta = 1 - \frac{C(V - V_T)^2}{2\gamma_{OL}} \tag{5}$$

Where V_T is the potential generated by the charge trapping. The electrostatic force on the oil is reduced because of the charge trapping, which causes a decrease in the aperture ratio of EWDs. In addition, the relationship between the amount of trapped charges and the driving voltage has been determined by measuring surface potential at a liquid–solid interface in electrowetting-on-dielectrics (EWOD) [30]. Trapped charges are increased when the driving voltage is increased. Therefore, the influence of driving voltages on charge trapping should be considered in the driving waveform.

EXPERIMENT AND DISCUSSION

Testing System

The response time and the luminance of EWDs need to be tested, then the performance of the driving waveform can be analyzed. So, an experimental platform was developed to test and record luminance data of EWDs. The experimental platform was composed of a driving system and a testing system, it is shown in **Figure 3**. The driving system was composed of a computer (H430, Lenovo, China), a function generator (AFG3022C, Tektronix, USA) and a voltage amplifier (ATA-2022H, Agitek, China), which was used to generate driving waveforms. The testing system was composed of the computer and a colorimeter (Arges-45, Admesy, The Netherlands), which was used to test and record the luminance data of EWDs.

In this experiment, an EWD was used as a tested object, and its parameters was shown in **Table 1**. In the testing process, a driving waveform was edited by Arbexpress (V3.4, Tektronix, USA) waveform editing software in the computer. Then, an edited driving waveform was imported into the function generator by a universal serial bus (USB) interface, and it was amplified by the voltage amplifier. Thirdly, the EWD was driven by the driving waveform from the voltage amplifier, and the luminance data of the EWD was tested by the colorimeter. Finally, collected luminance data was transmitted to the computer, and Admesy software was used to record the luminance data in real time.

Design of Driving Waveforms

The response time of EWDs depend on the design of driving waveforms. Traditional driving waveforms generally used a pulse width modulation (PWM) waveform with a voltage amplitude of 30 V. However, the traditional driving waveform has the disadvantages of a long response time [11]. The proposed driving waveform was composed of an overdriving stage and a driving stage. In the overdriving stage, an overdriving voltage was applied to increase the response speed of the oil, and the duration of the overdriving time was called overdriving time. In the driving

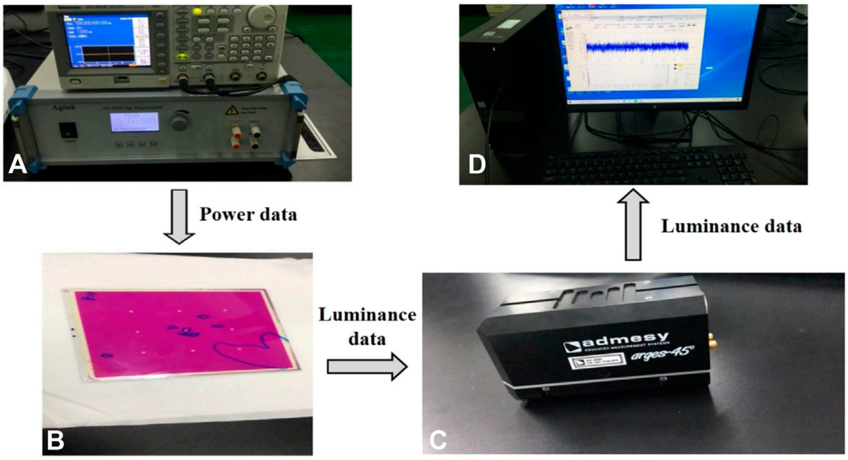

FIGURE 3 | An Experimental platform. It was composed of a driving system and a testing system. **(A)** a function generator and a voltage amplifier **(B)** an EWD **(C)** a computer **(D)** a colorimeter. The power data was the driving waveform from the voltage amplifier. The luminance data was tested by the colorimeter, then it was recorded by the computer.

TABLE 1 | Parameters of the EWD.

Panel size (cm^2)	Oil color	Resolution	Pixel size	Pixel wall size (um^2)	Pixel wall height	Hydrophobic insulating layer thickness
10 × 10	Purple	200 × 200	150 × 150	15 × 15	5.6 um	1 um

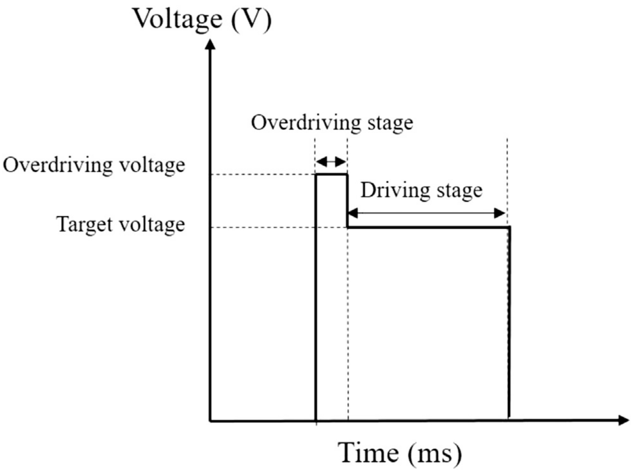

FIGURE 4 | The proposed driving waveform of EWDs in this paper. It was composed of an overdriving stage and a driving stage. An overdriving voltage was applied in the overdriving stage, and a target voltage was applied in the driving stage.

stage, a target voltage was applied to achieve a target luminance, and the target voltage was set to 30 V for comparing with the PWM driving waveform. The proposed driving waveform was shown in **Figure 4**. However, the response time and the luminance of EWDs were affected by the charge trapping. Therefore, the overdriving voltage and overdriving time need to be determined by the experiment to achieve an optimal performance.

The Effect of Overdriving Voltages

The effect of overdriving voltages was analyzed by testing the response time and the luminance of the EWD. In the driving waveform, overdriving voltages were set to 32 V, 34 V, 36 V, 38 V, and 40 V. The overdriving time was set to 4 ms. The luminance rising curves of difference overdriving voltages were shown in **Figure 5**. It can be seen that the luminance of the EWD was 181 when no voltage was applied. Then, the time which was required by the luminance to rise from 181 to 345 was defined as the response time. At the beginning of luminance rising curves, the rising speed of luminance was becoming faster when the overdriving voltage was increased. However, there were two situations during the transition from the overdriving stage to the driving stage. Specifically, the rising speed of luminance remained unchanged when the overdriving voltages were 32 V and 34 V. On the contrary, the rising speed of luminance was decreased when the overdriving voltages were 36 V, 38 V, and 40 V. The reason for this phenomenon was that the charge of the electrode plate in the EWD can be increased rapidly when the overdriving voltage was set higher than 34 V. At this time, the voltage of the equivalent capacitance *C* in the EWD was greater than the target voltage. So, a discharge process of the equivalent capacitance was formed, and the luminance was decreased. In addition, more charges would be trapped in the hydrophobic insulating layer when the overdriving voltage was set higher than

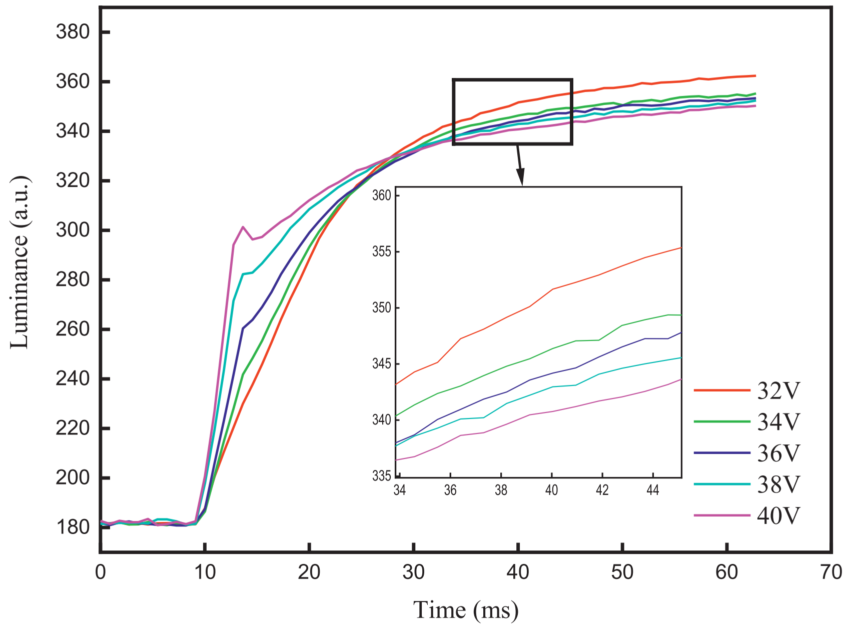

FIGURE 5 | The luminance rising curves of difference overdriving voltages. At the beginning, the rising speed of luminance was becoming faster when the overdriving voltage was increased. Then, the rising speed of luminance was decreased when the overdriving voltage was set higher than 32 V. The shortest response time was 26.39 ms when the overdriving voltage was 32 V.

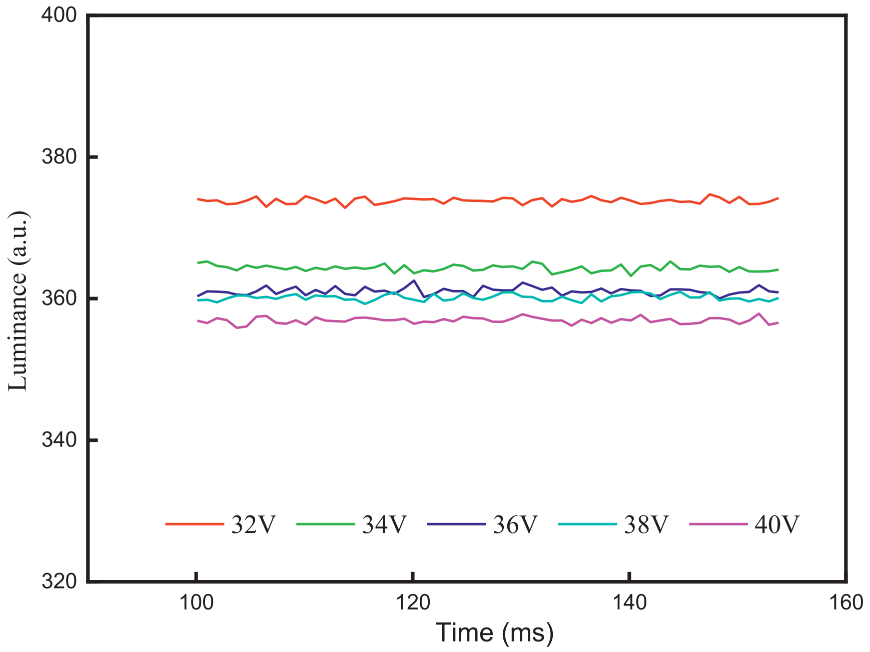

FIGURE 6 | The luminance of difference overdriving voltages. It was decreased when the overdriving voltage was increased. The highest luminance was 373.81 when the overdriving voltage was 32 V. The lowest luminance was 356.91 when the overdriving voltage was 40 V.

32 V. Therefore, the luminance was rose slowly in the driving stage. It can be seen that the response time was prolonged when the overdriving voltage was increased. The shortest response time was 26.39 ms when the overdriving voltage was 32 V. The luminance of difference overdriving voltages was shown in **Figure 6**. It can be seen that the luminance was decreased when the overdriving voltage was increased. The highest luminance was 373.81 when the overdriving voltage was 32 V.

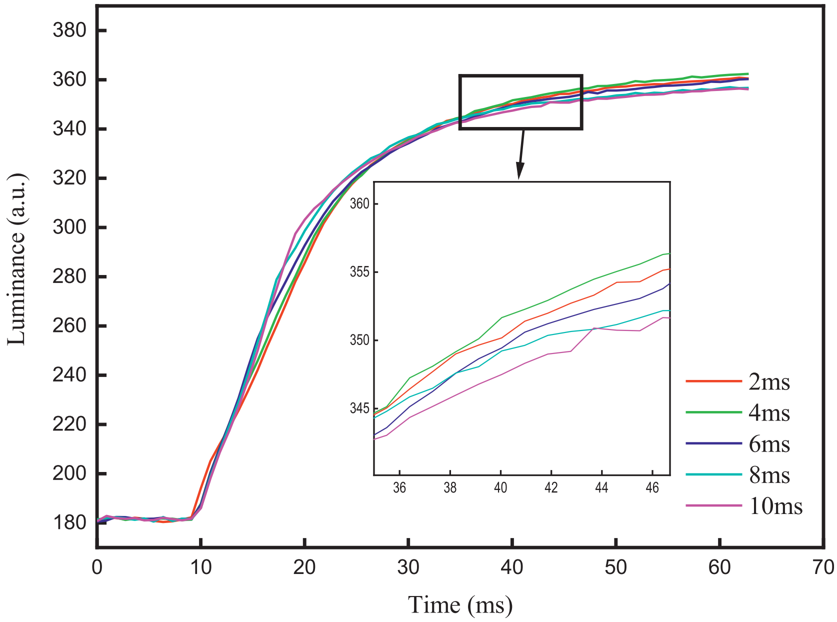

FIGURE 7 | The luminance rising curves of difference overdriving times. At the beginning of the luminance rising curves, the rising speed of the luminance was becoming faster when the overdriving time was increased. However, the rising speed of luminance was decreased during the transition from the overdriving stage to the driving stage when the overdriving time was longer than 4 ms. The shortest response time was 26.39 ms when the overdriving time was 4 ms.

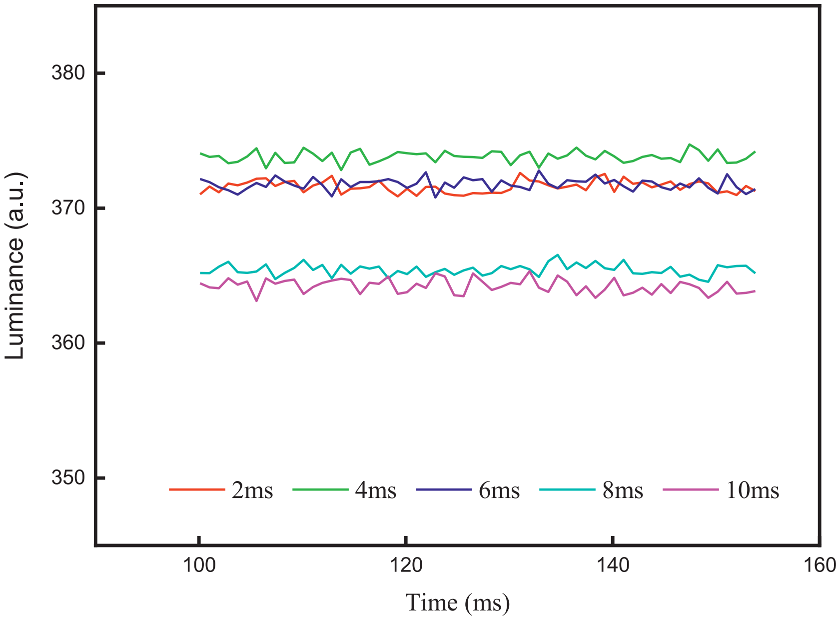

FIGURE 8 | The luminance of difference overdriving times. The highest luminance was 373.81 when the overdriving time was 4 ms. The lowest luminance was 364.21 when the overdriving time was 10 ms.

At this time, the decrease of the electrostatic force caused by the charge trapping was less than the increase of the electrostatic force caused by overdriving voltages. Therefore, the overdriving voltage should be set to 32 V for achieving a better performance.

The Effect of Overdriving Times

The effect of overdriving times was analyzed by testing the response time and luminance of the EWD. In the driving waveform, the overdriving voltage was set to 32 V, and the

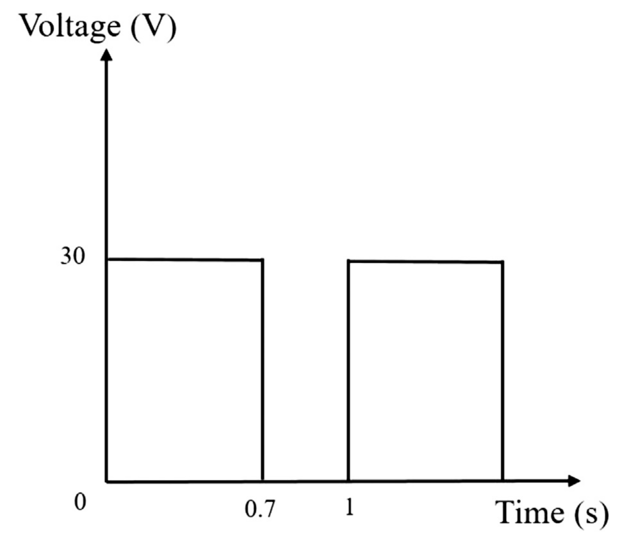

FIGURE 9 | A PWM driving waveform. Its voltage amplitude, frequency and duty cycle were 30 V, 1 Hz and 70% respectively.

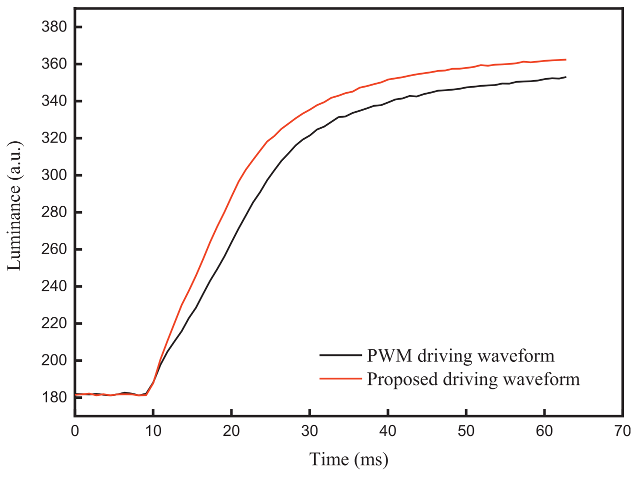

FIGURE 10 | The comparison of response times between the proposed driving waveform and the PWM driving waveform. The red line represented the proposed driving waveform, its response time was 26.39 ms. The black line represented the PWM driving waveform, its response time was 37.31 ms.

overdriving times were set to 2 ms, 4 ms, 6 ms, 8 ms, and 10 ms. The luminance rising curves of difference overdriving times were shown in **Figure 7**. At the beginning of luminance rising curves, the rising speed of luminance was becoming faster when the overdriving time was increased. However, the rising speed of luminance was decreased during the transition from the overdriving stage to the driving stage when the overdriving time was increased. The reason for this phenomenon was that more charges would be trapped in the hydrophobic insulating layer when the overdriving time was longer than 4 ms. Therefore, the luminance was rose slowly in the driving stage. The shortest response time was 26.39 ms when the overdriving time was 4 ms. The luminance of difference overdriving times was shown in **Figure 8**. The highest luminance was 373.81 when the overdriving voltage was 4 ms. At this time, the response speed and luminance were increased by overdriving voltages. Therefore, the overdriving time should be set to 4 ms for getting a better performance.

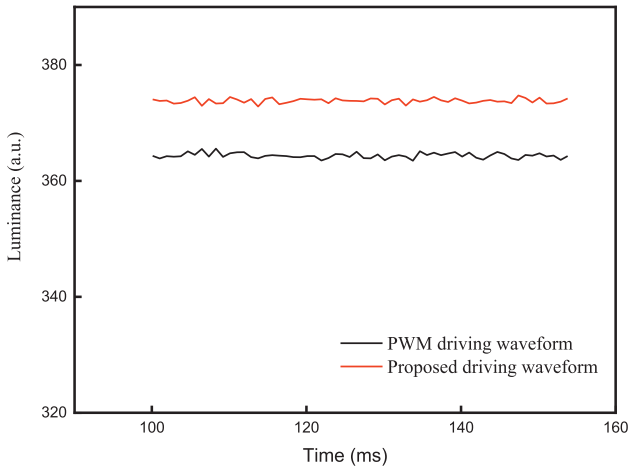

FIGURE 11 | The comparison of luminance between the proposed driving waveform and a PWM driving waveform. The red line represented the proposed driving waveform, its luminance was 373.81. The black line represented the PWM driving waveform, its luminance was 364.35.

Performance Testing

A PWM driving waveform was shown in **Figure 9**, and it was used to compare with the proposed driving waveform [11, 15]. The voltage amplitude, frequency and duty cycle of the PWM driving waveform were 30 V, 1 Hz and 70% respectively. The overdriving voltage and the overdriving time of the proposed driving waveform were 32 V and 4 ms respectively. The comparison of response time between the proposed driving waveform and the PWM driving waveform was shown in **Figure 10**. It can be seen that the response time of the proposed driving waveform was shorter than that of the PWM driving waveform. Specifically, the response time of the proposed driving waveform was 26.39 ms, and the response time of the PWM driving waveform was 37.31 ms. So, the response time was shortened by 29.27%. The comparison of luminance between the proposed driving waveform and the PWM driving waveform was shown in **Figure 11**. The luminance of the proposed driving was 373.81, and the luminance of the PWM driving waveform was 364.35. So, the luminance was increased by 2.60%. In the EWD, the response time and the luminance mainly depended on electrostatic force. The electrostatic force of the EWD was increased by the overdriving voltage in the proposed driving waveform. So, the response time can be shortened and the luminance can be increased compared with the PWM driving waveform.

CONCLUSION

In this paper, a driving waveform, which based on overdriving voltages and charge trapping theory, was proposed to shorten the response time in EWDs. The relationship between driving voltage and response time was established by a physical model of EWDs. Then, the response speed of oil was increased by an overdriving stage. In addition, a better performance of EWDs was achieved by charge trapping theory, and an experimental platform was developed to verify the effectiveness of the driving waveform. The response time of EWDs was shortened by using the driving waveform, which provided a certain reference for the application and development of EWDs.

DATA AVAILABILITY STATEMENT

The original contributions presented in the study are included in the article/Supplementary Material, further inquiries can be directed to the corresponding author.

AUTHOR CONTRIBUTIONS

WZ and ZY designed this project. WZ and MY carried out most of the experiments and data analysis. WZ, SM, and XZ performed part of the experiments and helped with discussions during manuscript preparation. HF, LL, and LS contributed to the data analysis and correction. GZ, JY, and GZ gave suggestions on project management and provided helpful discussions on the experimental results. All authors have read and agreed to the published version of the manuscript.

FUNDING

This research was funded by the Guangdong Basic and Applied Basic Research Foundation (No. 2020A1515010420), the Key Research Platforms and Research Projects in Universities and Colleges of Guangdong Provincial Department of Education (No. 2018KQNCX334), the Zhongshan Innovative Research Team Program (No. 180809162197886), Guangdong Provincial Key Laboratory of Optical Information Materials and Technology (No. 2017B030301007), the Zhongshan Institute high-level talent scientific research startup fund project (No. 416YKQ04), the Project for Innovation Team of Guangdong University (No. 2018KCXTD033), and the National Key R&D Program of China (No. 2018YFB0407100-02).

REFERENCES

1. Kim DY, Steckl AJ. Electrowetting on paper for electronic paper display. *ACS Appl Mater Interfaces* (2010) 2:3318–23. doi:10.1021/am100757g
2. Bai PF, Hayes RA, Jin ML, Shui LL, Yi Z, Wang L, et al. Review of paper-like display technologies. *Prog Electromagn Res* (2014) 147:95–116. doi:10.2528/PIER13120405
3. Kao WC, Tsai JC. Driving method of three-particle electrophoretic displays. *IEEE Trans Electron Dev* (2018) 65:1023–8. doi:10.1109/TED.2018.2791541
4. Wang L, Yi Z, Jin ML, Shui LL, Zhou GF. Improvement of video playback performance of electrophoretic displays by optimized waveforms with shortened refresh time. *Displays* (2017) 49:95–100. doi:10.1016/j.displa.2017.07.007
5. He W, Yi Z, Shen S, Huang Z, Liu L, Zhang T, et al. Driving waveform design of electrophoretic display based on optimized particle activation for a rapid response speed. *Micromachines* (2020) 11:498. doi:10.3390/mi11050498
6. Yi Z, Bai P, Wang L, Zhang X, Zhou G, An electrophoretic display driving waveform based on improvement of activation pattern. *J Cent S Univ* (2014) 21: 3133–7. doi:10.1007/s11771-014-2285-9
7. Shen S, Gong Y, Jin M, Yan Z, Xu C, Yi Z, et al. Improving electrophoretic particle motion control in electrophoretic displays by eliminating the fringing effect via driving waveform design. *Micromachines* (2018) 9:143. doi:10.3390/mi9040143
8. Van DR, Feenstra BJ, Hayes RA, Camps IGJ, Boom RGH, Wagemans MMH, et al. Gray scales for video applications on electrowetting displays. *Sid Symp Dig Tech Pap* (2006) 37:1926. doi:10.1889/1.2433427
9. Chae JB, Hong J, Lee SJ, Chung SK. Enhancement of response speed of viscous fluids using overdrive voltage. *Sensor Actuator B Chem* (2015) 209:56–40. doi:10.1016/j.snb.2014.11.076
10. Jin ML, Shen ST, Yi ZC, Zhou GF, Shui LL. Optofluid-based reflective displays. *Micromachines* (2018) 9:159. doi:10.3390/mi9040159
11. Yi Z, Shui L, Wang L, Jin M, Hayes R, Zhou G. A novel driver for active matrix electrowetting displays. *Displays* (2015) 37:86–93. doi:10.1016/j.displa.2014.09.004
12. Oh JM, Ko SH, Kang KH. Shape oscillation of a drop in ac electrowetting. *Langmuir* (2008) 24:8379–86. doi:10.1021/la8007359
13. Zhang XM, Bai PF, Hayes RA, Shui LL, Jin ML, Tang B, et al. Novel driving methods for manipulating oil motion in electrofluidic display pixels. *J Disp Technol* (2016).12:200–5. doi:10.1109/JDT.2015.2477947
14. Yi Z, Liu L, Wang L, Li W, ShuiZhou LG. A driving system for fast and precise gray-scale response based on amplitude–frequency mixed modulation in TFT electrowetting displays. *Micromachines* (2019) 10:732. doi:10.3390/mi10110732
15. Yi Z, Huang Z, Lai S, He W, Wang L, Chi F, et al. Driving waveform design of electrowetting displays based on an exponential function for a stable grayscale and a short driving time. *Micromachines* (2020) 11:313. doi:10.3390/mi11030313
16. Lin S, Zeng S, Qian M, Lin Z, Guo T, Tang B. Improvement of display performance of electrowetting displays by optimized waveforms and error diffusion. *J Soc Inf Disp* (2019) 27:619–29. doi:10.1002/jsid.790
17. Li W, Wang L, Zhang T, Lai S, Liu L, He W, et al. Driving waveform design with rising gradient and sawtooth wave of electrowetting displays for ultra-low power consumption. *Micromachines* (2020) 11:145. doi:10.3390/mi11020145
18. Xie N, Zhang N, Xu RQ. Effect of driving voltage polarity on dynamic response characteristics of electrowetting liquid lens. *Jpn J Appl Phys* (2018) 57:052201. doi:10.7567/JJAP.57.052201
19. Luo ZJ, Luo JK, Zhao WW, Cao Y, Lin WJ, Zhou GF. A high-resolution and intelligent dead pixel detection scheme for an electrowetting display screen. *Opt Rev* (2018) 25:18–26. doi:10.1007/s10043-017-0382-3
20. Luo ZJ, Zhang WN, Liu LW, Xie ST, Zhou GF. Portable multi-gray scale video playing scheme for high-performance electrowetting displays. *J Soc Inf Disp* (2016) 24:345–54. doi:10.1002/jsid.444
21. Zhou M, Zhao Q, Tang B, Groenewold J, Hayes RA, Zhou GF. Simplified dynamical model for optical response of electrofluidic displays. *Displays* (2017) 49:26–34. doi:10.1016/j.displa.2017.05.003
22. Shubhi B, Prosenjit S. Effect of electrowetting induced capillary oscillations on coalescence of compound droplets. *J Colloid Interface Sci* (2018) 530:223–32. doi:10.1016/j.jcis.2018.05.090
23. Gao J, Mendel N, Dey R, Baratian D, Mugele F. Contact angle hysteresis and oil film lubrication in electrowetting with two immiscible liquids. *Appl Phys Lett* (2018) 112:203703. doi:10.1063/1.5034510

24. Roghair I, Musterd M, van den Ende D, Kleijn CR, Kreutzer M, Muggle F. A numerical technique to simulate display pixels based on electrowetting. *Phys Fluids* (2015) 19:465–82. doi:10.1007/s10404-015-1581-5
25. Hayes RA, Feenstra BJ. Video-speed electronic paper based on electrowetting. *Nature* (2003) 425:383–5. doi:10.1038/nature01988
26. Roques CT, Hayes R, Schlangen L. A physical model describing the electro-optic behavior of switchable optical elements based on electrowetting. *J Appl Phys* (2004) 96:6267–71. doi:10.1063/1.1810192
27. Zhao Q, Tang B, Dong BQ, Li H, Zhou R, Guo YY, et al. Electrowetting on dielectric: experimental and model study of oil conductivity on rupture voltage. *J Phys D Appl Phys* (2018) 51:195102. doi:10.1088/1361-6463/aabb69
28. Roques CT, Hayes R, Feenstra B, Schlangen L. Liquid behavior inside a reflective display pixel based on electrowetting. *J Appl Phys* (2004) 95: 4389–96. doi:10.1063/1.1667595
29. Verheijen HJJ, Prins MWJ. Reversible electrowetting and trapping of charge: model and experiments. *Langmuir* (1999) 15:6616–20. doi:10.1021/la990548n
30. Li XM, Tian HM, Shao JY, Ding YC, Chen XL, Wang L, et al. Decreasing the saturated contact angle in electrowetting-on-dielectrics by controlling the charge trapping at liquid-solid interfaces. *Adv Funct Mater* (2016) 26: 2994–3002. doi:10.1002/adfm.201504705

Conflict of Interest: The authors declare that the research was conducted in the absence of any commercial or financial relationships that could be construed as a potential conflict of interest.

frontiers in Physics

ORIGINAL RESEARCH
published: 16 March 2021
doi: 10.3389/fphy.2021.655547

Driving Scheme Optimization for Electrowetting Displays Based on Contact Angle Hysteresis to Achieve Precise Gray-Scales

Li Wang[1], *Hu Zhang*[2], *Wei Li*[3]*, *Jiaxuan Li*[4], *Zhenyu Yi*[4], *Qiming Wan*[1], *Jitao Zhang*[1] and *Pengchang Ma*[1]

[1] School of Information Engineering, Zhongshan Polytechnic, Zhongshan, China, [2] School of Electronic Science and Engineering (National Exemplary School of Microelectronics), University of Electronic Science and Technology of China, Chengdu, China, [3] South China Academy of Advanced Optoelectronics, South China Normal University, Guangzhou, China, [4] College of Electron and Information, Zhongshan Institute, University of Electronic Science and Technology of China, Zhongshan, China

Edited by:
Qiang Xu,
Nanyang Technological University, Singapore

Reviewed by:
Xiaowen Zhang,
Guilin University of Electronic Technology, China
Zhijie Luo,
Zhongkai University of Agriculture and Engineering, China

***Correspondence:**
Wei Li
wei.li@guohua-oet.com

Specialty section:
This article was submitted to Optics and Photonics, a section of the journal Frontiers in Physics

Received: *19 January 2021*
Accepted: *22 February 2021*
Published: *16 March 2021*

Citation:
Wang L, Zhang H, Li W, Li J, Yi Z, Wan Q, Zhang J and Ma P (2021) Driving Scheme Optimization for Electrowetting Displays Based on Contact Angle Hysteresis to Achieve Precise Gray-Scales. Front. Phys. 9:655547. doi: 10.3389/fphy.2021.655547

As a new display technology, electrowetting display (EWD) has many excellent display characteristics, such as paper-like, low power consumption, quick response and full color. These characteristics make EWD devices very suitable for portable devices. However, the gray-scale distortion caused by the contact angle hysteresis of EWDs seriously affects the accuracy of gray-scale display. To improve this phenomenon, the hysteresis curve of an EWD panel was studied according to the motion characteristics of advancing contact angle and receding contact angle of oil in a pixel. Then, a driving scheme for EWDs using alternating current (AC) voltage instead of direct current (DC) voltage was proposed in this paper. And the advantages and disadvantages of the driving scheme at different AC frequencies from 90 to 2,700 Hz were analyzed through experiments. According to the stability of aperture ratio in EWDs, a 470 Hz AC driving scheme was determined. Experimental results showed that the aperture ratio distortion of EWDs could be reduced from 35.82 to 5.97%, which significantly improved the display performance of pixel units.

Keywords: electrowetting display, contact angle hysteresis, alternating current voltage, driving scheme, aperture ratio

INTRODUCTION

Electrowetting display (EWD) is a new type of electronic paper display technology with excellent display characteristics: (a) reflective display, paper-like reading experience [1]; (b) response speed of several milliseconds which can meet the needs of video playback [2]; (c) paper-like reflective display mode, with low power consumption [3]; (d) high reflectivity and true color display can be implemented [4]; (e) pixel structure can be attached to flexible backplanes [5]; (f) high degree of overlap with the existing liquid crystal display (LCD) manufacturing process, which means a low manufacturing cost [6]. These advantages make EWD technology to be known as the most promising next-generation paper-like display technology.

The EWD technology was first proposed by Beni and Hackwood [7]. In 2003, Hayes proposed a fast display EWD scheme, which could realize a simple video playback function [8]. However, when EWDs were driven, the phenomenon of contact angle hysteresis would occur, which had a bad effect on the gray-scale display performance of pixels in EWDs [9, 10]. The linear inconsistency of advancing contact angle and receding contact angle increased the complexity for controlling gray-scales [11]. In the process of pixel gray-scales display, it is difficult to control the gray-scale accurately, and gray-scale distortion may be caused. Therefore, it is necessary to analyze the influence of contact angle hysteresis and study how to optimize the contact angle hysteresis in EWDs.

Many scholars have studied the hysteresis phenomenon of EWDs. An AC voltage driving scheme was proposed by studying the balance among the surface tension of oil wetting, pinning force and electrostatic force on the contact line. It was proved that the hysteresis of the contact angle of a moving droplet could be reduced during a wetting process [12]. However, researchers did not further explore parameters of the AC voltage. Then, according to pixel characteristics, two driving methods of using hydrophilic patches or adding steps for pixels were proposed to enhance the motion control of oil and realize a hysteresis-free gray-scale conversion of pixels [13]. However, the transparent electrode of the pixel could be blocked by hydrophilic patches and the increased steps, which could reduce the reflectivity of a pixel. And then, a driving waveform with an optimized voltage slope was proposed, this method can improve the aperture ratio and reduce the hysteresis of pixels [14]. Although the PWM (pulse width modulation) could compensate for the hysteresis to a certain extent, it means an increase of response time, a decrease of effective frames, and an increase of power consumption [15]. At the same time, the PWM can only be used in fully opened and completely closed for driving a pixel, and the display ability of EWDs is limited by this feature.

In this paper, the influence of contact angle hysteresis on the gray-scale was analyzed when the driving voltage was turned on and off, and an AC voltage driving scheme was proposed, the influence of contact angle hysteresis on display performance could be significantly reduced by the proposed AC driving scheme compared with the traditional DC voltage driving scheme.

PRINCIPLES OF SYSTEM DESIGN

Display Principle of EWDs

Wettability is great significance for EWDs. Wettability describes the relationship between the contact angle and the surface tension of droplets. The surface tension can be expressed by equation (1), γ_{LG} is a liquid-gas surface tension, f is the frequency of the surface wave, λ is the wavelength of the surface wave, ρ is the density of droplets. The relationship between contact angle and surface tension can be expressed by equation (2) [16], θ_0 is a static contact angle, γ_{SG} is a solid-gas surface tension and γ_{SL} is a solid-liquid surface tension.

$$\gamma_{LG} = \frac{f^2\lambda^3\rho}{2\pi} \tag{1}$$

$$\cos\theta_0 = (\gamma_{SG} - \gamma_{SL})\frac{2\pi}{f^2\lambda^3\rho} \tag{2}$$

Lippmann-Young equation was first proposed by Gabriel Lippmann in 1898, and it is regarded as the theoretical foundation of electrowetting. This equation describes the changing process of the contact angle of droplets on the solid surface with an applied voltage. As shown in equation (3) [17]:

$$\cos\theta = \frac{\gamma_{se} - \gamma_{so}}{\gamma_{eo}} + \frac{1}{2}\frac{\varepsilon_0\varepsilon_r}{d\gamma_{eo}}V^2 \tag{3}$$

Where, θ is the contact angle when driving voltage is V, ε_0 is the vacuum dielectric constant, ε_r is the relative dielectric constant, d is the thickness of a hydrophobic insulation layer, γ_{eo} is the interface tension between oil and electrolyte solution, and V is the driving voltage. As shown in **Figure 1**, The other two interfacial tensions are γ_{so} and γ_{se}, γ_{so} is the interfacial tension between the hydrophobic insulation layer and oil. γ_{se} is the interfacial tension between the hydrophobic insulation layer and electrolyte solution. When the driving voltage is $0V$, the non-polar oil is laid on the hydrophobic insulation layer, and the contact angle is small, close to zero.

EWD is an optical switch for realizing gray-scale display by controlling the movement of colored oil by applying voltage. In practical application, the display is realized by an optical stack. It consists of a white substrate, a hydrophobic insulation layer, colored oil, water and an ITO (indium tin oxide) glass. When the voltage is turned off, the force among the colored oil, the hydrophobic insulation layer and the water is balanced. At this time, $\gamma_{eo} > \gamma_{so}$, and contact angle $\theta < 90$. The colored oil is laid between the water and the hydrophobic insulation, which can show a hydrophilicity and become a continuous spreading film. And we could see the color of oil, as shown in **Figure 2A**, the state is in the lowest energy state at this time.

Next, the voltage is connected to the upper and lower plates of ITO. As shown in **Figure 2B**, according to Lippmann-Young equation, with the increase of electric field, the surface tension among insulation layer, oil film and water can be increased, and the indirect antennae of the interface become larger. The original balance can be broken by the electric field force generated by the voltage difference. Water instead of the oil to contact with the hydrophobic insulation layer surface. At this time, $\gamma_{eo} < \gamma_{so}$, and contact angle $\theta > 90$. The oil is pushed to a corner of pixels, so pixels show color of the white substate. The colored oil shows hydrophobicity.

Principle of Contact Angle Hysteresis

In an EWD driving process, as the driving voltage increases from $0V$ to the maximum voltage V_m, the oil in the pixel is gradually gathered. When the driving voltage reaches the maximum value, the oil can be completely pushed to a corner. In this process, the higher the voltage, the larger the contact angle. The process of increasing voltage is the advancing process, and the contact angle is also called as advancing angle. On the contrary, the process of reducing the voltage from V_m to $0V$ is called as receding process, and the contact angle at this time is also called as the receding angle. With a same driving voltage value, the difference between the advancing angle and the receding angle is the contact angle hysteresis in EWDs.

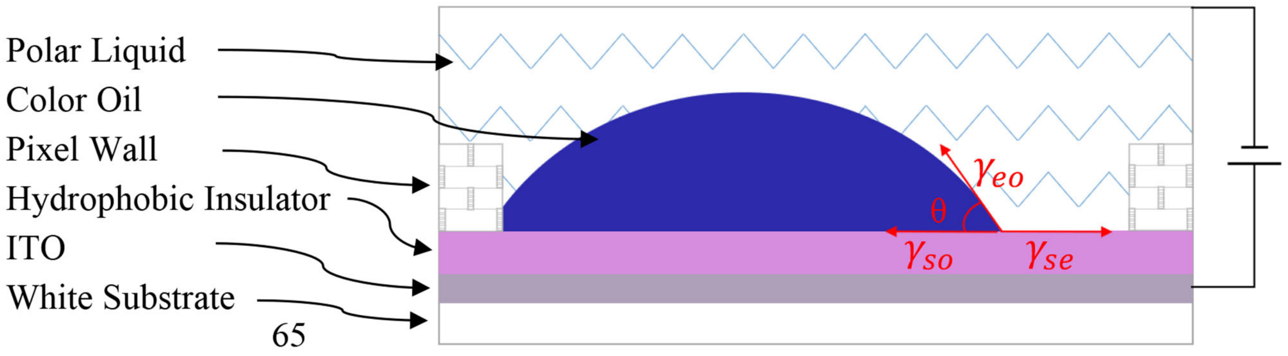

FIGURE 1 | The structure of an EWD pixel. The colored oil was pushed to a corner of the pixel by driving voltage. The pixel would display the color of oil and part of the white substrate.

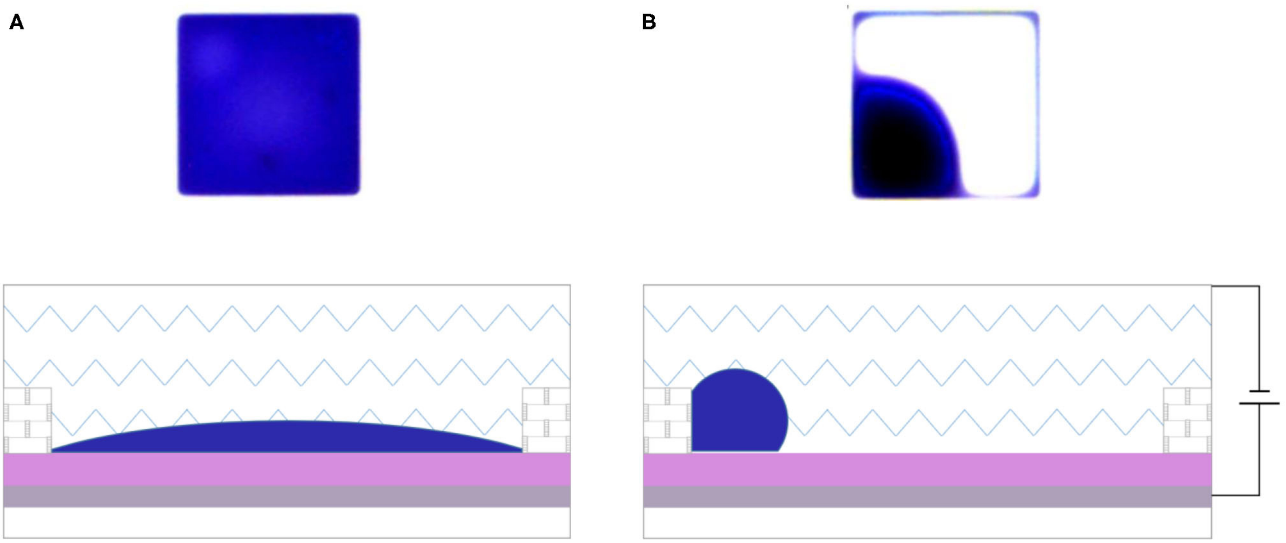

FIGURE 2 | Display principle of an EWD pixel. **(A)** When the pixel was turned off, the whole pixel was covered by oil, the color of oil was reflected. **(B)** When the pixel was turned on, the oil was pushed into a corner of the pixel, the color of substrate was reflected.

The aperture ratio is a proportion of the exposed white substrate area in a whole pixel. The different aperture ratio represents different optical states. The surface area of oil can be expressed as equation (4), and the aperture ratio can be defined as equation (5) [18].

$$S_{oil} = \pi \sin^2\theta \left(\frac{B_{oil}}{\frac{2}{3}\pi\left(1 - \frac{3}{2}cos\theta + \frac{1}{2}\cos^3\theta\right)} \right)^{\frac{2}{3}} \tag{4}$$

$$W_A(V) = \left(1 - \frac{\pi \sin^2\theta B_{oil}{}^{\frac{2}{3}}}{S_{pix}\left(\frac{2}{3}\pi\left(1 - \frac{3}{2}cos\theta + \frac{1}{2}\cos^3\theta\right)\right)^{\frac{2}{3}}} \right) \times 100\% \tag{5}$$

Where, $W_A(V)$ is the aperture ratio, S_{oil} represents the surface area of oil when voltage V is applied to EWDs. S_{pix} is the surface area of a whole pixel, and B_{oil} is the volume of the oil. The pixel wall can divide an EWD into several pixels. This transparent grid structure has a small area which can be ignored in calculating the aperture ratio.

EXPERIMENTAL RESULTS AND DISCUSSION

Experimental Platform and Experimental Materials

In order to measure the display state of pixels, a complete experimental platform was built. As shown in **Figure 3**, the experimental equipment mainly includes: (a) is a GDS-3354 oscilloscope (Shanghai GuWei Electronics Co., Ltd, Shanghai, China); (b) is an AFG3052C function generator, produced by Tektronix (United States); (c) is an ATA-2022H amplifier, produced by Agitek (Xi'an, China); (d) is a XTL-165 microscope, produced by Phenix (Jiangxi, China), and (e) is a computer. The experimental process was described as follows: First, the required waveform was edited by the computer. Second, the

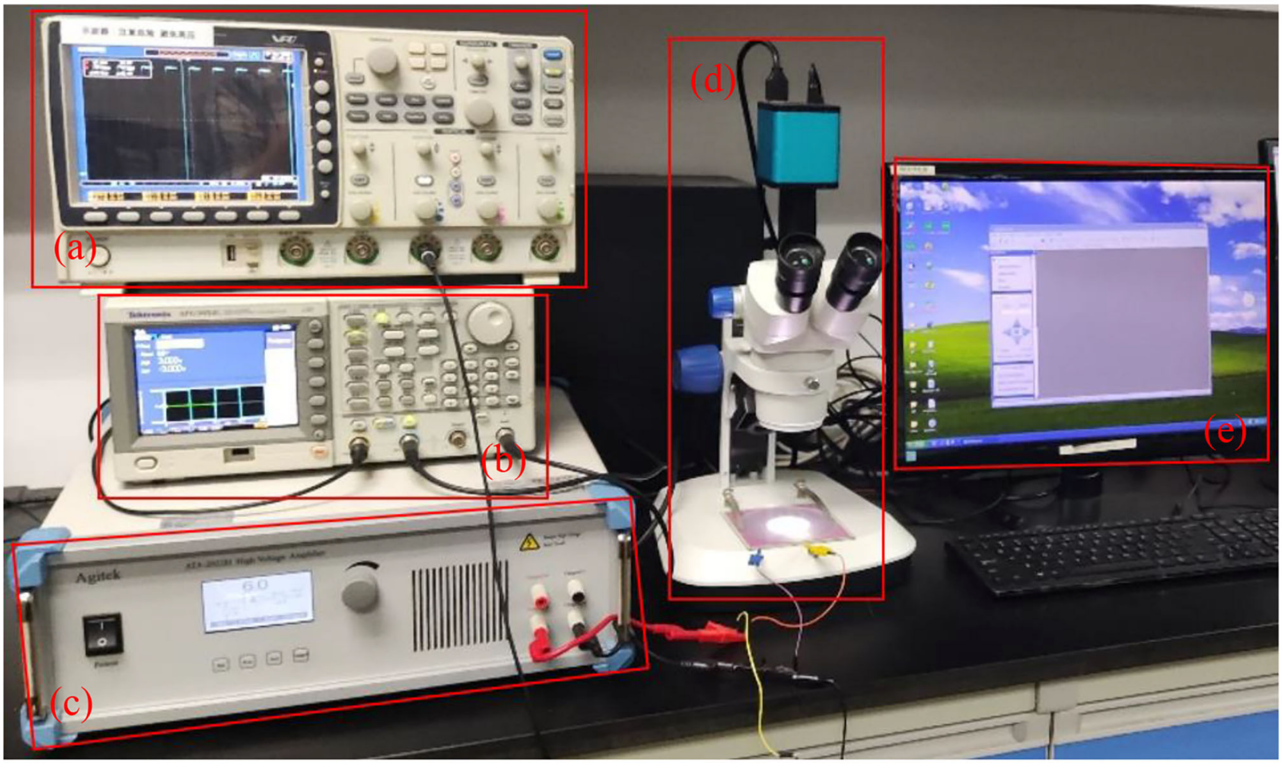

FIGURE 3 | Experimental platform for the testing of EWD contact angle hysteresis. It was composed of driving system and testing system. **(a)** Oscilloscope. **(b)** Function generator. **(c)** Amplifier. **(d)** Microscope. **(e)** Computer.

TABLE 1 | Parameters of the EWD panel.

Panel size (cm^2)	Oil color	Resolution	Pixel size (μm^2)	Height of pixel (μm)	ITO layer (nm)	Hydrophobic layer thickness
10 × 10	Blue	320 × 240	150 × 150	18	2.5	800 nm

voltage sequence of the waveform was generated by the waveform generator, and the voltage was amplified by the amplifier. Then the output voltage of the amplifier was applied to an EWD panel. Finally, the video stream was captured by the high-speed camera combined with the microscope and displayed on another computer. The aperture ratio was calculated by a software.

The materials of an EWD panel used in the experiment are as follows. The material of hydrophobic insulating layer was Teflon AF1600, and the solution was a fluorocarbon solvent FC-43 of 3M Company in United States. Transparent polyimide was used as the grid material of pixel walls. Photoresist was SU-83005 which came from Microchem. The ITO glass substrate came from Shenzhen Laibao High-Tech Co., Ltd, with a thickness of 0.7 mm and an impedance of 100 Ω/cm2. The electrolyte solution was sodium chloride solution with a concentration of 1 × 10-4 mol/L, deionized water was obtained by an ultra-pure ultraviolet water purification system. And the parameters of the EWD panel were listed in **Table 1**.

Effect of Contact Angle Hysteresis on EWDs

During the driving process of EWDs, the period that the driving voltage increases from 0V to the maximum voltage and then decreases from the maximum voltage to 0V is called a driving period T. In 0-T/2, the driving voltage can be gradually increased, and the pixel oil gradually shrinks from the flat state to a corner in a pixel. In the process from T/2 to T, the oil state should be completely opposite to the first half cycle. In this case, the oil could be controlled more precisely and achieve a multiple gray-scale display.

However, the state of oil is different from an ideal situation. Two identical EWD panels were used to test the impact of contact angle hysteresis. The driving voltage was increased from 0 to 20V and decreased from 30 to 20V respectively. When starting voltages were different, the gray-scale obtained was different with a same target driving voltage. As shown in **Figure 4**, when the driving voltage was increased from 0 to 20V, the pixel aperture ratio was 24.85%; when the driving voltage was decreased from

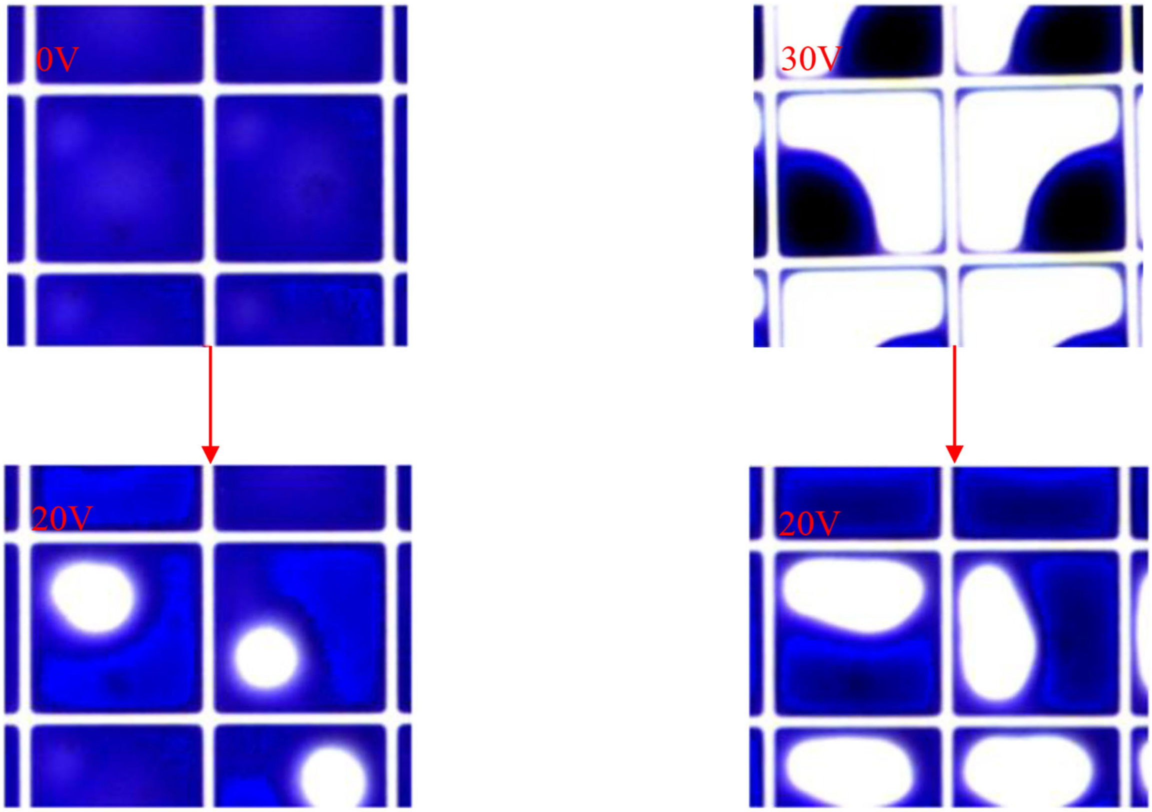

FIGURE 4 | Inconsistent performance of aperture ratio in a pixel. The driving voltage was increased from 0 to 20V and decreased from 30 to 20V, respectively, the aperture ratio was different at 20V.

30 to 20V, the pixel aperture ratio was 40.12%. The maximum difference of the aperture ratio was 15.27%. During the process of driving voltage increased from 0 to 20V, the electric field force increased, and the oil was pushed to achieve a balance state. During the process of driving voltage decreased from 30 to 20V, the electric field force decreased, and the oil spread naturally due to the wetting effect. Due to the coarseness of hydrophobic insulation layer and the existence of charge trapping, the rising and falling process was asymmetric. This phenomenon is called hysteresis effect, and also can be called gray-scale distortion. The smaller the difference, the smaller the gray-scale distortion. This gray-scale distortion phenomenon was caused by contact angle hysteresis.

Contact Angle Hysteresis in DC Driving Scheme and AC Driving Scheme

In order to study the effect of contact angle hysteresis on aperture ratio of EWDs, some experiments were designed in this paper. The traditional square wave was selected to drive an EWD panel, and 60 Hz was determined as the default driving frequency [3]. As shown in **Figure 5**, they are square waves in DC driving scheme and AC driving scheme, respectively. The relationship between driving voltage and aperture ratio in DC driving scheme and AC driving scheme were tested. During experiments, the overall trend of the pixel aperture ratio was increasing with the increasing of driving voltage. When the driving voltage was decreased, the aperture ratio was decreased, and finally returned to a flat state. When the voltage was increased from 0 to 30V, the oil state was in the forward process. When the voltage was decreased from 30 to 0V, the oil state was in the backward process. When the driving voltage was higher than 30V, the pixel could be broken down.

The test results are shown in **Figure 6**. **Figure 6A** shows the result of square wave in DC driving scheme, the range of aperture ratio was 1–61.48%. At both ends of the driving voltage value, the distortion of the aperture ratio was small. When the driving voltage was in the middle stage, the rate of the aperture ratio distortion was bigger. Among these situations, when the driving voltage was 16V, the maximum distortion could reach to 35.82%. During an entire EWD process, the scale distortion interval of gray-scale was 0–35.82%. **Figure 6B** shows the result of square wave in AC driving scheme, the range of aperture ratio was 1–58.71%. At both ends of the driving voltage value, the distortion of the aperture ratio was small. When the driving voltage was in the middle stage, the rate of the aperture ratio distortion was bigger. Among these situations, when the driving voltage was 13V, the maximum distortion could reach to 20.84%.

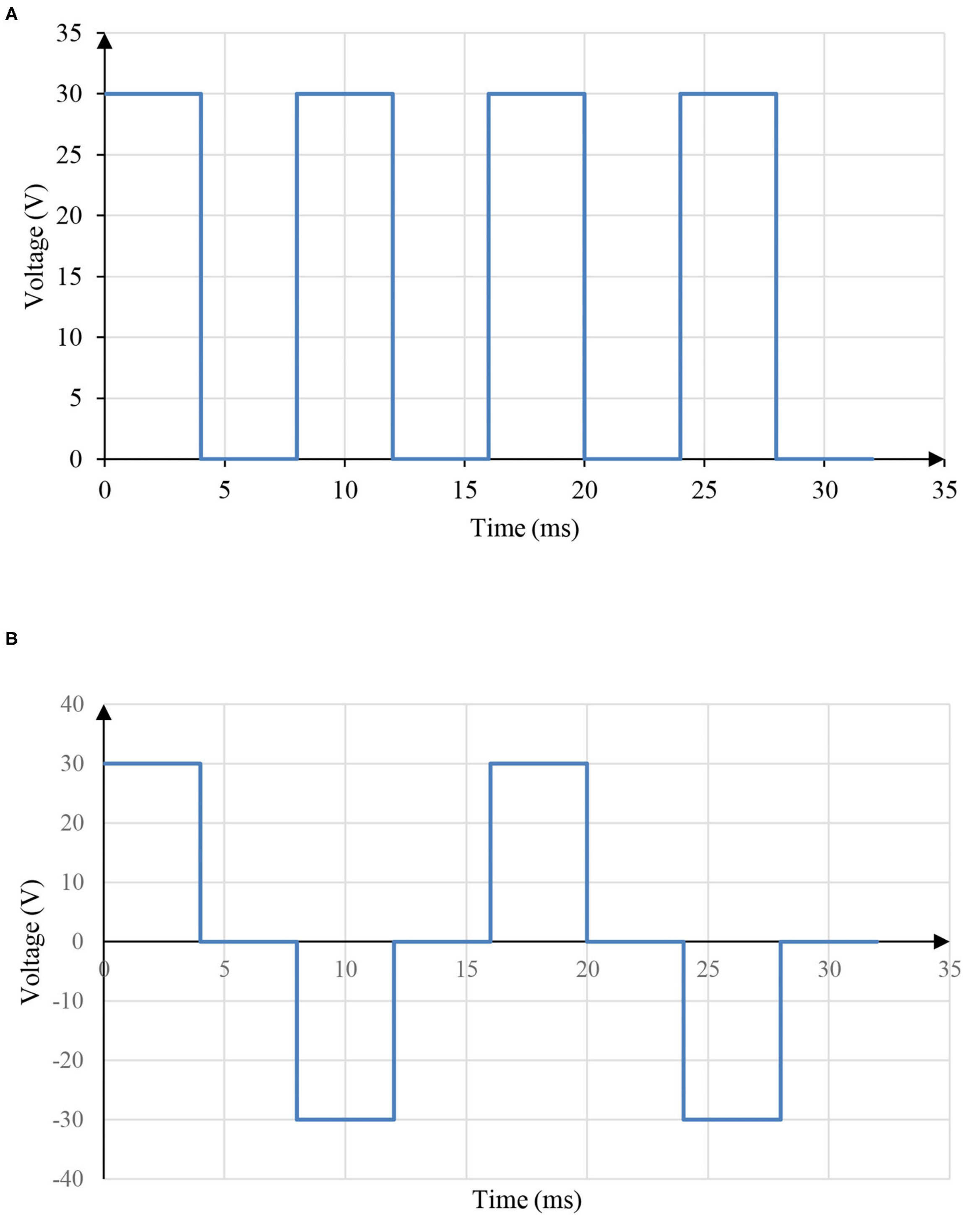

FIGURE 5 | Square waves in DC driving scheme and AC driving scheme. **(A)** The square wave in DC driving scheme. **(B)** The square wave in AC driving scheme.

During an entire EWD process, the scale distortion interval of gray-scale was 0–20.84%. It can be seen that the contact angle hysteresis of AC driving scheme is lower than that of DC driving scheme.

Frequency Optimization for the AC Driving Scheme

In order to determine the optimal driving frequency, more experiments were designed. The maximum voltage in AC driving

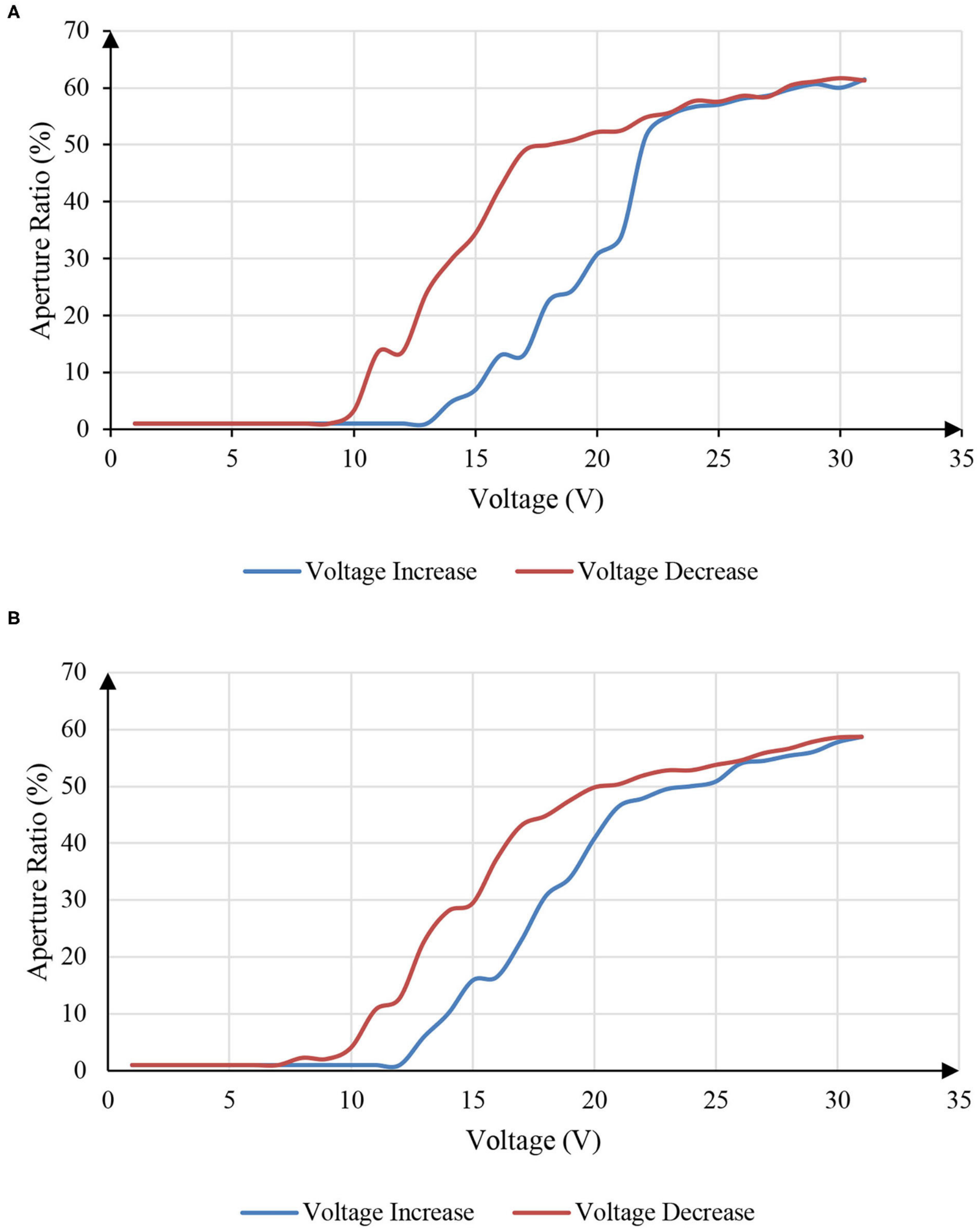

FIGURE 6 | Hysteresis curves of an EWD driven by DC driving scheme and AC driving scheme. The black curve showed the aperture ratio when driving voltage was increased from 0 to 30V, and the red curve showed the aperture ratio when driving voltage was decreased from 30 to 0V. **(A)** The hysteresis curve of an EWD driven by DC driving scheme. **(B)** The hysteresis curve of an EWD driven by AC driving scheme.

scheme used in this paper was 30V. And AC voltages with frequency of 90–2,700 Hz were applied to EWD panels. Then the average value of aperture ratio was recorded, simulated and calculated by a microscope.

As shown in **Figure 7**, when the frequency was from 90 to 350 Hz, the oil in pixels was unstable, and pixels were opened for a short time and closed in an instant. In addition, the unstable state of oil in the pixel led to an oil splitting. Although the driving voltage was remained unchanged, the aperture ratio of the pixel was decreased gradually with the passage of time, and the stability of the aperture ratio was insufficient.

When the frequency was 350–500 Hz. The oil in pixels was stable, pixels were fully opened, the aperture ratio was 70.96%, and pixels were hardly closed within 12 s. When the frequency was 500–1,200 Hz, some pixels were fully opened, and others were not fully opened. The oil state was not stable enough. The overall aperture ratio of pixels varied from 62.10 to 56.33%. When the frequency was 1,200–2,700 Hz, the oil state in pixels was stable, but pixels were not fully opened, and the aperture ratio was stable at about 51.89%. At the same time, when the driving voltage was unchanged, the oil state had almost no change by time, and the aperture ratio was remained stable. When the driving voltage frequency was higher than 2,700 Hz, as the frequency was changed, the aperture ratio was remained at about 50.73%. Therefore, when the frequency was higher than 2,700 Hz, the influence of driving voltage and frequency on aperture ratio was very small.

In the process of an AC voltage driving with a constant frequency, the oil movement path became more stable over time. We tested the stability of the aperture ratio within 12 s when the frequency was 90, 175, 350, 470, 670, 1,200, 1,700, and 2,700 Hz. As shown in **Figure 8**.

It can be seen from **Figure 8** that the aperture ratio reached the maximum with frequency of 90 Hz. But the oil was gradually spread out from the fully contracted state within 2 s. After 5 s, the aperture ratio was decreased from about 69.76% to 50.77%. In addition, during the oil shrinking process, the oil state was unstable and split. At the same time, the oil in pixels was driven randomly to four corners, and it could affect the display brightness of pixels. Compared with the frequency of 90 Hz, the oil was more stable under the frequency of 175 Hz. But within 1 s, aperture ratio was decreased from 58.38 to

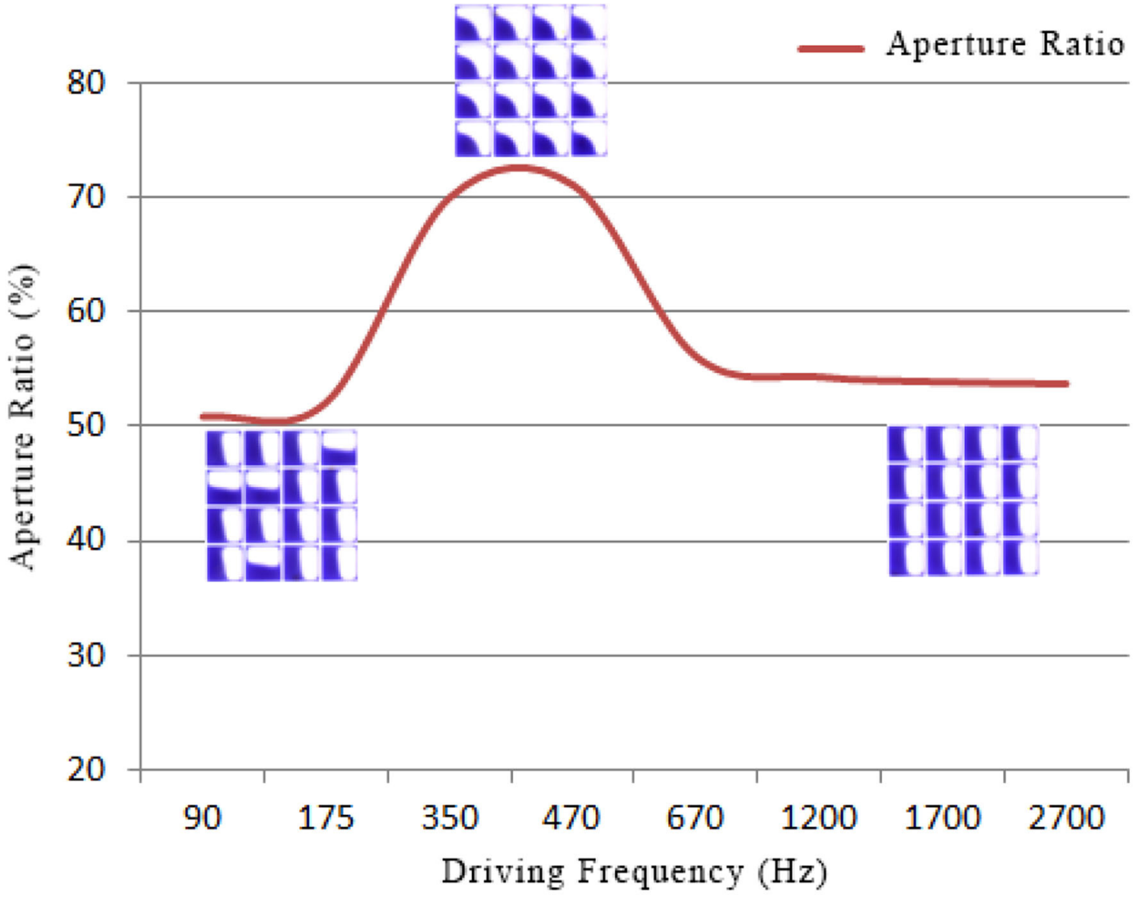

FIGURE 7 | The EWD was driven by a 30V AC driving voltage, the aperture ratio changed when the frequency was increased from 90 to 2,700 Hz. When the frequency was 350–500 Hz, pixels were fully opened.

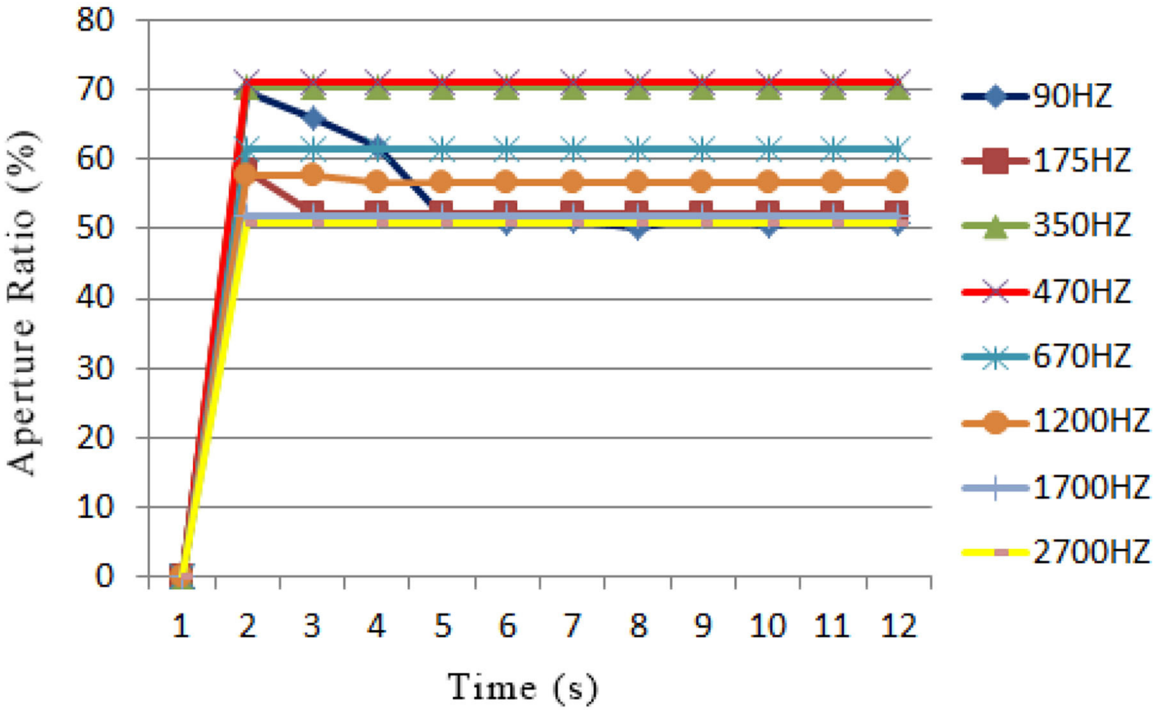

FIGURE 8 | The relationship between time and aperture ratio when an EWD was driven by a 30V AC driving voltage at different frequencies. The smoothness of curves represented the oil stability. The 470 Hz AC driving voltage had the largest aperture ratio and most stable aperture ratio.

52.11%. Then the aperture ratio was remained stable. When the frequency was higher than 350 Hz, the stability of aperture ratio was significantly improved. When the frequency was 350 and 470 Hz, the oil in pixels was completely contracted and remained stable within 12 s. When the frequency was 670 Hz, the aperture ratio was 61.33%, and pixels were not fully opened. At this time, the aperture ratio was stable. When the frequency was 1,200, 1,700, and 2,700 Hz, the aperture ratio and the oil state were stable, but pixels were not fully opened. Therefore, the 470 Hz AC driving voltage was selected in our driving scheme for EWDs.

The generation process of the 470 Hz AC driving voltage was as follows, the waveform generator can generate 470 Hz AC driving voltage with the maximum voltage difference of 10V. Therefore, the AC voltage was varied from +5 to −5V. Then the output of waveform generator was amplified 6 times by a high voltage amplifier, so that the AC driving voltage can be changed from +30 to −30V. During the AC driving process, the average value of the aperture ratio was calculated.

As shown in **Figure 9**, the red curve indicated that the driving voltage was increased from 10 to 25V and the blue curve indicated that the driving voltage was decreased from 25 to 10V. When the voltage was > 25V or < 10V, these two curves were coincident. In process (B), when the driving voltage was increased or decreased, the aperture ratio was basically the same, and the maximum difference between them was 3%. In process (A), when the difference of aperture ratio was the largest, the EWD is shown in the **Figure 10**. **Figure 10A** showed the aperture ratio of EWDs during the driving voltage increasing process, the average aperture ratio was 26.50%; **Figure 10B** showed the aperture ratio of EWDs during the driving voltage decreasing process, the average aperture ratio was 32.47%. Therefore, the maximum difference between them is 5.97%. When the traditional DC voltage was used, the maximum distortion was 35.82%. Although the distortion could not be completely eliminated, the aperture ratio distortion could be reduced by 29.85% with the AC driving scheme.

CONCLUSIONS

In order to reduce the distortion of aperture ratio and achieve precise control of gray-scales, an AC driving scheme was proposed for improving the performance of EWDs. This scheme can effectively reduce the influence of contact angle hysteresis. The advantages and disadvantages of AC driving voltages at different frequencies were analyzed by experiments. And then, according to the stability and aperture ratio of EWDs, a 470 Hz AC driving scheme was determined. Compared with traditional DC driving scheme, the aperture ratio distortion caused by contact angle hysteresis could be reduced to 5.97%. Therefore, this scheme could be applied

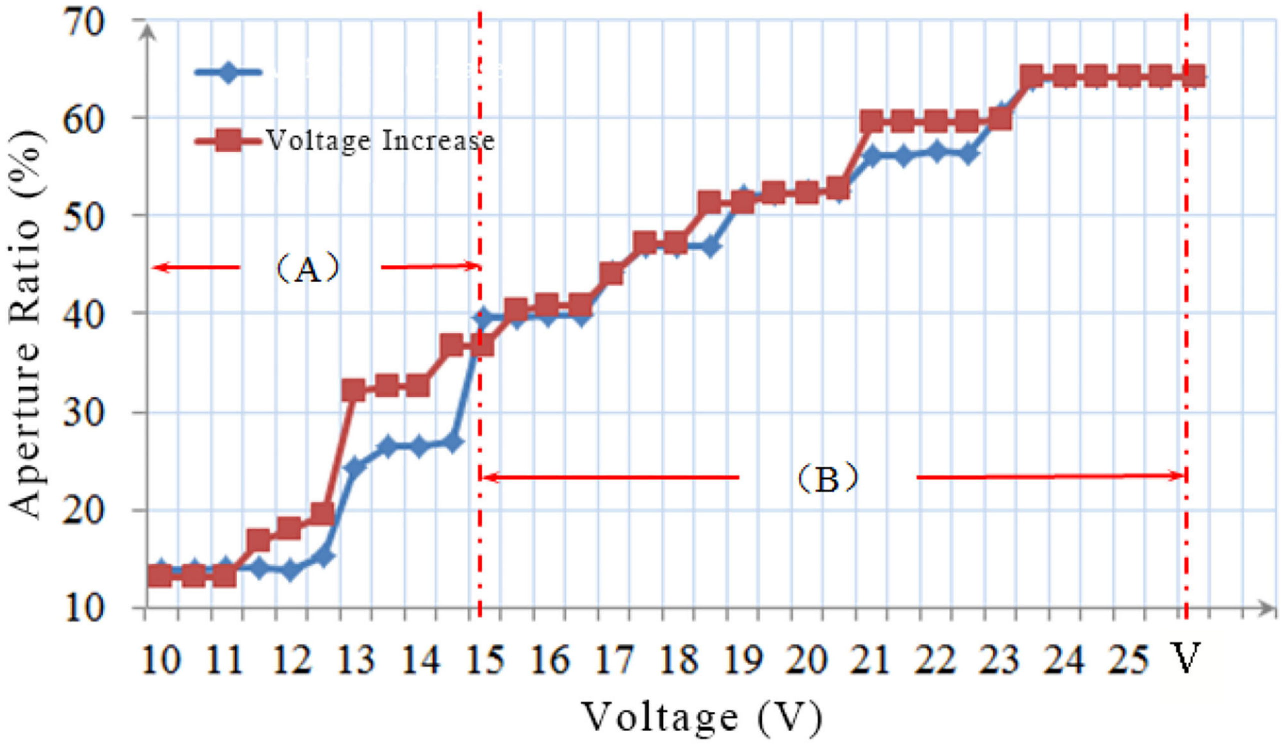

FIGURE 9 | Hysteresis characteristic curves of an EWD driven by a 470 Hz AC driving voltage. The red curve represented the aperture ratio when the driving voltage was increased from 10 to 25V, the blue curve represented the aperture ratio when the driving voltage was decreased from 25 to 10V. The maximum distortion is 5.97%. **(A)** Indicates the state where the difference of aperture ratio changes greatly, **(B)** indicates the stage where the difference of aperture ratio changes little.

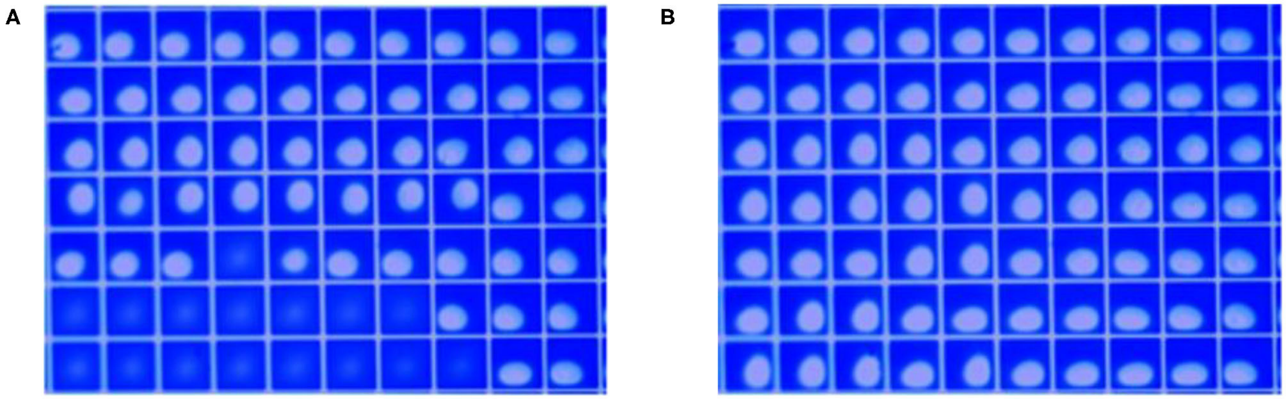

FIGURE 10 | The aperture ratio of pixels when the EWD was driven by 470 Hz AC driving voltage. **(A)** The pixel aperture ratio was 26.50% during the voltage increasing process. **(B)** The pixel aperture ratio was 32.47% during the voltage decreasing process. The maximum difference was 5.97%.

to EWDs system to achieve more accurate control for displaying gray-scales.

DATA AVAILABILITY STATEMENT

The raw data supporting the conclusions of this article will be made available by the authors, without undue reservation.

AUTHOR CONTRIBUTIONS

LW and WL designed this project. LW and HZ carried out most of the experiments and data analysis. JL and ZY carried out a few of the experiments and data analysis. WL, HZ, WL, JL, ZY, QW, JZ, and PM gave suggestions on the project management and conducted helpful discussion on the experimental results. All authors contributed to the article and approved the submitted version.

FUNDING

This research was supported by the Special Projects in Key Fields of Colleges and Universities of Guangdong in 2020 (No. 2020ZDZX3083), the Second Batch of Social Welfare and Basic Research Key Projects of Zhongshan (No. 2020B2021), the School Level Project of Zhongshan Polytechnic (No. 2018KQ22), the Key Technology Development of High Frequency Antenna Substrate Based on 5G Communication (No. 2020ZDZX2081), Key Project of Provincial Education Department, the Key Technology Research and Development of High Frequency Substrate Based on 5G Communication (No. KYA2002), and Key Scientific Research Project of the University.

REFERENCES

1. Heikenfeld J, Drzaic P, Yeo J S, Koch T. Review paper: a critical review of the present and future prospects for electronic paper. *J Soc Inform Display*. (2011) 19:129–56. doi: 10.1889/JSID19.2.129
2. Mingyong Q, Shanling L, Suyun Z, Zhixian L, Tailiang G, Biao T. Real-time dynamic driving system implementation of electrowetting display. *Opto-Electronic Eng*. (2019) 46:180623. doi: 10.12086/oee.2019.180623
3. Li W, Wang L, Zhang T, Lai S, Liu L, He W, et al. Driving waveform design with rising gradient and sawtooth wave of electrowetting displays for ultra-low power consumption. *Micromachines*. (2020) 11:145. doi: 10.3390/mi11020145
4. Heikenfeld J, Zhou K, Kreit E, Raj B, Yang S, Sun B, et al. Electrofluidic displays using young–laplace transposition of brilliant pigment dispersions. *Nat Photo.* (2009) 3:292–6. doi: 10.1038/nphoton.2009.68
5. Tröls A, Enser H, Jakoby B. Modeling and fabrication of low-cost electrowetting actuators for flexible microfluidic display applications. *2016 IEEE Sens*. (2016) 10:1–3. doi: 10.1109/ICSENS.2016.7808429
6. Zhao R, Cumby B, Russell A, Heikenfeld J. Large area and low power dielectrowetting optical shutter with local deterministic fluid film breakup. *Appl Phys Lett.* (2013) 103:223510. doi: 10.1063/1.4834095
7. Beni G, Hackwood S. Electro-wetting displays. *Appl Phys Lett*. (1981) 38:207–9. doi: 10.1063/1.92322
8. Hayes RA, Feenstra BJ. Video-speed electronic paper based on electrowetting. *Nature*. (2003) 425:383–5. doi: 10.1038/nature01988
9. Xu ZN. An algorithm for selecting the most accurate protocol for contact angle measurement by drop shape analysis. *Rev Sci Instrum*. (2014) 85:125107. doi: 10.1063/1.4903198
10. Yi Z, Huang Z, Lai S, He W, Wang L, Chi F, et al. Driving waveform design of electrowetting displays based on an exponential function for a stable grayscale and a short driving time. *Micromachines*. (2020) 11: 313. doi: 10.3390/mi11030313
11. Yi Z, Liu L, Wang L, Li W, Shui L, Zhou G. A driving system for fast and precise gray-scale response based on amplitude–frequency mixed modulation in TFT electrowetting displays. *Micromachines*. (2019) 10:732. doi: 10.3390/mi10110732
12. Li F, Mugele F. How to make sticky surfaces slippery: contact angle hysteresis in electrowetting with alternating voltage. *Appl Phys Lett*. (2008) 92:244108. doi: 10.1063/1.2945803
13. Giraldo A, Aubert J, Bergeron N, Li F, Slack A, Weijer M. Transmissive electrowetting-based displays for portable multi-media devices. *Sid Sympos Digest Techn Papers*. (2012) 40:479–82. doi: 10.1889/1.3256820
14. Yi Z, Feng W, Wang L, Liu L, Lin Y, He W, et al. Aperture ratio improvement by optimizing the voltage slope and reverse pulse in the driving waveform for electrowetting displays. *Micromachines*. (2019) 10:862. doi: 10.3390/mi10120862
15. Van Dijk R, Feenstra BJ, Hayes RA, Camps IGJ, Boom RGH, Wagemans MMH, et al. Gray scales for video applications on electrowetting displays. *Sid Sympos Digest Techn Papers*. (2006) 37:1926–9. doi: 10.1889/1.2433427
16. Seveno D, Blake TD, Coninck JD. Young's equation at the nanoscale. *Phys Rev Lett.* (2013) 111:096101. doi: 10.1103/PhysRevLett.111.096101
17. Dou Y, Wang B, Jin M, Yu Y, Zhou G, Shui L. A review on self-assembly in microfluidic devices. *J Micromech Microeng*. (2017) 27:113002. doi: 10.1088/1361-6439/aa84db
18. Chen Z, Lin S, Lin Z, Liao Q, Li T, Tang B. Design of video display driving system for low-power electrowetting display. *Acta Photo Sinica*. (2020) 49:222002. doi: 10.3788/gzxb20204902.0222002

Conflict of Interest: The authors declare that the research was conducted in the absence of any commercial or financial relationships that could be construed as a potential conflict of interest.

frontiers
in Physics

ORIGINAL RESEARCH
published: 26 March 2021
doi: 10.3389/fphy.2021.659782

Photo-Diodes Based on $CH_3NH_3PbCl_3$ Perovskite Single Crystals by Epitaxial Growth for Ultraviolet Photo-Detection

Jingda Zhao [1,2]***, Xin Wang*** [2]****, Yuzhu Pan*** [2]***, Yubing Xu*** [2]***, Yuwei Li*** [2]***, Jing Chen*** [2]***, Jun Wu*** [2]***, Qing Li*** [2]***, Zhiwei Zhao*** [2]***, Xiaobing Zhang*** [2]***, Javed Akram*** [3]***, Byung Seong Bae*** [4]***, Haining Yang*** [2] ***and Wei Lei*** [2]**

[1] State Key Laboratory of Nuclear Power Safety Monitoring Technology and Equipment, China Nuclear Power Engineering Co. Ltd., Shenzhen, China, [2] Joint International Research Laboratory of Information Display and Visualization, School of Electronic Science and Engineering, Southeast University, Nanjing, China, [3] Department of Physics, COMSATS University Islamabad, Islamabad, Pakistan, [4] Department of Electronics & Display Engineering, Hoseo University, Asan, South Korea

Organic-inorganic hybrid methylammonium lead halide perovskite MAPbX3 (where MA = CH_3NH_3, and X = Cl, Br, I) single crystals are potential semiconductors for photo-detection due to their excellent optoelectronic performance. In particular, $MAPbCl_3$ single crystal is a wide-band-gap (2.9 eV) semiconductor which is suitable for ultraviolet (UV) detection. In this work, n^--n^+ photo-diodes are fabricated through solution-processed epitaxial growth, growing Bi-doped $MAPbCl_3$ epitaxial layer on $MAPbCl_3$ single crystal substrate. The epitaxial layer effectively improves the interface between n^--type and n^+-type layers and leads to low dark current. This work provides useful information for UV detection based on perovskites.

Keywords: UV detection, perovskite, single crystal, epitaxial growth, photo-diodes

OPEN ACCESS

Edited by:
Feng Chi,
University of Electronic Science and Technology of China, China

Reviewed by:
Liming Liu,
University of Electronic Science and Technology of China, China
Bao Peng,
Shenzhen Institute of Information Technology, China

****Correspondence:***
Xin Wang
230159424@seu.edu.cn
Wei Lei
lw@seu.edu.cn

Specialty section:
This article was submitted to Optics and Photonics, a section of the journal Frontiers in Physics

Received: *28 January 2021*
Accepted: *25 February 2021*
Published: *26 March 2021*

Citation:
Zhao J, Wang X, Pan Y, Xu Y, Li Y, Chen J, Wu J, Li Q, Zhao Z, Zhang X, Akram J, Bae BS, Yang H and Lei W (2021) Photo-Diodes Based on $CH_3NH_3PbCl_3$ Perovskite Single Crystals by Epitaxial Growth for Ultraviolet Photo-Detection. Front. Phys. 9:659782. doi: 10.3389/fphy.2021.659782

INTRODUCTION

Recently, Organic-inorganic hybrid methylammonium lead halide perovskite ($MAPbX_3$, where MA = CH_3NH_3, and X = Cl, Br, I) perovskite have attracted a lot of attention due to their excellent optoelectronic properties, such as tunable band gap, low trap density, and long diffusion length [1, 2]. $MAPbX_3$ have been proved to have potential in a number of optoelectronic devices, such as photodetectors, light-emitting diodes, and solar cells [3–9]. There are reports on the visible and near infrared detection applications of $MAPbI_3$ and $MAPbBr_3$ single crystals because of their suitable band gap and high optical absorption coefficient [10, 11]. $MAPbCl_3$ single crystals are wide-bandgap (2.9 eV) semiconductors [12] which are insensitive to visible light while having a high absorption for ultraviolet (UV) radiation (wavelength ∼100–400 nm) [13]. These characters make $MAPbCl_3$ single crystals suitable in applications of UV detection [14–16]. To best our knowledge, little work carried out to study the optoelectronic characteristics of photo-diode based on $MAPbCl_3$, which is important to develop optoelectronic device based on PSCs. Therefore, it is necessary to obtain a photo-diode based on $MAPbCl_3$ with high performance.

The properties of conventional semiconductor could be adjusted by impurity doping, similarly, heterovalent metals doping into PSCs is an efficient way to change the electrical and optical properties [17–21]. $MAPbCl_3$ is proved to be a n^- type semiconductor [12], while doping Bi^{3+} into $MAPbX_3$ would move Femi level close to conduction band [22, 23]. Inspired by the above work, we suppose to fabricate n^{-}-n^{+} photo-diodes based on n^{-}-type $MAPbCl_3$ single crystal substrate with n^{+}-type Bi-doped $MAPbCl_3$ epitaxial layer. Different to conventional heterojunction, the PSCs homojunction has low lattice mismatch rate, continuous band alignments, and low trap densities [24–26] which allow the device to have a lower dark current when the device is under reverse bias.

In this work, a bulk $MAPbCl_3$ single crystal with cubic shape and high crystallization quality was synthesized by inverse temperature crystallization (ITC) method [27], and we fabricated a UV photo-diode by growing Bi-doped $MAPbCl_3$ epitaxial layer on $MAPbCl_3$ single crystal substrate. This photo-diode shows a low dark current density of $-2.15\ \mu Acm^{-2}$ at -20 V bias voltage while its photocurrent reaches $-82.69\ \mu Acm^{-2}$ under 393 nm LED with the illumination of 20 $mWcm^{-2}$. Due to the successful fabricating of the n^{-}-n^{+} junction, the responsibility reaches 404.7 mA/W, ∼1–2 orders of magnitude higher than pervious reported photodetector based on $MAPbCl_3$ [14, 28], and its detectivity reaches 4.87×10^{11} Jones, which is two orders of magnitude higher than that of the previously reported $MAPbCl_3$ photodetectors [14]. The relatively high carrier mobility makes the rise time reach 176.3 ns while decay reaches 11.6 μs, which is 1–3 orders of magnitude faster than that of the previously reported $MAPbCl_3$ photodetectors [14, 15, 28].

MATERIALS AND METHODS

Materials

Lead chloride (PbCl2, 99%) were purchased from Sigma Aldrich. N, N-Dimethylformamidel (DMF, 99.5%), and Dimethyl sulfoxide were purchased from Chinese reagents. Bismuth Chloride ($BiCl_3$, 98%) and Methylamine hydrochloride (MACl, 98%) were purchased from Aladdin. All commercial products were used as received.

Fabrication of Device

1 mol/L MACl and 1 mol/L $PbCl_2$ were dissolved in 50 ml dimethylformamide (DMF) and dimethylsulfoxide (DMSO) mixed solution (1:1 v/v) to act as precursor solutions. The poly tetra fluoroethylene (PTFE) filters with a 30 μm pore size were used to filter the solutions. Then, the precursor solutions, after being filtered, were transferred to a crystallizing dish by dropper. The crystallizing dish was placed on a programmable heating station (IKA-RET control-visc). The temperature was set to rise 0.5°C per hour from 40 to 60°C, the whole process is shown in **Figure 1A**. After two days, the pristine $MAPbCl_3$ single crystal could be obtained, **Figure 1B** shows the $MAPbCl_3$ substrate with the size of 6.95 × 6.96 × 2.52 mm.

Similarly, 1 mol/L MACl, 1 mol/L $PbCl_2$, and 0.1 mol/l $BiCl_3$ were dissolved in 10 ml dimethylformamide (DMF) and dimethylsulfoxide (DMSO) mixed solution (1:1 v/v) to prepare for epitaxial growth. The pristine $MAPbCl_3$ single crystal was put into the epitaxial solution. After the heating station temperature kept at 60°C for 4 h. the $MAPbCl_3$ with epitaxial layer could be obtained, and **Figure 1C** is a photograph of $MAPbCl_3$ single crystal with epitaxial layer after polishing the edges of the crystal, obviously, the color of the epitaxial layer is yellow and the thickness of the epitaxial layer is nearly 0.52 mm. To fabricated the photo-diodes, the gold electrode acted as anode is deposited on the side of the $MAPbCl_3$ substrate while the sliver electrode acted as cathode is deposited on the side of the epitaxial layer. The structure of this device is shown in **Figure 1D**.

Characterization and Measurements

X-ray diffraction (XRD) patterns were taken by X'TRA (Switzerland). Photoluminescence (PL) spectra were measured by UV–vis spectroscopy (Lab Tech Bluestar, USA). I-V curve was measured by a Keithley 4200 semiconductor analyzer. EQE was measured by Zolix tunable 500-W arc lamplight. A 355-nm pulsed Nd: YAG laser with 6-ns pulse width at 10 Hz as the illumination source and an Agilent oscilloscope were used to measure the carrier mobility.

RESULTS AND DISCUSSION

Firstly, we study the optical properties of the pristine $MAPbCl_3$ substrate, $MAPbCl_3$ with Bi-doped $MAPbCl_3$ epitaxial layer, and Bi-doped $MAPbCl_3$ single crystal, the PL spectra and absorption are shown in **Figures 2A,B**. The absorption edge of pristine $MAPbCl_3$ single crystal was located at 430 nm, and the PL peak is obtained at 436 nm with a narrow FWHM of 14.9 nm confirming the high quality of the single crystal [7]. Doping into single crystal would cause a larger increase of the lattice defect which is the reason why the PL of the Bi-doped $MAPbCl_3$ has a broadening effect [29]. The absorption of Bi-doped $MAPbCl_3$ single crystal is in good agreement with results that were previously reported [30]. The PL of $MAPbCl_3$ with Bi-doped $MAPbCl_3$ epitaxial layer is the stack of the pristine $MAPbCl_3$ and Bi-doped $MAPbCl_3$ single crystal, which indicated the successful growth of the Bi-doped $MAPbCl_3$ epitaxial layer. The absorption moves from 430 to 480 nm after epitaxial growth which approaches the Bi-doped $MAPbCl_3$ single crystal.

Figures 2C,D provide XRD spectra of pristine $MAPbCl_3$ single crystal, $MAPbCl_3$ with epitaxial layer, and Bi-doped $MAPbCl_3$. To (100) planes, the strongest peaks of $MAPbCl_3$ are observed at $2\theta = 31.48°, 48.00°, 65.68°$, while the strongest peaks of Bi-doped $MAPbCl_3$ at $2\theta = 31.50°, 48.02°, 65.70°$ indicating no phase change after doping Bi^{3+}. Besides, **Figure 2D** illustrates the FWHM of pristine $MAPbCl_3$ single crystal with the epitaxial layer is 0.113° which confirms the epitaxial layer remains single crystalline. The stagger XRD peak of $MAPbCl_3$ substrate and epitaxial layer causes the FWHM of photo-diode to be widened. The lattice constants could be calculated from the XRD spectra by Bragg law ($2d\sin\theta = n*\lambda$, where d is the distance between two atoms, θ is the angle of crystal plane and X-ray, n is constant, and λ is the wavelength of the X-ray), the lattice constants of $MAPbCl_3$ and Bi-doped $MAPbCl_3$ are 5.67902 Å and 5.67550 Å, respectively, the lattice constants of $MAPbCl_3$ is same as previously reported [31]. After doping Bi^{3+}, the lattice constant is smaller than pristine $MAPbCl_3$ single crystal indicating the Bi^{3+} ions are possibly substituting Pb^{2+} ions in the crystal. The mismatch rate (mismatch rate can be calculated by $\gamma = (a_1 - a_2)/(a_1 + a_2)$, where a_i is the lattice constants of the

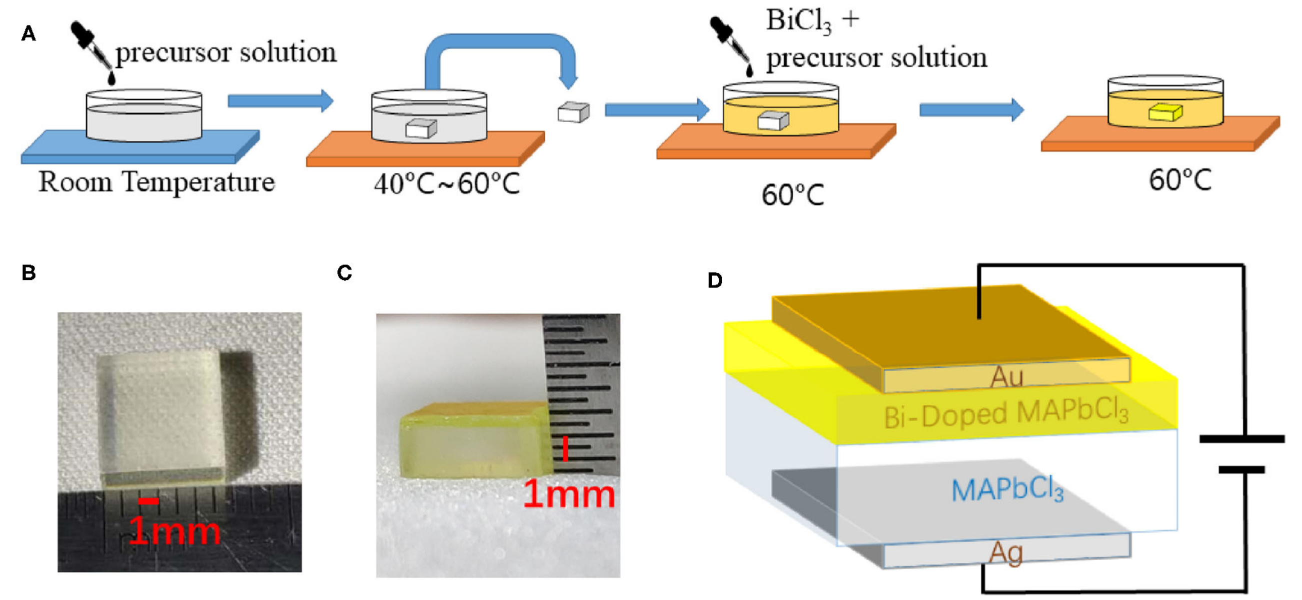

FIGURE 1 | (A) Processing of the growth of PSC and epitaxial. **(B)** Optical photo of pristine $MAPbCl_3$ PSC. **(C)** Optical photo of $MAPbCl_3$ single crystal with Bi-doped $MAPbCl_3$ epitaxial layer. **(D)** Schematic representation of the photodiode structure.

crystal) of $MAPbCl_3$ and Bi-doped $MAPbCl_3$ single crystal is 0.3%, suggesting that their lattice could match well.

Further, the charge mobility of the photo-diode is investigated by the TOF method. After the optical signal is received, the photo-induced holes could immediately be collected under forward bias, while electrons have to drift through the whole device to be collected, the electrons mobility could be calculated through the drift time. Similarly, under the reverse voltage, the holes' mobility could be calculated in the same way. A 355-nm pulsed Nd: YAG laser with 6-ns pulse width at 10 Hz is used as the illumination source, the direction of the light is shown in **Figure 3A**. The average electron mobility was measured as shown in **Figure 3B**. And the average hole mobility was measured as shown in **Figure 3C**. The carrier mobility can be calculated according to:

$$T_{tof} = \frac{L^2}{\mu} \times \frac{1}{V_s}$$

where μ is the carrier mobility, L is the thickness of the photo-diode, V_s is the bias voltage between two electrodes, and T_{tof} is the transmit time [32, 33]. The fitting plot of carrier mobility vs. reciprocal of the bias voltage is shown in the insets, the result shows that the average holes mobility is $55.06 \pm 0.61\ cm^2V^{-1}s^{-1}$ is faster than UV detector based on $MAPbCl_3$ single crystal ($26\ cm^2V^{-1}s^{-1}$) reported [16], the reason is Bi-Doped $MaPbCl_3$ has a high conductivity. And the average electrons mobility is $40.01 \pm 1.30\ cm^2V^{-1}s^{-1}$.

Figure 4A illustrates the EQE of the photo-diode under −20V, the EQE peak locates at 398 nm which prove the device can be applied in UV photo-detection. EQE is calculated by:

$$EQE = \frac{hv}{e} \times \frac{I_{Light} - I_{Dark}}{P \times S} \times 100\%$$

where I_{Light} is the photocurrent (A), I_{Dark} is the dark current (A), h is Plank's constant, ν is the frequency of incident light, S is the area being illuminated, and P is the incident illumination power density (W/cm^2), and e is the element charge [34].

To further study the optoelectronic performance of this photo-diode, an LED with an emission peak of 393 nm and the power intensity of the LED is 20 $mWcm^{-2}$, and the current-voltage characterization of the device in the dark and under illumination is shown in **Figure 4B**, respectively. The photocurrent under reverse bias is much larger than the photocurrent under forward bias. Because of the built-in electric field, holes are hard to transfer from $MAPbCl_3$ substrate to Bi-$MAPbCl_3$ epitaxial layer and electrons are hard to transfer from Bi-$MAPbCl_3$ epitaxial layer to $MAPbCl_3$ substrate when the device is under reverse bias and in a dark environment, and the homojunction restrains the dark current further. Thanks to the highly crystallized epitaxial layer, the dark current of the photo-diode is $-2.15\ \mu Acm^{-2}$ at −20 V, while its photocurrent reaches approximately $-82.69\ \mu Acm^{-2}$ under illumination. To analyze the response ability of the photo-diode to UV radiation, the responsivity (R) and detectivity (D) of the photo-diode was calculated as follow [35, 36]:

$$R = \frac{I_{Light} - I_{Dark}}{P \times S}$$

$$D = \frac{R}{\sqrt{2eJ_{dark}}}$$

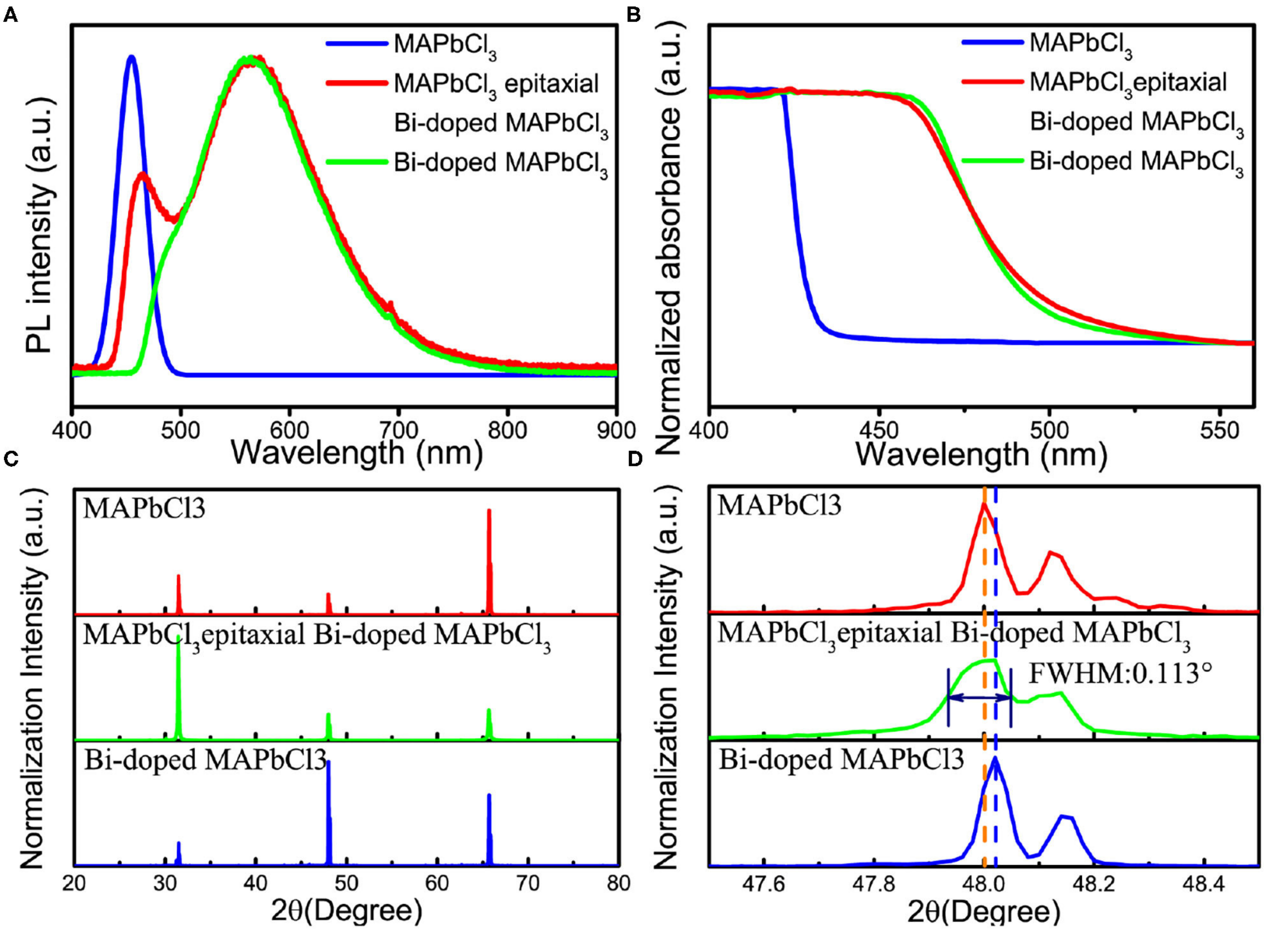

FIGURE 2 | (A) PL spectra of pristine $MAPbCl_3$ substrate, $MAPbCl_3$ with epitaxial layer, and Bi-doped $MAPbCl_3$. **(B)** Absorption of pristine $MAPbCl_3$ substrate, $MAPbCl_3$ with epitaxial layer, and Bi-doped $MAPbCl_3$. **(C)** XRD spectra of the pristine $MAPbCl_3$ substrate, $MAPbCl_3$ with Bi-doped $MAPbCl_3$ epitaxial layer, and Bi-doped $MAPbCl_3$ single crystal. **(D)** XRD spectra from 47.5° to 48.5° of the three kinds of PSCs.

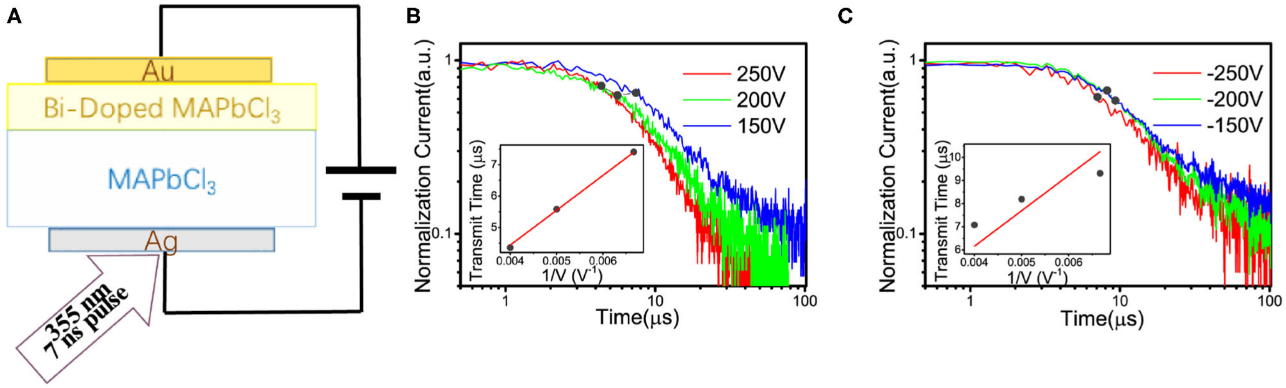

FIGURE 3 | (A) Illustration of the optoelectronic experiment. **(B)** Holes mobility measured by time-of-flight (TOF) method. **(C)** Electrons mobility measured by the TOF method.

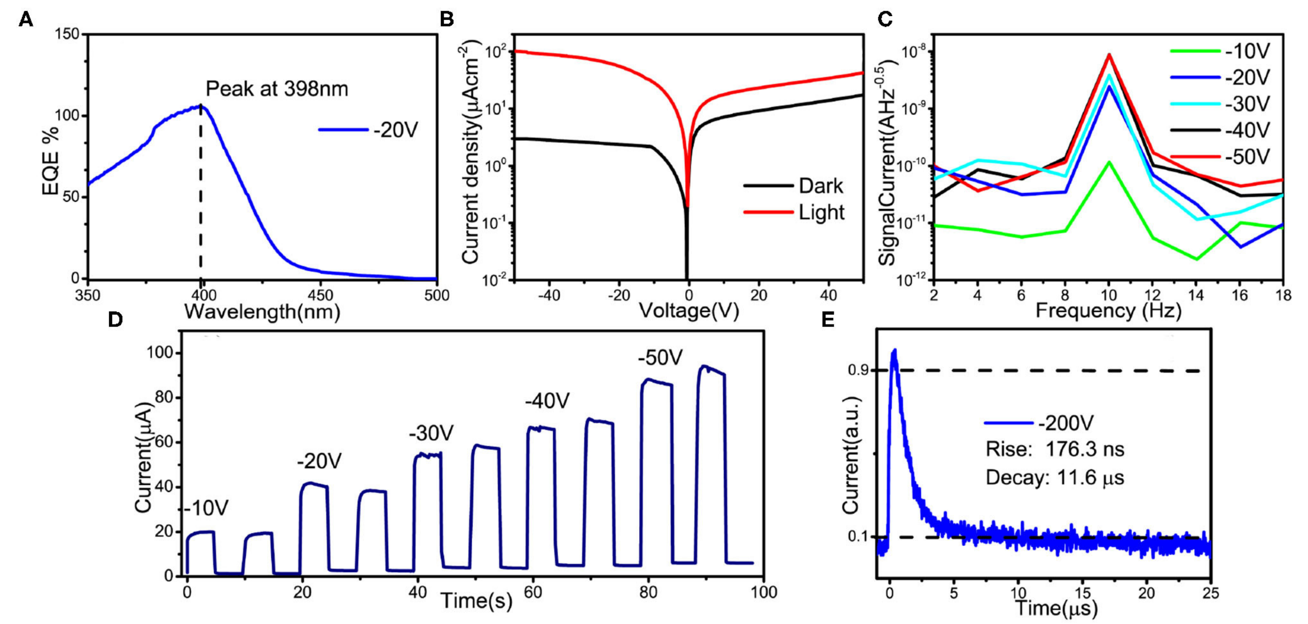

FIGURE 4 | (A) EQE curve under −20 V from 350 to 500 nm. **(B)** Current density vs. Voltage curve. **(C)** Signal current as a function of frequency under different voltage bias. **(D)** Temporal response of the photo-diode under different Voltage. **(E)** Rise time and decay time of the photo-diode at −200 V bias.

The responsivity is calculated to be 404.7 mA/W, detectivity is calculated to be 4.87 × 10^{11} Jones which is one order of magnitude larger compared to $MAPBCl_3$ film (6.87 × 10^{10} Jones) [37].

To study the signal noise at low frequency, we investigate 10 Hz temporal response of the photo-diode under different reverse voltage bias from −10 to −50 V, the Fast Fourier Transform (FFT) method is used to transfer the current vs. time curve to signal current vs. frequency curve. The signal noise from 2 to 18 Hz is calculated and the curve is shown in **Figure 4C**. The average noise current increases from 2.3 pAHz$^{-0.5}$ to 17.0 nAHz$^{-0.5}$ under illumination with bias voltage from −10 to −50 V.

Figure 4D illustrates the on–off switching properties of the photo-diode with the bias voltage range from −10 to −50 V. Obviously, the photo-diode could switch rapidly and stably under different bias. The response speed was measured as shown in **Figure 4E**, the rise time is 176.3 ns and the fall time is 11.6 μs under the bias of −150 V, the fast carrier mobility contributes to the rapid response speed.

The comparison of responsivity and response time between this work and previously reported $MAPbCl_3$ photodetector is summarized in **Table 1**. The photo-diode fabricated in this work has a higher responsivity than most UV detectors reported, and the decay time is the fastest.

TABLE 1 | Comparison between this work and previously reported $MAPbCl_3$ photodetectors.

UV Detector	Responsivity @light source	Decay time	Reference
$MAPbCl_3$ film	0.97 A/W @360 nm (2.2 mWcm^{-2})	220 μs	[38]
	71 mA/W@398 nm		[37]
	Below 1 mA/W @385 nm	20 ms	[16]
$MAPbCl_3$ single crystal	46.9 mA/W @365 nm	62 ms	[14]
	0. 60 mA/W @405 nm		[28]
	1.85 A/W @415 nm	368 μs	[15]
Photo-diode	404.7 mA/W @393 nm	11.6 μs	This work

CONCLUSION

In summary, we have fabricated a UV photo-diode by growing Bi-doped $MAPbCl_3$ epitaxial layer on a pristine $MAPbCl_3$ single crystal substrate. And we calculate the lattice constants of pristine $MAPbCl_3$ and Bi-doped $MAPbCl_3$ single crystal through XRD, which are lattice-matched. Further, we investigate the optoelectronic properties of the photo-diode. At −20 V voltage, the dark current is −2.15 μAcm^{-2} while the photocurrent reaches −82.69 μAcm^{-2}, the on-off ratio reaches nearly 40 under a 393 nm LED with 20 mW/cm^2. Moreover, the photo-diode has a responsivity of 404.7 mW/cm^2 and detectivity of 4.87 × 10^{11} Jones. The carrier mobility is calculated to be 55.06 ± 0.61 cm^{2}V^{-1}s^{-1} by TOF. The rise time and decay time are 176.3 ns and 11.6 μs, which is faster than the previously reported UV detector based on $MAPbCl_3$ single crystal and ploy-crystal film. This work provides useful information for UV detection and photoelectrical device based on $MAPbX_3$.

DATA AVAILABILITY STATEMENT

The raw data supporting the conclusions of this article will be made available by the authors, without undue reservation.

AUTHOR CONTRIBUTIONS

JZ and YP grew the perovskite single crystals. JZ did the epitaxial experiments. YX and JZ did the measurements. XW and JZ analyzed these results. JZ wrote this manuscript. All authors make comments on the manuscript.

FUNDING

This work was financially supported by the funding of State Key Laboratory of Nuclear Power Safety Monitoring Technology and Equipment (K-A2020.415), National Key Research and Development Program of China (2018YFE0125500, 2016YFB0401600), Program 111_2.0 in China (BP0719013), National Natural Science Foundation Project of China (61775034, 51879042, 61674029, 12005038), Research Fund for International Young Scientists (62050410350), International Cooperative Research Project of Jiangsu Province (BZ2018056), Leading Technology of Jiangsu Basic Research Plan (BK20192003).

REFERENCES

1. Shi D, Adinolfi V, Comin R, Yuan M, Alarousu E, Buin A, et al. Low trap-state density and long carrier diffusion in organolead trihalide perovskite single crystals. *Science*. (2015) 347:519–22. doi: 10.1126/science.aaa2725
2. Dong. Electron-hole diffusion lengths >175 µm in solution-grown $CH_3NH_3PbI_3$ single crystals. *Sci Expr*. (2015) 43210:1–8. doi: 10.1126/science.aaa5760
3. Yusoff ARBM, Nazeeruddin MK. Organohalide lead perovskites for photovoltaic applications. *J Phys Chem Lett*. (2016) 7:851–66. doi: 10.1021/acs.jpclett.5b02893
4. Jena AK, Kulkarni A, Miyasaka T. Halide perovskite photovoltaics: background, status, and future prospects. *Chem Rev*. (2019) 119:3036–103. doi: 10.1021/acs.chemrev.8b00539
5. Jaramillo-Quintero OA, Sanchez RS, Rincon M, Mora-Sero I. Bright visible-infrared light emitting diodes based on hybrid halide perovskite with Spiro-OMeTAD as a hole-injecting layer. *J Phys Chem Lett*. (2015) 6:1883–90. doi: 10.1021/acs.jpclett.5b00732
6. Wehrenfennig C, Liu M, Snaith HJ, Johnston MB, Herz LM. Homogeneous emission line broadening in the organo lead halide perovskite $CH_3NH_3PbI_{3-x}Cl_x$. *J Phys Chem Lett*. (2014) 5:1300–6. doi: 10.1021/jz500434p
7. Veldhuis SA, Boix PP, Yantara N, Li M, Sum TC, Mathews N, Mhaisalkar SG. Perovskite materials for light-emitting diodes and lasers. *Adv Mater*. (2016) 28:6804–34. doi: 10.1002/adma.201600669
8. Pan Y, Wang X, Xu Y, Li Y, Elemike EE, Shuja A, et al. Enhanced performance of perovskite single-crystal photodiodes by epitaxial hole blocking layer. *Front Chem*. (2020) 8:791. doi: 10.3389/fchem.2020.00791
9. Xu Y, Wang X, Pan Y, Li Y, Emeka Elemike E, Li Q, et al. Perovskite photodetectors based on p-i-n junction with epitaxial electron-blocking layers. *Front Chem*. (2020) 8:811. doi: 10.3389/fchem.2020.00811
10. Yakunin S, Dirin DN, Shynkarenko Y, Morad V, Cherniukh I, Nazarenko O, et al. Detection of gamma photons using solution-grown single crystals of hybrid lead halide perovskites. *Nat Photon*. (2016) 10:585–9. doi: 10.1038/nphoton.2016.139
11. Xu Q, Shao W, Li Y, Zhang X, Ouyang X, Liu J, et al. High-performance surface barrier x-ray detector based on methylammonium lead tribromide single crystals. *ACS Appl Mater Interfaces*. (2019) 11:9679–84. doi: 10.1021/acsami.8b21605
12. Liu Y, Yang Z, Cui D, Ren X, Sun J, Liu X, et al. Two-inch-sized perovskite $CH_3NH_3PbX_3$ ($X = Cl, Br, I$) crystals: growth and characterization. *Adv Mater*. (2015) 27:5176–83. doi: 10.1002/adma.201502597
13. Li D, Jiang K, Sun X, Guo C. AlGaN photonics: recent advances in materials and ultraviolet devices. *Adv Opt Photon*. (2018) 10:43. doi: 10.1364/AOP.10.000043
14. Maculan G, Sheikh AD, Abdelhady AL, Saidaminov MI, Haque MA, Murali B, et al. $CH_3NH_3PbCl_3$ single crystals: inverse temperature crystallization and visible-blind UV-photodetector. *J Phys Chem Lett*. (2015) 6:3781–6. doi: 10.1021/acs.jpclett.5b01666
15. Cheng Z, Liu K, Yang J, Chen X, Xie X, Li B, et al. High-performance planar-type ultraviolet photodetector based on high-quality $CH_3NH_3PbCl_3$ perovskite single crystals. *ACS Appl Mater Interfaces*. (2019) 11:34144–50. doi: 10.1021/acsami.9b09035
16. Adinolfi V, Ouellette O, Saidaminov MI, Walters G, Abdelhady AL, Bakr OM, et al. Fast and sensitive solution-processed visible-blind perovskite UV photodetectors. *Adv Mater*. (2016) 28:7264–8. doi: 10.1002/adma.201601196
17. Klug MT, Osherov A, Haghighirad AA, Stranks SD, Brown PR, Bai S, et al. Tailoring metal halide perovskites through metal substitution: Influence on photovoltaic and material properties. *Energy Environ Sci*. (2017) 10:236–46. doi: 10.1039/C6EE03201J
18. Sarkar P, Srivastava A, Tripathy SK, Baishnab KL, Lenka TR, Menon PS, et al. Exploring the effect of Ga^{3+} doping on structural, electronic and optical properties of $CH_3NH_3PbCl_3$ perovskites: an experimental study. *J Mater Sci Mater Electron*. (2020). doi: 10.1007/s10854-020-04019-w. [Epub ahead of print].
19. Zhang J, Shang MH, Wang P, Huang X, Xu J, Hu Z, et al. N-type doping and energy states tuning in $CH_3NH_3Pb_{1-x}Sb_{2x/3}I_3$ perovskite solar cells. *ACS Energy Lett*. (2016) 1:535–41. doi: 10.1021/acsenergylett.6b00241
20. Choi H, Jeong J, Kim HB, Kim S, Walker B, Kim GH, et al. Cesium-doped methylammonium lead iodide perovskite light absorber for hybrid solar cells. *Nano Energy*. (2014) 7:80–85. doi: 10.1016/j.nanoen.2014.04.017
21. Xiong Y, Xu L, Wu P, Sun L, Xie G, Hu B. Bismuth doping–induced stable seebeck effect based on $MAPbI_3$ polycrystalline thin films. *Adv Funct Mater*. (2019) 29:1–10. doi: 10.1002/adfm.201900615
22. Li C, Chen X, Li N, Liu J, Yuan B, Li Y, et al. Highly conductive n-type $CH_3NH_3PbI_3$ single crystals doped with bismuth donors. *J Mater Chem C*. (2020) 8:3694–704. doi: 10.1039/C9TC06854F
23. Abdelhady AL, Saidaminov MI, Murali B, Adinolfi V, Voznyy O, Katsiev K, et al. Heterovalent dopant incorporation for bandgap and type engineering of perovskite crystals. *J Phys Chem Lett*. (2016) 7:295–301. doi: 10.1021/acs.jpclett.5b02681
24. Shah JM, Li YL, Gessmann T, Schubert EF. Experimental analysis and theoretical model for anomalously high ideality factors ($n \gg 2.0$) in AlGaN/GaN p-n junction diodes. *J Appl Phys*. (2003) 94:2627–30. doi: 10.1063/1.1593218
25. Jin Y, Keum DH, An SJ, Kim J, Lee HS, Lee YH. A Van der waals homojunction: ideal p-n diode behavior in $MoSe_2$. *Adv Mater*. (2015) 27:5534–40. doi: 10.1002/adma.201502278
26. Li F, Li J, Gao L, Long X, Hu Y, Wang C, et al. Facile regrowth of Mg-Fe_2O_3/P-Fe_2O_3 homojunction photoelectrode for efficient solar water oxidation. *J Mater Chem A*. (2018) 6:13412–8. doi: 10.1039/C8TA05194A
27. Saidaminov MI, Abdelhady AL, Murali B, Alarousu E, Burlakov VM, Peng W, et al. High-quality bulk hybrid perovskite single crystals within minutes by inverse temperature crystallization. *Nat Commun*. (2015) 6:8586. doi: 10.1038/ncomms8586
28. Cheng X, Jing L, Zhao Y, Du S, Ding J, Zhou T. Crystal orientation-dependent optoelectronic properties of $MAPbCl_3$ single crystals. *J Mater Chem C*. (2018) 6:1579–86. doi: 10.1039/C7TC05156E

29. Wang R, Zhang X, He J, Ma C, Xu L, Sheng P, Huang F. Bi^{3+}-doped CH 3 NH 3 PbI 3: red-shifting absorption edge and longer charge carrier lifetime. *J Phys Chem C*. (2017) 695:555–60. doi: 10.1016/j.jallcom.2016.11.125
30. Zhang Z, Ren L, Yan H, Guo S, Wang S, Wang M, et al. Bandgap narrowing in bi-doped $CH_3NH_3PbCl_3$ perovskite single crystals and thin films. *J Phys Chem C*. (2017) 121:17436–41. doi: 10.1021/acs.jpcc.7b06248
31. Baikie T, Barrow NS, Fang Y, Keenan PJ, Slater PR, Piltz RO, et al. A combined single crystal neutron/X-ray diffraction and solid-state nuclear magnetic resonance study of the hybrid perovskites CH3NH3PbX3(X=I,Br and Cl). *J Phys Chem C*. (2015) 3:9298–307. doi: 10.1039/C5TA01125F
32. Huang J, Shao Y, Dong Q. Organometal trihalide perovskite single crystals: a next wave of materials for 25% efficiency photovoltaics and applications beyond *J Phys Chem Lett*. (2015) 6:3218–27. doi: 10.1021/acs.jpclett.5b01419
33. Thirimanne HM, Jayawardena KDGI, Parnell AJ, Bandara RMI, Karalasingam A, Pani S, et al. High sensitivity organic inorganic hybrid X-ray detectors with direct transduction and broadband response. *Nat Commun*. (2018) 9:2926. doi: 10.1038/s41467-018-05301-6
34. Li C, Wang H, Wang F, Li T, Xu M, Wang H, et al. Ultrafast and broadband photodetectors based on a perovskite/organic bulk heterojunction for large-dynamic-range imaging. *Light Sci Appl*. (2020) 9:31. doi: 10.1038/s41377-020-0264-5
35. Dou L, Yang YM, You J, Hong Z, Chang WH, Li G, Yang Y. Solution-processed hybrid perovskite photodetectors with high detectivity. *Nat Commun*. (2014) 5:5404. doi: 10.1038/ncomms6404
36. Li C, Lu J, Zhao Y, Sun L, Wang G, Ma Y. Highly sensitive, fast response perovskite photodetectors demonstrated in weak light detection circuit and visible light communication system. *Small*. (2019) 15:e1903599. doi: 10.1002/smll.201903599
37. Zheng E, Yuh B, Tosado GA, Yu Q. Solution-processed visible-blind UV-A photodetectors based on $CH_3NH_3PbCl_3$ perovskite thin films. *J Mater Chem*. (2017) 5:3796–806. doi: 10.1039/C7TC00639J
38. Wang W, Xu H, Cai J, Zhu J, Ni C, Hong F, et al. Visible blind ultraviolet photodetector based on $CH_3NH_3PbCl_3$ thin film. *Opt Expr*. (2016) 24:8411. doi: 10.1364/OE.24.008411

Conflict of Interest: JZ is employed by China Nuclear Power Engineering Co. Ltd., Shenzhen, Guangzhou, China.

The remaining authors declare that the research was conducted in the absence of any commercial or financial relationships that could be construed as a potential conflict of interest.

ORIGINAL RESEARCH
published: 29 April 2021
doi: 10.3389/fphy.2021.672541

Driving Waveform Design of Electrowetting Displays Based on a Reset Signal for Suppressing Charge Trapping Effect

Taiyuan Zhang[1] *and Yong Deng*[2]*

[1] *Guangdong Provincial Key Laboratory of Optical Information Materials and Technology & Institute of Electronic Paper Displays, South China Academy of Advanced Optoelectronics, South China Normal University, Guangzhou, China,*
[2] *Academy of Shenzhen Guohua Optoelectronics, Shenzhen, China*

Electrowetting display (EWD) device is a new type of reflective optoelectronic equipment with paper-like display performance. Due to the oil backflow phenomenon, it is difficult for pixels to be maintained a stable aperture ratio, so the grayscale of EWDs cannot be stabilized. To reduce the oil backflow in EWDs, a driving waveform composed of a driving signal and a periodic reset signal was proposed in this paper. A direct current (DC) signal was designed as the driving signal for driving pixels. The aperture ratio of pixels was determined by the amplitude of the DC signal. The periodic reset signal was divided into a charge release phase and a driving recovery phase. During the charge release phase, the driving voltage was abruptly dropped to 0 V for a period to release trapped charges. In the driving recovery phase, the driving voltage was rapidly increased from 0 V to a maximum value. To reach the same grayscale of EWDs, the driving waveform was returned to the driving signal at the end of the driving recovery phase. Experimental results showed that the aperture ratio of EWDs was unchanged when the driving waveform was applied. However, the aperture ratio of pixels was gradually decreased with the conventional driving waveform. It was indicated that the charge trapping effect and the oil backflow phenomenon can be effectively inhibited by the proposed driving waveform. Compared with the conventional driving waveform, the speed of oil backflow was reduced by 90.4%. The results demonstrated that the proposed driving waveform is beneficial for the achievement of stable grayscale in EWDs.

Keywords: electrowetting display, oil backflow, grayscale, charge trapping, driving waveform

Edited by:
Feng Chi,
University of Electronic Science and Technology of China Zhongshan Institute, China

Reviewed by:
Yulin Shi,
Shihezi University, China
Jingjing Yang,
Nanjing Xiaozhuang University, China

****Correspondence:***
Yong Deng
yong.deng@guohua-oet.com

Specialty section:
This article was submitted to Optics and Photonics, a section of the journal Frontiers in Physics

Received: *26 February 2021*
Accepted: *06 April 2021*
Published: *29 April 2021*

Citation:
Zhang T and Deng Y (2021) Driving Waveform Design of Electrowetting Displays Based on a Reset Signal for Suppressing Charge Trapping Effect. Front. Phys. 9:672541. doi: 10.3389/fphy.2021.672541

INTRODUCTION

As a reflective display technology, the electrophoretic display (EPD) technology [1] has been successfully applied in fields such as e-readers [2], electronic tags, and billboards. However, due to limitations of EPDs in response time [3] and color display [4], it is difficult to be used in application scenarios where rich colors and video display [5] are required.

The mentioned shortcomings of EPDs can be made up by the EWD technology [6] based on the electrowetting effect [7]. As a novel reflective display technology, the EWD has a response speed of milliseconds and can maintain high contrast and reflectivity in a strong light environment. In addition, the power consumption and the thickness of the device can be significantly reduced

[8]. Therefore, the power consumption of EWDs is much lower than liquid crystal display (LCD) of equivalent size and solution. As the new generation of display technology, the driving system for EWDs has received wide attention [9, 10]. However, the charge trapping phenomenon can cause an asymmetric electrowetting effect [11], contact angle saturation, and oil backflow [12]. These problems not only directly lead to dielectric failure [13], but also make a challenge for the stable display and precise control of grayscales. The strength of the charge trapping effect is related to the polarity of the driving voltage, type, and pH value of the solution. It has been found that increasing the size of ions in the solution could reduce the risk of charge trapping effects [14]. According to the previous research, it was possible to reduce the charge trapping effect by introducing an oil layer [15], but this hypothesis has not yet been confirmed. Research results demonstrated that the saturation effect of contact angle could be suppressed by driving waveform modulation [16]. However, the maximum voltage of proposed driving waveform was up to 200 V. In addition, some driving waveforms of EWDs with a low voltage were designed, whereas the effect of hysteresis in EWDs was not considered by these driving waveforms [17, 18]. Even so, these excellent research results provided valuable experience and an important reference for reducing the charge trapping effect.

A well-designed driving waveform is an important method to improve the display performance of displays [19, 20]. Therefore, we analyzed the formation mechanism of oil backflow caused by the charge trapping effect. And then a new driving waveform for suppressing the charge trapping was proposed. To reduce the charge trapping effect, a reset signal was introduced into the driving waveform. This method could provide a new idea for achieving stable and precise control of grayscales for EWDs.

PRINCIPLES OF EWDS

Principle of Electrowetting-on-Dielectric

Electrowetting is to change the surface tension between solid-liquid interface by applying a voltage between conductive liquid and electrode. The related dynamics of electrowetting and the concept of EWDs were proposed in 1981 [7, 21]. With the introduction of a dielectric layer between the conductive liquid and the metal electrode, the problem of electrolysis of the electrode has been solved [22]. And the electrowetting model with a dielectric layer introduced is called electrowetting-on-dielectric (EWOD) [23]. The structure diagram of an EWOD model was shown in **Figure 1**. The conductive liquid is placed on the surface of the dielectric layer with hydrophobic properties. One of the electrodes was immersed in the conductive liquid drop, and the other electrode was under the dielectric layer substrate. When a voltage was applied between two electrodes of a pixel, the wettability of conductive liquid droplet can be increased. In this case, the solid-liquid interface and the dielectric layer can be taken as a parallel plate capacitor.

When no voltage was applied between the conductive liquid and the metal electrode, the conductive liquid droplet can form an angle θ_0 between the three-phase contact line and the hydrophobic dielectric layer with the action of surface tension. The angle θ_0 is called the electrowetting contact angle. Since the size of a droplet is very small, the effect of gravity is negligible relative to the surface tension of the droplet. In the initial state, the relationship described by Formula (1) can be obtained according to the mechanical equilibrium along the surface of the hydrophobic insulating layer.

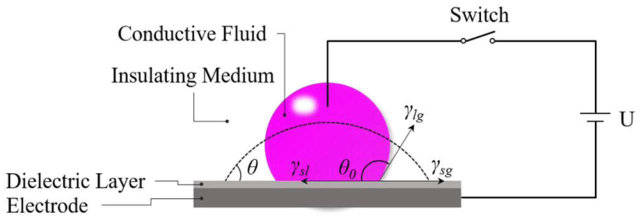

FIGURE 1 | Schematic diagram of an EWOD. When no external voltage was applied, the conductive fluid was in a contracted state, as shown in the red part. When an appropriate driving voltage was applied, the contracted conductive droplet can be spread out, as shown by the dotted line.

$$\gamma_{sl} = \gamma_{sg} + \gamma_{\mathrm{lg}} \cos(\pi - \theta_0) \tag{1}$$

Then, the contact angle in the initial state can be expressed by the Formula (2).

$$\cos\theta_0 = \frac{\gamma_{sg} - \gamma_{sl}}{\gamma_{\mathrm{lg}}} \tag{2}$$

In Formulas (1) and (2), θ_0 is the contact angle of the solid-liquid interface. γ_{sl}, γ_{sg}, and γ_{lg} represent the surface tension of the solid-liquid, solid-gas, and liquid-gas interface, respectively.

When a voltage U was applied between the conductive liquid and the electrode, the surface tension γ_{sl} at the solid-liquid interface could be decreased. The relationship between the surface tension γ_{sl} and the voltage U can be described by the Lippmann equation, as shown in Formula (3).

$$\gamma'_{sl} = \gamma_{sl} - \frac{\varepsilon_0 \varepsilon_r}{2d} U^2 \tag{3}$$

Where, γ'_{sl} is the surface tension between the hydrophobic insulating layer and the conductive liquid when the voltage was applied. ε_0 is the vacuum dielectric constant, ε_r is the relative dielectric constant of the dielectric layer. d is the effective thickness of the hydrophobic medium layer. Combined with Young's equation, the relationship between the contact angle of the solid-liquid interface and the applied voltage can be described by Formula (4), namely the Lippmann-Young equation.

$$cos\,\theta_u = cos\,\theta_0 + \frac{\varepsilon_0 \varepsilon_r}{2d\gamma_{\mathrm{lg}}} U^2 \tag{4}$$

According to Formulas (2) and (4), the relationship between contact angle and voltage can be written as Formula (5).

$$cos\,\theta_u = \frac{\gamma_{sg} - \gamma_{sl} + \varepsilon_0 \varepsilon_r U^2/2d}{\gamma_{\mathrm{lg}}} \tag{5}$$

Where, θ_u was the solid-liquid contact angle when U was applied.

Principle of EWDs

EWOD is widely used in many fields such as digital microfluidics (DMF) [24–26], lab-on-chip [27, 28], micro-lens [29–31], and EWDs. In 2003, a reflective display based on the principle of EWOD was proposed [6].

The basic structure of EWDs was shown in **Figure 2A**. The optical laminated structure of the display device is composed of a white reflective substrate, a hydrophobic insulating layer, an indium tin oxide (ITO) electrode, oil film, and water. The white reflective substrate at the bottom of the device is an electrode coated with a hydrophobic insulating layer, and the hydrophobic insulating layer is covered with a layer of the colored oil. The transparent conductive liquid is connected to the water electrode, and the oil film is confined inside the surrounding pixel grid by pixel wall.

When no voltage was applied between the upper and lower substrates, the sum of interfacial tension at the oil-water interface and interfacial tension at the oil-solid interface is less than the interfacial tension at the water-solid interface. According to the principle of the lowest energy of a stable system, oil droplets can naturally stretch into an oil film and spread between the transparent conductive liquid and the hydrophobic insulating layer. At this time, the pixel grid was in a closed state, and the color of oil film was displayed, as shown in **Figures 2A,C**.

When a voltage was applied between the upper and lower substrates, the original equilibrium state of the system was broken, and the solid-liquid contact angle can be gradually decreased. With the action of an external electric field, the transparent conductive liquid was deformed and displaced. And then the hydrophobic insulating layer was infiltrated by the liquid. With the push of the transparent conductive liquid, the stretched oil film can shrink to a corner in a pixel grid. The contact area between the shrinking oil and the hydrophobic insulating layer was gradually decreased, and eventually, the entire system can reach a new equilibrium state. With the action of an external electric field, the shape of the opened pixel grid was shown in **Figures 2B,D**. The magnitude of the applied voltage determines the balance position of the corresponding electrostatic force and capillary force. Thus, the opening degree of the pixel grid was determined by the voltage applied between the upper and lower electrodes. Therefore, the grayscale of EWDs can be controlled by adjusting the magnitude of the applied voltage. The opening degree of the pixel grid can be characterized by the aperture ratio. The aperture ratio is defined as the ratio of the aperture area S_o to the total area of a pixel grid S_p, which can be described by the Formula (6).

$$Aperture\ Ratio\ (\%) = \frac{S_o}{S_p} \times 100\% \tag{6}$$

Charge Trapping Effect and Oil Backflow Phenomenon

According to the Lippmann-Young equation, the change of the electrowetting contact angle in an ideal state is related to the square of U. Theoretically, the change in contact angle is only related to the magnitude of the applied voltage. The polarity of the applied voltage (positive or negative voltage) makes no difference in the change of a contact angle. However, it has been found that the change of contact angle during the electrowetting process showed a dependence on the polarity of driving voltages. The asymmetric electrowetting effect can be exacerbated because of the polarity dependence. The previous study has shown that the charge at the solid-liquid interface could be trapped by asymmetric electrowetting points with voltage polarity dependence [15]. To take the captured charges into account, a modification could be made to the Lippmann-Young equation. The modified Lippmann-Young equation can be described by Formula (7).

$$cos\,\theta_u = \frac{\gamma_{sg} - \gamma_{sl} + \varepsilon_0\varepsilon_r(U - U_T)^2/2d}{\gamma_{lg}} \tag{7}$$

$$\sigma_T = \frac{\varepsilon_0\varepsilon_r}{d}U_T \tag{8}$$

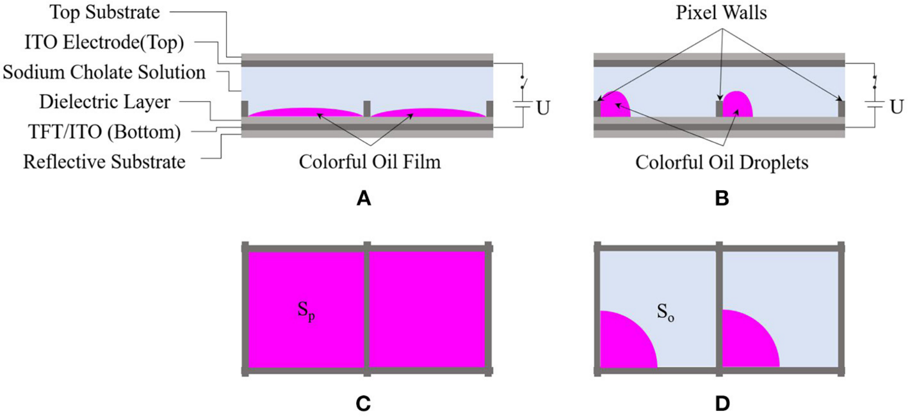

FIGURE 2 | Schematic diagram of EWDs. When no voltage was applied, the colored oil was evenly spread out in the pixel grid, **(A)** is a side sectional view, **(C)** is a top view. When a voltage was applied, the spread oil film was squeezed to a corner of the pixel grid, **(B)** is the side cross-sectional view, **(D)** is the top view.

Where, U_T represents the magnitude of the voltage generated by the trapped charges. σ_T represents the density of trapped charges, as shown in Formula (8). It has been found that there was indeed a charge trapping phenomenon during the electrowetting process [32]. According to the modified Lippmann-Young equation, a local reverse electric field can be formed at the interface between the dielectric and the water because of the charge trapping effect. The effective electric field at the three-phase contact line was weakened by the reverse electric field. The reverse electric field could be continuously strengthened by the accumulated charges. Therefore, the effective driving voltage between electrodes of pixel was indirectly reduced with the increasing of time. With a constant voltage applied, the electrowetting force would be reduced by the charge trapping effect. At the same time, the hydrophobicity of the medium layer was enhanced. In this situation, it is difficult for the three-phase contact line to be maintained in a fixed position. Therefore, the contracted oil droplets cannot be maintained in a stable state, and the oil droplets would be gradually spread out on the medium layers.

EXPERIMENTAL METHODS

Experimental System

For evaluating the performance of the proposed driving waveform, an experimental platform was developed to measure the brightness of EWDs. The block diagram of experimental system was shown in **Figure 3**, and the picture of experimental platform was shown in **Figure 4**. The proposed experimental platform was composed of a waveform design module, a driving module, and a detection module. In the waveform design module, the waveform data generated by MATLAB was imported into the host software to obtain the corresponding waveform file. The driving module was composed of an arbitrary waveform generator and a power amplifier. The generated waveform files can be transferred to the arbitrary waveform generator by Universal Serial BUS (USB) interface. Since the amplitude of the driving waveform was limited by the arbitrary waveform generator, a power amplifier was used to amplify the driving waveform. To ensure that the designed driving waveform can be output correctly, an oscilloscope was added to observe the amplified driving waveform in real-time. Then, the amplified driving waveform was used to drive an EWD panel. The detection work was undertaken by the detection module composed of a reflection colorimeter and its host software. To characterize the performance of the EPD panel, the reflective colorimeter was placed on the EWD panel during the experiment. The brightness data of EWDs was collected by the host software of colorimeter with the USB interface.

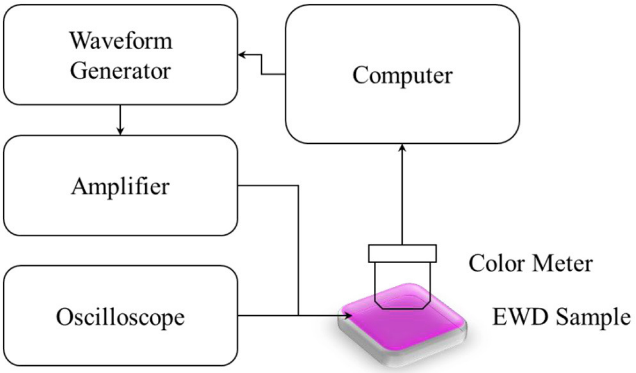

FIGURE 3 | System diagram of the experimental platform. The experimental platform was mainly composed of an arbitrary waveform generator, an amplifier, an oscilloscope, and a colorimeter. The magenta EWD panel was used in experiments.

Measurement of Hysteresis Characteristic Curve of EWDs

According to the Lippmann-Young equation, the relationship between contact angle and applied voltage was not linear. Due to the contact angle hysteresis of EWDs, the state of EWDs was different at the different stages with the same driving voltage. To intuitively observe the non-linear relationship, a stepwise voltage was applied between electrodes of pixel. The driving waveform for the measurement of the hysteresis curve was shown in **Figure 5**.

It can be seen from **Figure 5** that the driving waveform was consists of a rising phase and a falling phase. In the rising phase, the initial voltage applied to the EWD panel was 0 V, and then the voltage was increased by 0.5 V per second. When the voltage reached the maximum driving voltage of 30 V, the driving waveform was turned into a falling phase. In the falling phase, the voltage was reduced by 0.5 V per second until 0 V. The relationship between the luminance and driving voltage is shown in **Figure 6**.

It can be seen from **Figure 6** that the brightness of the EWD during the voltage rising phase could not be overlapped with the brightness during falling phase at the same voltage. A non-negligible difference between two curves could be observed in most voltage ranges, especially when pixels were turned on. With the same driving voltage, the brightness of an EWD in the falling phase was higher than that in the rising stage. The hysteresis effect of EWDs was mainly caused by the inconsistency between the advancing contact angle and the receding contact angle [33]. Due to the hysteresis effect of EWDs, aperture ratio in the rising phase and the falling phase were different with the same driving voltage. Similar differences have appeared in the brightness and reflectivity of EWDs. To obtain a repeatable grayscale with the same driving voltage, the influence of the hysteresis effect of EWDs cannot be ignored. The impact of the hysteresis effect on grayscales should be minimized by the design of driving waveform. Considering that the curve of luminance-voltage in the falling phase was smoother, the voltage of relatively flat area was always used to drive EWDs in this paper.

Design of Driving Waveform

Due to the phenomenon of oil backflow, the state of oil film in pixels was difficult to be maintained. To achieve a stable grayscale of EWDs, a reset signal was introduced to the driving waveform.

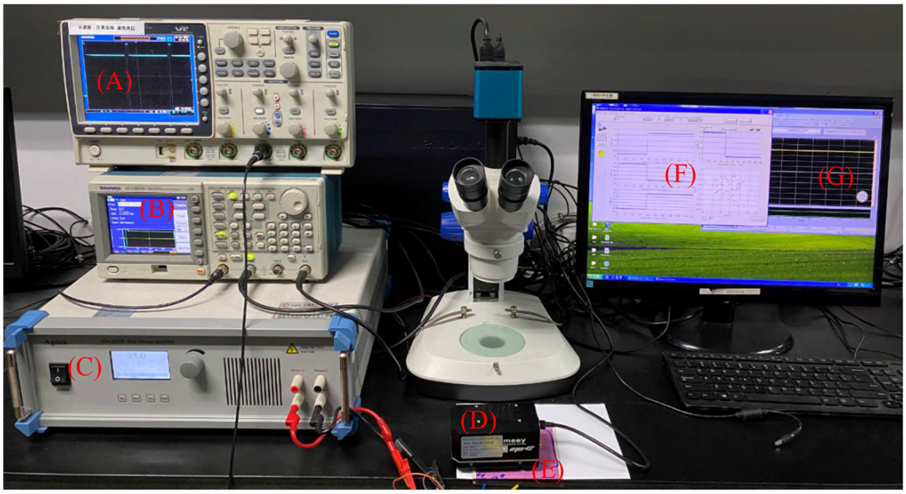

FIGURE 4 | The experimental platform for driving EWDs. **(A)** Oscilloscope. **(B)** Arbitrary waveform generator. **(C)** Power amplifier. **(D)** Colorimeter. **(E)** EWD panel. **(F)** Host software of colorimeter. **(G)** Host software of waveform generator.

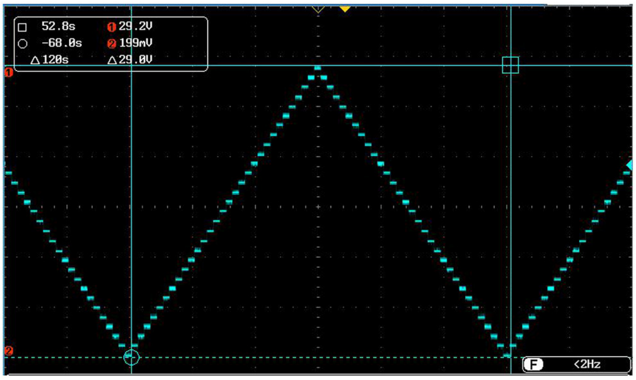

FIGURE 5 | The driving waveform used to measure the hysteresis curve of an EWD. When a stepwise changing voltage was applied to an EWD, the brightness value of the EWD was measured by a reflection colorimeter in real-time.

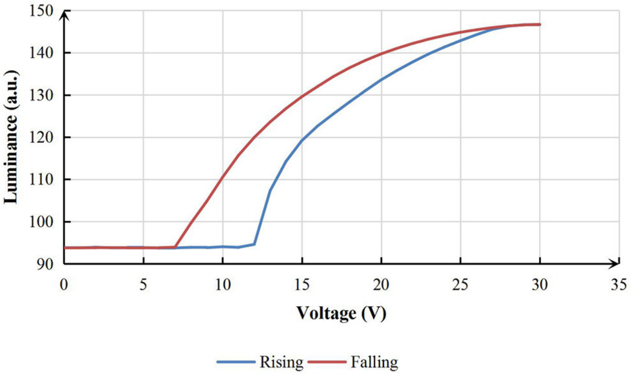

FIGURE 6 | Hysteresis characteristic curve of EWDs.

The shape of the proposed reset signal can be shown by the red line in **Figure 7**. The introduction of the reset signal was aimed at reducing the influence of oil backflow caused by the charge trapping effect.

As shown in **Figure 7**, the proposed driving waveform can be divided into two parts: a driving signal S_0 and a reset signal. The driving signal was used to turn on pixels, and the reset signal was used to release trapped charges. The effective driving voltage between electrodes of pixel could be maintained by discharging captured charges on time. In this way, the current equilibrium state of the oil film in pixel grids could be maintained. The reset signal can be divided into a charge release phase S_1 and a driving recovery phase S_2. V_{max} represented the maximum driving voltage. V_{Gn} and V_{Gn+1} represented the target voltage that was required to drive pixels to a grayscale. $V_{Release}$ represented a driving voltage used in the charge release phase. T_{reset} represented the period where the reset signal was applied. Durations of the charge release phase and the driving recovery phase in the reset signal were represented by t_1 and t_2, respectively. $t_1 + t_2$ represented the duration of the reset signal in one driving cycle.

The driving signal S_0 was a DC signal. The DC signal was used to drive the EWD to the target grayscale. The amplitude of the driving voltage of the target grayscale can be determined by the hysteresis characteristic curve of EWDs. The reset signal was used to release captured charges. In the charge release phase of the reset signal, the release efficiency of the trapped charge was related to $V_{Release}$ and t_1. In the driving recovery phase of the reset signal, the maximum voltage V_{max} was applied to obtain a better grayscale response. In an ideal state, a reset signal should be applied immediately before the oil backflow phenomenon appeared.

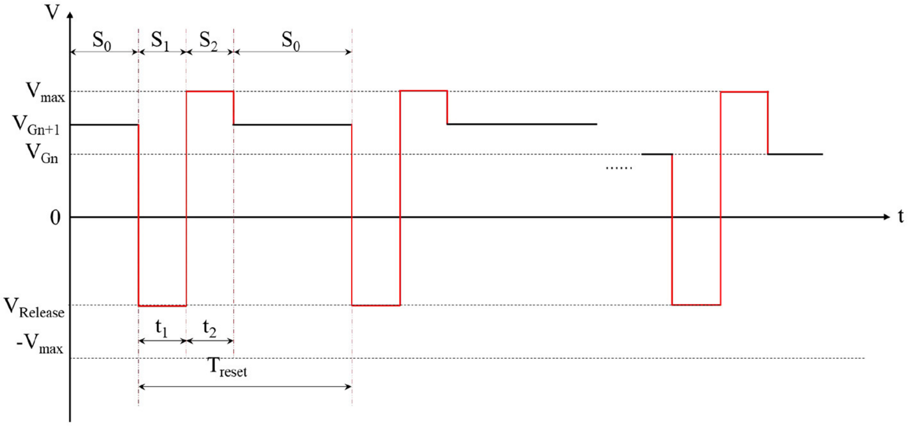

FIGURE 7 | The diagram of driving waveform with a reset signal introduced. It can be used to reduce the influence of oil backflow in EWDs.

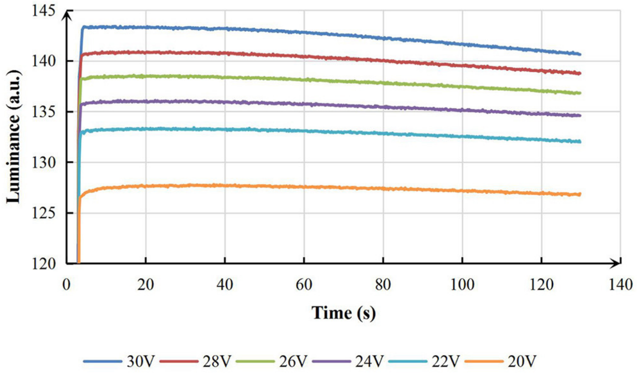

FIGURE 8 | The relationship between brightness and driving time when an EWD panel was driven by different DC voltages.

EXPERIMENTAL RESULTS AND DISCUSSION

The Brightness Change of EWDs With DC Driving Voltage

To obtain the brightness curve of an EWD with the DC voltage, several different DC driving voltages were sequentially applied to EWDs. The time-varying curve of the brightness of an EWD driven by different DC voltages as shown in **Figure 8**.

It can be seen from **Figure 8** that a higher brightness could be detected by the reflective colorimeter with a larger driving voltage. However, the state of EWDs cannot be maintained when the brightness reached the maximum value. The brightness value was gradually decreased at a certain rate as the driving time was increased. When the driving time was long enough, the brightness would be gradually decreased to a minimum value. When the amplitude of DC signal was reduced from 30 to 20 V, the decrease value of brightness was reduced from 2.770 to 0.729 a.u. within 109.4 s. The result showed that the drop gradient of brightness was faster with the higher driving voltage.

The Influence of Driving Waveforms With a Reset Signal on EWDs

According to the results of the DC driving experiment, it was found that the brightness of EWDs has different degrees of decline with different DC driving voltages due to the charge trapping effect. To suppress the charge trapping effect, a reset signal was introduced in the DC driving waveform. It can be seen that the shape of reset signal was determined by T_{reset}, $V_{Release}$, t_1 and t_2. The driving voltage of target grayscales in phase S_0 was set to 24 V. The brightness value of the EWD driven by different driving waveforms was used to characterize the performance of driving waveforms.

The brightness curve of an EWD at different frequencies was shown in **Figure 9**. Many peaks were observed in the curve of brightness when the driving frequency was set to 1 or 5 Hz. It was indicated that the brightness of the display had a large jitter. At this point, a strong flicker of EWDs can be directly observed. When the frequency of driving waveform was increased to 10 Hz, the number and amplitude of peaks were significantly decreased. At the same time, the obvious flicker cannot be observed on EWDs. When the frequency was increased to 50 Hz, there was no peak. It was shown that the high driving frequency was conducive to the stability of brightness or gray scales. However, the brightness of EWDs was decreased with the increase of driving frequency. In addition, an obvious downward trend has appeared when the driving frequency was increased to about 600 Hz. That's because the duration of the reset signal phase was shortened when the driving frequency was increased. If the duration of the reset signal was not enough, the target of suppressing charge trapping cannot be achieved. In this situation, it was difficult for EWDs to maintain a stable state. When the driving frequency was set to 50 Hz, the brightness can be stabilized at a higher value. In addition, the fluctuation cannot

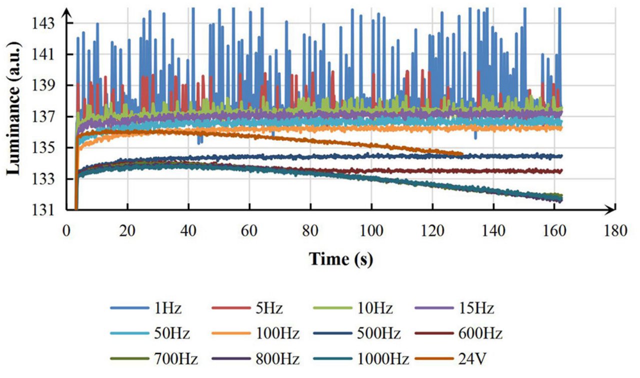

FIGURE 9 | The brightness curve of an EWD driven by driving waveform at different frequencies ($V_{Release} = -30$ V, $V_{max} = 30$ V, $t_1 = t_2$, $P_{reset} = 10\%$.).

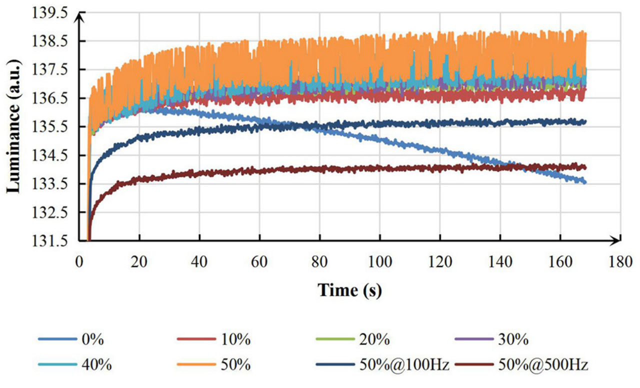

FIGURE 10 | The brightness curve of an EWD driven by reset signals with different proportions P_{reset} (F = 50 Hz, $V_{Release} = -30$ V, $V_{max} = 30$ V, $t_1 = t_2$.).

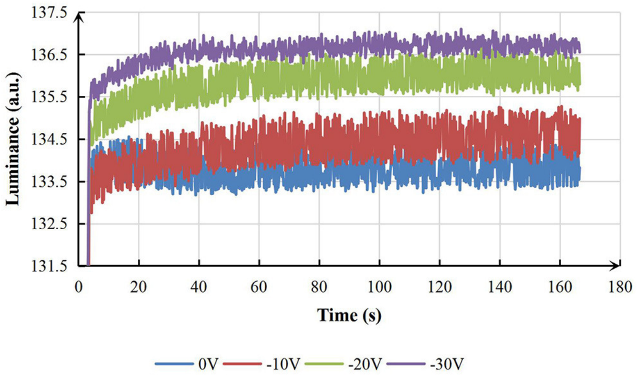

FIGURE 11 | Luminance curves of an EWD driven by reset signals with different release voltages (F = 50 Hz, $V_{max} = 30$ V, $t_1 = t_2$, $P_{reset} = 10\%$.).

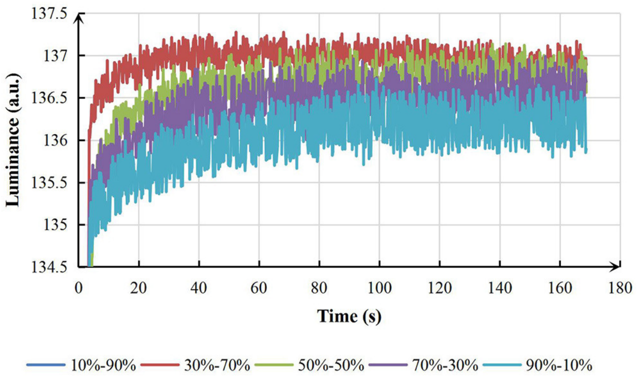

FIGURE 12 | The curve of brightness-voltage of an EWD with the different ratio of t_1/t_2 (F = 50 Hz, $V_{max} = 30$ V, $V_{Release} = -30$ V, $P_{reset} = 10\%$.).

be directly observed. So, the frequency of the proposed driving waveform was set to 50 Hz.

With the same frequency of driving waveform, the proportion of the reset signal in a whole driving cycle also had an influence on the stability of grayscales. The definition of proportion P_{reset} can be described as $P_{reset} = (t_1 + t_2)/T_{Reset}$. The brightness curve of an EWD at different P_{reset} was shown as **Figure 10**.

When the driving frequency was set to 50 Hz, all driving waveforms except $P_{reset} = 0\%$ (equivalent to DC driving waveform without a reset signal) can be used to keep the stability of brightness. With the increase of P_{reset} in a whole driving cycle, the brightness value was increased. However, the fluctuation amplitude of brightness was significantly increased at the same time. To reduce the fluctuation of brightness, the frequency of driving waveform was increased to 100 and 500 Hz. It turned out that the maximum brightness value of EWDs was decreased. Experimental rsults show that EWDs could reach a higher brightness with the lower fluctuation when Preset was set to 10%. Therefore, the proportion P_{reset} was set to 10% and the frequency was still set to 50 Hz.

The voltage applied in the release phase was also an important factor for the stability of EWDs. It can be seen from **Figure 11** that the brightness and stability of the EWD were significantly improved with the increase of $V_{Release}$. That's because a larger reverse voltage was beneficial to the release of trapped charges. Therefore, the effective driving voltage between electrodes of a pixel can be stabilized. Once the effective voltage was stabilized, the brightness of EWDs could be maintained.

In addition, the brightness stability of an EWD could be affected by the ratio of t_1 to t_2, which can be defined as $R_{reset} = \frac{t_1}{t_2}$. Curves of brightness-time with different R_{reset} was shown in **Figure 12**. Experimental results showed that the brightness was decreased and the fluctuation range of brightness was increased with the increase of R_{reset}. An obvious downward trend of the brightness curve was shown when the value of R_{reset} was set to 1/9 or 3/7. It was demonstrated that the charge trapping effect cannot be well-suppressed when the duration of the release phase was less than half of $t_1 + t_2$. So, the brightness of EWDs was decreased as the driving time increased. On the other hand, it was difficult for pixels to reach the maximum brightness when the duration of the release phase was more than half of $t_1 + t_2$.

Therefore, the decrease and fluctuation of the brightness can be noticed on EWDs. The experimental results showed that the best inhibition effect on the charge trapping can be obtained when t_1 was equal to t_2.

With the DC voltage was applied, the brightness of EWDs was decreased by 3.280 a.u. in 145 s. However, the brightness only decreased by 0.315 a.u. in the same period by applying the proposed driving waveform. To quantitatively analyze the display performance of EWDs, the speed of oil backflow can be defined as the falling value of the brightness within unit time. It was demonstrated that the speed of oil backflow was reduced by 90.4% when the EWD was driven by the proposed driving waveform.

CONCLUSIONS

To suppress the influence of the charge trapping effect in EWDs, a driving waveform based on a reset signal was proposed. The reset signal was composed of a charge release phase and a driving recovery phase. The performance of driving waveform was evaluated by the brightness of EWDs. Experiments were conducted to investigate the influence of reset signal on the oil backflow. By applying the proposed driving waveform, the speed of oil backflow can be reduced by 90.4%, and the charge trapping effect can be suppressed by the periodic reset signal. Therefore, the proposed driving waveform could be applied for achieving stable grayscales.

DATA AVAILABILITY STATEMENT

The original contributions presented in the study are included in the article/supplementary material, further inquiries can be directed to the corresponding author/s.

AUTHOR CONTRIBUTIONS

TZ and YD devised the project and experiments. TZ conceived the planned experiments and wrote the manuscript in consultation with YD. YD helped supervise the findings of this work. All authors discussed the results and contributed to the final version of the manuscript.

FUNDING

This research was funded by the National Key Research and Development Program of China (No. 2016YFB0401501), Science and Technology Program of Guangzhou (No. 2019050001), Program for Guangdong Innovative and Enterpreneurial Teams (No. 2019BT02C241), National Natural Science Foundation of China (No. 22008156), Guangdong Provincial Key Laboratory of Optical Information Materials and Technology (No. 2017B030301007), Guangzhou Key Laboratory of Electronic Paper Displays Materials and Devices (201705030007), MOE International Laboratory for Optical Information Technologies and the 111 Project.

REFERENCES

1. Bai P, Hayes R, Jin M, Shui L, Yi Z, Wang L, Zhang X, G Zhou. Review of paper-like display technologies. *Progr Electromagn Res*. (2014) 147:95–116. doi: 10.2528/PIER13120405
2. Wang Z, Liu Z. The key technology of ereader based on electrophoretic display. In: *2nd International Conference on Software Technology and Engineering*, San Juan, PR (2010) pp. V1-333–V1-336. doi: 10.1109/ICSTE.2010.5608873
3. Zhang Y, Zhen B, Al-Shuja'a S, Zhou G, Li X, Feng Y. Fast-response and monodisperse silica nanoparticles modified with ionic liquid towards electrophoretic displays. *Dyes Pigments*. (2018) 148:270–5. doi: 10.1016/j.dyepig.2017.09.014
4. Hiji N, Yoshinori M, Yasuo Y, Yoshihide S, Shigeaki O, Tadanobu S, et al. Novel color electrophoretic E-paper using independently movable colored particles. *SID Symp Digest Tech Papers*. (2012) 43:85–7. doi: 10.1002/j.2168-0159.2012.tb05716.x
5. Kao W, Liu S, Chang W. Signal processing for playing videos on electrophoretic displays. In: *IEEE 55th International Midwest Symposium on Circuits and Systems (MWSCAS)*, Boise, ID (2012) pp. 872–5. doi: 10.1109/MWSCAS.2012.6292159
6. Hayes R, Feenstra B. Video-speed electronic paper based on electrowetting. *Nature*. (2003) 425:383–5. doi: 10.1038/nature01988
7. Beni G, Tenan M. Dynamics of electrowetting displays. *J Appl Phys*. (1981) 52:6011–5. doi: 10.1063/1.329822
8. Li W, Wang L, Zhang T, Lai S, Liu L, He W, et al. Driving waveform design with rising gradient and sawtooth wave of electrowetting displays for ultra-low power consumption. *Micromachines*. (2020) 11:145. doi: 10.3390/mi11020145
9. Yi Z, Liu L, Wang L, Li W, Shui L, Zhou G. A driving system for fast and precise gray-scale response based on amplitude–frequency mixed modulation in TFT electrowetting displays. *Micromachines*. (2019) 10:732. doi: 10.3390/mi10110732
10. Yi Z, Shui L, Wang L, Jin M, Hayes R A, Zhou G. A novel driver for active matrix electrowetting displays. *Displays*. (2015) 37:86–93. doi: 10.1016/j.displa.2014.09.004
11. Yi Z, Feng W, Wang L, Liu L, Zhou G. Aperture ratio improvement by optimizing the voltage slope and reverse pulse in the driving waveform for electrowetting displays. *Micromachines*. (2019) 10:862. doi: 10.3390/mi10120862
12. Chevalliot S, Dhindsa M, Kuiper S, Heikenfeld, J. Experimental validation of the invariance of electrowetting contact angle saturation. *J Adhes Sci Technol*. (2012) 26:1909–30. doi: 10.1163/156856111X599580
13. Dong B, Tang B, Groenewold J, Li H, Zhou R, Henzen A, et al. Failure modes analysis of electrofluidic display under thermal ageing. *R Soc Open Sci*. (2018) 5:181121. doi: 10.1098/rsos.181121
14. Raj B, Dhindsa M, Smith NR, Laughlin R, Heikenfeld J. Ion and liquid dependent dielectric failure in electrowetting systems. *Langmuir*. (2009) 25:12387–92. doi: 10.1021/la9016933
15. Verheijen H, Prins M. Reversible electrowetting and trapping of charge: model and experiments. *Langmuir*. (1999) 15:6616–20. doi: 10.1021/la990548n
16. Li X, Tian H, Shao J, Ding Y, Chen X, Wang L, et al. Decreasing the saturated contact angle in electrowetting-on-dielectrics by controlling the charge trapping at liquid-solid interfaces. *Adv Funct Mater*. (2016) 26:2994–3002. doi: 10.1002/adfm.201504705
17. Yi Z, Huang Z, Lai S, He W, Wang L, Chi F, et al. Driving waveform design of electrowetting displays based on an exponential function for a stable grayscale and a short driving time. *Micromachines*. (2020) 11:313. doi: 10.3390/mi11030313
18. Chen Y C, Chiu Y H, Lee W Y, Liang CC. A charge trapping suppression method for quick response electrowetting displays. *SID Symp Digest Tech Papers*. (2010) 41:842–5. doi: 10.1889/1.3500607

19. Yi Z, Bai P, Wang L, Zhang X, Zhou G. An electrophoretic display driving waveform based on improvement of activation pattern. *J Central South Univ.* (2014) 21:3133–7. doi: 10.1007/s11771-014-2285-9
20. Wang L, Yi Z, Jin M, Shui L, Zhou G. Improvement of video playback performance of electrophoretic displays by optimized waveforms with shortened refresh time. *Displays.* (2017) 49:95–100. doi: 10.1016/j.displa.2017.07.007
21. Beni G, Hackwood S. Electro-wetting displays. *Appl Phys Lett.* (1981) 38:207–9. doi: 10.1063/1.92322
22. Xie N, Zhang N, Xu R. Effect of driving voltage polarity on dynamic response characteristics of electrowetting liquid lens. *Jpn J Appl Phys.* (2018) 57:052201. doi: 10.7567/JJAP.57.052201
23. Yi Z, Feng H, Zhou X, Shui M. Design of an open electrowetting on dielectric device based on printed circuit board by using a parafilm. *Front Phys.* (2020) 8:193. doi: 10.3389/fphy.2020.00193
24. Gong J, Kim C. All-electronic droplet generation on-chip with real-time feedback control for ewod digital microfluidics. *Lab Chip.* (2008) 8:898–906. doi: 10.1039/b717417a
25. Samiei E, Tabrizian M, Hoorfar M. A review of digital microfluidics as portable platforms for lab-on a-chip applications. *Lab Chip.* (2016) 16:2376. doi: 10.1039/C6LC00387G
26. Feng H, Yi Z, Yang R, Qin X, Shen S, Zeng W, et al. Designing splicing digital microfluidics chips based on polytetrafluoroethylene membrane. *Micromachines.* (2020) 11:1067. doi: 10.3390/mi11121067
27. Srinivasan V, Pamula V, Fair R. An integrated digital microfluidic lab-on-a-chip for clinical diagnostics on human physiological fluids. *Lab Chip.* (2004) 4, 310–5. doi: 10.1039/b403341h
28. Torabinia M, Asgari P, Dakarapu U, Jeon J, Moon, H. On-chip organic synthesis enabled using an engine-and-cargo system in an electrowetting-on-dielectric digital microfluidic device. *Lab Chip.* (2019) 19:3054–3064. doi: 10.1039/C9LC00428A
29. Yang S, Krupenkin T, Mach P, Chandross E. Tunable and latchable liquid microlens with photopolymerizable components. *Adv Mater.* (2003) 15:940–3. doi: 10.1002/adma.200304745
30. Berge B. Liquid lens technology: principle of electrowetting based lenses and applications to imaging. In: *18th IEEE International Conference on Micro Electro Mechanical Systems, 2005. MEMS 2005.* Miami Beach, FL (2005). p. 227–230. doi: 10.1109/MEMSYS.2005.1453908
31. Hu X, Zhang S, Qu C, Zhang Q, Lu L, Ma X, et al. Ionic liquid based variable focus lenses. *Soft Matter.* (2011) 7:5941–3. doi: 10.1039/c1sm05585b
32. Wu H, Dey R, Siretanu I, Ende D, Shui L, Zhou G, et al. Electrically controlled localized charge trapping at amorphous fluoropolymer–electrolyte interfaces. *Small.* (2019) 16:1905726. doi: 10.1002/smll.201905726
33. Van Dijk R, Feenstra BJ, Hayes RA, Camps IGJ, Boom RGH, Wagemans MMH, et al. Gray scales for video applications on electrowetting displays. *SID Symp Digest Tech Papers.* (2006) 37:1926–9. doi: 10.1889/1.2433427

Conflict of Interest: The authors declare that the research was conducted in the absence of any commercial or financial relationships that could be construed as a potential conflict of interest.

frontiers in Physics

ORIGINAL RESEARCH
published: 04 May 2021
doi: 10.3389/fphy.2021.684283

InGaN/Cu_2O Heterostructure Core-Shell Nanowire Photoanode for Efficient Solar Water Splitting

Yingzhi Zhao[1], *Lingyun Xie*[1], *Hedong Chen*[1], *Xingyu Wang*[1], *Yongjie Chen*[1], *Guofu Zhou*[1,2,3]* and *Richard Nötzel*[1,2]*

[1] Guangdong Provincial Key Laboratory of Optical Information Materials and Technology, South China Academy of Advanced Optoelectronics, South China Normal University, Guangzhou, China, [2] National Center for International Research on Green Optoelectronics, South China Normal University, Guangzhou, China, [3] Academy of Shenzhen, Guohua Optoelectronics, Shenzhen, China

The heterostructuring and doping concepts have proved to obtain a novel n-InGaN/p-Cu_2O nanowire (NW) photoanode by strong enhancement of the photocurrent compared to a bare InGaN NW photoanode in solar water splitting. The large photocurrent is due to the maximized photocarrier separation and hole transfer to the surface in the depletion zone of the p–n heterojunction established by the p-Cu_2O layer, forming a thin, uniform shell-layer around the n-InGaN NW core by electrodeposition. For sufficiently thin Cu_2O layers, the upward energy band bending in the depletion zone extends up to the surface for optimized hole transport and surface reaction. Thick Cu_2O layers on top of the InGaN NWs act as common photocathodes. The functional InGaN/Cu_2O heterostructure core-shell NW photoanode is chemically self-stabilized at positive applied voltage by a thin CuO surface layer. Final deposition of the earth-abundant NiOOH co-catalyst boosts the photocurrent of the InGaN/Cu_2O/NiOOH complete NW photoanode into the competitive mA/cm^2 range.

Keywords: Cu_2O, InGaN nanowires, core-shell, stability, co-catalyst

Edited by:
Qiang Xu,
Nanyang Technological University, Singapore

Reviewed by:
Xiaowen Zhang,
Guilin University of Electronic Technology, China
Liming Liu,
University of Electronic Science and Technology of China, China

***Correspondence:**
Richard Nötzel
richard.noetzel@scnu.edu.cn
Guofu Zhou
guofu.zhou@m.scnu.edu.cn

Specialty section:
This article was submitted to Optics and Photonics, a section of the journal Frontiers in Physics

Received: *23 March 2021*
Accepted: *12 April 2021*
Published: *04 May 2021*

Citation:
Zhao Y, Xie L, Chen H, Wang X, Chen Y, Zhou G and Nötzel R (2021) InGaN/Cu_2O Heterostructure Core-Shell Nanowire Photoanode for Efficient Solar Water Splitting. Front. Phys. 9:684283. doi: 10.3389/fphy.2021.684283

INTRODUCTION

The key strategies to boost the performance of photoelectrodes are nanostructuring, surface catalyst coupling, light management, heterostructuring, and doping to optimize the crucial processes of light absorption, photocarrier separation and transfer, and surface reaction [1, 2]. To begin with the right material, InGaN is one of the best choices due to the wide tunability of the direct optical bandgap over the whole visible range by varying the In content, the high absorption coefficient, high carrier mobility, and chemical and mechanical resilience [3–5]. In addition, for one of the most important reactions, the photoelectrochemical splitting of water into hydrogen and oxygen [6–8], InGaN possesses the required straddling alignment of the conduction band and valence band with the water H^+/H_2 reduction potential and O_2/H_2O oxidation potential for up to ∼50% of the In content and shows the best bandgap energy for solar light absorption for 30–40% In [9]. Solar hydrogen produced by this method of photoelectrochemical water splitting is the ideal green fuel to replace fossil fuels in a sustainable hydrogen energy economy[1].

Nanostructured n-type InGaN nanowires (NWs) and InGaN layers, activated with InN quantum dots (QDs), employed as photoanodes, showed high efficiencies in the oxygen evolution reaction (OER) in solar water splitting [10–16]. The underlying difference between these two approaches is

---

[1] Hydrogen program. Available online at: https://www.hydrogen.energy.gov.

the type of surface states for the m-plane InGaN NW sidewalls and the c-plane surface of the InGaN layers and InN QDs. m-Planes exhibit negatively charged surface states within the energy bandgap, causing near-surface upward energy band bending, which is most commonly encountered in the n-type semiconductors. The c-plane of In-rich InGaN layers exhibits positively charged surface states located within the conduction band [17–21]. These positively charged surface states catalyze the OER by attraction of electrons, which is strongly enhanced by the zero-dimensional electronic properties of InN QDs. For m-planes, in contrast, a low catalytic activity for the OER results from the negatively charged surface states. Therefore, to benefit from the largely increased surface area of NWs, additional measures need to be taken to obtain competitive water splitting efficiencies, such as the decoration of the NW sidewalls with co-catalysts. InGaN NWs have also demonstrated their successful light management and absorption enhancement, acting as efficient anti-reflection structures when grown on pyramid-patterned Si substrates [22].

In this study, we demonstrate the heterostructuring and doping routes for an InGaN/Cu_2O core-shell NW photoanode to boost solar water splitting by enhancing the separation and transport of photogenerated carriers. The underlying concept is as follows: A heterostructure with the right staggered band alignment, such that no energy barriers for the transport of electrons and holes are present, can improve the photogenerated carrier separation and transport. However, it is only effective together with the right band bending given by the doping. Based on an n-type photoanode with near-surface upward energy band bending, a p-type layer on top is optimum to increase the upward energy band bending at the p–n junction. Together with a positive band offset, this pushes the holes toward the surface more effectively for the OER and also enhances the electrons to travel toward the cathode for the hydrogen evolution reaction (HER). A p-type layer, however, exhibits the wrong near-surface downward energy band bending, opposing the hole transport toward the surface. Therefore, the p-type layer has to be sufficiently thin, such that it is fully depleted and the upward energy band bending proceeds all the way to the surface. This turns a p-type layer, usually acting as photocathode into an active surface layer, by boosting the efficiency of an n-type photoanode. For the optimized bandgap energy for solar light absorption of the n-type photoanode, the p-type layer on top ideally has a similar, medium bandgap energy to contribute to the absorption. Regarding the OER, however, the surface of the p-type layer is not necessarily reactive, still requiring the deposition of co-catalysts.

Considering the band alignment, doping, and bandgap energy, p-type Cu_2O fulfills all the requirements when combined with n-type In-rich InGaN as a heterostructure photoanode. Photogenerated carrier separation and transfer are strongly enhanced in the depletion zone of the p–n heterojunction formed at the n-InGaN/p-Cu_2O heterointerface with positive band offset. This is based on a previous study where we showed that Cu_2O, a deeply studied p-type metal-oxide, acts as an efficient hole injection and a collection layer on In-rich InGaN NWs, solving the p-type conductivity problem [23]. High-quality p-type InGaN with a high In content is hardly realized. The bandgap energy of Cu_2O of 2.1 eV is sufficiently small and the conduction band and valence band of Cu_2O are well-aligned with those of the In-rich InGaN with the right band offsets.

Cu_2O is electrodeposited on the InGaN NWs. Scanning electron microscopy (SEM), transmission electron microscopy (TEM), and energy dispersive X-ray spectroscopy (EDS) reveal that Cu_2O forms a uniform shell-layer on the m-plane InGaN NW sidewalls while nucleating as isolated Cu_2O nanocrystals on the c-plane NW tops. p-Type Cu_2O is well-known as a photocathode for the HER [24, 25]. This is reproduced for thick Cu_2O layers grown on top of the InGaN NWs. Similar to InGaN, Cu_2O also exhibits a straddling energy band alignment with the water redox potentials [25–28], making the energy band alignment with InGaN most obvious. For thin Cu_2O layer deposition, the Cu_2O shell-layers on the InGaN NWs are fully depleted for thicknesses of $\sim$10 nm with upward energy band bending up to the surface. The efficient photocarrier separation and hole transport to the surface strongly enhance the OER reaction for positive applied voltage, as shown by linear sweep voltammetry (LSV) measurements and current density vs. time (I–t) measurements under chopped illumination. For optimized Cu_2O deposition amount, an almost 7-fold enhancement of the photocurrent is observed. Electrochemical impedance spectroscopy (EIS), however, shows that the Cu_2O surface is catalytically not very active for the OER, such as the m-plane InGaN NW sidewalls, leading to an overall insufficient photocurrent. Therefore, to achieve competitive photocurrents, NiOOH co-catalyst is electrodeposited to complete the photoanode preparation process. NiOOH is chosen because it contains only earth-abundant elements. Functioning as InGaN/Cu_2O core-shell NW photoanode at positive applied voltage, the Cu_2O layer is chemically self-stabilized by the formation of a thin CuO surface layer due to the self-limiting oxidation of Cu_2O, as evidenced by the LSV measurements, cyclic voltammetry (CV) measurements, and X-ray photoelectron spectroscopy (XPS). Although imposing a small energy barrier for the hole transport, the thin CuO surface layer does not significantly influence the photocurrent. In contrast to Cu_2O employed as photocathode at negative applied voltage, no other surface passivation is needed. The InGaN/Cu_2O heterostructure core-shell NW photoanode, self-passivated with the thin CuO surface layer, shows no degradation for many hours of operation.

EXPERIMENTAL DETAILS

Growth of In-rich InGaN NWs

The InGaN NWs on planar p-type Si (111) substrates were fabricated by plasma-assisted molecular beam epitaxy (PA-MBE). The In and Ga metal fluxes were provided by standard Knudson effusion cells, and the active nitrogen species were generated with a radio frequency (RF) plasma source. Before loading into the MBE chamber, the Si substrates were etched in 10 wt% HF aqueous solution for 1 min to remove the native surface oxide layer. Then, the cleaned Si substrates were loaded into the MBE buffer chamber and degassed in the MBE middle chamber for 1 h at 300°C. The Si substrates were then transferred to the MBE growth chamber, outgassed for 10 min at 900°C (thermocouple reading) to remove any residual native surface oxide, and exposed to active N flux for 5 min to form a thin SiN_x layer. The RF power for the Si surface nitridation was 350 W, and the molecular N_2 flow rate was 1.7 standard cubic centimeters per minute (sccm). The SiN_x layer improves the InGaN crystal quality by enhancing strain relaxation and reducing the dislocation density. For not too extended nitridation, the SiN_x interlayer does not alter the electronic properties/near-ohmic behavior of the Si/InGaN interface [29]. For InGaN growth, the substrate temperature was ramped down to 610°C (thermocouple reading) and InGaN growth under N-rich conditions was performed by opening the In and Ga cell shutters for 1 h. The In and Ga beam equivalent pressure was 7.60×10^{-8} and 1.32×10^{-7} Torr, respectively, and the active N source parameters were 350 W and 1.7 sccm molecular N_2 flux.

Electrode Preparation

The samples were coated with In–Ga eutectic on the back side of the substrate to form an ohmic contact, glued on Cu-conductive adhesive tape, and fixed on a supporting glass plate. The surface was covered with non-transparent silicone rubber, leaving an opening for contact with the electrolyte.

Electrodeposition of Cu_2O

The Cu_2O layers were fabricated on the InGaN NWs by electrodeposition in a three-electrode electrochemical cell using an electrochemical work station. The InGaN NWs, a Pt mesh, and a saturated calomel electrode (SCE) were used as working, counter, and reference electrodes, respectively. The aqueous electrolyte comprised 0.4 M $CuSO_4$, 3 M lactic acid, and $C_3H_6O_3$. The pH was adjusted to 12 by adding 5 M NaOH. The deposition voltage was kept at −0.4 V vs. SCE. During deposition with magnetic stirring at 180 rpm, the temperature was set to 27°C by a hot plate with a temperature sensor in the solution.

Electrodeposition of NiOOH

The InGaN/Cu_2O/NiOOH structures were prepared by electrodeposition in a three-electrode electrochemical cell with the InGaN/Cu_2O working electrode, a Pt mesh counter electrode, and a saturated KCl Ag/AgCl reference electrode, connected to an electrochemical workstation. The electrolyte was 100 mL of 5 mM $Ni(NO_3)_2 \cdot 6H_2O$ aqueous solution. The potential was kept at −1.0 V vs. Ag/AgCl. The optimized electrodeposition time was 330 s.

Materials Assessment

Structural analysis of the InGaN NWs and Cu_2O layer was performed using X-ray diffraction (XRD) (PANalytical X'Pert PRO). Field-emission SEM (ZEISS Gemini 500), TEM (JEM-2100HR), and atomic force microscopy (AFM, Bruker MultiMode 8) were used to characterize the surface morphology and cross-section of the structures. EDS element mappings were carried out with energy disperse spectrometers (Aztec X-Max 80) attached to the SEM and TEM. XPS was conducted with XPS spectrometers (EscaLab 250Xi) attached to the SEM and TEM. The XPS spectra were calibrated with respect to the C 1s peak. Raman spectroscopy was performed with the 532 nm line of a Nd-YAG solid-state laser. The diameter of the laser spot was ~1 μm. Photoluminescence (PL) spectra were taken at room temperature with the 100 mW, 532 nm line of a Nd-YAG solid-state laser as excitation source, and a silicon charged coupled device (CCD) attached to a single monochromator for detection.

Electrochemical Measurements

The electrochemical measurements were performed in a three-electrode electrochemical cell with the InGaN, InGaN/Cu_2O, and InGaN/Cu_2O/NiOOH working electrodes; a Pt mesh counter electrode; and a saturated KCl Ag/AgCl reference electrode connected to an electrochemical workstation. A scheme of the experimental setup and sample structure is shown in **Supplementary Figure 1**. The electrolyte was 0.5 M Na_2SO_4 (pH = 7) aqueous solution. LSV current vs. voltage (I–V) measurements from +1 V to 0 V vs. Ag/AgCl [+1.6 V to +0.6 V vs. the reversible hydrogen electrode (RHE)] with 10 mV s^{-1} scan rate and I-t measurements at 0.6 V vs. Ag/AgCl (1.2 V vs. RHE) were performed under chopped 5 s on and 5 s off simulated sun light (1-sun, AM 1.5, 100 mW cm^{-2}, GLORIA-X500A). EIS measurements were conducted in the frequency range of 10 Hz to 1,000 kHz in the dark and light. CV measurements were performed in the voltage windows of −1 V to +1 V and 0 V to +1 V vs. Ag/AgCl with a 100 mV s^{-1} scan rate.

RESULTS AND DISCUSSION

Structure

Figures 1a,b shows the SEM top-view and cross-sectional images of the as-grown, bare InGaN NWs on a Si (111) substrate. The NWs have an average diameter of 40 nm, 600 nm length, and a flat top. After 40 s of Cu_2O electrodeposition, which turns out to be the optimum Cu_2O electrodeposition time, sparse, isolated Cu_2O nanocrystals are visible in the top-view SEM image in **Figure 1b**. AFM images are shown in **Supplementary Figure 2**. The nanocrystals are positioned on the NWs and also in-between NWs with arbitrary orientations. The shape of the nanocrystals reflects the cubic crystal symmetry of Cu_2O. The more connected appearance of the NWs in the cross-sectional image in **Figure 1c** indicates the deposition of Cu_2O on the InGaN NW sidewalls. Formation of the pure Cu_2O phase for the present electrodeposition condition is confirmed by the omega-two-theta XRD spectrum shown in **Supplementary Figure 3A** and by the Raman spectrum in **Supplementary Figure 3B** [23]. Only peaks from cubic Cu_2O, InGaN, and Si, as labeled, are observed. From the XRD spectrum, the In content of the InGaN NWs of 28% is deduced [30]. However, XPS measurements (**Figure 1e**) that were taken some days after fabrication of the Cu_2O layer revealed the presence of CuO. As XRD and Raman spectroscopy rather probe the bulk material, XPS is highly surface sensitive, indicating the self-limiting oxidation of Cu_2O to CuO in air to form a thin surface layer of CuO [31]. This is

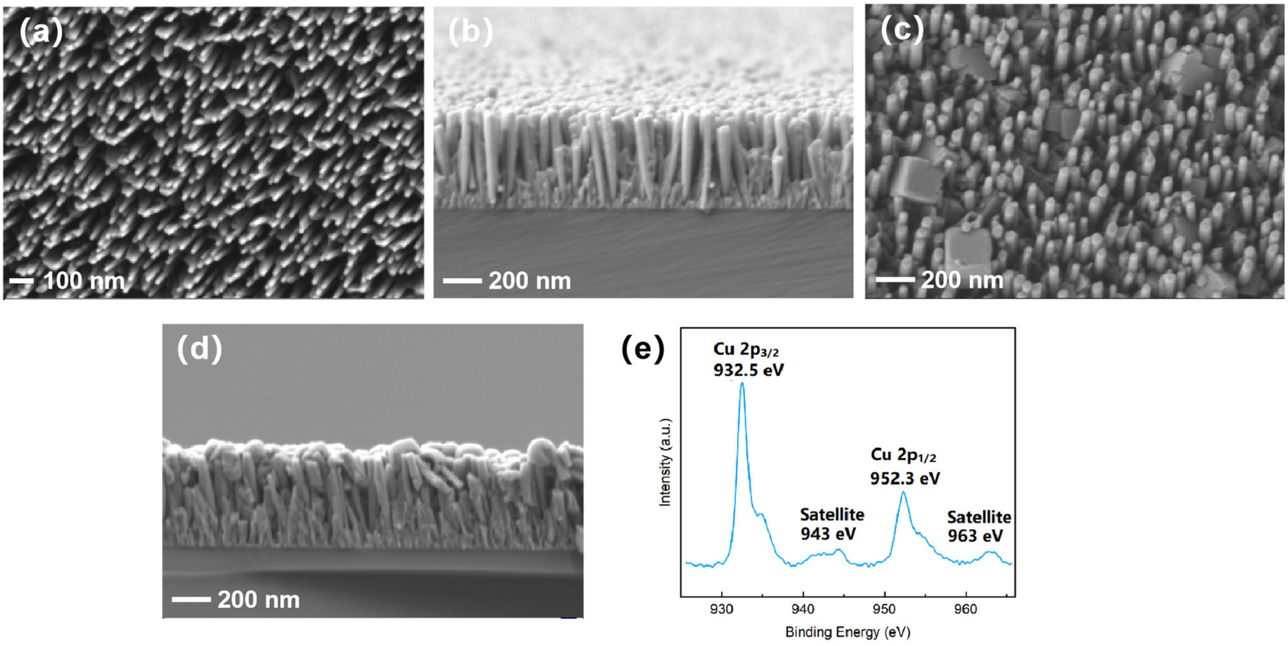

FIGURE 1 | Top-view- and cross-sectional SEM images of the **(a,b)** bare InGaN nanowires (NWs) and **(c,d)** InGaN NWs after 40 s Cu_2O electrodeposition. **(e)** X-ray photoelectron spectroscopy taken several days after Cu_2O electrodeposition.

further discussed in the section Stability on the stability of the InGaN/Cu_2O heterostructure operated as photoanode.

The element distributions are imaged by EDS mappings shown in **Figure 2**. The mappings are taken from the NW cross-sectional part shown in the SEM image in **Figure 2a**. **Figure 2b** displays the total EDS intensity. The individual mappings of In, Ga, N, Cu, O, and Si are shown in **Figures 2c–h**, respectively. The mappings of In, Ga, N, and Si show the uniform element distribution in the InGaN NWs on the Si substrate. The Cu and O element distributions reveal the deposition of Cu_2O on the NW sidewalls, penetrating from the top to the bottom with decreasing EDS intensities.

The deposition of Cu_2O on the InGaN NW sidewalls is directly resolved in the TEM image in **Figure 3a,** and the corresponding EDS element mappings of In, Ga, N, and Cu are shown in **Figures 3b–f**. **Figure 3b** gives the total EDS intensity and **Figures 3c–f** depict the individual In, Ga, N, and Cu element mappings. The element contrast for O, which is not shown, is very weak. Cu_2O forms a rather uniform shell on the InGaN NW sidewalls. The Cu_2O shell is composed of ultra-small nanocrystals, of ∼5 nm in diameter, with random orientation, seen in the high-resolution TEM image in the inset of **Figure 3a**. The spaces between the NWs are not completely filled. The element distributions of In, Ga, and N follow the straight geometry of the InGaN NWs. The element distribution of Cu is more blurred and smeared out, as expected for the InGaN/Cu_2O core-shell structure. The different Cu_2O electrodeposition behavior on the InGaN NW sidewalls and NW tops is addressed in the following section.

Photoelectrochemical Properties

Figure 4A depicts the LSV curves for the InGaN/Cu_2O core-shell NWs and for the bare InGaN NWs under chopped 1-sun (AM 1.5, 100 mW/cm^2) illumination. The Cu_2O electrodeposition time is 40 s. The LSV scan is taken from +1 V to 0 V vs. Ag/AgCl (1.6 V to 0.6 V vs. RHE) with a scan rate of 10 mV/s. In the presence of the Cu_2O shell, the photocurrent density at positive voltage is enhanced by up to 700%. At negative voltage, no photoresponse is observed, as seen in the CV scan from +1 V to −1 V in **Supplementary Figure 4A**. This demonstrates the role of Cu_2O in enhancing the OER when the InGaN/Cu_2O core-shell NWs operate as photoanodes. The optimum Cu_2O electrodeposition time of 40 s is provided from the plot of the photocurrent density vs. electrodeposition time, which is taken for an applied voltage of +0.6 V vs. Ag/AgCl (1.2 V vs. RHE), as shown in **Figure 4B**. When the Cu_2O deposition time is increased much longer, the individual cubic Cu_2O nanocrystals on top of the InGaN NWs, as shown in the SEM image in **Figure 1c**, increase in density and coalesce to form a compact layer. For such thick Cu_2O layers, the usual behavior of Cu_2O as a photocathode for the HER at negative voltage is recovered, as shown in the LSV and I–t curves in **Supplementary Figures 4B–D**. In this case, there is no photoresponse for positive voltage. This confirms that the thin Cu_2O shell-layer is responsible for the enhanced photoanode performance, whereas the much thicker/larger cubic Cu_2O nanocrystals act as photocathodes.

A first indication of the reproducibility and stability of the InGaN/Cu_2O core-shell NW photoanode is given by the I–t curve taken at +0.6 V vs. Ag/AgCl (1.2 V vs. RHE) under

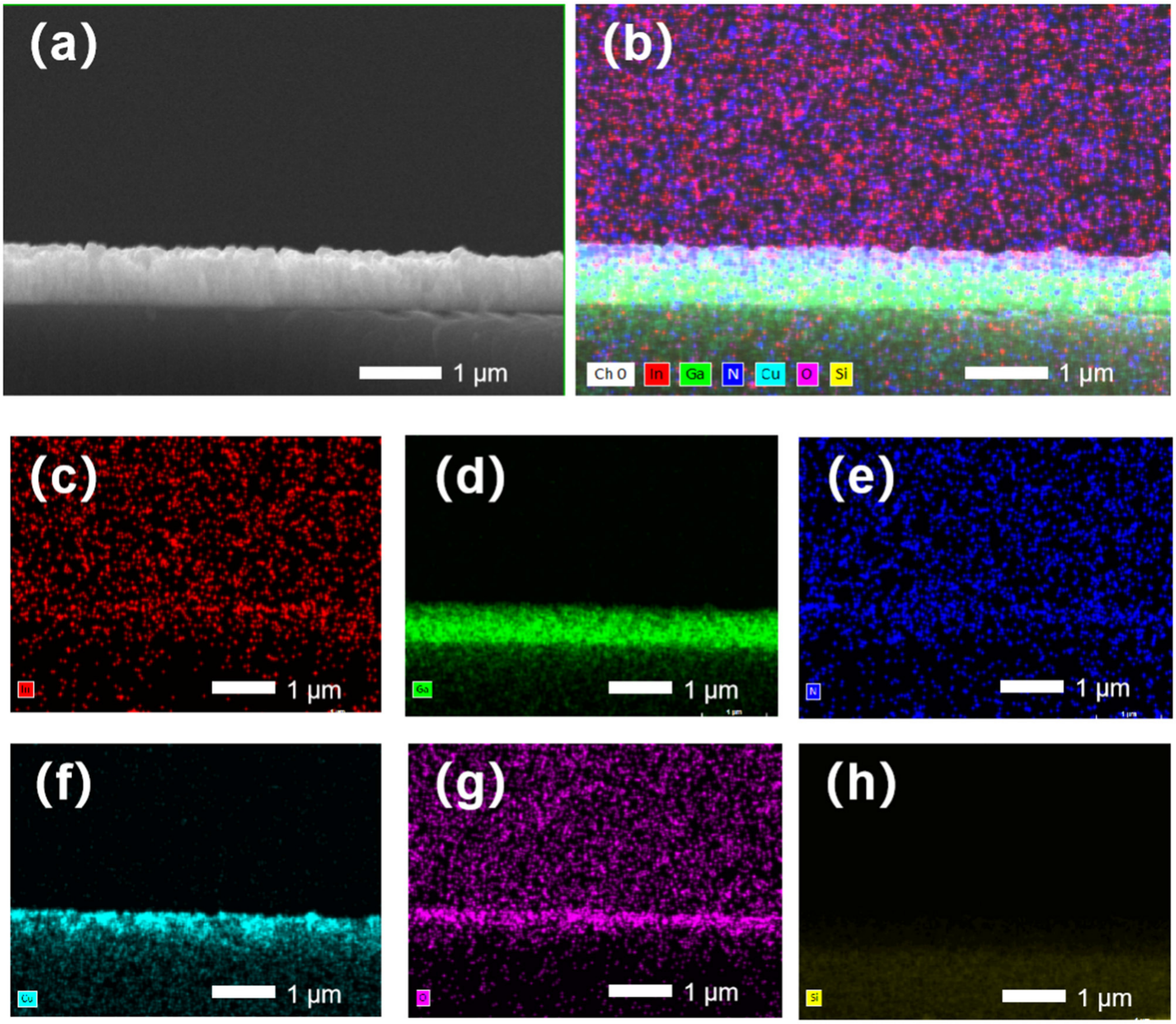

FIGURE 2 | **(a)** Cross-sectional SEM image and **(b–h)** energy dispersive X-ray spectroscopy (EDS) element mappings. **(b)** Total EDS intensity and **(c–h)** In, Ga, N, Cu, O, and Si element mappings.

chopped 1-sun illumination in **Figure 4C** with the curve for the bare InGaN NWs for comparison. The curves reproduce a 700% increase of the photocurrent density in the presence of the Cu_2O shell-layer, in agreement with the LSV measurements, and a good photo-switching behavior is observed.

The increased photocurrent density is attributed to the p–n junction with related upward energy band bending, formed at the InGaN/Cu_2O interface for the m-plane NW sidewalls. The upward energy band bending enhances the separation of the photogenerated carriers and the transport of photogenerated holes toward the surface. This is maximized for sufficiently thin and fully depleted Cu_2O layers on the NW sidewalls when the upward energy band bending continues to the surface. This is guaranteed for up to a Cu_2O thickness where the energy band positions at the surface, taking into account only the ionized acceptor density, reach the values given by the downward energy band bending for bulk Cu_2O of typically 0.4 V, which are, in turn, given by the surface Fermi-level pinning. This accounts for the increase of the photocurrent at positive voltage with increasing Cu_2O shell-layer thickness, passing up to a maximum and finally reverse with photoresponse at negative voltage for thick Cu_2O layers on the InGaN NW tops. The sparse cubic Cu_2O nanocrystals formed together with the Cu_2O shell-layers do not affect the photoanode behavior. Their size rather indicates near-surface downward energy band bending without photoresponse for positive voltage. A scheme of the described InGaN/Cu_2O energy band structure and photogenerated carrier transport for increasing Cu_2O shell-layer thickness is drawn in **Figure 4D**.

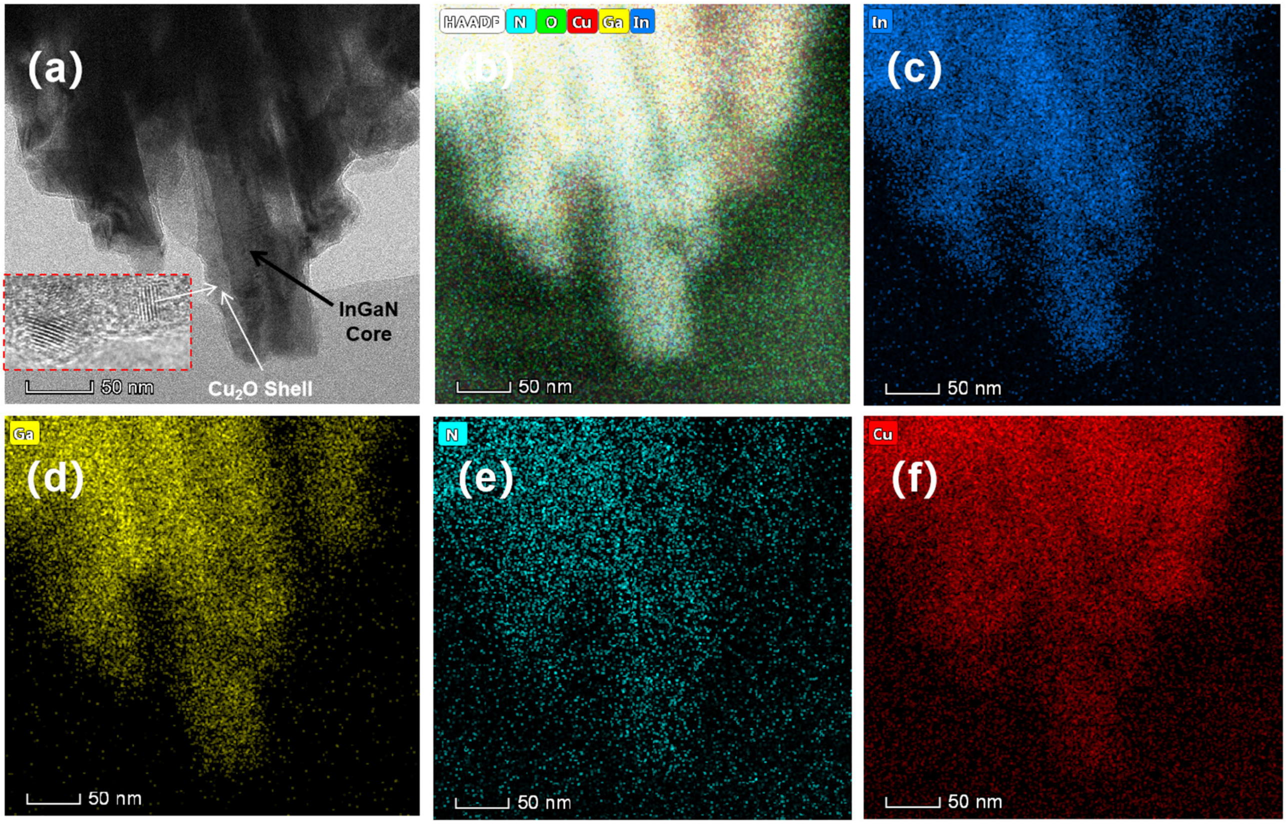

FIGURE 3 | **(a)** Cross-sectional TEM image and **(b–f)** EDS element mappings. **(b)** Total EDS intensity and **(c–f)** In, Ga, N, and Cu element mappings. The inset in **(a)** is a high-resolution TEM image of the Cu_2O shell-layer.

The thin CuO surface layer [32] formed due to the self-limiting oxidation of Cu_2O, which is discussed in more detail below, is also indicated.

The maximum photocurrent density for a Cu_2O shell-layer thickness of several 10 nm agrees with typical ionized acceptor densities for Cu_2O of 10^{15}–10^{16} cm^{-3} and the related width of the depletion zone [33, 34]. However, the decrease of the photocurrent density might set in before the maximum width of the Cu_2O depletion zone is utilized because of filling up of the spaces between the InGaN NWs with Cu_2O, whereas the light absorption in the Cu_2O layer might contribute to the increase of the photocurrent density with Cu_2O layer thickness. Unfortunately, we have no direct experimental access to the electrical properties of the thin Cu_2O shell-layers electrodeposited on the InGaN NW sidewalls.

Apart from that, in contrast to the rectifying p–n junction for Cu_2O on the m-plane InGaN NW sidewalls, leading to the upward energy band bending, the electrical contact is more ohmic for Cu_2O on the c-plane NW tops [23], not supporting the upward energy band bending. This has been attributed to the varying characteristics of the surface states for the m-plane and the c-plane of In-rich InGaN: Negatively charged surface states in the bandgap for the m-plane vs. positively charged surface states in the conduction band for the c-plane of In-rich InGaN, leading to upward/downward near-surface energy band bending for the m-plane/c-plane for In-rich InGaN and, accordingly, to near-surface electron depletion for the m-plane/near-surface electron accumulation for the c-plane of In-rich InGaN.

The different characteristics of the surface states and resulting InGaN/Cu_2O electrical contact for the m-plane and the c-plane of In-rich InGaN may also explain the different electrodeposition behavior of Cu_2O on the m-plane NW sidewalls and c-plane NW tops. The formation of the rectifying p–n junction for Cu_2O electrodeposition on the NW sidewalls, which is forward biased under the electrodeposition conditions, might lead to a more controlled, charge-transfer limited, quasi-two-dimensional growth with the nucleation and fast coalescence of ultra-small and dense Cu_2O nanocrystals. The more ohmic resistance for the NW tops might favor mass-transport limited growth, leading to the larger, randomly oriented three-dimensional Cu_2O nanocrystals with lower density, as usually observed on conductive substrates [35].

The PL spectra taken at room temperature from the InGaN/Cu_2O core-shell NWs and the bare InGaN NWs are shown in **Figure 5A**. The PL intensity for the InGaN/Cu_2O core-shell NWs is significantly reduced. This is the PL from InGaN. No PL is observed from Cu_2O. The PL process is fairly complex, involving light absorption, photogenerated carrier relaxation and

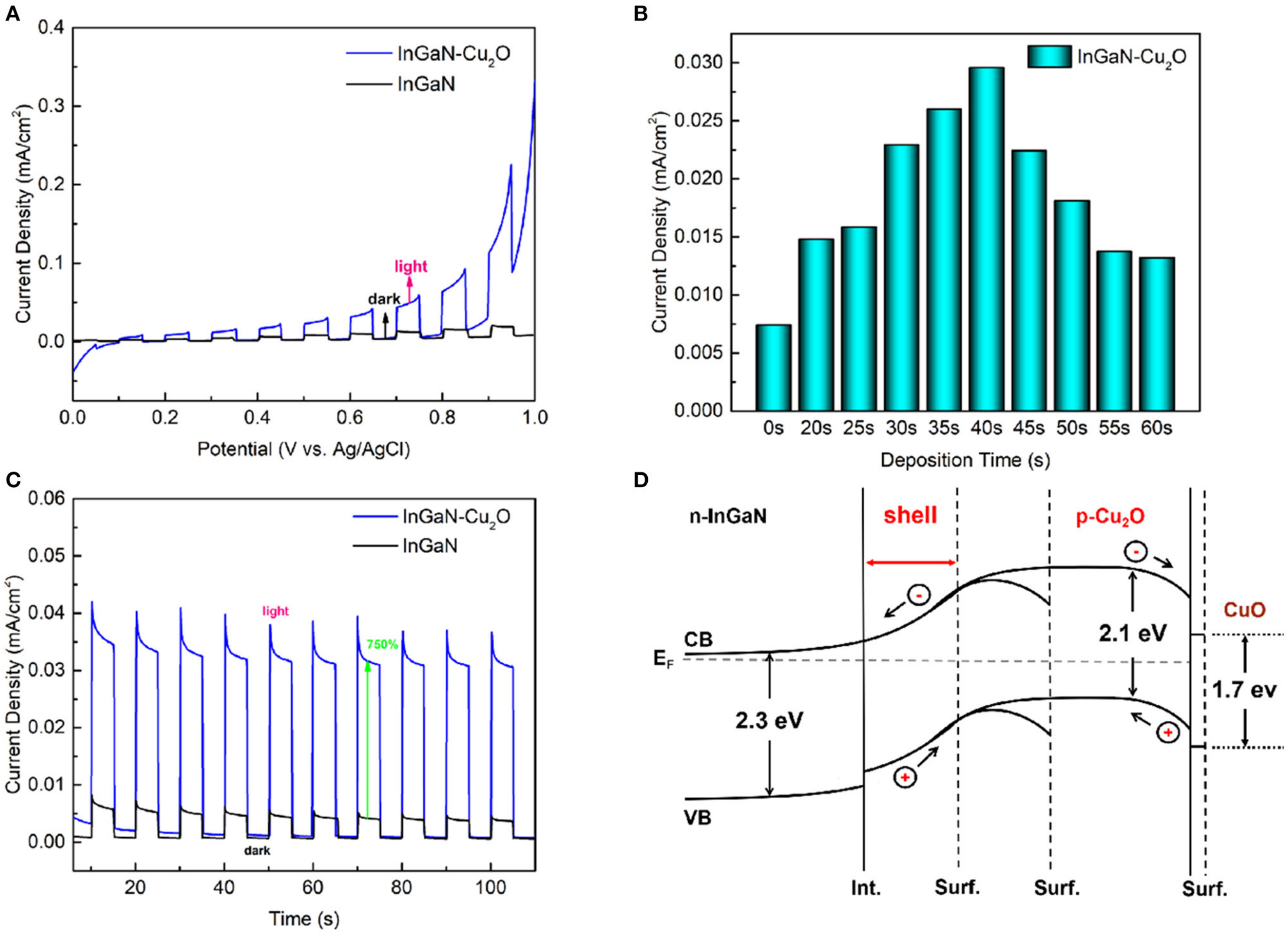

FIGURE 4 | (A) Linear sweep voltammetry measurements of the InGaN/Cu_2O core-shell NWs and the bare InGaN NWs under chopped illumination. **(B)** Photocurrent density at +0.6 V vs. Ag/AgCl (1.2 V vs. reversible hydrogen electrode [RHE]) as a function of the Cu_2O electrodeposition time. **(C)** I–t measurements at +0.6 V vs. Ag/AgCl (1.2 V vs. RHE) of the InGaN/Cu_2O core-shell NWs and the bare InGaN NWs under chopped illumination. **(D)** Scheme of the InGaN/Cu_2O energy band diagram and photogenerated carrier transport for increasing Cu_2O layer thickness. Int. indicates the InGaN/Cu_2O interface and Surf. indicates the surface of Cu_2O shell-layers with different thicknesses. The thin CuO surface layer is also shown.

diffusion, and radiative electron–hole recombination. However, the reduced PL intensity for InGaN and the absence of PL from Cu_2O strongly support the enhanced photogenerated carrier separation and transfer in the presence of the Cu_2O shell-layer. The radiative electron–hole recombination is suppressed, overcompensating the absorption, which might be enhanced by the Cu_2O shell-layer.

With regard to all the steps in photoanode operation, i.e., absorption, photocarrier separation and transfer, and surface reaction, however, the Cu_2O surface is not anticipated to exhibit particular surface catalytic activity for the OER reaction. This is seen in the EIS measurements shown in **Figure 5B** of the InGaN/Cu_2O core-shell NWs and the bare InGaN NWs taken at an applied voltage of +0.6 V in the dark and under illumination. The half-circle in the Nyquist plots, whose diameter gives the charge transfer resistance, R_{ct}, is large for the InGaN/Cu_2O core-shell NWs and for the bare InGaN NWs, indicating an overall large R_{ct}. To be precise, R_{ct} includes the charge transfer through the surface in the dark plus the charge transfer toward the surface inside the photoanode under illumination. Therefore, the large R_{ct} for the InGaN/Cu_2O core-shell NWs, which is also under illumination, indicates a dominating slow charge transfer through the surface, resulting in a slow surface reaction. Therefore, to demonstrate competitive photocurrent densities, the photoanode fabrication process is completed by the electrodeposition of NiOOH co-catalyst comprising only earth-abundant elements. As shown in **Figures 5C,D**, the LSV and I–t curves (at +0.8 V, where the dark current continues to be low) of the InGaN/Cu_2O/NiOOH complete NW photoanode and the InGaN/Cu_2O core-shell NW photoanode demonstrate that photocurrent densities, reaching the mA/cm^2 regime, are achieved.

Stability

Figure 6 shows the CV curves recorded from −1 V to +1 V vs. Ag/AgCl and back in the dark and under 1-sun illumination with a scan rate of 100 mV/s for the bare InGaN NWs in

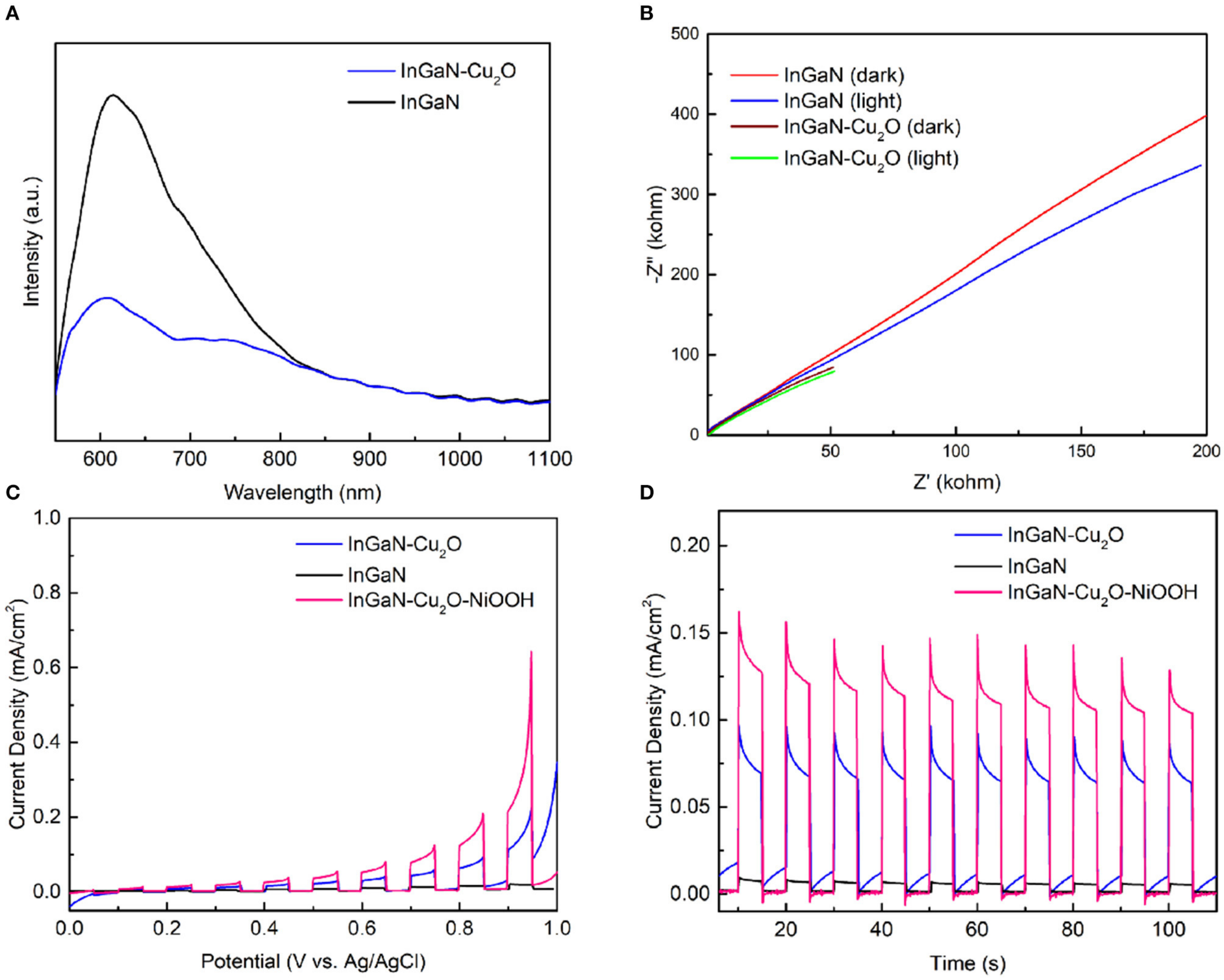

FIGURE 5 | (A) Photoluminescence (PL) spectra taken at room temperature of the InGaN/Cu_2O core-shell NWs and the bare InGaN NWs. **(B)** Electrochemical impedance spectroscopy (EIS) taken at +0.6 V vs. Ag/AgCl (1.2 V vs. RHE) in the dark and under illumination of the InGaN/Cu_2O core-shell NWs and the bare InGaN NWs. **(C)** LSV- and **(D)** I–t measurements at +0.8 V vs. Ag/AgCl (1.4 V vs. RHE) of the InGaN/Cu_2O/NiOOH complete NW photoanode and the InGaN/Cu_2O core-shell NWs under chopped illumination.

Figure 6A, the InGaN/Cu_2O core-shell NWs in **Figure 6B**, and the InGaN/Cu_2O/NiOOH complete NW photoanode in **Figure 6C**. The bare InGaN NWs show solely capacitative behavior without reaction peaks, whereas the InGaN/Cu_2O core-shell NWs exhibit distinct reduction and oxidation peaks at −0.46 V and +0.3 V, respectively. These are again absent for the InGaN/Cu_2O/NiOOH complete NW photoanode. This indicates excellent chemical stability of the bare InGaN NWs, which has been widely reported in previous studies, whereas the InGaN/Cu_2O core-shell NWs exhibit reduction and oxidation reactions. This is well-known and has been deeply investigated for the reduction and oxidation of thick Cu_2O layers used as photocathodes [25]. The NiOOH co-catalyst stabilizes the Cu_2O shell-layer by promoting the water splitting rather than the reduction and oxidation of Cu_2O.

Importantly, as we show in this study, the InGaN/Cu_2O core-shell NWs without NiOOH are stable when operated solely at positive voltage as photoanode. They are self-stabilized by a thin CuO surface layer. The chain of arguments goes as follows: (i) The oxidation peak at positive voltage occurs only after prior scanning over the reduction peak at negative voltage, as is done for the CV measurements (**Figure 6B**). When scanning only from 0 V to +1 V and back, while avoiding the reduction peak, no reaction peaks are visible in the CV curves (**Figure 6D**). Also, when scanning from +1 V to 0 V or to −1 V, no oxidation peaks were visible in the LSV measurements in **Figure 4A** and **Supplementary Figure 4A**. (ii) XPS shows that the oxidation peak originates from the oxidation of Cu_2O to CuO. In the XPS taken after scanning at positive voltages, as shown in **Figure 6E**, the CuO-related features are enhanced compared to those in the

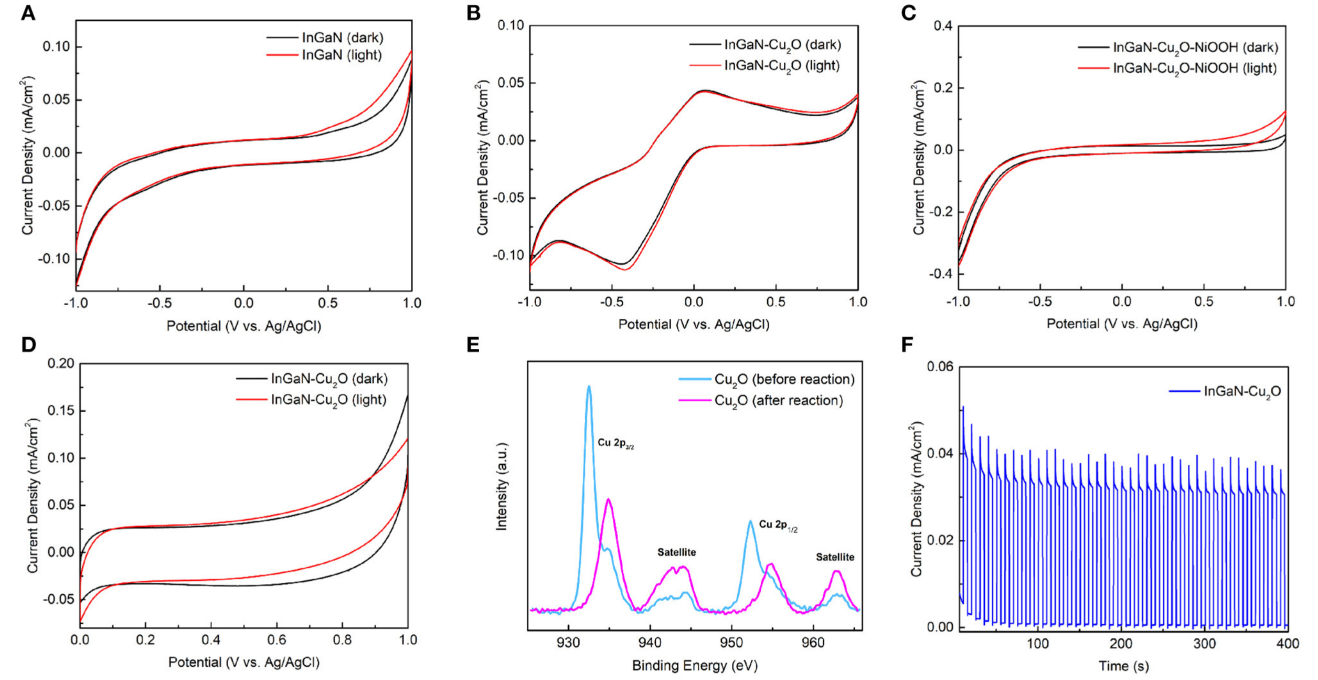

FIGURE 6 | Cyclic voltammetry (CV) curves taken in the dark and under illumination of the **(A)** bare InGaN NWs, **(B)** InGaN/Cu_2O core-shell NWs, **(C)** InGaN/Cu_2O/NiOOH complete photoanode, and **(D)** InGaN/Cu_2O core-shell NWs. **(E)** XPS spectra taken from the InGaN/Cu_2O core-shell NWs before and after the water splitting experiment. **(F)** I–t measurement at +0.6 V vs. Ag/AgCl (1.2 V vs. RHE) for the InGaN/Cu_2O core-shell NWs under chopped illumination.

XPS taken before, as shown in **Figure 1e**. We do not exclude that the oxidation of Cu contributes to the oxidation peak after prior reduction of Cu_2O [36]. However, this is irrelevant for the photoanode operation as no Cu-related features are observed in the XPS after scanning at positive voltage. (iii) In the I–t measurement taken over an extended duration of time at +0.6 V under chopped illumination, as shown in **Figure 6F**, an initial dark current is observed. This dark current appears when the measurement is started after prior to reduction at negative voltage. The dark current vanishes within 100 s. The photocurrent appears unaffected over the whole measurement. The total current and the dark current initially decrease with the same rate and finally, the total current equals the photocurrent and becomes very stable. Altogether, from observations (i)–(iii), there is oxidation of Cu_2O in air and at positive voltage, forming a thin surface layer of CuO, as already discussed in the context of the XRD, Raman, and XPS measurements. The oxidation quickly saturates such that the Cu_2O layer becomes self-stabilized by the thin CuO surface layer. Photo-oxidation is not involved in CuO formation as only the dark current changes but the photocurrent does not. The formation of a nanoscale thin, self-limiting surface oxide is all-too-common for materials which can undergo oxidation, such as those observed for the bare InGaN photoanode and Si. The self-limiting thickness is expected, considering that Cu_2O is the most stable Cu oxide. In TEM, the presence of the CuO layer is not seen. Importantly, the thin CuO surface layer does not significantly affect the photocurrent, although it imposes a small energy barrier for hole transport, as indicated in **Figure 4D**. Hole transport might be easy because of thermionic emission and tunneling or because the thin CuO layer is leaky for the transition of holes. Self-stabilized by the thin CuO surface layer, **Supplementary Figure 5** shows that the InGaN/Cu_2O photoanode only exhibits a very small photocurrent decrease after many hours of operation.

CONCLUSIONS

Large enhancement of the photocurrent is achieved for a novel n-InGaN/p-Cu_2O NW photoanode compared to a bare InGaN NW photoanode for the OER in solar water splitting. The electrodeposited Cu_2O layer forms a thin shell around the InGaN NW cores. The enhancement of the photocurrent is due to maximized photogenerated carrier separation and hole transfer to the surface in the fully depleted Cu_2O shell-layer of the p–n Cu_2O/InGaN heterojunction. Thick Cu_2O layers on top of the InGaN NWs act as usual photocathodes for the HER. The functional InGaN/Cu_2O heterostructure core-shell NW photoanode is chemically self-stabilized at positive applied voltage by a thin CuO surface layer. The photocurrent reaches the competitive mA/cm^2 range after final deposition of the earth-abundant NiOOH co-catalyst, establishing the InGaN/Cu_2O/NiOOH complete NW photoanode. Moreover, this is an important proof of the successful formation of a rectifying p–n junction at the InGaN/Cu_2O heterointerface with the Cu_2O layer acting as an efficient hole collection and transport layer on In-rich InGaN, solving the p-type doping problem with far-reaching impact for devices.

DATA AVAILABILITY STATEMENT

The original contributions presented in the study are included in the article/**Supplementary Material**, further inquiries can be directed to the corresponding author/s.

AUTHOR CONTRIBUTIONS

YZ performed the growth and the measurements with the support of LX. GZ and RN discussed and interpreted the results. RN supervised the research and drafted the manuscript together with YZ. All authors discussed and commented on the manuscript and read and agreed to the published version of the manuscript.

FUNDING

This study was supported by: the Program for Chang Jiang Scholars and Innovative Research Teams in Universities (No. IRT_17R40), the Science and Technology Program of Guangzhou (No. 2019050001), the Guangdong Provincial Key Laboratory of Optical Information Materials and Technology (Grant No. 2017B030301007), the Provincial Natural Science Foundation of Guangdong program (Grant No. 2018A030313368), the MOE International Laboratory for Optical Information Technologies, and the 111 Project.

SUPPLEMENTARY MATERIAL

The Supplementary Material for this article can be found online at: https://www.frontiersin.org/articles/10.3389/fphy.2021.684283/full#supplementary-material

REFERENCES

1. Jian J, Jiang G, van de Krol R, Wei B, Wang H. Recent advances in rational engineering of multinary semiconductors for photoelectrochemical hydrogen generation. *Nano Energy.* (2018) 51:457–80. doi: 10.1016/j.nanoen.2018.06.074
2. Cho S, Jang JW, Lee KH, Lee JS. Research update: strategies for efficient photoelectrochemical water splitting using metal oxide photoanodes. *Apl Mater.* (2014) 2:010703. doi: 10.1063/1.4861798
3. Wu J. When group-III nitrides go infrared: new properties and perspectives. *J Appl Phys.* (2009) 106:011101. doi: 10.1063/1.3155798
4. Zhou C, Ghods A, Saravade VG, Patel PV, Yunghans KL, Ferguson C, et al. The current and emerging applications of the III-nitrides. *ECS J Solid State Sci Technol.* (2017) 149:188–233. doi: 10.1149/2.0101712jss
5. Hwang YJ, Wu CH, Hahn C, Jeong HE, Yang P. Si/InGaN Core/Shell hierarchical nanowire arrays and their photoelectrochemical properties. *Nano Lett.* (2012) 12:1678–82. doi: 10.1021/nl3001138
6. Reece SY, Hamel JA, Sung K, Jarvi TD, Esswein AJ, Pijpers JJ, et al. Wireless solar water splitting using silicon-based semiconductors and earth-abundant catalysts. *Science.* (2011) 334:645–8. doi: 10.1126/science.1209816
7. Walter MG, Warren EL, McKone JR, Boettcher SW, Mi Q, Santori EA, et al. Solar water splitting cells. *Chem Rev.* (2010) 110:6446–73. doi: 10.1021/cr1002326
8. Grätzel M. Photoelectrochemical cells. In: Dusastre V, editor. *Materials for Sustainable Energy: A Collection of Peer-Reviewed Research and Review Articles From Nature Publishing Group*. World Scientific (2011). p. 26–32. doi: 10.1142/9789814317665_0003
9. Moses PG, Van de Walle CG. Band bowing and band alignment in InGaN alloys. *Appl Phys Lett.* (2010) 96:021908. doi: 10.1063/1.3291055
10. Lin J, Wang W, Li G. Modulating surface/interface structure of emerging InGaN manowires for efficient photoelectrochemical water splitting. *Adv Funct Mater.* (2020) 30:2005677. doi: 10.1002/adfm.202005677
11. Chowdhury FA, Mi Z, Kibria MG, Trudeau ML. Group III-nitride nanowire structures for photocatalytic hydrogen evolution under visible light irradiation. *APL Mater.* (2015) 77:104408. doi: 10.1063/1.4923258
12. Li J, Lin J, Jiang H. Direct hydrogen gas generation by using InGaN epilayers as working electrodes. *Appl Phys Lett.* (2008) 93:162107. doi: 10.1063/1.3006332
13. Benton J, Bai J, Wang T. Utilisation of gaN and InGaN/GaN with nanoporous structures for water splitting. *Appl Phys Lett.* (2014) 105:223902. doi: 10.1063/1.4903246
14. Nötzel R. InN/InGaN quantum dot electrochemical devices: new solutions for energy and health. *Natl Sci Rev.* (2017) 113:184–95. doi: 10.1093/nsr/nww101
15. Rodriguez PEDS, Aseev P, Gómez VJ, ul-Hassan W, Willander M, Nötzel R, et al. InN/InGaN quantum dot photoelectrode: efficient hydrogen generation by water splitting at zero voltage. *Nano Energy.* (2015) 13:291–7. doi: 10.1016/j.nanoen.2015.02.017
16. Baumann AE, Burns DA, Liu B, Thoi VS. Metal-organic framework functionalization and design strategies for advanced electrochemical energy storage devices. *Commun Chem.* (2019) 2:1–14. doi: 10.1038/s42004-019-0184-6
17. Van de Walle CG, Segev D. Microscopic origins of surface states on nitride surfaces. *J Appl Phys.* (2007) 101:081704. doi: 10.1063/1.2722731
18. Veal T, Jefferson P, Piper L, McConville C, Joyce T, Chalker P, et al. Transition from electron accumulation to depletion at InGaN surfaces. *Appl Phys Lett.* (2006) 89:202110. doi: 10.1063/1.2387976
19. Xie L, Wang P, Qian Y, Rao L, Yin H, Wang X, et al. Spatial surface charge engineering for electrochemical electrodes. *Sci Rep.* (2019) 9:1–8. doi: 10.1038/s41598-019-51048-5
20. Linhart WM, Veal TD, King PDC, Koblmüller G, Gallinat CS, Speck JS, et al. Surface, bulk, and interface electronic properties of nonpolar InN. *Appl Phys Lett.* (2010) 97:2–4. doi: 10.1063/1.3488821
21. King PDC, Veal TD, Mcconville CF, Fuchs F, Furthmüller J, Bechstedt FJ, et al. Universality of electron accumulation at wurtzite c-and a-plane and zinc-blende InN surfaces. *Appl Phys Lett.* (2011) 91:092101. doi: 10.1063/1.2775807
22. Chen H, Wang P, Ye H, Yin H, Rao L, Luo D, et al. Vertically aligned InGaN nanowire arrays on pyramid textured Si (1 0 0): A 3D arrayed light trapping structure for photoelectrocatalytic water splitting. *Chem Eng J.* (2021) 406:126757. doi: 10.1016/j.cej.2020.126757
23. Wang X, Wang P, Yin H, Zhou G, Nötzel R. Cu_2O as hole injection layer on In-rich InGaN nanowires. *J Appl Phys.* (2020) 128:025304. doi: 10.1063/1.5145035
24. De Jongh P, Vanmaekelbergh D, Kelly J. Cu_2O: electrodeposition and characterization. *Chem Mater.* (1999) 11:3512–7. doi: 10.1021/cm991054e
25. Paracchino A, Laporte V, Sivula K, Grätzel M, Thimsen, E. Highly active oxide photocathode for photoelectrochemical water reduction. *Nat Mater.* (2011) 10:456–61. doi: 10.1038/nmat3017
26. Chen S, Wang LW. Thermodynamic oxidation and reduction potentials of photocatalytic semiconductors in aqueous solution. *Chem Mater.* (2012) 24:3659–66. doi: 10.1021/cm302533s
27. Bagal IV, Chodankar NR, Hassan MA, Waseem A, Johar MA, Kim H, et al. Cu_2O as an emerging photocathode for solar water splitting-a status review. *Int J Hydrog Energy.* (2019) 44:21351–78. doi: 10.1016/j.ijhydene.2019.06.184
28. Azevedo J, Steier L, Dias P, Stefik M, Sousa CT, Araújo JP, et al. On the stability enhancement of suprous oxide water splitting photocathodes by low temperature steam annealing. *Energy Environ Sci.* (2014) 7:4044–52. doi: 10.1039/C4EE02160F

29. Wang X, Wang P, Yin H, Zhou G, Nötzel R. An InGaN/SiNx/Si uniband diode. *J Electron Mater*. (2020) 49:3577–82. doi: 10.1007/s11664-020-08038-5
30. Aseev P, Soto Rodriguez PED, Nötzel R. In-rich near-infrared InGaN layers grown directly on Si: towards the whole composition range. *Appl Phys Lett*. (2014) 106:072102. doi: 10.1063/1.4909515
31. Yu SY, Gao Y, Chen FZ, Fan C, Han DM, Wang C, et al. Fast electrochemical deposition of CuO/Cu_2O heterojunction photoelectrode: preparation and application for rapid cathodic photoelectrochemical detection of l-cysteine. *Sensors Actuators B: Chem*. (2019) 290:312–7. doi: 10.1016/j.snb.2019.03.104
32. Rafea MA, Roushdy N. Determination of the optical band gap for amorphous and nanocrystalline copper oxide thin films prepared by SILAR technique. *J Appl Phys*. (2009) 42:015413. doi: 10.1088/0022-3727/42/1/015413
33. Sullivan I, Zoellner B, Maggard PA. Copper (I)-based P-type oxides for photoelectrochemical and photovoltaic solar energy conversion. *Chem Mater*. (2016) 28:5999–6016. doi: 10.1021/acs.chemmater.6b00926
34. Wang Z, Nayak PK, Caraveo-Frescas JA, Alshareef HN. Recent developments in p-Type oxide semiconductor materials and devices. *Adv Mater*. (2016) 28:3831–92. doi: 10.1002/adma.201503080
35. Kaur J, Bethge O, Wibowo RA, Bansal N, Bauch M, Hamid R, et al. All-oxide solar cells based on electrodeposited Cu_2O absorber and atomic layer deposited ZnMgO on precious-metal-free electrode. *Solar Energy Mater Solar Cells*. (2017) 161:449–59. doi: 10.1016/j.solmat.2016.12.017
36. De Jongh P, Vanmaekelbergh D, Kelly JJ. Photoelectrochemistry of electrodeposited Cu_2O. *J Electrochem Soc*. (2000) 147:486. doi: 10.1149/1.1393221

Conflict of Interest: The authors declare that the research was conducted in the absence of any commercial or financial relationships that could be construed as a potential conflict of interest.

frontiers in Physics

ORIGINAL RESEARCH
published: 28 May 2021
doi: 10.3389/fphy.2021.687438

Photon-Assisted Seebeck Effect in a Quantum Dot Coupled to Majorana Zero Modes

Tian-Yu He[1], *Hailing Sun*[1,2]* *and Guofu Zhou*[1,2,3,4]

[1] *Guangdong Provincial Key Laboratory of Optical Information Materials and Technology, Institute of Electronic Paper Displays, South China Academy of Advanced Optoelectronics, South China Normal University, Guangzhou, China,* [2] *National Center for International Research on Green Optoelectronics, South China Normal University, Guangzhou, China,* [3] *Shenzhen Guohua Optoelectronics Tech. Co. Ltd., Shenzhen, China,* [4] *Academy of Shenzhen Guohua Optoelectronics, Shenzhen, China*

The Seebeck effect is investigated within the framework of a non-equilibrium Green's function technique in a quantum dot (QD) sandwiched between the left and right leads held at different temperatures. We consider that the QD is shelled by a photon field and is side-coupled to a topological superconductor nanowire hosting Majorana zero modes (MZMs). It is found that the thermopower (Seebeck coefficient) can be obviously enhanced by weak QD-MZMs coupling at low temperatures, in addition to its sign reversion that may be used for detecting the existence of MZMs. In the presence of a photon field, the thermopower can be further enhanced due to decreased electrical conductance when electrons' transport probability through each channel is reduced by photon-assisted tunneling (PAT). The hybridization between the MZMs will also induce sign reversion of the thermopower in the absence of a photon field, whereas it has less impact on the thermopower when the QD is shelled by the photon field.

Keywords: Seebeck effect, quantum dot, Majorana zero modes, photon, nanowire

Edited by:
Qiang Xu,
Nanyang Technological University, Singapore

Reviewed by:
Yingjie Chen,
Qufu Normal University, China
Lian-Liang Sun,
North China University of Technology, China

****Correspondence:***
Hailing Sun
sunsmile1225@163.com

Specialty section:
This article was submitted to Optics and Photonics, a section of the journal Frontiers in Physics

Received: *29 March 2021*
Accepted: *19 April 2021*
Published: *28 May 2021*

Citation:
He T-Y, Sun H and Zhou G (2021) Photon-Assisted Seebeck Effect in a Quantum Dot Coupled to Majorana Zero Modes. Front. Phys. 9:687438. doi: 10.3389/fphy.2021.687438

INTRODUCTION

Majorana zero modes (MZMs) [1, 2] are zero-energy excitations that have been extensively studied in the condensed matter physics community for much of the last decade. They are massless and of their own antiparticles, which are analogous to the electron-hole pair in superconductors. A pair of spatially separated MZMs obeys non-Abelian statistics and is robust against local sources of decoherence. This enables them to be used as quantum bits for fault-tolerant topological quantum computation [2–4]. The MZMs also play important roles in some other research subjects, such as spintronics [5] and thermoelectricity [6, 7].

Due to the similarities between MZMs and electron-hole pairs, researchers have been naturally trying to prepare MZMs in superconductors. Indeed, Kitaev has theoretically demonstrated that MZMs can be formed at the two ends of a p-wave superconductor chain [8]. However, it can hardly be realized in experiments as the p-wave superconductors are rare in nature. In 2008, Fu and Kane proved the theory that it is possible to induce MZMs in vortices by the means of the proximity effect between an s-wave superconductor and the surface states of a strong topological insulator. It was subsequently demonstrated in experiments and has led to numerous studies [9, 10]. Along with this kind of scheme, a variety of other platforms have been proposed as hosts of MZMs and intensively studied, including heavy metal surfaces [11], semiconductor nanowires [12, 13], magnetic atom chains [14], planar Josephson junctions in 2D electron gas [15] and iron superconductors [16, 17]. Owing to the unique properties of MZMs as mentioned above, the detection of it is very challenging. In early years, one of the signatures most likely to be induced by MZMs is the zero-bias anomaly (ZBA) of conductance in semiconductor superconductor nanowires [18–20]. However, ZBA cannot be solely attributed to the existence of MZMs in that an ordinary localized state can also give rise to this phenomenon, such as the Kondo effect [21]. In 2011, Liu and Baranger proposed to detect the MZMs by measuring the electrical conductance through a quantum dot (QD) attached to the edge of a topological nanowire [22]. In such a scheme, the MZMs at one end of the nanowire leak into the QD [22, 23] and reduce the zero-bias conductance through the dot to be half of its quantum value, i.e., $G(0) = e^2/2h$. Recently, hybridized topological nanowire-QD junctions have been successfully realized in experiments [24, 25], providing an excellent platform for the preparation, manipulation, and detection of MZMs. The introduction of QD offers a non-invasive measurement technique for the MZMs as there is no direct charge transfer between them and the QD. In addition, the origin of the ZBA in the conductance can also be excluded from the Kondo effect, even if the experiment is performed at temperatures below the Kondo temperature [26, 27]. Along with the preparation and detection of MZMs in tunneling experiments, thermoelectric effect in QD mediated by MZMs has also been studied in recent years. The previous research subject of thermoelectric effect concerned energy conversion between electrical and thermal energies, which has reacquired recognitions because of the significantly enhanced thermoelectric efficiency and thermopower [28]. In thermoelectricity, the most common studied issue is the Seebeck effect, which refers to the generation of an electrical voltage ΔV in response to a temperature difference ΔT applied across the two ends of the system. The thermopower (Seebeck coefficient) is then defined as $S = -\Delta V/\Delta T$ which is directly measured in experiments. It has been proved that thermopower in hybridized QD-superconductor nanowire hosting MZMs satisfies the Mott formula, and can be used for inferring the temperature of the Majorana edge state by measuring the differential conductance [29]. The enhancement and sign change of the thermopower in such a system have also been reported [30–34]. The optical techniques are widely used in manipulating particles' transportation in nanostructures, and were also proved to be promising in the study of MZMs [35, 36]. In [37], Chen and Zhu found that in the presence of the QD-MZMs interaction, if a strong pump laser is applied at the QD, the single peak in the probe absorption spectrum will be split into two. In [38, 39], as the photon-assisted tunneling (PAT) occurs, the PAT peaks are developed and the original zero-bias peak is suppressed to zero due to the MZMs, which turn to non-zero mode by emitting (absorbing) photons. Based on the features of MZMs in the PAT process, it is worthy to investigate the affection of MZMs on the thermoelectricity by the optical techniques.

In the present paper, we study the Seebeck effect in a hybridized QD-topological superconductor nanowire with a photon field shelled on the QD (see **Figure 1**). The dot is connected to the left and right leads at different temperatures. We calculate the electrical conductance and thermopower through the dot interacting with one mode of the MZMs prepared at the ends of the topological superconductor nanowire. Our numerical results show that the magnitude of the thermopower can be obviously enhanced by the combined effect of the MZMs and PAT. When the two modes of the MZMs are strongly overlapped with each other, the thermopower is less influenced by the MZMs in the presence of the photon field because the photon energy absorbed by one mode of the MZMs is subsequently emitted by the other one. We also find a sign change of the thermopower induced by changing either dot-MZMs coupling or temperature.

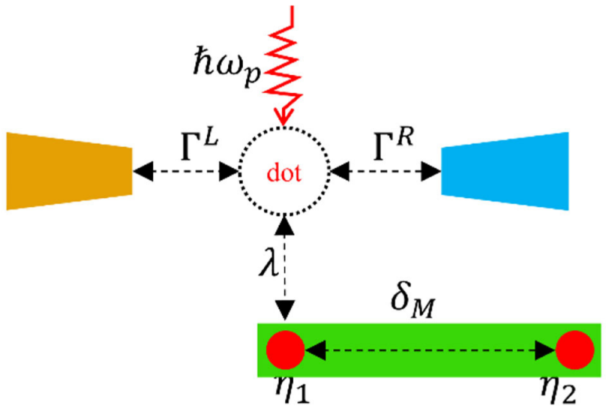

FIGURE 1 | Schematic plot of the scheme composing a quantum dot connected to the left and right leads at different temperatures of T_L and T_R, respectively. The dot is shelled by a microwave field with frequency ω_p and intensity Δ_d, and is side-coupled to a topological superconductor nanowire hosting a pair of MZMs (red circles). Here we consider that only one mode of the MZMs denoted by the operator of is coupled to the dot with strength λ. The hybridization amplitude between the MZMs is δ_M.

MODEL AND METHODS

The Hamiltonian of the system illustrated in **Figure 1** is written as the following [22, 40]

$$\begin{aligned} H &= \sum_{k\alpha} \varepsilon_{k\alpha} c^{+}_{k\alpha} c_{k\alpha} + \varepsilon_d(t) d^{+} d + \sum_{k,\alpha} (V_\alpha c^{+}_{k\alpha} d + H.c) \\ &\quad + i\delta_M \eta_1 \eta_2 \; + \; (\lambda d - \lambda d^{+}) \eta_1, \end{aligned} \tag{1}$$

in which the first term describes the left and right ($\alpha = L, R$) leads at temperatures of T_L and T_R, respectively. The annihilation (creation) operator $c_{k\alpha}\left(c^{+}_{k\alpha}\right)$ is for the electrons on the leads with wave-vector k and energy $\varepsilon_{k\alpha}$. The second term is for the electrons on the QD with annihilation (creation) operator $d\left(d^{+}\right)$, time-varying dot level $\varepsilon_d(t) = \varepsilon_d + \Delta_d \cos(\omega t)$ [40, 41], in which ε_d is the dot level in the absence of the photon field, Δ_d the field intensity applied on the dot, and ω_p the photon frequency. The third term represents the tunneling between the QD and the leads, with tunnel amplitude V_α. The last two terms in Equation

(1) are for the MZMs and their interaction to the QD. Following previous work [22], we transform the Majorana fermions into the regular ones by $\eta_1 = \frac{1}{\sqrt{2}}\left(f^+ + f\right)$, $\eta_2 = \frac{i}{\sqrt{2}}\left(f^+ - f\right)$ and then the Hamiltonian is rewritten as

$$\begin{aligned} H &= \sum_{k\alpha} \varepsilon_{k\alpha} c^+_{k\alpha} c_{k\alpha} + \varepsilon_d(t) d^+ d + \sum_{k,\alpha=L,R} (V_\alpha c^+_{k\alpha} d + H.c) \\ &+\delta_M \left(f^+ f - \frac{1}{2}\right) + \frac{1}{\sqrt{2}} \left(\lambda d - \lambda d^+\right)\left(f + f^+\right) \end{aligned} \qquad (2)$$

The electrical and heat currents from lead-α to the dot are individually calculated from the time rate of the electrons' average occupation number and the associated energy [41], i.e., $J_\alpha = -ed\left\langle N_\alpha \right\rangle/dt$ and $Q_\alpha = -ed\left\langle \sum_k \left(\varepsilon_{k\alpha} - \mu_\alpha\right) c^+_{k\alpha} c_{k\alpha} \right\rangle/dt$, in which $N_\alpha = \sum_k c^+_{k\alpha} c_{k\alpha}$ is the electrons' occupation number and μ_α the chemical potential in the lead. In the present paper, we focus the linear response regime with infinitesimal bias voltage ΔV and temperature difference ΔT between the two leads. The total electrical and heat currents through the dot are then given by [30, 31, 42]

$$J = eL_0 \Delta V + \frac{e}{T} L_1 \Delta T, \qquad (3)$$

$$Q = L_1 \Delta V + \frac{1}{T} L_2 \Delta T, \qquad (4)$$

where the integral $L_n \ (n = 0, 1, 2)$ is defined by [31, 42]

$$L_n = -\frac{1}{\hbar} \int d\varepsilon \left(\varepsilon - \mu\right)^n \frac{\partial f\left(\varepsilon\right)}{\partial \varepsilon} T\left(\varepsilon\right) \qquad (5)$$

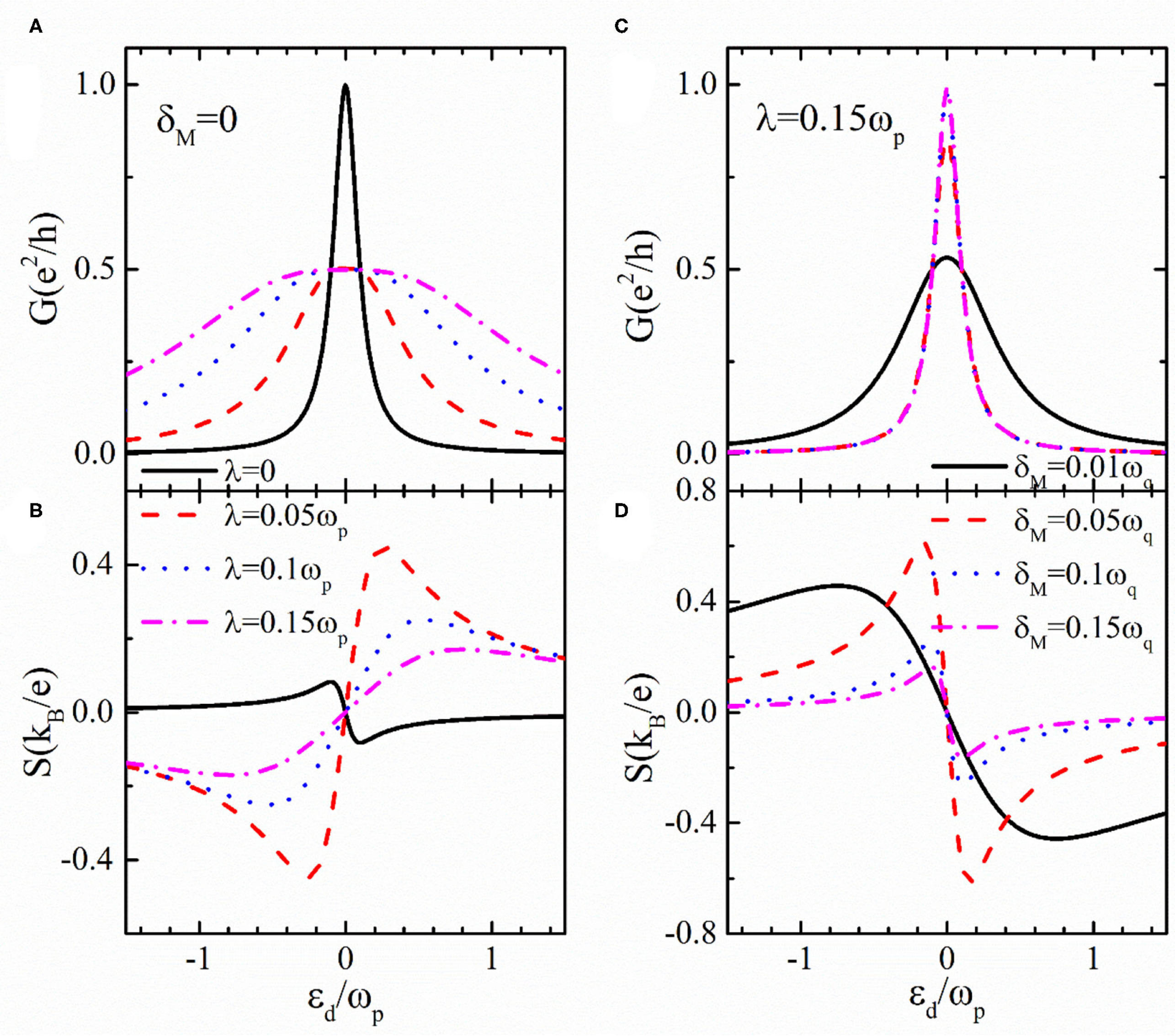

FIGURE 2 | Conductance and thermopower as functions of the dot level for different values of dot-MZMs coupling strength λ in **(A)**, **(B)** with a fixed value of $\delta_M = 0$, and for different δ_M in **(C)**, **(D)** with fixed $\lambda = 0.15\omega_p$. The other parameters are $T_e = 0.0025\omega_p$, $\Delta_d = 0$.

in which the Fermi distribution function is $f(\varepsilon)$=$[\exp[(\varepsilon-\mu)/k_BT]+1]^{-1}$, with the chemical potential $\mu=\mu_L=\mu_R$ in the linear response regime. By setting $J=0$ and $Q=0$, the electrical conductance and thermopower are given by $G=e^2L_0$ and $S=-L_1/(eTL_0)$, respectively. The remaining task is to calculate the transmission coefficient $T(\varepsilon)$ in Equation (5). In the framework of non-equilibrium Green's function technique, its expression is given by [39–41],

$$T(\varepsilon)=\frac{\Gamma_L\Gamma_R}{\Gamma_L+\Gamma_R}\sum_k \tilde{G}^r_{dd;k}(\varepsilon)J_k^2, \tag{6}$$

in which $\Gamma_\alpha=2\pi|V_{k\alpha}|^2\rho_\alpha$ is the line-width function with ρ_α being the local density of states in lead-α. In the above equation, J_k is the k-th order Bessel function with argument Δ_d/ω_p, and $\tilde{G}^r_{dd;k}(\varepsilon)$ the retarded Green's function given by [39–41]

$$\begin{aligned}&\tilde{G}^r_{dd;k}(\varepsilon)\\&=\left[g^{r-1}_{dd;k}(\varepsilon)-\sum\nolimits_n J^2_{k+n}\Sigma^r_{nn}(\varepsilon)-\sum\nolimits_{k'}\frac{\tilde{\Sigma}^{r2}_{kk'}(\varepsilon)}{\tilde{g}^{r-1}_{dd;k'}(\varepsilon)-\tilde{\Sigma}^r_{k'}(\varepsilon)}\right]^{-1},\end{aligned} \tag{7}$$

where the dot free Green's function in the absence of coupling to the leads and MZMs is $g^r_{dd;k}(\varepsilon)=\left[\varepsilon-\varepsilon_d-k\omega_p+i(\Gamma_L+\Gamma_R)/2\right]^{-1}$, and the associated hole free Green's function $\tilde{g}^r_{dd;k}(\varepsilon)=\left[\varepsilon+\varepsilon_d+k\omega_p+i(\Gamma_L+\Gamma_R)/2\right]^{-1}$. The self-energies in Equation (7) are individually given by$\Sigma^r_{nn}(\varepsilon)=\lambda^2(\varepsilon+n\omega_p)/\left[(\varepsilon+n\omega_p)^2+\delta_M^2\right]$,$\tilde{\Sigma}^r_{k'}(\varepsilon)=\sum_{k'}J_{k'-n}\Sigma^r_{nn}(\varepsilon)$, and $\tilde{\Sigma}^r_{kk'}(\varepsilon)=\sum_{k'}J_{k+n}J_{k'-n}\Sigma^r_{nn}(\varepsilon)$. One can check that in the absence of the photon field, i.e., $\Delta_d=0$, the Green's function $\tilde{G}^r_{dd;k}(\varepsilon)$ reduces to that in [22].

RESULTS AND DISCUSSION

In the following numerical calculations, the photon frequency ω_p is set as the energy unit, and the equilibrium chemical potential in the leads is fixed at $\mu_L=\mu_R=\mu=0$ as the energy zero point. Throughout the paper we fix the value of line-width functions $\Gamma_L=\Gamma_R=0.05\omega_p$. **Figure 2** shows the conductance and thermopower as functions of the dot level without the photon field shelled on the dot ($\Delta_d=0$). For $\lambda=0$ as indicated by the black solid in **Figure 2A**, the conductance G develops a resonant peak when the dot level ε_d is aligned to the chemical potential μ, where the maximum of the conductance reaches its quantum value $G(\mu=0)=e^2/h$. Turning on the coupling between the dot and MZMs ($\lambda\neq 0$), the value of conductance around the leads' chemical potentials μ reduces to half of its quantum value, i.e., $G=e^2/2h$ due to the half fermionic property of MZMs. This is regarded as a signature of the existence of MZMs in QD [22, 23]. Note that at ultra-low temperature, the half fermionic property of MZMs ($G=e^2/2h$) is independent of the dot's level [31]. At a rather high temperature, however, we find that only the conductance near the chemical potential is half of its quantum value, as shown in **Figure 2A**. This is because the interaction between the MZMs and electrons on the dot is weakened by increased thermal motion of the electrons.

The most prominent change of the thermopower is the sign reversion induced by dot-MZMs coupling, as shown in **Figure 2B**. For $\lambda=0$ as indicated by the black solid line, the thermopower is positive (negative) when the dot level is below (above) the chemical potential $\mu=0$. The reason is that in the presence of thermal gradient ΔT between the two leads that induces the thermoelectric effect, there are more electrons flowing from the left hotter lead to the right cooler one as $\varepsilon_d>\mu$. This will induce a positive voltage drop ΔV and correspondingly a negative thermopower $S=-\Delta V/\Delta T$ [42]. When $\varepsilon_d=\mu$, tunneling of electrons through the dot are compensated by that of holes and thus the thermopower is zero. In other words, there are the same amounts of electrons flowing in opposite directions and then the voltage drop is zero accordingly [42]. Just in the same way, one can explain the origin of the positive thermopower when $\varepsilon_d<\mu$. The dependence of thermopower on the dot-MZMs coupling λ can be derived by Sommerfeld expansion of the Fermi function $f(\varepsilon)$ up to second order in temperature, and its analytical expression when the dot level is near the chemical potential is [31, 34]

$$S=\frac{\pi^2k_B^2T}{3e}\frac{\varepsilon_d}{2\lambda^2} \tag{8}$$

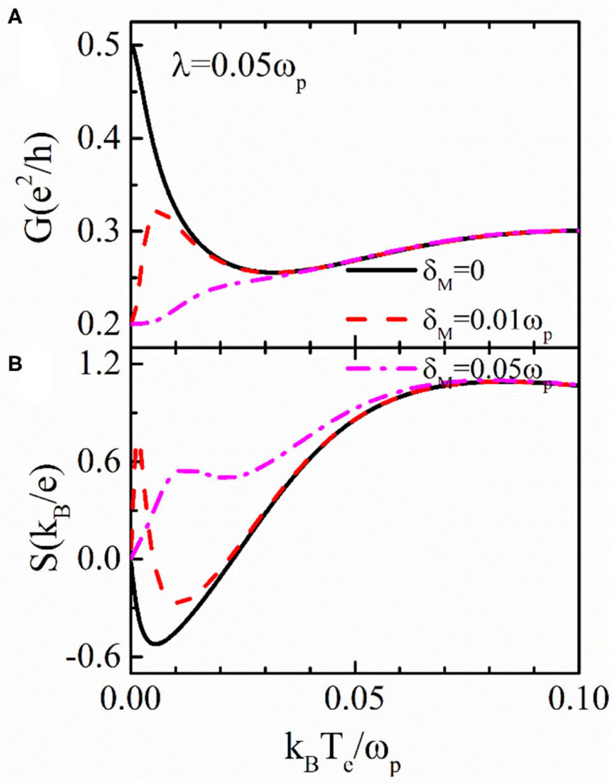

FIGURE 3 | (A) Conductance and **(B)** thermopower as functions of the temperature T_e for $\varepsilon_d=-0.2\omega_p$ and different values of the overlap amplitude between the MZMs δ_M. Other parameters are $\lambda=0.05\omega_p$ and $\Delta_d=0$.

Note that this result applies only to the case of finite dot-MZMs coupling, and clearly shows the sign reversion of the thermopower as compared to the case of zero λ. From Equation (8), one can also expect the magnitude of the thermopower to be enhanced by a small λ, as has been shown in previous works [6, 33].

The two modes of the MZMs at opposite ends of the topological nanowire interact with each other with strength of $\delta_M \sim e^{-\zeta/L}$, where L is the length of the topological superconductor wire and ζ is the superconducting coherence length [29, 30]. **Figure 2C** shows that when the hybridization strength between the MZMs is strong enough $\delta_M > 0.01\omega_q$, the property of $G(\mu) = e^2/2h$ is destroyed. For a sufficiently large value of $\delta_M \geq 0.1\omega_q$, the conductance reduces to the result of resonant level model $G(\mu) = e^2/h$ because the transportation is dominated by regular fermions as demonstrated in [22, 31]. As for the thermopower with finite δ_M, its analytical expression when the dot level is near the chemical potential can also be obtained by the Sommerfeld expansion as [31]

$$S = -\frac{\pi^2 k_B^2 T}{3e} \frac{\varepsilon_d}{4\Gamma^2 + \varepsilon_d^2} \frac{8\left(\delta_M^2 + \lambda^2\right)}{\delta_M^2} \tag{9}$$

By comparing Equations (8) and (9), one finds that the hybridization between the MZMs will also induce a sign reversion of the thermopower as seen from **Figure 2D**. The peaks at the two sides of the zero point become sharper and lower with increasing δ_M due to the increased level renormalization by coupling between the MZMs [22, 31, 33].

Figure 3 presents the conductance and thermopower varying as functions of the system equilibrium temperature T_e for different values of δ_M and a fixed value of $\lambda = 0.05$. The dot level is fixed at $\varepsilon_d = -0.2\omega_p$ where the thermopower develops a peak. With increasing temperature, the conductance for $\delta_M = 0$ in **Figure 3A** is essentially decreased and finally reaches a constant value at high temperature (solid line). The absolute value of the thermopower in **Figure 3B** is first enhanced, reaching a maximum, and then decreases with increasing temperature. With further increased temperature, the thermopower experiences a sign reversion and then increases. The sign change of the thermopower by temperature in the absence of dot-MZMs coupling has been previously found to be induced by the Kondo effect in single QD [43], and by interdot Coulomb interaction in double-QD [44]. In the presence of δ_M, both the conductance and thermopower depend on the temperature in a non-monotonous way. The sign reversion of the thermopower by δ_M can be clearly seen in **Figure 3B**, which agrees with the results in [31, 33].

We now study the case of finite photon field shelled on the dot, i.e., $\Delta_d \neq 0$. As has been demonstrated in previous works, the conductance develops a series of photon-assisted side peaks at $\varepsilon_d = \mu + n\omega_p$ with $n = 0, \pm1, \pm2 \cdots$,

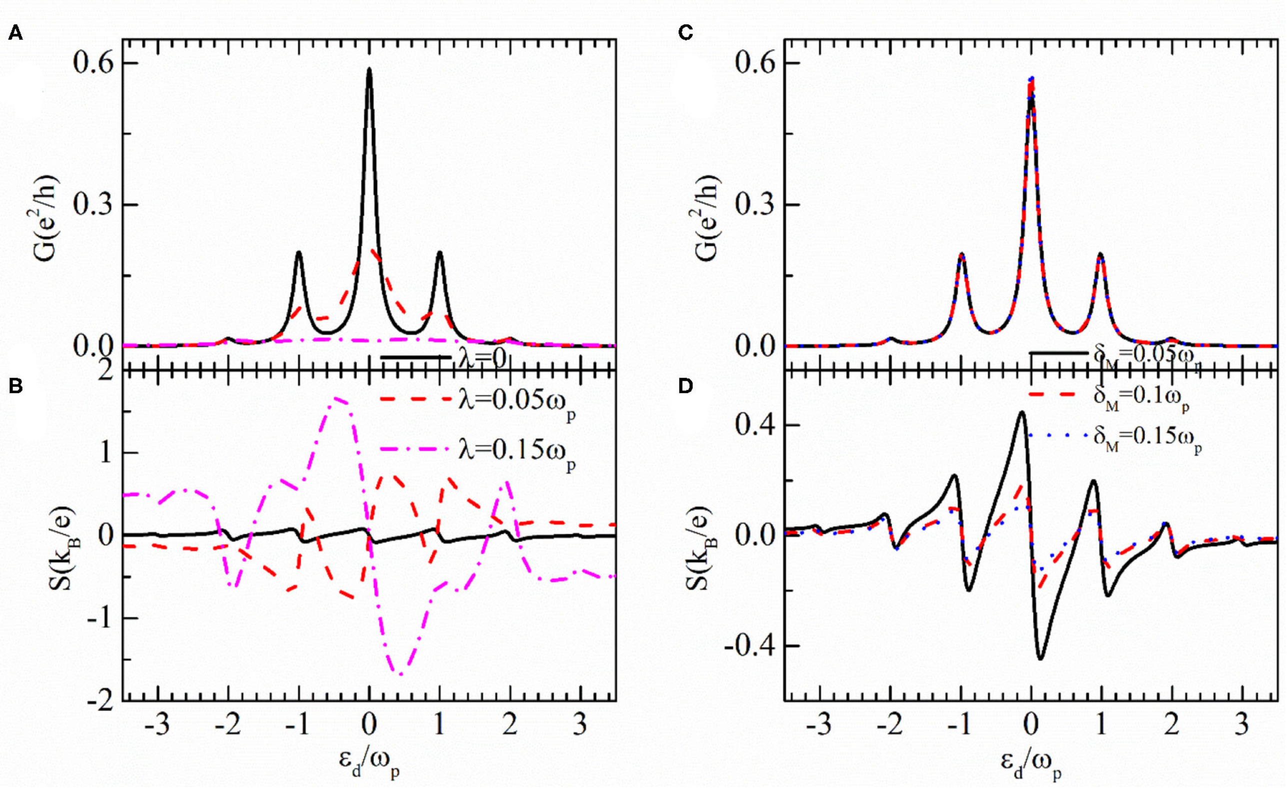

FIGURE 4 | Conductance and thermopower in the presence of the microwave field with $\Delta_d = \omega_p$ as functions of the dot level for different values of dot-MZMs coupling strength λ in **(A)**, **(B)** with $\delta_M = 0$, and for different δ_M in **(C)**, **(D)** with $\lambda = 0.05\omega_p$. The equilibrium temperature is chosen as $T_e = 0.0025\omega_p$.

due to the additional transport channels induced by photon absorption and emission processes [39–41]. Since now electrons can transport through the dot *via* more states, the tunneling probability through each channel is weakened and then the conductance's peak height is lowered, as shown by the solid line in **Figure 4A**. The thermopower in **Figure 4B** is zero at these photon-induced additional side bands $\varepsilon_d = \mu + n\omega_p$ (black solid line) correspondingly. The peaks' height of the conductance is further lowered by the dot-MZMs coupling as indicated by the dashed and dash-dotted lines in **Figure 4A**, which is consistent with the results in **Figure 2A**. For $\lambda = 0.15\omega_p$, the conductance is negligibly small. As a result of it, the thermopower in **Figure 4B** is significantly enhanced in addition to the sign reversion. This can be understood by the definition of the thermopower of $S = -eL_1/(TG)$. We find in **Figure 4C** that the magnitude of the conductance is slightly increased by the overlap between the MZMs as shown in **Figure 2C**. Such a change is amplified by the thermopower in **Figure 4D**, in which it shows the typical sawtooth configuration with weakened strength. By comparing **Figures 4B,D**, one can find that the sign reversion of the thermopower by δ_M is retained in the presence of the photon field.

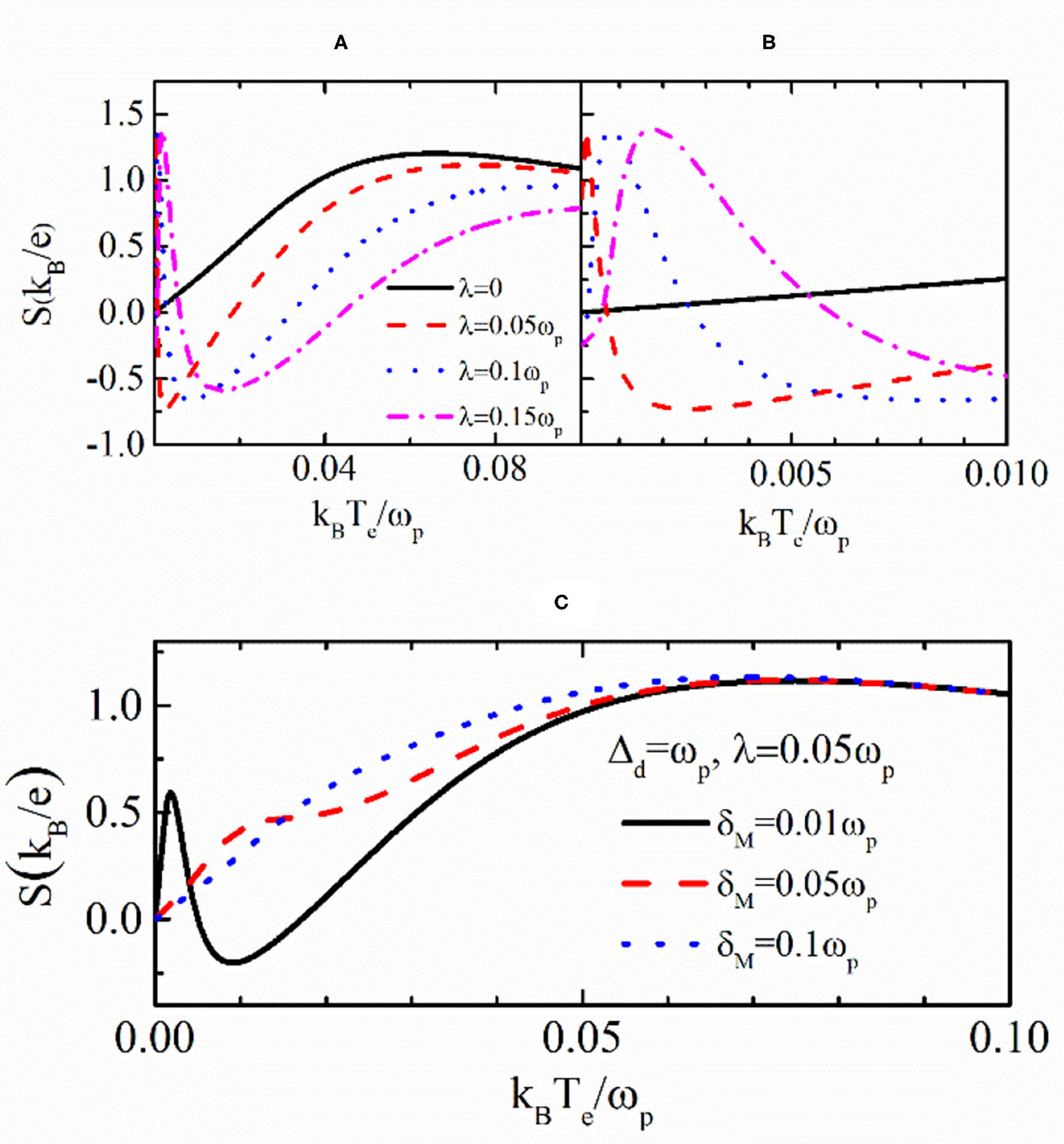

FIGURE 5 | Thermopower varying with the equilibrium temperature for $\varepsilon_d = -0.2\omega_p$ and different values of λ in **(A)**, and varying δ_M in **(C)**. **(B)** is the blow-up of **(A)** at lower temperatures.

Finally, in **Figure 5** we study the properties of thermopower varying as a function of the temperature. For zero δ_M and λ as indicated by the black solid line in **Figure 5A**, the magnitude of the thermopower is first increased with increasing temperature, reaching a maximum at about $k_BT_e = 0.05\omega_p$ and then decreases to a constant value. As compared to **Figure 3B**, one can see that the sign change of the thermopower induced by the varying temperature is eliminated in the presence of photon field. For non-zero λ, however, the thermopower changes sign by the varying of both temperature and λ, as shown in **Figure 5A**. At a lower temperature, the thermopower develops a peak, whose sign depends on the magnitude of λ. To show this more clearly, we present in **Figure 5B** the blow-up of the case of $k_BT_e < 0.01\omega_p$. For $\lambda < 0.05\omega_p$ represented by the red-dashed line, the thermopower is positive at $k_BT_e \sim 0$, whereas those for $\lambda < 0.1\omega_p$ and $\lambda < 0.15\omega_p$ are negative. In these three cases, the thermopower develops positive peaks at higher temperatures and then becomes negative with further increasing temperature. At sufficiently high temperature, the thermopower reaches a positive value regardless of the existence of MZMs. Behaviors of the thermopower in **Figure 5C** essentially resemble those in **Figure 3B** in which $\Delta_d = 0$. The reason can be attributed to the fact that when the MZMs are overlapped [39], the photon energy absorbed by one mode of the MZMs is subsequently emitted by the other mode, and then the electron transport through the dot is less influenced.

CONCLUSIONS

In conclusion, we have studied the properties of electrical conductance and thermopower in a quantum dot coupled to MZMs under the irradiation of a photon field. Our numerical results show that the conductance is fixed at half of its quantum value as the QD-MZMs coupling increases. The thermopower can be obviously enhanced by the combined effect of the MZMs and PAT. This mainly occurs in a low temperature regime, under which the MZMs are prepared at the two ends of a topological superconductor nanowire. When the two modes of the MZMs are strongly overlapped with each other, the thermopower is less influenced by the MZMs in the presence of the photon field because the photon energy absorbed by one mode of the MZMs is subsequently emitted by the other one. We also find a sign change of the thermopower induced by changing either dot-MZMs coupling or temperature.

DATA AVAILABILITY STATEMENT

The original contributions presented in the study are included in the article/supplementary material, further inquiries can be directed to the corresponding author.

AUTHOR CONTRIBUTIONS

HS and GZ contributed the ideas equally. HS and T-YH derived the formulae, performed the numerical calculations, and wrote the original manuscript. All authors contributed to the article and approved the submitted version.

FUNDING

This work was supported by Science and Technology Program of Guangzhou (No. 2019050001), Program for Guangdong Innovative and Entrepreneurial Teams (No. 2019BT02C241), Program for Chang Jiang Scholars and Innovative Research Teams in Universities (No. IRT_17R40), Key-Area Research and Development Program of Guangdong Province (No. 2019B010924005), Guangdong Provincial Key Laboratory of Optical Information Materials and Technology (No. 2017B030301007), and Guangzhou Key Laboratory of Electronic Paper Displays Materials and Devices (201705030007) and the 111 Project.

REFERENCES

1. Read N, Green D. Paired states of fermions in two dimensions with breaking of parity and time-reversal symmetries and the fractional quantum Hall effect N. *Phys Rev B*. (1999) 61:10267–97. doi: 10.1103/PhysRevB.61.10267
2. Nayak C, Simon SH, Stern A, Freedman M, Das Sarma S. Non-Abelian anyons and topological quantum computation. *Rev Mod Phys*. (2008) 80:1083–159. doi: 10.1103/RevModPhys.80.1083
3. Alicea J, Oreg Y, Refael G, Von Oppen F, Fisher MPA. Non-Abelian statistics and topological quantum information processing in 1D wire networks. *Nat Phys*. (2011) 7:412–7. doi: 10.1038/nphys1915
4. Karzig T, Knapp C, Lutchyn RM, Bonderson P, Hastings MB, Nayak C, et al. Scalable designs for quasiparticle-poisoning-protected topological quantum computation with Majorana zero modes. *Phys Rev B*. (2017) 95:1–32. doi: 10.1103/PhysRevB.95.235305
5. Liu X, Li X, Deng DL, Liu XJ, Das Sarma S. Majorana spintronics. *Phys Rev B*. (2016) 94:1–13. doi: 10.1103/PhysRevB.94.014511
6. Chi F, Fu ZG, Liu J, Li KM, Wang Z, Zhang P. Thermoelectric effect in a correlated quantum dot side-coupled to Majorana bound states. *Nanoscale Res Lett*. (2020) 15:79. doi: 10.1186/s11671-020-03307-y
7. Smirnov S. Universal Majorana thermoelectric noise. *Phys Rev B*. (2018) 97:1–14. doi: 10.1103/PhysRevB.97.165434
8. Kitaev AYu. Fault-tolerant quantum computation by anyons. *Ann Phys (N Y)*. (2003) 303:2–30. doi: 10.1016/S0003-4916(02)00018-0
9. Fu L, Kane CL. Superconducting proximity effect and majorana fermions at the surface of a topological insulator. *Phys Rev Lett*. (2008) 100:1–4. doi: 10.1103/PhysRevLett.100.096407
10. Qi XL, Zhang SC. Topological insulators and superconductors. *Rev Mod Phys*. (2011) 83:1057–110. doi: 10.1103/RevModPhys.83.1057
11. Potter AC, Lee PA. Topological superconductivity and Majorana fermions in metallic surface states. *Phys Rev B*. (2012) 85:1–9. doi: 10.1103/PhysRevB.85.094516
12. Lutchyn RM, Sau JD, Das Sarma S. Majorana fermions and a topological phase transition in semiconductor-superconductor heterostructures. *Phys Rev Lett*. (2010) 105:1–4. doi: 10.1103/PhysRevLett.105.077001
13. Lutchyn RM, Bakkers EPAM, Kouwenhoven LP, Krogstrup P, Marcus CM, Oreg Y. Majorana zero modes in superconductor-semiconductor heterostructures. *Nat Rev Mater*. (2018) 3:52–68. doi: 10.1038/s41578-018-0003-1

14. Nadj-Perge S, Drozdov IK, Bernevig BA, Yazdani A. Proposal for realizing Majorana fermions in chains of magnetic atoms on a superconductor. *Phys Rev B*. (2013) 88:1–5. doi: 10.1103/PhysRevB.88.020407
15. Pientka F, Keselman A, Berg E, Yacoby A, Stern A, Halperin BI. Topological superconductivity in a planar Josephson junction. *Phys Rev X*. (2017) 7:1–17. doi: 10.1103/PhysRevX.7.021032
16. Wang Z, Zhang P, Xu G, Zeng LK, Miao H, Xu X, et al. Topological nature of the FeSe0.5Te0.5 superconductor. *Phys Rev B*. (2015) 92:1–7. doi: 10.1103/PhysRevB.92.115119
17. Wu X, Qin S, Liang Y, Fan H, Hu J. Topological characters in Fe(Te1-xSex) thin films. *Phys Rev B*. (2016) 93:1–13. doi: 10.1103/PhysRevB.93.115129
18. Mourik V, Zuo K, Frolov SM, Plissard SR, Bakkers EPAM, Kouwenhoven LP. Signatures of majorana fermions in hybrid superconductor-semiconductor nanowire devices. *Science*. (2012) 336:1003–7. doi: 10.1126/science.1222360
19. Das A, Ronen Y, Most Y, Oreg Y, Heiblum M, Shtrikman H. Zero-bias peaks and splitting in an Al-InAs nanowire topological superconductor as a signature of Majorana fermions. *Nat Phys*. (2012) 8:887–95. doi: 10.1038/nphys2479
20. Deng MT, Yu CL, Huang GY, Larsson M, Caroff P, Xu HQ. Anomalous zero-bias conductance peak in a Nb-InSb nanowire-Nb hybrid device. *Nano Lett*. (2012) 12:6414–9. doi: 10.1021/nl303758w
21. Lee EJH, Jiang X, Aguado R, Katsaros G, Lieber CM, De Franceschi S. Zero-bias anomaly in a nanowire quantum dot coupled to superconductors. *Phys Rev Lett*. (2012) 109:1–5. doi: 10.1103/PhysRevLett.109.186802
22. Liu DE, Baranger HU. Detecting a Majorana-fermion zero mode using a quantum dot. *Phys Rev B*. (2011) 84:1–4. doi: 10.1103/PhysRevB.84.201308
23. Vernek E, Penteado PH, Seridonio AC, Egues JC. Subtle leakage of a Majorana mode into a quantum dot. *Phys Rev B*. (2014) 89:1–5. doi: 10.1103/PhysRevB.89.165314
24. Deng MT, Vaitiekenas S, Hansen EB, Danon J, Leijnse M, Flensberg K, et al. Majorana bound state in a coupled quantum-dot hybrid-nanowire system. *Science*. (2016) 354:1557–62. doi: 10.1126/science.aaf3961
25. Deng MT, Vaitiekenas S, Prada E, San-Jose P, Nygård J, Krogstrup P, et al. Nonlocality of Majorana modes in hybrid nanowires. *Phys Rev B*. (2018) 98:1–10. doi: 10.1103/PhysRevB.98.085125
26. Górski G, Barański J, Weymann I, Domański T. Interplay between correlations and Majorana mode in proximitized quantum dot. *Sci Rep*. (2018) 8:1–12. doi: 10.1038/s41598-018-33529-1
27. Silva JF, Da Silva LGGVD, Vernek E. Robustness of the Kondo effect in a quantum dot coupled to Majorana zero modes. *Phys Rev B*. (2020) 101:1–10. doi: 10.1103/PhysRevB.101.075428
28. Dubi Y, Di Ventra M. Colloquium: heat flow and thermoelectricity in atomic and molecular junctions. *Rev Mod Phys*. (2011) 83:131–55. doi: 10.1103/RevModPhys.83.131
29. Hou CY, Shtengel K, Refael G. Thermopower and Mott formula for a Majorana edge state. *Phys Rev B*. (2013) 88:1–8. doi: 10.1103/PhysRevB.88.075304
30. Leijnse M. Thermoelectric signatures of a Majorana bound state coupled to a quantum dot. *New J Phys*. (2014) 16:1–13. doi: 10.1088/1367-2630/16/1/015029
31. López R, Lee M, Serra L, Lim JS. Thermoelectrical detection of Majorana states. *Phys Rev B*. (2014) 89:1–7. doi: 10.1103/PhysRevB.89.205418
32. Ricco LS, Dessotti FA, Shelykh IA, Figueira MS, Seridonio AC. Tuning of heat and charge transport by Majorana fermions. *Sci Rep*. (2018) 8:1–8. doi: 10.1038/s41598-018-21180-9
33. Hong L, Chi F, Fu ZG, Hou YF, Wang Z, Li KM, et al. Large enhancement of thermoelectric effect by Majorana bound states coupled to a quantum dot. *J Appl Phys*. (2020) 127:1–10. doi: 10.1063/1.5125971
34. Bin NP, Liu L, Su X, Dong L, Shi Y, Luo HG. Spin Seebeck effect induced by a Majorana zero mode in a nanomagnet. *Phys E Low Dimensional Syst Nanostruct*. (2020) 124:1–7. doi: 10.1016/j.physe.2020.114313
35. Li Y, Kundu A, Zhong F, Seradjeh B. Tunable Floquet Majorana fermions in driven coupled quantum dots. *Phys Rev B*. (2014) 90:1–5. doi: 10.1103/PhysRevB.90.121401
36. Väyrynen JI, Rastelli G, Belzig W, Glazman LI. Microwave signatures of Majorana states in a topological Josephson junction. *Phys Rev B*. (2015) 92:1–5. doi: 10.1103/PhysRevB.92.134508
37. Chen HJ, Zhu KD. All-optical scheme for detecting the possible Majorana signature based on QD and nanomechanical resonator systems. *Sci China Phys Mech Astron*. (2015) 58:1–14. doi: 10.1007/s11433-014-5637-4
38. Tang HZ, Zhang YT, Liu JJ. Photon-assisted tunneling through a topological superconductor with Majorana bound states. *AIP Adv*. (2015) 5:1–8. doi: 10.1063/1.4939096
39. Chi F, He TY, Wang J, Fu ZG, Liu LM, Liu P, et al. Photon-assisted transport through a quantum dot side-coupled to Majorana bound states. *Front Phys*. (2020) 8:8–13. doi: 10.3389/fphy.2020.00254
40. Sun QF, Lin TH, Wang J. Photon-assisted andreev tunneling through a mesoscopic hybrid system. *Phys Rev B*. (1999) 59:13126–38. doi: 10.1103/PhysRevB.59.13126
41. Jauho AP, Wingreen NS, Meir Y. Time-dependent transport in interacting and noninteracting resonant-tunneling systems. *Phys Rev B*. (1994) 50:5528–44. doi: 10.1103/PhysRevB.50.5528
42. Liu J, Sun QF, Xie XC. Enhancement of the thermoelectric figure of merit in a quantum dot due to the Coulomb blockade effect. *Phys Rev B*. (2010) 81:1–6. doi: 10.1103/PhysRevB.81.245323
43. Krawiec M, Wysokiński KI. Thermoelectric phenomena in a quantum dot asymmetrically coupled to external leads. *Phys Rev B*. (2007) 75:155330–5. doi: 10.1103/PhysRevB.75.155330
44. Rajput G, Ahluwalia PK, Sharma KC. Thermoelectric properties of correlated double quantum dot system in Coulomb blockade regime. *Phys B Condens Matter*. (2011) 406:3328–34. doi: 10.1016/j.physb.2011.05.054

Conflict of Interest: GZ is employed by Shenzhen Guohua Optoelectronics Tech. Co. Ltd.

The remaining authors declare that the research was conducted in the absence of any commercial or financial relationships that could be construed as a potential conflict of interest.

frontiers
in Physics

ORIGINAL RESEARCH
published: 16 June 2021
doi: 10.3389/fphy.2021.690661

Enhanced Electrochemical Property of $Li_{1.2-x}Na_xMn_{0.54}Ni_{0.13}Co_{0.13}O_2$ Cathode Material for the New Optoelectronic Devices

Yumei Gao[1]*, *Yuchong Hui*[2] *and Hang Yin*[1]

[1]*College of Electron and Information, University of Electronic Science and Technology of China, Zhongshan Institute, Zhongshan, China,* [2]*State Key Laboratory of Electronic Thin Films and Integrated Devices, University of Electronic Science and Technology of China, Chengdu, China*

The Li-rich Mn-based oxide $Li_{1.2}Mn_{0.54}Ni_{0.13}Co_{0.13}O_2$ has been extensively studied as a cathode material of the battery module for new optoelectronic devices. To improve and enhance the electrochemical performance, sodium doping is one of the effective approaches. According to the density functional theory of first-principles, the band gap, partial density of states, lithiation formation energy, electron density difference, and potential energy of electrons for $Li_{1.2-x}Na_xMn_{0.54}Ni_{0.13}Co_{0.13}O_2$ were simulated with Materials Studio, Nanodcal, and Matlab. When the sodium doping amount x = 0.10 mol, simulations show that $Li_{1.2-x}Na_xMn_{0.54}Ni_{0.13}Co_{0.13}O_2$ has a better conductivity. The potential maps of $Li_{1.2-x}Na_xMn_{0.54}Ni_{0.13}Co_{0.13}O_2$ obtained in Matlab demonstrate that the potential barrier is lower and the rate capability is enhanced after sodium doping. Results of analyses and calculations agree with the experimental result of Chaofan Yang's group. This theoretical method could be a great avenue for the investigation of the battery application of new optoelectronic devices. Also, our findings could give some theoretical guidance for the subsequent electrochemical performance study on doping in the field of lithium-ion batteries.

Keywords: density functional theory, electrochemical performance, $Li_{12-x}Na_xMn_{054}Ni_{013}Co_{013}O_2$, optoelectronic device, cathode material

Edited by:
Qiang Xu,
Nanyang Technological University, Singapore

Reviewed by:
Liu Wenping,
Guilin University of Electronic Technology, China
Xiang Liu,
Nanjing Tech University, China

***Correspondence:**
Yumei Gao
yumeigao5697@163.com

Specialty section:
This article was submitted to Optics and Photonics, a section of the journal Frontiers in Physics

Received: *03 April 2021*
Accepted: *18 May 2021*
Published: *16 June 2021*

Citation:
Gao Y, Hui Y and Yin H (2021) Enhanced Electrochemical Property of $Li_{1.2-x}Na_xMn_{0.54}Ni_{0.13}Co_{0.13}O_2$ Cathode Material for the New Optoelectronic Devices.
Front. Phys. 9:690661.
doi: 10.3389/fphy.2021.690661

INTRODUCTION

The commercial lithium-ion batteries (LIBs) have many advantages, such as their energy saving, high energy density, good cycle performance, less pollution, no memory characteristics, and rechargeable property [1]. With the rapid development of new optoelectronic devices in recent decades, LIBs have been widely applied as the stationary energy storage of the electro-optical conversion devices. Nowadays, the actual specific capacity of conventional cathode materials, such as $LiCoO_2$, $LiMnO_2$, spinel $LiMn_2O_4$, ternary lithium nickel cobalt aluminum oxide, and olivine $LiFePO_4$, is less than 160 mAh/g, but that of the anode is much higher. Commercialized cathode materials are not adequate to match the next-generation power battery. In addition, the percentage of the cathode's cost in the whole battery's cost is very high. To meet the needs of people, the low-cost cathode materials with higher energy density and discharge/charge rate capability are urgent to be explored.

The layered Li-rich Mn-based Ni–Co–Mn (NCM) ternary cathode material xLi$_2$MnO$_3$·(1−x) LiMO$_2$ ($0 < x < 1$, M = Ni, Co, Mn, $Ni_{1/2}Mn_{1/2}$, $Ni_{1/3}Mn_{1/3}Co_{1/3}$) has attracted extensive attention owing to its lower price and good performance. Its space group is $R\bar{3}m$, and its layered structure is α-$NaFeO_2$–type like $LiCoO_2$; their synthesis is always thought as formed by two phases: monoclinic Li_2MnO_3-layered and rhombohedral $LiMO_2$-layered moieties [2]. However, their complex crystal structure has not yet been fully realized. It is known that Co is poisonous and expensive. In Li-rich Mn-based NCM, the percentage of Co is far lower than that of Mn; thus, with the advantages of low cost and high safety, this material is superior to the commonly used cathode material. Meanwhile, for the layered structural stability influenced by the Li_2MnO_3 component, when its first charging voltage is higher than 4.5 V (vs Li^+/Li), Li and O are removed together and its theoretical capacity is up to 377 mAh/g. Therefore, the layered Li-rich Mn-based NCM is a hot candidate for the new LIBs.

Recently, the Li-rich Mn-based oxide $Li_{1.2}Mn_{0.50}Ni_{0.13}Co_{0.13}O_2$ (or $Li[Li_{0.2}Mn_{0.54}Ni_{0.13}Co_{0.13}]O_2$) has aroused increasing attraction [3, 4], and it is considered one of the most promising layered cathode materials for the new battery of optoelectronic devices and LIBs. Its discharge-specific capacity is higher than 250 mAh/g in the voltage range from 2.0 to 4.8 V at 0.1 C. Its precursors are made by sol–gel, solid phase, coprecipitation, combustion, spray pyrolysis, and molten salt synthesis [5]. However, the application of this material has trapped seriously in higher-power systems due to high first irreversible specific capacity, poor cycling stability, and low rate capability [6]. To improve the electrochemical performance of $Li_{1.2}Mn_{0.54}Ni_{0.13}Co_{0.13}O_2$, many effective approaches, such as surface modification [7, 8] and doping [9, 10], had been employed experimentally. The cycling stability and the rate capacity can be dramatically improved by coating with the La–Co–O compound [7]. Since Cs doping can alleviate structural transition from layer to spinel, the Cs-doped $Li_{1.2}Mn_{0.54}Ni_{0.13}Co_{0.13}O_2$ has a better rate capability, a higher initial Coulombic efficiency, and a restrained discharge voltage [10]. Yb doping [11], Na^+ and F^- co-doping [12], and Mg^{2+} and $PO_4{}^{3-}$ dual doping [13] were taken to strengthen the electrochemical performance of $Li_{1.2}Mn_{0.54}Ni_{0.13}Co_{0.13}O_2$. The K-doped $Li_{1.2}Mn_{0.52}Ni_{0.2}Co_{0.08}O_2$ has a higher Coulombic efficiency, a larger reversible discharging capacity, and a more well-defined layered structure, which are mainly ascribable to the accommodation of bigger metal ions K^+ enlarging Li layers to facilitate the diffusion of Li^+ and stabilize the structure [14]. Sodium doping in $Li_{1.2}Mn_{0.54}Co_{0.13}Ni_{0.13}O_2$ had been extensively experimented by Chaofan Yang's group [15]; their results showed that $Li_{1.2-x}Na_xMn_{0.54}Ni_{0.13}Co_{0.13}O_2$ (or $Li_{1.0\text{-}x}Na_x[Li_{0.2}Mn_{0.54}Ni_{0.13}Co_{0.13}]O_2$) has an excellent electrochemical performance.

In parallel with these experimental efforts, the density functional theory (DFT) based on first-principles [16–19] is applied to investigate the physical and chemical mechanics of Li-ion binding and diffusion in the crystal lattice. The results of simulations and calculations can give some theoretical study directions about the relevant experiments, shorten greatly the entire period of experiments or investigations, and reduce the experimental cost [18]. Herein, in this work, $Li_{1.2-x}Na_xMn_{0.54}Ni_{0.13}Co_{0.13}O_2$ was studied theoretically with DFT by Materials Studio, Nanodcal, and Matlab. The results exhibited that the electrochemical performance of $Li_{1.2-x}Na_xMn_{0.54}Ni_{0.13}Co_{0.13}O_2$ is affected by the amount of sodium doping, and the best sodium doping in $Li_{1.2}Mn_{0.54}Ni_{0.13}Co_{0.13}O_2$, obtained by calculations, agreed with that of experiments [15].

PRINCIPLE

Density Functional Theory

DFT originates from the uniform electronic gas model, which is called the Thomas–Fermi model [16, 20]. On the assumption of no interaction between electrons, the Schrödinger equation of the electron's motion is the wave equation shown in the following:

$$-\frac{\hbar^2}{2m}\nabla^2\psi(\boldsymbol{r}) = E\psi(\boldsymbol{r}). \qquad (1)$$

Based on the distribution of free electrons' energy levels at absolute zero, the electron density ρ is shown in the following equation:

$$\rho = \frac{1}{3\pi^2}\left(\frac{2m}{\hbar^2}\right)^{\frac{3}{2}} E_{\mathrm{F}}^{\frac{3}{2}}. \qquad (2)$$

Here, E_{F} is the Fermi energy level, and the kinetic energy T_{e} of a single electron is shown in the following equation:

$$T_{\mathrm{e}} = \frac{3}{5}E_{\mathrm{F}}. \qquad (3)$$

And the system's kinetic energy density is shown in the following equation:

$$\rho T_{\mathrm{e}} = \frac{3}{5}\frac{h^2}{2m}\left(3\pi^2\right)^{\frac{3}{2}}\rho^{\frac{5}{3}} \quad = C_k\rho^{\frac{5}{3}}. \qquad (4)$$

Considering the external field $u(\boldsymbol{r})$ of the classical Coulombic interaction between nuclei and electrons, the total energy of the electron system can be obtained as shown in the following equation:

$$E_{\mathrm{TF}}(\boldsymbol{r}) = C_k\int r^{\frac{5}{3}}\mathrm{d}r + \int r(\boldsymbol{r})u(\boldsymbol{r})\mathrm{d}r + \frac{1}{2}\int\frac{r(\boldsymbol{r})r(\boldsymbol{r}')}{|\boldsymbol{r}-\boldsymbol{r}'|}\mathrm{d}r\mathrm{d}r'. \qquad (5)$$

The above equation shows the electronic systemic total energy is affected only by the electron density function $r(r)$; hence, this theory of Thomas–Fermi model is called DFT. But this model could not be used directly. Then, Hohenberg and Kohn proposed the more exact density functional method (HK theorems) [17, 21] considering the nonrelativistic, adiabatic, and single-electron approximations. In fact, the theoretical basis of DFT is HK theorems including the first theory and the second theory. According to HK theorems, when the particles' number is constant, the ground state of particles can be expressed by a variational function of energy function on the number density function of particles $\rho(\boldsymbol{r})$, and the total energy $E_v[\rho(\boldsymbol{r})]$ relevant to external potential is shown in the following equation:

$$E_v[\rho(\boldsymbol{r})] = F[\rho(\boldsymbol{r})] + V_{\mathrm{ne}}[\rho(\boldsymbol{r})], \qquad (6)$$

where the functional $F[\rho(\boldsymbol{r})] = T[\rho(\boldsymbol{r})] + \frac{1}{2}\int \frac{\rho(\boldsymbol{r})\rho(\boldsymbol{r}')}{|\boldsymbol{r}-\boldsymbol{r}'|}\mathrm{d}\boldsymbol{r}\mathrm{d}\boldsymbol{r}' + E_{\mathrm{xc}}[\rho(\boldsymbol{r})]$, which is independent of the external field, $V_{\mathrm{ne}}[\rho(\boldsymbol{r})]$ is the attraction potential between nuclei, $T[\rho(\boldsymbol{r})]$ is the kinetic energy of non-interacting particle models, $\frac{1}{2}\int \frac{\rho(\boldsymbol{r})\rho(\boldsymbol{r}')}{|\boldsymbol{r}-\boldsymbol{r}'|}\mathrm{d}\boldsymbol{r}\mathrm{d}\boldsymbol{r}'$ is the Coulombic repulsion, and $E_{\mathrm{xc}}[\rho(\boldsymbol{r})]$ is the exchange–correlation energy functional.

However, $\rho(\boldsymbol{r})$, $\boldsymbol{T}[\rho(\boldsymbol{r})]$, and $E_{\mathrm{xc}}[\rho(\boldsymbol{r})]$ had not been expressed in HK theorems.

Kohn–Sham Equation and Exchange–Correlation Functional

From the Kohn–Sham equation [22], $\rho(\boldsymbol{r})$ and $\boldsymbol{T}[\rho(\boldsymbol{r})]$ can be solved as shown in the following Hamiltonian:

$$\{-\nabla^2 + V_{\mathrm{KS}}[\rho(\boldsymbol{r})]\}\varphi_i(\boldsymbol{r}) = E_i\varphi_i(\boldsymbol{r}), \tag{7}$$

where $V_{\mathrm{KS}}[\rho(\boldsymbol{r})] = V_{\mathrm{ne}}[\rho(\boldsymbol{r})] + V_{\mathrm{coul}}[\rho(\boldsymbol{r})] + V_{\mathrm{xc}}[\rho(\boldsymbol{r})]$, $V_{\mathrm{coul}}[\rho(\boldsymbol{r})]$ is the Coulombic potential between electrons, and $V_{\mathrm{xc}}[\rho(\boldsymbol{r})]$ is the exchange–correlation potential.

$E_{\mathrm{xc}}[\rho(\boldsymbol{r})]$ is generally solved by the local density approximation (LDA) and the generalized gradients approximation (GGA) [23]. When the system's electron density in the space is not changed much, LDA is used to give more accurate results. Considering the uniformity of the electron density, GGA can get better energy features and more rigorous results than LDA. Now, GGA is one of the important thermotical methods employed by the first-principles and relevant researches of systemic properties. Under GGA, there are many kinds of exchange–correlation functionals, such as PW91 (Perdew–Wang) [24] and PBE (Perdew–Burke–Ernzerhof) [25]. With the development of computing power, theoretical investigation based on DFT is more and more important for the performance study of materials.

METHOD AND MODEL

Using the PW91 method with the PBE exchange–correlation functional and GGA, the electronic conductivity of $\mathrm{Li_{1.2-\mathit{x}}Na_{\mathit{x}}Mn_{0.54}Ni_{0.13}Co_{0.13}O_2}$ was implemented by CAmbridge Serial Total Energy Package (CASTEP) of Materials Studio 8.0, which is the quantum mechanical procedure. The plane wave pseudopotential method was used in CASTEP. The Coulombic attraction potential, between the inner layer electrons around the nucleus and those of the outer layer [26], was described by the ultrasoft pseudopotential. A plane wave cutoff was set at 440 eV. To relax all structures [27], a 4 × 4 × 1 mesh of k-points in the Monkhorst–Pack scheme was taken. The self-consistency energy tolerance was 1×10^{-6} eV. To obtain the local stable structure of the material, the structure geometry should be optimized; the maximum stress tolerance, the maximum displacement tolerance, and the average force on every atom were the same as those in our previous work [19]. And DFT calculations had been carried out with the virtual mixed atom method.

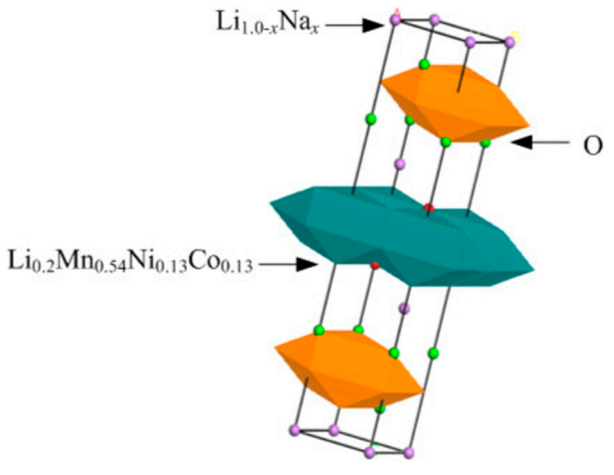

FIGURE 1 | Cell of $\mathrm{Li_{1.0-\mathit{x}}Na_{\mathit{x}}[Li_{0.2}Mn_{0.54}Ni_{0.13}Co_{0.13}]O_2}$. Li and Na occupy 3a, $\mathrm{Li_{0.2}Mn_{0.54}Ni_{0.13}Co_{0.13}}$ occupies 3b, and O occupies 6c.

The $\mathrm{Li_{1.0-\mathit{x}}Na_{\mathit{x}}[Li_{0.2}Mn_{0.54}Ni_{0.13}Co_{0.13}]O_2}$ cell model is shown in **Figure 1**, and a 4 × 3 × 2 supercell model was built. Li and sodium are assumed as 1.0 mol in this chemical formula; if the sodium doping amount is x mol, then Li is $1.0-x$ mol. The calculation of $\mathrm{Li_{1.2-\mathit{x}}Na_{\mathit{x}}Mn_{0.54}Ni_{0.13}Co_{0.13}O_2}$ (x = 0.01, 0.02, 0.03, . . . , 0.15) is analyzed as follows.

RESULTS AND DISCUSSION

Band Gap and Partial Density of States

The band gap of $\mathrm{Li_{1.2-\mathit{x}}Na_{\mathit{x}}Mn_{0.54}Ni_{0.13}Co_{0.13}O_2}$ is calculated, and the partial density of states (PDOS) is plotted with the sodium doping amount x = 0.01, 0.02, 0.03, . . . , 0.15 mol. The band gap and electrons in the conduction band are very important for the material's electronic conductivity. If the band gap is narrower, the conductivity of the material is better. After sodium doping, the band structure of $\mathrm{Li_{1.2-\mathit{x}}Na_{\mathit{x}}Mn_{0.54}Ni_{0.13}Co_{0.13}O_2}$ remains stable, but the energy gap has changed much. In **Table 1**, all band gap values are listed. **Figure 2** shows the relationship between the band gap and x. According to **Figure 2**, the band gap curve of $\mathrm{Li_{1.2-\mathit{x}}Na_{\mathit{x}}Mn_{0.54}Ni_{0.13}Co_{0.13}O_2}$ has three inflection points at x = 0.02 mol, x = 0.07 mol, and x = 0.12 mol, respectively, where the band gap has changed clearly. When x = 0.02 mol, the band gap value begins to decrease; at x = 0.07 mol, its value increases slightly, which may be ascribed to the expanding volume and disorder of $\mathrm{Ni^{2+}/Li^{+}}$ cation mixing, but from then on, it decreases continually. In other words, it basically decreases with increasing x until x = 0.12 mol, which indicates sodium doping can effectively improve the conductivity of $\mathrm{Li_{1.2}Mn_{0.54}Ni_{0.13}Co_{0.13}O_2}$ when $0.02 < x < 0.13$ mol.

The sodium doping influence on the conductivity of $\mathrm{Li_{1.2}Mn_{0.54}Ni_{0.13}Co_{0.13}O_2}$ was achieved by the PDOS, which can clearly describe the bonding and density of states near the Fermi level. **Figure 3** shows its PDOS, respectively, when x = 0, 0.01, 0.04, and 0.10 mol. The peak of the PDOS corresponds to the electron number at this energy level. The colored lines in **Figure 3** represent

TABLE 1 | Band gap values of $Li_{1.2-x}Na_xMn_{0.54}Ni_{0.13}Co_{0.13}O_2$ with different x.

***x* (mol)**	**0**	**0.01**	**0.02**	**0.03**	**0.04**	**0.05**	**0.06**	**0.07**
Band gap (eV)	1.577	1.573	1.574	1.536	1.479	1.423	1.364	1.429
***x* (mol)**	**0.08**	**0.09**	**0.10**	**0.11**	**0.12**	**0.13**	**0.14**	**0.15**
Band gap (eV)	1.381	1.315	1.100	1.008	1.000	1.100	1.215	1.237

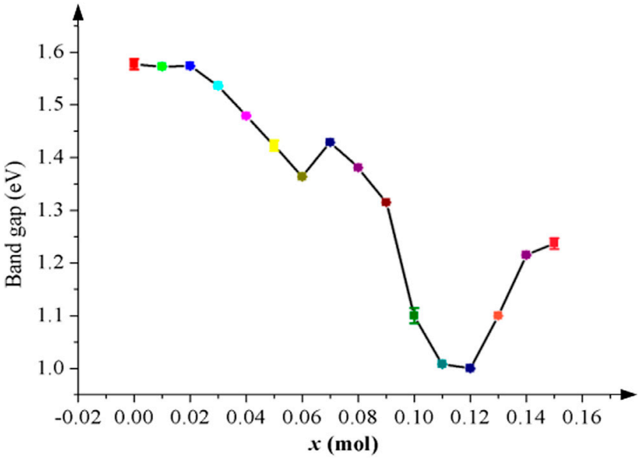

FIGURE 2 | The band gap of $Li_{1.2-x}Na_xMn_{0.54}Ni_{0.13}Co_{0.13}O_2$ becomes narrower after sodium doping, which means its conductivity is improved notably. The error bars show that the accuracy of our band gap values is reliable.

the density of different orbital states. In **Figure 3B**, when x = 0.01 mol, the PDOS peak is about 181 eV, which is subtly different from that of the pristine as shown in **Figure 3A**; when x = 0.02 ~ 0.03 mol, PDOS peaks have increased slowly; when x = 0.04 mol (shown in **Figure 3C**), the PDOS peak at the Fermi level around 201 eV may be ascribed to the wider Li–O layers made by the bigger sodium atoms' substitution, and the conductivity of $Li_{1.2}Mn_{0.54}Ni_{0.13}Co_{0.13}O_2$ is getting better distinctly; when x = 0.05 ~ 0.14 mol, the PDOS peaks have not changed much. **Figure 3D** shows the PDOS peak is about 207 eV when x = 0.10 mol; but when x = 0.15 mol, the peak of the PDOS declines. Therefore, the right amount of sodium doping can multiply greatly the electrons near the Fermi level, and sodium doping should be within x = 0.04 ~ 0.14 mol.

Cell Volume and Lithiation Formation Energy

The volume and formation energy of $Li_{1.2-x}Na_xMn_{0.54}Ni_{0.13}Co_{0.13}O_2$ were calculated. The volume data after doping indicate that x should be controlled at x < 0.11 mol. The volume is a little bigger at x = 0.07 mol than that at x = 0.06 mol; at x = 0.08 mol, it decreases again; when x > 0.10 mol, the volume expansion is huge, which will lead to the structural instability. Due to the bigger sodium atom than the lithium atom, the interslab distance of the Li–O layer can be enlarged, and the diffusion ability of Li^+ in the crystal lattice is strengthened to enhance the conductivity of $Li_{1.2}Mn_{0.54}Ni_{0.13}Co_{0.13}O_2$. More importantly, the proper sodium doping can stabilize the layered crystal structure.

It is very important to analyze the formation energy, which explicitly decides the difficulty of the lithiation/delithiation process. The greater the formation energy of metal oxide is, the higher the difficulty is for atoms to get free from the crystal lattice. The lithiation formation energy E is shown in the following equation:

$$E = E_t - E_{dl} - E_{dil}, \tag{8}$$

where E_t is the supercell's total energy, E_{dl} is the delithiation, and E_{dil} is the supercell's energy after delithiation. In **Figure 4**, the energies in **Eq. 8** are plotted to investigate the relationship between E and x. According to **Figure 4**, E has varied with x. When $0 < x < 0.09$ mol, E decreases extremely, which indicates Li^+ can be deintercalated more easily and the cycling stability and rate capability of $Li_{1.2-x}Na_xMn_{0.54}Ni_{0.13}Co_{0.13}O_2$ can be continually enhanced; when $0.09 < x < 0.12$ mol, E remains stable; when x = 0.10 mol, E is lowest and the rate capability is best; when x > 0.12 mol, E raises gradually. Therefore, the best doping amount x = 0.10 mol.

Electron Density Difference

To analyze the electrons' distribution near local atoms, the electron density difference of $Li_{1.2-x}Na_xMn_{0.54}Ni_{0.13}Co_{0.13}O_2$ was modulated. Compared with the pristine (**Figure 5A**), when $0 < x < 0.04$ mol, the color of the electron cloud around atoms has not changed obviously and the coverage of the electron cloud is getting bigger slowly; in **Figure 5B**, the color of the electron cloud has changed much and the electron cloud's coverage is bigger significantly, which exhibit that the conductivity of $Li_{0.08}Na_{0.04}Mn_{0.54}Ni_{0.13}Co_{0.13}O_2$ is better than that when x < 0.04 mol; when x = 0.10 mol (**Figure 5C**), the color is orange and the coverage expands much, meaning that free electrons have increased enormously and its conductivity is far better than before; when x = 0.11 mol (**Figure 5D**), the color of the electron cloud is the same as that of $Li_{1.1}Na_{0.1}Mn_{0.54}Ni_{0.13}Co_{0.13}O_2$; when $0 < x < 0.14$ mol, the coverage of the electron cloud is expanding continually until when x = 0.14 mol; when x > 0.14 mol, the electron cloud's coverage has shrunk a little. Therefore, sodium doping can improve the conductivity of $Li_{1.2}Mn_{0.54}Ni_{0.13}Co_{0.13}O_2$, and the excellent amount of sodium doping x = 0.05–0.13 mol.

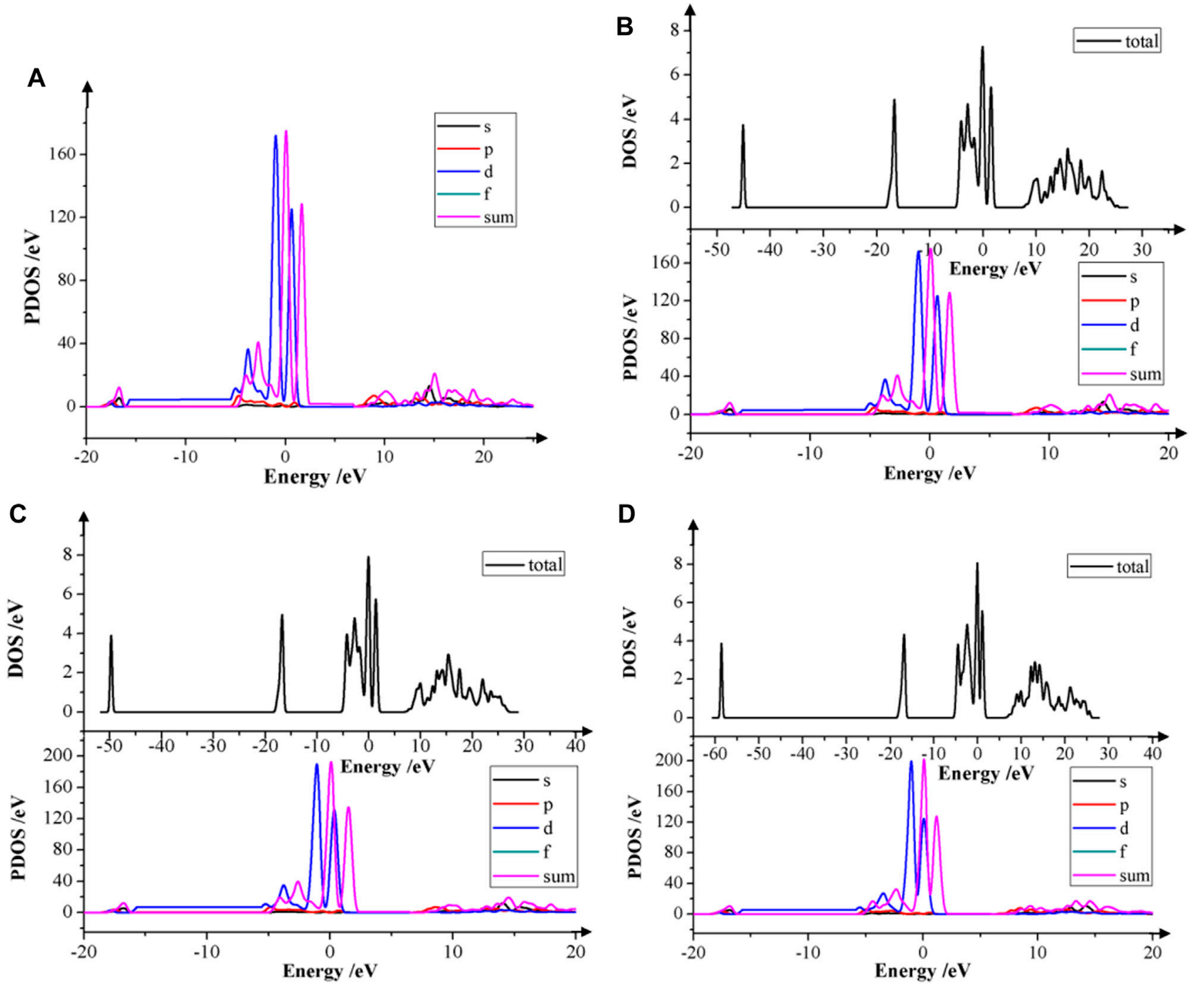

FIGURE 3 | PDOS schemas of $Li_{1.2-x}Na_xMn_{0.54}Ni_{0.13}Co_{0.13}O_2$ with different *x*. **(A)** When $x = 0$ mol, the PDOS peak of the pristine is about 173 eV. **(B)** The PDOS peak of $Li_{1.19}Na_{0.01}Mn_{0.54}Ni_{0.13}Co_{0.13}O_2$ is up to 181 eV, which is higher than that of $Li_{1.2}Mn_{0.54}Ni_{0.13}Co_{0.13}O_2$. **(C)** When $x = 0.04$ mol, the PDOS peak raises around to 201 eV. The bigger Li–O layers contribute to the better conductivity. **(D)** When $x = 0.10$ mol, the PDOS peak is approximately 207 eV, which is higher much than that of $Li_{1.2}Mn_{0.54}Ni_{0.13}Co_{0.13}O_2$.

Potential Energy of Electrons

To study the rate capability after doping, the electrons' potential energy of $Li_{1.2-x}Na_xMn_{0.54}Ni_{0.13}Co_{0.13}O_2$ had been profiled. In a potential well, if electrons have lower potential energy and get the extra external energy, they can cross freely over the potential well. In **Figure 6**, the 3D potential energy map of $Li_{1.1}Na_{0.1}Mn_{0.54}Ni_{0.13}Co_{0.13}O_2$ is shown. The different colors represent the potential energy change. In **Figure 6**, the taking turns of the potential barrier and well show $Li_{1.1}Na_{0.1}Mn_{0.54}Ni_{0.13}Co_{0.13}O_2$ is still a layered structure. And so do the potential energy maps of $Li_{1.2-x}Na_xMn_{0.54}Ni_{0.13}Co_{0.13}O_2$ when $x < 0.10$ mol, which means the right doping amount cannot lead to the phase transition.

For the purpose of investigating the sodium doping influence on the potential energy well, diffusion paths were simulated. The 2D potential energy image of $Li_{1.1}Na_{0.1}Mn_{0.54}Ni_{0.13}Co_{0.13}O_2$ is shown in **Figure 7**. Electrons will diffuse more facilely along the path marked with blue "*", which represents the minimum potential energy and can offer abundant channels to diffuse. And the energy barrier of Li^+ insertion/extraction is reduced in the crystal lattice. Therefore, electrons and Li^+ can be removed and migrated to other places almost without any energy barrier. In **Figure 7**, the potential energy of $Li_{1.1}Na_{0.1}Mn_{0.54}Ni_{0.13}Co_{0.13}O_2$ is from 36 to 1 eV, and each marked path is not the same. According to the calculations of potential energy for $Li_{1.2-x}Na_xMn_{0.54}Ni_{0.13}Co_{0.13}O_2$, the minimum potential energy decreases with rising *x*, which demonstrates that the potential well of $Li_{1.2-x}Na_xMn_{0.54}Ni_{0.13}Co_{0.13}O_2$ is lower, and electrons can be removed from the potential well more easily. Thus, its rate performance can be effectively promoted.

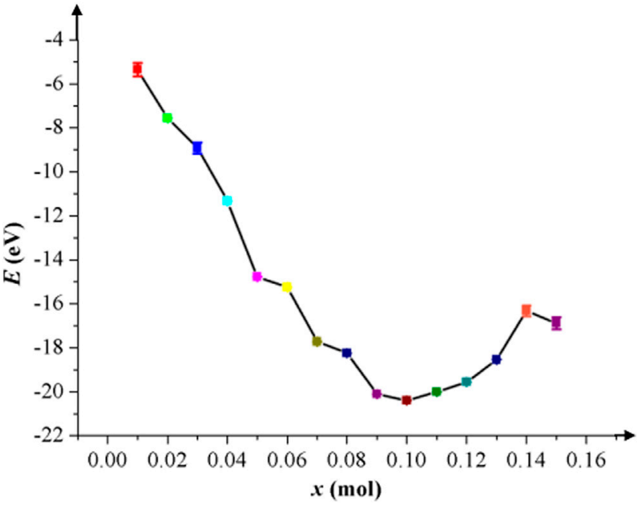

FIGURE 4 | Schematic diagram of the lithiation formation energy *E* with different *x*. The error bars show that the accuracy of our calculations is credible.

CONCLUSION

The physical and electrochemical performances of $Li_{1.2-x}Na_xMn_{0.54}Ni_{0.13}Co_{0.13}O_2$ were simulated and analyzed by DFT. The layered structure of $Li_{1.2-x}Na_xMn_{0.54}Ni_{0.13}Co_{0.13}O_2$ can be kept stably after sodium doping. According to the calculations of the band gap and PDOS, when x = 0.05–0.12 mol, $Li_{1.2-x}Na_xMn_{0.54}Ni_{0.13}Co_{0.13}O_2$ has better conductivity and cycling performance; when $x < 0.11$ mol, its volume remains invariable; when $x = 0.10$ mol, the lithiation formation energy E is lowest and Li^+ and electrons can be removed easily; based on the results of the electron density difference, when x = 0.05–0.13 mol, $Li_{1.2-x}Na_xMn_{0.54}Ni_{0.13}Co_{0.13}O_2$ has better conductivity and

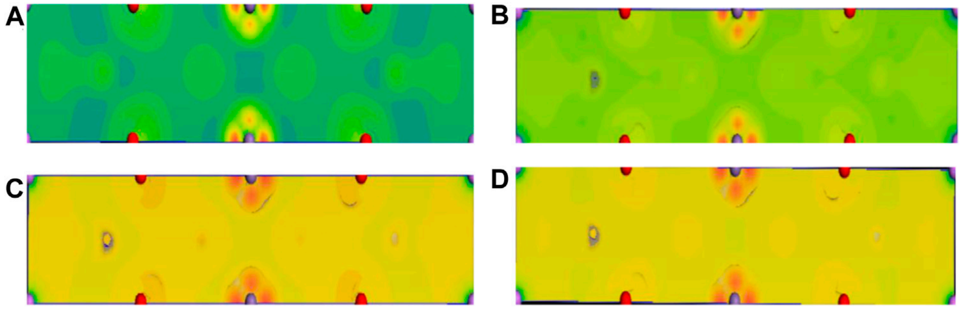

FIGURE 5 | Electron density difference of $Li_{1.2-x}Na_xMn_{0.54}Ni_{0.13}Co_{0.13}O_2$. **(A)** The electron cloud's color and coverage of the pristine are shown. **(B)** When x = 0.04 mol, the color has become orange and the electron cloud's coverage has expanded obviously, which mean its conductivity is distinguished. **(C)** When x = 0.10 mol, its color gets brighter and the electron cloud's coverage gets bigger, which indicate its conductivity is promoted extremely. **(D)** When x = 0.11 mol, there is no difference in color between x = 0.11 mol and x = 0.10 mol and the coverage of the electrons gets bigger continually.

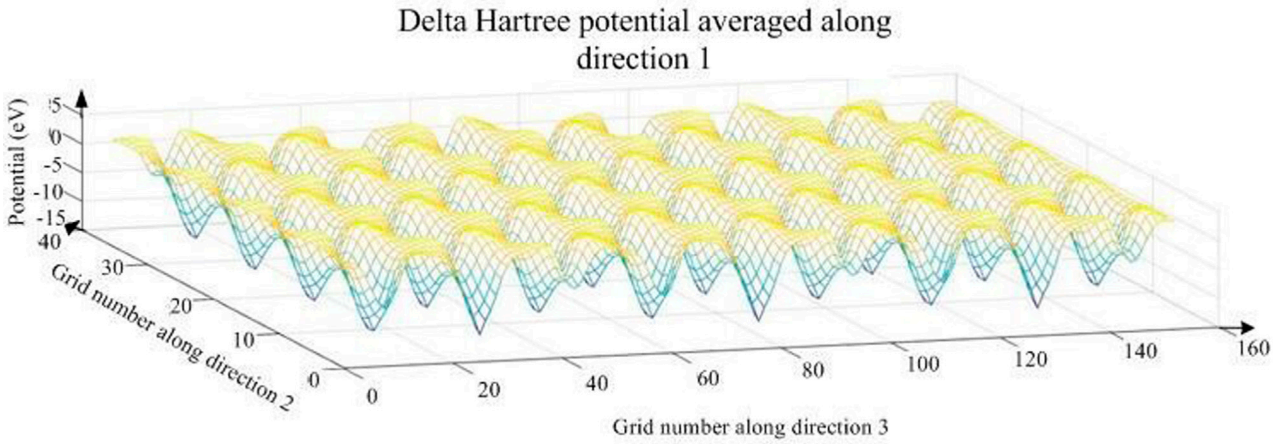

FIGURE 6 | 3D potential energy map of $Li_{1.1}Na_{0.1}Mn_{0.54}Ni_{0.13}Co_{0.13}O_2$.

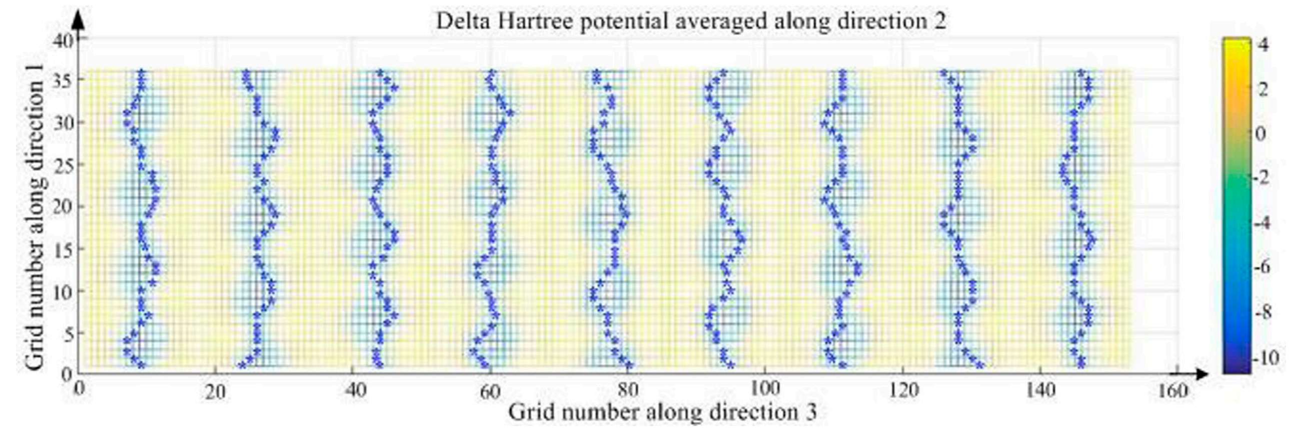

FIGURE 7 | 2D potential energy map of $Li_{1.1}Na_{0.1}Mn_{0.54}Ni_{0.13}Co_{0.13}O_2$.

electrons' potential energies are becoming lower with rising x. To sum up, when $x = 0.10$ mol, the electrochemical performance of sodium-doped $Li_{1.2}Mn_{0.54}Ni_{0.13}Co_{0.13}O_2$ is best, which is essentially in agreement with experimental results. The sample of $Li_{1.2-x}Na_xMn_{0.54}Ni_{0.13}Co_{0.13}O_2$ could be synthesized with a confinement method. Though $Li_{1.1}Na_{0.1}Mn_{0.54}Ni_{0.13}Co_{0.13}O_2$ has better electrochemical performance than $Li_{1.2}Mn_{0.54}Ni_{0.13}Co_{0.13}O_2$, other approaches should be taken as well to further improve the energy density, reversible charge capacity, and cycling performance. Our calculations, analyses, and simulations based on DFT can provide some theoretical proposals for the doping study about the electrochemical performance, and these methods can contribute to the performance study of the battery module for new electro-optical conversion devices.

DATA AVAILABILITY STATEMENT

The original contributions presented in the study are included in the article/Supplementary Material, and further inquiries can be directed to the corresponding author.

AUTHOR CONTRIBUTIONS

YG designed models, analyzed results, and wrote the manuscript. YH carried out calculations. HY gave some proposals.

FUNDING

This research was funded by the Science and Technology Project Foundation of Zhongshan City of Guangdong Province of China (no. 2018B1127), the Zhongshan Innovative Research Team Program (no. 180809162197886), the Educational Science and Technology Planning in Guangdong Province (no. 2018GXJK240), the National Natural Science Foundation of China (no. 11775047), the union project of the National Natural Science Foundation of China and Guangdong Province (no. U1601214), the Science and Technology Program of Guangzhou (no. 2019050001), and the Scientific and Technological Plan of Guangdong Province (no. 2018B050502010).

REFERENCES

1. Zhu C, Usiskin RE, Yu Y, and Maier J. The Nanoscale Circuitry of Battery Electrodes. *Science* (2017) 358(6369):eaao2808–08. doi:10.1126/science.aao2808
2. Thackeray MM, Kang S-H, Johnson CS, Vaughey JT, Benedek R, and Hackney SA. Li_2MnO_3-stabilized $LiMO_2$ (M = Mn, Ni, Co) Electrodes for Lithium-Ion Batteries. *J Mater Chem* (2007) 17(30):3112–25. doi:10.1039/B702425H
3. Song C, Feng W, Wang X, and Shi Z. Enhanced Electrochemical Performance of $Li_{1.2}Mn_{0.54}Ni_{0.13}Co_{0.13}O_2$ Cathode Material with Bamboo Essential Oil. *Ionics* (2020) 26(2):661–72. doi:10.1007/s11581-019-03233-9
4. Vivekanantha M, Senthil C, Kesavan T, Partheeban T, Navaneethan M, Senthilkumar B, et al. Reactive Template Synthesis of $Li_{1.2}Mn_{0.54}Ni_{0.13}Co_{0.13}O_2$ Nanorod Cathode for Li-Ion Batteries: Influence of Temperature over Structural and Electrochemical Properties. *Electrochimica Acta* (2019) 317:398–407. doi:10.1016/j.electacta.2019.05.095
5. Leifer N, Penki T, Nanda R, Grinblat J, Luski S, Aurbach D, et al. Linking Structure to Performance of $Li_{1.2}Mn_{0.54}Ni_{0.13}Co_{0.13}O_2$ (Li and Mn Rich NMC) Cathode Materials Synthesized by Different Methods. *Phys Chem Chem Phys* (2020) 22(16):9098–109. doi:10.1039/D0CP00400F
6. Zhang W, Liu Y, Wu J, Shao H, and Yang Y. Surface Modification of $Li_{1.2}Mn_{0.54}Ni_{0.13}Co_{0.13}O_2$ Cathode Material with Al_2O_3/SiO_2 Composite for Lithium-Ion Batteries. *J Electrochem Soc* (2019) 166(6):A863–A872. doi:10.1149/2.0171906jes
7. Luo Z, Zhou Z, He Z, Sun Z, Zheng J, and Li Y. Enhanced Electrochemical Performance of $Li_{1.2}Mn_{0.54}Ni_{0.13}Co_{0.13}O_2$ Cathode by Surface Modification Using La-Co-O Compound. *Ceramics Int* (2021) 47(2):2656–64. doi:10.1016/j.ceramint.2020.09.114
8. Liu Y, Yang Z, Li J, Niu B, Yang K, and Kang F. A Novel Surface-Heterostructured $Li_{1.2}Mn_{0.54}Ni_{0.13}Co_{0.13}O_2@Ce_{0.8}Sn_{0.2}O_{2-\sigma}$ Cathode Material for Li-Ion Batteries with Improved Initial Irreversible Capacity Loss Cathode Material for Li-Ion Batteries with Improved Initial Irreversible Capacity Loss. *J Mater Chem A* (2018) 6:13883–93. doi:10.1039/C8TA04568B
9. Zhou L, Liu J, Huang L, Jiang N, Zheng Q, and Lin D. Sn-doped $Li_{1.2}Mn_{0.54}Ni_{0.13}Co_{0.13}O_2$ Cathode Materials for Lithium-Ion Batteries with Enhanced Electrochemical Performance. *J Solid State Electrochem* (2017) 21(4):3467–77. doi:10.1007/s10008-017-3688-y

10. Xu L, Meng JX, Yang P, Xu H, and Zhang S. Cesium-doped Layered $Li_{1.2}Mn_{0.54}Ni_{0.13}Co_{0.13}O_2$ Cathodes with Enhanced Electrochemical Performance. *Solid State Ionics* (2021) 361:115551. doi:10.1016/j.ssi.2021.115551
11. Bao L, Yang Z, Chen L, Su Y, Lu Y, Li W, et al. The Effects of Trace Yb Doping on the Electrochemical Performance of Li-Rich Layered Oxides. *ChemSusChem* (2019) 12(10):2294–301. doi:10.1002/cssc.201900226
12. Zhang P, Zhai X, Huang H, Zhou J, Li X, He Y, et al. Synergistic Na^+ and F^- Co-doping Modification Strategy to Improve the Electrochemical Performance of Li-Rich $Li_{1.2}Mn_{0.54}Ni_{0.13}Co_{0.13}O_2$ Cathode. *Ceramics Int* (2020) 46(15):24723–36. doi:10.1016j.ceramint.2020.06.26310.1016/j.ceramint.2020.06.263
13. Liu Y, He B, Li Q, Liu H, Qiu L, Liu J, et al. Relieving Capacity Decay and Voltage Fading of $Li_{1.2}Ni_{0.13}Co_{0.13}Mn_{0.54}O_2$ by Mg^{2+} and PO_4^{3-} Dual Doping. *Mater Res Bull* (2020) 130:110923. doi:10.1016/j.materresbull.2020.110923
14. Liu Z, Zhang Z, Liu Y, Li L, and Fu S. Facile and Scalable Fabrication of K+-doped $Li_{1.2}Ni_{0.2}Co_{0.08}Mn_{0.52}O_2$ Cathode with Ultra High Capacity and Enhanced Cycling Stability for Lithium Ion Batteries. *Solid State Ionics* (2019) 332:47–54. doi:10.1016/j.ssi.2018.12.021
15. Yang C, Zhang X, Huang J, and AoZhang PG. Enhanced Rate Capability and Cycling Stability of $Li_{1.2-x}Na_xMn_{0.54}Co_{0.13}Ni_{0.13}O_2$. *Electrochimica Acta* (2016) 196:261–9. doi:10.1016/j.electacta.2016.02.18010.1016/j.electacta.2016.02.180
16. Fermi E. Eine statistische methode zur bestimmung einiger eigenschaften des atoms und ihre anwendung auf die theorie des periodischen systems der elemente. *Z Physik* (1928) 48(1):73–9. doi:10.1007/BF01351576
17. Hohenberg P, and Kohn W. Inhomogeneous Electron Gas. *Phys Rev* (1964) 136(3B):B864–B871. doi:10.1103/physrev.136.b864
18. Ng MF, and Sullivan MB. First-principles Characterization of Lithium Cobalt Pyrophosphate as a Cathode Material for Solid-State Li-Ion Batteries. *J Phys Chem C* (2019) 123(49):29623–9. doi:10.1021/acs.jpcc.9b09946
19. Gao Y, Shen K, Liu P, Liu L, Chi F, Hou X, et al. First-Principles Investigation on Electrochemical Performance of Na-Doped $LiNi_{1/3}Co_{1/3}Mn_{1/3}O_2$. *Front Phys* (2021) 8:1–8. doi:10.3389/fphy.2020.616066
20. Thomas LH. The Calculation of Atomic fields. *Math Proc Camb Phil Soc* (1927) 23:542–8. doi:10.1017/S0305004100011683
21. Jones RO, and Gunnarsson O. The Density Functional Formalism, its Applications and Prospects. *Rev Mod Phys* (1989) 61(3):689–746. doi:10.1103/RevModPhys.61.689
22. Kohn W, and Sham LJ. Self-consistent Equations Including Exchange and Correlation Effects. *Phys Rev* (1965) 140:A1133–A1138. doi:10.1103/physrev.140.a1133
23. Perdew JP, Chevary JA, Vosko SH, Jackson KA, Pederson MR, Singh DJ, et al. Atoms, Molecules, Solids, and Surfaces: Applications of the Generalized Gradient Approximation for Exchange and Correlation. *Phys Rev B* (1992) 46(11):6671–87. doi:10.1103/PhysRevB.46.6671
24. Kresse G, and Joubert D. From Ultrasoft Pseudopotentials to the Projector Augmented-Wave Method. *Phys Rev B* (1999) 59:1758–75. doi:10.1103/PhysRevB.59.1758
25. Perdew JP, Burke K, and Ernzerhof M. Generalized Gradient Approximation Made Simple. *Phys Rev Lett* (1996) 77:3865–8. doi:10.1103/PhysRevLett.77.3865
26. Vanderbilt D. Soft Self-Consistent Pseudopotentials in a Generalized Eigenvalue Formalism. *Phys Rev B* (1990) 41(11):7892–5. doi:10.1103/PhysRevB.41.7892
27. Monkhorst HJ, and Pack JD. Special Points for Brillouin-Zone Integrations. *Phys Rev B* (1976) 13:5188–92. doi:10.1103/PhysRevB.16.174810.1103/physrevb.13.5188

Conflict of Interest: The authors declare that the research was conducted in the absence of any commercial or financial relationships that could be construed as a potential conflict of interest.

frontiers
in Physics

BRIEF RESEARCH REPORT
published: 22 June 2021
doi: 10.3389/fphy.2021.704493

Heat Generation by Electrical Current in a Quantum Dot Hybridized to Majorana Nanowires

Zhu-Hua Wang*

College of Physics and Electromechanics, Fujian Longyan University, Longyan, China

Heat current generated by electronic transport through a quantum dot (QD) coupled to both a phonon bath and a Majorana nanowire hosting Majorana bound states (MBSs) is theoretically studied in the framework of non-equilibrium Green's function technique. The calculated numerical results show that electrical current can be either enhanced or suppressed by the combined influences of the phonon bath and the MBSs at certain bias voltage regimes. The enhancement and suppression of the current's magnitude for a fixed bias voltage will be reversed due to the direct hybridization between the MBSs. The simultaneous coupling between both MBSs will amplify the function of the MBSs on the current, with the same unchanged and essential qualitative impacts. Heat generation by the electrical current can be fully adjusted by the dot–MBS coupling, direct hybridization between the MBSs, and positions of the dot level. By properly choosing the above parameters, heat generation can be suppressed even for increased electrical current, which is favorable in removing waste heat generated by electrical current flowing through low-dimensional circuits.

Keywords: quantum dot, phonon, Majorana bound states, electrical current, heat generation

Edited by:
Feng Chi,
University of Electronic Science and Technology of China, China

Reviewed by:
Jia Liu,
Inner Mongolia University of Science and Technology, China
Xiu Qing Wang,
Inner Mongolia University for Nationalities, China

***Correspondence:**
Zhu-Hua Wang
lywzh666@163.com

Specialty section:
This article was submitted to Optics and Photonics, a section of the journal Frontiers in Physics

Received: *03 May 2021*
Accepted: *27 May 2021*
Published: *22 June 2021*

Citation:
Wang Z-H (2021) Heat Generation by Electrical Current in a Quantum Dot Hybridized to Majorana Nanowires. Front. Phys. 9:704493. doi: 10.3389/fphy.2021.704493

1 INTRODUCTION

With continuing decreased size and increased density of electronic devices integrated in circuits, the issue of heat generation by electrical current becomes progressively vital. In mesoscopic and nanoscale systems, heat is mainly generated from electron–phonon interaction (EPI), by which the energy accompanying the electric current flowing through the scattering region is transferred to the phonon bath as heat. In fact, recent progresses in nano-fabrication and characterization have brought about a new subject of phononics, which is interested in carrying heat current and information by phonons in addition to electrons or photons [1, 2]. Similar to the case in the usual electronics, the elementary unit in phononics is the preparation, detection, and manipulation of the thermal diode and memory devices. The thermal diode is to switch on–off or to amplify heat current [3, 4], and the thermal memory devices are building blocks for a quantum computer in terms of phonons [5, 6]. Up to now, phononics is still in its primary stage in that the movement of phonons is quite difficult to be controlled, which is contrary to the case of electrons. This is mainly because those phonons are quasiparticles behaving as energy elements without either bare mass or charge [1, 2], which is totally different from the characteristics of electrons. In addition, there are no interactions between single phonon modes. Thus, understanding the nature and controlling the movement of phonons with the help of EPI has become a much interesting research subject, and many theoretical and experimental works about phonon-assisted tunneling through low-dimensional systems have been performed [2–10].

Very similar to the characteristics of phonons, another quasiparticle known as Majorana bound states (MBSs) with zero mass and charge has recently been extensively studied both theoretically and experimentally [11]. The MBSs are of their own antiparticles having no energy and have been successfully formed in various platforms, including superconductors with a non-centrosymmetric center [12, 13], topological insulators in proximity to superconductors [14], defects located in topological superconductors [15], and p-wave superconductors [16]. They are also realizable even in the semiconductor [17] or ferromagnetic [18] nanowires having strong spin–orbit interaction or Josephson junctions [19]. They are very promising in both fault-tolerant quantum computation and energy conservation electronic setups. In line with the preparation of MBSs, their detection is also an important task due to the unique zero-energy, chargeless, and massless nature. Motivated by this, many detection schemes for the existence of MBSs have been proposed, among which the most important one is the electrical transport spectroscopy which applies an electric field on the setup having MBSs and then detects the associated electrical current. The MBS induces an abnormal zero-bias peak in the differential conductance, by which the existence of MBSs can be deduced [20, 21]. This zero-bias peak in the differential conductance, however, can also be induced by other mechanisms, such as the Kondo effect [16] and Andreev bound states [20]. Some other schemes, for example, the unusual sign change or enhancement of thermopower by MBSs, were proposed recently [22–24]. Moreover, a semiconductor quantum dot (QD) side-coupled to MBSs and sandwiched between leads was also introduced to break electron–hole symmetry to avoid null thermoelectric signatures. A previous work shows that the sign change induced by changes in the dot level, dot–MBS coupling strength, and direct MBS–MBS coupling are an efficient demonstration of MBSs. The thermoelectric effect assisted by MBSs was studied in structures composed of a QD connected to more than one lead. Moreover, universal Majorana thermoelectric noise in such similar systems was proposed as a non-invasive electrical detection scheme for the MBSs [24]. Optical detection schemes were also put forward in recent years [25–28]. For example, Liu *et al.* demonstrated that MBSs will absorb and emit photons and then induce photon-assisted side band in the conductance, which can split the MBSs and result in a novel non-zero MBS mode. This provides a new detection means for the MBSs which are very different from the previously proposed ones [25]. All-optical detecting plans for the MBSs were put forward by Zhu *et al.* [26] relying on a QD coupled to nanomechanical resonators, and they found that the optical signatures are enhanced by MBSs. Tang *et al.* [29] have proved that the existence of MBSs will induce a sign change of the tunnel magnetic resistance, which measures the relative change in the electronic currents when the magnetic moments of two leads are changing from parallel to antiparallel configurations.

Heat generation by electrical current in universal nanostructures was theoretically investigated by Sun *et al.* by the non-equilibrium Keldysh Green's function method [30], in which the heat originates from the EPI. The authors proved that the behaviors of the heat current in low-dimensional systems are quite different from Joule's law valid in macroscopic structures. This issue then arouse many investigations [31–33], and it was found that phonon emission processes occur if the Coulomb repulsion equals the phonon energy and induces a high peak in heat generation at even a small electric current [32]. By changing the energy levels in the QD, the heat current decreases regardless of increased electrical bias voltage as the electrons emit phonons in this process. This may induce a negative differential of heat generation [32]. If the scattering region is under a temperature difference between its two ends, it was found that the electrons tunneling through the dot will absorb heat current from the phonon bath to the scattering region and then serve as a nano-refrigerator [32, 33]. In view of the similarities between phonons and MBSs, here we study electrical current and heat exchanged between electrons passing through a QD and a phonon bath interacting with the QD under the influence of a Majorana nanowire hosting MBSs (see **Figure 1**). Our results show that both the electrical current and heat generation can be fully adjusted by the existence of MBSs. Under some conditions, the electrical current can be enhanced with small heat generation, which is useful in energy-saving devices.

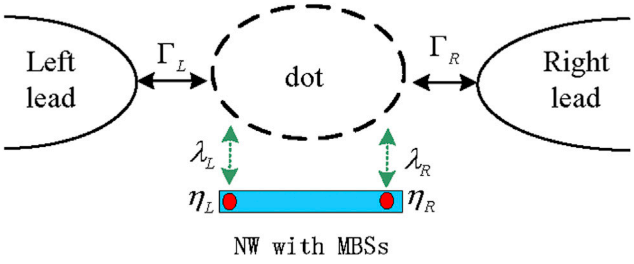

FIGURE 1 | Plot of a quantum dot connected to MBSs prepared at the ends of a topological superconductor nanowire. The dot is coupled to the left and right leads and to a phonon bath with phonon frequency ω_q.

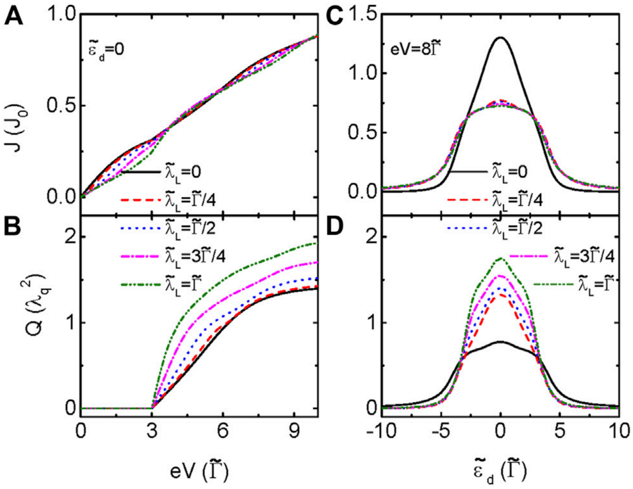

FIGURE 2 | Electrical current **(A)** and heat generation **(B)** as functions of the bias voltage for $\tilde{\varepsilon}_d = 0$ at different $\tilde{\lambda}_L$. **(C, D)** Electrical current and heat generation vs the dot level for $eV = 8\tilde{\Gamma}$ and different $\tilde{\lambda}_L$. Other parameters are $\omega_q = \lambda_q = 3\tilde{\Gamma}$, $\delta_M = \tilde{\lambda}_R = 0$, and $T_e = T_p = 0.00025\tilde{\Gamma}$.

2 MODEL AND METHODS

The Hamiltonian of the considered system composed of a semiconductor QD coupled to two leads and a Majorana nanowire is written as follows ($\hbar = 1$) [30, 34–37]:

$$H = \sum_{k,\beta} \varepsilon_{k\beta} c_{k\beta}^{\dagger} c_{k\beta} + \left[\varepsilon_d + \lambda_q \left(a^{\dagger} + a\right)\right] d^{\dagger} d + \omega_q a^{\dagger} a + \sum_{k,\beta} \left(t_{k\beta} c_{k\beta}^{\dagger} d + H.c\right) + H_{MBSs}, \tag{1}$$

where the first term is for the left ($\beta = L$) and the right ($\beta = R$) electron lead with $c_{k\beta}^{\dagger}$ ($c_{k\beta}$) being the electron creation (annihilation) operator having momentum k and energy $\varepsilon_{k\beta}$. The second term denotes the electron on the QD, and $d_{\sigma}^{\dagger}$ (d_{σ}) creates (annihilates) an electron with a quantized energy level ε_d. $a^{\dagger}$ (a) accounts for the creation (annihilation) operator of a phonon with frequency ω_q, and the quantity λ_q is the electron–phonon coupling magnitude. The third term denotes the single phonon mode, and the fourth term describes hopping between the QD and the leads with $t_{k\beta}$ being the matrix element. The last term in **Eq. 1** is for the MBSs and their coupling to the QD [34–37], given as follows:

$$H_{MBSs} = i\delta_M \eta_L \eta_R + \left(\lambda_L d - \lambda_L^{*} d^{\dagger}\right)\eta_L + \left(\lambda_R d + \lambda_R^{*} d^{\dagger}\right)\eta_R, \tag{2}$$

where the operator $\eta_{L/R}$ stands for the mode located on the left/right end of the nanowire and is coupled to the QD with the strength of $\lambda_{L/R}$, with ε_M being the overlap strength bewteen them. The Majorana operators satisfy $\{\eta_{\alpha}, \eta_{\beta}\} = 2\delta_{\alpha\beta}$ and $\eta_{\alpha} = \eta_{\alpha}^{\dagger}$. We follow the previous work to switch from the Majorana fermion representation to the equivalent regular fermion one by defining [34] $\eta_L = (1/\sqrt{2})(f + f^{\dagger})$ and $\eta_R = (-i/\sqrt{2})(f - f^{\dagger})$; the Hamiltonian H_{MBSs} is rewritten as follows:

$$H_{MBSs} = \varepsilon_M\left(f^{\dagger} f - \frac{1}{2}\right) + \frac{1}{\sqrt{2}}\left(\lambda_L d - \lambda_L^{*} d^{\dagger}\right)\left(f + f^{\dagger}\right) - \frac{1}{\sqrt{2}}\left(\lambda_R d + \lambda_R^{*} d^{\dagger}\right)\left(f - f^{\dagger}\right). \tag{3}$$

We then perform a canonical transformation to eliminate the electron–phonon coupling, that is, [30–32] $\tilde{H} = XHX^{\dagger}$ with $X = \exp\left[(\lambda_q/\omega_q)(a_q^{\dagger} - a_q)d^{\dagger} d\right]$. The transformed Hamiltonian reads as follows:

$$\tilde{H} = \sum_{k,\beta} \varepsilon_{k\beta} c_{k\beta}^{\dagger} c_{k\beta} + \tilde{\varepsilon}_d d^{\dagger} d + \sum_{k,\alpha} \left(\tilde{t}_{k\beta} c_{k\alpha}^{\dagger} d + H.c\right) + \tilde{H}_{MBSs}, \tag{4}$$

where the dot level is *transformed* into $\tilde{\varepsilon}_d = \varepsilon_d - g\omega_q$ with $g = (\lambda_q/\omega_q)^2$. The tunneling matrix element $t_{k\beta}$ and the dot–MBS coupling strengths $\lambda_{L/R}$ are individually transformed into $\tilde{t}_{k\alpha} = t_{k\alpha} X$ and $\tilde{\lambda}_{L/R} = \lambda_{L/R} X$ with $X = \exp[-g(a^{\dagger} - a)]$. When $t_{k\alpha}$ is small compared to λ_q, X can be replaced by its expectation value $\langle X \rangle = \exp[-g(N_{ph} + 1/2)]$, in which $N_{ph} = 1/[\exp(\omega_q/k_B T_p) - 1]$ describes the phonon distribution function with T_p being the phonon temperature [12, 13]. The Fourier transform of heat generation $Q(t) = \omega_q \langle d a_q^{\dagger}(t) a_q(t)/dt \rangle$ can be calculated from the above Hamiltonian and is as follows [30]:

$$Q = \mathrm{Re}\,\omega_q \lambda_q^2 \int \frac{d\varepsilon}{2\pi} \left\{\tilde{G}^{<}(\varepsilon)\tilde{G}^{>}(\bar{\varepsilon}) - 2N_{ph}\left[\tilde{G}^{>}(\varepsilon)\tilde{G}^{a}(\bar{\varepsilon}) + \tilde{G}^{r}(\varepsilon)\tilde{G}^{>}(\bar{\varepsilon})\right]\right\}, \tag{5}$$

where $\bar{\varepsilon} = \varepsilon - \omega_q$ and $\tilde{G}^{r,a,\langle,\rangle}(\varepsilon)$ are the electron single-particle Green's function. By using the equation of motion method, the retarded Green's function is given by [30, 34–37]

$$\tilde{G}^{r}(\varepsilon) = \frac{1}{\varepsilon - \tilde{\varepsilon}_d + i\tilde{\Gamma} - K_1 - \left|\tilde{\lambda}_L^2 - \tilde{\lambda}_R^2\right|^2 K\tilde{K},} \tag{6}$$

where $\tilde{\Gamma} = (\tilde{\Gamma}_L + \tilde{\Gamma}_R)/2$, with $\tilde{\Gamma}_{\beta} = \exp[-g(2N_{ph} + 1)]\Gamma_{\beta}$ and $\Gamma_{\beta} = 2\pi\left|t_{k\beta}\right|^2 \rho_{\beta}$ (ρ_{β} is the local density of states in the lead β). The advanced Green's function in the above equation is $\tilde{G}^{a}(\varepsilon) = [\tilde{G}^{r}(\varepsilon)]^{*}$, and the lesser (greater) one is $\tilde{G}^{<(>)}(\varepsilon) = \tilde{G}^{r}(\varepsilon)\tilde{\Sigma}^{<(>)}\tilde{G}^{a}(\varepsilon)$, in which the self-energies are individually given by $\tilde{\Sigma}^{<} = i[\tilde{\Gamma}_L f_L(\varepsilon) + \tilde{\Gamma}_R f_R(\varepsilon)]$ and $\tilde{\Sigma}^{>} =$

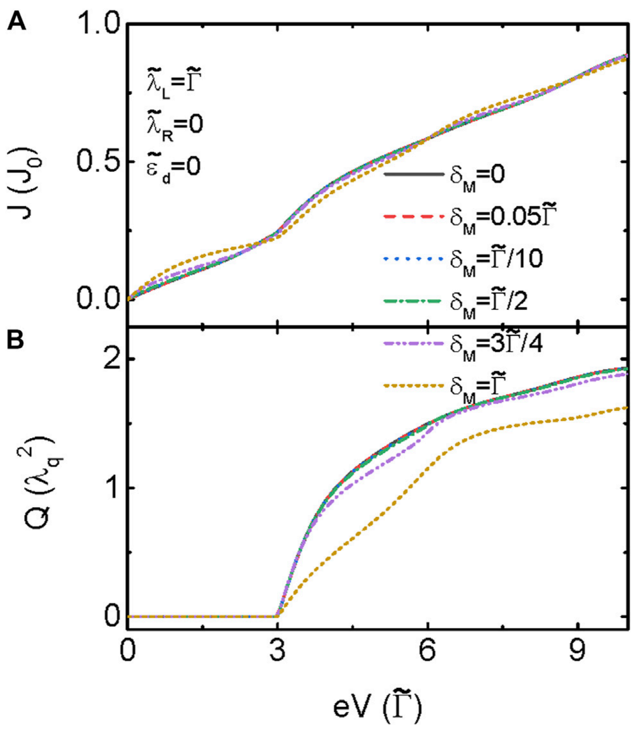

FIGURE 3 | (A) Electrical current and **(B)** heat generation as functions of the bias voltage at different δ_M. Other parameters are the same as in **Figure 2**.

$-i\{\tilde{\Gamma}_L[1-f_L(\varepsilon)]+\tilde{\Gamma}_R[1-f_R(\varepsilon)]\}$ [15]. The Fermi distribution function is $f_\beta(\varepsilon)=1/\{\exp[(\varepsilon-\mu_\beta)/k_BT_e]+1\}$, with chemical potential μ_β. The quantities K, K_1, and $\tilde{K}$ in the above equation are given as $K=\varepsilon/(\varepsilon^2-\delta_M^2)$, $K_1=\left|\tilde{\lambda}_L-\tilde{\lambda}_R\right|^2/2(\varepsilon-\delta_M)+\left|\tilde{\lambda}_L+\tilde{\lambda}_R\right|^2/2(\varepsilon+\delta_M)\tilde{K}=1/(\varepsilon-\tilde{\varepsilon}_d+i\tilde{\Gamma}-K_2)$, and $K_2=\left|\tilde{\lambda}_L+\tilde{\lambda}_R\right|^2/2(\varepsilon-\delta_M)+\left|\tilde{\lambda}_L-\tilde{\lambda}_R\right|^2/2(\varepsilon+\delta_M)$. In terms of the above canonical transformation, $G^r(\varepsilon)$ is related to $\tilde{G}^r(\varepsilon)$ by [7, 30] $G^r(\varepsilon)=\sum_{n=-\infty}^{n=\infty}L_n\{\tilde{G}^r(\varepsilon-n\omega_q)+[\tilde{G}^<(\varepsilon-n\omega_q)-\tilde{G}^<(\varepsilon+n\omega_q)]/2\}$, and $\tilde{G}^<(\varepsilon)=-2i(\Gamma_Lf_L(\varepsilon)+\Gamma_Rf_R(\varepsilon)/(\Gamma_L+\Gamma_R)\mathrm{Im}\tilde{G}^r(\varepsilon)$, and L_n is given by $L_n=\exp[-g(2N_{ph}+1)]\exp(n\omega_q/2k_BT)I_n[2g\sqrt{2N_{ph}(N_{ph}+1)}]$, with $I_n(x)$ being the modified nth Bessel function. Finally, the electric current through the system reads as [7, 30]

$$J=-\frac{e}{h}\int\frac{d\varepsilon}{2\pi}[f_L(\varepsilon)-f_R(\varepsilon)]\frac{\Gamma_L\Gamma_R}{\Gamma_L+\Gamma_R}\mathrm{Im}G^r(\varepsilon). \tag{7}$$

3 RESULTS AND DISCUSSION

In this section, we present our numerical results of heat generation Q and electrical current J versus either the bias voltage eV or the renormalized dot level $\tilde{\varepsilon}_d$. We assume identical coupling between the dot and the two leads, that is, $\Gamma_L=\Gamma_R=\Gamma$, and choose $\tilde{\Gamma}=1$ as the energy unit. To compare our results with those in the absence of MBSs given in Ref. 10, we set $\omega_q=\lambda_q=3\tilde{\Gamma}$ and symmetrical bias $\mu_L=-\mu_R=eV/2$. Usually, the QD and the phonon bath are at the same temperature $T_{ph}=T_e$, which is fixed at a rather low value of $0.00025\tilde{\Gamma}$ favorable in experiments concerning the MBSs. When the dot is decoupled from the Majorana $\tilde{\lambda}_L=\tilde{\lambda}_R=0$, the electrical current in **Figure 2A** increases with the increasing bias voltage and shows several small steps due to the phonon-assisted transport processes [7, 30–33]. The reason is that the dot's level shifts to $\tilde{\varepsilon}_d=\varepsilon_d-g\omega_q$ in the presence of EPI [7, 30–33], and then electrons transport through the dot whenever $\mu_L=\tilde{\varepsilon}_d+n\omega_q$ or $\mu_R=\tilde{\varepsilon}_d-n\omega_q$ for the present case of $V\geq0$. The electric differential conductance $G_{dif}=\partial J/\partial V$ then will develop sharp peaks at the above leads' chemical potentials [7], which is not illustrated here. Heat generation in **Figure 2B** also increases with the increasing bias voltage, but with a delay of ω_q as compared to the case in electric current [30]. The reason is that the heat Q is generated by the phonon emission processes from the state of ε to an empty state of $\varepsilon-\omega_q$ [30]. Under the condition of $eV<\omega_q$, the energy provided by the external electric field is smaller than the phonon energy $\hbar\omega_q$, and then electrons cannot tunnel through the state and heat generation is zero. As shown in previous studies, such a delay effect of heat generation with respect to the current is more distinct at lower temperatures [30, 31]. It is worth pointing out that the steps in heat generation emerge at a different value of bias voltage in the electric current. It is well known that the current plateau is induced as the dot level $\tilde{\varepsilon}_d$ and is in between the bias window, but that of heat generation emerges *at* $eV=2\omega_q$.

When the dot is hybridized to the MBSs formed at the left side of the nanowire ($\tilde{\lambda}_L\neq0$, $\tilde{\lambda}_R=0$), the magnitude of the electrical current in **Figure 2A** can be either enhanced or suppressed depending on the value of the bias voltage. More specifically, the current is suppressed in the bias regimes of $0\leq eV\leq\omega_q$ and $2\omega_q\leq eV\leq3\omega_q$, whereas it is enhanced in the bias regime of $\omega_q\leq eV\leq2\omega_q$. The reason is that, in these two regimes, the electrons emit and absorb phonons and the energy is lost and gained, respectively. As a consequence of it, the differential conductance will develop peaks at $eV=n\omega_q$ (not illustrated in the present manuscript), which is qualitatively consistent with the results found in Ref. [30]. Moreover, the peaks in the differential conductance may be positive corresponding to current's increment or negative due to current's decrement. The variation of the current or the differential conductance also indicates the phonon emission and absorption processes. The reason of the above results is that, in the presence of side-coupled MBSs [34], the jumps in the current are consistent with the eigenstates of the QD, which are at $\varepsilon=\pm\sqrt{\tilde{\varepsilon}_d^2+\tilde{\lambda}_L^2}$ and 0 [34–36]. From this, one can see that the electric current depends on EPI and hybridization between electrons in the dot and the MBSs. Heat generation in **Figure 2B**, however, is monotonously enhanced in the bias regimes of $eV\geq\omega_q$ in the presence of dot–MBS coupling. Such a behavior of heat generation proves that the relationship between the electrical current and the heat does not follow Joule's law of $Q=JV$ valid in mesoscopic systems [30]. The enhancement of heat generation can be explained as follows [30]: heat generation arises from the phonon emission processes as an electron located at an energy state of ε transmitting to an empty state of $\varepsilon-\omega_q$. On the condition of

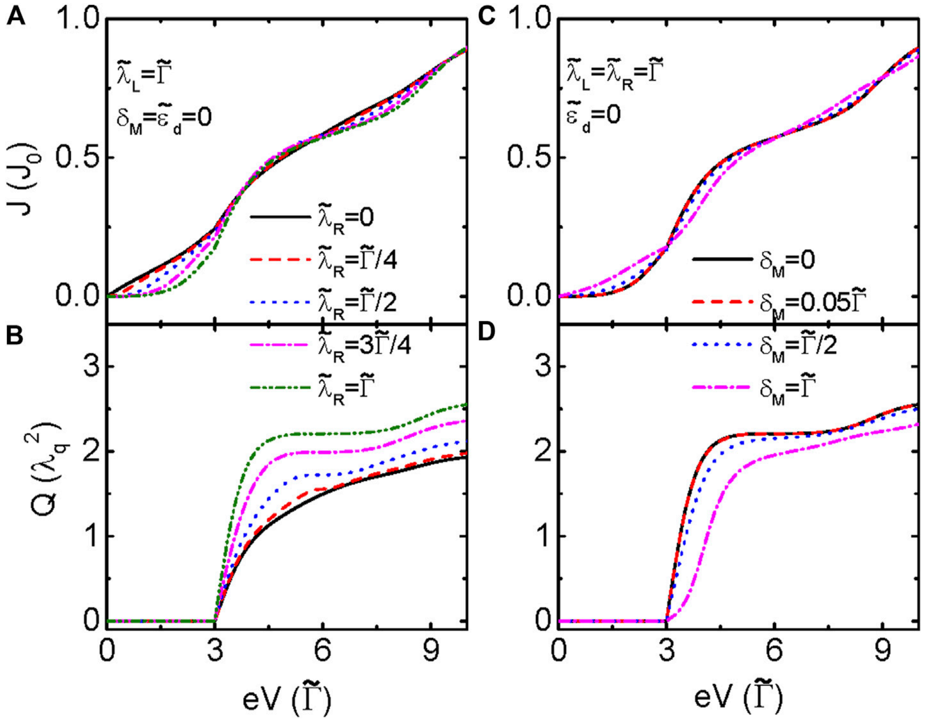

FIGURE 4 | Electrical current and heat generation **(A, B)** as functions of the bias voltage and **(C, D)** vs the dot level at different values of $\tilde{\lambda}_R$. Other parameters are given in the figure and the same as in **Figure 2**.

$eV < \omega_q$, the electric field cannot supply enough energy for electrons to fulfill such a process, and then the heat current is zero, which is the delay effect as shown in **Figure 2**. When the bias voltage $eV \geq \omega_q$, electrons will absorb enough energy to emit phonons and the magnitude of heat generation is increased accordingly. In the presence of coupling between the dot and MBSs, additional molecular states $\varepsilon = \pm\sqrt{\tilde{\varepsilon}_d^2 + \tilde{\lambda}_L^2}$ are induced as discussed above, and then the phonon emission processes will become easier and heat generation is then increased. As the value of $\tilde{\lambda}_L$ is increased, heat generation is further enhanced as indicated in **Figure 2B** because the roles of the molecular states induced by dot–MBS coupling become more and more important. **Figures 2B,C** present the electrical current and heat generation versus the dot level $\tilde{\varepsilon}_d$ for fixed $eV = 8\tilde{\Gamma}$ and different values of $\tilde{\lambda}_L$. The current is suppressed by the dot–MBS coupling when the dot level locates within $-(\omega_q - \tilde{\Gamma}) \leq \tilde{\varepsilon}_d \leq \omega_q - \tilde{\Gamma}$, which is qualitatively in agreement with the results obtained in Ref. [30] and **Figure 2A**. As $\tilde{\varepsilon}_d \geq |\omega_q - \tilde{\Gamma}|$, it is found that the current is increased by hybridization between the dot and the MBSs. This is induced by the newly emerged molecular state from the MBSs. The change in heat generation in **Figure 2D** is essentially opposite to the electrical current in **Figure 2C**. When the dot level is within $-(\omega_q - \tilde{\Gamma}) \leq \tilde{\varepsilon}_d \leq \omega_q - \tilde{\Gamma}$, the magnitude of heat generation is obviously enhanced due to the molecular states arisen from the coupling between the dot and the MBSs, which makes the phonon-emitting processes to become easier [30]. Out of this regime, heat generation is slightly enhanced by the increasing value of $\tilde{\lambda}_L$. The reason is that the zero-energy MBSs only play dominant roles near around $\tilde{\varepsilon}_d = 0$. When the dot level is much higher or lower than zero, the phonon-emitting processes due to the MBS-induced molecular states become difficult, and then heat generation is decreased. From **Figure 2**, it can be seen that, by tuning the dot level and the bias voltage, one can effectively adjust the magnitude of either the electrical current or heat generation, which is favorable in device design [30].

In real experiments, the two modes of the MBSs formed at different ends of a nanowire interact with each other with an amplitude of $\delta_M \propto e^{-\xi/L}$, where L is the length of the nanowire and ξ is the electrons' coherence length [34–37]. Some previous works have demonstrated that this hybridization between the MBSs results in a sharp peak in the conductance when the dot level is aligned to the leads' chemical potential and another two side peaks at about $\varepsilon = \pm\sqrt{\tilde{\varepsilon}_d^2 + \tilde{\lambda}_L^2 + \delta_M^2}$[34]. If the MBS–MBS coupling is strong enough, the central peak in the conductance reduces to the case of resonant level. Under the condition of $\delta_M \neq 0$ as shown in **Figure 3A**, the magnitude of the electrical current J increases when the bias voltage locates within $2n\omega_q \leq eV \leq (2n+1)\omega_q$ and decreases as the bias voltage is $(2n+1)\omega_q \leq eV \leq 2(n+1)\omega_q$ with $n = 0, 1, 2.......$ Such a change in the current induced by the MBS–MBS coupling is totally different from that in **Figure 2A**, where $\delta_M = 0$. The reason is that the impact of hybridization between the MBSs will be suppressed due to their overlapping. The magnitude of heat generation in **Figure 3B**, however, is monotonously suppressed in the whole bias voltage regime except when $eV \leq \omega_q$. For large enough MBS–MBS coupling strength ($\delta_M = \tilde{\lambda}_L = \tilde{\Gamma}$), the magnitude of heat generation reduces almost to the case of the single dot decoupled from the MBSs ($\tilde{\lambda}_L = 0$). This can be seen by comparing the yellow dotted line in **Figure 3B** and the black solid one in **Figure 2B**. The reduction of heat generation by the inter-MBS coupling is because that the impact of each isolated mode of the MBSs is weakened if the MBSs at the two ends of the nanowire overlap with each other. In other words, the phonon absorbed by one MBS formed at one end of the nanowire will be subsequently emitted by the other MBS at the other end of the nanowire. As a result of it, the MBS-assisted heat generation is reduced as shown in **Figure 3B**. By comparing the curves in **Figure 3B** of $\delta_M = 0$ (black solid line) with those of $\delta_M \neq 0$, one can find that the direct hybridization between the MBSs δ_M will strengthen the jumps in heat generation. As indicated above, the phonon absorbed (emitted) by one mode of the MBSs will be subsequently emitted (absorbed) by the other mode. Such phonon absorption and emission processes will change the behaviors of heat generation and induce additional jumps. We emphasize that even the impacts of the MBSs on the heat generation processes are weakened in the presence of hybridization between the MBSs, and the behavior of heat generation is quite different from the case of no MBSs because there are more phonon absorption and emission processes by interaction between the QD and the MBSs.

If both ends of the nanowire are close to the QD [34, 35], the MBSs prepared may couple to the dot simultaneously. In 2011, Flensberg proposed a scheme composed of a QD that couples to both modes of the MBSs to implement a $\pi/8$ phase gate. The author proved that, by adding or removing one electron, non-Abelian rotations at the ground state with Majorana fermions are realizable and also proposed a scheme based on a QD with intradot Coulomb interaction. Moreover, the state of the system with Majorana fermions can also be read out with the help of the QD by a charge measurement. We present the electrical current J and heat generation Q in **Figure 4** with finite values of $\tilde{\Gamma}_L$ and $\tilde{\Gamma}_R$. The behavior of the current in **Figure 4A** resembles that in **Figure 2A**, is further enhanced when the bias voltage is $2n\omega_q \leq eV \leq (2n+1)\omega_q$, and decreases as $(2n+1)\omega_q \leq eV \leq 2(n+1)\omega_q$ by the increasing value of $\tilde{\lambda}_R$. The reason is that, for $\delta_M = 0$, the dot is coupled to both isolated MBSs, which contribute to the tunneling processes almost independently. Heat generation in **Figure 4B** also resembles that in **Figure 2B** and is monotonously enhanced due to the presence of $\tilde{\lambda}_R$ as long as $eV \geq \omega_q$. The jumps in **Figure 4A** are more obvious if both modes of the MBSs are coupled to the dot than those in **Figure 2A** in which only the left mode of the MBSs is coupled to the dot. **Figures 4C,D** show the electrical current and heat generation on the condition of the dot are symmetrically coupled to the two modes of the MBSs with $\tilde{\Gamma}_L = \tilde{\Gamma}_R = \tilde{\Gamma}$. Similar to the results in **Figure 3B**, the current's magnitude in **Figure 4C** is enhanced (suppressed) by MBS–MBS coupling δ_M when the bias voltage is within $(2n+1)\omega_q \leq eV \leq 2(n+1)\omega_q$ ($2n\omega_q \leq eV \leq (2n+1)\omega_q$). Again, the amplitude of heat generation in **Figure 4D** is monotonously suppressed with the increasing value of δ_M for $eV \geq \omega_q$. Interestingly, the current can be enhanced when the bias voltage is within $6\omega_q \leq eV \leq 9\omega_q$, whereas heat generation is suppressed in the presence of direct hybridization between the MBSs, a phenomenon favorable in designing energy conservation devices.

4 SUMMARY

In summary, the present paper studies electric transport and heat generation in a QD side-coupled to MBSs formed at opposite ends of a topological nanowire. It is found that the amplitude of the phonon-assisted current can be either enhanced or suppressed depending on the value of bias voltage compared to the phonon energy. If the dot is simultaneously coupled to the two isolated modes of the MBSs, the change in the current becomes more obvious, but it essentially resembles the case when it is coupled to only one mode of the MBSs. The direct overlap between the MBSs will totally reverse the functions of the MBSs on the current's magnitude, which is individually enhanced and suppressed by hybridization between the MBSs in the bias regimes between which the current is suppressed and enhanced when the dot is only coupled to one isolated mode of the MBSs. The magnitude of heat generation is monotonously enhanced when the dot is coupled to either one or both of the isolated MBSs, whereas it is monotonously suppressed in the presence of direct overlap between the two MBSs. The variation of the electrical current and heat generation due to the MBSs enables the possibility of simultaneously enhancing the current while suppressing the generated heat and is ideal in designing energy conservation devices.

DATA AVAILABILITY STATEMENT

The original contributions presented in the study are included in the article/supplementary material, and further inquiries can be directed to the corresponding author.

AUTHOR CONTRIBUTIONS

ZW derived the formulae, performed the numerical calculations, and wrote the original manuscipt.

FUNDING

This work was supported by the thirteenth five-year plan of educational science in Fujian Province (Grant No. 2019CG0707).

REFERENCES

1. Li NB, Ren J, Wang L, Zhang G, Hanggi P, and Li BW. Colloquium: Phononics: Manipulating Heat Flow with Electronic Analogs and Beyond. *Rev Mod Phys* (2012) 84:1045–66. doi:10.1103/RevModPhys.84.1045
2. Balandin AA. Nanophononics: Phonon Engineering in Nanostructures and Nanodevices. *J Nanosci Nanotech* (2005) 5:1015–22. doi:10.1166/jnn.2005.175
3. Liang B, Yuan B, and Cheng J-c. Acoustic Diode: Rectification of Acoustic Energy Flux in One-Dimensional Systems. *Phys Rev Lett* (2009) 103:104301. doi:10.1103/PhysRevLett.103.104301
4. Li B, Wang L, and Casati G. Thermal Diode: Rectification of Heat Flux. *Phys Rev Lett* (2004) 93:184301. doi:10.1103/PhysRevLett.93.184301
5. Xie R, Bui CT, Varghese B, Zhang Q, Sow CH, Li B, et al. An Electrically Tuned Solid-State Thermal Memory Based on Metal-Insulator Transition of Single-Crystalline VO2 Nanobeams. *Adv Funct Mater* (2011) 21:1602–7. doi:10.1002/adfm.201002436
6. Dubi Y, and Di Ventra M. Colloquium: Heat Flow and Thermoelectricity in Atomic and Molecular Junctions. *Rev Mod Phys* (2011) 83:131–55. doi:10.1103/RevModPhys.83.131
7. Chen Z-Z, Lü R, and Zhu B-f. Effects of Electron-Phonon Interaction on Nonequilibrium Transport through a Single-Molecule Transistor. *Phys Rev B* (2005) 71:165324. doi:10.1103/PhysRevB.71.165324
8. Balandin A, and Wang KL. Significant Decrease of the Lattice thermal Conductivity Due to Phonon Confinement in a Free-Standing Semiconductor Quantum Well. *Phys Rev B* (1998) 58:1544–9. doi:10.1103/PhysRevB.58.1544
9. Shamsa M, Liu W, Balandin AA, and Liu J. Phonon-hopping thermal Conduction in Quantum Dot Superlattices. *Appl Phys Lett* (2005) 87: 202105. doi:10.1063/1.2130711
10. Rego LGC, and Kirczenow G. Quantized thermal Conductance of Dielectric Quantum Wires. *Phys Rev Lett* (1998) 81:232–5. doi:10.1103/PhysRevLett.81.232
11. Fu L, and Kane CL. Superconducting Proximity Effect and Majorana Fermions at the Surface of a Topological Insulator. *Phys Rev Lett* (2008) 100:096407. doi:10.1103/PhysRevLett.100.096407
12. Alicea J, Oreg Y, Refael G, von Oppen F, and Fisher MPA. Non-abelian Statistics and Topological Quantum Information Processing in 1d Wire Networks. *Nat Phys* (2011) 7:412–7. doi:10.1038/nphys1915
13. Karzig T, Knapp C, Lutchyn RM, Bonderson P, Hastings MB, Nayak C, et al. Scalable Designs for Quasiparticle-Poisoning-Protected Topological Quantum Computation with Majorana Zero Modes. *Phys Rev B* (2017) 95:1–32. doi:10.1103/PhysRevB.95.235305
14. Sato M, and Fujimoto S. Topological Phases of Noncentrosymmetric Superconductors: Edge States, Majorana Fermions, and Non-abelian Statistics. *Phys Rev B* (2009) 79:1–16. doi:10.1103/PhysRevB.79.09450410.1103/physrevb.79.094504
15. Qi X-L, and Zhang S-C. Topological Insulators and Superconductors. *Rev Mod Phys* (2011) 83:1057–110. doi:10.1103/RevModPhys.83.1057
16. Wang R, Su W, Zhu J-X, Ting CS, Li H, Chen C, et al. Kondo Signatures of a Quantum Magnetic Impurity in Topological Superconductors. *Phys Rev Lett* (2019) 122:1–6. doi:10.1103/PhysRevLett.122.087001
17. Mourik V, Zuo K, Frolov SM, Plissard SR, Bakkers EPAM, and Kouwenhoven LP. Signatures of Majorana Fermions in Hybrid Superconductor-Semiconductor Nanowire Devices. *Science* (2012) 336:1003–7. doi:10.1126/science.1222360
18. Choy T-P, Edge JM, Akhmerov AR, and Beenakker CWJ. Majorana Fermions Emerging from Magnetic Nanoparticles on a Superconductor without Spin-Orbit Coupling. *Phys Rev B* (2011) 84:1–6. doi:10.1103/PhysRevB.84.195442
19. San-Jose P, Prada E, and Aguado R. Ac Josephson Effect in Finite-Length Nanowire Junctions with Majorana Modes. *Phys Rev Lett* (2012) 108:1–5. doi:10.1103/PhysRevLett.108.257001
20. Ricco LS, de Souza M, Figueira MS, Shelykh IA, and Seridonio AC. Spin-dependent Zero-Bias Peak in a Hybrid Nanowire-Quantum Dot System: Distinguishing Isolated Majorana Fermions from Andreev Bound States. *Phys Rev B* (2019) 99:1–9. doi:10.1103/PhysRevB.99.155159
21. Liu C-X, van Heck B, and Wimmer M. Josephson Current via an Isolated Majorana Zero Mode. *Phys Rev B* (2021) 103:1014510. doi:10.1103/PhysRevB.103.014510
22. López R., Lee M., Serra L., and Lim J. S. Thermoelectrical detection of majorana states. *Phys Rev B* (2014) 89:1–7. doi:10.1103/PhysRevB.89.205418
23. Ricco LS, Dessotti FA, Shelykh IA, Figueira MS, and Seridonio AC. Tuning of Heat and Charge Transport by Majorana Fermions. *Sci Rep* (2018) 8:2790–7. doi:10.1038/s41598-018-21180-9
24. Smirnov S. Universal Majorana Thermoelectric Noise. *Phys Rev B* (2018) 97: 1–14. doi:10.1103/PhysRevB.97.165434
25. Tang H-Z, Zhang Y-T, and Liu J-J. Photon-assisted Tunneling through a Topological Superconductor with Majorana Bound States. *AIP ADVANCES* (2015) 5:1–8. doi:10.1063/1.4939096
26. Chen H, and Zhu K. All-optical Scheme for Detecting the Possible Majorana Signature Based on Qd and Nanomechanical Resonator Systems. *Sci China Phys Mech Astron* (2015) 58:1–14. doi:10.1007/s11433-014-5637-4
27. Väyrynen JI, Rastelli G, Belzig W, and Glazman LI. Microwave Signatures of Majorana States in a Topological Josephson junction. *Phys Rev B* (2015) 92: 1345081–5. doi:10.1103/PhysRevB.92.134508
28. Chi F, He T-Y, Wang J, Fu Z-G, Liu L-M, Liu P, et al. Photon-assisted Transport through a Quantum Dot Side-Coupled to Majorana Bound States. *Front Phys* (2020) 8:2541–7. doi:10.3389/fphy.2020.00254
29. Tang L-W, and Mao W-G. Detection of Majorana Bound States by Sign Change of the Tunnel Magnetoresistance in a Quantum Dot Coupled to Ferromagnetic Electrodes. *Front Phys* (2020) 8:1471–8. doi:10.3389/fphy.2020.00147
30. Sun Q-f., and Xie XC. Heat Generation by Electric Current in Mesoscopic Devices. *Phys Rev B* (2007) 75:155306. doi:10.1103/PhysRevB.75.155306
31. Liu J, Song J, Sun Q-f., and Xie XC. Electric-current-induced Heat Generation in a Strongly Interacting Quantum Dot in the Coulomb Blockade Regime. *Phys Rev B* (2009) 79:161309. doi:10.1103/PhysRevB.79.161309
32. Chi F, Zheng J, Liu Y-S, and Guo Y. Refrigeration Effect in a Single-Level Quantum Dot with thermal Bias. *Appl Phys Lett* (2012) 100:233106. doi:10.1063/1.4720093
33. Chi F, and Sun L-L. Photon-assisted Heat Generation by Electric Current in a Quantum Dot Attached to Ferromagnetic Leads. *Chin Phys. Lett.* (2016) 33: 1–6. doi:10.1088/0256-307X/33/11/117201
34. Liu DE, and Baranger HU. Detecting a Majorana-Fermion Zero Mode Using a Quantum Dot. *Phys Rev B* (2011) 84:201308R. doi:10.1103/PhysRevB.84.201308
35. Prada E, Aguado R, and San-Jose P. Measuring Majorana Nonlocality and Spin Structure with a Quantum Dot. *Phys Rev B* (2017) 96:085418. doi:10.1103/PhysRevB.96.085418
36. Deng MT, Vaitiekenas S, Prada E, San-Jose P, Nygard J, Krogstrup P, et al. Nonlocality of Majorana Modes in Hybrid Nanowires. *Phys Rev B* (2018) 98: 085125. doi:10.1103/physrevb.98.085125
37. Stefański P. Properties of the Majorana-State Tunneling Josephson junction Mediated by an Interacting Quantum Dot. *J Phys Condens Matter* (2019) 31: 1–18. doi:10.1088/1361-648X/ab052a

Conflict of Interest: The author declares that the research was conducted in the absence of any commercial or financial relationships that could be construed as a potential conflict of interest.

frontiers in Physics

ORIGINAL RESEARCH
published: 02 July 2021
doi: 10.3389/fphy.2021.709151

A Combined Pulse Driving Waveform With Rising Gradient for Improving the Aperture Ratio of Electrowetting Displays

*Lixia Tian and Pengfei Bai**

Guangdong Provincial Key Laboratory of Optical Information Materials and Technology and Institute of Electronic Paper Displays, South China Academy of Advanced Optoelectronics, South China Normal University, Guangzhou, China

As a reflective display technology, electrowetting displays (EWDs) have the advantages of paper-like display, low power consumption, fast response, and full color, but the aperture ratio of EWDs is seriously affected by oil dispersion and charge trapping. In order to improve the aperture ratio and optimize the display performance of EWDs, a combined pulse driving waveform with rising gradient design was proposed. First, an initial driving voltage was established by the threshold voltage of oil film rupture (V_{th}). And then, a rising gradient was designed to prevent oil from dispersing. At last, the oil splitting and movement were controlled to achieve the target aperture combined with the pulse waveform. Experimental results showed that the oil dispersion of EWDs can be effectively improved by using the proposed driving waveform, the aperture ratio of EWDs was increased by 3.16%, and the stability was increased by 71.43%.

Keywords: electrowetting display, driving waveform, aperture ratio, charge trapping, threshold voltage, oil dispersion

Edited by:
Qiang Xu,
Nanyang Technological University, Singapore

Reviewed by:
Liming Liu,
University of Electronic Science and Technology of China, China
Zhixian Lin,
Fuzhou University, China

****Correspondence:***
Pengfei Bai
baipf@scnu.edu.cn

Specialty section:
This article was submitted to Optics and Photonics, a section of the journal Frontiers in Physics

Received: *13 May 2021*
Accepted: *11 June 2021*
Published: *02 July 2021*

Citation:
Tian L and Bai P (2021) A Combined Pulse Driving Waveform With Rising Gradient for Improving the Aperture Ratio of Electrowetting Displays. Front. Phys. 9:709151. doi: 10.3389/fphy.2021.709151

INTRODUCTION

Electrowetting displays (EWDs) are a kind of reflective display technology with the ability of video-speed display applications; its fluidic pixels can respond and switch quickly by controlling electronic [1]. And it shows excellent electro-optic characteristics like low operating voltage, thinness, fast response, wide viewing angle, and low power consumption [2, 3]. EWD makes up the performance bottlenecks in full-color display and real-time dynamic video display [4–8]; it is known to be one of the most attractive emerging display technologies [15].

The concept of EWD was first proposed by Beni and Hackwood in 1981 [9]. In addition, Hayes developed a new type of the EWD scheme which was based on the principle of microfluidic motion at low driving voltages in 2003 [10]. To achieve fast response EWDs with an accurate multiple gray-level performance for video applications [11], it is necessary to solve the influence of hysteresis effect, charge trapping, and oil splitting in EWDs [12]. The driving waveform controls the motion state of the oil and affects the gray-scale display of EWDs [13]. By changing the applied voltage to control the aperture ratio of EWDs, multiple gray-scale displays can be realized [14]. Amplitude modulation (AM) and pulse width modulation (PWM) are the two main methods to obtain gray scales [15, 16]. But the hysteresis effect is obvious if using AM to drive EWDs. Although the hysteresis of the PWM driving method is much smaller, the gray scales and the frame update rate are limited. Therefore, an amplitude–frequency mixed modulation driving system was proposed to improve the response speed and oil stability when the gray scale was displayed [17]. Also, a driving waveform based on overdriving voltages was proposed to shorten

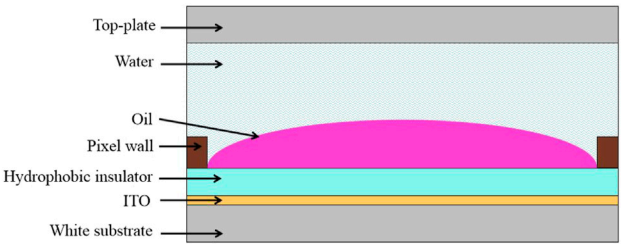

FIGURE 1 | Pixel structure of EWDs. The optical stack consists of glass substrate, indium tin oxide (ITO), hydrophobic insulator layer, pixel wall, colored oil, and water.

the response time of EWDs [18]. Moreover, a decoupling driving waveform was developed to diminish the induced voltage stress on thin film transistor (TFT) backplane of EWDs [19]. For dealing with the charge trapping phenomenon properly, an asymmetrical alternating polarity driving waveform was proposed [20]. The asymmetry in the driving energy is the difference between an alternating polarity signal with symmetrical energy and a common signal with variable DC voltage. The objective of the asymmetrical driving energy was used to provide the consistent electric field on EWDs with the alternating polarity method, so as to obtain a faster response time and a higher reflectivity. In addition, it was found that the oil film has a higher aperture ratio and a higher reflectivity by applying driving voltage waveforms with different rising gradients, which has the same final voltage on EWDs [21]. The driving voltage gradient was proven to be useful in the microfluidic behavior for electrowetting devices. When the voltage increased slowly, the oil droplets had more time to coalesce or merge, and then the oil splitting phenomena decreased. Although the voltage gradient could improve the reflectivity of EWDs, the response time becomes longer. Therefore, both reflectivity and response time should be taken into account fully. Traditional driving waveforms often cause oil dispersion, which affects the optical performance seriously and reduces the aperture ratio greatly. Analysis of the oil motion behavior in the driving process is helpful to improve the performance of EWDs.

In this study, the relationship among threshold voltage of oil film rupture, luminance value, and response time was analyzed, and a combined pulse waveform with rising gradient design was proposed for improving the aperture ratio and optimizing the display performance of EWDs.

PRINCIPLES

Display Principle of EWDs

Electrowetting refers to the electrical modulation of the interfacial tension between a conducting liquid phase and a solid electrode [22, 23]. It is a convenient method to actively control the contact angle [24]. As shown in **Figure 1**, the structure of an EWD is mainly composed of glass substrate, indium tin oxide (ITO), hydrophobic insulator layer, pixel wall, colored oil, and water [25, 26]. The principle is based on the movement of colored oil across a hydrophobic insulator [27].

Without driving voltage, the oil forms a continuous film between the hydrophobic insulator and water. In this case, the relationship of the interfacial tension in a three-phase system is presented as **Eq. 1**.

$$\gamma_{ow} + \gamma_{oi} < \gamma_{wi}, \tag{1}$$

where γ is the interfacial tension, and o, w, and i denote oil, water, and insulator, respectively. γ_{ow} is the interfacial tension between oil and water, γ_{oi} is the interfacial tension between oil and the hydrophobic insulator layer, and γ_{wi} is the interfacial tension between water and the hydrophobic insulator layer.

The display principle of EWDs is presented in **Figure 2**. For a pixel unit, the surface of the insulator layer is hydrophobic when no driving voltage is applied. The oil covers the insulator layer and absorbs the incident light, as shown in **Figure 2A**, and the pixel is in a dark state. **Figure 2C** shows the top view of a pixel in colored off-state. When driving voltage is applied on pixel electrodes, the surface polarity of an insulator layer changes from hydrophobic to hydrophilic, which leads to the change of interfacial tension. As shown in **Figure 2B**, the oil would be pushed to corners of a pixel by interfacial tension, and the underlying reflective layer would reflect the incident light. **Figure 2D** is the top view when a pixel is in white on-state. In this way, the optical switch is formed and the monochromatic display of a pixel unit is realized [28].

Electro-optic Characteristics of EWDs

Electrowetting behavior is governed by the Lippmann–Young equation for electrowetting in a three-phase system [29]. The Lippmann–Young equation is defined as **Eq. 2**.

$$\cos\theta = cos\alpha - \frac{1}{2}\frac{\varepsilon_0\varepsilon_r}{d\gamma_{ow}}V^2, \tag{2}$$

where θ is a contact angle with the applied voltage, α is a contact angle without the applied voltage, and ε_0, ε_r, d, γ_{ow}, and V are the vacuum dielectric constant, dielectric permittivity, insulator layer thickness, oil/water interface tension, and driving voltage, respectively. When no driving voltage is applied, the oil film completely covers the hydrophobic insulator layer, and the contact angle is close to zero, that is, $cos\alpha \sim 1$. Then **Eq. 2** can be reduced to **Eq. 3**.

$$\cos\theta = 1 - \frac{1}{2}\frac{\varepsilon_0\varepsilon_r}{d\gamma_{ow}}V^2. \tag{3}$$

The aperture ratio is an important index to describe the performance of EWDs, which refers to the percentage of white area in the pixel when the driving voltage is applied. During oil contraction, the aperture ratio is defined as **Eq. 4**.

$$WA\%(V) = \left(1 - \frac{S_{oil}}{S_{pix}}\right) \times 100\% \tag{4}$$

where $WA\%(V)$ is the aperture ratio, S_{oil} and S_{pix} represent the pixel area occupied by oil and total area of a pixel, respectively, when driving voltage V is applied to EWDs. With the applied driving voltage, S_{oil} in a pixel in terms of contact angle θ can be written as **Eq. 5**. Similarly, S_{oil} can be written as **Eq. 6** when no driving voltage is applied.

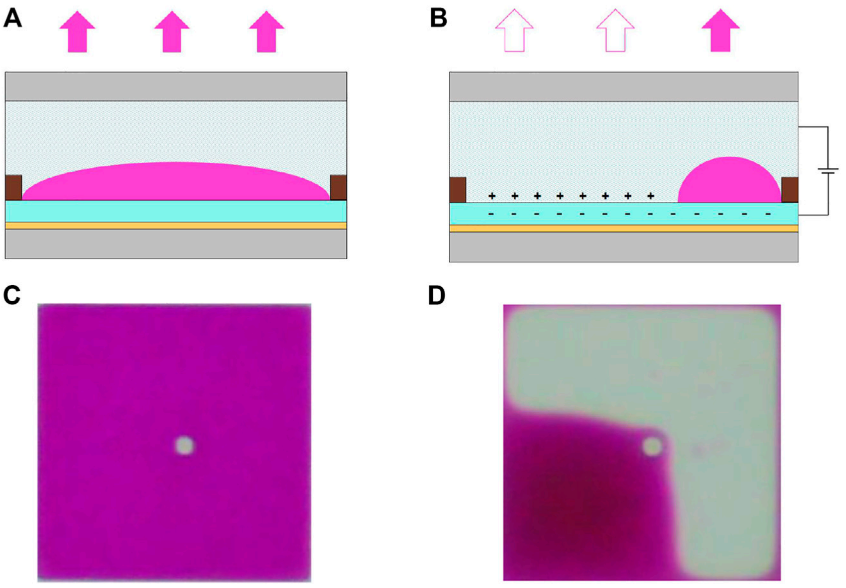

FIGURE 2 | Display principle of an EWD pixel. **(A)** A homogeneous oil film is present when no driving voltage is applied, and the pixel is in colored off-state. **(B)** When a driving voltage is applied, oil is shrunk to a corner, and the pixel is in white on-state. **(C)** Top view of the pixel in colored off-state. **(D)** Top view of the pixel in white on-state.

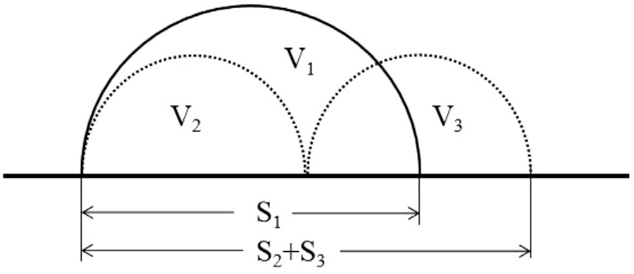

FIGURE 3 | Schematic diagram of different oil contraction patterns in an EWD pixel; when an oil droplet splits into two droplets, the covered area between the oil and the hydrophobic insulator layer becomes larger, although the volume remains the same, that is, $V_1 = V_2 + V_3$, $S_1 < S_2 + S_3$.

$$S_{oil}(V) = \pi sin^2\theta(V) \times \left(\frac{V_{oil}}{1 - \frac{3}{2}cos\theta(V) + \frac{1}{2}cos^3\theta(V)}\right)^{\frac{2}{3}} \tag{5}$$

$$S_{oil} = \pi sin^2\alpha \times \left(\frac{V_{oil}}{1 - \frac{3}{2}cos\alpha + \frac{1}{2}cos^3\alpha}\right)^{\frac{2}{3}} \tag{6}$$

where V_{oil} is the volume of colored oil. Substituting **Eq. 5** and **Eq. 6** in **Eq. 4**, the aperture ratio can be calculated theoretically, and finally defined as **Eq. 7**.

$$WA\%(V) = \left(1 - \left(\frac{sin^2\theta(V)}{sin^2\alpha}\right)\left(\frac{1 - \frac{3}{2}cos\alpha + \frac{1}{2}cos^3\alpha}{1 - \frac{3}{2}cos\theta(V) + \frac{1}{2}cos^3\theta(V)}\right)^{\frac{2}{3}}\right) \times 100\%. \tag{7}$$

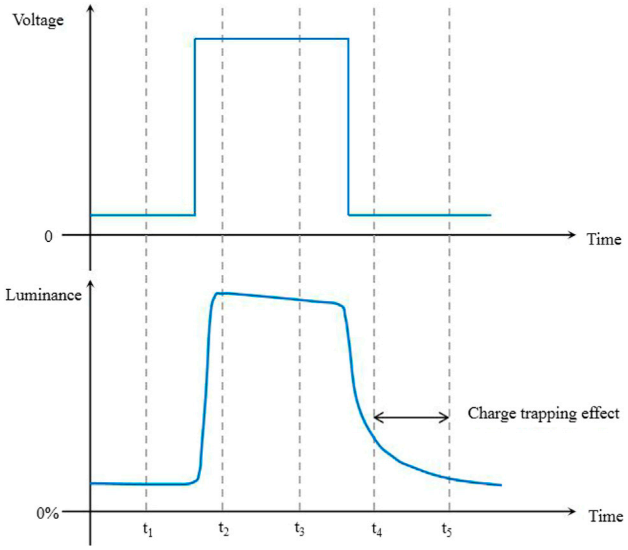

FIGURE 4 | Charge trapping phenomenon of EWDs. When applying a driving voltage, ions in the water move toward the insulator due to the electrostatic force, and then the oil is pushed aside. Some ions move into the insulator and become trapped. Even when removing the driving voltage, the oil could not cover the entire hydrophobic layer.

When the colored oil film in a pixel splits into small droplets, the contact area between the oil and the hydrophobic insulator layer becomes larger. For example, if a single droplet with 90°contact angle splits into two droplets, the whole area of the two oil droplets occupied is $\sqrt[3]{2}$ times that of the original one.

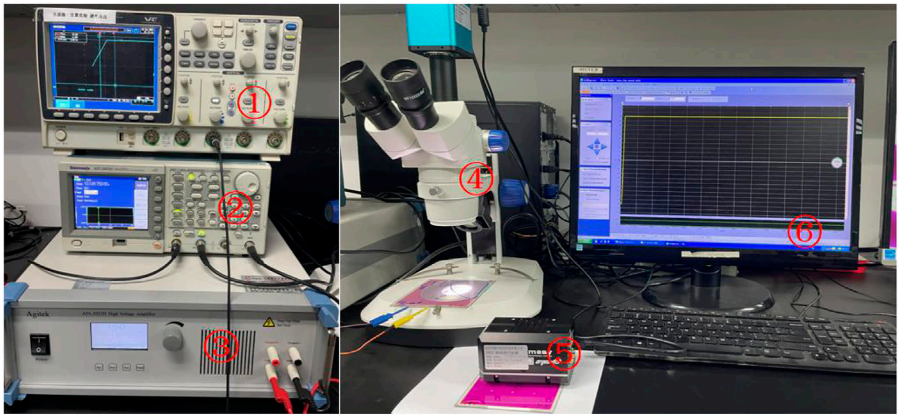

FIGURE 5 | Experimental platform for driving EWDs. ① Oscilloscope. ② Arbitrary waveform generator. ③ Power amplifier. ④ Microscope. ⑤ Colorimeter. ⑥ Computer.

As shown in **Figure 3** [21], $S_2 + S_3 > S_1$, where S_1 is the covered area of the original oil droplet on the substrate, and S_2 and S_3 are the covered area of two splitting oil droplets. Obviously, oil pattern with less oil droplets covers less area on the substrate. Oil contraction patterns in pixels is one of the important factors that affect the aperture ratio of EWDs. Therefore, improving the oil dispersion phenomenon in EWDs is one of the useful methods to increase the aperture ratio of EWDs.

Charge Trapping Phenomenon of EWDs

The phenomenon of charge trapping exists in EWDs. The charge trapping on the dielectric layer of EWDs can influence the stability of display effect, resulting in slow response speed and few gray scales [2]. **Figure 4** illustrates the charge trapping phenomenon in an EWD. When the driving voltage is continuously applied to the pixel, ions in water move toward the insulator by the electrostatic force, and then the colored oil would be pushed away. In this process, some ions enter the insulator and can be trapped. Even when removing the driving voltage, the oil could not cover the whole hydrophobic layer. And trapped ions must be discharged by waiting enough time or applying a special driving waveform. Otherwise, the colored oil cannot be completely spread out. Worse still, the charge trapping can lead to the slow response speed of EWDs, which has serious impact on the aperture ratio value.

EXPERIMENTAL RESULTS AND DISCUSSION

Experimental Platform

In order to evaluate the performance of the proposed driving waveform, an optical experimental platform was built to measure the aperture ratio of EWDs. As shown in **Figure 5**, the experimental platform consisted of a GDS-3354 oscilloscope, an AFG3052C function generator, an ATA-2022H amplifier, an XTL-165 microscope, an Arges-45 colorimeter, and a computer. Relevant equipment information is shown in **Table 1**. The tested object was an EWD panel whose parameters are listed in **Table 2**. The maximum voltage of the texted EWD panel was 30 V. The detailed experimental procedure was as follows.

First, the required driving waveform was edited by the computer with ArbexPress software and sent to arbitrary waveform generator by serial communication. Then the required driving waveform was generated, which was amplified by the power amplifier to drive the EWD. During the experiment, the colorimeter was placed on the EWD panel, and the host software of colorimeter collected luminance values of the specified pixel in real time. In addition, the high-speed camera captured the display state of the EWD by the microscope.

Driving Waveform Design

The aperture ratio of EWDs is seriously influenced by oil dispersion and charge trapping. In order to improve the aperture ratio and optimize the display stability of EWDs, a combined pulse waveform with rising gradient design was proposed. As shown in **Figure 6**, the proposed driving waveform included two stages.

At the first stage, initial driving voltage was established by the threshold voltage of oil film rupture (V_{th}), and a rising gradient was designed to prevent oil from dispersing. Without driving voltage, the oil is in a balanced state of natural spreading; therefore, V_{th} needs to be applied to break the static balance. In addition, a rising gradient from V_{th} to 30 V was introduced to prevent the decrease of the aperture ratio caused by oil dispersion. It gives the oil droplets more time to coalesce or merge with adjacent oil droplets when the driving voltage increased slowly so that the oil splitting phenomena could be decreased. The pixel was supposed to reach a larger aperture ratio if the oil distribution is stable. To remove the electric charge which is trapped in the dielectric layer of EWDs, the pulse waveform was introduced at the second stage. As the polarization phenomenon was avoided, the oil splitting and movement could be controlled to achieve a target aperture ratio. With the combination of the pulse waveform, the stability of oil shrinkage could be maintained.

TABLE 1 | Experimental platform for testing EWDs.

Category	Oscilloscope	Arbitrary waveform generator	Power amplifier	Microscope	Colorimeter	Computer
Model	GDS-3354	AFG3052C	ATA-2022H	XTL-165	Arges-45	M425
Country	China	United States	China	China	Netherlands	China
Manufacturer	GuWei	Tektronix	Agitek	Phenix	Admesy	Lenovo

TABLE 2 | Parameters of the EWD.

Panel size (cm^2)	Oil color	Resolution	Pixel size (μm^2)	Height of pixels (μm)	ITO layer (nm)	Hydrophobic layer thickness (nm)
10 × 10	Magenta	320 × 240	150 × 150	18	2.5	800

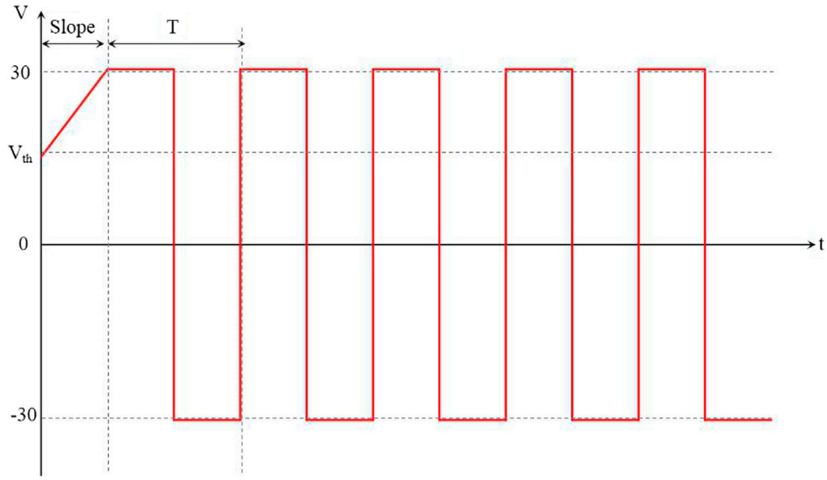

FIGURE 6 | Schematic diagram of a combined pulse waveform with rising gradient design. The proposed driving waveform contained two stages. The first stage was a rising gradient with slope from V^{th} to 30 V. The second stage was a pulse waveform with a suitable period.

Threshold Voltage of Oil Film Rupture

The precise location of oil film rupture depends on the applied voltage to EWDs. In order to confirm the threshold voltage of the oil film rupture, a traditional DC voltage driving waveform was used to drive the EWD panel. The driving voltage was increased by 1 V per second from the initial voltage 0 V to the final voltage 30 V. During the experiment, the aperture ratio was increased while the driving voltage was increased gradually. As shown in **Figure 7**, the pixel in colored off-state turned in to white on-state when the applied voltage was increased from 0 V to 30 V. The threshold voltage of oil film rupture could be found by analyzing the relationship between the brightness and the applied voltage with DC voltage driving.

As the DC voltage increased, there was a clear threshold with the rupture of oil film. The results of the experiment showed that when the voltage was above the threshold voltage, the brightness value increases sharply. As the capillary force became dominant and the charge distribution increase quickly at the three-phase contact line, the optical response speed of EWDs was increased gradually. When the driving voltage reached 15 V, the EWD began to response quickly, so the threshold voltage of the oil film rupture was determined to be 15 V.

Effects of Different Slopes on the Aperture Ratio of EWDs

Driving waveforms with various slope values were applied to study the influence of rising gradient driving waveforms on the aperture ratio of EWDs. When the voltage was increased slowly, oil droplets have more time to coalesce with adjacent oil droplets, so it can effectively suppress the violent vibration of oil, which would result in the oil splitting, and obtain a higher aperture ratio. We applied different slopes to rising gradient driving waveforms from 15 V to 30 V for observing the influence of rising gradient waveforms with different slopes. Voltage rising speeds of 0.2 V/ ms, 0.4 V/ ms, 0.9 V/ ms, 1.4 V/ ms, and 2.0 V/ ms were tested in this study. **Figure 8** shows the schematic diagram of a driving waveform with rising gradient design.

The luminance curve of EWDs driven by different slope rising gradient driving waveforms is shown in **Figure 9**. And the comparison of driving effects is listed in **Table 3**. The experimental results showed that the response speed was 1.73 ms when the slope was 0.2 V/ s, whereas the response speed was 0.96 ms when the slope was 0.4 V/ s; it was 0.77 ms

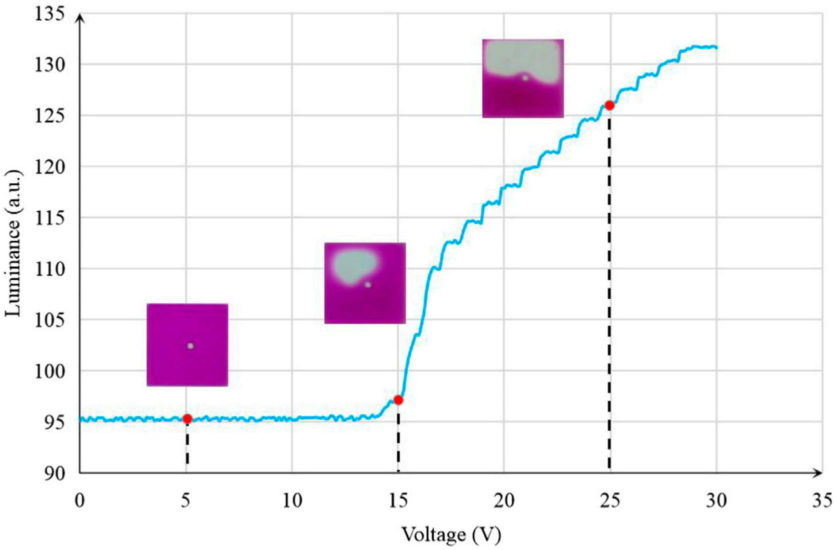

FIGURE 7 | Luminance–voltage curve of an EWD when it was driven by a DC voltage. The EWD began to respond quickly when the voltage was 15 V. The threshold voltage of the oil film rupture was confirmed to be 15 V.

FIGURE 8 | Schematic diagram of a driving waveform with rising gradient design. The rising gradient waveform with slope from V^{th} to 30 V. V^{th} = 15 V.

faster than the slope of 0.2 V/ ms. When the slope of the waveform was 0.4 V/ ms, the mean square error of the luminance value was smaller than that of other waveforms; that is, the aperture ratio and oil state of EWDs were more stable. Therefore, the rising gradient driving waveform with the slope of 0.4 V/ s was selected in our driving waveform for EWDs.

Performance Testing of the Rising Gradient Pulse Waveform

The charge trapping phenomenon of EWDs can cause oil backflow and affect the stability of display directly. Therefore, at the end of the 0.4 V/ s rising gradient waveform, a pulse waveform was introduced as the driving force to keep the aperture ratio stable. By adjusting the period of the applied square waveform, the shape of oil contraction was supposed to be maintained stable. Square waveforms with periods of 5 ms, 15 ms, 25 ms, and 35 ms were applied to the EWD panel. The time-varying curve of the brightness of the EWD driven by different periods is shown in **Figure 10**. And the comparison of driving effect is listed in **Table 4**.

The experimental results showed that when the period of the square waveform was 5 ms, the stale brightness value of the EWD was 138.77, which was lower than that of other driving waveforms, with periods of 15 ms, 25 ms, and 35 ms. However,

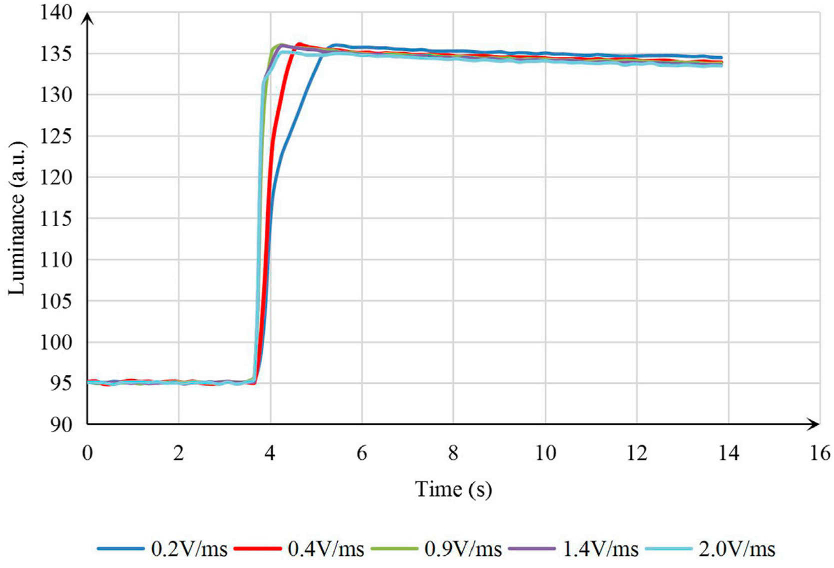

FIGURE 9 | Brightness–duration curve of an EWD when it was driven by different rising gradient driving waveforms. The 0.4 V/ ms slope driving waveform had the most stable aperture ratio.

TABLE 3 | Driving effect comparison when different rising gradient driving waveforms were used to drive EWDs.

Slope (V/ms)	0.2	0.4	0.9	1.4	2.0
Average (a.u.)	135.01	134.52	134.40	134.25	134.09
Standard deviation	0.48	0.44	0.46	0.47	0.45
Response time (ms)	1.73	0.96	0.58	0.58	0.77

TABLE 4 | Driving effect comparison when different period pulse waveforms were used to drive EWDs.

Period (ms)	5	15	25	35
Average (a.u.)	138.77	139.35	139.50	139.71
Standard deviation	0.12	0.40	1.41	1.62

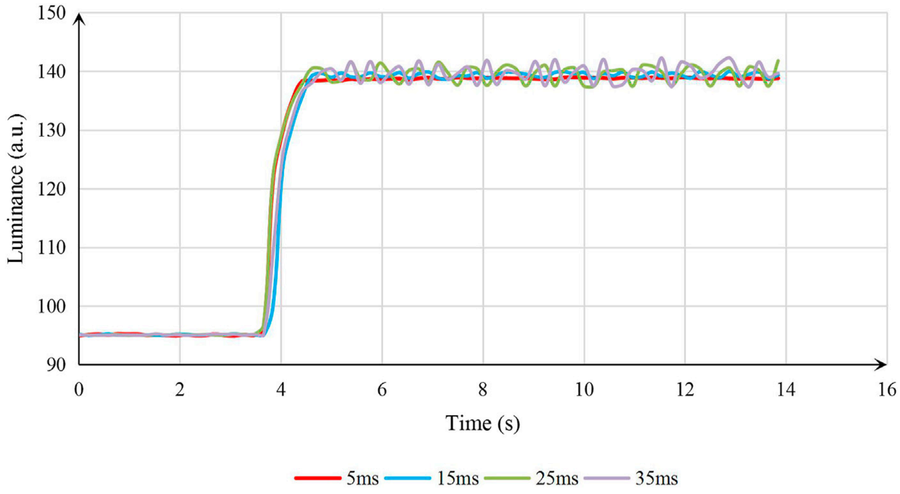

FIGURE 10 | The brightness curve of an EWD driven by rising gradient pulse waveform at different periods. Square waveforms with periods of 5, 15, 25, and 35 ms were applied to the EWD panel. The curve was relatively stable when the period was 5 ms.

the mean square error of the stable luminance value was smaller than that of other waveforms; that is, the aperture ratio and the stability of oil were the best with the period of 5 ms.

In addition, the luminance–time curve of an EWD driven by four different driving waveforms is shown in **Figure 11**, including the traditional square waveform, the existing rising gradient driving

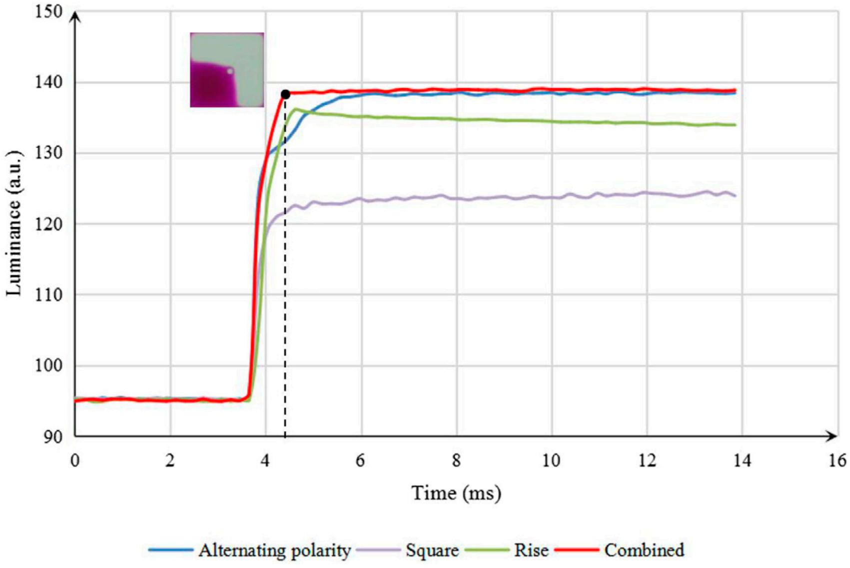

FIGURE 11 | Luminance–time curve of an EWD panel with four different driving waveforms. The traditional square waveform, the existing rising gradient driving waveform proposed by Zhang [21], the asymmetrical alternating polarity driving waveform proposed by Chen [20], and the proposed combined driving waveform in this study.

TABLE 5 | Driving effect comparison by four different driving waveforms used to drive EWDs.

Driving Waveform	Asymmetrical alternating polarity	Square	Rising gradient	Combined
Average (a.u.)	138.18	123.69	134.52	138.77
Standard deviation	0.46	0.42	0.44	0.12

waveform proposed by Zhang [21], the asymmetrical alternating polarity driving waveform proposed by Chen [20], and the proposed combined pulse waveform with rising gradient in this study. It was proved that the proposed driving waveform eliminated the oil dispersion phenomenon and inhibited oil backflow effectively. It not only decreased oil splitting but also avoided the polarization phenomenon. As listed in **Table 5**, the average of the brightness value was 138.77, which was higher than that of other three driving waveforms. Compared with the asymmetrical alternating polarity driving waveform, the aperture ratio was increased by 3.16%. Moreover, the mean square error of the stable brightness value was 0.12; it was much lower than that of the other driving waveforms. The brightness standard deviation was increased by 71.43% compared with the traditional square wave. Hence, both the aperture ratio and the stability of oil were the best by applying the proposed driving waveform. Therefore, the proposed driving waveform in this study could effectively suppress the charge trapping of EWDs and keep the state of oil film more stable.

CONCLUSION

In order to improve the aperture ratio and optimize the display performance of EWDs, a combined pulse driving waveform with rising gradient design was proposed in this study. It can significantly reduce the influence of oil dispersion and charge trapping in EWDs. Experimental results showed that EWD has a higher aperture ratio than the former waveforms. The aperture ratio was increased by 3.16%, and the stability was increased by 71.43%. It was proved that the proposed driving waveform can control oil splitting and movement. It is helpful to realize a more stable EWD and achieve target aperture.

DATA AVAILABILITY STATEMENT

The original contributions presented in the study are included in the article/Supplementary Material; further inquiries can be directed to the corresponding author.

AUTHOR CONTRIBUTION

LT and PB designed this project. LT carried out most of the experiments. PB performed part of the experiments and helped with discussions during manuscript preparation. LT contributed to the data analysis and correction. PB provided helpful discussions on the experimental results. All authors have discussed the results and agreed to the published version of the manuscript.

FUNDING

This research was supported by Program for Chang Jiang Scholars and Innovative Research Teams in Universities (No. IRT_17R40), Program for Guangdong Innovative and Enterpreneurial Teams (No. 2019BT02C241), Science and Technology Program of Guangzhou (No. 2019050001), Guangdong Provincial Key Laboratory of Optical Information Materials and Technology (No. 2017B030301007), Guangzhou Key Laboratory of Electronic Paper Displays Materials and Devices (201705030007), and the 111 Project.

REFERENCES

1. Bai PF, Hayes RA, Jin M, Shui L, Yi ZC, Wang L, et al. REVIEW of PAPER-LIKE DISPLAY TECHNOLOGIES (Invited Review). *Pier* (2014) 147:95–116. doi:10.2528/PIER13120405
2. Palanivelu S, and Surjya S. Display Applications of Electrowetting. *J Adhes Sci Tech* (2012) 26(12-17):1947–63. doi:10.1163/156856111X600532
3. Li W, Wang L, Zhang T, Lai S, Liu L, He W, et al. Driving Waveform Design with Rising Gradient and Sawtooth Wave of Electrowetting Displays for Ultra-low Power Consumption. *Micromachines* (2020) 11(2):145. doi:10.3390/mi11020145
4. Chen J, Cranton W, and Fihn M. Droplet-Driven Electrowetting Displays. *Handbook Vis Display Tech* (2012) 104:1747–59. doi:10.1007/978-3-540-79567-4_104
5. Yi Z-c., Bai P-f., Wang L, Zhang X, and Zhou G-f. An Electrophoretic Display Driving Waveform Based on Improvement of Activation Pattern. *J Cent South Univ* (2014) 21(8):3133–7. doi:10.1007/s11771-014-2285-9
6. Wang L, Yi Z, Jin M, Shui L, and Zhou G. Improvement of Video Playback Performance of Electrophoretic Displays by Optimized Waveforms with Shortened Refresh Time. *Displays* (2017) 49(9):95–100. doi:10.1016/j.displa.2017.07.007
7. Shen S, Gong Y, Jin M, Yan Z, Xu C, Yi Z, et al. Improving Electrophoretic Particle Motion Control in Electrophoretic Displays by Eliminating the Fringing Effect via Driving Waveform Design. *Micromachines* (2018) 9(4):143. doi:10.3390/mi9040143
8. He W, Yi Z, Shen S, Huang Z, Liu L, Zhang T, et al. Driving Waveform Design of Electrophoretic Display Based on Optimized Particle Activation for a Rapid Response Speed. *Micromachines* (2020) 11(5):498. doi:10.3390/mi11050498
9. Beni G, and Hackwood S. Electro-wetting Displays. *Appl Phys Lett* (1981) 38(4):207–9. doi:10.1063/1.92322
10. Hayes RA, and Feenstra BJ. Video-speed Electronic Paper Based on Electrowetting. *Nature* (2003) 425(6956):383–5. doi:10.1038/nature01988
11. Liu L, Bai P, Yi Z, and Zhou G. A Separated Reset Waveform Design for Suppressing Oil Backflow in Active Matrix Electrowetting Displays. *Micromachines* (2021) 12(5):491. doi:10.3390/mi12050491
12. Chiu Y-H, Liang C-C, Chen Y-C, Lee W-Y, Chen H-Y, and Wu S-H. Accurate-gray-level and Quick-Response Driving Methods for High-Performance Electrowetting Displays. *J Soc Inf Display* (2011) 19(11):741–8. doi:10.1889/JSID19.11.741
13. Luo ZJ, Zhang WN, Liu LW, Xie S, and Zhou G. Portable Multi-gray Scale Video Playing Scheme for High-Performance Electrowetting Displays. *Jnl Soc Info Display* (2016) 24(6):345–54. doi:10.1002/jsid.444
14. Yi Z, Shui L, Wang L, Jin M, Hayes RA, and Zhou G. A Novel Driver for Active Matrix Electrowetting Displays. *Displays* (2015) 37:86–93. doi:10.1016/j.displa.2014.09.004
15. Van R, Feenstra B, Hayes R, Camps I, Boom R, Wagemans M, et al. Gray Scales for Video Applications on Electrowetting Displays. *SID Symp Dig Tech Pap* (2006) 37(1):1926–9. doi:10.1889/1.2433427
16. Yi Z, Huang Z, Lai S, He W, Wang L, Chi F, et al. Driving Waveform Design of Electrowetting Displays Based on an Exponential Function for a Stable Grayscale and a Short Driving Time. *Micromachines* (2020) 11(3):313. doi:10.3390/mi11030313
17. Yi Z, Liu L, Wang L, Li W, Shui L, and Zhou G. A Driving System for Fast and Precise Gray-Scale Response Based on Amplitude-Frequency Mixed Modulation in TFT Electrowetting Displays. *Micromachines* (2019) 10(11):732. doi:10.3390/mi10110732
18. Zeng W, Yi Z, Zhao Y, Zeng W, Ma S, Zhou X, et al. Design of Driving Waveform Based on Overdriving Voltage for Shortening Response Time in Electrowetting Displays. *Front Phys* (2021) 9:642682. doi:10.3389/fphy.2021.642682
19. Liang C-C, Chen Y-C, Chiu Y-H, Chen H-Y, Cheng W-Y, and Lee W-Y. 27.3: A Decoupling Driving Scheme for Low Voltage Stress in Driving a Large-Area High-Resolution Electrowetting Display. *SID Symp Dig* (2009) 40(1):375–8. doi:10.1889/1.3256791
20. Chen Y-C, Chiu Y-H, Lee W-Y, and Liang C-C. 56.3: A Charge Trapping Suppression Method for Quick Response Electrowetting Displays. *SID Symp Dig* (2010) 41(1):842–5. doi:10.1889/1.3500607
21. Zhang X-M, Bai P-F, Hayes R, Shui L-L, Jin M-L, Tang B, et al. Novel Driving Methods for Manipulating Oil Motion in Electrofluidic Display Pixels. *J Display Technol* (2015) 12(2):1. doi:10.1109/jdt.2015.2477947
22. Yi Z, Feng H, Zhou X, and Shui L. Design of an Open Electrowetting on Dielectric Device Based on Printed Circuit Board by Using a Parafilm M. *Front Phys* (2020) 8:193. doi:10.3389/fphy10.3389/fphy.2020.00193
23. Feng H, Yi Z, Yang R, Qin X, Shen S, Zeng W, et al. Designing Splicing Digital Microfluidics Chips Based on Polytetrafluoroethylene Membrane. *Micromachines* (2020) 11(12):1067. doi:10.3390/mi11121067
24. Prins MWJ, Welters W, and Weekamp J. Fluid Control in Multichannel Structures by Electrocapillary Pressure. *Science* (2001) 291(5502):277–80. doi:10.1126/science.291.5502.277
25. Feenstra J. Video-Speed Electrowetting Display Technology. *Handbook Vis Display Tech* (2016) 1(13):2443–58. doi:10.1007/978-3-319-14346-0_103
26. Jin M, Shen S, Yi Z, Zhou G, and Shui L. Optofluid-Based Reflective Displays. *Micromachines* (2018) 9(4):159. doi:10.3390/mi9040159
27. Roques C, Hayes R, Feenstra B, and Schlangen L. Liquid Behavior inside a Reflective Display Pixel Based on Electrowetting. *J Appl Phys* (2004) 95(8):4389–96. doi:10.1063/1.1667595
28. Feenstra BJ, Hayes RA, Camps IGJ, Hage LM, Johnson MT, Roques-Carmes T, et al. A Video-Speed Reflective Display Based on Electrowetting: Principle and Properties. *J Soc Inf Display* (2004) 12(3):293–9. doi:10.1889/1.1825703
29. Yi Z, Feng W, Wang L, Liu L, Lin Y, He W, et al. Aperture Ratio Improvement by Optimizing the Voltage Slope and Reverse Pulse in the Driving Waveform for Electrowetting Displays. *Micromachines* (2019) 10(12):862. doi:10.3390/mi10120862

Conflict of Interest: The authors declare that the research was conducted in the absence of any commercial or financial relationships that could be construed as a potential conflict of interest.

frontiers in Physics

ORIGINAL RESEARCH
published: 15 July 2021
doi: 10.3389/fphy.2021.720515

Driving Waveform Optimization by Simulation and Numerical Analysis for Suppressing Oil-Splitting in Electrowetting Displays

Shufa Lai[1], *Qinghua Zhong*[2]* and *Hailing Sun*[1]

[1]Guangdong Provincial Key Laboratory of Optical Information Materials and Technology and Institute of Electronic Paper Displays, South China Academy of Advanced Optoelectronics, South China Normal University, Guangzhou, China, [2]School of Physics and Telecommunication Engineering, South China Normal University, Guangzhou, China

Electrowetting display (EWD) is a new reflective display device with low power consumption and fast response speed. However, the maximum aperture ratio of EWDs is confined by oil-splitting. In order to suppress oil-splitting, a two-dimensional EWD model with a switch-on and a switch-off process was established in this paper. The process of oil-splitting was obtained by applying different voltage values in this model. Then, the relationship between the oil-splitting process and the waveforms with different slopes was analyzed. Based on this relationship, a driving waveform with a narrow falling ramp, low-voltage maintenance, and a rising ramp was proposed on the basis of square waveform. The proposed narrow falling ramp drove the oil to rupture on one side. The low-voltage maintenance stage drove the oil to shrink with a whole block. The proposed rising ramp was pushed the oil into a corner quickly. The experimental results showed that the oil splitting can be suppressed effectively by applying the proposed driving waveform. The aperture ratio of the proposed driving waveform was 2.9% higher than that of the square waveform with the same voltage.

Keywords: driving waveform, electrowetting display, oil-splitting, modeling and simulation, oil movement

Edited by:
Feng Chi,
University of Electronic Science and Technology of China, China

Reviewed by:
Jiasheng Li,
South China University of Technology, China
Xiaowen Zhang,
Guilin University of Electronic Technology, China

Correspondence:
Qinghua Zhong
zhongqinghua@m.scnu.edu.cn

Specialty section:
This article was submitted to Optics and Photonics, a section of the journal Frontiers in Physics

Received: *04 June 2021*
Accepted: *02 July 2021*
Published: *15 July 2021*

Citation:
Lai S, Zhong Q and Sun H (2021) Driving Waveform Optimization by Simulation and Numerical Analysis for Suppressing Oil-Splitting in Electrowetting Displays. Front. Phys. 9:720515. doi: 10.3389/fphy.2021.720515

INTRODUCTION

Electrowetting (EW) is a phenomenon which can change the wettability of solid-liquid surface by using electric field [1]. The theory of EW was first proposed in 1981 [2]. In recent years, EW technology has been widely used in the chemical industry, bioengineering, display, and other fields [3–5]. Among them, the EWD is a new reflective display technology after electrophoretic display technology [6, 7]. Compared with conventional display technologies [8, 9], the EWD technology has the advantages of low power consumption, high contrast, fast response, and full color [10, 11], which is considered one of the most attractive emerging display technologies [12].

An EWD pixel is mainly composed of substrate, ITO (Indium Tin Oxides) guide electrode, hydrophobic insulation layer, pixel wall, colored oil, polar liquid, and top plate as shown in **Figure 1** [13, 14]. A complete driving process of EWD can be divided into two stages. In the first stage, a suitable voltage is applied between upper and lower electrodes, the colored oil is pushed into a corner. The color of bottom substrate is displayed in pixels. When the voltage is removed, the hydrophobic layer is completely covered by the colored oil again. The color of colored oil is displayed in pixels [15].

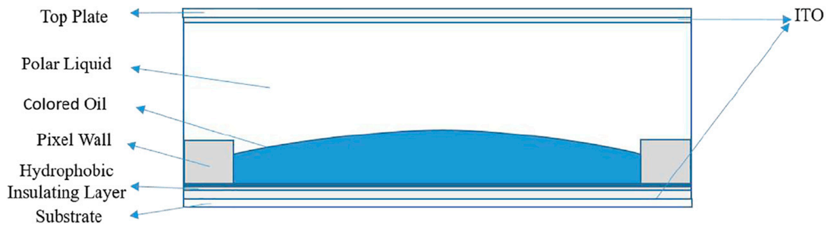

FIGURE 1 | Pixel structure of an EWD panel. The structure includes a top plate, ITO, fluid (colored oil and polar liquid), pixel wall, hydrophobic insulating layer, and substrate. The pixel wall is hydrophilic, and the hydrophobic insulating layer is hydrophobic and lipophilic.

At present, there are still some defects in EWDs, such as oil-splitting, charge trapping, oil overflow, and so on [10]. To solve these defects and further improve the display performance of EWDs, many researchers have made many attempts. For example, a three-dimensional EWD model was established and the process of fluid flow was simulated. In the simulation, the principle of phase-field was used to simulate the movement of oil interface successfully, and the influence of contact angle of the pixel wall on oil-splitting was studied [16]. However, the problem of oil-splitting caused by high voltage had not been solved. For oil-splitting, the influence of surface tension and contact angle in the fluid was considered. Through model simulation and numerical analysis, the influence of contact angle and surface tension on oil-splitting was proved [17]. In addition, the oil-splitting was affected by the oil thickness. The oil in the EWDs pixel was non-uniform, and the oil was split at the thinnest point [18]. However, the influence of thickness change on the process of oil movement was not considered. To suppress the oil-splitting, a driving waveform which consisted of four stages: starting, rising, displaying, and recovering was proposed. Starting from a low voltage to drive the oil can suppress oil-splitting effectively [19]. However, the speed of oil movement was slowed down.

In order to suppress the oil-splitting, a simulation model was established by COMSOL Multiphysics software. The relationship between electrostatic field force and oil shape change was studied by this model. And then, the change characteristic of oil shape was obtained in a switch-on process. According to this characteristic, a driving waveform which can suppress the oil-splitting effectively was proposed.

NUMERICAL METHODOLOGY

The simulation of EWDs was implemented by establishing and calculating numerical equations. It was done to track the change of the oil-water interface in the model [20]. By using COMSOL Multiphysics software and Finite-Element method to simulate Two-Phase laminar flow with the electrostatic field, the physical field of laminar flow was coupled with the phase-field and the electrostatic field [21]. The finite element analysis method can be used to solve numerical calculation problems including the Cahn-Hilliard equation, Laplace equation, and Navier-Stokes equation [22]. Meanwhile, to solve Maxwell's stress tensor equation, an electrostatic field module was added to the simulation. The electrostatic field force of the electrostatic field module was fed back into the laminar flow module. The Navier-Stokes equation and phase-field equation were solved according to specified boundary conditions and calculation results of electrostatic field.

Governing Equations

Phase-field is used to describe the dynamic process of a two-phase flow interface. The movement of interface is tracked indirectly by solving two equations. One of them is used to solve phase-field variable $\varnothing$ and the other is used to solve the mixed energy density ψ [16, 23, 24]. The position of the interface is determined by minimum free energy [23]. A large number of data have been proved that the phase-field method could effectively predict droplet movement on the solid surface [25, 26]. **Eqs. 1–3** represent the governing equation of phase-field [27]. **Eq. 4** describes the relationship between γ and ε.

$$\frac{\partial\varnothing}{\partial t} + u\cdot\nabla\varnothing = \nabla\cdot\frac{\gamma\lambda}{\varepsilon^2}\nabla\psi \tag{1}$$

$$\psi = -\nabla\cdot\varepsilon^2\nabla\varnothing + \left(\varnothing^2 - 1\right)\varnothing + \left(\frac{\varepsilon^2}{\lambda}\right)\frac{\partial f_{ext}}{\partial\varnothing} \tag{2}$$

$$\sigma = \frac{2\sqrt{2}}{3}\frac{\lambda}{\varepsilon} \tag{3}$$

$$\gamma = \chi\varepsilon^2 \tag{4}$$

Where λ is the energy density and ε is the capillary width. **Eq. 3** describes the relationship between these two parameters and the surface tension coefficient σ. The γ is the mobility parameter and χ is the mobility tuning parameter in **Eq. 4**. $\varnothing$ was set to 1 for oil and −1 for water. In order to couple the electrostatic field with the laminar flow field, the dielectric constant, density, and viscosity between diffusion interfaces need to be calculated by **Eqs. 5–7**.

$$\rho = \rho_1 + \left(\rho_2 - \rho_1\right)\varnothing \tag{5}$$

$$\mu = \mu_1 + \left(\mu_2 - \mu_1\right)\varnothing \tag{6}$$

$$\varepsilon_r = \varepsilon_{r1} + \left(\varepsilon_{r2} - \varepsilon_{r1}\right)\varnothing \tag{7}$$

Where ρ, μ, and ε_r represent the density, viscosity, and dielectric constant of fluids, respectively. The mean curvature between the two liquids interfaces was calculated by **Eqs. 8,9** [27].

$$\kappa = 2(1 + \varnothing)(1 - \varnothing)\frac{G}{\sigma} \tag{8}$$

$$G = \lambda\left(-\nabla^2\varnothing + \frac{\varnothing(\varnothing^2 - 1)}{\varepsilon^2}\right) + \frac{\partial f}{\partial \varnothing} \tag{9}$$

Where κ and G represent the mean curvature and the chemical potential, respectively.

The laminar flow field can be solved by the Navier-Stokes equation and continuity equation [28]. The Navier-Stokes equation is described as **Eq. 10**. To depict the movement of two immiscible liquids, the transport of mass and momentum are governed by incompressible Navier–Stokes equations.

$$\rho\left(\frac{\partial u}{\partial t} + u \cdot \nabla u\right) = -\nabla p + \nabla \cdot \left(\mu\left(\nabla u + (\nabla u)^T\right) - \frac{2}{3}u(\nabla \cdot u)I\right) + F \tag{10}$$

$$F = F_{st} + \rho g + F_{vf} \tag{11}$$

Where u, p, ρ, and μ represent the velocity, pressure, density, and dynamic viscosity of the fluid respectively. Each term in **Eq. 10** corresponds to the inertial force, pressure, viscous force, and external force, respectively. The external force consists of surface tension, gravity, and a volume force, the F_{st}, g and F_{vf} represent the surface tension, gravity acceleration, and volume force, respectively.

As stated in **Eqs. 10, 11**, the coupling between the laminar flow field and the electrostatic field is achieved by applying the electrostatic volume force to the Navier-Stokes equation. The electrostatic field force is the main factor that can cause fluid-flowing [16]. In addition, the electrostatic field force can be obtained by calculating the divergence based on Maxwell Stress Tensor (MST) [16], and the calculation is expressed in **Eq. 12**.

$$F_{vf} = \nabla T_{ik} \tag{12}$$

MST formula is described by **Eq. 13**.

$$T = ED^T - \frac{1}{2}(D \cdot EI) \tag{13}$$

Where I is the identity matrix, E is the electric field and D is the electric displacement field, and their relationship is described by **Eqs. 14, 15**.

$$E = -\nabla V \tag{14}$$

$$D = \varepsilon_0\varepsilon_r E \tag{15}$$

In a two-dimensional model simulation, the MST is expressed as **Eq. 16**.

$$T = \begin{bmatrix} T_{xx} & T_{xy} \\ T_{yx} & T_{yy} \end{bmatrix} \tag{16}$$

Eq. 17 can be obtained by substituting parameters.

$$T = \begin{bmatrix} \varepsilon_0\varepsilon_r E_x^2 - \frac{1}{2}\varepsilon_0\varepsilon_r\left(E_x^2 + E_y^2\right) & \varepsilon_0\varepsilon_r E_x E_y \\ \varepsilon_0\varepsilon_r E_x E_y & \varepsilon_0\varepsilon_r E_y^2 - \frac{1}{2}\varepsilon_0\varepsilon_r\left(E_x^2 + E_y^2\right) \end{bmatrix} \tag{17}$$

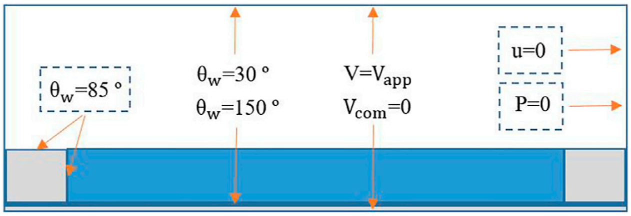

FIGURE 2 | The boundary conditions for the electrostatic field, phase field, and laminar flow field. Where u, P, θ_w, and V represents the velocity, pressure, contact angle, and voltage of the boundary conditions respectively. The pixel wall and outlet are symmetrical boundary conditions.

Where E_x and E_y represent the horizontal and vertical electric fields respectively. The variation of volume force caused by the electrostatic field acts on the interface between oil and water, and the calculation can be expressed in **Eq. 18**.

$$F = \begin{bmatrix} \dfrac{\partial(T_{xx})}{\partial x} & \dfrac{\partial\left(T_{xy}\right)}{\partial y} \\ \dfrac{\partial\left(T_{yx}\right)}{\partial x} & \dfrac{\partial\left(T_{yy}\right)}{\partial y} \end{bmatrix} \tag{18}$$

When an electric field is applied, the water is in contact with the hydrophobic insulation layer with the action of electrostatic field force [29, 30], the electrostatic field force can be described by **Eq. 19**.

$$F_e = \frac{1}{2} d_{hyd}\varepsilon_0\varepsilon_{hyd}E_{hyd}^2 \tag{19}$$

Where d_{hyd}, ε_{hyd} and E_{hyd} represent the thickness of the hydrophobic insulation layer, dielectric constant, and electric field strength on the hydrophobic insulation layer, respectively. Therefore, the force balance on the contact line can be derived from the Lippmann-Young equation, as shown in **Eq. 20**.

$$\cos\theta_e = \cos\theta_{hyd} + \frac{\varepsilon_0\varepsilon_{hyd}V^2}{2d_{hyd}\gamma_{ow}} \tag{20}$$

Where θ_e, θ_{hyd}, and γ_{ow} are the EW contact angle, Young's contact angle of the hydrophobic dielectric layer, and the surface tension, respectively.

Boundary Conditions

In the simulation model, boundary conditions are the prerequisites for determining the solution of governing equations on the boundary. The zero-charge boundary condition should be set on all sides of the model. For electrostatic field boundary conditions, the voltage V and the ground need to be specified. The wetted wall, the initial interface, and the outlet need to be specified in phase-field boundary conditions. The wetted wall boundary can be calculated by **Eqs. 21, 22**.

$$n \cdot \varepsilon^2\nabla\varnothing = \varepsilon^2\cos(\theta_w)|\nabla\varnothing| \tag{21}$$

TABLE 1 | Structure, material, and interface parameters of the model.

Parameters	Quantity	Symbol	Value	Unit
Material	Density of oil	ρ_{oil}	800	kg/m³
	Density of water	ρ_{water}	1,000	kg/m³
	Dynamic viscosity of oil	μ_{oil}	0.0005–0.003	Pa·s
	Dynamic viscosity of water	μ_{water}	0.001	Pa·s
	Dielectric constant of oil	ε_{oil}	2.8	1
	Dielectric constant of water	ε_{water}	88	1
	Dielectric constant of a hydrophobic dielectric layer	ε_{hyd}	1.6	1
	Dielectric constant of a grid	ε_{grid}	3.6	1
Structure	Width of a pixel	w_{pixel}	160	μm
	Height of a grid	d_{grid}	6	μm
	Width of a grid	w_{grid}	15	μm
	Thickness of a hydrophobic dielectric layer	d_{hyd}	1	μm
	Thickness of oil	d_{oil}	6	μm
Interfacial	Surface tension of oil and water	γ_{ow}	0.02	N/m
	Contact angle of a grid	θ_{grid}	85	deg
	Contact angle of a hydrophobic insulating layer	θ_{hyd}	150	deg
	Contact angle of the top plate	θ_{top}	30	deg

$$n\cdot\frac{\gamma\lambda}{\varepsilon^2}\nabla\psi = 0 \tag{22}$$

The interface of the two-phase flow was selected as an initial boundary condition. Both sides of the model (except the pixel walls) were selected as inlet and outlet boundary conditions. In addition, initial values of pressure and velocity in the laminar flow field were set to 0. The wall condition was set to no slip. These setting of boundary conditions were shown in **Figure 2**. The dotted box in **Figure 2** represents the symmetric boundary condition.

PROCESS AND DISCUSSION

The parameters used in the simulation were shown in **Table 1**. The fluid (oil and water) in the model was set to incompressible flow. It was assumed that the temperature (25°C) was kept constant during the fluid movement, so the thermal expansion of the fluid was ignored. The influence of pressure on dynamic viscosity was ignored. In addition, the Bond number describes the relationship between gravity and surface tension in the EWDs model, and it is far less than 1. So the gravity can be neglected [16]. In the simulation, the polar liquids were replaced by water [31].

The proposed simulation model was shown in **Figure 2**. The natural spreading and shrinking process of oil were realized in this model. To describe the display performance of EWDs, it is necessary to calculate the aperture ratio. The aperture ratio is an important performance index of EWDs, which is a proportion of opening area in a whole pixel [20]. When the aperture ratio was calculated in two dimensions, the bottom of the EWD was considered as a square, and A_r is used to represent the aperture ratio, L is the length of the contact line between the oil and the hydrophobic insulating layer in two dimensions structure, and d is the area of the hydrophobic insulating layer. The aperture ratio was calculated by using **Eq. 23**.

$$A_r = \frac{4\times d^2 - \pi L^2}{4\times d^2}\times 100\% \tag{23}$$

When the electric field inside a pixel was analyzed, the electric field formula was used, as shown in **Eq. 24**. Where E, U, d represents the electric field, the voltage, and the distance between the two potentials, respectively.

$$E = \frac{U}{d} \tag{24}$$

In this paper, the EWD model was implemented by COMSOL Multiphysics 5.4. The aperture ratio test platform was shown in **Figure 3**. This test platform included a waveform editing system, a signal amplifier, and a detection system. The waveform editing system was used to edit and generate waveform signals, which was consisted of a computer and a function signal generator. The signal was amplified by the signal amplifier to drive the oil. The detection system was used to collect oil movement image of EWD panel in real time, which was consisted of a high-speed camera and an image processing system. The aperture ratio was obtained by the image processing platform.

Influence of Dynamic Viscosity

The dynamic viscosity is an important parameter in fluid. The dynamic viscosity of oil can affect the aperture ratio and response time [20]. The response time is expressed as T. In one driving cycle, the time for applying the driving waveform is represented by T1, and the time when the pixel reaches the maximum aperture ratio is represented by T2. The response time is equal to the difference between T2 and T1. In this paper, an experiment of oil dynamic viscosity from 0.0005 Pa·s to 0.003 Pa·s with an interval of 0.0005 Pa·s was designed, and the experimental results were shown in **Figure 4**. When the dynamic viscosity was changed from 0.002 Pa·s to 0.003 Pa·s, the response time was shorter and the aperture ratio was larger. **Figure 5** showed that when the dynamic viscosity of oil was less than 0.0015 Pa·s, the oil was split into two pieces. Otherwise, the oil was pushed into a

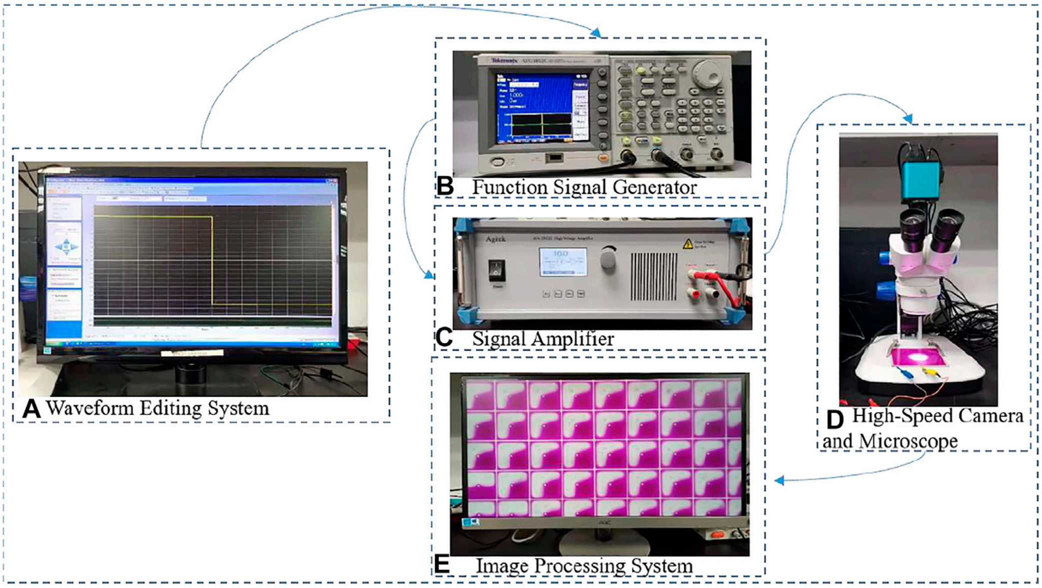

FIGURE 3 | An aperture ratio test platform for EWDs **(A)** A waveform editing system **(B)** A function signal generator **(C)** A signal amplifier **(D)** A high-speed camera and a microscope **(E)** An image processing system.

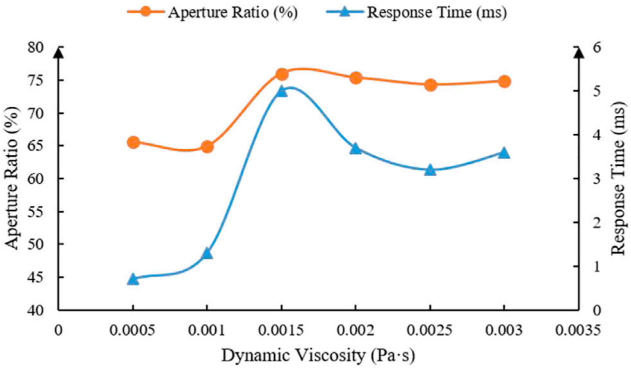

FIGURE 4 | The influence of oil dynamic viscosity on pixel aperture ratio and response time.

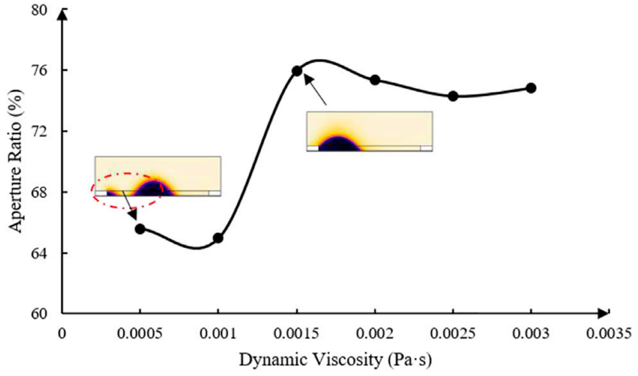

FIGURE 5 | The influence of oil with different dynamic viscosity on oil-splitting. When the dynamic viscosity of the oil was higher than 0.0015 Pa·s, the oil was pushed with a whole block. Otherwise, the oil was divided into two pieces.

corner with a whole block. Therefore, the oil with a dynamic viscosity from 0.002 Pa·s to 0.003 Pa·s should be selected in current conditions. **Figure 6** showed the process of a switch-on and a switch-off in a pixel with specific conditions. The conditions were that the voltage was 32 V and the oil dynamic viscosity was 0.002 Pa·s. The results showed that the oil was pushed into a corner with a whole block. So, the dynamic viscosity of oil was set to 0.002 Pa·s.

Influence of Driving Waveforms

In a pixel, the voltage of driving waveform was converted into electrostatic field force and applied to the water and oil. In the simulation, the gradually increasing voltage was set by the parametric scanning method, and the results were shown in **Figure 7**. When the voltage was lower than 16 V, the shape of oil was squeezed down at both sides of a pixel, but the oil was not split. When the voltage was changed from 16 to 36 V, the aperture ratio was almost increased linearly. When the voltage was higher than 36 V, the aperture ratio was increased slowly and reached the maximum. At the same time, the oil was split into two pieces. The blue curve in **Figure 7** represented the maximum aperture ratio of an actual EWD pixel when the voltage was changed from 16 to 36 V. The length and width of an actual pixel were 150 and 150 μm, respectively. The aperture ratio of the actual pixel was measured on the test platform in **Figure 3**. The results showed that the value of simulation was close to the actual before 20 V. In the range of 20–28 V, the simulation value was 4.3% higher than the actual, and in the range of 28–36 V, the simulation value was 10.5% higher than the actual. Altogether, the trends between

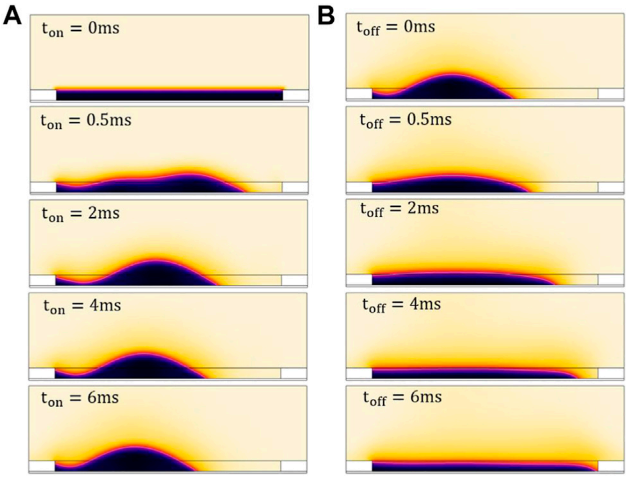

FIGURE 6 | In COMSOL software, the movement process of oil and water (black represents oil, light yellow represents water) was intercepted **(A)** After applying 32 V voltage, the oil was shrunk with the action of electrostatic field force, which was completed in 4 ms. **(B)** When the driving voltage was removed, the oil was naturally spread, and the process was completed in 6 ms.

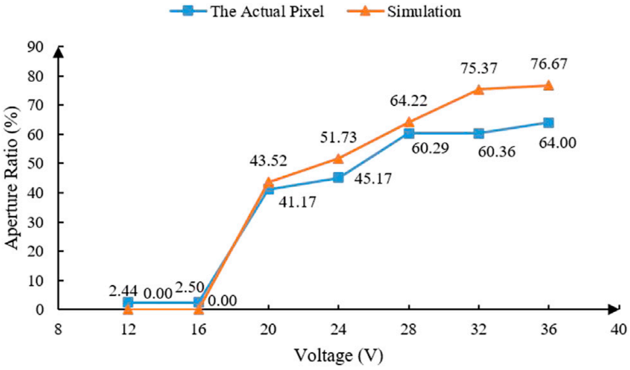

FIGURE 7 | The aperture ratio between simulation and an actual pixel. When the voltage was changed from 16 to 36 V, the change curve of aperture ratio between the actual pixel and simulation was obtained. The length and width of an actual pixel were 150 and 150 μm respectively. The changing trend of aperture ratio was consistent between simulation and actual EWD pixel.

these two were consistent. Therefore, the accuracy of this simulation model was verified.

The driving waveform has influence on the movement of oil [32–34]. To comprehend the acceleration ability of oil with the action of driving waveforms in one cycle, these driving waveforms with a different rising slope were designed, as shown in **Figure 8**. The change of aperture ratio with the action of four driving waveforms was shown in **Figure 9**. With the slope increased, the response time was shorter. When the slope was infinite (square waveform), the oil was split into two pieces. The experimental data showed that the moment when the pixel reached the maximum aperture ratio later

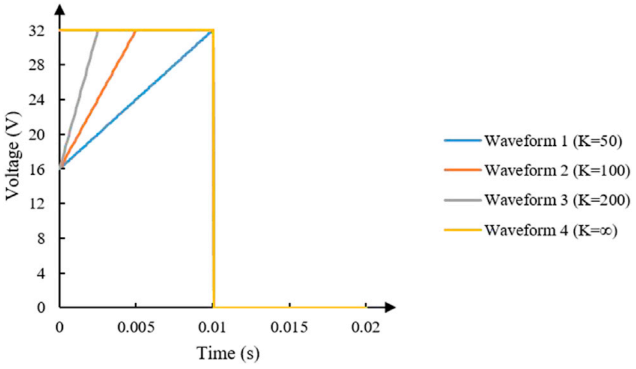

FIGURE 8 | Four driving waveforms with different slopes were designed. The starting voltage was set to 16 V. K in the cleft was the slope, and the slopes of the four waveforms are 50, 100, 200, and infinite, respectively. The effective driving cycle was 10 ms, and the latter 10 ms was set to 0 V.

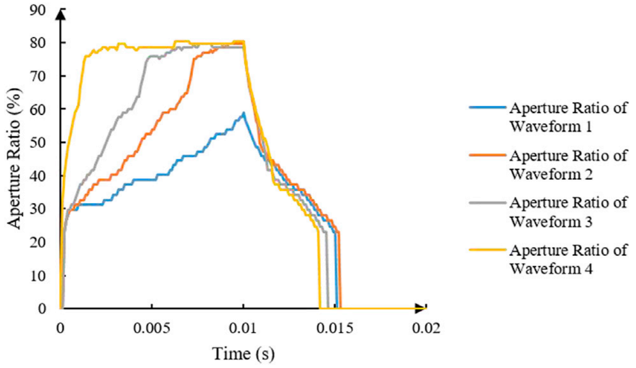

FIGURE 9 | The pixel aperture ratio was obtained with four driving waveforms.

than the moment that the driving waveform reached the maximum voltage for 2–5 ms. The greater the slope, the stronger the oil acceleration. So, a maintenance period of 2–5 ms should be set to drive a pixel for reaching the maximum aperture ratio. It took more than 6 ms in the natural spreading stage.

Relationship Between Electrostatic Field Force and Oil Movement

The forces on the fluid can be divided into volume force and external force. The volume force can be divided into surface tension and electrostatic field force. The electrostatic field force is a key factor that affects the oil movement of EWDs [35, 36]. To obtain the relationship between the movement status of oil with a whole block and the internal electrostatic field force. Parameters were determined based on Waveform 2 in **Figure 8**, the voltage was set to 32 V and the oil dynamic viscosity was 0.002 Pa·s.

The change of the internal electric field inside a pixel was shown in **Figure 10**. In the vertical direction, the internal space of the pixel was divided into a water channel and an oil-water mixed

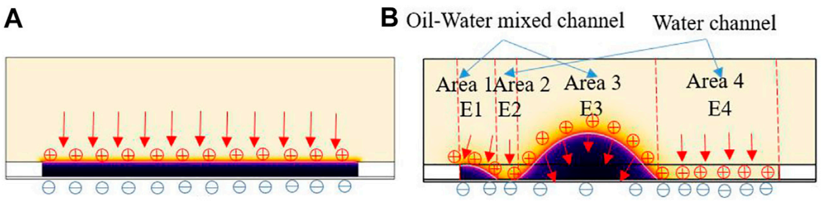

FIGURE 10 | The change of the internal electric field inside of a pixel **(A)** The internal electric field of the initial interface **(B)** The internal electric field in the process of oil movement. E1, E2, E3, and E4 represented the internal electric fields formed by areas 1, 2, 3, and 4, respectively.

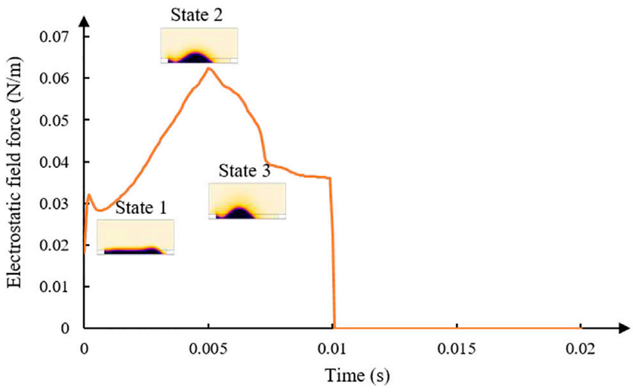

FIGURE 11 | The relationship between fluid status and electrostatic field force. Taking Waveform 2 as the input term, the electrostatic field force in a pixel space was integrated, and the results of the electrostatic field force in the driving period were obtained.

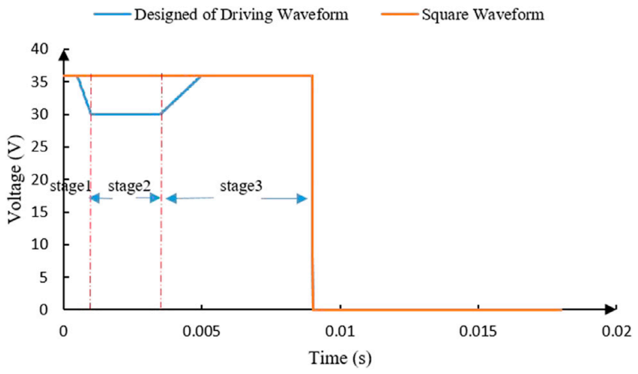

FIGURE 12 | The proposed driving waveform and the traditional square waveform. The proposed driving waveform had three stages which were maintained for 1 ms, 2.5 ms, and 5.5 ms, respectively, and the period of the square waveform and the proposed driving waveform were both 18 ms. The rest of the blue curve overlapped with the square waveform.

channel. As shown in **Figure 10B**, the internal space of the pixel can be divided into areas 1, 2, 3, and 4, respectively, areas 1, 3 were oil-water mixed channels, and areas 2, 4 were water channels. E1, E2, E3, and E4 represented the internal electric fields formed by areas 1, 2, 3, and 4, respectively. In the analysis process, the water with a high dielectric constant (80) as a conductor of electricity and oil as an insulator was considered. According to **Eq. 24**, the internal voltage U was 0 V in the water channel, so the internal electric field E was 0 (V/m). In the area of the oil-water mixed channel, if U remained unchanged and d was increased, the internal electric field was decreased. On the contrary, the internal electric field was increased. Therefore, the internal electric field force was proportional to the thickness of the oil, and the oil was split easier in the thin area. The red arrows in **Figure 10B** indicated the direction of the internal electric field. When the water was considered as a conductor of electricity, the voltage at the oil-water interface was the same. As the height of the oil increased, the electric field at the high of the oil was smaller, and the electric field at both sides was greater than the highest. Therefore, a non-uniform electric field was formed in the oil, and the oil formed a spherical cap shape with the action of the non-uniform internal electrostatic field.

The change of the internal electrostatic field force inside a pixel was shown in **Figure 11**. The result was obtained by the integral calculation of electrostatic field forces in a pixel space (except the pixel walls). When the oil was in State 1, a new water channel was formed in the oil ruptured area, and the internal electric field was reduced in this area. So, the electrostatic field force was reduced at this stage. Then, the voltage was increased linearly, the electric field in the pixel space was increased overall. As a result, the electrostatic field force was also increased. When the oil became State 2, the oil was pushed to the highest. Although the voltage kept the maximum, the internal electrostatic field force was reduced. This was mainly due to the larger water channel area.

DRIVING WAVEFORM DESIGN FOR SUPPRESSING OIL-SPLITTING

In a two-dimensional EWD model simulation, a pixel switch-on process can be divided into three stages. In the first stage, oil was ruptured randomly on one side of a pixel. The other side was squeezed down, but not ruptured. This stage was maintained about 1 ms. In the second stage, oil was continuously squeezed, the oil was driven both vertically and horizontally with the action of the non-uniform electrostatic field force. If the voltage was large enough, oil on the side which was not ruptured previously was split. This stage was maintained about 2–5 ms. In the third stage, oil was driven horizontally, and the height of oil was almost unchanged. By analyzing these stages, the conclusions were obtained as follows. The oil was thin and the electrostatic field force applied to the oil was large in the first stage. When a high voltage more than 36 V was

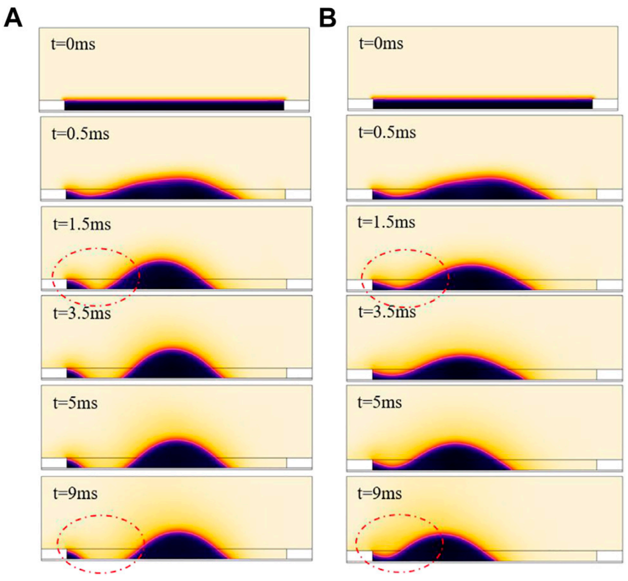

FIGURE 13 | When the proposed driving waveform and the square waveform were applied, the change of oil status was obtained **(A)** With the driving of the square waveform, the oil was split into two pieces, the aperture ratio was 76.67% **(B)** With the driving of the proposed driving waveform, the oil was pushed into a corner with a whole block, and the aperture ratio was 78.89%.

applied, the oil was split into two pieces. The oil-splitting appeared in the first and second stages. So, combined with the analysis of oil movement in the first and second stages, a driving waveform was proposed for suppressing the oil-splitting. The proposed driving waveform was divided into three stages as shown in **Figure 12.** In the first stage, the waveform started at 36 V (high voltage), then was dropped to 30 V rapidly, and maintained for 0.5 ms, respectively. The purpose of this stage was mainly to drive the oil to rupture on one side. In stage 2, the voltage value was maintained at 30 V for 2.5 ms. At this stage, oil was mainly driven in one direction horizontally. In stage 3, when the oil was pushed thick enough, the voltage can be increased, and the oil was not split anymore. This stage was to improve the response speed of the pixel. When the square waveform was applied to this model, the oil was split into two pieces at 1.5 ms as shown in **Figure 13A**, and then the oil was driven to the middle of a pixel at 5 ms. When the proposed driving waveform was applied to this model, the oil was pushed a corner with a whole block as shown in **Figure 13B**. The result showed that the proposed driving waveform can effectively suppress oil-splitting, and the aperture ratio was increased by 2.9% compared to the square waveform.

CONCLUSION

In this paper, a two-dimensional EWD model was established. This model was used to simulate the influence of dynamic viscosity, voltage, and waveform on oil-splitting. The oil was easily broken into two pieces with a high voltage. In addition, the internal electrostatic field force and oil movement were affected by each other. On the basis of the traditional square waveform, the proposed narrow falling ramp drove the oil to rupture quickly on one side of a pixel. The proposed low voltage maintenance stage can effectively suppress the oil-splitting. After applying this optimized waveform, the aperture ratio of a pixel was increased. The simulation model can provide a prediction scheme for the selection of oil and the design of the driving system in practical application. By adjusting part of the structure or material parameters of the model, it can be applied to other schemes of EWDs.

DATA AVAILABILITY STATEMENT

The raw data supporting the conclusions of this article will be made available by the authors, without undue reservation.

AUTHOR CONTRIBUTIONS

SL, HS, and QZ: investigation, methodology, formal analysis, editing.SL: writing – review, and editing. All authors contributed to the article and approved the submitted version.

FUNDING

Supported by the National Key Research and Development Program of China (2016YFB0401501), Program for Guangdong Innovative and Enterpreneurial Teams (No. 2019BT02C241), Science and Technology Program of Guangzhou (No. 2019050001), Program for Chang Jiang Scholars and Innovative Research Teams in Universities (No. IRT_17R40), Guangdong Provincial Key Laboratory of Optical Information Materials and Technology (No. 2017B030301007), Guangzhou Key Laboratory of Electronic Paper Displays Materials and Devices (201705030007), and the 111 Project.

REFERENCES

1. Jones TB. An Electromechanical Interpretation of Electrowetting. *J Micromech Microeng* (2005) 15(6):1184–7. doi:10.1088/0960-1317/15/6/008
2. Beni G., and Hackwood S.. Electro-wetting Displays. *Appl Phys Lett* (1981) 38(4):207–9. doi:10.1063/1.92322
3. Bai PF., Hayes RA., Jin M., Shui L., Yi ZC., Wang L., et al. Review of Paper-Like Display Technologies (Invited Review). *Pier* (2014) 147:95–116. doi:10.2528/PIER13120405
4. Yi Z., Feng H., Zhou X., and Shui L. Design of an Open Electrowetting on Dielectric Device Based on Printed Circuit Board by Using a Parafilm M. *Front Phys* (2020) 8:193. doi:10.3389/fphy.2020.00193
5. Feng H., Yi Z., Yang R., Qin X., Shen S., Zeng W., et al. Designing Splicing Digital Microfluidics Chips Based on Polytetrafluoroethylene Membrane. *Micromachines* (2020) 11(12):1067. doi:10.3390/mi11121067
6. Wang L., Yi Z., Jin M., Shui L., and Zhou G. Improvement of Video Playback Performance of Electrophoretic Displays by Optimized Waveforms with Shortened Refresh Time. *Displays* (2017) 49:95–100. doi:10.1016/j.displa.2017.07.007

7. Shen S., Gong Y., Jin M., Yan Z., Xu C., Yi Z., et al. Improving Electrophoretic Particle Motion Control in Electrophoretic Displays by Eliminating the Fringing Effect via Driving Waveform Design. *Micromachines* (2018) 9(4): 143. doi:10.3390/mi9040143
8. Li JS., Tang Y., Li ZT., Li JX., Ding XR., Yu BH., et al. Toward 200 Lumens Per Watt of Quantum-Dot White-Light-Emitting Diodes by Reducing Reabsorption Loss. *ACS Nano* (2021) 15(1):550–62. doi:10.1021/acsnano.0c05735
9. Li Z., Cao K., Cao K., Li J., Tang Y., Ding X., et al. Review of Blue Perovskite Light Emitting Diodes with Optimization Strategies for Perovskite Film and Device Structure. *Opto-Electronic Adv* (2021) 4(2):20001901–15. doi:10.29026/oea.2021.200019
10. Li W., Wang L., Zhang T., Lai S., Liu L., He W., et al. Driving Waveform Design with Rising Gradient and Sawtooth Wave of Electrowetting Displays for Ultra-low Power Consumption. *Micromachines* (2020) 11(2):145. doi:10.3390/mi11020145
11. Yi Z., Huang Z., Lai S., He W., Wang L., Chi F., et al. Driving Waveform Design of Electrowetting Displays Based on an Exponential Function for a Stable Grayscale and a Short Driving Time. *Micromac* (2020) 11(3):313. doi:10.3390/mi11030313
12. Jin M., Shen S., Yi Z., Zhou G., and Shui L. Optofluid-Based Reflective Displays. *Micromac* (2018) 9(4):159. doi:10.3390/mi9040159
13. Yi Z., Shui L., Wang L., Jin M., Hayes RA., and Zhou G. A Novel Driver for Active Matrix Electrowetting Displays. *Displ* (2015) 37:86–93. doi:10.1016/j.displa.2014.09.004
14. Yi Z., Liu L., Wang L., Li W., Shui L., and Zhou G. A Driving System for Fast and Precise Gray-Scale Response Based on Amplitude-Frequency Mixed Modulation in TFT Electrowetting Displays. *Micromac* (2019) 10(11):732. doi:10.3390/mi10110732
15. Liu L., Bai P., Yi Z., and Zhou G. A Separated Reset Waveform Design for Suppressing Oil Backflow in Active Matrix Electrowetting Displays. *Micromac* (2021) 12(5):491. doi:10.3390/mi12050491
16. Hsieh WL., Lin CH., Lo KL., Lee KC., Cheng WY., and Chen KC. 3D Electrohydrodynamic Simulation of Electrowetting Displays. *J Micromech Microeng* (2014) 24(12):125024. doi:10.1088/0960-1317/24/12/125024
17. Walker S. W., and Shapiro B. Modeling the Fluid Dynamics of Electrowetting on Dielectric (EWOD). *J Microelectromech Syst* (2006) 15(4):986–1000. doi:10.1109/JMEMS.2006.878876
18. Zhou M., Zhao Q., Tang B., Groenewold J., Hayes RA., and Zhou G. Simplified Dynamical Model for Optical Response of Electrofluidic Displays. *Displ* (2017) 49:26–34. doi:10.1016/j.displa.2017.05.003
19. Luo Z., Fan J., Xu J., Zhou G., and Liu S. A Novel Driving Scheme for Oil-Splitting Suppression in Electrowetting Display. *Opt Rev* (2020) 27(4):339–45. doi:10.1007/s10043-020-00601-z
20. Roques-Carmes T., Hayes RA., and Schlangen LJM. A Physical Model Describing the Electro-Optic Behavior of Switchable Optical Elements Based on Electrowetting. *J Appl Phys* (2004) 96(11):6267–71. doi:10.1063/1.1810192
21. Yang G., Zhuang L., Bai P., Tang B., Henzen A., and Zhou G. Modeling of Oil/Water Interfacial Dynamics in Three-Dimensional Bistable Electrowetting Display Pixels. *ACS Omega* (2020) 5(10):5326–33. doi:10.1021/acsomega.9b04352
22. Kim J.. Phase-Field Models for Multi-Component Fluid Flows. *Commun Comput Phys* (2012) 12(3):613–61. doi:10.4208/cicp.301110.040811a
23. Zhao Q., Tang B., Dong B., Li H., Zhou R., Guo Y., et al. Electrowetting on Dielectric: Experimental and Model Study of Oil Conductivity on Rupture Voltage. *J Phys D: Appl Phys* (2018) 51(19):195102. doi:10.1088/1361-6463/aabb69
24. Yue P., Feng JJ., Liu C., and Shen J. A Diffuse-Interface Method for Simulating Two-phase Flows of Complex Fluids. *J Fluid Mech* (2004) 515:293–317. doi:10.1017/S0022112004000370
25. Yurkiv V., Yarin AL., and Mashayek F. Modeling of Droplet Impact onto Polarized and Nonpolarized Dielectric Surfaces. *Langmuir* (2018) 34(34): 10169–80. doi:10.1021/acs.langmuir.8b01443
26. Zhu G., Yao J., Zhang L., Sun H., Li A., and Shams B. Investigation of the Dynamic Contact Angle Using a Direct Numerical Simulation Method. *Langmuir* (2016) 32(45):11736–44. doi:10.1021/acs.langmuir.6b02543
27. Cahn JW., and Hilliard JE.. Free Energy of a Nonuniform System. I. Interfacial Free Energy. *J Chem Phys* (1958) 28(2):258–67. doi:10.1063/1.1744102
28. Dolatabadi A., Arzpeyma A., Wood-Adams P., and Bhaseen S. A Coupled Electro-Hydrodynamic Numerical Modeling of Droplet Actuation by Electrowetting. *Colloids Surfa, A Physicoche Eng Aspects* (2008) 323(1/3): 28–35. doi:10.1016/j.colsurfa.2007.12.025
29. Jones TB., Gunji M., Washizu M., and Feldman MJ. Dielectrophoretic Liquid Actuation and Nanodroplet Formation. *J Appl Phys* (2001) 89(2):1441–8. doi:10.1063/1.1332799
30. Jones TB., Fowler JD., Chang YS., and Kim CJ. Frequency-based Relationship of Electrowetting and Dielectrophoretic Liquid Microactuation. *Langmuir* (2003) 19(18):7646–51. doi:10.1021/la0347511
31. Jones TB. On the Relationship of Dielectrophoresis and Electrowetting. *Langmuir* (2002) 18(11):4437–43. doi:10.1021/la025616b
32. Yi Z., Feng W., Wang L., Liu L., Lin Y., He W., et al. Aperture Ratio Improvement by Optimizing the Voltage Slope and Reverse Pulse in the Driving Waveform for Electrowetting Displays. *Micromachines* (2019) 10(12): 862. doi:10.3390/m11012086210.3390/mi10120862
33. Feng HQ., Yi ZC., Sun ZZ., Zeng WJ., Wang L., Yang JJ., et al. A Spliceable Driving System Design for Digital Microfluidics Platform Based on Indium Tin Oxide Substrate. *J Nanoelectronics Optoelectronics* (2020) 15(9):1127–36. doi:10.1166/jno.2020.2838
34. Zeng W., Yi Z., Zhao Y., Zeng W., Ma S., Zhou X., et al. Design of Driving Waveform Based on Overdriving Voltage for Shortening Response Time in Electrowetting Displays. *Front Phys* (2021) 9:642682. doi:10.3389/fphy.2021.642682
35. Kang KH. How Electrostatic fields Change Contact Angle in Electrowetting. *Langmuir* (2002) 18(26):10318–22. doi:10.1021/la0263615
36. Brabcova Z., McHale G., Wells GG., Brown CV., and Newton MI. Electric Field Induced Reversible Spreading of Droplets into Films on Lubricant Impregnated Surfaces. *Appl Phys Lett* (2017) 110(12):121603. doi:10.1063/1.4978859

Conflict of Interest: The authors declare that the research was conducted in the absence of any commercial or financial relationships that could be construed as a potential conflict of interest.

MINI REVIEW
published: 16 July 2021
doi: 10.3389/fphy.2021.728804

Review of Driving Waveform for Electrowetting Displays

Zichuan Yi[1]*, *Hu Zhang*[1,2], *Wenjun Zeng*[1,3], *Haoqiang Feng*[3], *Zhengxing Long*[3], *Liming Liu*[1], *Yunfeng Hu*[1], *Xichen Zhou*[1] and *Chongfu Zhang*[1,4]

[1]School of Electronic Information, University of Electronic Science and Technology of China, Zhongshan Institute, Zhongshan, China, [2]School of Electronic Science and Engineering (National Exemplary School of Microelectronics), University of Electronic Science and Technology of China, Chengdu, China, [3]South China Academy of Advanced Optoelectronics, South China Normal University, Guangzhou, China, [4]School of Information and Communication Engineering, University of Electronic Science and Technology of China, Chengdu, China

Electrowetting display (EWD) is the most potential technology among new electronic paper technologies. It not only has the advantages of electrophoretic display (EPD) technology but also can realize color video playback. Therefore, this technology has been widely studied in recent years. Driving waveform is a voltage sequence which can drive pixels to display gray scales in EWDs. As one of the key technologies, it directly affects the display effect of pixels. In this paper, we give a review of the display principle of EWDs and the research status of driving waveforms. At the same time, the contact angle hysteresis, charge trapping, and oil splitting are also reviewed, which can provide a reference value for designing driving waveforms.

Keywords: electrowetting displays, driving waveform, charge trapping, response time, aperture ratio

Edited by:
Qiang Xu,
Nanyang Technological University,
Singapore

Reviewed by:
Ji-Pei Chen,
Guangzhou University, China
Jia Liu,
Inner Mongolia University of Science and Technology, China

Correspondence:
Zichuan Yi
yizichuan@163.com

Specialty section:
This article was submitted to Optics and Photonics, a section of the journal Frontiers in Physics

Received: *22 June 2021*
Accepted: *05 July 2021*
Published: *16 July 2021*

Citation:
Yi Z, Zhang H, Zeng W, Feng H, Long Z, Liu L, Hu Y, Zhou X and Zhang C (2021) Review of Driving Waveform for Electrowetting Displays. Front. Phys. 9:728804. doi: 10.3389/fphy.2021.728804

INTRODUCTION

Display is one of the most important modes of human-computer interactions, and display devices play a key role in daily life. Along with the rapid increase of network information, people expect better displays to meet various requirements. At present, the most common displays are liquid crystal displays (LCD) and light-emitting diode (LED) displays [1, 2]. These self-luminous displays have the defect of high power consumption which can severely limit the using time of electronic products. Nevertheless, electronic paper displays, such as electrophoretic displays (EPDs) and electrowetting displays (EWDs), have the advantages of paper-like reading experience and low power consumption due to its reflective display. EPDs are the most widely used electronic paper. It has been widely used in e-books, e-labels, etc. However, it cannot achieve video playback and the luminance of color is not enough [3–6]. As a result, many scholars began to pay attention to EWDs for obtaining better paper-like display performance in recent years.

The principle of EWDs was first proposed by Beni in 1981 [7]. In 2003, Hayes and Feenstra have successfully demonstrated that the electrowetting technology can be used to form a basis of a new reflective display. Its display principle is to utilize the voltage-controlled movement of a colored oil [8]. As a new reflective electronic paper display, EWDs have excellent display characteristics, such as paper-like reading experience [9, 10]; low power consumption [11, 12]; color display [13–16]; fast response speed which can meet the requirements of video playback [17]; low manufacturing cost because part of the manufacturing process is the same as LCDs [18, 19]. Hence, EWD technology becomes the most potential paper-like display technology. The voltage sequence which can control gray scales in EWDs is driving waveform [20–23]. The earliest driving waveform of EWDs is a pulse width modulated (PWM) square wave [24]. However, some defects are caused by this driving

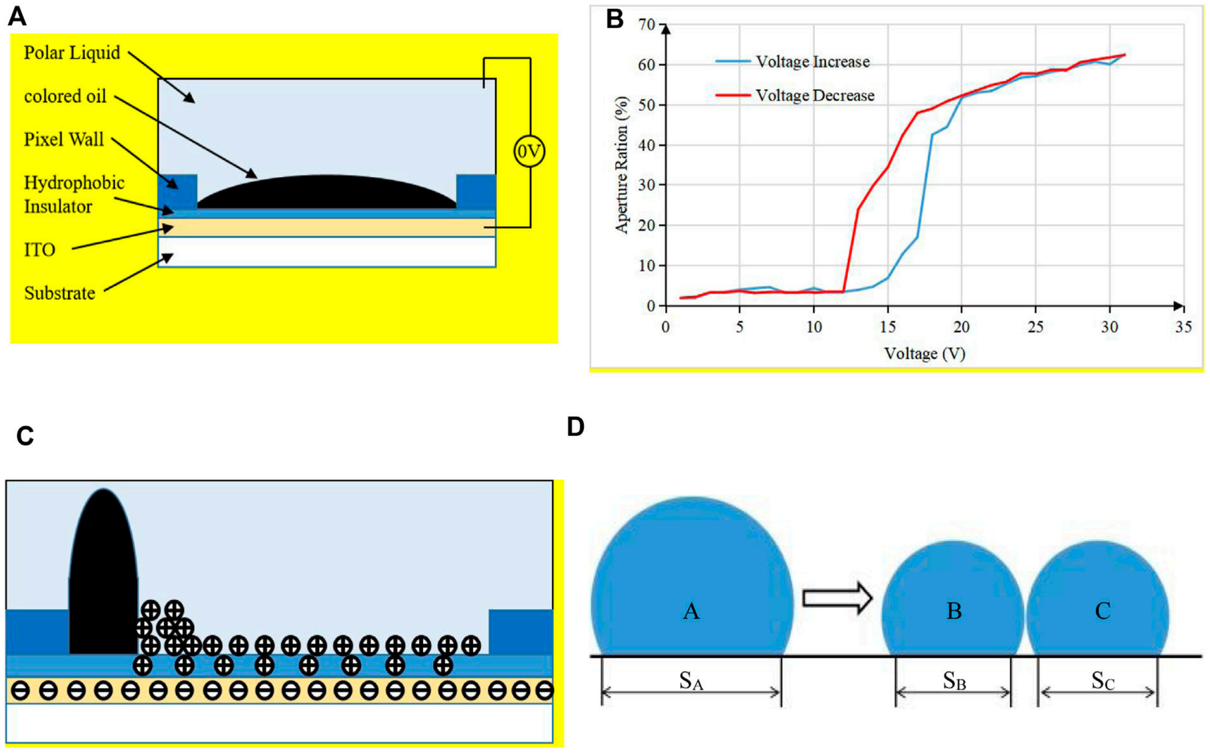

FIGURE 1 | The structure of an EWD pixel and the phenomenon of defects in EWDs. **(A)** The whole pixel is covered with oil and the color of oil is displayed when the driving voltage is 0 V. **(B)** Phenomenon of contact angle hysteresis. The blue curve is the aperture ratio when the driving voltage is increased from 0 to 30 V, and the red curve is the aperture ratio when the driving voltage is decreased from 30 to 0 V. **(C)** Phenomenon of charge trapping. When the oil shrinks to one corner of a pixel, the charge distribution in a pixel. Charge trapping would be caused when the interaction between ions and hydrophobic insulating layer is stronger than that between ions and conductive liquid. **(D)** Phenomenon of oil splitting. *A* is the colored oil which shrinks to one corner of a pixel. *B* and *C* are oil which is split into two parts.

waveform, such as gray scale distortion which is caused by contact angle hysteresis [25–28]; maximum aperture ratio is reduced due to oil splitting [29–31]; oil backflow caused by charge trapping in the hydrophobic insulator [32–36]. The movement of oil is directly controlled by the driving waveform, the optimization of driving waveform can affect the display effect of EWDs. Hence, the equivalent circuit models, capacitor-voltage (C-V) characteristics and contact angle hysteresis characteristic of EWDs have been studied by scholars, and some new driving waveforms were proposed for better performance of EWDs.

In this paper, driving waveforms of EWDs are summarized, and classified with different categories according to functions. It includes optimizing contact angle hysteresis, reducing charge trapping and oil splitting. The display quality of EWDs was greatly improved by these driving waveforms. Furthermore, it provided an important reference for the further study of EWDs.

PRINCIPLE

Principle of Electrowetting Displays

EWD is essentially an optical switch [37, 38]. Its structure is shown in **Figure 1A**. Each pixel is composed of a hydrophobic insulating layer, colored oil, polar liquid, pixel walls, a electrode which is made by ITO (Indium tin oxide) glass, a substrate. The colored oil is controlled by driving voltage to turn pixels on or off. The state of oil shrinkage can be described by the contact angle. The Lippmann-Young equation is considered as the basic theory of electrowetting technology. As shown in **Eq. 1** [39–42]. The relationship between the voltage and the contact angle can be described by this equation.

$$\cos\theta = \cos\theta_0 + \frac{1}{2}\frac{\varepsilon_0\varepsilon_r}{d\gamma}V^2 \tag{1}$$

Where θ is the contact angle when the driving voltage is V. θ_0 is the contact angle when the driving voltage is 0 V ε_0 is a vacuum dielectric constant and ε_r is a relative dielectric constant. d is the thickness of a hydrophobic insulation layer, γ is interfacial tension between oil and electrolyte solution. V is the driving voltage.

When the driving voltage is 0 V, the contact angle is approximately equal to zero due to Lippmann-Young equation. At this stage, because the oil is spread on the substrate, the pixel displays the color of colored oil, as shown in **Figure 1A**. With the increase of driving voltage, the electric field force is increased. Therefore, the oil original force balance is broken and oil begins to shrink to one corner of a pixel. The oil completely shrinks in one corner of the pixel when the voltage increases to V_{max}. The aperture ratio cannot become bigger when the voltage is greater than V_{max} [43]. The value of V_{max} depends on the size of the pixel and the thickness of hydrophobic insulating layer. At this stage, the pixel displays the color of substrate. Therefore, the pixel can display different gray scales by applying different driving voltages [44–47].

Contact Angle Hysteresis

Ideally, in the process of driving voltage rise or fall, the aperture ratio of the same driving voltage value should be the same. But experimental result is completely inconsistent with the expectation. The relationship between aperture ratio and voltage when the driving voltage rises from 0 to 30 V and falls from 30 to 0 V can be tested, respectively. As shown in **Figure 1B** [48]. The blue curve represents the relationship between the aperture ratio and the voltage when the driving voltage is rising. The red curve represents the relationship between the aperture ratio and the voltage when the driving voltage is falling. When the driving voltage is close to 0 and 30 V, the aperture ratio of these two curves almost coincide. But the difference of the aperture ratio is big when the driving voltage is in the middle stage. When the aperture ratio increases as the voltage increases, the contact angle is called as advancing angle. On the contrary, when the aperture ratio decreases as the voltage decreases, the contact angle is called as receding angle. Therefore, this distortion is called contact angle hysteresis [48]. The accurate gray scale display cannot be achieved because of this phenomenon.

Charge Trapping

Theoretically, the aperture ratio of a pixel is related to the applied voltage due to Lippmann-Young equation. But the oil can backflow when the same voltage is applied continuously. Thus, the aperture ratio is reduced. It has been found that some charge is trapped in the hydrophobic insulator when driving voltage is applied to EWDs [49]. The charge distribution is shown in **Figure 1C**. A three-phase contact line is formed where the oil, water and hydrophobic insulator are in contact. Positive ions gather on the three-phase contact line, and then, the nearby electric field can be distorted. The backflow can be caused due to the imbalance between Laplace pressure and Maxwell pressure at the three-phase contact line [50]. It can also reduce the maximum aperture ratio of EWDs.

Oil Splitting

Ideally, the oil shrinks in one corner of a pixel when driving voltage is applied to EWD in the process of oil shrinkage. However, oil may be split to two or more parts. The reason is that the charges in the hydrophobic insulator can cause a sudden change in electric field. When the capacitance value of a pixel increases rapidly, it is likely to cause oil splitting [51]. As shown in **Figure 1D**, the oil is divided into B and C from A in a pixel. The areas covered by oil are S_A, S_B, S_C. The sum of S_B and S_C is greater than S_A. Therefore, the aperture ratio becomes smaller when the oil is divided into two parts. The more the oil is divided, the smaller the aperture ratio.

DRIVING WAVEFORMS DESIGN

Driving Waveforms for Optimizing Contact Angle Hysteresis

The fundamental reason of contact angle hysteresis is the rough surface of hydrophobic insulation layer and the viscous resistance of two-phase liquid [52]. The precise gray scale cannot be displayed by EWDs because of contact angle hysteresis. The contact angle hysteresis can be reduced by optimizing driving waveforms. A multi-waveform adaptive driving scheme was proposed [53]. In this scheme, the contact angle hysteresis curves of EWDs driven by a square wave, a sine wave and a triangle wave were tested. Then, the optimal waveform of each stage could be selected by superimposing the three hysteresis curves, and an activation voltage sequence was added in front of the first stage. The maximum distortion caused by contact angle hysteresis could be effectively reduced by this driving scheme. Besides, the inhibitory effect of alternating current (AC) voltage on contact angle hysteresis was proved in another driving scheme [48].

Driving Waveforms for Reducing Charge Trapping and Oil Backflow

With an applied constant voltage, the shrinking oil cannot be maintained in a stable state because of charge trapping. This defect can also be solved by optimizing driving waveforms. A method showed that charge trapping can be reduced by a reverse electrode pulse voltage which takes a few milliseconds, and the proposed driving waveform is shown in **Figure 2A** [54]. Furthermore, the influence of oil backflow caused by charge trapping can also be reduced by the reset signal [55], as shown in **Figure 2B**. The proposed driving waveform was divided into a driving signal and a reset signal. The driving signal S_0 and S_3 were direct current (DC) signals. They were used to drive the pixel to a target gray scale, and the reset signal was used to release trapped charges. S_2 in the reset signal was a driving recovery phase. It was used to obtain a faster gray scale response speed. But it has been proved that the higher the brightness of the target gray scale, the more serious the charge trapping [56]. Therefore, the dwell time of the reset signal needed to be adjusted according to the gray scale. However, the additional power consumption of EWDs caused by charge trapping and oil backflow cannot be reduced by these methods. A driving waveform with a rising gradient and a sawtooth wave was proposed to reduce the power consumption by reducing charge trapping [57]. The power consumption of various waveforms was compared, and the driving waveform is shown in **Figure 2C**. It was proved that the sawtooth wave can prevent oil backflow caused by charge trapping, and lower power consumption can be obtained by sacrificing the maximum aperture ratio. Besides, charge trapping can slow down the turn-off time of EWDs, which makes it difficult to achieve high quality video playback. It is important to solve this problem when the driving waveform is designed for video playback. The earliest two methods for video playback were amplitude modulation and pulse width modulation. These methods can divide the driving waveform into a display phase and a reset phase. The Charge trapping can be reduced due to the reset phase. But a multi-gray scale video could not be obtained in previous studies [58]. An improved multi-gray scales dynamic symmetrical driving waveform was proposed [59]. In this method, the display stage was divided into two identical parts. The probability of applying a constant voltage for a long time can

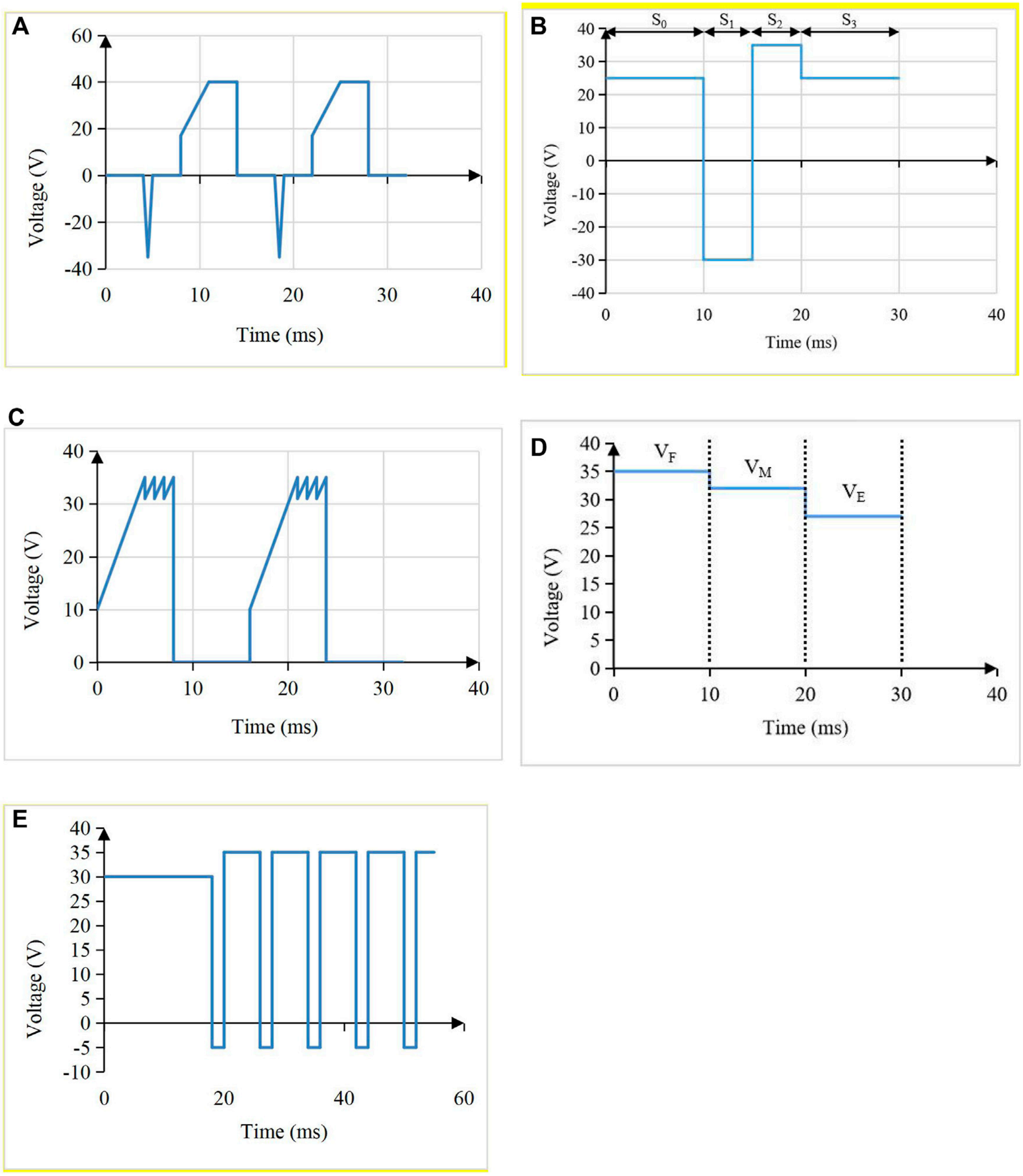

FIGURE 2 | Different driving waveforms. **(A)** The multi structural driving waveform was designed to increase aperture ratio. **(B)** Driving waveform with a rising gradient and a sawtooth wave was designed to reduce power consumption. **(C)** The driving waveform with a reset signal. The reset signal consisted of S_1 and S_2. The driving signal S_0 was a DC signal. The DC signal was used to drive the EWD to the target gray scale. **(D)** Amplitude-frequency mixed modulation driving waveform was designed to reduce response time. **(E)** The DC and AC mixed waveform. The DC driving stage was used to drive the EWD to the target gray scale and the AC driving stage was used to prevent oil backflow.

be greatly reduced. Thus, this method could achieve 16 gray scales and reduce oil splitting and charge trapping.

Driving Waveforms for Reducing Response Time

In order to obtain a higher frame rate video playback and a better display effect, it is necessary to shorten the response time of EWDs. There are several different methods to achieve this goal. First, although some defects are caused by contact angle hysteresis, the hysteresis curve can help to design new waveforms. An amplitude-frequency mixed modulation driving system was proposed according to the contact angle hysteresis, as shown in **Figure 2D** [60]. The driving voltage and driving time of each stage were determined by the hysteresis curve of a target gray scale. Next, a driving waveform based on an exponential function was proposed to reduce the response time [51]. The optimal time constant of the exponential function was designed by testing the influence of the time constant on the aperture ratio oscillation range. Then, it has been proved that excessive reverse voltage can cause a chemical reaction between water and ITO [50]. In order to solve this problem, a mixed DC and AC waveform was proposed, as shown in **Figure 2E**. The driving waveform was composed of two parts. The first part was a DC driving stage. It was used to drive pixels to reach target aperture ratios. The second part was an AC driving stage, and a reverse voltage was used to prevent oil backflow. This scheme could effectively reduce the response time. Lastly, due to the response speed of the oil was increased when the driving voltage was increased, the work showed that overdriving voltage can reduce the response time [61]. The influence of different overdriving voltages on response time was tested in this work.

Driving Waveforms for Reducing Oil Splitting

The reset frame is often used to solve the problem of charge trapping in EWDs. However, the reset frame could affect the instantaneous display state, such as flickers and the decrease of reflective luminance [57]. Therefore, a separated reset waveform was proposed to solve this problems [62]. The instantaneous reverse driving voltage can be achieved by adjusting the voltage of the common electrode. The charges can be released quickly with the overdriving voltage, and another lower instantaneous reverse driving can keep the oil active. In addition, DC balance is not complied in the improved multi-gray scales dynamic symmetrical driving scheme, which may cause polarization in EWDs. Therefore, a DC balanced driving waveform was proposed [63]. In this work, a long frame was divided into two short frames. In the two short frames, DC balance can be complied due to the reversal of polarity.

Generally, the oil splitting caused by the sudden change of electric field force could be prevented by a rising voltage. In a previous study, the sinusoidal waveform could reduce oil splitting effectively [64]. Therefore, a novel driving scheme was proposed to reduce oil splitting [65]. The driving voltage increased gradually from a value which was below the threshold voltage to a final voltage with a sinusoidal curve. It was proved that this driving waveform could reduce oil splitting and increase the aperture ratio of pixels.

CONCLUSION

The design of driving waveform plays a key role for improving the display quality of EWDs. In this paper, we reviewed new driving waveforms. At first, the shortcomings of EWDs were described, including contact angle hysteresis, charge trapping phenomenon and oil splitting. Then, driving waveforms for improving these shortcomings were classified. It provide a reference value for reducing response time, increasing aperture ratio and improving oil stability of EWDs. In the future, driving waveforms design would become an important part of driving system design with the development of EWDs, and an excellent driving waveform design is expected to achieve higher quality performance for EWDs.

AUTHOR CONTRIBUTIONS

ZY and HZ discussed and wrote the manuscript together. WZ, HF, ZL, LL, and YH discussed and corrected the manuscript. XZ and CZ also helped with drawing the figures. All authors have read and agreed to the published version of the manuscript.

FUNDING

This research was funded by the Guangdong Basic and Applied Basic Research Foundation (No. 2020A1515010420), Construction project of professional quality engineering in 2020 (No. YLZY202001), the Key Research Platforms and Research Projects in Universities and Colleges of Guangdong Provincial Department of Education (No. 2018KQNCX334), the Zhongshan Innovative Research Team Program (No. 180809162197886), Guangdong Provincial Key Laboratory of Optical Information Materials and Technology (No. 2017B030301007), the Project for Innovation Team of Guangdong University (No. 2018KCXTD033), and the National Key R&D Program of China (No. 2018YFB0407100-02).

REFERENCES

1. Lee S-M, Kwon JH, Kwon S, and Choi KC. A Review of flexible OLEDs toward highly durable unusual displays. *IEEE Trans Electron Devices* (2017) 64(5): 1922–31. doi:10.1109/TED.2017.2647964
2. Han J-W, Hwang M-C, Kim S-G, You T-H, and Ko S-J. Vector quantizer based block truncation coding for color image compression in LCD overdrive. *IEEE Trans Consumer Electron* (2008) 54(4):1839–45. doi:10.1109/TCE.2008.4711243
3. Jin M, Shen S, Yi Z, Zhou G, and Shui L. Optofluid-based Reflective displays. *Micromachines* (2018) 9(4):159. doi:10.3390/mi9040159
4. Bai PF, Hayes RA, Jin M, Shui L, Yi ZC, Wang L, et al. REVIEW OF PAPER-LIKE DISPLAY TECHNOLOGIES (Invited Review). *Pier* (2014) 147:95–116. doi:10.2528/PIER13120405
5. Kao W-C, and Tsai J-C. Driving method of three-particle electrophoretic displays. *IEEE Trans Electron Devices* (2018) 65(3):1023–8. doi:10.1109/TED.2018.2791541
6. Yi Z, Zeng W, Ma S, Feng H, Zeng W, Shen S, et al. Design of driving waveform based on a damping oscillation for optimizing Red saturation in three-color electrophoretic displays. *Micromachines* (2021) 12(2):162. doi:10.3390/mi12020162
7. Beni G, and Hackwood S. Electro-wetting displays. *Appl Phys Lett* (1981) 38(4):207–9. doi:10.1063/1.92322
8. Hayes RA, and Feenstra BJ. Video-speed electronic paper based on electrowetting. *Nature* (2003) 425(6956):383–5. doi:10.1038/nature01988
9. Heikenfeld J, Drzaic P, Yeo J-S, and Koch T. Review Paper: A critical Review of the present and future prospects for electronic paper. *J Soc Inf Display* (2011) 19(2):129–56. doi:10.1889/JSID19.2.129

10. Giraldo A, Aubert J, Bergeron N, Li F, Slack A, and van de Weijer M. 34.2: Transmissive Electrowetting-Based Displays for Portable Multi-Media Devices. *SID Symp Dig* (2009) 40(1):479–82. doi:10.1889/1.3256820
11. Dou Y, Wang B, Jin M, Yu Y, Zhou G, and Shui L. A Review on self-assembly in microfluidic devices. *J Micromech Microeng* (2017) 27(11):113002. doi:10.1088/1361-6439/aa84db
12. Chen Z, Lin S, Lin Z, Liao Q, Li T, and Tang B. Design of Video Display Driving System for Low-power Electrowetting Display. *Acta Photonica Sinica* (2020) 49(2):222002. doi:10.3788/gzxb20204902.0222002
13. Heikenfeld J, Zhou K, Kreit E, Raj B, Yang S, Sun B, et al. Electrofluidic displays using Young-Laplace transposition of brilliant pigment dispersions. *Nat Photon* (2009) 3(5):292–6. doi:10.1038/nphoton.2009.68
14. You H, and Steckl AJ. Three-color electrowetting display device for electronic paper. *Appl Phys Lett* (2010) 97(2):023514:doi:10.1063/1.3464963
15. Hayes RA, Feenstra BJ, Camps IGJ, Hage LM, Roques-Carmes T, Schlangen LJM, et al. 52.1: A high brightness colour 160 PPI Reflective display technology based on electrowetting. *SID Symp Dig* (2004) 35(1):1412–5. doi:10.1889/1.1825770
16. Massard R, Mans J, Adityaputra A, Leguijt R, Staats C, and Giraldo A. Colored oil for electrowetting displays. *J Inf Display* (2013) 14(1):1–6. doi:10.1080/15980316.2012.751939
17. Mingyong Q, Shanling L, Suyun Z, Zhixian L, Tailiang G, and Biao T. Real-time dynamic driving system implementation of electrowetting display. *Opto-Electronic Eng* (2019) 46(06):180623. doi:10.12086/oee.2019.180623
18. Zhao R, Cumby B, Russell A, and Heikenfeld J. Large area and low power dielectrowetting optical shutter with local deterministic fluid film breakup. *Appl Phys Lett* (2013) 103(22):223510. doi:10.1063/1.4834095
19. Tröls A, Enser H, and Jakoby B. Modeling and fabrication of low-cost electrowetting actuators for flexible microfluidic display applications. *IEEE SENSORS* (2016) 1–3. doi:10.1109/ICSENS.2016.7808429
20. Roques-Carmes T, Hayes RA, Feenstra BJ, and Schlangen LJM. Liquid behavior inside a Reflective display pixel based on electrowetting. *J Appl Phys* (2004) 95(8):4389–96. doi:10.1063/1.1667595
21. Zhou M, Zhao Q, Tang B, Groenewold J, Hayes RA, and Zhou G. Simplified dynamical model for optical Response of electrofluidic displays. *Displays* (2017) 49:26–34. doi:10.1016/j.displa.2017.05.003
22. Tang B, Groenewold J, Zhou M, Hayes RA, and Zhou G. Interfacial electrofluidics in confined systems. *Sci Rep* (2016) 6:26593. doi:10.1038/srep26593
23. Feng H, Yi Z, Sun Z, Zeng W, Wang L, Yang J, et al. A spliceable driving system design for digital microflfluidics platform based on indium tin oxide substrate. *J Nanoelectronics Optoelectronics* (2020) 15(9):1127–36. doi:10.1166/jno.2020.2838
24. Yi Z, Shui L, Wang L, Jin M, Hayes RA, and Zhou G. A novel driver for active matrix electrowetting displays. *Displays* (2015) 37:86–93. doi:10.1016/j.displa.2014.09.004
25. Xu ZN. An algorithm for selecting the most accurate protocol for contact angle measurement by drop shape analysis. *Rev Scientific Instr* (2014) 85(12):125107. doi:10.1063/1.4903198
26. Li F, and Mugele F. How to make sticky surfaces slippery: Contact angle hysteresis in electrowetting with alternating voltage. *Appl Phys Lett* (2008) 92(24):244108. doi:10.1063/1.2945803
27. Gao J, Mendel N, Dey R, Baratian D, and Mugele F. Contact angle hysteresis and oil film lubrication in electrowetting with two immiscible liquids. *Appl Phys Lett* (2018) 112(20):203703. doi:10.1063/1.5034510
28. Kulinich SA, and Farzaneh M. Effect of contact angle hysteresis on water droplet evaporation from super-hydrophobic surfaces. *Appl Surf Sci* (2009) 255(7):4056–60. doi:10.1016/j.apsusc.2008.10.109
29. Andrea G, Paul V, Daniel F, Marco S, Jasper A, Mathieu W, et al. 46.3: Improved oil motion control and hysteresis-free pixel switching of electrowetting displays. *SID Symp Dig Tech Pap* (2012) 43(1):625–8. doi:10.1002/j.2168-0159.2012.tb05859.x
30. Bansal S, and Sen P. Effect of electrowetting induced capillary oscillations on coalescence of compound droplets. *J Colloid Interf Sci* (2018) 530:223–32. doi:10.1016/j.jcis.2018.05.090
31. Zhao Q, Tang B, Dong B, Li H, Zhou R, Guo Y, et al. Electrowetting on dielectric: experimental and model study of oil conductivity on Rupture voltage. *J Phys D: Appl Phys* (2018) 51(19):195102. doi:10.1088/1361-6463/aabb69
32. Lu Y, Sur A, Pascente C, Ravi Annapragada S, Ruchhoeft P, and Liu D. Dynamics of droplet motion induced by Electrowetting. *Int J Heat Mass Transfer* (2017) 106:920–31. doi:10.1115/HT2016-733110.1016/j.ijheatmasstransfer.2016.10.040
33. Ounnunkad K, Patten HV, Velický M, Farquhar AK, Brooksby PA, Downard AJ, et al. Electrowetting on conductors: anatomy of the phenomenon. *Faraday Discuss* (2017) 199:49–61. doi:10.1039/c6fd00252h
34. Buehrle J, Herminghaus S, and Mugele F. Interface profiles near three-phase contact lines in electric fields. *Phys Rev Lett* (2003) 91(8):086101. doi:10.1103/PhysRevLett.91.086101
35. Li X, Tian H, Shao J, Ding Y, Chen X, Wang L, et al. Decreasing the saturated contact angle in electrowetting-on-dielectrics by controlling the charge trapping at liquid-solid interfaces. *Adv Funct Mater* (2016) 26(18): 2994–3002. doi:10.1002/adfm.201504705
36. Kilaru MK, Heikenfeld J, Lin G, and Mark JE. Strong charge trapping and bistable electrowetting on nanocomposite fluoropolymer:BaTiO3 dielectrics. *Appl Phys Lett* (2007) 90(21):212906. doi:10.1063/1.2743388
37. Roques-Carmes T, Hayes R, and Schlangen L. A physical model describing the electro-optic behavior of switchable optical elements based on electrowetting. *J Appl Phys* (2004) 96(11):6267–71. doi:10.1063/1.1810192
38. Duan MZ, Hayes RA, Zhang X, and Zhou GF. A Reflective display technology based on electrofluidics. *Amm* (2014) 670-671:976–81. doi:10.4028/www.scientific.net/AMM.670-671.976
39. Seveno D, Blake TD, and De Coninck J. Young's equation at the nanoscale. *Phys Rev Lett* (2013) 111(9):096101. doi:10.1103/PhysRevLett.111.096101
40. Navascues G. Liquid surfaces: theory of surface tension. *Rep Prog Phys* (2001) 42(7):1131–86. doi:10.1088/0034-4885/42/7/002
41. Moon H, Cho SK, Garrell RL, and Kim C-JC. Low voltage electrowetting-on-dielectric. *J Appl Phys* (2002) 92(7):4080–7. doi:10.1063/1.1504171
42. Feng H, Yi Z, Yang R, Qin X, Shen S, Zeng W, et al. Designing Splicing Digital Microfluidics Chips Based on Polytetrafluoroethylene Membrane. *Micromachines* (2020) 11(12):1067. doi:10.3390/mi11121067
43. Luo Z, Luo J, Zhao W, Cao Y, Lin W, and Zhou G. A high-Resolution and intelligent dead pixel detection scheme for an electrowetting display screen. *Opt Rev* (2018) 25(1):18–26. doi:10.1007/s10043-017-0382-3
44. Zhou K, Heikenfeld J, Dean KA, Howard EM, and Johnson MR. A full description of a simple and scalable fabrication process for electrowetting displays. *J Micromech Microeng* (2009) 19(6):065029. doi:10.1088/0960-1317/19/6/065029
45. Sun B, Zhou K, Lao Y, Heikenfeld J, and Cheng W. Scalable fabrication of electrowetting displays with self-assembled oil dosing. *Appl Phys Lett* (2007) 91(1):011106. doi:10.1063/1.2753697
46. Wu H, Tang B, Hayes R, Dou Y, Guo Y, Jiang H, et al. Coating and patterning functional materials for large area electrofluidic arrays. *Materials* (2016) 9(8): 707. doi:10.3390/ma9080707
47. Yi Z, Zeng W, Ma C, Feng H, Yang J, Liu L, et al. A Real-time touch control system design based on field-programmable gate array via optimizing Bresenham algorithm for electrowetting displays. *J Soc Inf Display* (2021) 29:573–83. doi:10.1002/jsid.1001
48. Wang L, Zhang H, Li W, Li J, Yi Z, Wan Q, et al. Driving scheme optimization for electrowetting displays based on contact angle hysteresis to achieve precise gray-scales. *Front Phys* (2021) 9:655547. doi:10.3389/fphy.2021.655547
49. Wu H, Dey R, Siretanu I, Ende D, Shui L, Zhou G, et al. Electrically controlled localized charge trapping at amorphous fluoropolymer-electrolyte interfaces. *Small* (2019) 16(2):1905726. doi:10.1002/smll.201905726
50. Liu L, Wu Z, Wang L, Zhang T, Li W, Lai S, et al. Design of an AC driving waveform based on characteristics of electrowetting stability for electrowetting displays. *Front Phys* (2020) 8:618752. doi:10.3389/fphy.2020.618752
51. Yi Z, Huang Z, Lai S, He W, Wang L, Chi F, et al. Driving Waveform Design of Electrowetting Displays Based on an Exponential Function for a Stable Grayscale and a Short Driving Time. *Micromachines* (2020) 11(3):313. doi:10.3390/mi11030313
52. Zhao R, Liu Q-C, Wang P, and Liang Z-C. Contact Angle Hysteresis in Electrowetting on Dielectric. *Chin Phys. B* (2015) 24(8):086801–496. doi:10.1088/1674-1056/24/8/086801
53. Li W, Wang L, and Henzen A. A Multi Waveform Adaptive Driving Scheme for Reducing Hysteresis Effect of Electrowetting Displays. *Front Phys* (2020) 8: 618811. doi:10.3389/fphy.2020.618811

54. Yi Z, Feng W, Wang L, Liu L, Lin Y, He W, et al. Aperture Ratio improvement by optimizing the voltage slope and Reverse pulse in the driving waveform for electrowetting displays. *Micromachines* (2019) 10(12):862. doi:10.3390/m110120862
55. Zhang T, and Deng Y. Driving Waveform Design of Electrowetting Displays Based on a Reset Signal for Suppressing Charge Trapping Effect. *Front Phys* (2021) 9:672541. doi:10.3389/fphy.2021.672541
56. Luo ZJ, Zhang WN, Liu LW, Xie S, and Zhou G. Portable multi-gray scale video playing scheme for high-performance electrowetting displays. *Jnl Soc Info Display* (2016) 24(6):345–54. doi:10.1002/jsid.444
57. Li W, Wang L, Zhang T, Lai S, Liu L, He W, et al. Driving waveform design with Rising gradient and sawtooth wave of electrowetting displays for ultra-low power consumption. *Micromachines* (2020) 11(2):145. doi:10.3390/mi11020145
58. Van Dijk R, Feenstra BJ, Hayes RA, Camps IGJ, Boom RGH, Wagemans MMH, et al. 68.3: Gray Scales for Video Applications on Electrowetting Displays. *SID Symp Dig* (2006) 37(1):1926–9. doi:10.1889/1.2433427
59. Qian M, Lin S, Zeng S, Lin Z, Guo T, and Tang B. Real-time dynamic driving system implementation of electrowetting display. *Opto-Electronic Eng* (2019) 46(6):180623. doi:10.12086/oee.2019.180623
60. Yi Z, Liu L, Wang L, Li W, Shui L, and Zhou G. A Driving System for Fast and Precise Gray-Scale Response Based on Amplitude-Frequency Mixed Modulation in TFT Electrowetting Displays. *Micromachines* (2019) 10(11): 732. doi:10.3390/mi10110732
61. Zeng W, Yi Z, Zhao Y, Zeng W, Ma S, Zhou X, et al. Design of driving waveform based on overdriving voltage for shortening Response time in electrowetting displays. *Front Phys* (2021) 9:642682. doi:10.3389/fphy.2021.642682
62. Liu L, Bai P, Yi Z, and Zhou G. A separated Reset waveform design for suppressing oil backflow in active matrix electrowetting displays. *Micromachines* (2021) 12(5):491. doi:10.3390/mi12050491
63. Lin S, Zeng S, Qian M, Lin Z, Guo T, and Tang B. Improvement of display performance of electrowetting displays by optimized waveforms and error diffusion. *J Soc Inf Display* (2019) 27(10):619–29. doi:10.1002/jsid.790
64. Zhang X-M, Bai P-F, Hayes R, Shui L-L, Jin M-L, Tang B, et al. Novel Driving Methods for Manipulating Oil Motion in Electrofluidic Display Pixels. *J Display Technol* (2015) 12(2):1. doi:10.1109/JDT.2015.24779471
65. Luo Z, Fan J, Xu J, Zhou G, and Liu S. A Novel Driving Scheme for Oil-Splitting Suppression in Electrowetting Display. *Opt Rev* (2020) 27(4):339–45. doi:10.1007/s10043-020-00601-z

Conflict of Interest: The authors declare that the research was conducted in the absence of any commercial or financial relationships that could be construed as a potential conflict of interest.

frontiers
in Physics

BRIEF RESEARCH REPORT
published: 09 August 2021
doi: 10.3389/fphy.2021.723106

Driving Waveform Design Based on Driving Process Fusion and Black Reference Gray Scale for Electrophoretic Displays

Li Wang, Pengchang Ma*, Jitao Zhang and Qiming Wan*

School of Information Engineering, Zhongshan Polytechnic, Zhongshan, China

An electrophoretic display (EPD) is a kind of paper display technology, which has the advantages of ultra-low power consumption and readability under strong light. However, in an EPD-driving process, four stages are needed to finish the driving of a pixel erase original images, reset to black state, clear-to-white state, and write a new image. A white reference gray scale can be obtained before writing a new image, and this driving process may take too long for the comfort of reading. In this article, an EPD-driving waveform, which takes the black state as the reference gray, is proposed to reduce the driving time. In addition, the rules of direct current (DC) balance are also followed to prevent the charge from getting trapped in the driving backplane. The driving process is fused and there are two stages in the driving waveform: reset to black state and write the next image. First, the EPD is written to a stable black state according to the original gray scale driving waveform and the black state is used as the reference gray for the next image. Second, the new image is written by the second stage of the new driving waveform. The experimental results show that the proposed driving waveform has a better performance. Compared with the traditional driving waveform which has four stages, the driving time of the new driving waveform is reduced by nearly 50%.

Keywords: electrophoretic display, driving waveform, driving process, reference gray scale, direct current balance

Edited by:
Qiang Xu,
Nanyang Technological University,
Singapore

Reviewed by:
Weimin Li,
Shenzhen Institutes of Advanced Technology, CAS, China
Jingling Yan,
Ningbo Institute of Materials Technology and Engineering, CAS, China

****Correspondence:***
Li Wang
wangli_oet@163.com
Pengchang Ma
mpcmyc99@aliyun.com

Specialty section:
This article was submitted to Optics and Photonics, a section of the journal Frontiers in Physics

Received: *10 June 2021*
Accepted: *05 July 2021*
Published: *09 August 2021*

Citation:
Wang L, Ma P, Zhang J and Wan Q (2021) Driving Waveform Design Based on Driving Process Fusion and Black Reference Gray Scale for Electrophoretic Displays. Front. Phys. 9:723106. doi: 10.3389/fphy.2021.723106

INTRODUCTION

EPD has become the most widely used paper-like display due to its good market potential. As a reflective display technology, the light reflection characteristic provides it with a paper-like comfortable reading experience [1–4]. In addition, EPDs also have the advantages of ultra-low power consumption and a good bistable characteristic [5, 6]. Therefore, EPDs have been widely used in electronic labels, e-books, etc. But video playback cannot be achieved due to the long response time of EPDs [7]. Particles in microcapsules of EPDs are driven by voltages, and pixels can display different gray scales by adjusting the position of particles [7–10]. The voltage sequence which can drive particles to display gray scales is called the driving waveform. Hence, it is of great significance to reduce the response time and improve the display effect by optimizing the driving waveform design [11, 12].

A traditional driving waveform can be divided into four stages: erasing the original image, resetting to the black state, clearing to the white state, and writing a new image [13–15]. When a particle is in a same position for a long time, its mobility is much lower than that of other particles.

The particle activity can be improved by resetting to the black state and clearing to the white state [16–18]. This driving process may be continued from hundreds of milliseconds to 1 s [19, 20]. Therefore, there are some scholars who have conducted a series of research on the driving waveform, and some principles and methods of driving waveform editor are put forward to shorten the driving time or reduce flickers. Kao et al. [21] studied the property of the suspension viscosity, characterized the response latency of the EPD, and put forward a new driving waveform, which set the white gray scale as a reference gray scale, to shorten the driving time and reduce the number of flickers. However, the proposed driving method did not take into account an important factor-DC balance. Moreover, the reference gray scale is unstable. Wang et al. [22] used four kinds of screen update modes to update the EPD according to different images, and it could improve the update speed. However, the form of driving waveforms in four modes was not changed, and it could not improve the refresh speed fundamentally. In a traditional driving waveform, stages of resetting to the black state and clearing to the white state are longer than the other two stages [23, 24], so some scholars have studied new driving schemes to reduce the driving time of these two stages. Yi et al. [25] found that high-frequency voltage can be used to activate particles, and the new driving waveform could effectively reduce the ghost image and flicker. But it is difficult to get a stable gray scale display. He et al. [26] proposed a driving waveform based on the optimization of particle activation by analyzing the electrophoresis performance of particles. It can effectively reduce the driving time. However, the DC balance is not considered in the design of the driving waveform, which may cause damage to the EPD [27].

In this article, a new driving waveform, which is based on the black reference gray, is proposed to reduce the driving time. The new driving waveform obeys the rule of DC balance and is divided into two stages: reset to black state and write the new image. The first stage is used to get an accurate reference gray, and some principles are proposed to get a uniform reflectance value for black state at the same time. The second stage is used to write a new gray value by comparing it with the black reference gray.

MICROENCAPSULATED EPD SYSTEM

The introduction of microcapsule technology is an important breakthrough in EPD technology. There are two kinds of particles in a microcapsule [28]. Here, the microcapsule is a pixel in EPD. It solves the long-term display instability problem in EPD. The

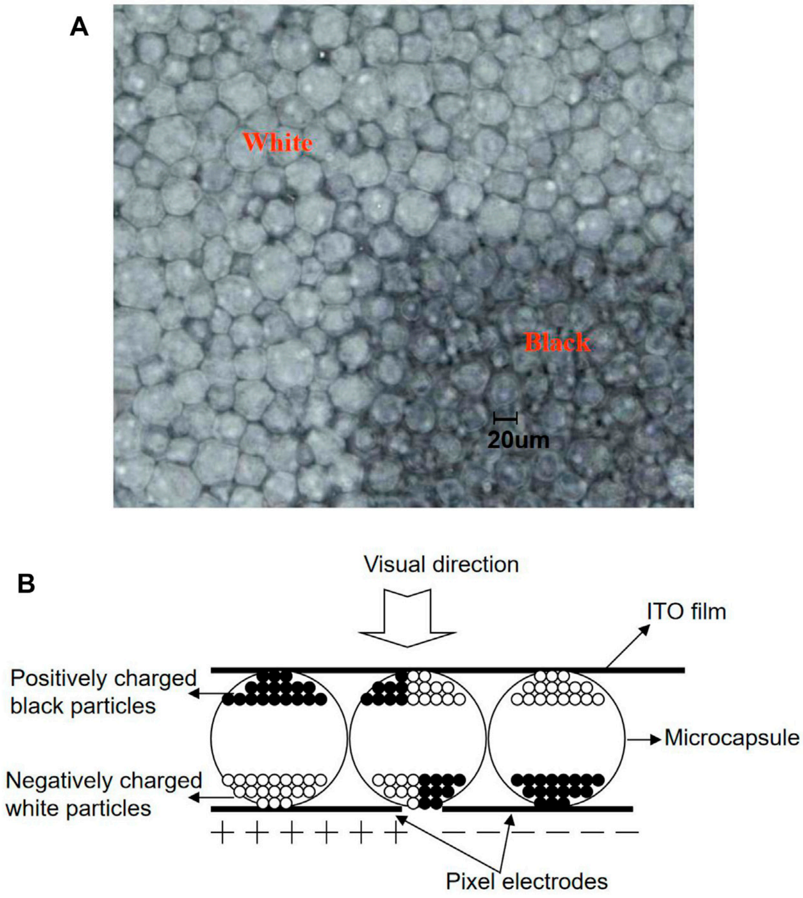

FIGURE 1 | The structure of a microcapsule EPD. **(A)** An enlargement image of microcapsules in an EPD. **(B)** EPD model.

movement and aggregation of particles are limited in microcapsules, and the different gray scales could be realized by controlling the voltage which is applied on electrodes. In the display process, the white SiO_2 particles of the EPD are charged with a negative charge and black carbon particles are charged with a positive charge. The structure of an EPD is shown in **Figure 1**. In **Figure 1A**, the electrode of a pixel in the upper left part is provided with a negative voltage and the positively charged white particles move upward, the EPD shows white, the lower right part is provided with a positive voltage and the negatively charged black particles move upward, and the EPD shows black.

In the interior of a microcapsule, as is shown in **Figure 1B**, in order to ensure the good electrophoretic performance of electrophoretic particles, a charged control agent is injected into the display capsule, which can effectively prevent the accumulation of charged particles and deposit on the capsule wall. The display particles in the capsule are mainly affected by gravity, buoyancy, electric power, and the viscosity of nonpolar solvent. In order to avoid the settlement of display particles, gravity is equal to buoyancy, as shown in **Eq. 1**.

$$\left[\frac{(3m-4\pi R^3\rho)g}{3}\right]=0. \tag{1}$$

Here, m is the mass of a particle, R is the radius of a particle, ρ is the density of nonpolar solvents, and g is the gravity constant. The electric force can be expressed by **Eq. 2**.

$$\overrightarrow{F_E} = q\vec{E} + \vec{m}\nabla\vec{E} + \frac{1}{6}\nabla\left(\vec{Q}:\nabla\vec{E}\right) + O\left(\nabla^3 E\right). \tag{2}$$

Here, $\overrightarrow{F_E}$ is the electric force, q is the charge of the particle, $\vec{E}$ is electric field, and $\vec{Q}$ is the total charge of particles. The first term of **Eq. 2** is the Coulomb interaction between particles and electric field, and the other term is the interaction of dielectric polarization components induced by particles. The viscosity can be expressed by **Eq. 3** [29, 30].

$$\overrightarrow{F_S} = 6\pi\eta R\vec{v}. \tag{3}$$

Here, $\overrightarrow{F_S}$ is the viscosity, η is the viscosity coefficient of the nonpolar solvent, and $\vec{v}$ is the velocity of the particle. $\vec{v}$ can be obtained by solving **Eq. 3**, and it is shown in **Eq. 4** [31].

$$\vec{v} = \frac{q\overrightarrow{F_E}}{6\pi\eta R}\left(1 \pm e^{-\frac{6\pi\eta R t}{m}}\right). \tag{4}$$

In general, the charged particle zeta potential could reach a level which could make a particle whose radius is 1 μm with 50–100 charges by using the charge control agent, at the same time, the electrophoretic mobility reaches $10^{-4} - 10^{-5}\, cm^2/Vs$. The expression of response time is shown as **Eq. 5**.

$$T = \frac{6\pi d^2\eta}{V\xi\varepsilon}, \tag{5}$$

where T is the response time, d is the distance between the common electrode and the pixel electrode, V is the voltage applied between two kinds of electrodes, ξ is the particle zeta potential, and ε is the dielectric constant of suspension liquid.

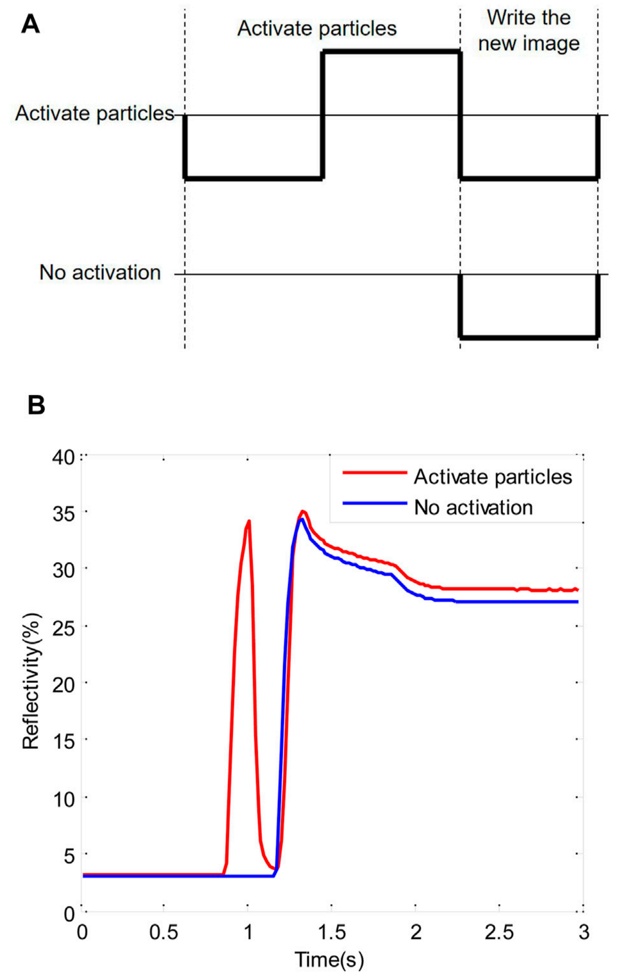

FIGURE 2 | Reflectance curves of an EPD which is driven by two kinds of driving waveform **(A)** EPD driving waveforms. **(B)** Reflectance curves of an EPD according to driving waveforms, the driving waveform with an active particles stage can obtain higher reflectivity.

Generally speaking, the voltage of the driving waveform could be set as 15, 0, or −15 V, and the EPD may spend 1 s or so on updating the image.

RESULTS AND DISCUSSION

Particle Performance Analysis

In the process of driving particles, the EPD may not display a desired gray scale if we drive particles to realize gray scales directly. In the traditional driving waveform, a four-stage driving waveform is used to drive particles to realize gray scales accurately [7]: erase the original image, reset to black state, clear to white state, and write a new image. In a driving waveform, a unit of time is 1/50 = 20 ms if the frame rate is 50 frames/s, so the time of four stages must be an integer multiple of 20 ms, the second stage and the third stage form a process of activating particles. Then, an accurate white reference gray scale

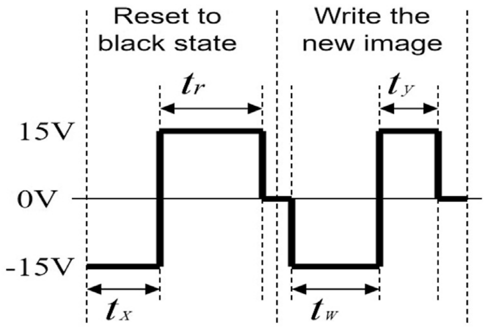

FIGURE 3 | An example of the new driving waveform which includes a resetting to black state stage and a writing the new image stage.

can be obtained at the end point of the third stage. The new image can be displayed in the fourth stage by using the reference gray scale.

In the design process of a driving waveform, the DC balance is a factor which must be considered. In the traditional driving waveform, the time of positive voltage and negative voltage must equal in the one gray scale change path to reach the DC balance.

The process of activating particles is very important in the driving waveform. The particles in microcapsules may be affected by various forces, and the driving force of electric potential must overcome other external forces to drive the particles. However, the resistance increases with the increase of speed. The forces that hinder the movement of particles are particle gravity, viscous resistance of electrophoretic solution, collision between particles, wall collision of microcapsules, Coulomb force between particles, and so on. When the resistance of particles is greater than the electric field force, the particle velocity will decrease. Only after a long enough residence time, the particles can reach a stable state, and the force acting on the particles can reach equilibrium. This reaction time has a direct impact on the refresh speed of the display screen. At this time, the motion ability of the moving particles is obviously lower than that of the activated particles [6]. Therefore, it is necessary to design a longer voltage duration to obtain the same gray level as the driving waveform with the active particle stage. Therefore, at the beginning of the driving waveform, we always use the limited driving time to activate the particles as much as possible. There are two driving waveforms, which are designed to drive the EPDs from a black state to a white state, in **Figure 2A**. The final reflectivity difference of an EPD which is driven by two driving waveforms are shown in **Figure 2B**.

Driving Process Fusion in the Driving Waveform

In this article, a new driving waveform, which is based on the black reference gray, is proposed. In this waveform, the driving process is fused, and there are two stages which include a resetting to black state stage and writing the new image stage. In the first stage, the particles are activated as far as possible, and a stable reflectivity black state is obtained at the end of this stage; then, the black state is taken as the reference gray. In the second stage, the positive voltage and negative voltage can cooperate with each other to realize the display of multilevel gray scales. An example of the new driving waveform is shown in **Figure 3**.

The second stage of the driving waveform, which could drive the EPD to realize the original image, must be considered in the design of the new driving waveform. For example, t_w is the negative voltage driving time and t_y is the positive voltage driving time of second stage which could drive the EPD to display the original image. And t_x is the negative voltage driving time and t_r is the positive voltage driving time of the first stage which could drive the EPD to display a new image. The relationship among four driving times is shown in **Eq. 6**.

$$t_w - t_y = t_r - t_x. \tag{6}$$

The driving waveform could reach the DC balance if **Eq. 6** is obeyed. In the first stage of the driving waveform, there is not enough time for refreshing between the white state and the black state, so the EPD is written to a middle gray scale, and this method could reduce the activation time greatly [8]. The detail design of the driving waveform is shown in **Figure 4**. For the sake of convenience, B represents black gray, DG represents dark gray, LG represents light gray, and W represents white gray, respectively. In **Figure 4**, the original gray scale is LG, both t_1 and t_2 are square waves whose duty ratio is 50%, so it has no effect on DC balance. t_3 is used to realize the DC balance and write to black state. At the end point of the first stage, a black state which has a stable reflectance value is obtained. The first stage of driving

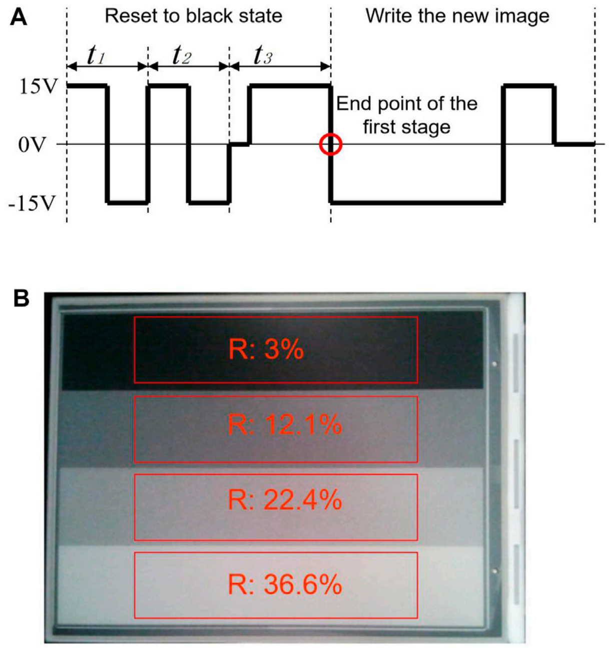

FIGURE 4 | (A) Design details of the new driving waveform, at the end point of the first stage, a black state which has a stable reflectance value can be obtained. **(B)** The real EPD has four-level gray scales which are driven by the proposed driving waveform.

waveforms should be filled with a positive voltage when the original gray scale is white, but it cannot get a black gray as the black reference gray. This is because the black reference gray is obtained in the case of activating particles, but there is no space for the activated particles stage when this stage is full of positive voltage. So, the first stage must be prolonged to form a longer time of positive voltage to get the black reference gray. The prolonged part could occupy the driving time of the second stage, or else, the driving waveform must be prolonged a little to meet the requirement.

Display Effect of the Proposed Driving Waveform

We carried out a driving experiment on an EPD device according to the proposed driving waveform, and the result is shown in **Figure 4B**. The experimental results showed that the driving waveform could realize multilevel gray scales. Among them, four testing areas are marked, the reflectivity of the first testing area is 3%, the second testing area is 12.1%, the third testing area is 22.4%, and the fourth testing area is 36.3%. According to the principle of gamma correction, the human eye sensitive to brightness transformation when the brightness is low. So, the change of the reflectivity value is nonlinear.

CONCLUSION

In this article, a new driving waveform based on two stages is proposed, and the driving process of gray scales is effectively fused. The first stage of the driving waveform can erase the original image, and the second stage is used to realize a multilevel gray scales display. In addition, the black state is used as the reference gray scale according to the mechanical analysis of particles in microcapsules. The driving waveform proposed by us has the advantages of short driving time and less voltage conversion times. It can effectively reduce the flicker sense and improve the reading comfort while shortening the screen switching time. What is more, the DC balance rule is applied to the design, which can effectively prevent the display breakdown caused by charge trapping. So, the proposed driving waveform provides a reference for the continuous improvement of the EPD display quality.

DATA AVAILABILITY STATEMENT

The original contributions presented in the study are included in the article/Supplementary Material; further inquiries can be directed to the corresponding authors.

AUTHOR CONTRIBUTIONS

LW designed this project. PM and JZ carried out most of the experiments and data analysis. QW performed part of the experiments and helped with discussions during manuscript preparation. All authors have read and agreed to the published version of the manuscript.

FUNDING

This research was funded by the Key Projects of the Second Batch of Social Welfare and Basic Research in Zhongshan City (No. 2020B2021), the High-level Scientific Research Startup Project in Zhongshan Polytechnic (No. KYG2104), and the Special Projects in Key Fields of Colleges and Universities in Guangdong Province in 2020 (No. 2020ZDZX3083).

REFERENCES

1. Heikenfeld J, Drzaic P, Yeo J-S, and Koch T. Review Paper: A Critical Review of the Present and Future Prospects for Electronic Paper. *J Soc Inf Display* (2011) 19(2):129–56. doi:10.1889/JSID19.2.129
2. Meng X, Wen T, Qiang L, Ren J, and Tang F. Luminescent Electrophoretic Particles via Miniemulsion Polymerization for Night-Vision Electrophoretic Displays. *ACS Appl Mater Inter* (2013) 5(9):3638–42. doi:10.1021/am400103d
3. Lee J-K, Kim S-S, Park Y-I, Kim C-D, and Hwang Y-K. In-cell Adaptive Touch Technology for a Flexible E-Paper Display. *Solid-state Electron* (2011) 56(1): 159–62. doi:10.1016/j.sse.2010.10.008
4. Yi Z, Huang Z, Lai S, He W, Wang L, and Chi F. Driving Waveform Design of Electrowetting Displays Based on an Exponential Function for a Stable Grayscale and a Short Driving Time. *Micromachines* (2020) 11(3):313. doi:10.3390/mi11030313
5. Kao W-C, Wu G-F, Shih Y-L, Chang W-T, Lin F-S, and Hsieh Y-J. Design of Real-Time Image Processing Engine for Electrophoretic Displays. *J Display Technol* (2011) 7(10):556–61. doi:10.1109/JDT.2011.2159360
6. Li W, Wang L, Zhang T, Lai S, Liu L, and He W. Driving Waveform Design with Rising Gradient and Sawtooth Wave of Electrowetting Displays for Ultra-low Power Consumption. *Micromachines* (2020) 11(2):145. doi:10.3390/mi11020145
7. Bai PF, Hayes RA, Jin M, Shui L, Yi ZC, and Wang L. Review of Paper-Like Display Technologies (Invited Review). *Prog Electromagn Res C* (2014) 147: 95–116. doi:10.2528/PIER13120405
8. Zeng W, Yi Z, Zhao Y, Zeng W, Ma S, and Zhou X. Design of Driving Waveform Based on Overdriving Voltage for Shortening Response Time in Electrowetting Displays. *Front Phys* (2021) 9:642682. doi:10.3389/fphy.2021.642682
9. Kao W-C, Liu C-H, Liou S-C, Tsai J-C, and Hou G-H. Towards Video Display on Electronic Papers. *J Display Technol* (2016) 12(2):129–35. doi:10.1109/JDT.2015.2469539
10. Yi Z, Feng H, Zhou X, and Shui L. Design of an Open Electrowetting on Dielectric Device Based on Printed Circuit Board by Using a Parafilm M. *Front Phys* (2020) 8:193. doi:10.3389/fphy.2020.00193
11. Kao W-C. Electrophoretic Display Controller Integrated with Real-Time Halftoning and Partial Region Update. *J Display Technol* (2010) 6(1):36–44. doi:10.1109/JDT.2009.2030774
12. Yi Z, Zeng W, Ma C, Feng H, Yang J, and Liu L. A Real-time Touch Control System Design Based on Field-programmable Gate Array via Optimizing Bresenham Algorithm for Electrowetting Displays. *J Soc Inf Display* (2021) 29: 573–83. doi:10.1002/jsid.1001
13. Kao W-C, Chen H-Y, Liu Y-H, and Liou S-C. Hardware Engine for Supporting Gray-Tone Paintbrush Function on Electrophoretic Papers. *J Display Technol* (2014) 10(2):138–45. doi:10.1109/JDT.2013.2289364

14. Lu C-M, and Wey C-L. A Controller Design for Micro-Capsule Active Matrix Electrophoretic Displays. *J Display Technol* (2011) 7(8):434–42. doi:10.1109/JDT.2011.2142173
15. Yi Z, Zeng W, Ma S, Feng H, Zeng W, and Shen S. Design of Driving Waveform Based on a Damping Oscillation for Optimizing Red Saturation in Three-Color Electrophoretic Displays. *Micromachines* (2021) 12(2):162. doi:10.3390/mi12020162
16. Yang S-H, Lin F-C, Huang Y-P, Shieh H-PD, Yang B-R, and Chang M-J. P-83: Ghosting Reduction Driving Method in Electrophoretic Displays. *SID Int Symp Dig Tech Pap* (2012) 43(1):1361–4. doi:10.1002/j.2168-0159.2012.tb06057.x
17. Yi Z, Liu L, Wang L, Li W, Shui L, and Zhou G. A Driving System for Fast and Precise Gray-Scale Response Based on Amplitude-Frequency Mixed Modulation in TFT Electrowetting Displays. *Micromachines* (2019) 10(11):732. doi:10.3390/mi10110732
18. Li WC, and Keh HJ. Electrophoretic Mobility of Charged Porous Shells or Microcapsules and Electric Conductivity of Their Dilute Suspensions. *Colloids Surf A: Physicochemical Eng Aspects* (2016) 497:154–66. doi:10.1016/j.colsurfa.2016.02.028
19. Wang L, Yi Z, Jin M, Shui L, and Zhou G. Improvement of Video Playback Performance of Electrophoretic Displays by Optimized Waveforms with Shortened Refresh Time. *Displays* (2017) 49:95–100. doi:10.1016/j.displa.2017.07.007
20. Yi Z, Feng W, Wang L, Liu L, Lin Y, and He W. Aperture Ratio Improvement by Optimizing the Voltage Slope and Reverse Pulse in the Driving Waveform for Electrowetting Displays. *Micromachines* (2019) 10(12):862. doi:10.3390/mi10120862
21. Kao W-C, Chang W-T, and Ye J-A. Driving Waveform Design Based on Response Latency Analysis of Electrophoretic Displays. *J Display Technol* (2012) 8(10):596–601. doi:10.1109/JDT.2012.2205896
22. Wang Z, and Liu Z. The Key Technology of Ereader Based on Electrophoretic Display. In: 2010 2nd International Conference on Software Technology and Engineering, San Juan, PR, October 3-5, 2010 (2010). 333–6. doi:10.1109/ICSTE.2010.5608873
23. Shen S, Gong Y, Jin M, Yan Z, Xu C, and Yi Z. Improving Electrophoretic Particle Motion Control in Electrophoretic Displays by Eliminating the Fringing Effect via Driving Waveform Design. *Micromachines* (2018) 9(4):143. doi:10.3390/mi9040143
24. Zeng W, Yi Z, Zhou X, Zhao Y, Feng H, and Yang J. Design of Driving Waveform for Shortening Red Particles Response Time in Three-Color Electrophoretic Displays. *Micromachines* (2021) 12(5):578. doi:10.3390/mi12050578
25. Yi Z-C., Bai P-F., Wang L, Zhang X, and Zhou G-F. An Electrophoretic Display Driving Waveform Based on Improvement of Activation Pattern. *J Cent South Univ* (2014) 21(8):3133–7. doi:10.1007/s11771-014-2285-9
26. He W, Yi Z, Shen S, Huang Z, Liu L, and Zhang T. Driving Waveform Design of Electrophoretic Display Based on Optimized Particle Activation for a Rapid Response Speed. *Micromachines* (2020) 11(5):498. doi:10.3390/mi11050498
27. Duan F, Bai P, Henzen A, and Zhou G. Driving Waveform Optimization in electrophoretic Display Based on DC-balance. *Chin J Liquid Crystals Displays* (2016) 31(10):943–8. doi:10.3788/YJYXS20163110.0943
28. Bert T, and De Smet H. Dielectrophoresis in Electronic Paper. *Displays* (2003) 24(4-5):223–30. doi:10.1016/j.displa.2004.01.009
29. Kang H-L, Kim CA, Lee S-I, Shin Y-K, Lee Y-H, and Kim Y-C. Analysis of Particle Movement by Dielectrophoretic Force for Reflective Electronic Display. *J Display Technol* (2016) 12(7):747–52. doi:10.1109/JDT.2016.2524023
30. Crowder TM, Rosati JA, Schroeter JD, Hickey AJ, and Martonen TB. Fundamental Effects of Particle Morphology on LungDelivery: Predictions of Stokes'Law and the Particular Relevance to Dry Powder Inhaler Formulation and Development. *Pharm Res* (2002) 19(3):239–45. doi:10.1023/A:1014426530935
31. He W, Yi Z, Shen S, Huang Z, Liu L, and Zhang T. Driving Waveform Design of Electrophoretic Display Based on Optimized Particle Activation for a Rapid Response Speed. *Micromachines* (2020) 11(5):498. doi:10.3390/mi11050498

Conflict of Interest: The authors declare that the research was conducted in the absence of any commercial or financial relationships that could be construed as a potential conflict of interest.

ORIGINAL RESEARCH
published: 12 August 2021
doi: 10.3389/fphy.2021.737336

An Improved Sum of Squared Difference Algorithm for Automated Distance Measurement

Yue Lin, Yixun Gao and Yao Wang*

Guangdong Provincial Key Laboratory of Optical Information Materials and Technology and Institute of Electronic Paper Displays, South China Academy of Advanced Optoelectronics, South China Normal University, Guangzhou, China

In recent years, with improvement of photoelectric conversion efficiency and accuracy, photoelectric sensor was arranged to simulate binocular stereo vision for 3D measurement, and it has become an important distance measurement method. In this paper, an improved sum of squared difference (SSD) algorithm which can use binocular cameras to measure distance of vehicle ahead was proposed. Firstly, consistency matching calibration was performed when images were acquired. Then, Gaussian blur was used to smooth the image, and grayscale transformation was performed. Next, the Sobel operator was used to detect the edge of images. Finally, the improved SSD was used for stereo matching and disparity calculation, and the distance value could be obtained corresponding to each point. Experimental results showed that the improved SSD algorithm had an accuracy rate of 95.06% when stereo matching and disparity calculation were performed. This algorithm fully meets the requirements of distance measurement.

Keywords: sum of squared difference, photoelectric sensor, distance measurement, binocular cameras, stereo matching

Edited by:
Feng Chi,
University of Electronic Science and Technology of China Zhongshan Institute, China

Reviewed by:
Xue wei cheng,
Jiangsu Broadcasting Corporation, China
Peng Bao,
Shenzhen Institute of Information Technology, China

***Correspondence:**
Yao Wang
wangyao@m.scnu.edu.cn

Specialty section:
This article was submitted to Optics and Photonics, a section of the journal Frontiers in Physics

***Received:** 06 July 2021*
***Accepted:** 02 August 2021*
***Published:** 12 August 2021*

Citation:
Lin Y, Gao Y and Wang Y (2021) An Improved Sum of Squared Difference Algorithm for Automated Distance Measurement. Front. Phys. 9:737336. doi: 10.3389/fphy.2021.737336

INTRODUCTION

A photoelectric sensor is a semiconductor device which can convert light signals into electrical signals based on photoelectric effect. Photoelectric effect means that the energy of photons was absorbed by electrons of material when light is irradiated on materials, and then corresponding electric effect occurs. Photoelectric sensors were widely used in detection field because it has advantages of short response time, long detection distance and high resolution [1].

In recent years, three-dimensional measurement has been carried out by arranging photoelectric sensors to simulate binocular stereo vision. This method has the advantages of long detection distance, recognizable color, and wide application range. It has become an important distance measurement method. Binocular stereo vision is also an application of machine vision. It uses left and right cameras to imitate human left and right eyes. Based on the parallax principle, the imaging device is used to obtain two images of the measured object from different positions, and the three-dimensional geometric information of the object is obtained by calculating the position deviation between corresponding points of an image [2]. Binocular camera sensor ranging method has gradually become the most common stereo ranging method [3, 4]. Therefore, in order to match different parts at the same time, a real-time binocular stereo vision system which used Field Programmable Gate Array (FPGA) for full line design was proposed to improve the processing speed [5]. This algorithm took advantage of parallel computing and fast operation speed in FPGA, but the versatility was poor and targeted program development was needed. Then, high and low texture scenes were processed separately, a time of flight (TOF) depth camera was used to measure the low texture scene, and a binocular camera was used to measure the high-resolution scene, so as to improve the accuracy of three-dimensional measurement [6]. It needed to equip with TOF sensors, and the hardware design was complicated. In addition, in two sets of binocular vision systems with different accuracy levels, the method of triangulation analysis and spatial plane fitting were proposed to calculate relative poses [7]. This algorithm had a higher accuracy than other methods, but it required four cameras, which had a high cost. And algorithms that recognize objects first was proposed. For example, Canny edge detection was used to extract the target contour in order to determine the three-dimensional coordinates of the target [8]. Likewise, precise position of the target was used to determine robustness of the ellipse fitting strategy after located its approximate area [9]. And Canny edge detection based on binocular vision was used to identify and locate the target [10]. But these algorithms cannot be applied to other occasions. Then, roll angles of the binocular measurement system were calculated to compensate for dynamic measurement errors by installing a tilt angle sensor horizontally [11]. This algorithm required additional sensors to assist in attitude detection, which could increase the complexity of the system. And then a method based on the parallel binocular vision system and similarity judgment function was established by using cluster analysis method, and the distance was calculated by combining features of gradient histogram and cascade classifier [12]. This method had high a computational complexity and a slow operation speed. And combined with polar line matching, the Multi-line centerline detection stereo matching method was proposed for distance estimation [13]. This algorithm required multiple mathematical model conversions, which was not conducive to the real-time performance of the system.

Therefore, we proposed the improved SSD algorithm for automated distance measurement. It could improve the accuracy of automated distance measurement. The algorithm mainly includes five algorithms: gray-scale transformation, Gaussian Blur transformation, edge detection by Sobel operator, model of a binocular stereo camera, improved Sum of Squared Difference. It can accurately perform stereo matching and distance measurement.

SYSTEM DESIGN PRINCIPLE

Gray-Scale Transformation

In order to reduce the amount of calculation and improve the real-time performance, the image data is grayscale transformed. Grayscale transformation is a combination of three channel gray value calculation. According to the importance of three primary colors, three components of RGB are weighted and averaged with different weights, **Eq. 1** can obtain a grayscale image [14], where i and j represent coordinates of horizontal and vertical of images, $R(i, j)$, $G(i, j)$ and $B(i, j)$ respectively represent components of a points in row i and column j of three primary colors.

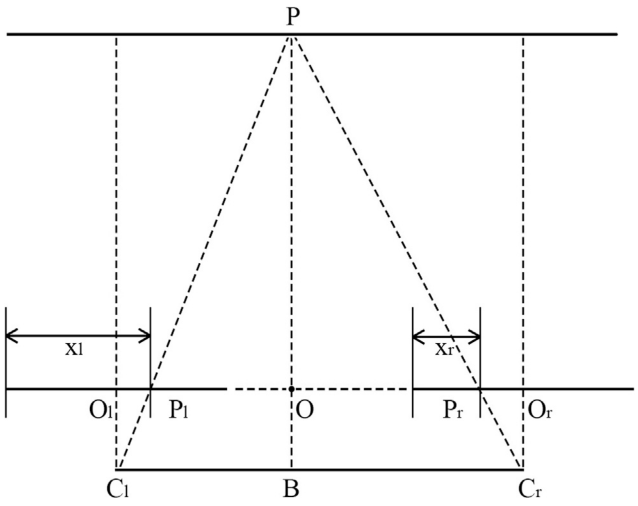

FIGURE 1 | | Parallax distance similar triangle calculation model diagram.

$$f(i,j) = 0.299 * R(i,j) + 0.587 * G(i,j) + 0.114 * B(i,j) \quad (1)$$

Gaussian Blur Transformation

Before edge detection, the image is filtered and denoised. It can reduce the interference of the original noise on edge detection. Therefore, Gaussian blur transformation is used to reduce the level of image detail and noise interference, so that images can become smoother and easier to perform stereo matching [15, 16]. Gaussian Blur transformation is defined as **Eq. 2**, where u is abscissa of pixel, v is ordinate of pixel, σ is blur radius, and it is standard deviation of normal distribution.

$$G(u,v) = \frac{1}{2\pi\sigma^2} e^{-\left(u^2+v^2\right)/\left(2\sigma^2\right)} \quad (2)$$

Edge Detection by Sobel Operator

The surface of some objects is smooth, whose features are not obvious. And stereo matching may be affected seriously. In order to obtain a high-level feature and improve the accuracy of stereo matching, the first derivative Sobel operator can be used to perform gradient extraction operation of spatial convolution. And edge can be extracted from the image to make the feature more obvious [17, 18], the Sobel operator is shown in **Eq. 3**, where I is original image, G_x and G_y are Convolution factor of longitudinal and horizontal axis direction.

$$\begin{aligned} G &= \sqrt{(G_x * I)^2 + \left(G_y * I\right)^2} \\ &= \sqrt{\begin{bmatrix} -1 & 0 & +1 \\ -2 & 0 & +2 \\ -1 & 0 & +1 \end{bmatrix}^2 * I^2 + \begin{bmatrix} -1 & 2 & -1 \\ 0 & 0 & 0 \\ +1 & +2 & +1 \end{bmatrix}^2 * I^2} \end{aligned} \quad (3)$$

Model of the Binocular Stereo Camera

The depth of an object refers to the distance between the camera and object. It is measured for distance by ultrasonic, laser, etc. But these methods can only measure a specific point. We measured distance by arranging left and right cameras to simulate parallax of the image, which can be obtained by human binocular. Binocular parallax is a position difference of imaging pixel coordinates in left and right cameras. Therefore, stereo matching can be performed on images which are obtained by the left and right cameras. Cost calculation can obtain three-dimensional information of each point in an image in the real scene [19, 20]. This algorithm uses the principle of similar triangles to construct a parallax distance calculation model. The model is shown in **Figure 1**.

Among them, C_l and C_r are left and right camera sensors respectively, and O_l and O_r are corresponding focal points. P is a point to be measured, P_l and P_r are imaging points on a camera lens, and x_l and x_r are corresponding offset pixel point distances respectively. B is a baseline of left and right cameras, that is, the distance between C_l and C_r. Triangle PP_lO and $C_lO_lP_l$ are similar triangles, so are PP_rO and $C_rO_rP_r$. And triangles PP_lP_r and PC_lC_r are also similar triangles, so **Eq. 4** can be obtained, where Z is the distance from the image sensor to the target object, which is a distance value from point P to baseline B, f is the focal length of the camera, x_l is the abscissa of the image on left, and x_r is the ordinate of the image on left.

$$\frac{Z}{B} = \frac{Z - f}{B - (x_l - x_r)} \tag{4}$$

The available distance between the image sensor to the target object is shown in **Eq. 5**.

$$Z = \frac{Bf}{x_l - x_r} \tag{5}$$

Improved Sum of Squared Difference

Stereo matching cost calculation can be used to compare similarity between a certain area of an image and a certain area of another image. Common stereo matching algorithms include Sum of Absolute Difference (SAD), Sum of Squared Difference (SSD), Normalization Cross- Correlation (NCC), Census, etc [21–23]. Among these algorithms, SSD has lowest implementation complexity, but the matching accuracy is relatively poor. So we optimized the basis of SSD and proposed an improved SSD, which can improve matching accuracy and maintain original lightweight calculation at the same time.

The improved Sum of Squared Difference is shown in **Eq. 6**, where I_l is left image, I_r is the right image, c is the center area of target window, r is edge area of target window, and d is target window in coordinate difference between left image and right image, x is left horizontal axis, y is coordinate vertical axis, and a is weight coefficient.

$$\begin{aligned} ISSD(x, y, d) = &\sum_{(x,y)\in c} \left[I_l(x, y) - I_r(x - d, y)\right]^2 \\ &+ a * \sum_{(x,y)\in r} \left[I_l(x, y) - I_r(x - d, y)\right]^2 \end{aligned} \tag{6}$$

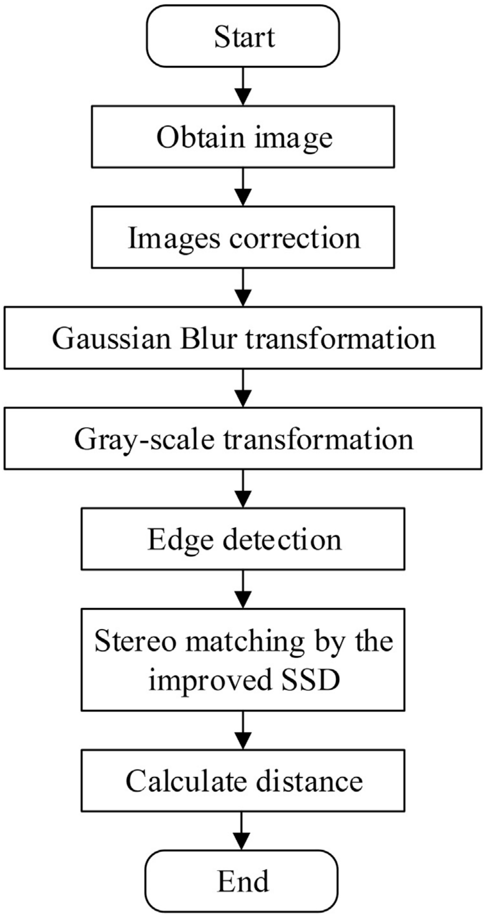

FIGURE 2 | | System processing flow chart.

EXPERIMENT AND DISCUSSION

The platform was equipped with a left camera and a right camera. Before acquiring images, it was necessary to match parameters of the binocular camera, and obtain the correction matrix parameters between left and right cameras to keep them consistent. During the measurement, two frames of images were obtained by each camera at the same time, and parameters of images were calibrated. Then Gaussian blur was used to smooth image, gray scale transformation was performed and Sobel operator was used for edge detection. Finally, improved SSD was used to perform stereo matching and disparity calculation on a target image, and then the distance value could be obtained corresponding to each point, which was combined into a distance value matrix. The specific processing flowchart of system is shown in **Figure 2**.

System Hardware Architecture

The experimental platform is shown in **Figure 3**. Embedded computer Raspberry Pi 4B was used as the main processor to build an experimental platform. An ARM Cortex-A72 quad-core processor with a main frequency of 1.5 GHz was used with

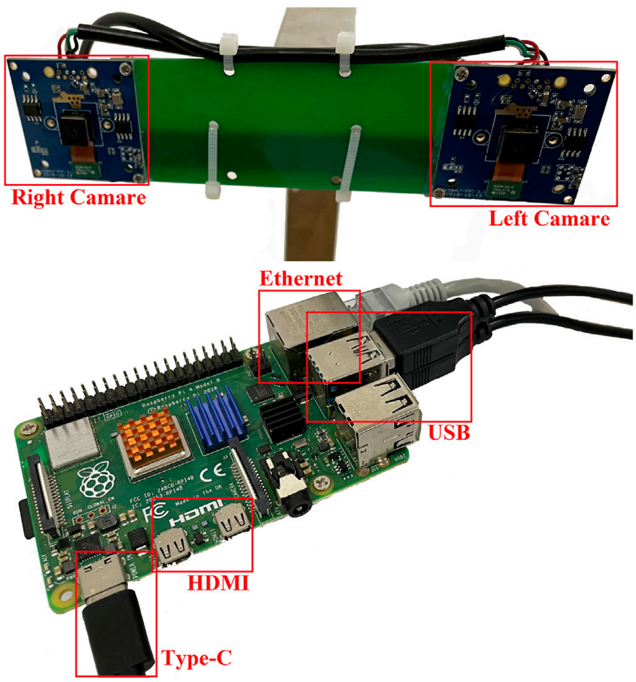

FIGURE 3 | | Physical image of the experimental platform. The one on the left was embedded computer Raspberry Pi 4B with USB ports, Ethernet port, HDMI interface and Type-C interface. On the right was the binocular camera with a bracket. The left and right cameras were distributed on it.

Raspberry Pi 4B. It was equipped with 2 GB of LPDDR4 memory, it also had two USB 3.0 ports and two USB 2.0 ports, two external micro HDMI ports and a gigabit Ethernet port. It can be directly powered by a USB Type-C port with 5 V. The operating system was UBUNTU18.04, PYTHON3.7, and OPENCV2.0 environments were deployed. The image sensor was composed of two left and right cameras placed in parallel, and the space was 10 cm between the left and right cameras, which was called a center baseline. The camera was connected to the laptop by USB ports. The camera used a low-sensitivity Sony high-speed CMOS camera with a resolution of 1,920*1,080 pixels and it could obtain 60 frames of images per second. In order to reduce the difficulty of stereo matching, two cameras were guaranteed on the same horizontal line, and the inclination of the horizontal plane was set to be consistent.

Image Preprocessing

Image preprocessing mainly included image correction, Gaussian smoothing, and grayscale transformation. Pre-calibrated differential parameters of the left and right camera were applied for image correction, so that initial coordinates of the left and right image were consistent. The transformation effect is shown in **Figure 4**. We could draw a red straight line on the image. It could be seen from the part in the yellow box, the left car light before calibration was completely above the red line in the left image, but there was still a small part below the red line in the right image. Moreover, the left car light was relatively close to the red line in the left and right images after calibration. And pixels with the same feature were almost in the same row on the left and right images. That was a prerequisite for stereo matching to improve accuracy, which was conducive to subsequent accurate feature matching.

Then, Gaussian smoothing was performed for the image. All noise must be filtered on the image so that the image level was excessively relaxed, and the influence of noise on subsequent stereo matching was reduced. The license plate area was used as an example, the transformation effect is shown in **Figure 5**. After Gaussian smooth transformation, the gradient of the image was smoother, the sense of hierarchy was reduced, and the feature difference between the left and right cameras, which was caused by different viewing angles, was reduced. Then, it was easier to perform stereo matching and improve matching accuracy.

Finally, the grayscale transformation was performed to reduce the amount of calculation for stereo matching. By mixing RGB channels in proportions, two-dimensional matrix data was generated, the original features of the image were retained as much as possible when the amount of data was reduced.

Edge Extraction

Some objects in an image had a smooth surface. For example, there is a slight reflection on the body surface. Due to the reflection, the image appears to lack texture features. Unobvious features would lead to inaccurate matching results and low stereo matching recognition rate. In order to highlight the details of the smooth part, edge extraction was performed on the image. Gradient operations were performed on the vertical and horizontal directions of the image, which could magnify the small edge changes of inconspicuous texture surface, and the advanced features of smooth part were highlighted on the image. The transformation effect is shown in **Figure 6**. It could be seen that the processed image had obvious features in the areas near the license plate and the lower part of a car body. The original smooth surface had gradient edge features, so the accuracy of stereo matching could be improved with their inconspicuous textures, and the stereo matching recognition rate could be also improved.

Stereoscopic Matching of Left and Right Photos

Stereo matching was the most critical step of this algorithm. The same feature areas of the left and right images were matched. It meant that the feature recognition of the left image was performed on the same horizontal line in the right image. After calculation, it could find out the area with the highest similarity to the left image. According to the horizontal coordinate migration of the same feature, the depth value of the feature area could be calculated. The migration was the distance value from the baseline to objects. The recognition accuracy of stereo matching determined the ranging accuracy. Compared with other stereo matching algorithms, the gray value of the pixel in

FIGURE 4 | | Comparison images of correction. **(A)** is the left image before calibration, and **(B)** is the right image before calibration. **(C)** is the left image after calibration, and **(D)** is the right image after calibration.

FIGURE 5 | | Comparison images of Gaussian Blur Transform in the license plate area. **(A)** was the image before transformation, and **(B)** was the image after transformation.

FIGURE 6 | | Comparison images of edge detection. **(A)** was the original image, and **(B)** was the effect image after edge detection by using the SOBEL operator.

the corresponding area was distinguished, and then the absolute value of the result was obtained by using the improved SSD. So that the matching of the central region played a more important and dominant role in the whole

TABLE 1 | Measurement results.

Distance (m)	0.5	1	1.5	2	2.5	3	3.5	4	4.5	5
Ours (m)	0.51	1.03	1.55	2.09	2.63	3.17	3.7	4.24	4.8	5.37
Du Jiang's (m)	0.48	0.95	1.41	1.88	2.34	2.8	3.26	3.72	4.16	4.58
Gap (%)	2.00	2.00	2.67	1.50	1.20	1.00	1.14	1.00	0.89	1.00

The first line was the actual distance between binocular camera and target, the second line was measurement distance by using improved SSD algorithm, the third line was measurement distance of the comparison algorithm, the unit was meter. The fourth line was the actual accuracy difference between our algorithm and the comparison algorithm, the unit was a percentage.

matching results. In order to verify the accuracy and performance of our algorithm, an experimental platform was used to control the binocular camera at a specific distance from the target, and image acquisition was performed. Then, Du Jiang et al. proposed the binocular matching (BM) algorithm which run at the same time to record the data [24]. Measurement results were shown in **Table 1**. It can be seen that the actual measurement accuracy of the improved SSD algorithm was 95.06% on average. It was 1.44% higher than the comparison algorithm. So, it had a higher accuracy and smaller accuracy error fluctuations, which meets actual measurement requirements.

CONCLUSION

In this paper, an algorithm, which could configure the left and right cameras, to obtain images from different angles of the target was proposed. The images were smoothed to reduce noise, and grayscale transformation was performed to reduce stereo matching operations. Then, corresponding area pixels were matched on the same horizontal line of the right image. The absolute value of the degree was made difference and then summed, and the central key area was weighted, and the matching of the central area played a more important role in entire matching results. The algorithm improved the matching accuracy and could obtain measurement results more accurately, which fully met the requirements of distance measurement.

DATA AVAILABILITY STATEMENT

The original contributions presented in the study are included in the article/supplementary material, further inquiries can be directed to the corresponding author.

AUTHOR CONTRIBUTIONS

YW and YL designed this project. YL carried out most of the experiments and data analysis. YG performed part of the experiments and helped with discussions during manuscript preparation. YW and YL contributed to the data analysis and correction and provided helpful discussions on the experimental results. All authors have read and agreed to the published version of the manuscript.

FUNDING

This research was funded by Science and Technology Program of Guangzhou (No. 2019050001), Program for Chang Jiang Scholars and Innovative Research Teams in Universities (No. IRT_17R40), National Natural Science Foundation of China (Grant No. 51973070), Guangdong Basic and Applied Basic Research Foundation (No. 2021A1515012420), Innovative Team Project of Education Bureau of Guangdong Province, Startup Foundation from SCNU, Guangdong Provincial Key Laboratory of Optical Information Materials and Technology (No. 2017B030301007) and the 111 Project.

REFERENCES

1. Yi Z-C, Chen Z-B, Peng B, Li S-X, Bai P-F, Shui L-L, et al. Vehicle Lighting Recognition System Based on Erosion Algorithm and Effective Area Separation in 5G Vehicular Communication Networks. *IEEE Access* (2019) 7:111074–83. doi:10.1109/ACCESS.2019.2927731
2. Liu Y, Wang H, Dong C, and Chen Q. A Car-Following Data Collecting Method Based on Binocular Stereo Vision. *IEEE ACCESS* (2020) 8:25350–63. doi:10.1109/ACCESS.2020.2965833
3. Zhou Y, Li Q, Chu L, Ma Y, and Zhang J. A Measurement System Based on Internal Cooperation of Cameras in Binocular Vision. *Meas Sci Technol* (2020) 31(6):065002. doi:10.1088/1361-6501/ab6ecd
4. Wang Q, Wang Z, Yao Z, Forrest J, and Zhou W. An Improved Measurement Model of Binocular Vision Using Geometrical Approximation. *Meas Sci Technol* (2016) 27(12):125013. doi:10.1088/0957-0233/27/12/125013
5. Ma J, Yin W, Zuo C, Feng S, and Chen Q. Real-time Binocular Stereo Vision System Based on FPGA. In: *2018 Optical & Photonic Engineering*. Shanghai: ICOPEN (2018). doi:10.1117/12.2500769
6. Yang Y, Meng X, and Gao M. Vision System of Mobile Robot Combining Binocular and Depth Cameras. *J Sensors* (2017) 2017:1–11. doi:10.1155/2017/4562934
7. Chen Y, Zhou F, Zhou M, Zhang W, and Li X. Pose Measurement Approach Based on Two-Stage Binocular Vision for Docking Large Components. *Meas Sci Technol* (2020) 31(12):125002. doi:10.1088/1361-6501/aba5c7
8. Han Y, Zhao K, Chu Z, and Zhou Y. Grasping Control Method of Manipulator Based on Binocular Vision Combining Target Detection and Trajectory Planning. *IEEE Access* (2019) 7:167973–81. doi:10.1109/ACCESS.2019.2954339
9. Han Y, Chu Z, and Zhao K. Target Positioning Method in Binocular Vision Manipulator Control Based on Improved Canny Operator. *Multimed Tools Appl* (2020) 79(13-14):9599–614. doi:10.1007/s11042-019-08140-9

10. Wan G, Li F, Zhu W, and Wang G. High-precision Six-Degree-Of-freedom Pose Measurement and Grasping System for Large-Size Object Based on Binocular Vision. *Sr* (2020) 40(1):71–80. doi:10.1108/SR-05-2019-0123
11. Cai C, Qiao R, Meng H, and Wang F. A Novel Measurement System Based on Binocular Fisheye Vision and its Application in Dynamic Environment. *IEEE Access* (2019) 7:156443–51. doi:10.1109/ACCESS.2019.2949172
12. Zhang S, Li B, Ren F, and Dong R. High-Precision Measurement of Binocular Telecentric Vision System with Novel Calibration and Matching Methods. *IEEE Access* (2019) 7:54682–92. doi:10.1109/ACCESS.2019.2913181
13. Yu X, Liu S, Pang M, Zhang J, and Yu S. Novel SGH Recognition Algorithm Based Robot Binocular Vision System for Sorting Process. *J Sensors* (2016) 2016:1–8. doi:10.1155/2016/5479152
14. Wen K, Li D, Zhao X, Fan A, Mao Y, and Zheng S. "Lightning Arrester Monitor Pointer Meter and Digits Reading Recognition Based on Image Processing," In Proceedings of 2018 IEEE 3rd Advanced Information Technology, Electronic and Automation Control Conference; Chongqing. IEEE (2018). doi:10.1109/iaeac.2018.8577545
15. Kostková J, Flusser J, Lébl M, and Pedone M. Handling Gaussian Blur without Deconvolution. *Pattern Recognition* (2020) 103:107264. doi:10.1016/j.patcog.2020.107264
16. Zhao F, Zhao J, Han X, Wang H, and Liu B. Robust Image Reconstruction Enhancement Based on Gaussian Mixture Model Estimation. *J Electron Imaging* (2016) 25(2):023007. doi:10.1117/1.JEI.25.2.023007
17. Yang SH, and Hsiao SJ. H.266/VVC Fast Intra Prediction Using Sobel Edge Features. *Electron Lett* (2020) 57:11–3. doi:10.1049/ell2.12011
18. Joe H, and Kim Y. Compact and Power-Efficient Sobel Edge Detection with Fully Connected Cube-Network-Based Stochastic Computing. *Jsts* (2020) 20(5):436–46. doi:10.5573/JSTS.2020.20.5.436
19. Liu Z, Liu X, Duan G, and Tan J. Precise Pose and Radius Estimation of Circular Target Based on Binocular Vision. *Meas Sci Technol* (2019) 30(2):025006. doi:10.1088/1361-6501/aaf8c8
20. Jiang J, Liu L, Fu R, Yan Y, and Shao W. Non-horizontal Binocular Vision Ranging Method Based on Pixels. *Opt Quant Electron* (2020) 52(4):52. doi:10.1007/s11082-020-02343-3
21. Wang Z, Yue J, Han J, Jin Y, and Li B. Regional Fuzzy Binocular Stereo Matching Algorithm Based on Global Correlation Coding for 3d Measurement of Rail Surface. *Optik* (2020) 207:164488. doi:10.1016/j.ijleo.2020.164488
22. Vazquez-Delgado HD, Perez-Patricio M, Aguilar-Gonzalez A, Arias-Estrada MO, Palacios-Ramos MA, Camas-Anzueto JL, et al. Real-time Multi-Window Stereo Matching Algorithm with Fuzzy Logic. *IET Comp Vis* (2021) 15(3):208–23. doi:10.1049/cvi2.12031
23. Zhang B, and Zhu D. Local Stereo Matching: an Adaptive Weighted Guided Image Filtering-Based Approach. *Int J Patt Recogn Artif Intell* (2021) 35(3):2154010. doi:10.1142/S0218001421540100
24. Jiang D, Zheng Z, Li G, Sun Y, Kong J, Jiang G, et al. Gesture Recognition Based on Binocular Vision. *Cluster Comput* (2019) 22:13261–71. doi:10.1007/s10586-018-1844-5

Conflict of Interest: The authors declare that the research was conducted in the absence of any commercial or financial relationships that could be construed as a potential conflict of interest.

ORIGINAL RESEARCH
published: 13 August 2021
doi: 10.3389/fphy.2021.731851

Improvement of the High-Performance Al-Doped $LiNi_{1/3}Co_{1/3}Mn_{1/3}O_2$ Cathode Material for New Electro-Optical Conversion Devices

Yumei Gao, Wangran Yuan and Xinqi Dou*

College of Electron and Information, Zhongshan Institute, University of Electronic Science and Technology of China, Zhongshan, China

The ternary cathode material $LiNi_{1/3}Co_{1/3}Mn_{1/3}O_2$ has been extensively focused on as the power sources for new electro-optical conversion devices and lithium-ion batteries. To improve the electrochemical performance, Al doping is one of the effective strategies. Based on the density functional theory of first-principles, the band gap, volume, partial density of states, lithiation formation energy, electron density difference, and electrons' potential energy of $Li_{1.0\text{-}x}Al_xNi_{1/3}Co_{1/3}Mn_{1/3}O_2$ were simulated and analyzed with Materials Studio, Nanodcal and Matlab. Results show that $Li_{0.9}Al_{0.1}Ni_{1/3}Co_{1/3}Mn_{1/3}O_2$ has a better conductivity and cycling capability. The potential energy maps of $Li_{1.0\text{-}x}Al_xNi_{1/3}Co_{1/3}Mn_{1/3}O_2$ simulated in Matlab indicate that the rate capability of $LiNi_{1/3}Co_{1/3}Mn_{1/3}O_2$ is promoted after Al doping. Our theoretical advice could be an important choice for the power application of new optoelectronic devices. In addition, our methods could provide some theoretical guidance for the subsequent electrochemical performance investigations on doping of optoelectronic devices or lithium-ion battery materials.

Keywords: density functional theory, $Li_{1.0\text{-}x}Al_xNi_{1/3}Co_{1/3}Mn_{1/3}O_2$, conductivity, rate capability, electro-optical conversion devices

Edited by:
Qiang Xu,
Nanyang Technological University, Singapore

Reviewed by:
Hongdong Liang,
Guangzhou University, China
Qiming Zhu,
Guangxi University for Nationalities, China

****Correspondence:***
Yumei Gao
yumeigao5697@163.com

Specialty section:
This article was submitted to Optics and Photonics, a section of the journal Frontiers in Physics

Received: *28 June 2021*
Accepted: *27 July 2021*
Published: *13 August 2021*

Citation:
Gao Y, Yuan W and Dou X (2021) Improvement of the High-Performance Al-Doped $LiNi_{1/3}Co_{1/3}Mn_{1/3}O_2$ Cathode Material for New Electro-Optical Conversion Devices. Front. Phys. 9:731851. doi: 10.3389/fphy.2021.731851

INTRODUCTION

In recent years, rechargeable lithium-ion batteries (LIBs) are the leading power sources for new electro-optical conversion devices, portable electronic devices, electric vehicles and hybrid electric vehicles for their less pollution, good cycle property, no memory effect, high energy density, and high specific capacity at high voltage (4.5 V) [1]. In fact, the specific capacity of commercial cathode materials of LIBs is far lower than that of the anode. With the growing demand for the increasing energy and power densities, conventional cathode materials such as $LiCO_2$ and spinel $LiMn_2O_4$ are not satisfied with the new generation power sources. Moreover, the cathode's cost is much higher than that of the anode. Therefore, it is a major challenge to pursuit the appropriate cathode material for the power module of electro-optical conversion devices or LIBs.

Nowadays, the layered ternary lithium nickel-cobalt-manganese oxide has been well studied and widely applied into LIBs and the power module of optoelectronic devices for their lower price, good cycle performance and high thermal stability [2]. Among various ternary cathode materials, $LiNi_{1/3}Co_{1/3}Mn_{1/3}O_2$, whose structure likes $LiCoO_2$ with α-$NaFeO_2$-type, is extensively investigated owing

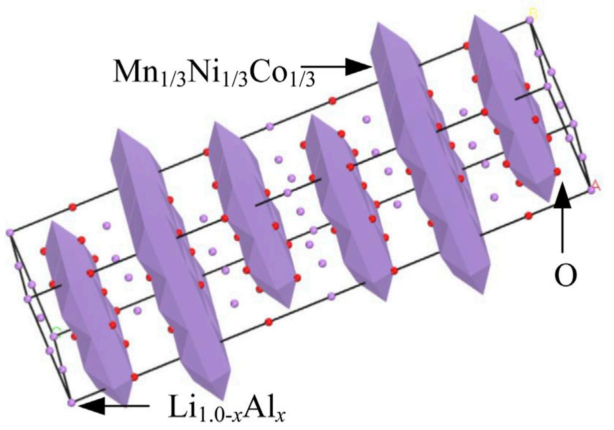

FIGURE 1 | The 2 × 2 × 2 supercell of $Li_{1.0\text{-}x}Al_xNi_{1/3}Co_{1/3}Mn_{1/3}O_2$.

to high reversible capacity, low cost and enhanced thermal stability [3], and it is considered as an attractive candidate of cathode material for LIBs. Its precursors are synthesized by solid state, co-precipitation, sol-gel, hydrothermal synthesis, combustion, and chemical solution [4]. However, its drawbacks, such as low electronic conductivity, poor cycling performance at the high rate, and phase deterioration during the charging/discharging process, have hindered seriously its practical application [5].

To improve the electrochemical properties of $LiNi_{1/3}Co_{1/3}Mn_{1/3}O_2$, many useful strategies, for instance, novel synthesis method [6, 7], morphology control [8, 9], composite cathode [10, 11], surface modification [12, 13], and doping [14–16], had been carried out experimentally. Shao Z C et al [14] reported $LiNi_{1/3}Co_{1/3\text{-}x}Mn_{1/3}O_2$ doped with Al_2O_3 has the enhanced electrochemical properties when x was 5%. Also, Mg-doped (Zhu JP et al [15]) and Na-doped (Li YH et al [16]) cathode materials can keep the crystal structure stable with least capacity loss, their cycling stability and conductivity can be improved much comparison with their pristines. Al^{3+} has the similar outer shell and ionic radius as $Mg^{2+}$and Na^+, hence, Al doping has aroused more attention to improve the electrochemical performance of $LiNi_{1/3}Co_{1/3}Mn_{1/3}O_2$. Kim S et al [17] found that residual Al in Li $[Ni_{1/3}Mn_{1/3}Co_{1/3}]Al_xO_2$ has an adverse effect on capacity and cycle ability when $x > 0.05\%$. Zhang ZH et al [18] claimed that Al doping in the Ni site can inhibit the mixing of cations, $LiNi_{1/3\text{-}0.04}Co_{1/3}Mn_{1/3}Al_{0.04}O_2$ has an excellent reversible discharge capacity. Li ZY [19] synthesized $LiNi_{1/3}Co_{1/3\text{-}x}Al_xMn_{1/3}O_2$ and the experimental results showed that the new Al-doped $LiNi_{1/3}Co_{1/3}Mn_{1/3}O_2$ has a better rate performance and cycling stability; Zhu JP et al [20] prepared the $LiNi_{1/3}Co_{1/3\text{-}x}Al_xMn_{1/3}O_2$ and employed hollow 3D-birdnest-shaped MnO_2 to provide a large amount of free space, measurements revealed this Al-doped cathode material has an outstanding cyclic performance and capacity. Accordingly, the right doping amount of Al^{3+} in $LiNi_{1/3}Co_{1/3}Mn_{1/3}O_2$ can effectively ameliorate the stability of materials during charging/discharging and enhance the electrochemical performance.

To investigate the physical diffusion mechanics of electrons and Li-ions in the crystal lattice, the density functional theory (DFT) based on first-principles is widely employed [21–23]. In this work, Al^{3+} as the doping ion has substituted for Li in $LiNi_{1/3}Co_{1/3}Mn_{1/3}O_2$, and $Li_{1\text{-}x}Al_xNi_{1/3}Co_{1/3}Mn_{1/3}O_2$ had been theoretically simulated and calculated based on DFT by Materials Studio, Nanodcal and Matlab. The more details about the first-principles and DFT were introduced in my previous work [24, 25]. The simulations and calculations indicate that Al-doped $LiNi_{1/3}Co_{1/3}Mn_{1/3}O_2$ has a better electrochemical performance. Our findings can give some theoretical advice about studies of the power module for new electro-optical conversion devices and investigations on LIBs; methods we presented can shorten greatly the whole period of experiments or investigations and reduce the experimental cost [26].

METHODS AND MODEL

Using the exchange-correlation potentials with the generalized gradient approximation [27] of the Perdew-Burke-Ernzerhof [28], calculations about the electronic conductivity of Al-doped $LiNi_{1/3}Co_{1/3}Mn_{1/3}O_2$ were carried out by CAmbridge Serial Total Energy Package (CASTEP) of Materials Studio 8.0, which the plane wave pseudopotential method is used. The interaction between electrons and ions is described by the projector-augmented-wave method [29]. The ultrasoft pseudopotential is used to depict the Coulombic attraction potential between the inner layer electrons around the nucleus and those of the outer layer. All parameters involved in the calculations, including a plane wave cutoff, k-points in the Monkhorst-Pack scheme, the self-consistency energy tolerance, the maximum stress tolerance, the maximum displacement tolerance, and the average force on every atom, were set as same as those in our previous work [24, 25]. The structure geometry should be optimized firstly before calculations.

Figure 1 shows a 2 × 2 × 2 supercell model of $Li_{1.0\text{-}x}Al_xNi_{1/3}Co_{1/3}Mn_{1/3}O_2$ built by virtual mixed atom method. Li and Al occupy 3a, $Ni_{1/3}Co_{1/3}Mn_{1/3}$ occupies 3b, O occupies 6c. In $Li_{1.0\text{-}x}Al_xNi_{1/3}Co_{1/3}Mn_{1/3}O_2$, Li and Al are assumed as 1.0 mol. If Al is x mol, and then Li is 1.0-x mol. The simulations and analyses of $Li_{1.0\text{-}x}Al_xNi_{1/3}Co_{1/3}Mn_{1/3}O_2$ (x = 0.01, 0.02, 0.03, ……, 0.13) are studied as followed.

RESULTS AND DISCUSSION

Band Gap and Partial Density of States

The conductivity is determined by the band gap of materials, the wider band gap means the worst conductivity. The band gaps of $Li_{1.0\text{-}x}Al_xNi_{1/3}Co_{1/3}Mn_{1/3}O_2$ were calculated when Al doping amount x = 0.01, 0.02, 0.03, ……, 0.13 mol. All band gap values at every x mol are plotted in **Figure 2**. After Al doping, the band structure of Al-doped $LiNi_{1/3}Co_{1/3}Mn_{1/3}O_2$ can keep stable. The substitution of bigger Al atoms can widen Li-O layers which provides many tunnels to help electrons to immigrate more easily, thus, band gap values have decreased obviously, which means band gaps are narrower. According to **Figure 2**, between $x = 0.04$ mol and $x = 0.05$ mol, the decreasing tendency pauses, and

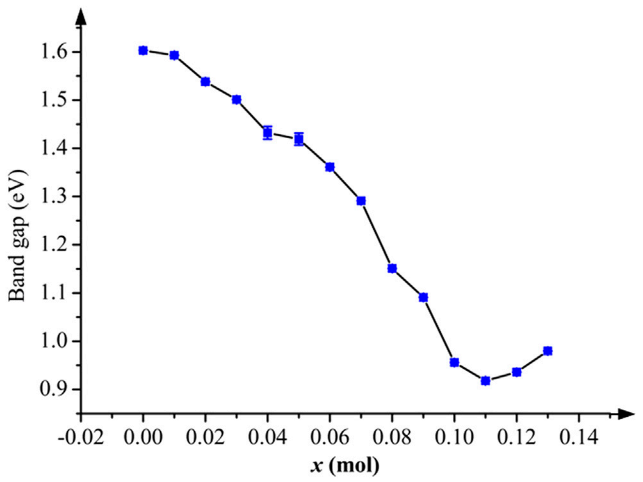

FIGURE 2 | The band gap of $Li_{1.0\text{-}x}Al_xNi_{1/3}Co_{1/3}Mn_{1/3}O_2$ with error bars. The curve goes down generally, which indicates its conductivity is enhanced effectively after Al doping.

the error bars are conspicuous, which may be caused by the slight disorder of Ni^{2+}/Li^+ cation mixing. From $x = 0.06$ mol, the curve goes down continually. At $x = 0.11$ mol, there is a minimum, and then the curve begins to go up. If only considering the band gap, the conductivity of $Li_{1.0\text{-}x}Al_xNi_{1/3}Co_{1/3}Mn_{1/3}O_2$ is best at $x = 0.11$ mol. Factually, from $x = 0.10$ mol to $x = 0.12$ mol, the band gap remains lowly, and the conductivity keeps excellent.

The peak of the partial density of state (PDOS) reflects electrons at this level, which directly demonstrates the conductivity. Herein, PDOS of $Li_{1.0\text{-}x}Al_xNi_{1/3}Co_{1/3}Mn_{1/3}O_2$ was implemented. **Figure 3** shows its PDOS when $x = 0$, 0.05, 0.10 and 0.13 mol, respectively. The colored lines in **Figure 3** represent the density of different orbital states. In **Figure 3A**, the peak of PDOS is about 168 eV, clearly describing the bonding and density of states near the Fermi level. When $0 < x < 0.05$ mol, the peak of PDOS increases continually, and the conductivity has been enhanced substantially. In **Figure 3B**, at $x = 0.05$ mol, the peak goes up to 519 eV which is several times higher than that of the pristine, and the conductivity has been enhanced dramatically. When $x = 0.06$–0.09 mol, the peak of PDOS increases slightly, the conductivity has been enhanced further with the increasing x. When $x = 0.10$ mol (shown in **Figure 3C**), the peak of PDOS is a maximum around 644 eV, which shows the best conductivity. When $x > 0.10$ mol, the peak goes down quickly. At $x = 0.13$ mol (shown in **Figure 3D**), the peak goes closely that of the pristine, which indicates too much Al-doping amount will not be useful to the high-performance of conductivity. Considering the results of PDOS, the right Al-doping amount should be controlled within $x = 0.06$–0.10 mol.

Cell Volume and Lithiation Formation Energy

For rechargeable power sources, good cycling and stable structure are very important. At different x mol, volumes of $Li_{1.0\text{-}x}Al_xNi_{1/3}Co_{1/3}Mn_{1/3}O_2$ were achieved by Material Studio.

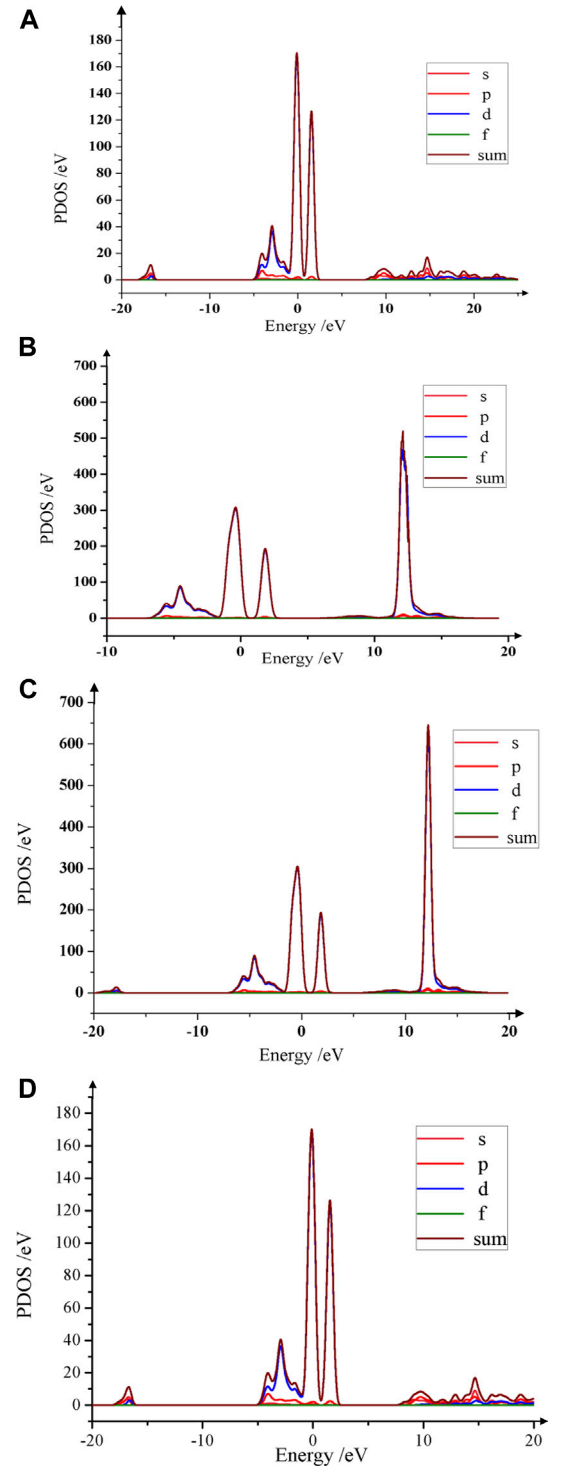

FIGURE 3 | PDOS curves of $Li_{1.0\text{-}x}Al_xNi_{1/3}Co_{1/3}Mn_{1/3}O_2$. **(A)** The PDOS peak of the pristine near the Fermi level is about 168 eV. **(B)** When $x = 0.05$ mol, the PDOS peak raises around 519 eV, which is much higher than that of the pristine. **(C)** When $x = 0.10$ mol, the PDOS peak is high up to 644 eV. The bigger Al atoms make Li-O layers wider, and abundant tunnels are provided, which electrons can cross over freely, and then the conductivity is strengthened strongly. **(D)** When $x = 0.13$ mol, the PDOS peak is down to 170 eV, which is close to the PDOS peak of $LiNi_{1/3}Co_{1/3}Mn_{1/3}O_2$.

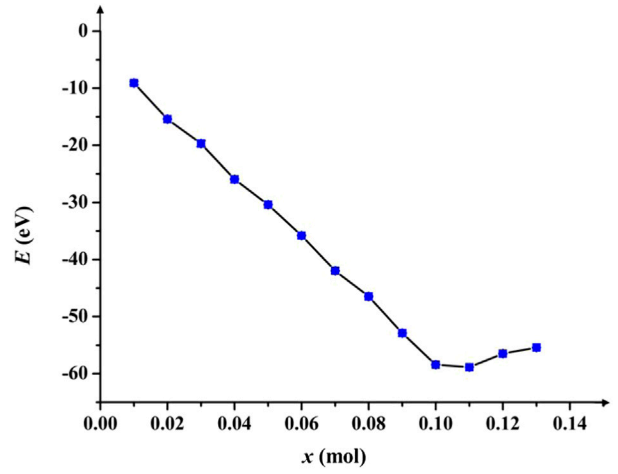

FIGURE 4 | Diagram about the relationship between *E* and *x*. The curve decreases until $x < 0.12$ mol, which demonstrates the lithiation/delithiation process can benefit from the appropriate Al doping amount. From $x = 0.11$ mol, *E* begins to get bigger slightly. The small error bars mean our high-accuracy calculations.

When $x < 0.12$ mol, the volumes can keep stable basically, which is consistent to the band gap. At $x = 0.04$ mol, the slight disorder of Ni^{2+}/Li^{+} cation mixing perhaps lead to a slight volume expanding. When $x > 0.12$ mol, the volume has expanded distinctly, and the structure is instable which is caused by structure transition from layer-to-spinel. In other word, when $x < 0.12$ mol, Al doping can stabilize the layered crystal structure and keep good cycling performances.

In general, the difficulty of the lithiation/delithiation process can be reflected by the formation energy. If the formation energy of metal oxide is low, atoms can be separated easily from the crystal lattice. The equation of lithiation formation energy *E* is the same as referred in my previous work [25]. **Figure 4** plots the formation energy *E* of $Li_{1.0\text{-}x}Al_xNi_{1/3}Co_{1/3}Mn_{1/3}O_2$ varying with different *x*. According to **Figure 4**, *E* goes down straight when $x < 0.12$ mol, and there is minimum at $x = 0.11$ mol which the rate capability of material is best; when $x > 0.12$ mol, the curve increases gradually, electrons and Li-ions will be apart difficultly from the lattice crystal. Hence, analyses of **Figure 4** states explicitly that too much Al doping will be harmful to the lithiation/delithiation process, the proper Al doping amount is within $x < 0.11$ mol.

Electron Density Difference

To investigate electrons' distribution near local atoms, we simulated the electron density difference of $Li_{1.0\text{-}x}Al_xNi_{1/3}Co_{1/3}Mn_{1/3}O_2$. **Figure 5** shows the simulations at $x = 0$, 0.06, 0.10, and 0.11 mol. Some blocks with heavy colors are reflections of atoms. In comparison with that of the pristine (shown in **Figure 5A**), when $0 < x < 0.06$ mol, the coverage and color of the electron cloud have changed a little, which means electrons near local atoms have not increased much; when $x = 0.06$ mol (shown in **Figure 5B**), its coverage has distinguished from the before, but its color has still remained; when $x > 0.08$ mol, its color has turned into orange which means electrons have increased enormously, and its coverage has expanded further; especially, at $x = 0.10$ mol (shown in **Figure 5C**), its color is still orange, and its coverage is biggest, which exhibits that there are abundant of free electrons around atoms, and $Li_{0.9}Al_{0.1}Ni_{1/3}Co_{1/3}Mn_{1/3}O_2$ has superior conductivity; when $x = 0.11$ mol (shown in **Figure 5D**), its coverage has shrunk greatly, free electrons near local atoms have decreased significantly, and its conductivity has become poor. Therefore, the appropriate doping amount is $x =$ 0.08–0.10 mol which Al doping can notably boost the conductivity.

Potential Energy of Electrons

To study the electrons' transfer and rate capability of $LiNi_{1/3}Co_{1/3}Mn_{1/3}O_2$ after Al doping, their electrons' potential energy had been

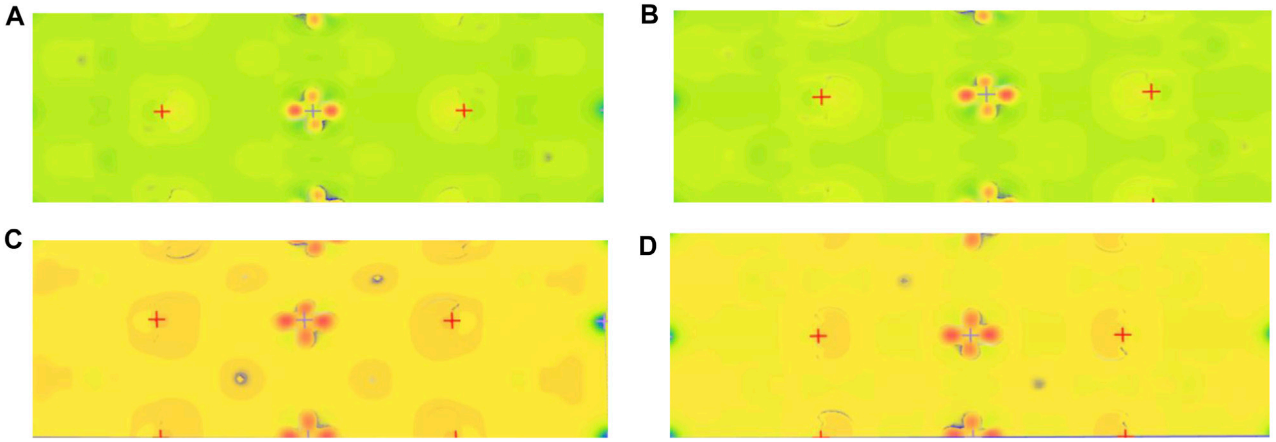

FIGURE 5 | Electron density difference of $Li_{1.0\text{-}x}Al_xNi_{1/3}Co_{1/3}Mn_{1/3}O_2$. **(A)** The electron density difference image of the pristine is shown. **(B)** When $x = 0.06$ mol, the color has not changed, and the coverage of electron cloud has expanded significantly, which suggests the conductivity has been enhanced due to more free electrons around atoms. **(C)** When $x = 0.10$ mol, the color of electron cloud gets orange, and the electron cloud's coverage is biggest, which indicates its conductivity is promoted extremely. **(D)** When $x = 0.11$ mol, its color has not changed, and its coverage has shrunk much.

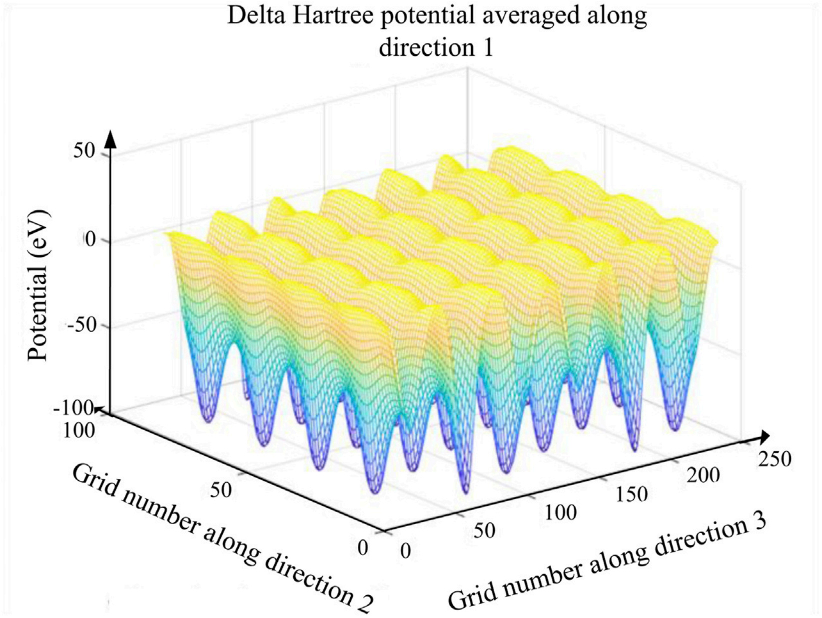

FIGURE 6 | 3D potential energy profile of $Li_{0.9}Al_{0.1}Ni_{1/3}Co_{1/3}Mn_{1/3}O_2$. The different colors correspond to the different potential energy. When $x < 0.11$ mol, all 3D potential energy maps show that the potential barrier is getting lower after Al doping.

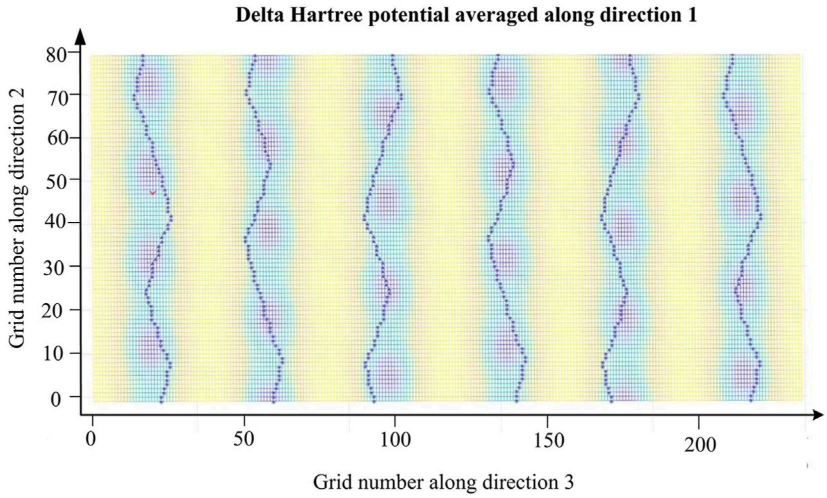

FIGURE 7 | 2D potential energy plot of $Li_{0.9}Al_{0.1}Ni_{1/3}Co_{1/3}Mn_{1/3}O_2$. Blue marks “*” represent the paths of electrons, and each marked route is not the same.

mapped. If electrons in a potential well can obtain some external energy, they can transport freely from the potential well. **Figure 6** shows the 3D potential energy map of $Li_{0.9}Al_{0.1}Ni_{1/3}Co_{1/3}Mn_{1/3}O_2$. From **Figure 6**, the potential barrier and well are regularly in turn, which indicates layered $Li_{0.9}Al_{0.1}Ni_{1/3}Co_{1/3}Mn_{1/3}O_2$ has not occurred the phase transition during the charging/discharging process. The right Al-doping amount can remain its layered structure invariantly.

To analyze the transfer of electrons in potential well after Al doping, diffusion paths were implemented in 2D potential energy image. **Figure 7** shows the electrons’ diffusion paths of $Li_{0.9}Al_{0.1}Ni_{1/3}Co_{1/3}Mn_{1/3}O_2$. Electrons will immigrate freely along the route marked blue “*”, where is the minimum potential energy and numerous channels to diffuse are offered. And the energy barrier of Li-ion insertion/extraction is reduced in the crystal lattice. Consequently, electrons and Li-ions can be removed and transfer to other places with lower energy barrier. In **Figure 7**, the potential energy of $Li_{0.9}Al_{0.1}Ni_{1/3}Co_{1/3}Mn_{1/3}O_2$ is from around 80 to 0 eV. When $x < 0.11$ mol, the minimum potential energy of $Li_{1.0\text{-}x}Al_xNi_{1/3}Co_{1/3}Mn_{1/3}O_2$ decreases with rising x, and electrons can be apart from the potential well more facilely. Thus, this new material has excellent rate capacity and electrochemical performances when $x < 0.11$ mol.

CONCLUSION

The physical mechanism of enhanced electrochemical properties for Al-doped $LiNi_{1/3}Co_{1/3}Mn_{1/3}O_2$ was investigated by DFT. After Al doping, $Li_{1.0\text{-}x}Al_xNi_{1/3}Co_{1/3}Mn_{1/3}O_2$ has a layered structural stability when $x < 0.12$ mol; the band gap has a minimum at $x = 0.11$ mol, and the conductivity is best; the peak of PDOS remains highly within $x = 0.06$–0.10 mol, which electrons are multiplied than the pristine, and its conductivity is enhanced dramatically; the lithiation formation energy E is lowest at $x = 0.11$ mol, and electrons and Li-ions can be separated easily within $x < 0.12$ mol; based on the simulations of the electron density difference, $Li_{1.0\text{-}x}Al_xNi_{1/3}Co_{1/3}Mn_{1/3}O_2$ has a better conductivity when $x = 0.08 - 0.10$ mol; and electrons' potential barrier is decreasing with rising x, electrons and Li-ions can be removed and diffused quickly, which means its rate capability is improved effectively. Considering all above calculations and analyses, the electrochemical performance of $Li_{1.0\text{-}x}Al_xNi_{1/3}Co_{1/3}Mn_{1/3}O_2$ is best at $x = 0.10$ mol. Up to now, it is few reported about the experimental investigations on $Li_{1.0\text{-}x}Al_xNi_{1/3}Co_{1/3}Mn_{1/3}O_2$. We believe that samples of $Li_{1.0\text{-}x}Al_xNi_{1/3}Co_{1/3}Mn_{1/3}O_2$ can be prepared experimentally by traditional syntheses, and suggest that its superior electrochemical performances of $Li_{0.9}Al_{0.1}Ni_{1/3}Co_{1/3}Mn_{1/3}O_2$ will be verified experimentally by physical and chemical tests. Moreover, the electrochemical performance of $Li_{1.0\text{-}x}Al_xNi_{1/3}Co_{1/3}Mn_{1/3}O_2$ can be improved further combining with other modifications. This study provides an insight to understand the physical improvement mechanism of Al-doped $LiNi_{1/3}Co_{1/3}Mn_{1/3}O_2$. Our results and theoretical advice based on DFT could be important for the investigations of $Li_{1.0\text{-}x}Al_xNi_{1/3}Co_{1/3}Mn_{1/3}O_2$, doping materials studies about the power sources of new electro-optical conversion devices, and applications in LIBs. Our simulations and calculations have concerned only on the conductivity, cycling and rate capability. Certainly, Al-doped $LiNi_{1/3}Co_{1/3}Mn_{1/3}O_2$ can be further improved its energy density and reversible charge capacity by structural optimization, coating, and composite etc.

DATA AVAILABILITY STATEMENT

The original contribution presented in the study are included in the article/**Supplementary Material**, further inquiries can be directed to the corresponding author.

AUTHOR CONTRIBUTIONS

YG designed models, analyzed results, and wrote the manuscript. WY carried out calculations. XD gave some proposals.

FUNDING

This research was funded by the Science and Technology Project Foundation of Zhongshan City of Guangdong Province of China (no. 2018B1127), the Educational Science and Technology Planning in Guangdong Province (no. 2018GXJK240), the Investigations of Lithium-ion Batteries and Display Modules for Mobile Machine Equipment (no. 421P06 and 421P15), the Characteristic Innovation Project of Guangdong Province, the National Natural Science Foundation of China (no. 11775047), the union project of National Natural Science Foundation of China and Guangdong Province (no. U1601214), Science and Technology Program of Guangzhou (no. 2019050001), the Scientific and Technological Plan of Guangdong Province (no. 2018B050502010).

SUPPLEMENTARY MATERIAL

The Supplementary Material for this article can be found online at: https://www.frontiersin.org/articles/10.3389/fphy.2021.731851/full#supplementary-material

REFERENCES

1. Lee GH, Wu JP, Kim D, Cho K, Cho M, and Yang WL. Reversible Anionic Redox Activities in Conventional $LiNi_{1/3}Co_{1/3}Mn_{1/3}O_2$ Cathodes. *Angewandte Chemie* (2020) 132:8759–66. doi:10.1002/anie.202001349
2. Zou BK, Ding CX, and Chen CH. Research Progress in Ternary Cathode Materials Li (Ni, Co, Mn) O_2 for Lithium Ion Batteries. *Scientia Sinica: Chim* (2014) 44(7):1104–15. doi:10.1360/N032014-00019
3. Refly S, Floweri O, Mayangsari TR, Sumboja A, Santosa SP, and Ogi T. Regeneration of $LiNi_{1/3}Co_{1/3}Mn_{1/3}O_2$ Cathode Active Materials from End-Of-Life Lithium-Ion Batteries through Ascorbic Acid Leaching and Oxalic Acid Coprecipitation Processes. *ACS Sustainable Chem Eng* (2020) 8(43):16104–14. doi:10.1021/acssuschemeng.0c01006
4. Zhu LM, Bao CG, Xie LL, Yang XL, and Cao XY. Review of Synthesis and Structural Optimization of $LiNi_{1/3}Co_{1/3}Mn_{1/3}O_2$ Cathode Materials for Lithium-Ion Batteries Applications[J]. *J Alloys Compounds* (2020) 831: 154864–80. doi:10.1016/j.jallcom.2020.154864
5. Nguyen VH, Ngo MD, and Kim YH. Effect of Soybean Oil as a Carbon Source on the Electrochemical Property of $LiNi_{1/3}Co_{1/3}Mn_{1/3}O_2$ Cathode Material for Lithium Ion Battery. *Carbon Lett* (2020) 30:621–6. doi:10.1007/s42823-020-00133-1
6. Zheng JL, Zhou W, Ma YR, Jin H, and Guo L. Combustion Synthesis of $LiNi_{1/3}Co_{1/3}Mn_{1/3}O_2$ Powders with Enhanced Electrochemical Performance in LIBs. *J Alloys Compounds* (2015) 635:207–12. doi:10.1016/j.jallcom.2015.02.114
7. David P, Jérémie S, Colin JF, Boulineau A, Fabre F, and Bourbon C. Submicronic $LiNi_{1/3}Co_{1/3}Mn_{1/3}O_2$ Synthesized by Co-precipitation for Lithium Ion Batteries-Tailoring a Classic Process for Enhanced Energy and

Power Density. *J Power Sourc* (2018) 396:527–32. doi:10.1016/j.jpowsour.2018.06.075

8. Song YJ, Wang MR, Li J, Cui HT, Su HJ, and Liu YY. Controllable Synthesis of $LiNi_{1/3}Co_{1/3}Mn_{1/3}O_2$ Electrode Material via a High Shear Mixer-Assisted Precipitation Process. *Chem Eng J* (2021) 5:129281–91. doi:10.1016/j.cej.2021.129281
9. Aida T, and Toma TKanada S. A Comparative Study of Particle Size and Hollowness of $LiNi_{1/3}Co_{1/3}Mn_{1/3}O_2$ Cathode Materials for High-Power Li-Ion Batteries: Effects on Electrochemical Performance. *J Solid State Electrochemistry* (2020) 24:1415–25. doi:10.1007/s10008-020-04640-z
10. Liu WJ, Sun XZ, Zhang X, Li C, Wang K, and Wen W. Structural Evolution of Mesoporous graphene/$LiNi_{1/3}Co_{1/3}Mn_{1/3}O_2$ Composite Cathode for Li-Ion Battery. *Rare Met* (2021) 40:521–8. doi:10.1007/s12598-020-01406-4
11. Zhu LM, Xie LL, Bao CG, Yan XY, and Cao XY. $LiNi_{1/3}Co_{1/3}Mn_{1/3}O_2$ Polypyrrole Composites as Cathode Materials for High-Performance Lithium-Ion Batteries. *Int J Energ Res* (2020)(2) 44. doi:10.1002/er.4916
12. Chen ZL, Zhang ZB, Liu P, Wang SF, Zhang WH, and Chen DJ. Facile Preparation of Carbon- $LiNi_{1/3}Co_{1/3}Mn_{1/3}O_2$ with Enhanced Stability and Rate Capability for Lithium-Ion Batteries. *J Alloys Compounds* (2019) 780:643–52. doi:10.1016/j.jallcom.2018.11.387
13. Li BY, Li GS, Zhang D, Fan JM, Chen DD, and Liu XQ. Zeolitic Imidazolate Framework-8 Modified $LiNi_{1/3}Co_{1/3}Mn_{1/3}O_2$: A Durable Cathode Showing Excellent Electrochemical Performances in Li-Ion Batteries. *Electrochimica Acta* (2020) 336:135724–33. doi:10.1016/j.electacta.2020.135724
14. Shao ZC, Guo J, Zhao Z, Xia J, Ma M, and Zhang Y. Preparation and Properties of Al_2O_3-Doping $LiNi_{1/3}Co_{1/3}Mn_{1/3}O_2$ Cathode Materials. *Mater Manufacturing Process* (2016) 31(8):1004–8. doi:10.1080/10426914.2015.1117618
15. Zhu JP, Yan JW, and Zhang L. High Specific Capacity Mg-Doping $LiNi_{1/3}Co_{1/3}$-$Mn_{1/3}O_2$ Cathode Materials Synthesized by a Simple Stepwise Co-precipitation Method. *Micro Nano Lett* (2018) 14(2). doi:10.1049/mnl.2018.5011
16. Li YH, Liu JY, Lei YK, Lai CY, and Xu QJ. Enhanced Electrochemical Performance of Na-Doped Cathode Material $LiNi_{1/3}Co_{1/3}Mn_{1/3}O_2$ for Lithium-Ion Batteries. *J Mater Sci* (2017) 52:13596–605. doi:10.1007/s10853-017-1449-z
17. Kim S, Park S, Jo M, Beak M, Park J, and Jeong G. Electrochemical Effects of Residual Al in the Resynthesis of $Li[Ni_{1/3}Mn_{1/3}Co_{1/3}]O_2$ Cathode Materials. *J Alloys Compounds* (2020) 857(9):157581. doi:10.1016/j.jallcom.2020.157581
18. Zhang ZH, Yu M, Yang B, Jin CZ, Guo GH, and Qiu JH. Regeneration of Al-Doped $LiNi_{1/3}Co_{1/3}Mn_{1/3}O_2$ Cathode Material via a Sustainable Method from Spent Li-Ion Batteries. *Mater Res Bull* (2020) 126:110855–61. doi:10.1016/j.materresbull.2020.110855
19. Li ZY. The Improvement for the Electrochemical Performances of $LiNi_{1/3}Co_{1/3}$-$Mn_{1/3}O_2$ Cathode Materials for Lithium-Ion Batteries by Both the Al-Doping and an Advanced Synthetic Method. *Int J Electrochem Sci* (2019) 14(4):3524–34. doi:10.20964/2019.04.57
20. Zhu JP, Yan JW, Chen J, Guo X, and Zhao SG. Structuring Al^{3+}-Doped $LiNi_{1/3}$-$Co_{1/3}Mn_{1/3}O_2$ by 3D-Birdnest-Shaped MnO_2. *Funct Mater Lett* (2019) 12(4): 1950051–4. doi:10.1142/S1793604719500516
21. Pana TY, Thanh NTT, Chang YC, and Hsu WD. First-principles Study on the Initial Reactions at $LiNi_{1/3}Co_{1/3}Mn_{1/3}O_2$ Cathode/electrolyte Interface in Lithium-Ion Batteries. *Appl Surf Sci* (2020) 507:144842–8. doi:10.1016/j.apsusc.2019.144842
22. Shen KX, Chen HD, Hou XH, Wang SF, Qin HQ, and Gao YM. Mechanistic Insight into the Role of N-Doped Carbon Matrix in Electrospun Binder-free Si@C Composite Anode for Lithium-Ion Batteries. *Ionics* (2020) 26:3297–305. doi:10.1007/s11581-020-03484-x
23. Chen SD, Sood A, Pop E, Goodson KE, and Donadio D. Strongly Tunable Anisotropic thermal Transport in MoS_2 by Strain and Lithium Intercalation: First-Principles Calculations. *2D Mater* (2019) 6:025033–42. doi:10.1088/2053-1583/ab0715
24. Gao YM, Shen KX, Liu P, Liu LM, Chi F, and Hou XH. First-principles Investigation on Electrochemical Performance of Na-Doped $LiNi_{1/3}Co_{1/3}Mn_{1/3}O_2$. *Frontier Phys* (2021) 8:616066–73. doi:10.3389/fphy.2020.616066
25. Gao YM, Hui YC, and Yin H. Enhanced Electrochemical Property of $Li_{1.2-x}Na_xMn_{0.54}Ni_{0.13}Co_{0.13}O_2$ Cathode Material for the New Optoelectronic Devices. *Frontier Phys* (2021) 9:690661–8. doi:10.3389/fphy.2021.690661
26. Ng MF, and Sullivan MB. First-principles Characterization of Lithium Cobalt Pyrophosphate as a Cathode Material for Solid-State Li-Ion Batteries. *J Phys Chem C* (2019) 123(49):29623–9. doi:10.1021/acs.jpcc.9b09946
27. Perdew JP, Chevary JA, Vosko SH, Jackson KA, Pederson MR, and Singh DJ. Erratum: Atoms, Molecules, Solids, and Surface: Applications of the Generalized Gradient Approximation for Exchange and Correlation. *Phy Rev B* (1992) 46(11):6671–87. doi:10.1103/PhysRevB.46.6671
28. Perdew JP, Burke K, and Ernzerhof M. Generalized Gradient Approximation Made Simple. *Phys Rev Lett* (1996) 77:3865–8. doi:10.1103/PhysRevLett.77.3865
29. Kresse G, and Joubert D. From Ultrasoft Pseudopotentials to the Projector Augmented-Wave Method. *Phys Rev B* (1999) 59:1758–75. doi:10.1103/PhysRevB.59.175

Conflict of Interest: The authors declare that the research was conducted in the absence of any commercial or financial relationships that could be construed as a potential conflict of interest.

frontiers
in Physics

BRIEF RESEARCH REPORT
published: 20 August 2021
doi: 10.3389/fphy.2021.720539

Faster-Than-Nyquist 400 G Implementation Using 126-GBaud QPSK-OFDM With 88-GSa/s Undersampling

*Peng Liu[1], Hongxian Chen[2], Weihao Ni[3] and Fan Li[3]**

[1]The School of Computer, Guangdong University of Technology, Guangzhou, China, [2]PLA Troops, Guangzhou, China, [3]The Key Laboratory of Optoelectronic Materials, School of Electronics and Information Technology, Sun Yat-Sen University, Guangzhou, China

In this study, we demonstrated generation and transmission of 114 Gbaud and 126 Gbaud faster-than-Nyquist (FTN) discrete Fourier transform-spread (DFT-spread) quadrature phase shift keying orthogonal frequency division multiplexing (QPSK-OFDM) with 88-Gsa/s sampling rate digital-to-analog converters (DACs) experimentally. It is the first time to realize 400G FTN DFT-spread QPSK-OFDM signal per optical carrier for metro and regional applications, which will be a solution for network operators to address the issue of increasing bandwidth derived from the rapid popularization of mobile Internet and the wide application of IoT (Internet of Things technology). Delay-and-add filter (DAF) is adopted to realize frequency shaping at the transmitter to keep higher portions of energy of signal at low frequencies, which makes the OFDM much more robust to strong filtering effect. After pre-equalization, bit error rate (BER) performance of 114 GBaud and 126 GBaud FTN DFT-spread QPSK-OFDM has been significantly improved, and maximum-likelihood sequence estimation (MLSE) shows a better effect than binary decoding in the aspect of against the inter symbol interference (ISI) introduced by spectrum compression. The effective bit rate of dual polarization 126 Gbaud FTN DFT-spread QPSK-OFDM which is generated with 88 GSa/s sampling rate is 410.08 Gb/s, to the exclusion of all overhead including TSs, cyclic prefix (CP), and 20% forward error correction (FEC) coding. We successfully transmit 8 × 400 Gbit/s FTN DFT-spread QPSK-OFDM signal generated from 88 Gsa/s sampling rate DAC over 420 km single mode fiber (SMF) with the BER under 2.4×10^{-2}.

Keywords: orthogonal frequency division multiplexing, discrete fourier transform-spread, WDM, pre-equalization, faster-than-nyquist

Edited by:
Qiang Xu,
Nanyang Technological University,
Singapore

Reviewed by:
Jia Lu,
Hebei University of Technology, China
Zhou Hui,
Hunan Normal University, China

***Correspondence:**
Fan Li
lifan39@mail.sysu.edu.cn

Specialty section:
This article was submitted to
Optics and Photonics,
a section of the journal
Frontiers in Physics

Received: *04 June 2021*
Accepted: *12 July 2021*
Published: *20 August 2021*

Citation:
Liu P, Chen H, Ni W and Li F (2021)
Faster-Than-Nyquist 400 G
Implementation Using 126-GBaud
QPSK-OFDM With 88-GSa/s
Undersampling.
Front. Phys. 9:720539.
doi: 10.3389/fphy.2021.720539

INTRODUCTION

Faster-than-Nyquist (FTN) is extensively studied to improve the spectrum efficiency by transmitting symbols within a bandwidth less than the Nyquist bandwidth [1–9]. This technique has been put forward and performed in 400G single-carrier coherent optical transmission systems recently [10]. Faster-than-Nyquist root-raised cosine (FTN-RRC) filter has been proposed to generate sub-symbol-rate sampling signal. 483 Gb/s (120.75 Gbaud) single-carrier polarization-division-multiplexed quadrature phase-shift keying (PDM-QPSK) signal is demonstrated by using a 92 GSa/s digital-to-analog convertor (DAC) with sampling rate 0.76 sample/symbol. We consider that transmission of higher order quadrature amplitude modulation (QAM) signal is a method to effectively improve spectrum efficiency, however, the optical signal-to-noise ratio (OSNR) and stringent system linearity requirements prevent the transmission of high-order QAM modulated signal from optical fiber communication system. Compared to high-order QAM modulated signal transmission, there are following advantages to enhance spectral efficiency with FTN techniques. First, low-order modulation formats with a relatively high spectrum compression factor that can effectively solve the system linearity requirement problem. Second, we can set the signal compression ratio flexibly within the maximum compression ratio in our experiment, which can better approach the theoretical maximum transmission capacity of the channel.

FTN orthogonal frequency division multiplexing (OFDM) is first reported in Ref. [11] with discrete Fourier transform-spread (DFT-spread) and duo-binary spectrum shaping techniques. In the DFT-spread technique, using all in-band subcarriers delivers each data symbol [12, 13]. The single carrier–alike characteristic of DFT-spread OFDM signals show much better filtering effect tolerance than conventional OFDM signals. In addition, digital delay addition filter (DAF) is used to perform spectrum shaping to further improve the filtering effect tolerance [6]. In Ref. [11], as several sub-bands are applied to transmit signal, inter-sub-band interference (ISBI) appears in multi-band FTN OFDM, complicated digital signal processing (DSP) algorithms is necessary to compensate ISBI. Also, it is still questionable whether it could be a potential option to its single-carrier counterpart delivering 400G services per wavelength for metro and regional applications, which requires further investigation. Recently we have succeeded in transmitting the highest equivalent baud rate (120 Gbaud) FTN DFT-spread QPSK-OFDM signal within 80 GHz channel bandwidth over 80 km SMF with the BER under SD-FEC limitation of 2.4×10^{-2}. We make use of 80 GSa/s sampling rate to generate dual polarization 120 Gbaud FTN DFT-spread QPSK-OFDM and the pay-load bit rate is 384.54 Gb/s excluding all overhead including TSs, cyclic prefix (CP), and 20% FEC coding. In order to further improve the spectral efficiency, we integrated wavelength division multiplexing (WDM) system with FTN DFT-spread system, and increased the single-channel pay-load bit rate to more than 400G by using 88 Gsa/s sampling rate DACs.

In this study, generation and transmission of 400G FTN QPSK-OFDM signal are experimentally demonstrated with single DFT-spread band to avoid multi-band ISBI. To achieve a symbol rate higher than the Nyquist bandwidth, spectral of single-band DFT spread is compressed and ISBI cancellation technique is avoided in the receiver. Maximum likelihood sequence estimation (MLSE) decoding [6, 14] and pre-equalization [15, 16] are implemented to compensate inter symbol interference (ISI) caused by insufficient bandwidth and spectral compression, which can improve the receiver sensitivity significantly. We generate and transmit a record high baud rate (126 Gbaud) QPSK-OFDM signal with 88 GSa/s Sampling rate DAC. Finally, 8 × 400 Gb/s WDM FTN QPSK-OFDM with 22.8% spectral compression ratio within 100 GHz grid are successfully transmitted over 420-km with the BER under soft-decision FEC (SD-FEC) threshold (2.4×10^{-2}).

PRINCIPLE

Compared to the scheme proposed in Ref. [11], only one sub-band is discussed in this article, and ISBI between sub-channels is avoided. Directly subcarriers discarding at high frequencies instead of spectrum overlapping are applied to achieve symbol rate higher than the Nyquist bandwidth. After duo-binary DAF encoding, the signal becomes a cosine-alike spectrum shape. Because the serious ISI of high-frequency subcarriers will be induced when the channel bandwidth less than signal baud rate, transmitting a conventional OFDM signal *via* this channel is not practical. For DFT-spread OFDM signal, each QPSK symbol is carried on all data-carried subcarriers when single-band DFT spread is realized. In the circumstances, serious ISI on high-frequency subcarriers are spread over all symbols equally and still lead to BER performance deterioration. In FTN DFT-spread OFDM scheme, duo-binary encoding is realized by differential encoding and DAF. Compared to DFT-spread OFDM, FTN DFT-spread OFDM shows better performance in overcoming severe ISI, as the cosine-alike shape spectral density of FTN DFT-spread OFDM signal is much more robust to strong brick-wall filtering effect.

Principle diagram for FTN DFT-spread QPSK-OFDM generation is described in our previous work in detail [17], QPSK samples are divided into in-phase/quadrature (I/Q) branches and then fed into duo-binary encoding. With differential encoding, the symbols can be easily demodulated [18, 19], or else the symbols should be demodulated with MLSE for nine-level quadrature amplitude modulation (9QAM) [6, 11]. MLSE takes advantage of duo-binary memorability between adjacent codes to select the largest possible path to minimize BER and to further reduce ISI and noise. In this study, the transmitted symbols of FTN DFT-spread OFDM signal are duo/poly-binary encoded in the transmitter. In the DAF, the memory length is only one symbol, which coincides with the algorithm idea of MLSE. In the receiver, we can make use of the inherent memory length of symbols to minimize the BER by MLSE decoding. In addition, since the memory length of symbols is only 1, using MLSE algorithm is not computationally difficult. For QPSK and M-QAM modulation schemes, we usually divide them into in-phase and orthogonal components. In this way, the signals of the two components are in the M-level pulse amplitude modulation (M-PAM) format. Therefore, the following algorithm introduction is based on M-PAM modulation. **Figure 1A** shows the duo-binary signal frame diagram of M-PAM (where M = 2 and 4). **Figure 1C** and **Figure 1D** display the spectra of 4-PAM signal before and after through duo-binary process, respectively. Generally, the transmission process of a binary channel can be explained by a finite state machine. The state transition frame diagram is used to represent this state machine, where $x(n)$ represents the states at the moment n, when M = 2,

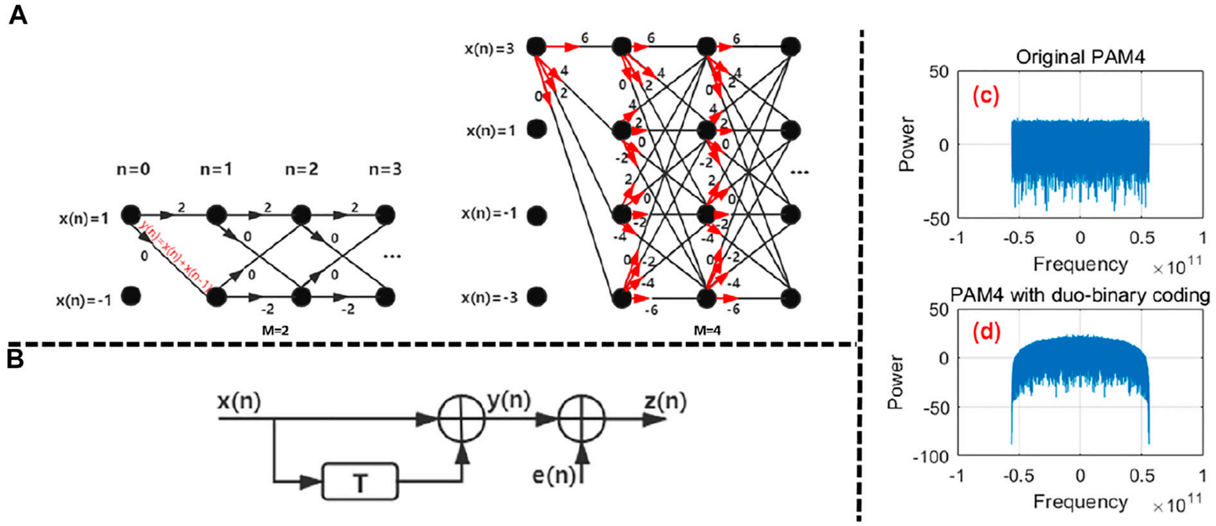

FIGURE 1 | (A) Duo-binary signal frame diagram of M-PAM, **(B)** simplified channel model of Duo-binary pulse shaping, **(C)** spectrum of 4-PAM signal, and **(D)** spectrum of duo-binary 4-PAM signal.

$x(n) \in \{1, -1\}$ and when M = 4, $x(n) \in \{3, 1, -1, -3\}$.$x(1)$ is the input at the first time. And $x(n) + x(n\text{-}1)$ which is attached to the branch stands for the transition of states between moment n-1 and n.

As can be seen from equation $y(n) = x(n) + x(n-1)$, it is obvious that the input of the node $y(1)$ is needed for the output $x(0)$ at the first moment, and we can take any value in $x(0) \in \{1, -1\}$ because the influence of the selection of the initial state on the MLSE algorithm in the long-distance transmission is negligible. The marked value of the line between nodes at two adjacent moments in the figure is determined by $y(n) = x(n) + x(n-1)$. It can be found that any node has M conversion possibilities, and from the moment $n = 2$, each node has M possible input paths. In order to more intuitively explain the implementation principle of MLSE, we simplified the duo-binary channel model as shown in **Figure 1B**.

$z(n)$ and $e(n)$ represent the sampling value of the received signal and the sampling value of the noise at the moment n, respectively, and T represents the delay of a sign time. The basic idea of the MLSE algorithm is to find the most likely path that maximizes the conditional probability of $P(Z(n)|X(n))$, where $Z(n) = [z(1), z(2), \ldots, z(n)]$ is the vector representation of the sampled value of the received signal and $X(n) = [x(1), x(2), \ldots, x(n)]$ is the vector representation of the input signal. We define $Y(n) = [y(1), y(2), \ldots, y(n)]$ to be an ideal vector representation of the output signal. It can be seen from formula $y(n) = x(n) + x(n-1)$ that $y(n)$ is uniquely determined by $x(n)$, so the maximum value of conditional probability $P(Z(n)|X(n))$ can be converted into the maximum value of conditional probability $P(Z(n)|Y(n))$, that is, the minimum value of Euclidean distance $D(Z(n), Y(n))_{\min}$ between vector $Y(n)$ and $Z(n)$. Based on the definition of Euclidean distance, it can be expressed as the sum of independent one-dimensional variables as follows:

$$\begin{aligned} D(Z(n), Y(n)) &= \sum_n (z(n) - y(n))^2 \\ &= \sum_n [z(n) - (x(n) + x(n-1))]^2. \end{aligned} \tag{1}$$

For the Euclidean distance $DM(x(1))$ between node $x(1)$ at the first receiver-side and the initial node $x(0)$, where $x(1)$ has M values, at the moment $n = 1$, each different node has corresponding Euclidean distance $DM(x(1))$ with sampling received signal $z(1)$ so $DM(x(1))$ has M values.

As shown in **Figure 1A** from the moment $n = 2$, each node $x(n)$ has M input paths and M different values of $x(n)$. So for every moment n, M^2Euclidean distance $DM(x(n))$ can be calculated by the Euclidean distance at the current time and the Euclidean distance that we calculated before. The maximum of conditional probability $P(Z(n)|Y(n))$ at the moment n can be converted to finding time n of $D(Z(n), Y(n))_{\min}$. For a specific $x(n)$ of one of M values at the moment n, the minimum value of M Euclidean distances can be used as $DM(x(n))$ of the current node, and $DM(x(n))$ can be defined as follows:

$$\begin{aligned} DM(x(n)) = \min\{&DM(x(n-1)) \\ &+ [z(n) - (x(n) + x(n-1))]^2\}. \end{aligned} \tag{2}$$

It can be seen that for the specific input path $x(n)$ at the moment n, which originally had M different input paths, only one surviving path would be left through the above formula, and the other M-1 paths would be discarded to reduce the storage capacity required by the algorithm. However, in the actual MLSE algorithm, the input sequence is often very long. It is not possible to store a minimum Euclidean distance for each time node. Therefore, the common processing method is to truncate the signal once after the time of K symbols. In this way,

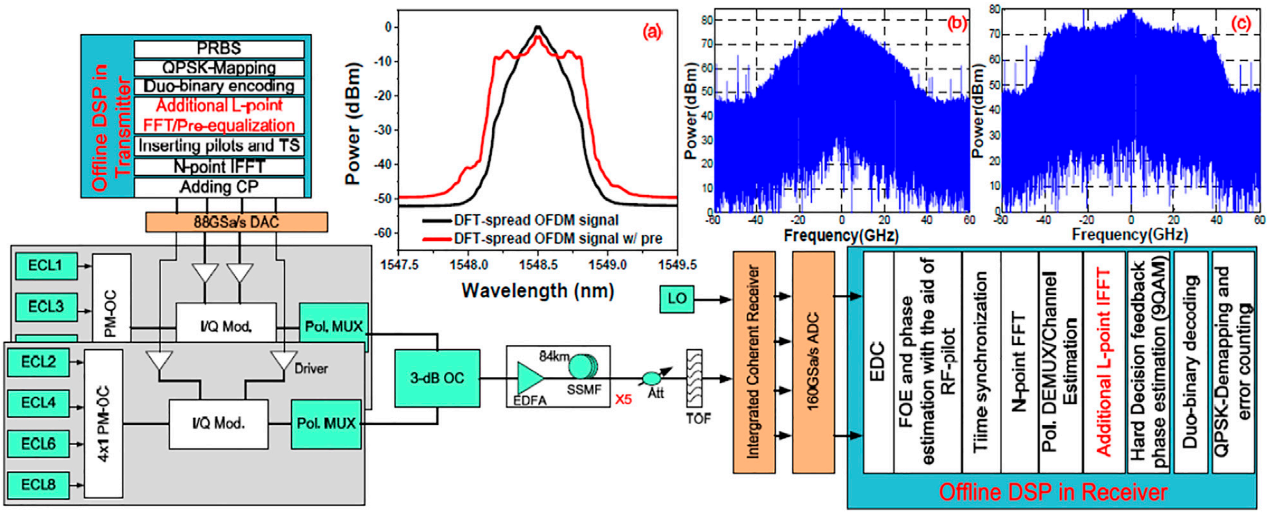

FIGURE 2 | Experimental setup (ECL: external cavity lasers; DAC: time-division Multiplexer; I/Q Mod.: IQ modulator; Pol. MUX: polarization multiplexer; OC: optical coupler; ATT: attenuator; TOF: tunable optical filter; LO: local oscillator; ADC: analog-to-digital convertor). Insets: **(A)** 114 Gbaud FTN-QPSK-OFDM optical spectrum, 114 Gbaud FTN-QPSK-OFDM electrical spectrum **(B)** without and **(C)** with pre-equalization.

we only need to store M viable paths within K symbols, which greatly reduces the load of memory. However, the value of K often has a great impact on the performance of MLSE algorithm. First of all, K must be greater than the memory length of the symbol, otherwise the Euclidean distance calculated and survived may not be the minimum value. Moreover, if the value of K is too large, the consistency of memory will be increased. For double/multiple binary signals with a memory length of one for M = 2 and 4, the performance penalty for MLSE is almost negligible when the K value is above 20.

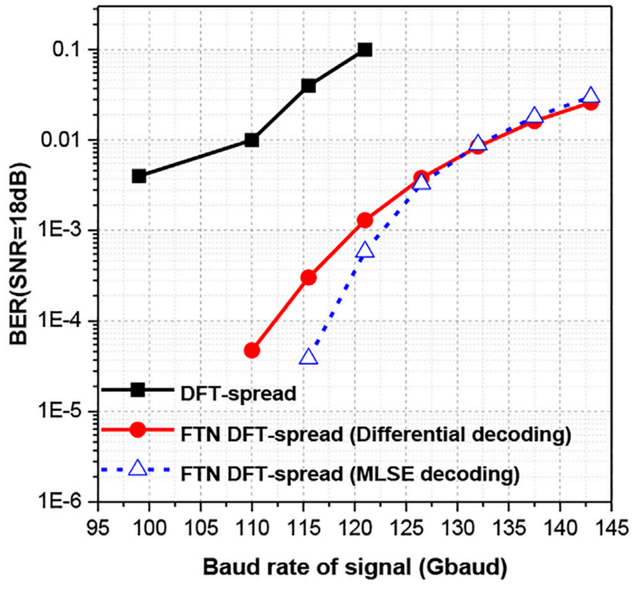

FIGURE 3 | BER versus baud rate of FTN-DFT-spread QPSK-OFDM in AWGN channel.

EXPERIMENTAL SETUP AND RESULTS

The experimental setup for 8 × 400 Gbit/s FTN-DFT-spread QPSK-OFDM signal generation, transmission, and reception is shown in **Figure 2**. In the transmitter, we use 8 100-GHz channel spacing external cavity lasers (ECLs) with <100-kHz linewidth and 14.5 dBm output power as the light sources in the transmitter. They are divided into two groups as the odd and even channels to form the WDM channel setup in 100 GHz-grid. The odd and even channels are combined with two sets of polarization multiplexer optical couplers (PM-OCs). FTN QPSK-OFDM is generated with MATLAB as described above and then uploaded into an 88 Gsa/s sampling rate DAC and the 3-dB bandwidth of the DAC is 16 GHz. The 3-dB bandwidth of driver and optical modulator are 30 GHz and 25 GHz, respectively. The odd and even channels I/Q modulators biased at null point are independently modulated by the four output ports of the DAC. We employ the polarization multiplexer to realize the polarization multiplexing of the signal [20], in our experiment, the even and odd channels are combined by a 2 × 1 optical coupler (OC). We can take advantage of effective OFDM signal baud rate **B** to adjust the DFT-spread fast Fourier transform/inverse fast Fourier transform (FFT/IFFT) size M. The relationship between them can be expressed as: $M = (N \times B)/88$. Among the $N = 1{,}024$ subcarriers. The first subcarrier of FTN DFT-spread signal is reserved null for direct-current bias (DC-bias). As frequency offset estimation (FOE) and phase noise estimation is realized with radio frequency pilot (RF-pilot) scheme [17], another five subcarriers around zero frequency are reserved for RF-pilot insertion, and the rest L ($L = N\text{-}6$)

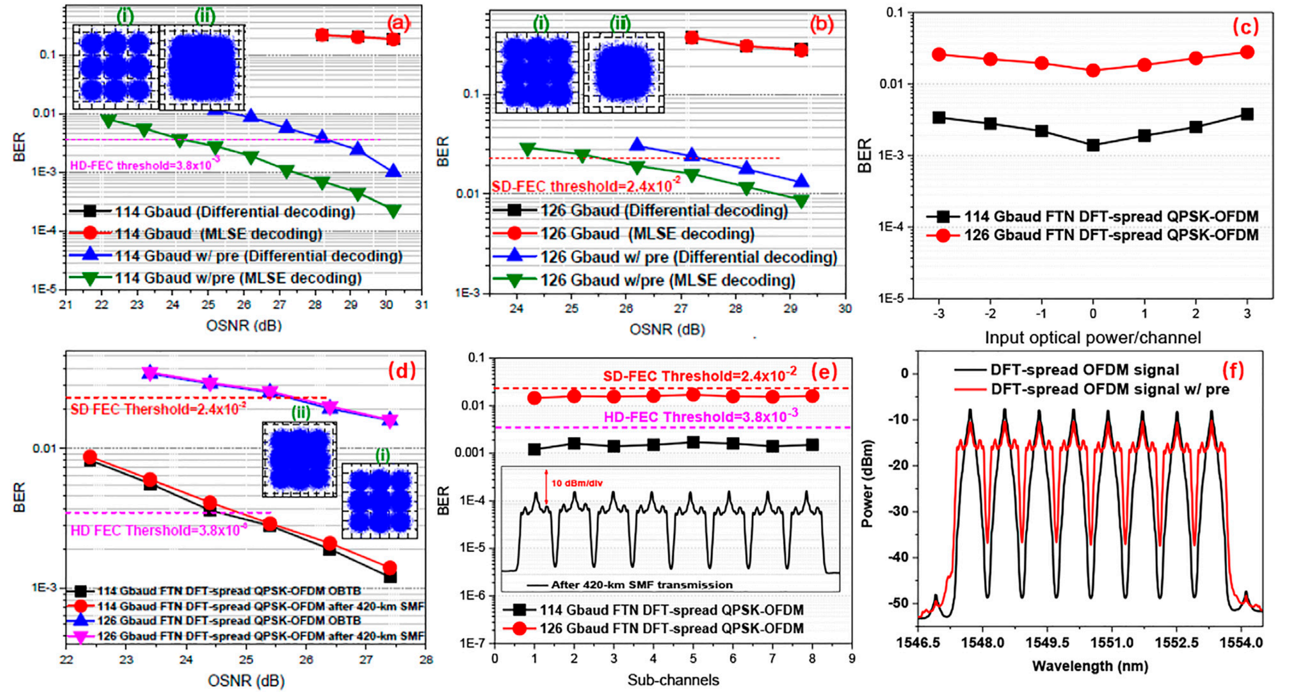

FIGURE 4 | (A) BER versus OSNR of 114 Gbaud FTN-DFT-spread QPSK-OFDM after 420-km fiber transmission, **(B)** BER versus OSNR of 126 Gbaud FTN-DFT-spread QPSK-OFDM after 420-km fiber transmission. BER versus OSNR of the 3rd sub-channel of WDM in OBTB and after 420-km fiber transmission, **(C)** BER versus input power per channel of the 3rd sub-channel of WDM after 420-km transmission, **(D)** BER versus OSNR of the 3rd sub-channel of WDM in OBTB and after 420-km fiber transmission, **(E)** BERs versus all sub-channels of 114 and 126 Gbaud FTN-DFT-spread QPSK-OFDM after 420-km fiber transmission, and **(F)** optical spectrum (0.02 nm) of WDM signal after 420-km fiber transmission.

subcarriers excluding above-mention six subcarriers are adopted to carry FTN DFT-spread QPSK symbols. The length of CP is eight sample and a pair of training symbols (TSs) is inserted between every 123 OFDM symbols for synchronization and channel estimation. The modulated signal is launched into five spans of 84-km SMF link. There are 18-dB average loss and 17.5-ps/km/nm chromatic dispersion (CD) at 1,550 nm in each span. An erbium doped fiber amplifier (EDFA) is used before each span to compensate for the fiber loss. At the receiver, an ECL with linewidth <100 kHz is used as a local oscillator (LO). We use an integrated coherent receiver (ICR) to achieve the O/E detection. The signal is captured by a 160 GSa/s sampling rate real-time oscilloscope and then processed with offline DSP shown in **Figure 2**.

Figure 3 gives out the simulation results of 99–143 GBaud DFT-spread QPSK-OFDM signal, in which FTN DFT-spread QPSK-OFDM signal is generated with 88 Gsa/s sampling rate DAC and an additive white Gaussian noise (AWGN) channel with signal-to-noise ratio (SNR) = 18 dB is used to emulate the fiber link. When the baud rate is higher than the sampling rate of DAC, the BER performance of conventional DFT-spread QPSK-OFDM is very poor as part of conventional DFT spread is not robust to brick-wall filter effect–induced ISI. However, the BER performance is better when FTN DFT-spread QPSK-OFDM signal is transmitted, as less proportion of power of signal is filtered out with brick-wall filter in frequency spectrum compression. After that, we prove MLSE decoding is more robust to resist ISI and can be used to further compensate the penalty induced by ISI. In this study, BER performance of single-channel 114 Gbaud and 126 Gbaud FTN DFT-spread QPSK-OFDM signal are measured and shown in **Figure 4A** and **Figure 4B**, respectively. We realize pre-equalization to resist bandwidth limitation induced ISI to some extent. Single-channel 114 Gbaud FTN DFT-spread QPSK-OFDM optical spectrums (0.02 nm) with and without pre-equalization are inserted in **Figure 2A**. The electrical spectrums of 114 Gbaud FTN-DFT-spread QPSK-OFDM optical spectrums with and without pre-equalization are inserted in **Figure 2B** and **Figure 2C**, respectively. After pre-equalization, BER performance of both 114 Gbaud and 126 Gbaud FTN DFT-spread QPSK-OFDM can be improved significantly, and MLSE decoding is also proved to be effective to resist ISI. Insets i) and ii) in **Figure 4A** show the constellations of 114 Gbaud FTN DFT-spread QPSK-OFDM with and without pre-equalization with OSNR at 30.4-dB, and insets i) and ii) in **Figure 4B** show the constellations of 126 Gbaud FTN DFT-spread QPSK-OFDM with and without pre-equalization with OSNR at 29.4-dB.

Figure 4C shows the measured BER versus input power per channel of the 3rd sub-channel of WDM after 420-km transmission. We measure the optimal input power per channel of all channels to be 0 dBm. It is easy to explain because high-power signals into the fiber will lead to chromatic dispersion and the nonlinear effect, which can damage signal quality. If the input fiber power is too low, the signal-to-noise ratio will be low, and the noise will also affect the transmission quality of the signal. There is supposed to be a compromised power that makes the system perform optimally. The optimal input power of the other seven sub-channels is also measured to be 0 dBm.

Figure 4D shows the measured BER versus optical signal-to-noise ratio (OSNR) of the 3rd sub-channel of WDM in optical back-to-back (OBTB) and after 420-km fiber transmission. We observe no OSNR penalty compared to single-channel transmission. And negligible OSNR is observed after 420-km SMF transmission. After 420-km SMF transmission, the required OSNRs for 114 and 126 Gbaud FTN-DFT-spread QPSK-OFDM to achieve hard decision forward error correction (HD-FEC) threshold (3.8×10^{-3}) and SD-FEC threshold (2.4×10^{-2}) are 24.8 and 25.5 dB, respectively. Both the effective data rates of 114 and 126 Gbaud FTN-DFT-spread QPSK-OFDM are larger than 400 Gbit/s after removing overheads which includes TSs, CP, and corresponding FEC overheads. Insets i) and ii) in **Figure 4E** show the constellations of 114 and 126 Gbaud FTN DFT-spread QPSK-OFDM in WDM case with OSNR at 27.4-dB.

For all sub-channels 114 and 126 Gbaud FTN DFT-spread QPSK-OFDM, the measured BERs after 420-km SMF transmission shown in **Figure 4** are below 3.8×10^{-3} and 2.4×10^{-2}, respectively. Optical spectrum (0.02 nm) of WDM signal after 420-km transmission is inset in **Figure 4F**. While the computational complexity of SD-FEC is significantly higher, it is practical to transmit 114 Gbaud FTN-DFT-spread QPSK-OFDM to realize 400G services per wavelength for metro and regional applications.

CONCLUSION

In this study, for the first time we realize 400G FTN-DFT-spread QPSK-OFDM signal transmission per optical carrier for metro and regional applications. With the aid of DAF-based spectrum shaping and MLSE decoding in the receiver, we successfully transmit 8 × 400 Gbit/s FTN-DFT-spread QPSK-OFDM signal generated from 88 Gsa/s sampling rate DAC over 420 km SMF with the BER under 2.4×10^{-2}.

DATA AVAILABILITY STATEMENT

The raw data supporting the conclusion of this article will be made available by the authors, without undue reservation.

AUTHOR CONTRIBUTIONS

FL supervised the project and proposed the idea. PL wrote the article and did the experiment. HC did the simulation and discussed the results. WN drew the figures and analyzed the data.

FUNDING

This work is partly supported by the State Key Laboratory of Computer Architecture (ICT, CAS) under Grant (No. CARCH201907); Guangdong Basic and Applied Basic Research Foundation under Grant (Nos. 2019A1515110284, 2021A1515011962); Fundamental and Applied Basic Research Project of Guangzhou City under Grant (No. 202002030326).

REFERENCES

1. Zhang J, Yu J, and Chi N. Generation and Transmission of 512-Gb/s Quad-Carrier Digital Super-nyquist Spectral Shaped Signal. *Opt Express* (2013) 21(25):31212. doi:10.1364/OE.21.031212
2. Jia Z, Yu J, Chien H-C, Dong Z, and Di Huo D. Field Transmission of 100 G and Beyond: Multiple Baud Rates and Mixed Line Rates Using Nyquist-WDM Technology. *J Lightwave Technol* (2012) 30(24):3793–804. doi:10.1109/JLT.2012.2207373
3. Cai JX, Davidson CR, Lucero A, Zhang H, Foursa DG, Sinkin OV, et al. 20 Tbit/s Transmission over 6860 Km with Sub-nyquist Channel Spacing. *J lightwave Technol* (2011) 30(4):651–7.
4. Chien HC, Yu J, Jia Z, Dong Z, and Xiao X. 512-Gb/s Quad-Carrier PM-QPSK Transmission over 2400-km SMF-28 Subject to Narrowing 100-GHz Optical Bandwidth. In: 2012 38th European Conference and Exhibition on Optical Communications; 2012 Sept 16–20; Amsterdam, Netherlands. IEEE (2012). p. 1–3.
5. Zhang J, Yu J, Jia Z, and Chien H-C. 400 G Transmission of Super-nyquist-filtered Signal Based on Single-Carrier 110-GBaud PDM QPSK with 100-GHz Grid. *J Lightwave Technol* (2014) 32(19):3239–46. doi:10.1109/jlt.2014.2343016
6. Jia Z, Cai Y, Chien H-C, and Yu J. Performance Comparison of Spectrum-Narrowing Equalizations with Maximum Likelihood Sequence Estimation and Soft-Decision Output. *Opt Express* (2014) 22(5):6047. doi:10.1364/OE.22.006047
7. Zhang J, Huang B, and Li X. Improved Quadrature Duobinary System Performance Using Multi-Modulus Equalization. *IEEE Photon Technol Lett* (2013) 25(16):1630–3. doi:10.1109/lpt.2013.2273034
8. Zhang J, Yu J, Dong Z, Jia Z, Chien HC, Cai Y, et al. Transmission of 20× 440-Gb/s Super-nyquist-filtered Signals over 3600 Km Based on Single-Carrier 110-GBaud PDM QPSK with 100-GHz Grid. In *OFC 2014*. San Francisco, CA: IEEE (2014). p. 1–3.
9. Yu J, Zhang J, Dong Z, Jia Z, Chien H-C, Cai Y, et al. Transmission of 8 × 480-Gb/s Super-nyquist-filtering 9-QAM-like Signal at 100 GHz-Grid over 5000-km SMF-28 and Twenty-Five 100 GHz-Grid ROADMs. *Opt Express* (2013) 21(13):15686–91. doi:10.1364/oe.21.015686
10. Lu Y, Yu Y, Liu L, Huang Y, Wang X, and Li L. Faster-Than-Nyquist Signal Generation of Single Carrier 483-Gb/s (120.75-GBaud) PDM-QPSK with 92-GSa/s DAC. In: Optical Fiber Communication Conference. Los Angeles, CA: Optical Society of America (2017). p. W2A–44.
11. Zhu C, Corcoran B, Morshed M, Zhuang L, and Lowery AJ. Faster-Than-Nyquist DFT-S-OFDM Using Overlapping Sub-bands and Duobinary Filtering. In: Optical Fiber Communication Conference. Los Angeles, CA: Optical Society of America (2015). p. Th3G–5. doi:10.1364/ofc.2015.th3g.5
12. Li F, Li X, and Yu J. Performance Comparison of DFT-Spread and Pre-equalization for 8× 244.2-Gb/s PDM-16qam-OFDM. *J Lightwave Tech* (2014) 33(1):227–33. doi:10.1109/JLT.2014.2375794
13. Li F, Li X, Yu J, Chen L, and Yu C. Optimization of Training Sequence for DFT-Spread DMT Signal in Optical Access Network with Direct Detection Utilizing DML. *Opt Express* (2014) 22(19):22962. doi:10.1364/OE.22.022962
14. Li J, Tipsuwannakul E, Eriksson T, Karlsson M, and Andrekson PA. Approaching Nyquist Limit in WDM Systems by Low-Complexity Receiver-Side Duobinary Shaping. *J Lightwave Technol* (2012) 30(11): 1664–76. doi:10.1109/jlt.2012.2190972

15. Chien H-C, Yu J, Jia Z, Dong Z, and Xiao X. Performance Assessment of Noise-Suppressed Nyquist-WDM for Terabit Superchannel Transmission. *J Lightwave Technol* (2012) 30(24):3965–71. doi:10.1109/jlt.2012.2207430
16. Zhang J, Chien HC, Xia Y, Chen Y, and Xiao J. A Novel Adaptive Digital Pre-equalization Scheme for Bandwidth Limited Optical Coherent System with DAC for Signal Generation. In: *OFC*. IEEE (2014). p. 1–3.
17. Ding L, Zou D, Wang W, Li F, and Li Z. Generation of faster-Than-Nyquist Coherent Optical DFT-Spread OFDM Signals with High-Baud and High-Order Modulations. *Opt Fiber Tech* (2021) 64:102526. doi:10.1016/J.YOFTE.2021.102526
18. Shankar H. *Duobinary Modulation for Optical Systems*. Santa Clara, CA: Inphi corporation (2002).
19. Xu X, Zhou E, Liu GN, Zuo T, Zhong Q, Zhang L, et al. Advanced Modulation Formats for 400-Gbps Short-Reach Optical Inter-connection. *Opt Express* (2015) 23(1):492–500. doi:10.1364/oe.23.000492
20. Xiao X, Li F, Yu J, Li X, Xia Y, and Chen F. 100-Gb/s Single-Band Real-Time Coherent Optical DP-16qam-OFDM Transmission and Reception. In: Optical Fiber Communication Conference. San Francisco, CA: Optical Society of America (2014). p. Th5C–6. doi:10.1364/ofc.2014.th5c.6

Conflict of Interest: The authors declare that the research was conducted in the absence of any commercial or financial relationships that could be construed as a potential conflict of interest.

BRIEF RESEARCH REPORT
published: 20 August 2021
doi: 10.3389/fphy.2021.727934

Dual Negative Differential of Heat Generation in a Strongly Correlated Quantum Dot Side-Coupled to Majorana Bound States

Zhu-Hua Wang and Wen-Cheng Huang*

College of Physics and Electromechanics, Fujian Longyan University, Longyan, China

We study theoretically the properties of local heat originated from energy exchange between electrons passing through a quantum dot (QD) coupled to a phonon bath. The dot is sandwiched between two normal metal leads and also side-coupled to Majorana bound states (MBSs) formed at opposite ends of a topological superconductor nanowire. We find that in addition to the negative differential of heat generation (NDHG) in the Coulomb blockade regime, another NDHG emerges near the leads' Fermi level due to the dot-MBS coupling. This dual NDHG effect is robust against the variation of intradot Coulomb interaction strength, and disappears if the QD is coupled to regular Fermions. Direct hybridization between the MBSs reduces their impacts on the electronic transport processes, and eliminates the dual NDHG effect. Our results show that the dual NDHG effect is quite efficient for inferring the existence of MBSs, and may remedy some limitations of the detection schemes relying on tunneling spectroscopy technique.

Keywords: heat current, electron-phonon interaction, majorana fermions, quantum dot, negative differential heat generation

Edited by:
Feng Chi,
Zhongshan Institute, China

Reviewed by:
Yingjie Chen,
Qufu Normal University, China
Lian-Liang Sun,
North China University of Technology, China

****Correspondence:***
Zhu-Hua Wang
lywzh666@163.com

Specialty section:
This article was submitted to Optics and Photonics, a section of the journal Frontiers in Physics

Received: *20 June 2021*
Accepted: *12 July 2021*
Published: *20 August 2021*

Citation:
Wang Z-H and Huang W-C (2021) Dual Negative Differential of Heat Generation in a Strongly Correlated Quantum Dot Side-Coupled to Majorana Bound States. Front. Phys. 9:727934. doi: 10.3389/fphy.2021.727934

1 INTRODUCTION

Majorana bound states (MBSs) are zero energy quasi-particles of Majorana fermions typically formed in low-dimensional topological superconductors [1, 2]. They obey non-Abelian statistics and can serve as anyons whose braiding can be used for constructing elementary logic gates for quantum computation [3–6]. Such a kind of logic gate depends only on the topology of the braiding path, and then small imperfections in the braiding are tolerable on the condition that the manipulations are topologically equivalent. Correspondingly, MBSs have been extensively investigated in the past decades as a prominent candidate for fault-tolerant topological quantum computation [7]. In addition, the MBSs are also promising in spintronics and thermoelectric effects. For example, the MBSs will strengthen the intrinsic π phase difference between spin-triplet pairings in Josephson junction [8]. Such a *π-phase shift* is demonstrated to induce a spin-dependent superconducting phase, i.e., spin-phase that is adjustable with the help of electric gates and the coupling energy between MBSs. This effect suggests an all-electrical spin control scheme and can also be used to manipulate and detect the MBSs [8]. If the electron-hole symmetry property of the MBSs is broken (e.g. by side-coupling one mode of the MBSs to a quantum dot (QD)) [9], the sign of the thermopower, which measures the generated bias voltage in response to a temperature difference applied at different ends of the system, can be reversed by changing the hybridization amplitude between the QD and the MBS [10, 11], or direct coupling between the MBSs [12, 13].

Moreover, the magnitude of the thermopower or thermoelectric efficiency can be significantly enhanced due to the existence of the MBSs [12, 13]. These results are useful in designing thermoelectric devices or detecting MBSs.

Experimentally, topological superconductors have been successfully realized in heterostructures comprised of a one-dimensional semiconductor nanowire having strong Rashba spin-orbit interaction and a proximitizing s-wave superconductor [1, 2, 14, 15]. With the help of a strong external magnetic field, the phase of the heterostructure can be driven into topological superconductor one and thus enable the formation of MBSs at opposite ends of the nanowire. As for the detection of MBSs, the most efficient scheme is the tunneling spectroscopy in Majorana nanowires sandwiched between normal metal leads. The MBSs will manifest itself by a zero-bias anomalous conductance peak [15]. Since this anomalous peak in the electric conductance may also originate from other reasons, such as the Kondo effect [16], anti-localization [17] and subgap states [18], some other detection schemes for the MBSs were then continuingly put forward. For example, signatures of MBSs can be inferred from the sign change or abnormal enhancement of the thermopower as was indicated above [9–13]. The existence of the MBSs can be deduced by measuring the Majorana entropy of an initial equilibrium state of the system [19]. Generally, the Majorana entropy will be ruined even when the transport amplitude of one mode of the MBSs is significantly blockaded, which can be directly measured in experiments. To avoid the above general issues, Smirnov very recently proposed to adjust the tunneling phases of one mode of the MBSs to bring out the universal Majorana plateau. Meanwhile, an experimental scheme that is realizable within present techniques was also proposed to measure entropy of the MBSs [19]. Signatures induced by MBSs may also be deduced from transport phenomena such as the abnormal changes of the shot noise [20–22], quantum noise [23, 24], thermoelectric noise [25], sign change of the tunnel magnetoresistance [26], splitting of the photon-assisted subbands [27], etc.

In fact, due to the unique charge neutral and zero energy properties, the above detection schemes still come with great difficulties and it is not sure if the existence of the MBSs can be completely determined. Recently, impacts of electron-phonon interaction on the MBSs-assisted transport have been studied [28, 29]. This is triggered by two motivations: one is that the electron-phonon interaction will induce significant decoherence effects that will change the transport behaviors and roles in quantum computation [30]; the other is that the phonons will play important roles in Majorana-induced Andreev reflection processes [28]. With continuing improvement of nanofabrication techniques, the length of the device becomes smaller than that of electron-phonon scattering, and thus the electron-phonon interaction is the main cause of heat generation by electrical current [30–34]. With increasing integration density on a chip, the issue of generated heat becomes more and more vital [35]. If the waste heat can not be removed as quickly as possible, the chips may not function properly. As was demonstrated by Sun *et. al.* [31, 32], the behaviors of the heat generation in nanodevices are quite different from those in the usual macroscopic ones. The Joule heating law $Q = JV$ for the local heat power density, where J is current density and V is the bias voltage applied across the system, is violated. Electrons transporting through a QD may absorb energy from a phonon bath attached to it even at zero temperature [36]. In the presence of intradot Coulomb interaction, the magnitude of heat generation may be quite small even under a large current [32]. In the Coulomb blockade regime, the heat generation decreases although the current's amplitude is monotonously enhanced *for* increasing bias voltage, a phenomenon was named as negative differential of the heat generation (NDHG) [32]. The NDHG is very similar to the negative differential conductance effect unique in nanodevices, and is expected to play an important role in phonon engineering subjects. In our previous work, MBSs-mediated heat generation by electrical current in a QD without Coulomb interaction was investigated [37]. It was found that the magnitude of the heat generation and electrical current is sensitive to the existence of MBSs. Under some conditions, the heat generation and electrical current can be individually suppressed and enhanced by changing the dot-MBSs or MBS-MBS couplings, which is ideal for energy-saving instruments. In the present manuscript, we revisit the problem of heat generation by taking the intradot Coulomb interaction into consideration. We find that the MBSs will induce another NDHG in addition to that in the absence of MBSs, which is named as dual NDHG that can be used for inferring the existence of the MBSs.

2 MODEL AND METHODS

The system under investigation can be described by the following Hamiltonian ($\hbar = 1$) [28, 29, 31, 32, 37].

$$H = \sum_{k,\beta,\sigma} \varepsilon_{k\beta\sigma} c^{\dagger}_{k\beta\sigma} c_{k\beta\sigma} + [\varepsilon_d + \lambda_q (a^{\dagger} + a)] \sum_{\sigma} d^{\dagger}_{\sigma} d_{\sigma} + U d^{\dagger}_{\uparrow} d_{\uparrow} d^{\dagger}_{\downarrow} d_{\downarrow} + \omega_q a^{\dagger} a + \sum_{k,\beta,\sigma} (t_{k\beta} c^{\dagger}_{k\beta\sigma} d_{\sigma} + H.c) + H_{MBSs}, \tag{1}$$

where the first term in the right side of **Eq. 1** describes the β-th ($\beta = L/R$) lead with $c^{\dagger}_{k\beta\sigma}$ ($c_{k\beta\sigma}$) being the electron creation (annihilation) operator having momentum k, energy $\varepsilon_{k\beta\sigma}$ and spin σ. The second term is for electrons on the QD and their interaction *to* the phonon with strength λ_q. The operator $d^{\dagger}_{\sigma}$ (d_{σ}) creates (annihilates) an electron having quantized single energy level ε_d. $a^{\dagger}(a)$ is for the creation (annihilation) operator of a phonon with frequency ω_q. The third term in the right side of **Eq. 1** is for Coulomb interaction between electrons on the QD, and the fourth term denotes the single phonon mode. The fifth term describes overlapping between the QD and the leads with $t_{k\beta}$ being the matrix element. The last term in **Eq. 1** is for the MBSs and their coupling to the QD, [15, 37–39]

$$H_{MBSs} = i\delta_M \eta_1 \eta_2 + \lambda \sum_{\sigma} (d_{\sigma} - d^{\dagger}_{\sigma}) \eta_1, \tag{2}$$

where the operator $\eta_{1/2}$ denotes the two modes of the MBSs located at opposite ends of the nanowire. In the present paper, we consider that the QD is only coupled to one mode of the MBSs with coupling amplitude λ. The quantity ε_M is the overlap strength between the MBSs. The Majorana operators follow $\{\eta_\alpha, \eta_\beta\} = 2\delta_{\alpha\beta}$ and $\eta_\alpha = \eta_\alpha^\dagger$. According to previous work, we replace the Majorana operators by the regular fermion via [15] $\eta_1 = (1/\sqrt{2})(f + f^\dagger)$, and $\eta_2 = (-i/\sqrt{2})(f - f^\dagger)$, the Hamiltonian H_{MBSs} then is given by.

$$H_{MBSs} = \varepsilon_M\left(f^\dagger f - \frac{1}{2}\right) + \frac{\lambda}{\sqrt{2}}\sum_\sigma (d_\sigma - d_\sigma^\dagger)(f + f^\dagger). \tag{3}$$

To decouple the electron-phonon interaction in **Eq. 1**, we next perform a canonical transformation, [28, 29, 31, 32, 37], $\tilde{H} = XHX^\dagger$ with $X = \exp[(\lambda_q/\omega_q)(a_q^\dagger - a_q)\sum_\sigma d_\sigma^\dagger d_\sigma]$, and then **Eq. 1** becomes.

$$\tilde{H} = \sum_{k,\beta,\sigma} \varepsilon_{k\beta\sigma} c_{k\beta\sigma}^\dagger c_{k\beta\sigma} + \tilde{\varepsilon}_d \sum_\sigma d_\sigma^\dagger d_\sigma + \sum_{k,\alpha,\sigma}(\tilde{t}_{k\beta} c_{k\alpha\sigma}^\dagger d_\sigma + H.c) + \tilde{H}_{MBSs}, \tag{4}$$

where the dot level is $\tilde{\varepsilon}_d = \varepsilon_d - g\omega_q$ and Coulomb interaction strength $\tilde{U} = U - 2g\omega_q$ with $g = (\lambda_q/\omega_q)^2$. The tunnelling amplitude $t_{k\beta}$ and the coupling strengths between the dot and MBSs λ are individually given by $t_{k\alpha} = t_{k\alpha}X$ and $\lambda = \lambda X$ with $X = \exp[-g(a^\dagger - a)]$ [28, 29]. The other quantities in $\tilde{H}_{MBSs}$ are the same as in **Eq. 3**. If $t_{k\alpha}$ and λ are weak as compared to λ_q, X can be replaced by the expectation value $< X > = \exp[-g(N_{ph} + 1/2)]$, in which $N_{ph} = 1/[\exp(\omega_q/k_B T_p) - 1]$ the phonon distribution function with T_p the phonon temperature [12, 13]. The heat generation $J_q(t) = \omega_q \langle d a_q^\dagger(t) a_q(t)/dt \rangle$ in frequency space is written based on the Green's functions as the following form, [31]

$$J_q = \mathrm{Re}\,\omega_q \lambda_q^2 \sum_\sigma \int \frac{d\varepsilon}{2\pi}\{\tilde{G}_\sigma^<(\varepsilon)\tilde{G}_\sigma^>(\bar{\varepsilon}) - 2N_{ph}[\tilde{G}_\sigma^>(\varepsilon)\tilde{G}_\sigma^a(\bar{\varepsilon}) + \tilde{G}_\sigma^r(\varepsilon)\tilde{G}_\sigma^>(\bar{\varepsilon})]\}, \tag{5}$$

where $\bar{\varepsilon} = \varepsilon - \omega_q$, and $\tilde{G}_\sigma^{r,a,<,>}(\varepsilon)$ are the electron retarded, advanced, lesser and greater Green's functions. The retarded Green's function $\tilde{G}_\sigma^r(\varepsilon)$ is calculated from **Eq. 4** by the equation of motion method as, [38, 39]

$$\tilde{G}_\sigma^r(\varepsilon) = \frac{1 + (1 - \tilde{\lambda}^4 \tilde{K}\tilde{K}_U)\Pi_\sigma}{\varepsilon - \tilde{\varepsilon}_d - \Sigma_{0,M}^r + i\tilde{\Gamma}}. \tag{6}$$

where $\tilde{\Gamma} = (\tilde{\Gamma}_L + \tilde{\Gamma}_R)/2$, with $\tilde{\Gamma}_\beta = \exp[-g(2N_{ph} + 1)]\Gamma_\beta$ and $\Gamma_\beta = 2\pi|t_{k\beta}|^2\rho_\beta$, where ρ_β is the local density of states in lead β. The quantities $\Pi_\sigma = \tilde{U}n_{\bar{\sigma}}/(\varepsilon - \tilde{\varepsilon}_d - \tilde{U} - \Sigma_{1,M}^r + i\tilde{\Gamma})$, $\tilde{\varepsilon}_d - \tilde{\lambda}^2 K + i\tilde{\Gamma})$, $\tilde{K}_U = K/(\varepsilon + \tilde{\varepsilon}_d + \tilde{U} - \tilde{\lambda}^2 K + i\tilde{\Gamma})$, and $K = \varepsilon/(\varepsilon^2 - \delta_M^2)$. The advanced Green's function in the above equation is $\tilde{G}_\sigma^a(\varepsilon) = [\tilde{G}_\sigma^r(\varepsilon)]^*$, and the lesser (greater) one is $\tilde{G}_\sigma^{<(>)}(\varepsilon) = \tilde{G}_\sigma^r(\varepsilon)\tilde{\Sigma}^{<(>)}\tilde{G}_\sigma^a(\varepsilon)$, in which the self-energies are individually given by $\tilde{\Sigma}^< = i[\tilde{\Gamma}_L f_L(\varepsilon) + \tilde{\Gamma}_R f_R(\varepsilon)]$, and $\tilde{\Sigma}^> = -i\{\tilde{\Gamma}_L[1 - f_L(\varepsilon)] + \tilde{\Gamma}_R[1 - f_R(\varepsilon)]\}$ [31]. The Fermi distribution function is $f_\beta(\varepsilon) = 1/\{\exp[(\varepsilon - \mu_\beta)/k_B T_e] + 1\}$, with chemical potential μ_β. $G^r(\varepsilon)$ is related to $\tilde{G}^r(\varepsilon)$ by [31] $G_\sigma^r(\varepsilon) = \sum_{n=-\infty}^{n=\infty} L_n\{\tilde{G}_\sigma^r(\varepsilon - n\omega_q) + [\tilde{G}_\sigma^<(\varepsilon - n\omega_q) - \tilde{G}_\sigma^<(\varepsilon + n\omega_q)]/2\}$, and $\tilde{G}_\sigma^<(\varepsilon) = -2i\Gamma_L f_L(\varepsilon) + \Gamma_R f_R(\varepsilon)/(\Gamma_L + \Gamma_R)\mathrm{Im}\tilde{G}_\sigma^r(\varepsilon)$, where $L_n = \exp[-g(2N_{ph} + 1)]\exp(n\omega_q/2k_B T)I_n[2g\sqrt{2N_{ph}(N_{ph} + 1)}]$, with $I_n(x)$ the modified nth Bessel function. The occupation number is calculated self-consistently from $n_\sigma = -i\int d\varepsilon/2\pi G_\sigma^<(\varepsilon)$, and the spin-dependent electric current is obtained also by the Green's function as [7, 30] $J_e = -e\Gamma_L\Gamma_R/[2\pi h(\Gamma_L + \Gamma_R)]\sum_\sigma \int d\varepsilon[f_L(\varepsilon) - f_R(\varepsilon)]\mathrm{Im}G_\sigma^r(\varepsilon)$.

3 RESULTS AND DISCUSSION

In the following numerical calculations, we *choose* the phonon frequency $\omega_q \equiv 1$ as energy unit ($\hbar = 1$), and consider the case of the dot is symmetrically coupled to the left and right leads with $\tilde{\Gamma}_L = \tilde{\Gamma}_R = 0.1\omega_q$. The electron-phonon coupling strength is fixed as $\lambda_q = \omega_q$, and the temperatures of the electrons and phonons are $T_e = T_p = 0.02\omega_q$. The chemical potential of the right lead μ_R is set to be zero as the energy zero point, and the bias voltage is $eV = \mu_L$. **Figure 1** shows the total electrical current J_e and heat generation J_q varying with respect to the bias voltage when the QD is coupled to one of the *MBSs* with different strengths. For dot level $\tilde{\varepsilon}_d = 0$, the electrical current J_e in **Figure 1A** has two steps respectively around bias values of $eV = \tilde{\varepsilon}_d$ and $eV = \tilde{\varepsilon}_d + \tilde{U}$. Between these two steps, the current's lineshape shows the typical Coulomb blockade effect [32]. The origination of this effect can be explained as follows: in the absence of bias voltage, i.e., $\tilde{\varepsilon}_d = \mu_L = \mu_R$, *there are an equal number of electrons in the left and right leads tunnel through the QD in opposite directions, and then results in zero charge current. In the presence of bias voltage* $eV = \mu_L$, *there are more electrons in the left lead than the right one entering into the QD and then tunneling out to the right lead, so the current is positive. For even larger bias voltage, the electron occupation number in the QD increases since the electrons' probability of dwelling on the dot becomes larger.* Correspondingly, the probability of other electrons to enter into the dot becomes smaller, and then the current's magnitude will not increase further. As shown in **Figure 1A**, the current reaches a plateau when the bias voltage is $\tilde{\varepsilon}_d < eV < \tilde{\varepsilon}_d + \tilde{U}$ due to the so-called Coulomb blockade effect. When $eV > \tilde{\varepsilon}_d + \tilde{U}$, the QD level $\tilde{\varepsilon}_d + \tilde{U}$ enters into the transport window and then the current's magnitude increases again. At the bias voltages of $eV = \tilde{\varepsilon}_d$ and $\tilde{\varepsilon}_d + \tilde{U}$, the electrical differential conductance $G_{dif} = dJ_e/dV$ has two sharp peaks, but is zero when $\tilde{\varepsilon}_d < eV < \tilde{\varepsilon}_d + \tilde{U}$, which is not shown here. There are some small steps in the curves of J_q versus eV due to the electron-phonon interaction, by which the QD energy level is modified into $\tilde{\varepsilon}_d = \varepsilon_d - g\omega_q$ [31, 32]. Now electrons can transport through the system whenever the energy states $\tilde{\varepsilon}_d + n\omega_q$ or $\tilde{\varepsilon}_d - n\omega_q$ enter into the bias window, which results in an abrupt increase of the electrical current. *In the presence of QD-MBSs coupling* ($\tilde{\lambda} \neq 0$), *we find that the current near zero bias voltage is obviously changed, whereas that at relatively larger bias voltage is less influenced. This is because the MBSs are zero in energy and only exert impacts on the current around zero bias voltage, which is consistent with the results of zero bias anomaly of the conductance serving as evidence of the MBSs.* [17, 20].

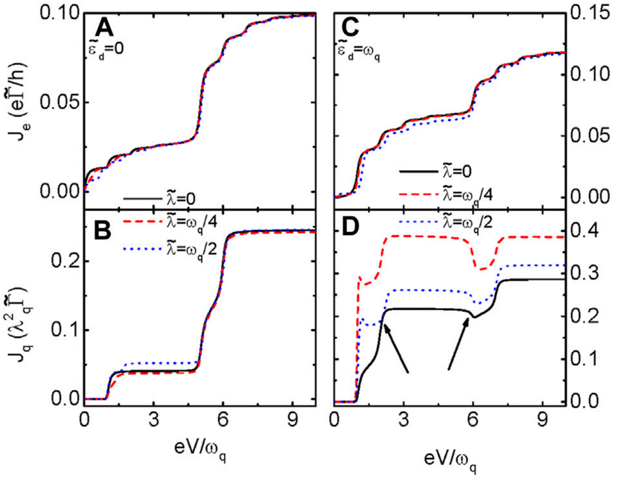

FIGURE 1 | Electrical current and heat generation varying with respective to the bias voltage when the QD is coupled to MBSs. **(A)** and **(B)** are for $\tilde{\varepsilon}_d = 0$ whereas $\tilde{\varepsilon}_d = \omega_q$ in **(C)** and **(D)**. The two arrows in **Figure 1D** indicate the two NDHG. The dot-MBSs coupling strength λ is set at different values. Other parameters are $\lambda_q = \omega_q$, $\tilde{\Gamma}_L = \tilde{\Gamma}_R = 0.1\omega_q$, $T_e = T_{ph} = 0.02\omega_q$, $\delta_M = 0$, $U = 5\omega_q$.

The line-shape of the heat generation in **Figure 1B** resembles that of the current influenced by the Coulomb blockade effect, but has no small steps induced by the electron-phonon interaction. The reason is that the heat generation in **Eq. 5** is calculated from the transformed Hamiltonian in which the electron and phonon is decoupled. Therefore, the plateaus in the heat generation are much flatter compared to those in the current. The heat generation has a delay of ω_q as compared to the electric current in **Figure 1A** [32]. This *is* because the heat generation J_q is caused by the phonon absorption and emission processes occurred between energy states ε and $\varepsilon \pm \omega_q$ [31, 32]. When the bias voltage is small $eV < \omega_q$, the electrons can not absorb enough energy from the external electrical field to emit phonon having energy $\hbar\omega_q$, and therefore the magnitude of the heat generation is zero. It is worth pointing out that this delay effect is absent in macroscopic systems and is more distinct at low temperature regimes. It emerges regardless of the existence of intradot Coulomb interaction or some other fields [31–34, 36]. In the presence of interaction between the MBSs *at the ends of a nanowire* ($\tilde{\lambda} \neq 0$), the magnitude of the electrical current in **Figure 1A** near the Fermi level $eV = 0$ is slightly decreased, with that at other bias voltage mainly remain unchanged which is indicated above. The heat generation in **Figure 1B**, however, can be either enhanced or suppressed. During the bias voltage of $\omega_q \leq eV \leq \tilde{U} + \omega_q$, the magnitude of the heat generation can be slightly enhanced for nonzero $\tilde{\lambda}$, but when $eV > \tilde{U} + \omega_q$ the magnitude of the heat generation is slightly suppressed.

When the dot level is tuned by gate voltage to be $\tilde{\varepsilon}_d = \omega_q$, positions of the steps in the current are changed accordingly (**Figure 1C**). The magnitude of the current changes more obviously by the dot-MBS coupling $\tilde{\lambda}$ as compared to the case of $\tilde{\varepsilon}_d = 0$ in **Figure 1A**. As found in Ref. [10], the electron transmission will become asymmetric for $\tilde{\varepsilon}_d \neq 0$ and develops a sharp peak at negative energy due to the dot-MBS coupling, which is out of the transport window. As a result of it, the current's magnitude is weakened for $\lambda \neq 0$. The line-shape of heat generation in **Figure 1D** is quite different from that in **Figure 1B**. First, the amplitude of the abrupt jump in heat generation at $eV = \tilde{\varepsilon}_d + \omega_q$ is much larger than that at $eV = \omega_q + \tilde{\varepsilon}_d + \tilde{U}$. This result is consistent with that in Ref. [32]. Second, in the absence of dot-MBS coupling, there is an obvious NDHG effect when the bias voltage is between $\tilde{\varepsilon}_d + \tilde{U} - \omega_q$ and $\tilde{\varepsilon}_d + \tilde{U}$, where the heat generation decreases with increasing bias voltage. This is because the electron passing through the QD can either absorb or emit a phonon. If the bias voltage V is between $\tilde{\varepsilon}_d + \tilde{U} - \omega_q$ and $\tilde{\varepsilon}_d + \tilde{U}$, the tunneling process can only be realized when the electron absorbs a phonon while electrons transport through the QD, inducing a NDHG. Third, we find in **Figure 1D** that another NDHG emerges when the bias voltage is between ω_q and $\omega_q + \lambda$ in the presence of dot-MBS hybridization, which is called dual NDHG in the present paper. The origination of the NDHG near ω_q is because the hybridization between the QD and MBS induces new states at $\tilde{\varepsilon}_d \pm \tilde{\lambda}$. Meanwhile, the NDHG in the Coulomb blockade regime is also enhanced by increasing $\tilde{\lambda}$. This enhanced and newly emerged NDHG can be used for deducing the existence of MBSs. We emphasize that the NDHG effect is more likely to emerge in the presence of intradot Coulomb interaction, as was shown in previous works [31, 32, 37].

To show the novel dual NDHG effect induced by the MBSs, we present the results when the dot is side-coupled to another QD serving as regular fermion in **Figure 2**. For the sake of notational consistency, we use the same symbols δ_M and $\tilde{\lambda}$ to individually denote the QD energy level and the coupling amplitude between the two dots. The Hamiltonian of the present system is given by $H_{MBSs} = \delta_M f^\dagger f + \tilde{\lambda}\sum_\sigma (f^\dagger d_\sigma + d_\sigma^\dagger f)$, and the Green's function is calculated as [40, 41]

$$\tilde{G}_\sigma^r(\varepsilon) = \frac{1 - n_{\bar{\sigma}}}{\varepsilon - \tilde{\varepsilon}_d - \Sigma_{1,M}^r + i\tilde{\Gamma}} + \frac{n_{\bar{\sigma}}}{\varepsilon - \tilde{\varepsilon}_d - \tilde{U} - \Sigma_{1,M}^r + i\tilde{\Gamma}}, \quad (7)$$

in which $\Sigma_{1,M}^r = \tilde{\lambda}^2/(\varepsilon - \delta_M)$. The molecular states of the structure of QD coupled to regular fermion are calculated

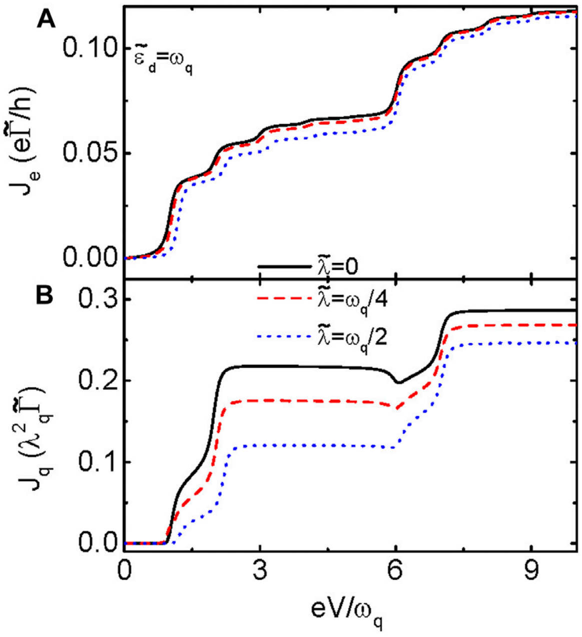

FIGURE 2 | J_e in **(A)** and J_q in **(B)** versus the bias voltage when the QD is coupled to regular fermions in another QD. As the present manuscript focuses on the NDHG occurred at non-zero dot level, here only the results of $\lambda_q = \omega_q$ is presented. Other parameters are the same to those in **Figure 2**.

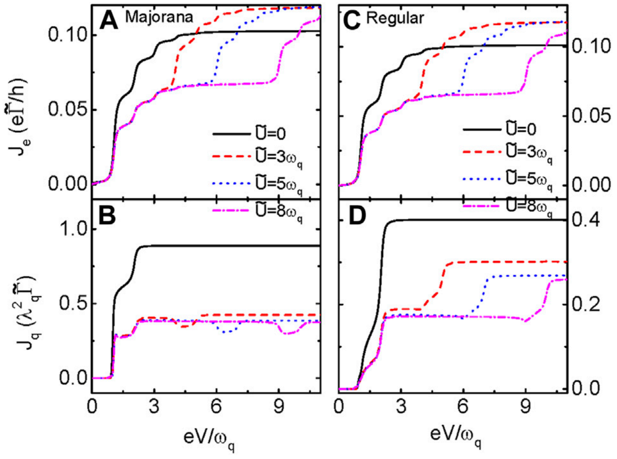

FIGURE 3 | (A) and **(B)** are individually for J_e and J_q in QD coupled to MBSs, and **(C)** and **(D)** are J_e and J_q in QD connected to regular fermions, respectively. The Coulomb interaction is chosen at different values with fixed $\lambda = \omega_q/4$. Other parameters are as in **Figure 2**.

from the above retarded Green's to be $\varepsilon = 0$ and $\varepsilon_\pm = (\delta_M \pm \sqrt{\delta_M^2 + 4\tilde{\lambda}^2})/2$, whereas those of the dot hybridized to MBSs are at $\varepsilon = 0$ and $\varepsilon_\pm = \pm\sqrt{\delta_M^2 + 2\tilde{\lambda}^2}$. Moreover, the phase shift of the two kinds of systems are different, [41] resulting in different behaviors of the current and heat generation in **Figure 2**. The electrical current in **Figure 2A** resembles that in **Figure 1C** only with changed positions of the steps, which indicates that the current is less influenced by the MBSs. The heat generation in **Figure 2B**, however, is very different from that in **Figure 1D**. Firstly, when the dot is coupled to regular fermion (another QD), the heat generation decreases with increasing $\tilde{\lambda}$ as shown in **Figure 2B**. But if the dot is coupled to MBS, the heat generation increases with increasing $\tilde{\lambda}$ which can be seen from **Figure 1D**. Secondly, the NDHG in the Coulomb blockade regime is eliminated by the stronger coupling between QD and regular fermion (**Figure 2B**), whereas that in QD-MBS structure is enhanced. Thirdly, the NDHG around $\omega_q + \tilde{\lambda}$ is also eliminated by increasing $\tilde{\lambda}$ when the QD is coupled to regular

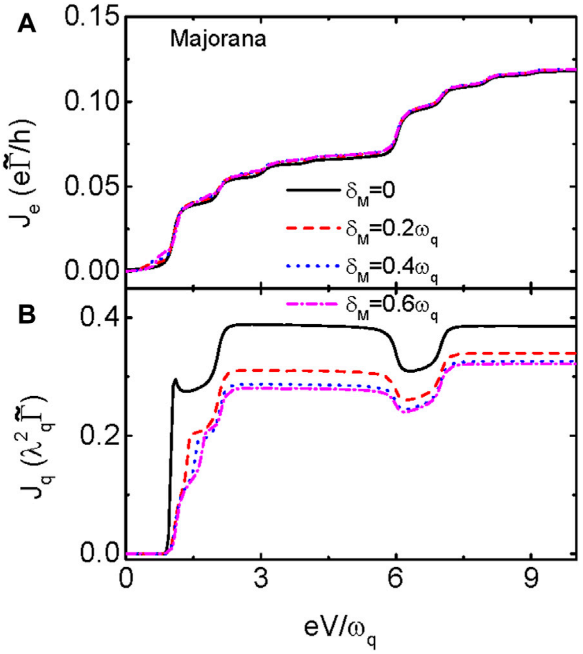

FIGURE 4 | J_e in **(A)** and J_q in **(B)** as functions of the bias voltage when the QD is coupled to MBSs for different values of δ_M and fixed. The Coulomb interaction is chosen at different values with fixed $\lambda = \omega_q/4$. Other parameters are as in **Figure 2**.

fermion given in **Figure 2B**. The above changes of the heat generation represents the unique properties of the MBSs as compared to those of the regular fermions, and then can be used for detection means for the MBSs. We have also calculated the case when the dot level is aligned to the Fermi level ($\tilde{\varepsilon}_d = 0$) and found that the phenomenon of NDHG disappears similar to the result in **Figure 1B**, and then we do not show them in the figure.

Figure 3 presents the impacts of different intradot Coulomb interaction on the electrical current and heat generation in both QD-MBS and QD-QD structures. The electrical current in **Figure 3A** when the dot is coupled to MBS shows small phonon-induced steps and plateaus. The intradot Coulomb interaction results in another plateau in higher voltage regimes and changes the strength of the current. The current in **Figure 3C** of QD-QD structure resembles that in **Figure 3A** and indicates the insufficiency of detecting MBS by transport means. The magnitude of the heat generation in **Figure 3B** for QD-MBS is decreased even for a weak $\tilde{U}$, and then almost *remains at* the same amount with further increasing $\tilde{U}$. Meanwhile, two NDHGs emerge as soon as the intradot Coulomb interaction is turned on. Further increase of the value of $\tilde{U}$ only changes the position of the NDHG in the Coulomb blockade regime, with the behavior at $eV = \omega_q + \tilde{\lambda}$ remains essentially unchanged. The heat generation in QD-QD structure, however, only has one NDHG in the Coulomb blockade regime. The above results show that the dual NDHG induced by MBS is quite robust against the variation of the amplitude of intradot Coulomb interaction.

Finally in **Figure 4**, we study the influences of direct hybridization between the MBSs δ_M, which is determined by the length and material properties of the nanowire, on the electrical current and heat generation when the QD is coupled to MBS. The case of the dot connected to another QD has been extensively studied [40], and we do not show it here. When the two modes of the MBSs are overlapped ($\delta_M \neq 0$), their impacts on the electrical current and heat generation is weakened. We find that the current in **Figure 4A** is slightly enhanced by increasing δ_M, with the positions of the steps and plateaus remaining unchanged. The magnitude of the heat generation, however, decreases in the presence of δ_M as shown in **Figure 4B**. The NDHG in the Coulomb blockade regime is almost unchanged by δ_M, whereas that near $\omega_q + \tilde{\lambda}$ is eliminated if the MBS-MBS coupling strength is large. The reason is that when the two modes of the MBSs interact with each other, they behave like regular fermions.

4 SUMMARY

In summary, we study properties of electric current and heat generation in a QD hybridized to one mode of MBSs prepared at the one end of a nanowire. Our results show that the properties of the electric current under the influence of MBS are quite similar to those when the dot is coupled to regular fermions. In the presence of intradot Coulomb interaction, the heat generation has a NDHG effect in the Coulomb blockade regime when there is no coupling between the QD and MBS. But another NDHG in lower bias voltage regime emerges, which is called the dual NDHG effect unique to the MBSs, when the dot interacts with the MBS. We find that the dual NDHG arises even for quite weak intradot Coulomb interaction and disappears if the MBS is replaced by regular fermions. The overlap between the two modes of the MBSs destroys the dual NDHG effect, and reduces the magnitude of the electrical current because now the MBSs resemble regular fermions. The present results indicate that the behaviors of the heat current may be rather efficient for detecting the MBSs as compared to the pure electrical method.

DATA AVAILABILITY STATEMENT

The original contributions presented in the study are included in the article/supplementary material, further inquiries can be directed to the corresponding author.

AUTHOR CONTRIBUTIONS

Z-HW derived the formulae, performed partial numerical calculations, and wrote the original manuscipt. W-CH discussed the physical model, performed partial numerical calculations, and contributed in the paper writting.

FUNDING

This work was supported by Thirteenth five-year plan of educational science in Fujian province (Grant Nos. FJJKCG19-297 and 2019CG0707).

REFERENCES

1. Fu L, and Kane C. Superconducting Proximity Effect and Majorana Fermions at the Surface of a Topological Insulator. *Phys Rev Lett* (2008) 100:096407. doi:10.1103/PhysRevLett.100.096407
2. Qi X, and Zhang S. Topological Insulators and Superconductors. *Rev Mod Phys* (2011) 83:1057. doi:10.1103/RevModPhys.83.1057
3. Nayak C, Simon S, Stern A, Freedman M, and Sarma S. Non-abelian Anyons and Topological Quantum Computation. *Rev Mod Phys* (2008) 80:1083. doi:10.1103/RevModPhys.80.1083
4. Alicea J, Oreg Y, Refael G, von Oppen F, and Fisher M. Non-abelian Statistics and Topological Quantum Information Processing in 1d Wire Networks. *Nat Phys* (2011) 7:412. doi:10.1038/nphys1915
5. Karzig T, Knapp C, Lutchyn R, Bonderson P, Hastings M, Nayak C, et al. Scalable Designs for Quasiparticle-Poisoning-Protected Topological Quantum Computation with Majorana Zero Modes. *Phys Rev B* (2017) 95:235305. doi:10.1103/PhysRevB.95.235305
6. Huang H, Narozniak M, Liang F, Zhao Y, Castellano A, Gong M, et al. Emulating Quantum Teleportation of a Majorana Zero Mode Qubit. *Phys Rev Lett* (2021) 126:090502. doi:10.1103/PhysRevLett.126.090502
7. Karzig T, Cole W, and Pikulin D. Quasiparticle Poisoning of Majorana Qubits. *Phys Rev Lett* (2021) 126:057702. doi:10.1103/PhysRevLett.126.057702
8. Liu X, Li X, Deng D, Liu X, and Sarma S. Majorana Spintronics. *Phys Rev B* (2016) 94:014511. doi:10.1103/PhysRevB.94.014511
9. Hou C, Shtengel K, and Refael G. Thermopower and mott Formula for a Majorana Edge State. *Phys Rev B* (2013) 88:075304. doi:10.1103/PhysRevB.88.075304
10. López R, Lee M, Serra L, and Lim J. Thermoelectrical Detection of Majorana States. *Phys Rev B* (2014) 89:205418. doi:10.1103/PhysRevB.89.205418
11. Leijinse M. Thermoelectric Signatures of a Majorana Bound State Coupled to a Quantum Dot. *New J Phys* (2014) 16:015029. doi:10.1088/1367-2630/16/1/015029
12. Hong L, Chi F, Fu Z, Hou Y, Wang Z, Li K, et al. Large Enhancement of Thermoelectric Effect by Majorana Bound States Coupled to a Quantum Dot. *J Appl Phys* (2020) 127:124302. doi:10.1063/1.5125971
13. Chi F, Fu Z, Liu J, Li K, Wang Z, and Zhang P. Thermoelectric Effect in a Quantum Dot Side-Coupled to Majorana Bound States. *Nanoscale Res Lett* (2020) 15:79. doi:10.1186/s11671-020-03307-y
14. Mourik V, Zuo K, Frolov S, Plissard S, Bakkers E, and Kouwenhoven L. Signatures of Majorana Fermions in Hybrid Superconductor-Semiconductor Nanowire Devices. *Science* (2012) 336:1003. doi:10.1126/science.1222360
15. Liu D, and Baranger H. Detecting a Majorana-Fermion Zero Mode Using a Quantum Dot. *Phys Rev B* (2011) 84:201308. doi:10.1103/PhysRevB.84.201308
16. Wang R, Su W, Zhu J, Ting C, Li H, Chen C, et al. Kondo Signatures of a Quantum Magnetic Impurity in Topological Superconductors. *Phys Rev Lett* (2019) 122:1–6. doi:10.1103/PhysRevLett.122.087001
17. Pikulin D, Dahlhaus J, Wimmer M, Schomerus H, and Beenakker C. A Zero-Voltage Conductance Peak from Weak Antilocalization in a Majorana Nanowire. *New J Phys* (2012) 14:125011. doi:10.1088/1367-2630/14/12/125011
18. Kells G, Meidan D, and Brouwer P. Low-energy Subgap States in Multichannel P-Wave Superconducting Wires. *Phys Rev B* (2012) 85:060507. doi:10.1103/PhysRevB.85.060507
19. Smirnov S. Majorana Entropy Revival via Tunneling Phases. *Phys Rev B* (2021) 103:075440. doi:10.1103/PhysRevB.103.075440
20. Liu D, Cheng M, and Lutchyn R. Probing Majorana Physics in Quantum-Dot Shot-Noise Experiments. *Phys Rev B* (2015) 91:081405. doi:10.1103/PhysRevB.91.081405
21. Smirnov S. Non-equilibrium Majorana Fluctuations. *New J Phys* (2017) 19:063020. doi:10.1088/1367-2630/aa70a9
22. Bathellier D, Raymond L, Jonckheere T, Rech J, Zazunov A, and Martin T. Finite Frequency Noise in a normal Metal-Topological Superconductor junction. *Phys Rev B* (2019) 99:104502. doi:10.1103/PhysRevB.99.104502
23. Smirnov S. Majorana Finite-Frequency Nonequilibrium Quantum Noise. *Phys Rev B* (2019) 99:165427. doi:10.1103/PhysRevB.99.165427
24. Smirnov S. Dynamic Majorana Resonances and Universal Symmetry of Nonequilibrium Thermoelectric Quantum Noise. *Phys Rev B* (2019) 100:245410. doi:10.1103/PhysRevB.100.245410
25. Smirnov S. Universal Majorana Thermoelectric Noise. *Phys Rev B* (2018) 97:165434. doi:10.1103/PhysRevB.97.165434
26. Tang L, and Mao W. Detection of Majorana Bound States by Sign Change of the Tunnel Magnetoresistance in a Quantum Dot Coupled to Ferromagnetic Electrodes. *Front Phys* (2020) 8:147. doi:10.3389/fphy.2020.00147
27. Chi F, He T, Wang J, Fu Z, Liu L, Liu P, et al. Photon-assisted Transport through a Quantum Dot Side-Coupled to Majorana Bound States. *Front Phys* (2020) 8:254. doi:10.3389/fphy.2020.00254
28. Dai N, and Sun Q. Phonon-assisted Andreev Reflection at a Majorana Zero Mode. *Phys Rev B* (2019) 99:085436. doi:10.1103/PhysRevB.99.085436
29. Wang X, Wu B, Zhang S, Wang Q, and Gong W. Influences of Electron–Phonon Interaction on Quantum Transport through One Quantum-Dot System with Side-Coupled Majorana Zero Mode. *Ann Phys* (2020) 415:168127. doi:10.1016/j.aop.2020.168127
30. Li N, Ren J, Wang L, Zhang G, Hänggi P, and Li B. Colloquium: Phononics: Manipulating Heat Flow with Electronic Analogs and beyond. *Rev Mod Phys* (2012) 84:1045. doi:10.1103/RevModPhys.84.1045
31. Sun Q, and Xie X. Heat Generation by Electric Current in Mesoscopic Devices. *Phys Rev B* (2007) 75:155306. doi:10.1103/PhysRevB.75.155306
32. Liu J, Song J, Sun Q, and Xie X. Electric-current-induced Heat Generation in a Strongly Interacting Quantum Dot in the Coulomb Blockade Regime. *Phys Rev B* (2009) 79:161309. doi:10.1103/PhysRevB.79.161309
33. Chi F, Zheng J, Liu Y, and Guo Y. Refrigeration Effect in a Single-Level Quantum Dot with thermal Bias. *Appl Phys Lett* (2012) 100:233106. doi:10.1063/1.4720093
34. Chi F, and Sun L. Photon-assisted Heat Generation by Electric Current in a Quantum Dot Attached to Ferromagnetic Leads. *Chin Phys Lett* (2016) 33:117201. doi:10.1088/0256-307X/33/11/117201
35. Lebedev A, and Vinokur V. Heat Generation Due to the anderson Catastrophe in Mesoscopic Devices. *Phys Rev B* (2020) 102:195111. doi:10.1103/PhysRevB.102.195111
36. Pei W, and Sun Q. Time-averaged Heat Generation in a Quantum Dot Driven by an Alternating Current Bias. *J Appl Phys* (2012) 112:124306. doi:10.1063/1.4769804

37. Wang Z. Heat Generation by Electrical Current in a Quantum Dot Hybridized to Majorana Nanowires. *Front Phys* (2021) 9:704493. doi:10.3389/fphy.2021.704493
38. Stefański P. Properties of the Majorana-State Tunneling Josephson junction Mediated by an Interacting Quantum Dot. *J Phys Condens Matter* (2019) 31: 185301. doi:10.1088/1361-648X/ab052a
39. Ricco L, de Souza M, Figueria M, Shelykh I, and Seridonio A. Spin-dependent Zero-Bias Peak in a Hybrid Nanowire-Quantum Dot System: Distinguishing Isolated Majorana Fermions from Andreev Bound States. *Phys Rev B* (2019) 99:155159. doi:10.1103/PhysRevB.99.155159
40. Ramos-Andrade JP, Pena FJ, Gonzalez A, Avalos-Ovando O, and Orellana PA. Spin-seebeck Effect and Spin Polarization in a Multiple Quantum Dot Molecule. *Phys Rev B* (2017) 96:165413. doi:10.1103/PhysRevB.96.165413
41. Zeng QB, Chen S, and Lu R. Fano Effect in an Ab Interferometer with a Quantum Dot Side-Coupled to a Single Majorana Bound State. *Phys Lett A* (2016) 380:951. doi:10.1016/j.physleta.2015.12.026

Conflict of Interest: The authors declare that the research was conducted in the absence of any commercial or financial relationships that could be construed as a potential conflict of interest.

frontiers in Physics

ORIGINAL RESEARCH
published: 27 August 2021
doi: 10.3389/fphy.2021.730078

Design Method of Equivalent Driving Waveform Based on Electrowetting Response Characteristics

*Lixia Tian and Hao Li**

Guangdong Provincial Key Laboratory of Optical Information Materials and Technology, Institute of Electronic Paper Displays, South China Academy of Advanced Optoelectronics, South China Normal University, Guangzhou, China

As a new reflective display technology, electrowetting displays (EWDs) have many important characteristics, such as high reflectivity, low power consumption, and paper-like display. However, the contact angle hysteresis, which is the inconsistency between the advancing contact angle and the receding contact angle of oil droplet movement, seriously affects the response speed of EWDs in the driving process. According to the hysteresis phenomenon of contact angle in an oil switch motion with the action of interface tension, the brightness curve of EWDs in the process of pixel switching by different driving voltages was tested in this paper, and driving voltage was changed from 30 to 100 V at the same time. Then, in order to reduce the influence of the hysteresis effect, an equivalent driving waveform design method with overdriving voltage was proposed, and the overvoltage was set to 100 V according to the hysteresis effect and driving characteristic of EWDs. Experimental results showed that the response rising time of EWDs was reduced to 21 ms by using the proposed driving waveform, and the response performance of EWDs can be effectively improved.

Keywords: electrowetting display, equivalent driving, response time, hysteresis, driving waveform

Edited by:
Feng Chi,
University of Electronic Science and Technology of China, China

Reviewed by:
Hui Li,
Shenzhen University, China
Chongfu Zhang,
University of Electronic Science and Technology of China, China

****Correspondence:***
Hao Li
haoli@m.scnu.edu.cn

Specialty section:
This article was submitted to Optics and Photonics, a section of the journal Frontiers in Physics

Received: *24 June 2021*
Accepted: *26 July 2021*
Published: *27 August 2021*

Citation:
Tian L and Li H (2021) Design Method of Equivalent Driving Waveform Based on Electrowetting Response Characteristics. Front. Phys. 9:730078. doi: 10.3389/fphy.2021.730078

INTRODUCTION

Reflective display has become common in e-readers. The most successfully commercialized e-book reader was produced by Amazon and Sony. At present, electrowetting displays (EWDs) have excellent characteristics of high reflectivity [1], fast response [2, 3], and paper-like display and low power consumption [4, 5], which is completely superior to electrophoresis displays (EPDs) [6, 7]. Moreover, the manufacturing engineering of EWDs is based on the liquid crystal display, which makes it cost-effective and easier to manufacture [8, 9]. Therefore, many scholars and investors have been attracted by EWD technology.

EWDs can realize an optical switch by controlling the movement of colored oil films. It was first proposed and implemented by Hayes in 2003 and published in Nature [10]. When a pixel unit was on-switching or off-switching, the brightness curve corresponding to the splitting, moving, and restructuring of the oil film in pixels was usually called the on-off curve, which is also called the response curve of EWDs [11]. Response time refers to the response speed of EWDs for displaying gray scales. Generally speaking, the response time is divided into two parts: rising time and falling time, and the sum of the two is called the response time of EWDs. However, in a response process, the oil backflow and hysteresis could lead to a negative effect on reducing the response time of EWDs [12]. So, research on response time is of great significance to analyze the oil film hysteresis, backflow, interface mechanics, and electrodynamics of EWDs.

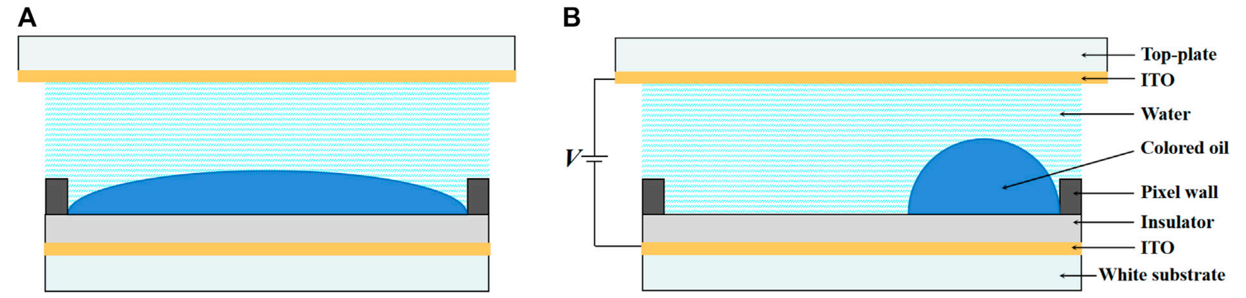

FIGURE 1 | Driving principle and pixel structure of EWDs. The optical stack consists of the glass substrate, indium tin oxide (ITO), a hydrophobic insulator layer, pixel wall, colored oil, and water. **(A)** Without applied voltage, a homogeneous oil film is present and the pixel is in colored off-state. **(B)** With an applied voltage, the oil film is shrunk to a corner and the pixel is in white on-state.

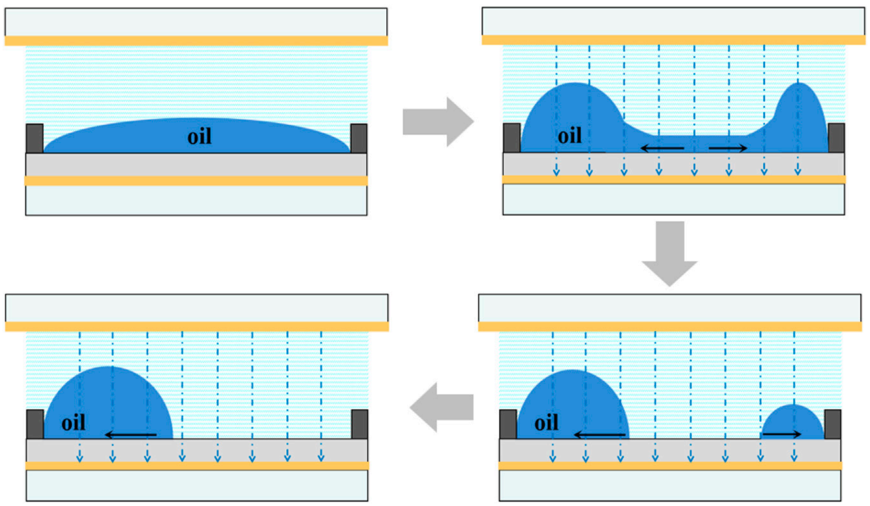

FIGURE 2 | The process of oil film rupture in a pixel from off-state to on-state. For the on-switching process, after applying external electric field force, the oil film begins to rupture with slight fluctuation. The fluctuation amplitude becomes larger with the increase of external force, and then, the oil can be shrunk to corners.

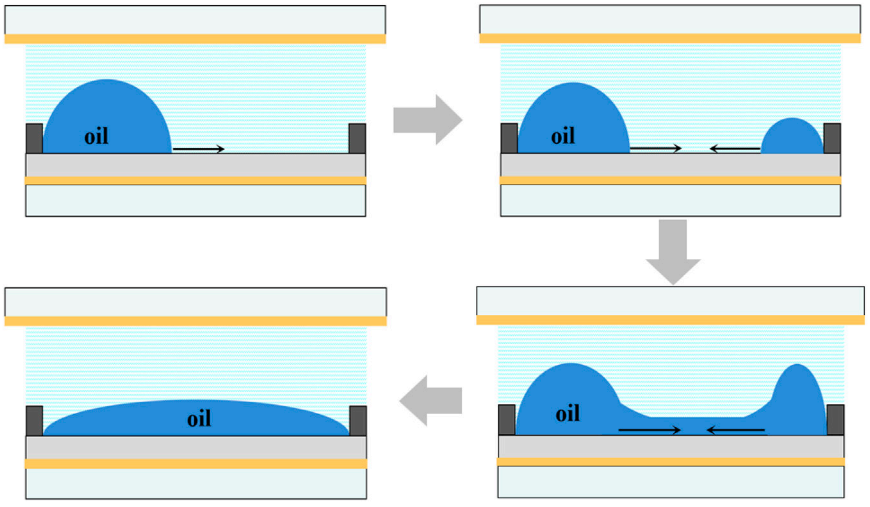

FIGURE 3 | The process of oil film recombination in a pixel from on-state to off-state. For the off-switching process, when the driving voltage is decreased, the oil begins to recombine with slight fluctuation, and the oil is spread out in the pixel gradually.

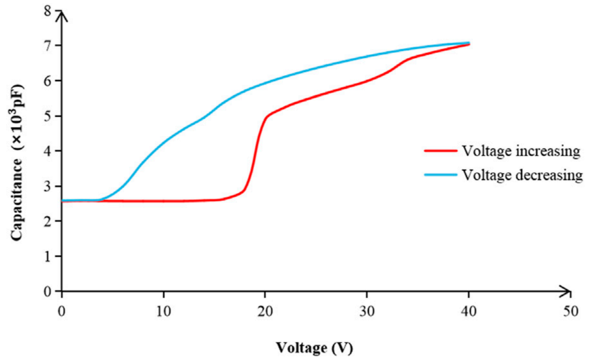

FIGURE 4 | | Hysteresis characteristic curve of an EWD panel. A step voltage from 0 to 40 V was used to measure the rising edge curve. The step time was 2 s and the step voltage was 2 V. A step voltage from 40 to 0 V was used to measure the falling edge curve. The step time was 2 s and the step voltage was −2 V.

The hysteresis effect, which is caused by the inconsistent contact angle and the persistence of oil backflow, can increase the complexity of shortening the response time [13, 14]. In 2011, Yung [15] studied the method of controlling grayscales and fast response of EWDs and proposed an asymmetric gray scales driving scheme, which changed the hysteresis characteristic curve of EWDs. It not only accelerated the response time but also effectively suppressed the phenomenon of oil backflow. However, researchers did not further explore the parameters of response time and backflow. In 2015, Yi [16] used electrophoretic chips to drive a matrix EWD system and used a unipolar PWM waveform modulation to realize EWD gray scales display. And a reset sub-frame was set to release charge trapping for weakening the oil backflow phenomenon, so as to keep a stable on-state for a longer time in a pixel. But this method prolonged the response time. In 2019, Yi [17] adopted a method of amplitude-frequency mixed modulation to drive EWDs. The oil was driven at 30 V to quickly approach a target reflectivity, and then the driving voltage was reduced to stabilize the oil reflectivity to the target reflectivity. But the response time of EWDs was limited. Lately, Zeng [18] introduced a 4 ms overdriving stage at 32 V to improve the response speed of EWDs, but the situation of much higher overdriving voltages had not been studied. In addition, it did not give a general method to design a waveform, and the proposed waveform was only limited to the EWD used in its verification. Once the technological process of EWDs changes, it will result in an inevitable redesign of the waveform.

In this paper, by recording the brightness curve of EWDs during the on- and off-switching process, the influence of oil motion hysteresis on response time was analyzed, and the hysteresis phenomenon of EWDs was summarized. Then, a driving method with an equivalent driving constant for EWDs was proposed. Furthermore, an overvoltage driving waveform was designed to shorten the response rising time of EWDs. The proposed driving constraint method enabled overvoltage driving to be used in EWDs. The validity of this method was verified by experimental data.

PRINCIPLES

Driving Principle of EWDs

The principle of EWDs is based on the movement of colored oil droplets by applying an external voltage [19–21]. Its essence is an optical switch [22]. The structure of an EWD is mainly composed of the glass substrate, indium tin oxide (ITO), hydrophobic insulator layer, pixel wall, colored oil, and water [23, 24]. The EWD operating principle and pixel structure are shown in **Figure 1**. When no driving voltage is applied between the electrodes, the colored oil film lies naturally between the water and the hydrophobic insulator layer; as shown in **Figure 1A**, the pixel is in a dark off-state. However, when a driving voltage is applied between the substrate electrode and the water, the oil film can be pushed aside by water with the electrowetting effect. As shown in **Figure 1B**, the reflective substrate electrode is exposed, different wavelengths of reflected light are superimposed to form a white optical sense, and the pixel is in a white on-state. In this way, the optical properties of the stack can be switched between a colored off-state and a white on-state [25, 26].

Hysteresis Effect of EWDs

In a pixel, the inconsistency between the advancing contact angle and the receding contact angle of oil droplet movement results in the hysteresis of EWDs [27, 28]. On the non-ideal surface, the droplet is in a metastable equilibrium state. When the droplet is deformed, there is a difference between the forward contact angle and the backward contact angle. This phenomenon is called contact angle hysteresis. In EWDs, the hysteresis phenomenon of contact angle would lead to the hysteresis effect, which shows that the reflected light intensity curves of the EWDs cannot coincide in the open phase and the closed phase. The main reasons for hysteresis include slight fluctuation in the process of oil film rupture and recombination and the viscous dissipation between the oil and dielectric layer at the same time.

The fluctuation of oil film rupture in an on-switching process is mainly caused by the fluctuation inside the oil after applying an external electric field force. **Figure 2** shows the process of oil film rupture in a pixel from off-state to on-state. During oil contraction, with the increase of the external force, the fluctuation amplitude can be increased. When the fluctuation is large enough, the oil film can be ruptured. This is related to the pixel structure and oil material parameters, as shown in **Equations 1**, **2** [29].

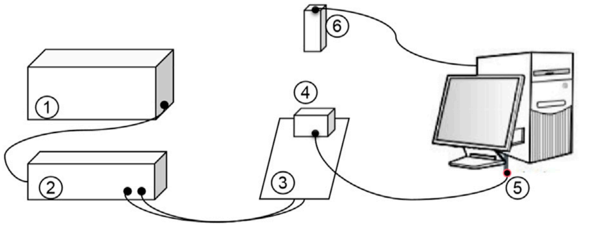

FIGURE 5 | The response testing platform of EWDs. ① Waveform generator. ② Voltage amplifier. ③ EWD panel. ④ Colorimeter. ⑤ Computer. ⑥ Microscope.

TABLE 1 | Parameters of the EWD panel.

Panel size (inch)	Pixel size (μm)	Pixel wall thickness (μm)	Pixel wall width (μm)	Oil color	Top ITO (nm)	Hydrophobic layer (nm)
5.5	185 × 185	6	10	Cyan	25	800

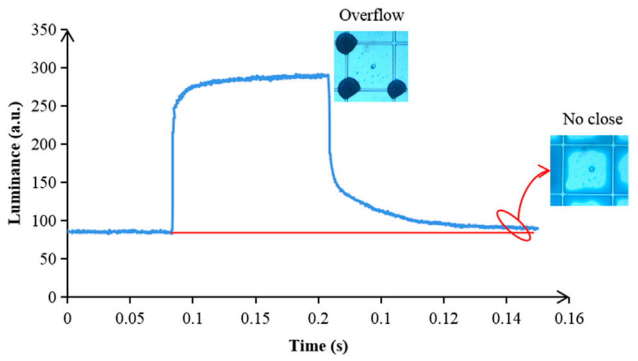

FIGURE 6 | The brightness curve of an EWD driven by a DC voltage for 15 ms. The applied driving voltage was 100 V. The oil film overflowed to the pixel wall, and it could not cover the whole pixel even power off.

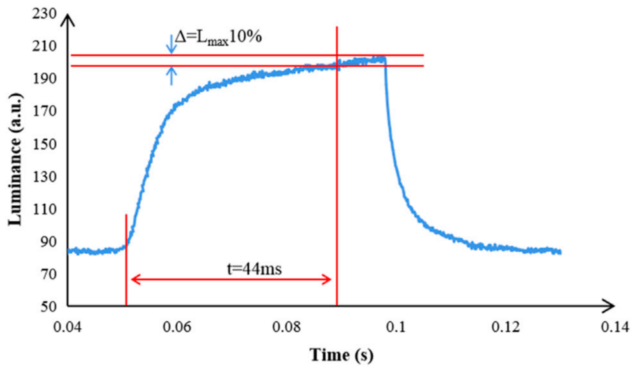

FIGURE 7 | The switch response curve of EWDs with a 30 V driving voltage and the calculation diagrammatic sketch of the constant E.

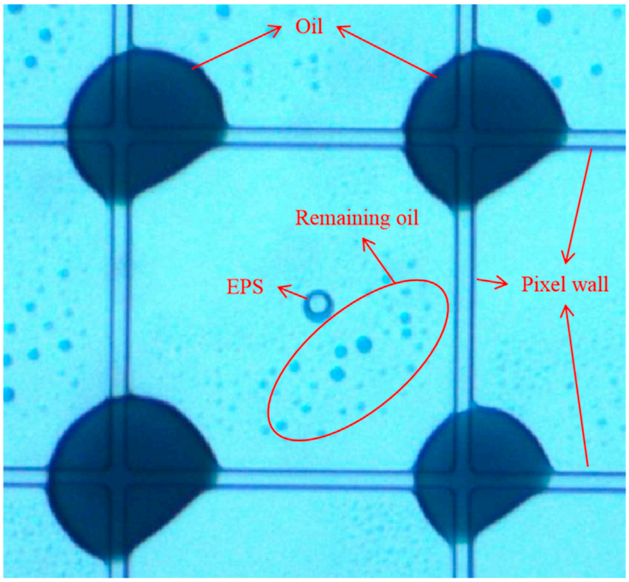

FIGURE 8 | Top view of pixels when the oil film overflowed to the pixel wall. When the EWD panel was driven by a high voltage, the oil film gathered on the pixel wall. When the driving voltage was removed, the amount of oil film in the pixel grid changed, and the oil film could not cover the whole pixel, which made the pixel unable to close. The circle in the middle of the pixel was an extra pinning structure (EPS). The random black spots in pixels were the residual oil.

$$\tau_{mn} = \frac{3\mu}{\gamma_{ow} h^3 \left(k^2 (V) - k_{mn}^2\right) k_{mn}^2}, \tag{1}$$

$$k^2 (V) = V^2 C(h) / \gamma_{ow} / 2, \tag{2}$$

where τ_{mn} is the voltage-dependent induction time caused by the oil film rupture, and μ, γ_{ow}, h, and $k(V)$ are viscosity, oil/water interface tension, oil film thickness, and electrostatic driving force, respectively. Modes (m,n) are characterized by a wavenumber k_{mn} which must be compatible with pixel dimensions [30]. When the driving voltage is low, the hysteresis phenomenon of EWDs is more obvious and the response time becomes longer.

The oil recombination process is the off-switching stage of an EWD pixel, as shown in **Figure 3**. The capillary force existing in the oil/water interface and the net force on the contact line are key elements in this reforming process. The timescale τ_{mn} which governs this reforming process is defined as **Eq. 3**.

$$\tau_{mn} = \frac{3\mu}{\gamma_{ow} k_{mn}^4 h^3}. \tag{3}$$

The oil recombination time is inversely proportional to the thickness of the oil film. When the oil film fluctuation is much smaller than the thickness of the film, the equation is strictly valid. However, when the thickness of oil becomes thinner, the hysteresis effect can be increased dramatically. In the driving process, the thickness of the oil film varies as the voltage becomes larger. When the voltage is removed, the oil reforming time will be affected by different potential energy in the recombination process. When the conductive liquid contacts with the hydrophobic insulator layer, there is a resistance force in the three-phase contact line among the hydrophobic insulator layer, the oil, and the conductive liquid. This is because the surface of the hydrophobic dielectric insulation is not completely smooth. The force which hinders the oil movement in the three-phase contact line can lead to viscous dissipation.

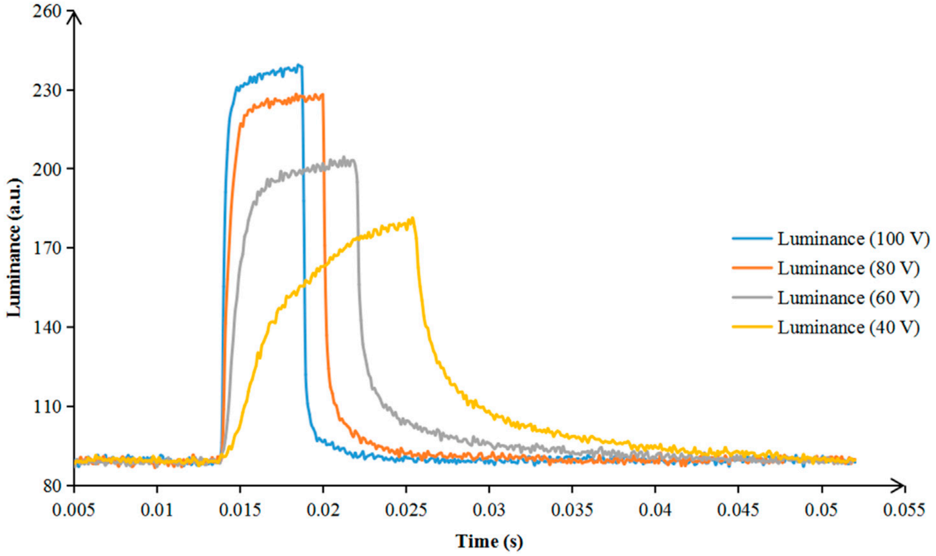

FIGURE 9 | Comparison of oil film opening time among different voltages with equivalent driving constraints. The larger the driving voltage, the steeper the rising edge of the response curve.

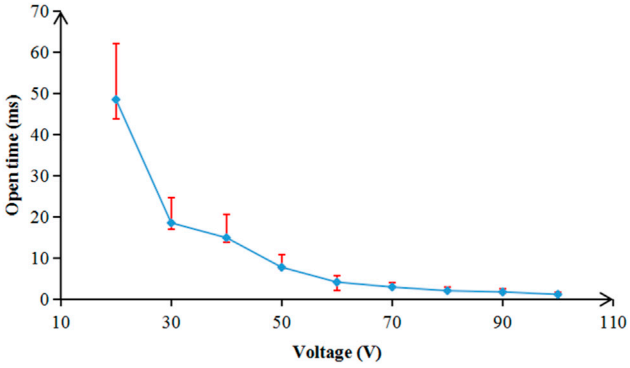

FIGURE 10 | The relationship between driving voltage and pixel opening time. The dot in the figure represented the response rising time of the pixel when the applied driving voltage was from 20 to 100 V. The pixel opening time was decreased exponentially with the increase of driving voltage.

A C-V curve for a segment of an EWD panel was shown in **Figure 4**. In the process of driving colored oil in pixels, when the driving voltage increased from 0 to 40 V, the colored oil film changed from lipophilic to hydrophilic. At the same time, with the combined action of electric field force, the polar liquid oil film ruptured and gradually gathered to corners. Ideally, the oil film would gather in a pixel corner. In this process, the voltage at the point at which the oil film began to be ruptured was called the threshold voltage. Above the threshold voltage, the optical response could be increased gradually. When the driving voltage decreased from 40 to 0 V, the optical response decreased linearly. The oil film rewets the interface until the fluoropolymer surface was completely covered. There was a clear hysteresis between switching-on and switching-off electro-optic curves.

EXPERIMENTAL RESULTS AND DISCUSSION

Optical Measurement Platform

To measure the Luminance-Time relationship of EWDs, a response testing platform was set up as shown in **Figure 5**. The main optical measuring equipment was a colorimeter (Arges-45, Admesy, Netherlands) which was used to measure the EWD luminance. Its measuring speed is 10,000 times/s, and the size of the measuring point is 3 mm. The optical system adopted a 45-degree incident light source and a 90-degree measuring angle. It was connected with a computer (M425, Lenovo, China) to save and display measured data graphically. In addition, experimental equipment also included a function waveform generator (AFG3052C, Tektronix, United States), an amplifier (ATA-2022H, Agitek, China), and a microscope (XTL-165, Phenix, China). The system used an adjustable DC power supply for providing a voltage that could change from 0 to 30 V. Programmable driving voltages were generated by the function waveform generator in combination with the voltage amplifier. And the fluidic pattern in pixels was recorded by the camera with a microscope synchronously. This system could record the brightness change of the reflected light during the driving process of EWDs.

In the tested EWD panel, Teflon AF1600 was used as the hydrophobic insulator layer material. The insulator was spin-coated on the ITO glass substrate with a resistivity of 100 Ω Sq. Transparent polyimide was used as the grid material of pixel walls and the photoresist was Microchem SU8 3005. The conductive

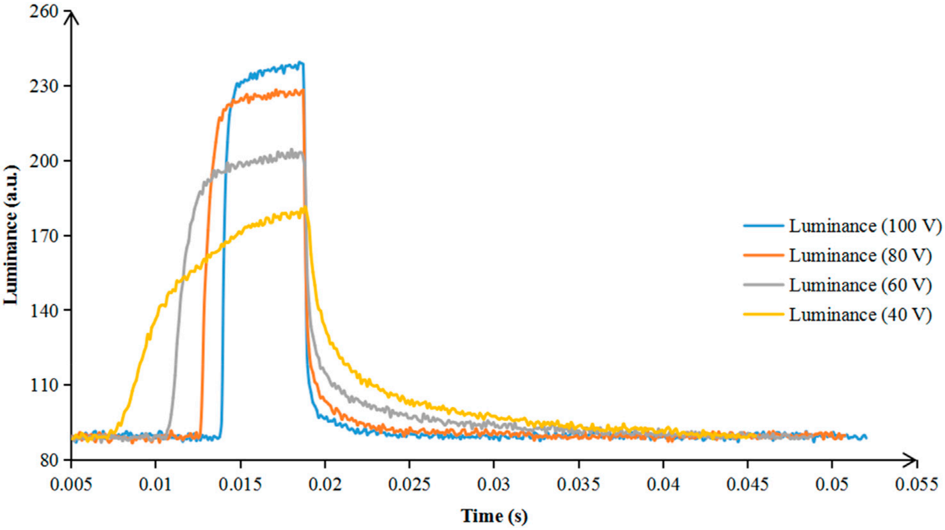

FIGURE 11 | Comparison of oil film closing time among different driving voltages with equivalent driving constraints. The larger the pixel aperture ratio, the faster of rewetting the whole pixel.

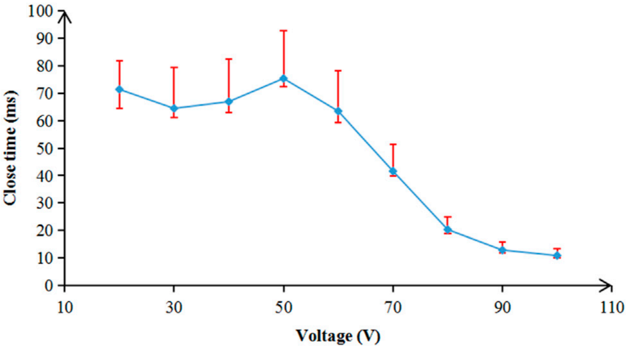

FIGURE 12 | The relationship between different driving voltages and oil film closing time. The dot in the figure represented the closing time of the pixel when the applied driving voltage was from 20 to 100 V. The larger the driving voltage, the shorter the closing time.

fluid was NaCl with a concentration of 0.001 M. The parameters of the EWD panel used in the experiment were shown in **Table 1**.

Driving Waveform Design

Driving waveforms were designed to study the influence of the hysteresis effect and oil backflow on the response time of EWDs; the response time of the traditional driving scheme and that of equivalent voltage driving scheme were compared. In the experiment, with the increase of voltage, the reflected brightness curve of EWDs became steeper from off-state to on-state. However, from on-state to off-state, the reflected brightness of EWDs was decreased with the rewetting of the oil. Finally, the oil was tiled again in the pixel.

As shown in **Figure 6**, when the applied DC voltage was 100 V and the EWD was driven for 15 ms, the reflected light intensity of the EWD was stronger than that of the low voltage. When pixels were observed with a microscope, the aperture ratio of the pixel was increased from 60% (at 30 V) to 65% (at 100 V), but the oil film overflowed to the pixel wall after the voltage driving, resulting in an increase of the light transmission intensity of pixels, and this process was irreversible. Through the analysis of the brightness curve, the brightness value could not be restored to the value before power on. At the same time, the slope of the descent curve could be changed and the descent time was prolonged.

In order to prevent the oil film from overflowing, an equivalent driving constant E = UT was designed, where U was the driving voltage, and T is the driving time of no oil film overflowing to the pixel wall. In this case, T was defined as the time when the oil film was driven from 0 to 90% of the maximum pixel aperture. As shown in **Figure 7**, the EWD was driven at 30 V, T was 44 ms, and then, the equivalent driving constant E was 1,320. When the product of applied voltage and driving time was greater than the equivalent driving constant, the oil film shrinkage state could exceed the limit. Excessive electric field force would make the oil film overflow the pixel wall, resulting in a reduction of the oil film. When the pixel was closed, some areas could not cover with the oil film, which showed that the pixel was always in on-state. **Figure 8** showed a top view of oil film when oil overflowed to the pixel wall with a high voltage.

Figure 9 showed brightness-time curves of an EWD when it was turned on and off with applied voltages of 40, 60, 80, and 100 V. After switching off the device, the brightness value could return to the value before the EWD was turned on, which proved that the equivalent driving method could make EWDs work without being damaged. With the constraint of the equivalent driving constant 1,000, the driving times were 25, 16, 12, and 10 ms, respectively, when the applied voltages were 40, 60, 80, and 100 V. The larger the driving voltage was, the steeper the rising edge of the response curve was. Meanwhile, the aperture ratio was

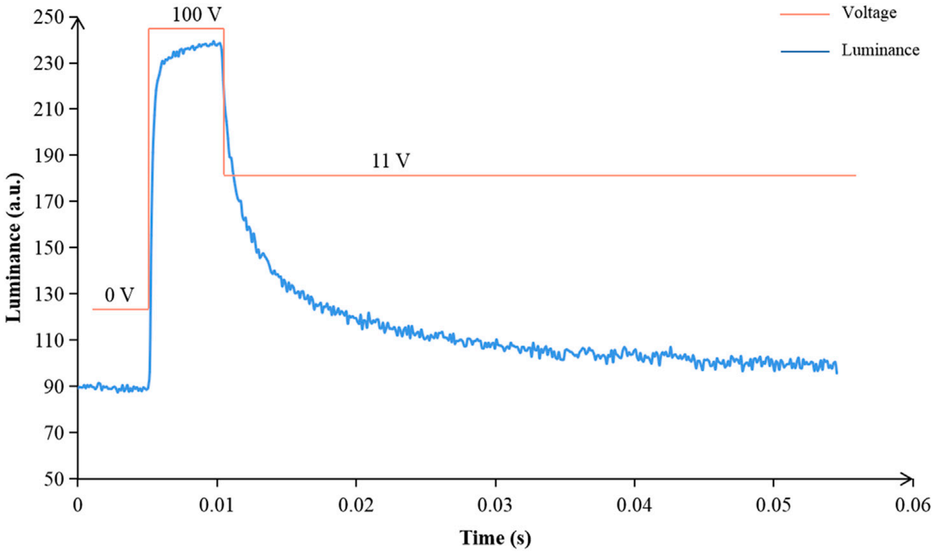

FIGURE 13 | Diagram of an overvoltage driving waveform and the response curve of EWDs with a 100 V overvoltage. The proposed driving waveform contained two stages. The first stage was an overvoltage for accelerating the oil film motion. The second stage was used to maintain the pixel opening state by a normal driving voltage.

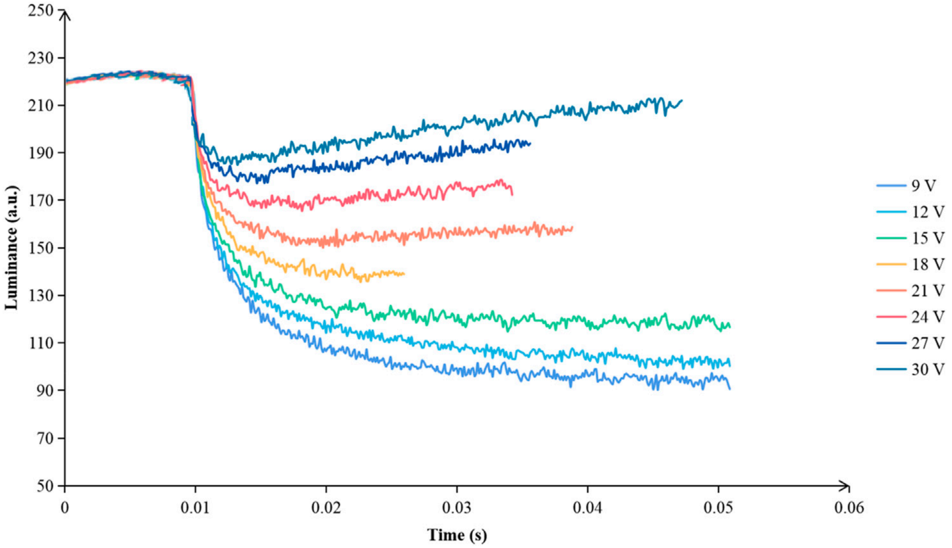

FIGURE 14 | The brightness curve of an EWD which was driven by different voltages from 7 to 21 V in the second stage. The lower the driving voltage, the more obvious reduction of pixel opening time.

larger, and the light reflection intensity of the pixel was higher. The response rising time took 1.2 ms for 100 V driving voltage, 1.95 ms for 80 V driving, 3.9 ms for 60 V driving, and 10.7 ms for 40 V driving. With the increase of driving voltage, the pixel opening time decreased exponentially, as shown in **Figure 10**.

Figure 11 showed the comparison of the oil film closing process with different driving voltages. The falling curve was a process of pixel closing. The larger the pixel aperture ratio, the higher the concentration height of the oil film. And the potential energy of the oil film in a pixel was larger, which made the timescale of rewetting shorter when it was in the off-switching process. When the EWD panel was driven by 40, 60, 80, and 100 V, the oil film closing time was 31.7, 24.6, 14.8, and 10.9 ms, respectively. **Figure 12** showed the relationship between the driving voltage and the oil film closing time. The larger the driving voltage, the shorter the closing time. The curve showed an obvious linear relationship.

The overvoltage driving waveform was shown in **Figure 13**. The proposed driving waveform was divided into two stages, including 100 and 11 V driving voltages. In the first stage, an overdriving voltage was used to accelerate the oil film motion. The pixel opening time was reduced by an overdriving voltage (100 V). The driving waveform of the second stage was used to maintain the pixel opening state and maintain the aperture ratio by a normal driving voltage (11 V). In **Figure 13**, the driving time in the first stage was 10 ms, and the oil film stabilization time was 11 ms in the second stage, which shortened the pixel opening time of 11 V to 21 ms, and it improved the response performance of a pixel.

When the overvoltage was 100 V in the first stage, the luminance curve of an EWD driven by different voltages from 9 to 30 V in the second stage was shown in **Figure 14**. The lower driving voltage in the second stage had little effect on the pixel opening time. However, the pixel opening time increased exponentially with the decrease of driving voltage when the EWD panel was driven by a DC voltage. Moreover, due to the hysteresis characteristic of EWDs, it was difficult to turn on pixels at a low DC voltage. On the contrary, the proposed driving waveform could still turn on pixels at 9 V. That is to say, the proposed driving waveform significantly improved the lowest aperture of pixels and enhanced the grayscale display ability of EWDs.

CONCLUSION

In this paper, an equivalent driving waveform design method was proposed according to the driving hysteresis characteristics of EWDs. The brightness changes of an EWD pixel during the switching process were statistically analyzed, and the equivalent driving constants were proposed as parameters for driving waveform design. Response curves of the pixel switching process with different driving voltages from 30 to 100 V were analyzed experimentally. It was proved that the equivalent driving constant could effectively protect EWDs from damage. Meanwhile, the overvoltage driving waveform of 100 V was designed to shorten the response rising time to 21 ms with an 11 V driving voltage. The proposed driving waveform could improve the display performance of pixels and facilitate the process of market application of EWDs.

DATA AVAILABILITY STATEMENT

The original contributions presented in the study are included in the article/supplementary material; further inquiries can be directed to the corresponding author.

AUTHOR CONTRIBUTIONS

LT and HL designed this project. LT carried out most of the experiments. HL performed part of the experiments and helped with discussions during manuscript preparation. LT contributed to the data curation and analysis. HL provided helpful discussions on the experimental results. All authors contributed to the article and approved the submitted version.

FUNDING

This article is supported by the Program for Guangdong Innovative and Entrepreneurial Teams (No. 2019BT02C241), Science and Technology Program of Guangzhou (No. 2019050001), Program for Chang Jiang Scholars and Innovative Research Teams in Universities (No. IRT_17R40), Guangdong Provincial Key Laboratory of Optical Information Materials and Technology (No. 2017B030301007), Guangzhou Key Laboratory of Electronic Paper Displays Materials and Devices (201705030007), and MOE International Laboratory for Optical Information Technologies and the 111 Project.

REFERENCES

1. Heikenfeld J., Zhou K., Kreit E., Raj B., Yang S., Sun B, et al. Electrofluidic displays using Young-Laplace transposition of brilliant pigment dispersions. *Nat Photon* (2009) 3(5):292–6. doi:10.1038/NPHOTON.2009.68
2. Qian M, Lin S, Zeng S, Lin Z, Guo T, and Tang B. Real-time dynamic driving system implementation of electrowetting display. *Opto-Electronic Eng* (2019) 46(06):87–95. doi:10.12086/oee.2019.180623
3. Yi Z., Zeng W., Ma C., Feng H., Yang J., Liu L, et al. A real-time touch control system design based on field-programmable gate array via optimizing Bresenham algorithm for electrowetting displays. *J Soc Inf Display* (2021) 29(7):573–83. doi:10.1002/jsid.1001
4. Li W., Wang L., Zhang T., Lai S., Liu L., He W, et al. Driving Waveform Design with Rising Gradient and Sawtooth Wave of Electrowetting Displays for Ultra-Low Power Consumption. *Micromachines* (2020) 11(2):145. doi:10.3390/mi11020145
5. Liu L., Bai P., Yi Z., and Zhou G. A Separated Reset Waveform Design for Suppressing Oil Backflow in Active Matrix Electrowetting Displays. *Micromachines* (2021) 12(5):491. doi:10.3390/mi12050491
6. Shen S., Gong Y., Jin M., Yan Z., Xu C., Yi Z, et al. Improving electrophoretic particle motion control in electrophoretic displays by eliminating the fringing effect via driving waveform design. *Micromachines* (2018) 9(4):143. doi:10.3390/mi9040143
7. Wang L., Yi Z., Jin M., Shui L., and Zhou G. Improvement of video playback performance of electrophoretic displays by optimized waveforms with shortened refresh time. *Displays* (2017) 49(9):95–100. doi:10.1016/j.displa.2017.07.007
8. Tröls A., Enser H., and Jakoby B. Modeling and fabrication of low-cost electrowetting actuators for flexible microfluidic display applications. *IEEE SENSORS* (2016) 10:1–3. doi:10.1109/ICSENS.2016.7808429
9. Zhao R., Cumby B., Russell A., and Heikenfeld J. Large area and low power dielectrowetting optical shutter with local deterministic fluid film breakup. *Appl Phys Lett* (2013) 103(33):223510. doi:10.1063/1.4834095
10. Hayes R. A., and Feenstra B. J. Video-speed electronic paper based on electrowetting. *Nature* (2003) 425(6956):383–5. doi:10.1038/nature01988
11. Palanivelu S, and Surjya S. Display Applications of Electrowetting. *J Adhes Sci Tech* (2012) 26(12-17):1947–63. doi:10.1163/156856111X600532
12. Yi Z., Huang Z., Lai S., He W., Wang L., Chi F, et al. Driving Waveform Design of Electrowetting Displays Based on an Exponential Function for a Stable Grayscale and a Short Driving Time. *Micromachines* (2020) 11(3):313. doi:10.3390/mi11030313
13. Zhang X-M., Bai P-F., Hayes R., Shui L-L., Jin M-L., Tang B, et al. Novel driving methods for manipulating oil motion in electrofluidic

display pixels. *J Display Technol* (2015) 12(2):1. doi:10.1109/jdt.2015.2477947

14. Lin S., Zeng S., Qian M., Lin Z., Guo T., and Tang B. Improvement of display performance of electrowetting displays by optimized waveforms and error diffusion. *J Soc Inf Display* (2019) 27(10):619–29. doi:10.1002/jsid.790
15. Chiu Y-H., Liang C-C., Chen Y-C., Lee W-Y., Chen H-Y., and Wu S-H. Accurate-gray-level and quick-response driving methods for high-performance electrowetting displays. *J Soc Inf Display* (2011) 19(11):741–8. doi:10.1889/JSID19.11.741
16. Yi Z., Shui L., Wang L., Jin M., Hayes R. A., and Zhou G. A novel driver for active matrix electrowetting displays. *Displays* (2015) 37:86–93. doi:10.1016/j.displa.2014.09.004
17. Yi Z., Liu L., Wang L., Li W., Shui L., and Zhou G. A Driving System for Fast and Precise Gray-Scale Response Based on Amplitude-Frequency Mixed Modulation in TFT Electrowetting Displays. *Micromachines* (2019) 10(11): 732. doi:10.3390/mi10110732
18. Zeng W., Yi Z., Zhao Y., Zeng W., Ma S., Zhou X, et al. Design of Driving Waveform Based on Overdriving Voltage for Shortening Response Time in Electrowetting Displays. *Front Phys* (2021) 9(642682):1–9. doi:10.3389/fphy.2021.642682
19. Roques C, Hayes R, Feenstra B, and Schlangen L. Liquid behavior inside a reflective display pixel based on electrowetting. *J Appl Phys* (2004) 95(8): 4389–96. doi:10.1063/1.1667595
20. Yi Z., Feng H., Zhou X., and Shui L. Design of an Open Electrowetting on Dielectric Device Based on Printed Circuit Board by Using a Parafilm M. *Front Phys* (2020) 8(193):1–10. doi:10.3389/fphy.2020.00193
21. Zhang C. Z., Yi Z, de Rooij N, de Rooij N., Zhou G., and Gravina R. Editorial: Modeling and Applications of Optoelectronic Devices for Access Networks. *Front Phys* (2021) 9(678269):1–3. doi:10.3389/FPHY.2021.678269
22. Yi Z., Feng W., Wang L., Liu L., Lin Y., He W, et al. Aperture ratio improvement by optimizing the voltage slope and reverse pulse in the driving waveform for electrowetting displays. *Micromachines* (2019) 10(12): 862. doi:10.3390/mi10120862
23. Feenstra J. Video-Speed Electrowetting Display Technology. *Handbook Vis Display Tech* (2016) 1(13):2443–58. doi:10.1007/978-3-319-14346-0_103
24. Jin M., Shen S., Yi Z., Zhou G., and Shui L.. Optofluid-Based reflective displays. *Micromachines* (2018) 9(4):159. doi:10.3390/mi9040159
25. Feenstra B. J., Hayes R. A., Camps I. G. J., Hage L. M., Johnson M. T., Roques-Carmes T, et al. A video-speed reflective display based on electrowetting: principle and properties. *J Soc Inf Display* (2004) 12(3):293–9. doi:10.1889/1.1825703
26. Jung H-Y., Choi U-C., Park S-H., Hwang H-S., Park C-W., You B-H, et al. P-48: Development of Driver IC with Novel Driving Method for the Electrowetting Display. *SID Symp Dig Tech Pap* (2012) 43(1):1239–42. doi:10.1002/j.2168-0159.2012.tb06022.x
27. Li W., Wang L., and Henzen A. A Multi Waveform Adaptive Driving Scheme for Reducing Hysteresis Effect of Electrowetting Displays. *Front Phys* (2020) 8(618811):1–10. doi:10.3389/fphy.2020.618811
28. Berthier J. Electrowetting Theory. In: *Micro-Drops and Digital Microfluidics*. Amsterdam, Netherlands: Elsevie (2013). p. 161–224. doi:10.1016/B978-1-4557-2550-2.00004-3
29. Zhou M., Zhao Q., Tang B., Groenewold J., Hayes R. A., and Zhou G. Simplified dynamical model for optical response of electrofluidic displays. *Displays* (2017) 49:26–34. doi:10.1016/j.displa.2017.05.003
30. Tang B., Groenewold J., Zhou M., Hayes R. A., and Zhou G. Interfacial electrofluidics in confined systems. *Sci Rep* (2016) 6:6. doi:10.1038/srep26593

Conflict of Interest: The authors declare that the research was conducted in the absence of any commercial or financial relationships that could be construed as a potential conflict of interest.

frontiers in Physics

BRIEF RESEARCH REPORT
published: 06 September 2021
doi: 10.3389/fphy.2021.750102

Spin Seebeck Effect in a Hybridized Quantum-Dot/Majorana-Nanowire With Spin Heat Accumulation

Lian-Liang Sun[1] *and Zhen-Guo Fu*[2]*

[1]*College of Science, North China University of Technology, Beijing, China,* [2]*Institute of Applied Physics and Computational Mathematics, Beijing, China*

Properties of spin Seebeck effect (SSE) in a quantum dot (QD) connected to a topological superconductor or semiconductor nanowire with strong spin-orbit interaction are theoretically studied by the noneqilibrium Green's function method combined with Dyson equation technique. At low temperatures, Majorana zero modes (MZMs) are prepared at the ends of topological superconductor or semiconductor nanowire, and are hybridized to the QD with spin-dependent strength. We consider that the QD is coupled to two leads in the presence of spin heat accumulation (SHA), i.e., spin-dependent temperature in the leads. We find that the thermopower is spin-polarized when the hybridization strength between the QD and one mode of the MZMs depends on electron spin direction, and its spin-polarization can be effectively adjusted by changing the magnitude of SHA. By proper variation of the spin-polarization of the QD-MZM hybridization strength, magnitude of the SHA, dot level, or the direct coupling between the MZMs, 100% spin-polarized or pure thermopower can be generated. Our results may find real usage in high efficiency spintronic devices or detection of the MZMs, which are under current extensive study. The present model is within the reach of current nano-technologies and may by used in high efficiency spin caloritronics devices.

Keywords: spin-dependent temperature, quantum dot, Majorana zero modes, spin seebeck effect, spin-polarized coupling

Edited by:
Qiang Xu,
Nanyang Technological University, Singapore

Reviewed by:
Jia Liu,
Inner Mongolia University of Science and Technology, China
Xiu Qing Wang,
Inner Mongolia University for Nationalities, China

***Correspondence:**
Zhen-Guo Fu
zgfu2021@163.com

Specialty section:
This article was submitted to Optics and Photonics, a section of the journal Frontiers in Physics

Received: *30 July 2021*
Accepted: *23 August 2021*
Published: *06 September 2021*

Citation:
Sun L-L and Fu Z-G (2021) Spin Seebeck Effect in a Hybridized Quantum-Dot/Majorana-Nanowire With Spin Heat Accumulation. Front. Phys. 9:750102. doi: 10.3389/fphy.2021.750102

1 INTRODUCTION

In the last decades, generating and manipulating spin current in closed circuits or spin bias in open ones by thermal bias have been successfully realized in experiments. This interdisciplinary subject of thermoelectric effect and spintronics is referred to as spin caloritronics aiming at spin control in terms of thermal means [1, 2]. In the usual thermoelectric effect, the Seebeck effect known as generation of electrical current or bias voltage in response to a temperature difference between two ends of a system is the most frequently investigated issue [3, 4]. The measured quantity is the thermopower $S = \sum_\sigma S_\sigma$ with $S_\sigma = -\Delta V_\sigma/\Delta T$ the spin-resolved one denoting induced spin bias voltage ΔV_σ by a temperature gradient ΔT. In spin caloritronics, the counterpart of Seebeck effect is the spin Seebeck effect (SSE) [5]. It refers to the generation of pure spin current in the absence of charge electrical current, or spin bias denoting spin-resolved chemical potentials. Since the interaction strength between electron spins is much weaker as compared to the electrostatic force, and then the SSE suggests a possibility of high-efficiency and low-energy nano-scale thermoelectric devices. It is also promising in the detection of small temperature difference in low-dimensional systems [5], and has been extensively investigated in the fields of spin current rectifier [6], magnetic heat valves [7], quantum cooling [8], thermal spin-transfer torque [9], thermovoltaic transistor [10], thermal logic gates and thermal memory for quantum information processing [11]. After the pioneering work of K. Uchida in 2008 [5], the SSE has been continuously observed in various materials [12–21], including magnetic metals, ferromagnetic insulators, ferromagnetic metals, ferromagnetic semiconductors, nonmagnetic materials with a magnetic field, paramagnetic materials, antiferromagnetic materials, and even topological insulators.

In the definition of spin-dependent thermopower S_σ, the generated spin bias voltage ΔV_σ denotes the split mechanical potentials as $\Delta V_\sigma = \hbar(\mu_\sigma - \mu_{\bar{\sigma}})/2$, and the spin-up and spin-down electrons are individually at different states μ_σ due to the existence of thermal bias ΔT. The spin bias is the driving force for electron transport and induces spin-polarized currents. In fact, from the Fermi-Dirac function $f_\sigma = 1/\{\exp[(\varepsilon - \mu_\sigma)/k_B T_\sigma] + 1\}$, one can expect that the driving force for spin-dependent electronic transport to come from a spin-dependent electrons' temperatures T_σ, whose function is similar to the spin bias μ_σ. This is called as spin heat accumulation (SHA) realizable by an electric current from a ferromagnet into a nonmagnetic material [7, 22–26]. Usually, the SHA emerges with the accompany of spin bias voltage and is quite weak as compared to the latter. In recent experiment [24], the magnitude of SHA can be enhanced to as high as about several kelvins.

Very recently, thermoelectric effect [27–31] was proposed to be used for detecting Majorana zero modes (MZMs), a kind of quasi-particles of Majorana fermions having zero energy that can be realized in nano-scale topological superconductors [32, 33]. They are of their own antiparticle and charge neutral [32–35], and have potential applications in fault-tolerant quantum computation and energy-saving spintronic devices [36]. Due to their exotic zero-energy, chargeless properties, *the detection of them* is the central topic in studies relating to MZMs. Currently, the most important detection means is the electrical tunnel spectroscopy by applying a voltage ΔV across the nanowire with MZMs and to observe the associate current. The MZMs induce a zero-bias anomaly in the differential of electrical conductance [32, 33, 37], which is viewed as the evidence of MZMs. But this zero-bias anomaly in the conductance may also induced by some other mechanisms, for example, the Kondo effect [35]. Therefore, some other schemes, including the thermoelectric effect tuned by MZMs, were then continuously proposed in recent years. It was proved that the electron-hole symmetric nature of the MZMs which results in null thermoelectric effect can be effectively broken in a structure with a quantum dot (QD) coupled to topological superconductor hosting MZMs [27, 28]. Large value of thermopower satisfying Mott formula was proposed for detecting temperature of MZMs [19]. Such a system is possible to deduce information of the dissipative decay of MZMs [29]. In a two-terminal structure with a QD sandwiched between two leads and side-coupled to MZMs, a global sign reversion of the thermopower induced by MZMs was studied by López et. al. Such a phenomenon is caused by the direct MZM-MZM coupling [28]. The sign change and abnormal enhancement of thermopower by coupling between the QD and MZMs were also studied in some subsequent works [30, 31].

In our recent work, we have proposed a scheme composing of a QD side-coupled to MZMs to detect the SHA in terms of sign change of thermopower [38]. The mechanism is that the thermopowers of different spin components will change signs at different temperatures due to the QD-MZMs coupling. The SHA denoting spin-dependent temperature then can be inferred by the change of spin-polarized thermopower varying with respect to the magnitude of SHA. This task can also be fulfilled by observing the charge thermpower, which is much easier to be measured in experiments. In the previous work [38], we proved that the transition temperature of the thermopower depends on the QD-MZMs coupling strength, and the ferromagnetism of the two leads connected to the QD. Above or below the transition temperature, both 100% spin-polarized or pure spin thermopower will emerge due to the influences of SHA and MZMs. In the present paper, we study the properties of thermopower in a QD connected to the left and right leads with SHA, and also to a topological superconductor nanowire hosting MZMs. We focus our attention of the spin-resolved thermopower induced by the existence of MZMs, which are coupled to electrons on the QD with spin-dependent coupling strength. Our numerical results show that 100% spin-polarized and pure spin thermopower can be obtained by varying several system parameters, such as spin-polarization of the QD-MZM hybridization interaction, inter-MZM coupling strength, magnitude of the SHA, and the dot levels.

2 MODEL AND METHODS

The system Hamiltonian we study can be written in the following form [30, 31, 38].

$$H = \sum_{k\beta\sigma} \varepsilon_{k\beta} c^\dagger_{k\beta\sigma} c_{k\beta\sigma} + \sum_\sigma \varepsilon_d d^\dagger_\sigma d_\sigma + U d^\dagger_\uparrow d_\uparrow d^\dagger_\downarrow d_\downarrow + \sum_{k\beta\sigma} (V_{k\beta} c^\dagger_{k\beta\sigma} d_\sigma + H.c) + H_{MZMs}, \tag{1}$$

where $c^\dagger_{k\beta\sigma}$ ($c_{k\beta\sigma}$) is the creation (annihilation) operator for an electron with momentum k, energy $\varepsilon_{k\beta}$ in the non-interacting leads $\beta = L, R$. $d^\dagger_\sigma$ (d_σ) is the electron creation (annihilation) operator having gate voltage tunable energy level ε_d, spin-σ and intradot Coulomb interaction U. The coupling strength between the QD and the leads is described by $V_{k\beta}$. The last term H_{MZMs} in **Eq. 1** is for the MZMs formed at the ends of a topological superconductor nanowire. Here we assume that the QD is side-coupled to one mode of the MZMs and [39],

$$H_{MZMs} = i\Delta_M \eta_1 \eta_2 + \sum_\sigma \lambda_\sigma (d_\sigma - d^\dagger_\sigma)\eta_1, \tag{2}$$

in which Δ_M is the inter-MZM coupling strength with $\eta_j = \eta_j^\dagger (j = 1, 2)$ and $\{\eta_i, \eta_j\} = \delta_{i,j}$. The spin-dependent hybridization strength between the MZM and electrons on the QD is λ_σ. We transform the Majorana operator η_j to the regular

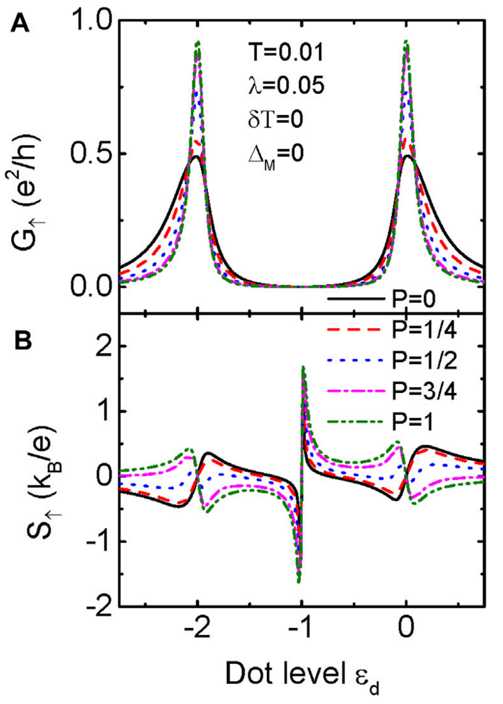

FIGURE 1 | The spin-up electrical conductance $G_\uparrow$ in **(A)**, and thermopower $S_\uparrow$ in **(B)** as functions of the dot level ε_d for indicated parameters, respectively. Due to the arrangement of λ_σ, $G_{\uparrow,P=0} = G_{\downarrow,P=1}$, $G_{\uparrow,P=1/4} = G_{\downarrow,P=3/4}$, and $G_{\uparrow,P=1/2} = G_{\downarrow,P=1/2}$. The same holds true for the thermopower, and then we only illustrate the results of spin-up component.

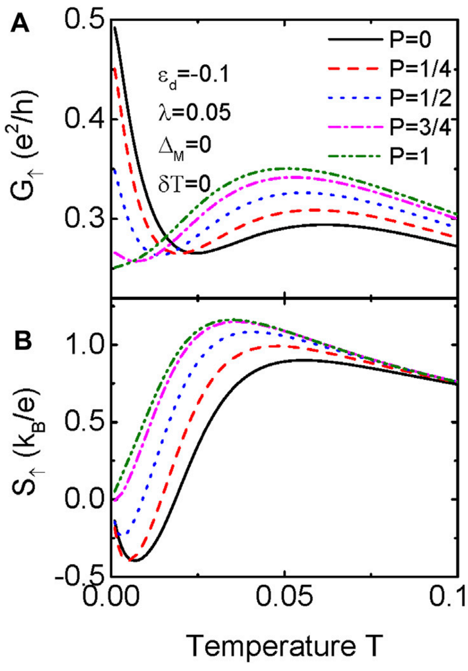

FIGURE 2 | $G_\uparrow$ in **(A)** and thermopower $S_\uparrow$ in **(B)** as functions of system equilibrium temperature T for the given parameters. The thermpower changes sign by varying the temperature with the help of the MZMs.

fermionic operators f as [39] $\eta_1 = (f^\dagger + f)/\sqrt{2}$ and $\eta_2 = i(f^\dagger - f)/\sqrt{2}$, and then H_{MZMs} is rewritten as

$$H_{MZMs} = \Delta_M\left(f^\dagger f - \frac{1}{2}\right) + \frac{1}{\sqrt{2}}\sum_\sigma \lambda_\sigma \left(d_\sigma - d_\sigma^\dagger\right)\left(f^\dagger + f\right). \tag{3}$$

In this paper, we study the thermopower in linear response regime (infinitesimal bias voltage ΔV and temperature bias ΔT) which is calculated from $S_\sigma = -K_{1,\sigma}/(eT_\sigma K_{0,\sigma})$, where the integrals are [28–31],

$$K_{n,\sigma} = \frac{1}{\hbar}\int (\varepsilon - \mu)^n \left[-\frac{\partial f_\sigma(\varepsilon)}{\partial \varepsilon}\right]\zeta_\sigma(\varepsilon)\frac{d\varepsilon}{2\pi}, \tag{4}$$

in which $\hbar$ is the reduced Planck's constant, and $\mu = 0$ is the leads' chemical potential. The spin-dependent equilibrium Fermi distribution function is written as $f_\sigma(\varepsilon) = 1/\{1 + \exp[(\varepsilon - \mu)/k_B T_\sigma]\}$ with k_B the Boltzmann constant and T_σ the spin-dependent equilibrium temperature known as SHA in the leads. Here we set the spin-resolved temperatures in the leads to be $T_\uparrow = T + \delta T/2$ and $T_\downarrow = T - \delta T/2$ with T the system equilibrium temperature. The transmission coefficient $\zeta_\sigma(\varepsilon)$ in the above equation can be obtained by using the Dyson equation method combined with Keldysh nonequilibrium Green's function technique as [28–31], $\zeta_\sigma(\varepsilon) = -2\tilde{\Gamma}\mathrm{Im}G^r_{e,\sigma}(\varepsilon)$, where $\tilde{\Gamma} = \Gamma_L\Gamma_R/(\Gamma_L + \Gamma_R)$ and the line-width function $\Gamma_{L(R)} = 2\pi\sum_k |V_{kL(R)}|^2\delta[\varepsilon - \varepsilon_{kL(R)}]$ is independent of electron spin for normal metal leads. The electron retarded Green's function in the transmission coefficient can be calculated by the Dyson equation method as [40, 41].

$$\mathbf{G} = \begin{bmatrix} g^{r-1}_{e,\uparrow} + i\Gamma/2 & 0 & 0 & 0 & \frac{\lambda_\uparrow}{\sqrt{2}} & \frac{\lambda_\uparrow}{\sqrt{2}} \\ 0 & g^{r-1}_{h,\uparrow} + i\Gamma/2 & 0 & 0 & -\frac{\lambda_\uparrow}{\sqrt{2}} & -\frac{\lambda_\uparrow}{\sqrt{2}} \\ 0 & 0 & g^{r-1}_{e,\downarrow} + i\Gamma/2 & 0 & \frac{\lambda_\downarrow}{\sqrt{2}} & \frac{\lambda_\downarrow}{\sqrt{2}} \\ 0 & 0 & 0 & g^{r-1}_{h,\downarrow} + i\Gamma/2 & -\frac{\lambda_\downarrow}{\sqrt{2}} & -\frac{\lambda_\downarrow}{\sqrt{2}} \\ \frac{\lambda_\uparrow}{\sqrt{2}} & -\frac{\lambda_\uparrow}{\sqrt{2}} & \frac{\lambda_\downarrow}{\sqrt{2}} & -\frac{\lambda_\downarrow}{\sqrt{2}} & \varepsilon - \delta_M & 0 \\ \frac{\lambda_\uparrow}{\sqrt{2}} & -\frac{\lambda_\uparrow}{\sqrt{2}} & \frac{\lambda_\downarrow}{\sqrt{2}} & -\frac{\lambda_\downarrow}{\sqrt{2}} & 0 & \varepsilon + \delta_M \end{bmatrix}^{-1}, \tag{5}$$

where $\Gamma = \Gamma_L + \Gamma_R$, and the electron (hole) free retarded Green's function is calculated from the equation of motion method as [40, 41].

$$g^r_{e(h),\sigma} = \frac{1 - n_{\bar{\sigma}}}{\varepsilon \mp \varepsilon_d} + \frac{n_{\bar{\sigma}}}{\varepsilon \mp \varepsilon_d \mp U}. \tag{6}$$

The interacting electron Green's function then is obtained as $G^r_{e,\uparrow(\downarrow)} = \mathbf{G}^r_{11(33)}$. The occupation number n_σ in the above free retarded Green's function needs to be calculated self-consistently from the equation of $n_\sigma = -2\tilde{\Gamma}\int d\varepsilon f_\sigma(\varepsilon)G^r_{e,\sigma}(\varepsilon)/2\pi$.

3 RESULTS AND DISCUSSION

In the following numerical calculations, we set the band width in the leads $D = 40$ as the energy unit, and fix $\Gamma_L = \Gamma_R = 0.1$. Other

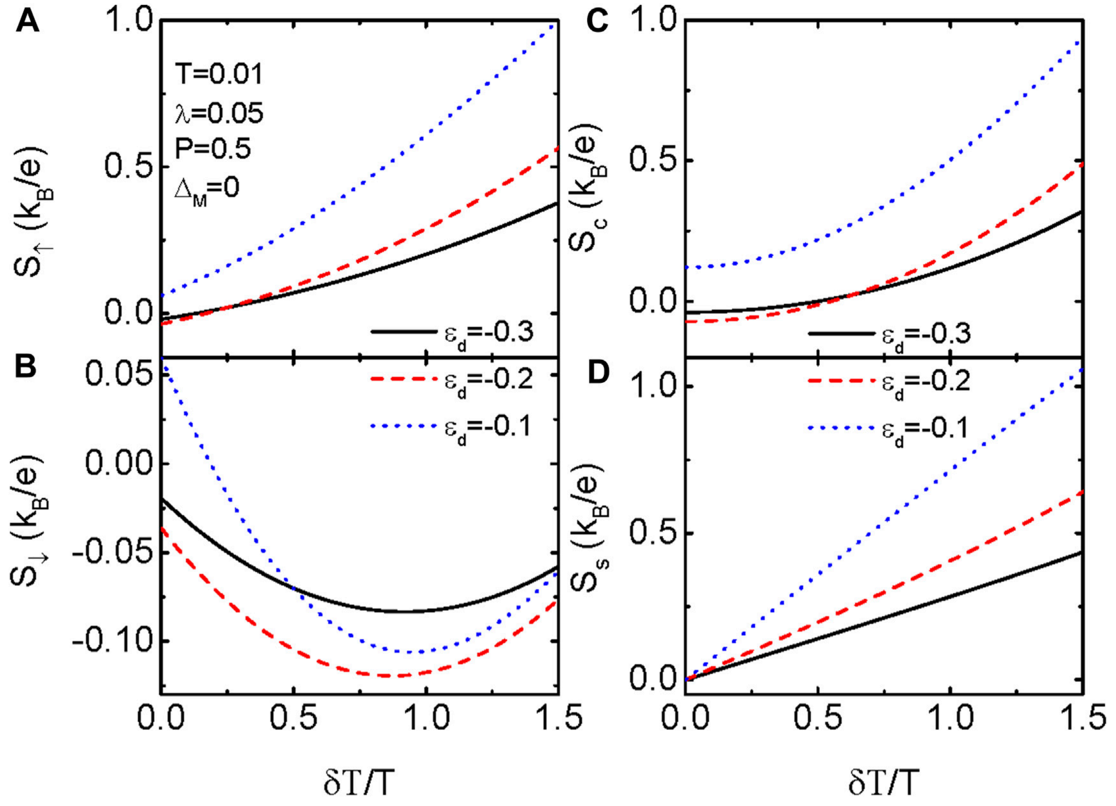

FIGURE 3 | Spin-up thermopower in **(A)**, spin-down thermopower in **(B)**, charge thermopower in **(C)** and spin thermopower in **(D)** as functions of SHA magnitude δT for indicated parameters.

constants are $e = \hbar = k_B = 1$, with the leads' chemical potentials $\mu_L = \mu_R = \mu = 0$. **Figure 1** shows the influences of QD-MZM coupling strength on the electrical conductance and thermopower without SHA (δT = 0). In numerical calculations, the spin-dependent hybridization λ_σ is set to be $\lambda_\uparrow = \lambda(1 - \mathrm{P})$ and $\lambda_\downarrow = \lambda P$, with P the spin-polarization of the QD-MZM hybridization [40]. For the particular arrangement of λ_σ, we only present $G_\uparrow$ in **Figure 1A** and $S_\uparrow$ in **Figure 1B**, the behaviors of the spin-down component can be easily deduced. For $P = 0$, $\lambda_\uparrow = \lambda$ whereas $\lambda_\downarrow = 0$, and $G_\uparrow$ in **Figure 1A** shows the typical double-peak configuration due to the Coulomb-blockade effect [30, 31]. The peaks' height is half of its quantum value e^2/h. With increasing P, the magnitude of $\lambda_\uparrow$ decreases and the peak' height of $G_\uparrow$ increases, accordingly. For $p = 1$, the spin-up electrons on the QD are totally decoupled from the MZM as $\lambda_\uparrow = 0$ and then the peak of $G_\uparrow = e^2/h$. If the QD is coupled to a regular fermion, the peak value of the electrical conductance is zero, which is not shown here [39]. Such a change of the conductance G induced by the QD-MZM coupling originates from the half-fermionic properties of MZM and was first found by Liu et. al., and is a strong evidence of the existence of MZMs. [39].

Figure 1B shows the spin-up thermopower $S_\uparrow$ *varying with respect to the dot level* ε_d for different value of spin-polarization of QD-MZM coupling strength. For $\lambda_\uparrow = 0$ ($P = 1$), the thermpower has three zero points individually at $\varepsilon_d = 0$, $\varepsilon_d = -U/2$, and $\varepsilon_d = -U$ as shown by the green dash-dot-dot line [30, 31]. At the two sides of each zero point, $S_\uparrow$ develops two sharp peaks with opposite signs. From the calculation formulae of the thermopower and $K_{n,\sigma}$, one can see that the integrand of $K_{1,\sigma}$ is antisymmetric with respective to the chemical potential for symmetrical transmission coefficient $\zeta_\sigma(\varepsilon)$. *This indicates that*, for $\lambda_\sigma = 0$ the magnitude of S_σ will be obviously suppressed in left-right symmetrical system as the tunneling of electrons will be compensated by the holes at the three zero points [27–30], which leads to null thermoelectric effect, i.e., zero thermopower. With increasing $\lambda_\uparrow$ (decreasing P), the value of the thermopower at the zero points keep unchanged, whereas at other dot level except for the electron-hole symmetric point $\varepsilon_d = -U/2$, it fist decreases, reaching zero and then changes its sign. Such a sign change of the thermpower induced by QD-MZM coupling was also predicted by Chi et. al. in a recent work [30, 31]. We emphasize that in their work, the spin-up and spin-down electrons couple to the MZM with equal strength, i.e., the coupling strength between the QD and the MZM is spin-independent, and then the thermpower changes sign in the whole dot level regime. In the present paper, however, the consider the case of the spin-dependent QD-MZM coupling and find that the thermopower will not change its sign around $S_\sigma = -U/2$. The sign of S_σ can be reversed by varying the value of P indicates that the electron or hole tunneling direction is tunable by the MZM. As is known that the thermoelectric effect arises from the thermal bias applied between the two leads. We assume the left lead is hotter as compared to the right one, and then there

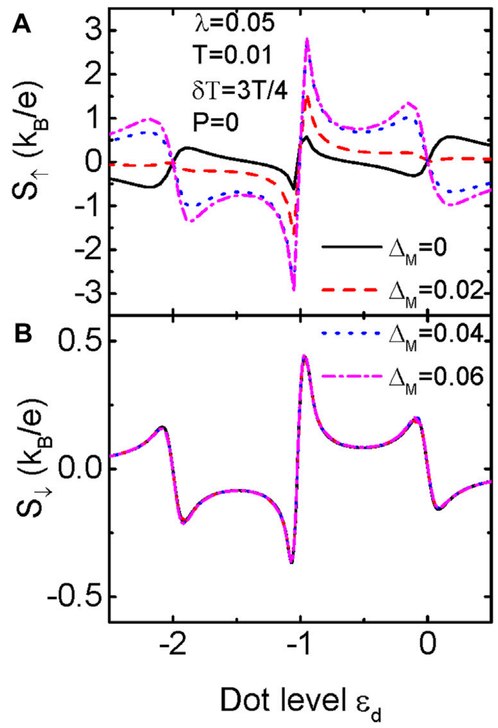

FIGURE 4 | Thermopower for spin-up electrons in **(A)** and spin-down ones in **(B)** as functions of the dot level for varying MZM-MZM coupling strength Δ_M for indicated parameters.

are more electrons above the chemical potential in the left lead and more empty states below the chemical potential. If the dot energy level is below the chemical potential, electrons in the right lead will transport to the left one and occupy the empty states. This induces a positive thermopower. If the dot level is above the chemical potential, electrons in the left lead will tunnel into the right one and induces negative thermopower [27–29]. For non-zero λ_σ, the electron energy levels are modified by the QD-MZM coupling [39]. Therefore, electron transport is converted into that of holes at different energy states, inducing sign change of the thermopower. It is worth noting that the sign change of the thermopower induced by MZM-MZM coupling Δ_M was early predicted [28] and proposed to be an detection means for the existence of Majorana fermions. The sign change of the thermpower by QD-MZM coupling may provide a more feasible means to probe the existence of the MZMs as compared to the direct coupling between the MZMs. This is because that in experiments the value of Δ_M is adjusted by the length of nanowire hosting MZMs [32, 33]. For long enough nanowire, Δ_M vanishes. The strength of QD-MZM coupling, however, can be adjusted in experiments by the capacitive coupling of the tunnel-gate between QD and MZMs [32, 33]. The sign change of the thermpower can be explained as follows: in definition of the thermopower and $K_{1,\sigma}$, one can see that S_σ is proportional to $\int \varepsilon d\varepsilon$ and is zero for symmetric $\zeta_\sigma(\varepsilon)$ when $\varepsilon_d = 0$ or $-U$. Because $-\partial f_\sigma(\varepsilon)/\partial\varepsilon$ is symmetric with respective to $\varepsilon = 0$ and $-U$, the peaks of the $\zeta_\sigma(\varepsilon)$ induced by QD-MZM coupling in the positive (negative) energy regime moves toward (away from) the chemical potential. At low temperatures, the Sommerfeld expansion of the Fermi function shows that the thermopower obey the relationship of $S_\sigma = S_0\varepsilon_d/2\lambda_\sigma^2$, and induces negative (positive) thermopower at the corresponding dot level. Note this relationship between S_σ and λ_σ is valid for only nonzero λ_σ.

Figure 2 presents spin-up conductance $G_\uparrow$ in (a) and $S_\uparrow$ in (b) varying with the system temperature T for different values of P ($\lambda_\uparrow$) and fixed $\lambda = 0.05$. Since $S_\uparrow = 0$ at $\varepsilon_d = 0$, we then fix $\varepsilon_d = -0.1$. **Figure 2A** indicates that at ultra-low temperature, the conductance for $p = 0$ is $G_\uparrow = e^2/2h$ showing the exotic half-fermionic character of the MZMs [39], see the solid line. It is worth of noting that the property of $G_\uparrow = e^2/2h$ is independent on the value of dot level. With increasing temperature, the thermal motion of electrons becomes stronger and the impacts of QD-MZM coupling is weakened. As a result of it, the value of conductance is suppressed accordingly. When $P > 0$, the coupling between spin-up electrons on the QD with MZM becomes weaker, and then the conductance is also suppressed. For $P = 1$, the spin-up electrons is free from interaction with the MZM, and the conductance becomes normal as shown by the green dash-dot-dot line. The thermopower in **Figure 2B** shows a clear sign reversion at a particular system temperature T for small spin-polarization of the dot-MZM coupling strength P [or, equivalently large $\lambda_\uparrow = \lambda(1 - P)$]. It is found that the transition temperature of $S_\uparrow$ become lower with smaller $\lambda_\uparrow$. For very weak $\lambda_\uparrow$, $S_\uparrow$ is positive in the whole temperature regime. As was explained in our previous work, the sign reversion of the thermopower is induced by the asymmetric transmission in the presence of the QD-MZM coupling. Since the sign reversion of the thermopower depends on both the system temperature and magnitude of QD-MZM coupling, it enable that one spin component thermopower is zero whereas the other component is finite. In this way, a 100% spin polarized thermopower can be obtained. It is also possible that the thermopowers of the two spin components are of the same amplitude but have opposite signs, i.e., a pure spin thermpower without the accompany of charge thermopower. In spintronics, 100% spin-polarized and pure spin thermopowers are the corresponding currents or bias voltages.

We study influences of the SHA denoted by δT [7, 23, 24] on the thermopowers at different dot levels in **Figure 3**. Here we set $p = 0.5$ so as to $\lambda_\uparrow = \lambda_\downarrow$ and $S_\uparrow = S_\downarrow$ for $\delta T = 0$. It is found that $S_\uparrow$ in **Figure 3A** and $S_\downarrow$ in (**Figure 3B**) respectively approach to positive and negative values with increasing δT [38]. This is because the spin-up and spin-down electrons are in different temperatures for finite value of δT, and then have corresponding different transition temperature of the thermpower. The charge thermopower $S_c = S_\uparrow + S_\downarrow$ in **Figure 3C** may also change its sign at dot levels of $\varepsilon_d = -0.3$ and -0.2, whereas it keeps positive at $\varepsilon_d = -0.1$. *Interestingly, the charge thermpower* $S_c = 0$ *at about* $\delta T = 3T/4$ for both $\varepsilon_d = -0.3$ and -0.2, which provides a feasible way of changing the charge thermopower. In **Figure 3D** we present the result of pure spin thermpower $S_s = S_\uparrow - S_\downarrow$. There are three characters worth to be pointing out: one is that S_s shows the perfect linear relationship with δT, which is ideal in detecting the strength of SHA; and the other is that S_s is positive in the whole range of δT. This indicates that a pure spin thermopower in the absence of charge thermopower can be generated by properly adjusting some system parameters, such as the dot level, magnitude of SHA, QD-MZM coupling strength or its spin polarization. At last, the magnitude of S_s is comparable to that of the charge one, which is important in thermospin devices.

Finally in **Figure 4** we present the influences of MZM-MZM coupling strength Δ_M on the spin-dependent thermopower. The most important property of the spin-up thermpower in **Figure 4A** is the sign change induced by Δ_M, which has also been found in some previous work [28, 30, 31, 38]. The sign change of the thermopower by Δ_M can also been explained in terms of the shape of the electronic transmission function $\zeta_\sigma(\varepsilon)$, [1, 2] which not shown here. For the particular value of P, the spin-down thermopower in **Figure 4B** keeps unchanged. From the two figures one can see that $S_\uparrow$ and $S_\downarrow$ of the same amplitude may be opposite in sign, which enable the emerge of 100% spin polarized or pure spin thermpowers.

4 SUMMARY

In conclusion, we study properties of spin-dependent thermopower adjusted by MZMs in a QD connected to two normal metal leads. Our numerical results *show* that the spin-polarized thermopower will change its sign by varying the system equilibrium temperature with the help of interaction between the dot and one mode of the MZMs, which is useful in generating 100% spin-polarized or pure spin thermopowers. The SHA will *change the signs of spin-up and spin-down thermpowers* with enhanced magnitude. By the combined effect of the SHA and hybridization between the dot and MZM, the spin-polarized thermpower can be fully adjusted and enhanced, which is vital in energy-saving nanoscale devices.

DATA AVAILABILITY STATEMENT

The original contributions presented in the study are included in the article/Supplementary Material, further inquiries can be directed to the corresponding author.

AUTHOR CONTRIBUTIONS

L-LS derived the formulae, performed partial numerical calculations, and wrote the original manuscipt. Z-GF discussed the physical model, performed partial numerical calculations, and contributed in the paper writting.

FUNDING

This work was supported by Research Funds for Beijing Universities (NO.KM201910009002).

REFERENCES

1. Johnson M. Spin Caloritronics and the Thermomagnetoelectric System. *Solid State Commu* (2010) 150:543. doi:10.1016/j.ssc.2009.10.027
2. Bauer G, Saitoh E, and van Wees B. Spin Caloritronics. *Nat Mater* (2012) 11: 391. doi:10.1038/nmat3301
3. Dresselhaus M, Dresselhaus G, Sun X, Zhang Z, Cronin S, and Koga T. Low-dimensional Thermoelectric Materials. *Phys Solid State* (1999) 41:679. doi:10.1134/1.1130849
4. Dubi Y, and Ventra M. Colloquium: Heat Flow and Thermoelectricity in Atomic and Molecular Junctions. *Rev Mod Phys* (2011) 83:131. doi:10.1103/RevModPhys.83.131
5. Uchida K, Takahashi S, Harii K, Ieda J, Koshibae W, Ando K, et al. Observation of the Spin Seebeck Effect. *Nat* (2008) 455:778. doi:10.1038/nature07321
6. Ren J, Fransson J, and Zhu J. Nanoscale Spin Seebeck Rectifier: Controlling thermal Spin Transport across Insulating Magnetic Junctions with Localized Spin. *Phys Rev B* (2014) 89:214407. doi:10.1103/PhysRevB.89.214407
7. Heikkilä T, Hatami M, and Bauer G. Spin Heat Accumulation and its Relaxation in Spin Valves. *Phys Rev B* (2010) 81:100408. doi:10.1103/PhysRevB.81.100408
8. Hatami M, Bauer G, Zhang Q, and Kelly P. Thermoelectric Effects in Magnetic Nanostructures. *Phys Rev B* (2009) 79:174426. doi:10.1103/PhysRevB.79.174426
9. Yu H, Granville S, Yu D, and Ansermet J. Evidence for thermal Spin-Transfer Torque. *Phys Rev Lett* (2010) 104:146601. doi:10.1103/PhysRevLett.104.146601
10. Gu L, Fu H, and Wu R. How to Control Spin-Seebeck Current in a Metal-Quantum Dot-Magnetic Insulator junction. *Phys Rev B* (2016) 94:115433. doi:10.1103/PhysRevB.94.115433
11. Ren J. Predicted Rectification and Negative Differential Spin Seebeck Effect at Magnetic Interfaces. *Phys Rev B* (2013) 88:220406. doi:10.1103/PhysRevB.88.220406
12. Uchida K, Adachi H, Ota T, Nakayama H, Maekawa S, and Saitoh E. Observation of Longitudinal Spin-Seebeck Effect in Magnetic Insulators. *Appl Phys Lett* (2010) 97:172505. doi:10.1063/1.3507386
13. Uchida K, Xiao J, Adachi H, Ohe J, Takahashi S, Ieda J, et al. Spin Seebeck Insulator. *Nat Mater* (2010) 9:894. doi:10.1038/nmat2856
14. Bosu S, Sakuraba Y, Uchida K, Saito K, Ota T, Saitoh E, et al. Spin Seebeck Effect in Thin Films of the Heusler Compound Co2mnsi. *Phys Rev B* (2011) 83: 224401. doi:10.1103/PhysRevB.83.224401
15. Jaworski C, Yang J, Mack S, Awschalom D, Heremans J, and Myers R. Observation of the Spin-Seebeck Effect in a Ferromagnetic Semiconductor. *Nat Mater* (2010) 9:898. doi:10.1038/nmat2860
16. Jaworski C, Myers R, Johnston-Halperin E, and Heremans J. Giant Spin Seebeck Effect in a Non-magnetic Material. *Nat* (2012) 487:210. doi:10.1038/nature11221
17. Wu SJE, Pearsonand Bhattacharya A. Paramagnetic Spin Seebeck Effect. *Phys Rev Lett* (2015) 114:186602. doi:10.1103/PhysRevLett.114.186602
18. Wu S, Zhang W, Kc A, Borisov P, Pearson J, Jiang J, et al. Antiferromagnetic Spin Seebeck Effect. *Phys Rev Lett* (2016) 116:097204. doi:10.1103/PhysRevLett.116.097204
19. Tang G, Chen X, Ren J, and Wang J. Rectifying Full-Counting Statistics in a Spin Seebeck Engine. *Phys Rev B* (2018) 97:081407. doi:10.1103/PhysRevB.97.081407
20. Chang P, Mahfouzi F, Nagaosa N, and Nikolić B. Spin-seebeck Effect on the Surface of a Topological Insulator Due to Nonequilibrium Spin-Polarization Parallel to the Direction of Thermally Driven Electronic Transport. *Phys Rev B* (2014) 89:195418. doi:10.1103/physrevb.89.195418
21. Okuma N, Masir M, and MacDonald A. Theory of the Spin-Seebeck Effect at a Topological-Insulator/ferromagnetic-Insulator Interface. *Phys Rev B* (2017) 95:165418. doi:10.1103/PhysRevB.95.165418
22. Hatami M, Bauer G, Zhang Q, and Kelly P. Thermal Spin-Transfer Torque in Magnetoelectronic Devices. *Phys Rev Lett* (2007) 99:066603. doi:10.1103/PhysRevLett.99.066603
23. Dejene F, Flipse J, Bauer G, and van Wees B. Spin Heat Accumulation and Spin-dependent Temperatures in Nanopillar Spin Valves. *Nat Phys* (2013) 9: 636. doi:10.1038/nphys2743
24. Vera-Marun I, van Wees B, and Jansen R. Spin Heat Accumulation Induced by Tunneling from a Ferromagnet. *Phys Rev Lett* (2014) 112:056602. doi:10.1103/PhysRevLett.112.056602

25. Kimling J, Wilson R, Rott K, Kimling J, Reiss G, and Cahill D. Spin-dependent thermal Transport Perpendicular to the Planes of Co/cu Multilayers. *Phys Rev B* (2015) 91:144405. doi:10.1103/PhysRevB.91.144405
26. Kimling J, and Cahill D. Spin Diffusion Induced by Pulsed-Laser Heating and the Role of Spin Heat Accumulation. *Phys Rev B* (2017) 95:014402. doi:10.1103/PhysRevB.95.014402
27. Hou C, Shtengel K, and Refael G. Thermopower and mott Formula for a Majorana Edge State. *Phys Rev B* (2013) 88:075304. doi:10.1103/PhysRevB.88.075304
28. López R, Lee M, Serra L, and Lim J. Thermoelectrical Detection of Majorana States. *Phys Rev B* (2014) 89:205418. doi:10.1103/PhysRevB.89.205418
29. Leijinse M. Thermoelectric Signatures of a Majorana Bound State Coupled to a Quantum Dot. *New J Phys* (2014) 16:015029. doi:10.1088/1367-2630/16/1/015029
30. Hong L, Chi F, Fu Z, Hou Y, Wang Z, Li K, et al. Large Enhancement of Thermoelectric Effect by Majorana Bound States Coupled to a Quantum Dot. *J Appl Phys* (2020) 127:124302. doi:10.1063/1.5125971
31. Chi F, Fu Z, Liu J, Li K, Wang Z, and Zhang P. Thermoelectric Effect in a Quantum Dot Side-Coupled to Majorana Bound States. *Nanoscale Res Lett* (2020) 15:79. doi:10.1186/s11671-020-03307-y
32. Mourik V, Zuo K, Frolov S, Plissard S, Bakkers E, and Kouwenhoven L. Signatures of Majorana Fermions in Hybrid Superconductor-Semiconductor Nanowire Devices. *Science* (2012) 336:1003. doi:10.1126/science.1222360
33. Ricco L, de Souza M, Figueira M, Shelykh I, and Seridonio A. Spin-dependent Zero-Bias Peak in a Hybrid Nanowire-Quantum Dot System: Distinguishing Isolated Majorana Fermions from Andreev Bound States. *Phys Rev B* (2019) 99:155159. doi:10.1103/PhysRevB.99.155159
34. Qi X, and Zhang S. Topological Insulators and Superconductors. *Rev Mod Phys* (2011) 83:1057. doi:10.1103/RevModPhys.83.1057
35. Nayak C, Simon S, Stern A, Freedman M, and Sarma S. Non-abelian Anyons and Topological Quantum Computation. *Rev Mod Phys* (2008) 80:1083. doi:10.1103/RevModPhys.80.1083
36. Alicea J, Oreg Y, Refael G, von Oppen F, and Fisher M. Non-abelian Statistics and Topological Quantum Information Processing in 1d Wire Networks. *Nat Phys* (2011) 7:412. doi:10.1038/nphys1915
37. Pikulin D, Dahlhaus J, Wimmer M, Schomerus H, and Beenakker C. A Zero-Voltage Conductance Peak from Weak Antilocalization in a Majorana Nanowire. *New J Phys* (2012) 14:125011. doi:10.1088/1367-2630/14/12/125011
38. Sun LL, and Chi F. Detecting Spin Heat Accumulation by Sign Reversion of Thermopower in a Quantum Dot Side-Coupled to Majorana Bound States. *J Low Temp Phys* (2021) 203:381. doi:10.1007/s10909-021-02593-9
39. Liu D, and Baranger H. Detecting a Majorana-Fermion Zero Mode Using a Quantum Dot. *Phys Rev B* (2011) 84:201308. doi:10.1103/PhysRevB.84201308
40. Gorski G, and Kucab K. The Spin-dependent Coupling in the Hybrid Quantum Dot–Majorana Wire System. *Phys Status Solidi B* (2019) 256:1800492. doi:10.1002/pssb.201800492
41. Chi F, Wang J, He TY, Fu ZG, Zhang P, Zhang XW, et al. Quantum Interference Effects in Quantum Dot Molecular with Majorana Bound States. *Front Phys* 8 (2021) 631031. doi:10.3389/fphy.2020.631031

Conflict of Interest: The authors declare that the research was conducted in the absence of any commercial or financial relationships that could be construed as a potential conflict of interest.

frontiers
in Physics

ORIGINAL RESEARCH
published: 09 September 2021
doi: 10.3389/fphy.2021.752476

Efficiency Boosting by Thermal Harvesting in InGaN/GaN Light-Emitting Diodes

Shunpeng Lu[1†*], *Yiping Zhang*[1†], *Ying Qiu*[2], *Xiao Liu*[3], *Menglong Zhang*[3] and *Dongxiang Luo*[3,4*]

[1]School of Electrical and Electronic Engineering, Nanyang Technological University, Singapore, Singapore, [2]Guangdong Research and Design Center for Technological Economy, Guangzhou, China, [3]Institute of Semiconductors, South China Normal University, Guangzhou, China, [4]School of Chemistry and Chemical Engineering, Institute of Clean Energy and Materials, Guangzhou Key Laboratory for Clean Energy and Materials, Huangpu Hydrogen Innovation Center, Guangzhou University, Guangzhou, China

Edited by:
Feng Chi,
University of Electronic Science and Technology of China, Zhongshan Institute, China

Reviewed by:
Ming Chen,
Shenzhen Institutes of Advanced Technology CAS, China
Lei Jin,
McGill University, Canada

***Correspondence:**
Shunpeng Lu
lush0007@e.ntu.edu.sg
Dongxiang Luo
luodx@gdut.edu.cn

†These authors have contributed equally to this work

Specialty section:
This article was submitted to Optics and Photonics, a section of the journal Frontiers in Physics

Received: *03 August 2021*
Accepted: *30 August 2021*
Published: *09 September 2021*

Citation:
Lu S, Zhang Y, Qiu Y, Liu X, Zhang M and Luo D (2021) Efficiency Boosting by Thermal Harvesting in InGaN/GaN Light-Emitting Diodes. Front. Phys. 9:752476. doi: 10.3389/fphy.2021.752476

On the same micro-LED display panel, LED pixels are always operated with high and low biased voltages simultaneously to show different brightness and colors. Thus, it is vitally important to understand the effect of the heat transmission between LEDs under high and low biased voltages. In this work, we design two different LED groups: Group A is two LEDs bonded together for heat transmission and Group B is two LEDs separated from each other. Then, the two LEDs are operated at one fixed and one tuned biased voltage respectively in each group in a vacuum chamber and the efficiency of the two groups is studied both experimentally and numerically. Here, our experimental results demonstrate that Group A exhibits a maximum improvement of 15.36% in optical output power compared with Group B. The underlying reason is that the wall-plug efficiency of the LED with a voltage lower than photon voltage ($V < \hbar\omega/q$) is surprisingly enhanced by elevated temperature owing to the heat transmission by the LED under a high biased voltage in Group A. Our further study shows that in such a low voltage region the improvement in the efficiency is attributed to the enhanced carrier concentrations with elevated temperature. On the other hand, the LED in Group A under a high biased voltage further raises the overall efficiency by alleviating the thermal droop due to reduced temperature. Device temperature measurement and numerical calculation of radiative recombination under different temperatures further support the superior performance of Group A LEDs. Our research results can act as the research prototype to design the high-efficient LED arrays for better energy recycling and thermal control.

Keywords: thermal heat, light emitting diode (LED), ingan/ GaN, thermal harvesting, micro-LED display

INTRODUCTION

Semiconductor optoelectronic materials and devices develop very fast recent decades [1–6]. InGaN/GaN based materials is one of the most promising materials for optoelectronic applications. As one of the most important devices, GaN-based light-emitting diodes (LEDs) are recognized as next-generation lighting sources and have become increasingly prevalent in the lighting, display, and optical communication industries owing to great advantages of high emission efficiency, long lifetime, robust reliability, multi-color properties, and low cost [7–10]. However, high self-heating and low heat dissipation are the critical issues needed to be addressed during the operation of LEDs. Therefore, extensive research and development efforts have been devoted to reducing the thermal heat generated in the InGaN/GaN-based LEDs to reduce the thermal droop, which rapidly drops the device efficiency under a high input electrical power especially in the high voltage regime($qV > \hbar\omega$) [11–18]. Over the past couple of decades, plenty of architectures and solutions have been proposed to address the scientific and technological challenges introduced by the thermal heat, including adding the heat sink, increasing the heat dissipation area, changing n-electrode length, and exploiting the thermoelectric generator [19–23]. However, all these methods seem to be failed when it comes to the devices with small dimensions and thin films, which have no sufficient space for installing external heat dissipation architectures, for example, Ribbon Filament LED Lamp where LEDs are lined up in a filament. More importantly, the rapidly growing development of the mini- and micro-LEDs has become a driving force to study the thermal management and exploring the possible thermal harvesting [24–31]. Nevertheless, the thermal heat is always regarded as undesirable in most of the previous designs and approaches, rather than considering the solutions from the perspective of heat energy recycling and thermoelectric energy transition, which can in turn boost the efficiency of the device and promote the energy saving. The Energy recycling is a thermoelectric pumping process of carriers under the coupling effect of electrical work and lattice heat (phonon field), and the recent advancements in Energy recycling for semiconductors under low bias voltage condition, especially in GaAs materials, is provoking an increasing interest in GaN-based LEDs [32–37]. Despite intense research on a relatively comprehensive understanding of the principle of Energy recycling in GaN-based LEDs, the utilization of Energy recycling is rare in practice [38–41].

In this work, we propose a new approach on the device level to address thermal heat issues by connecting LEDs for thermal transmission and applying varied voltages to different LED devices. The proposed method is observed to achieve thermal harvesting in InGaN/GaN LEDs with improved optical output power, enhanced energy efficiency, and alleviated thermal droop. Device temperature measurement and numerical calculation of Energy recycling further support the superior edge of the proposed design. The findings in this work reveal the cooling potential of LEDs and can provide guidelines on thermal management in designing the high-efficient LED arrays, especially for the mini- and micro-LEDs applications, and support the possibility of removing the heat sink.

MATERIALS AND METHODS

The blue InGaN/GaN MQW LED wafers used in this work were grown on (0001) c-plane pattern sapphire substrates using an AIXTRON close-coupled showerhead metal-organic chemical-vapor deposition (MOCVD) system. Initially, the epitaxial growth was grown on a 30-nm thick low-temperature GaN nucleation layer followed by a 4 μm unintentionally doped n-type GaN (u-GaN) layer. Then a 2 μm thick Si-doped n-GaN layer was grown with the Si doping concentration of $5 \times 10^{18}\ \mathrm{cm}^{-3}$. Subsequently, six pairs of InGaN/GaN MQWs were grown with a 3 nm thick quantum well (QW) and a 9 nm thick quantum barrier (QB). The indium composition of the InGaN layer was 18% and the emission peak wavelength of the grown samples was centered at ~ 460 nm. After the MQWs, a 20 nm $\mathrm{Al}_{0.15}\mathrm{Ga}_{0.85}\mathrm{N}$ electron blocking layer (EBL) was grown, followed by a 150 nm thick Mg-doped p-GaN layer with the Mg doping concentration of $1 \times 10^{18}\ \mathrm{cm}^{-3}$. Finally, the *in-situ* 720°C thermal annealing treatment in N_2 ambient was carried out to activate the Mg dopants. After epitaxial growth was completed, the LED wafers were fabricated into vertical structured LED chips with a dimension of 1 mm × 1 mm by standard fabrication and packing processes. To facilitate the experimental measurement of these LED devices within the varied temperature range, the InGaN/GaN LEDs used in this work are bare dies without encapsulation or packaging, which leads to slightly lower wall-plug efficiency values than commercial LED devices or ones with optimized light extraction architectures [35].

The optical output power of these LED devices used in this work was measured by Si-photodiode connected to the Thorlabs Dual Channel Optical Power and Energy Meter. And the surface temperature of these LED devices was measured by the TELOPS High-Speed IR Cameras, and meanwhile thermal couples were connected to these LED devices to double confirm the accuracy of the experimentally measured data. In order to reduce the devices' thermal dissipation into the ambient, all the experimental measurements were carried out in a high vacuum ambient, which was achieved by allocating the LEDs into a chamber and then pumping down the chamber to a high vacuum with a vacuum pressure of 4.05×10^{-7} mBar. During all the measurements, all the data were collected after the LEDs had reached thermal equilibrium.

In order to precisely reveal the mechanism that how the temperature influences the LED performance, numerical calculations were conducted by the Advanced Physical Models of Semiconductor Devices (APSYS) simulator, which self-consistently solves the Schrödinger equation, continuity equation, and Poisson equation with proper boundary conditions. In the simulations, the Auger recombination coefficient was set to $1 \times 1042\ \mathrm{m}^6/\mathrm{s}$ and 40% of the polarization charges were assumed such that 60% of the theoretical polarization charges were released because of the crystal strain relaxation by generating dislocations [42–44].

RESULTS AND DISCUSSION

In the research community of InGaN/GaN-based LEDs, operating at elevated temperatures is considered always undesirable, as this causes thermal droop and therefore degrades the device efficiency. Due to this reason, various structures and external cooling designs have been deployed in III-nitride LEDs including modifying device architectures and providing external cooling designs to alleviate the thermal droop by reducing operating temperature. However, in contrast to the common knowledge and practice of operating GaN-based LEDs, the increased device temperature may not necessarily lead to the degradation of efficiency. According to the well-known ABC model [45], internal quantum efficiency (*IQE*) can be expressed as follows at a low current injection level:

$$IQE = Bn^2/\left(An + Bn^2 + Cn^3\right) \tag{1}$$

where n is the carrier concentration, A is the Shockley-Read-Hall (SRH) nonradiative recombination rate, B is the radiative recombination rate, and C is the Auger nonradiative recombination rate. The SRH nonradiative recombination and Auger recombination has been reported to be increased with elevated temperature [46–48], however, the carrier concentration is significantly increased with the temperature, as shown in the equations below, which may improve the *IQE* in one certain voltage region [37, 49], especially in the low voltage region.

$$n^2 = n_i^2 \exp\left(\frac{qV}{kT}\right) \tag{2}$$

$$n_i^2 = N_c N_v \exp\left(\frac{-E_g}{kT}\right) = 2.33\times10^{31}\left(\frac{m_e^* m_h^*}{m_e^2}\right)^{3/2} T^3 \exp\left(\frac{-E_g}{kT}\right) \tag{3}$$

where n_i is the intrinsic concentration, q is the elementary charge, V is the applied voltage, k is the Boltzmann constant, T is the temperature, N_c is the effective density of states at conduction band edge, N_v is the effective density of states at valence band edge, m_e* is the effective electron mass, m_h* is the effective hole mass, m_e is the free electron mass, and E_g is the energy bandgap of the material. From the above **Eqs 1–3**, it can be understood that for a low voltage when the device temperature is increased, the carrier concentration is considerably increased, which leads to the improved radiative recombination and possibly causes the enhanced *IQE* even though the nonradiative recombination is simultaneously increased. In that case, the elevated temperature effect becomes beneficial.

More importantly, when it turns to the voltage region ($qV < ħω$), the Peltier effect is changed from Peltier heat to Peltier cooling. The total heating power Q_{total} (per unit area) generated in the LED device consisting of Peltier heat $Q_{Peltier}$ (phonon emission or absorption), nonradiative recombination heat $Q_{nonradiative}$, and Joule heat Q_{Joule} can be expressed as below:

$$Q_{total} = Q_{Peltier} + Q_{nonradiative} + Q_{Joule} = JV \times \left(1 - \eta_{WPE}\right) \tag{4}$$

where J is the injection current density, V is the applied voltage, and η_{WPE} is the wall-plug efficiency of the LED device. Then an approximate magnitude of the Peltier heat can be obtained as [35]:

$$Q_{Peltier} = J \times \left(V - IR_s - \frac{\hbar\omega}{q}\right) \tag{5}$$

where I is the injection current and R_s is the total series resistance of the LED device. As inferred from the above **Eq. 5**, the Peltier heat is changed to Peltier cooling when the applied voltage is lower than the photon voltage ($ħω/q$). As InGaN/GaN LEDs are typically driven under high bias ($qV > ħω$), the possible positive effect of the increased temperature is never taken into consideration in the LED designs, even less to utilize in the operation. Our hypothesis is that, when the operating voltage of InGaN/GaN LEDs falls into the bias region of $V < ħω/q$, the elevated temperature should become beneficial and enhance the device efficiency due to the enhanced carrier concentrations. Normally, there are more than one LED device embedded in the common lighting lamps and they suffer from severe thermal droop due to the considerable thermal heat generated when the applied voltages are higher than $ħω/q$. If the positive effect of the temperature can be utilized in the LED lamps or arrays, it will alleviate the thermal droop and boost energy efficiency.

Therefore, in this work, we propose a creative and simple approach to take advantage of the positive effect of temperature and achieve thermal harvesting by applying the varied voltages to different LED devices embedded in the LED arrays, which is in contrast to the common operation. In our design, these LED devices are biased at different voltages and the high voltage-biased LEDs are operated at the working voltage regime $V > ħω/q$ normally falling into the efficiency-droop, high-voltage region, in which the LEDs suffer from severe thermal droop and elevated temperature is undesirable. Thus, a large amount of thermal heat is generated in these LED devices while less heat is generated for the low voltage-biased ones whose voltages are within the high-efficiency, mid-voltage region ($V < ħω/q$), in which Energy recycling occurs. All these LED devices are close to each other in physical distance, thus the thermal heat transition among these devices occurs if there is a temperature gradient among them. The superior edge of this proposed configuration lies in two aspects. Firstly, the thermal heat flow among these devices enables heating the low-biased LEDs so that the device temperature is elevated, and the device efficiency is improved owing to the enhanced Energy recycling and the increased carrier concentrations. Secondly, because much thermal heat is transferred out from the LEDs under high biased voltage, the alleviated thermal droop is obtained, which boosts the efficiency and improves the device lifetime. Thus, the total energy efficiency of the whole LED system is increased. Even more importantly, the thermal heat generated is recycled and utilized and the total device temperature is tuned, which allows more energy-saving and efficient operation.

In order to demonstrate the proposed configuration and investigate its performance and advantages, we simplify the proposed configuration into a two-combined-LEDs design (named Group A Combined-LEDs setup), in which two behavior-similar LEDs are attached to each other in the way of back-to-back for highly efficient thermal transmission as illustrated in **Figure 1A**. In this simplified design, two LEDs are directly attached to each other in order to minimize the heat loss during the transition and maximize the amount of thermal heat that the LED under low voltage can receive. In this way, the beneficial effect of thermal heat can be maximized. This simplified configuration can be regarded as the research prototype and basic component for the LED arrays and the findings in the simplified model can be multiplied and applied to the whole LED arrays. A control group (called Group B Separated-LEDs setup) is also introduced as shown in **Figure 1A** by separating two LEDs far away from each other to eliminate the heat flow or any interference between them.

Figure 1B shows the experimental measured *I-V* curve and wall-plug efficiency (WPE) curve for two behavior-similar LEDs.

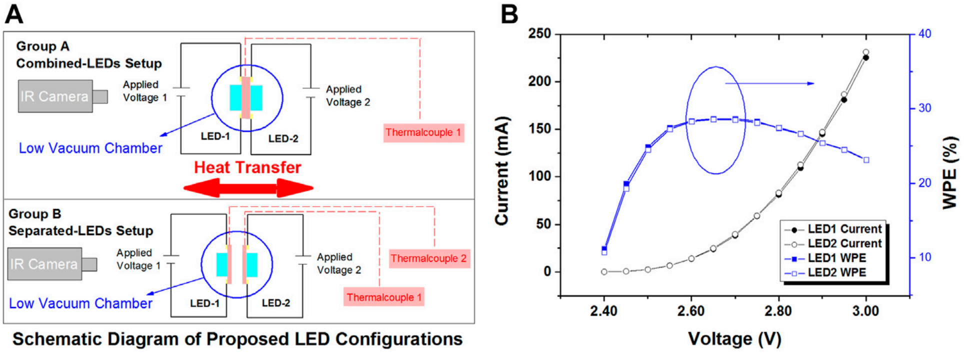

FIGURE 1 | (A) Schematic diagram of the experimental measurements for proposed LEDs configuration (Group A) and the control group (Group B); **(B)** Experimental measured *I-V* curve and WPE versus applied voltages for two behavior-similar LEDs.

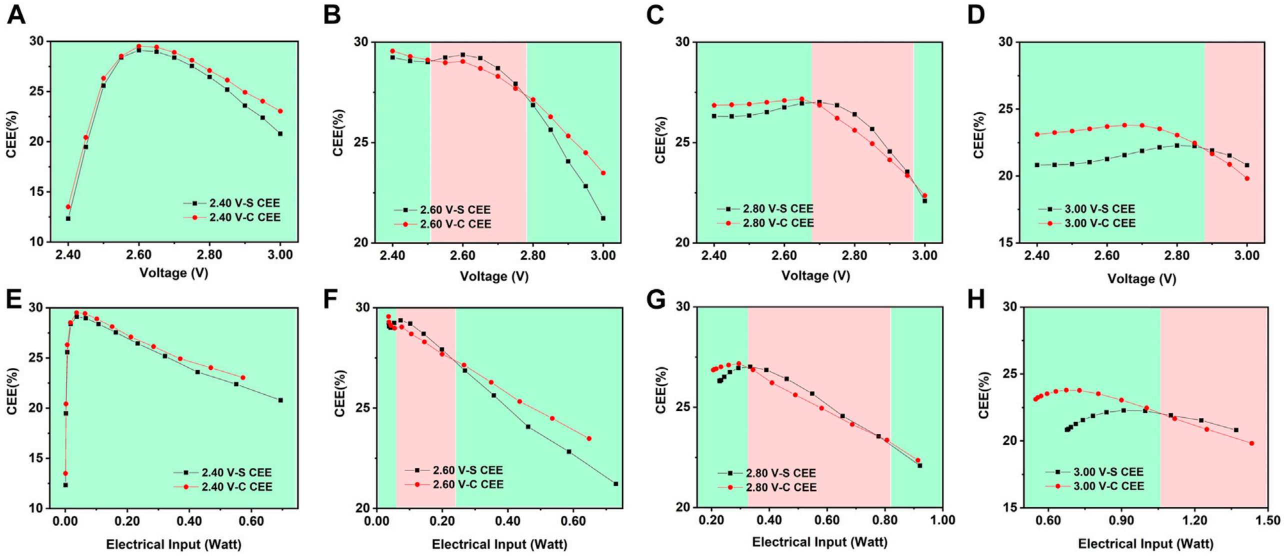

FIGURE 2 | Experimental measured CEE for two LED groups versus applied voltage of LED-1, while LED-2 under a fixed voltage of **(A)** 2.40, **(B)** 2.60, **(C)** 2.80, and **(D)** 3.00 V; CEE versus total electrical power for two LED groups, while LED-2 under a fixed voltage of **(E)** 2.40, **(F)** 2.60, **(G)** 2.80, and **(H)** 3.00 V. Here, V-C is Group A combined LED setup and V-S is Group B Separated-LEDs setup.

It can be clearly seen from **Figure 1B** that both the electrical and optical behaviors of two LEDs used in the experiments are similar when the applied voltage is increased from 2.40 to 3.00 V. Due to the high similarity between these two LEDs, it is reasonable to believe that the influence of such minor variation in the performance of these two LEDs on the experimental results is limited. In order to investigate the overall performance of the proposed design and demonstrate its advantages, the experimental measurements are conducted in the way that the applied voltage for one of the LEDs (called LED-1) is changing (increased from 2.40 to 3.00 V), while the voltage of the other one (LED-2) is fixed at several values (2.40, 2.60, 2.80, and 3.00 V). The experimental measurements are carried out in a high vacuum chamber to reduce the heat dissipation into the ambient. Here, these two LEDs are regarded as one system, hence the coupled energy efficiency (CEE) of these two LEDs is calculated by:

$$CEE = \frac{Total\ Optical\ Output\ Power\ of\ Two\ LEDs}{Total\ Electrical\ Input\ of\ Two\ LEDs} \tag{6}$$

Figures 2A–D show the experimental measured CEE of the system versus the applied voltage of LED-1, while LED-2 under a fixed voltage of 2.40, 2.60, 2.80, and 3.00 V for the Combined-LEDs and Separated-LEDs setups. When LED-2 is fixed at 2.4 V, as shown in **Figure 2A**, the proposed approach Group A Combined-LEDs has a higher CEE than the control group Group B separated LEDs at all voltages of LED-1. Such improvement is attributed to two aspects. On one hand, for LED-2 whose voltage is fixed at 2.40 V, Group A in the proposed configuration allows the thermal heat transition so that the thermal heat generated in the whole system can be easily absorbed by LED-2 before dissipating into the ambient and transfer the energy to the carriers through the Energy

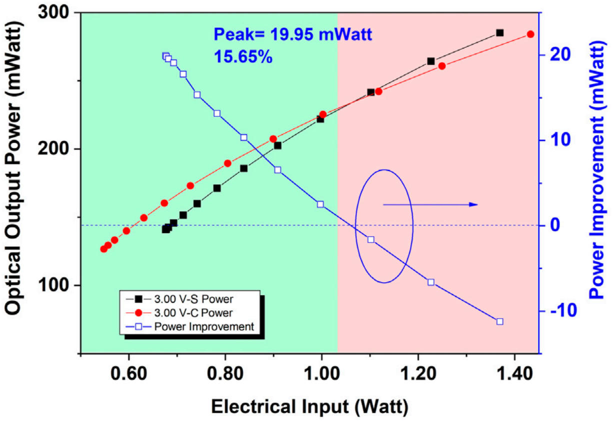

FIGURE 3 | The total optical output power versus total electrical input for two setups and corresponding power improvement for group A compared to group B. Here, LED-2 is under a voltage of 3.00 V for both groups. V-C is Group A combined LED setup and V-S is Group B Separated-LEDs setup.

recycling. Thus, improve the efficiency of LED-2. On the other hand, for LED-1 whose voltage is increased from 2.40 to 3.00 V, when the voltage is lower than photon voltage (2.69 V in our case) the elevated temperature and enhanced Energy recycling because of a smaller heat dissipation area contribute to the improved efficiency. When the voltage is increased to a value higher than photon voltage, the effect of elevated temperature turns to negative for LED-1. However, in our designed LED group A, the LED-2 acts as the heat sink by absorbing part of the thermal heat generated by LED-1, which significantly reduces the device temperature of LED-1, thus leading to alleviated thermal droop and improved efficiency for LED-1. While it is worth noting that at the voltage of 2.40 V, Group A has a higher CEE than Group B. This is because the back-to-back bonded LEDs Group A has a smaller heat dissipation area than that of Group B. Based on our calculation, the heat dissipation area of group A is 3.76 mm^2 and the heat dissipation area of group B is 5.76 mm^2 for two LEDs. Hence, Group A holds more heat, which contributes to improved efficiency enhanced by Energy recycling and higher current density improved by the heat. The trend in **Figure 2B** is almost the same as that in **Figure 2A**, except for one small voltage region around 2.60 V, which will be analyzed in the following discussion. The proposed setup also outperforms the control group when the voltage of LED-1 is in the low voltage region even though the voltage of LED-2 is increased to 2.80 and 3.00 V, as shown in **Figures 2C,D** . However, when the voltage variation between LED-1 and LED-2 gets smaller even negative, the lower heat dissipation capability of the Combined-LEDs setup with back-to-back configuration causes more severe thermal droop than the Separated-LEDs setup, thus degrading the efficiency, as shown in the high voltage regions of **Figures 2C,D**. It is noteworthy that when the variation of these two LEDs becomes larger, the LED with lower voltage plays the role of heat sink even though the voltages of both two LEDs are higher than photon voltage, for example, $V_{LED\text{-}1}$ = 2.80 V, $V_{LED\text{-}2}$ = 3.00 V, and $V_{LED\text{-}1}$ = 3.00 V, $V_{LED\text{-}2}$ = 2.80 V. Further analysis of the experimental measured CEE curves versus the total electrical input of two LEDs for two setups presented in **Figures 2E,F,G,H** also show the same trend. The improvement in the CEE of the presently studied configuration becomes relatively more pronounced when the applied voltage of LED-2 increased to 3.00 V.

Further analysis of the optical output power shown in **Figure 3** gives a peak power improvement of 19.95 mWatt (15.65% in terms of percentage) for the proposed configuration Group A studied here compared to the control group. The results in **Figure 3** suggest that under the same electrical input the proposed configuration with varied voltages has higher optical output power than the control group when the electrical input is smaller than 1.02 Watt. This improvement originates mainly from the beneficial effect of the increased temperature of the low-biased LED, as well as the alleviated thermal droop in the high-biased LED. Such improvement in the performance of the Combined-LEDs setup becomes relatively more pronounced under low electrical input. It is worth mentioning that the starting point of group A is smaller than that of group B, as indicated in **Figure 3**. The difference in the starting point of the electrical input between these two groups is due to the difference of the current for the whole system caused by the varied temperature. As LED-2 is under a voltage of 3.00 V for both groups and group A is two LEDs combined together for good heat transmission, LED-2 in group A has lower temperature and smaller current than that of group B, and LED-1 in group A has higher temperature and larger current than that of group B. We further calculate the current of LED-2 for two groups. The current of LED-2 for group A is 180 mA and that for group B is 230 mA. As the electrical input of LED-2 dominates the electrical input for two groups at the start point, the starting point of group A is smaller than that of group B.

Figure 4A presents the device surface temperature of LEDs versus applied voltage of LED-1 for two setups with $V_{LED\text{-}2}$ = 3.00 V, from which we can see that the device temperature of LED-2 in the proposed model is reduced compared to that in the control group at most of the voltages with a maximum reduction of 40 K at the voltage of 2.40 V. Such reduction becomes smaller with the increasing voltage and eventually changes to negative when the applied bias is higher than 2.85 V. In contrast to LED-2, the temperature of LED-1 in Group A is increased at all the voltages and the increase becomes smaller with the increasing applied biased voltage. It is worth noting that the temperature of Group A is a little higher than that of the control group (the average of the temperatures of LED-1 and LED-2) and the variation between them becomes more considerable with the increase of the applied bias. Such variation is caused by the difference in heat dissipation capability between two groups during the experimental measurement, which cannot be neglected when the input electrical power is high even though the measurement is carried out in the high vacuum chamber to reduce the thermal heat dissipation to the ambient.

To further support the claim that the elevated temperature caused by the heat absorption contributes to a higher average kinetic energy of the carrier and higher carrier concentration in

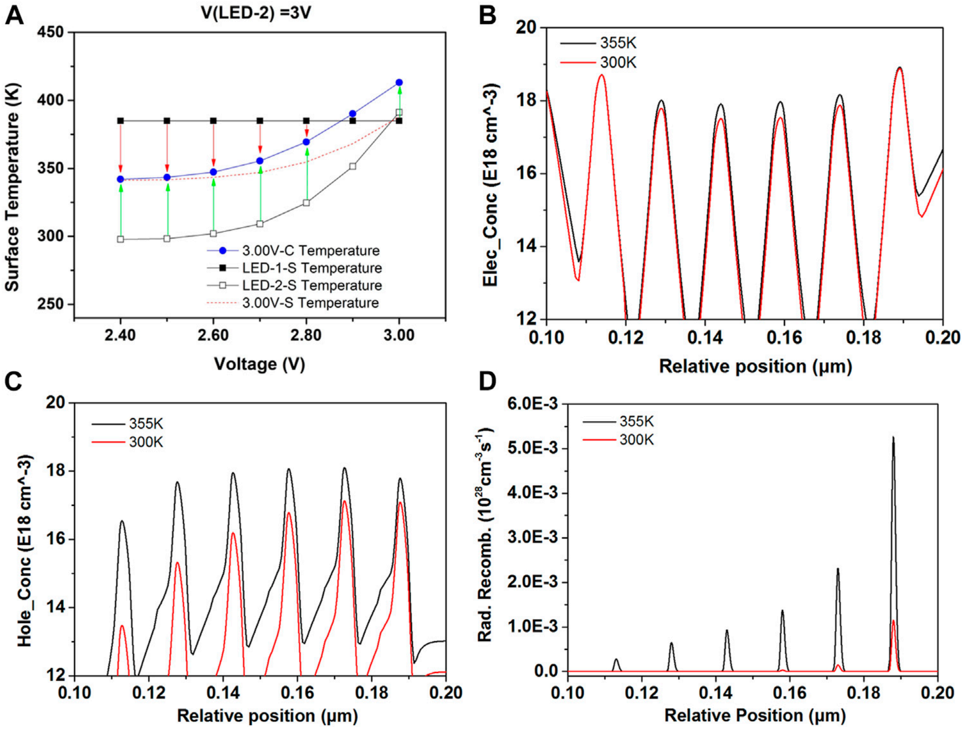

FIGURE 4 | (A). The device temperature of LEDs versus applied voltage for Combined-LEDs and Separated-LEDs setups with the voltage of LED-2 fixed at 3.00 V. Numerical results of the **(B)** electron concentration, **(C)** hole concentration, and **(D)** radiative recombination rate in the InGaN/GaN LEDs with the device temperature of 300 and 355 K under the voltage of 2.6 V.

the quantum wells, numerical calculation of the electron and hole concentrations, and the radiative recombination rate in the LEDs is conducted. **Figures 4B,C** show the calculated electron and hole concentrations of the InGaN/GaN LEDs at temperatures of 300 K and 355 K under the voltage of 2.6 V, from which it can be seen that the electron and hole concentrations increase at a higher temperature, suggesting that the total energy absorbed by the carriers from the phonon field is increased when the carriers climb up the potential barriers. The carriers overcome the potential barrier under the force of the electrical field, while for those without sufficient energy, the remaining energy is drawn from the phonon field to overcome the potential barriers. From **Figure 4D**, we can also observe that the radiative recombination rate is enhanced as the electron and hole concentrations increased due to higher temperature. Therefore, the elevated temperature leads to an increased carrier concentration, thus the improved efficiency is obtained in the voltage region of $V \lesssim \hbar\omega/q$. The improved performance in the proposed configuration is mainly caused by the elevated temperature that leads to increased carrier concentration, and minor reduced energy bandgap under the small and moderate electrical input [50, 51]. However, when the applied voltage is increased to further higher, e.g., 3.00 V in our experiments where the LED suffers from serious thermal droop, the contribution of the elevated temperature effect turns negative. Thus the proposed setup shows inferior performance due to its smaller thermal dissipation area compared to the control group, as indicated in **Figure 3**.

In order to further support the advantages of applying varied biases in the proposed approach, the measurements are modified to bias two LEDs at the same voltage simultaneously. **Figure 5** shows the measured CEE as a function of applied voltage and input electrical power, from which an enhanced CEE in the Combined-LEDs setup compared to the Separated-LEDs setup is observed when the applied voltage is smaller than 2.50 V and the corresponding electrical power of 12.77 mWatt is much lower than 19.95 mWatt shown in **Figure 3**. Furthermore, the maximum improvement in the CEE is also much lower than that observed in **Figure 3**, which further supports the superior edge of applying varied biases in the studied setup.

In order to further investigate the underlying mechanism of the enhanced performance in the proposed approach, the wall-plug efficiency and device temperature of LED-1 are also identified for the Combined-LEDs setup and Separated-LEDs setup, as shown in **Figure 6**. It can be clearly seen from **Figure 6B** that the device temperature of LED-1 in the case of V_{LED-2} = 3.00 V is always higher than that in the control group. Due to such increase, as shown in **Figure 6A**, the LED-1 is observed to have a pronounced enhancement in efficiency with a maximum improvement of 5.93% (27.91% in terms of percentage) in the proposed setup when the voltage is lower than 2.70 V. It can be clearly seen that the influence of temperature on efficiency varies in different operating regions separately by one inflection points: High-efficiency, Mid-voltage Region (2.15 V < V < 2.70 V); and Efficiency-

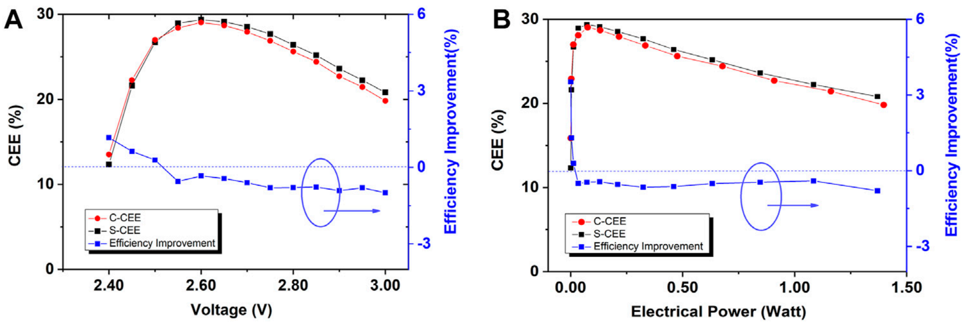

FIGURE 5 | (A) Experimental CEE and corresponding efficiency improvement for modified Combined-LEDs and Separated-LEDs setups versus applied voltage and **(B)** electrical input power.

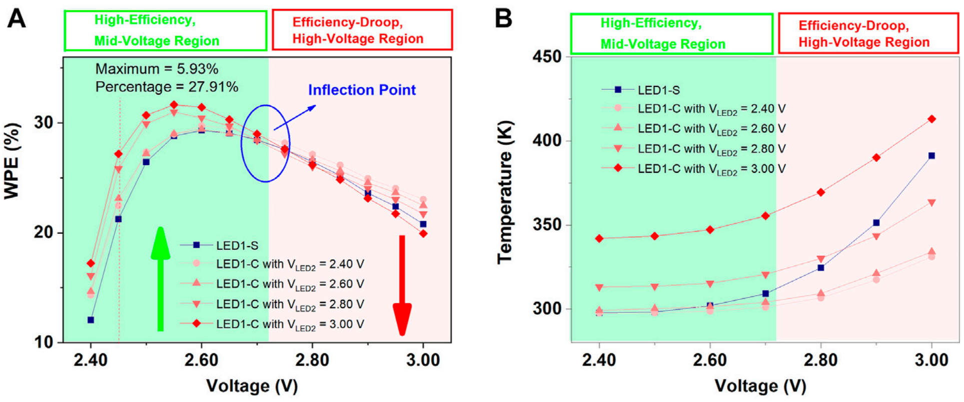

FIGURE 6 | (A) The WPE and **(B)** device temperature of LED-1 as a function of applied voltage for the Separated-LEDs and Combined-LEDs setups under $V_{LED\text{-}2}$ = 2.40, 2.60, 2.80, and 3.00 V.

droop, High-voltage Region (V ≥ 2.70 V). While the efficiency becomes worsen than that in the control group when the applied voltage of LED-1 is further increased to higher than 2.70 V (efficiency-droop, high-voltage region). The analysis of the device temperature and measured WPE for LED-1 in the Combined-LEDs setup and control group suggest that the increased temperature has a beneficial effect on device efficiency when the operating voltage falls in the high-efficiency, mid-voltage region due to the increased spontaneous radiative as well as the enhanced Energy recycling which allows the carriers to absorb the remaining energy from thermal heat as shown in **Figure 4B** . However, the effect of elevated temperature becomes negative when the applied voltage is increased to the efficiency-droop, high-voltage region, where the increased temperature leads to the more serious carrier overflow, reduced hole injection efficiency, and Auger recombination [52].

As indicated in **Figure 6A** the voltage corresponding to the peak efficiency for LED-1 is around 2.60 V and is slightly shifted with the increasing temperature. However, the corresponding current density at which the efficiency reaches the maximum remains constant. According to **Eq. 1**, the peak efficiency of *IQE* is achieved when [45, 53]:

$$\frac{d(IQE)}{dn} = 0 \tag{7}$$

Hence, the carrier concentration corresponding to the maximum efficiency is obtained at $n_0 = \sqrt{A/C}$. The relationship between the current density and carrier concentration is shown below:

$$J_0 = n_0 * e * v \tag{8}$$

where J_0 is the current density at n_0, and e is the elementary electronic charge while v is the carrier drift velocity. Therefore, the peak-efficiency current density is almost constant with the increased temperature. Since the elevated temperature leads to the increased current, the peak-efficiency current density can be achieved under lower voltage. For both LED-1 and LED-2 without combined configuration, the peak-efficiency current is around 13.86 mA, corresponding to the voltage of 2.60 V. Thus, the elevated temperature in the proposed setup will drive the efficiency away from the peak efficiency when the voltages of the two LEDs are close to 2.60 V, as shown in the **Figure 2B**.

Even though the LEDs are always driven by constant current and have additional cooling architectures, the thermal issues remain a great challenge for GaN-based LEDs, and achieving thermal dissipation through external architecture needs more space thus increasing the design difficulty of the system. Furthermore, using a larger size LED device is a common approach to increase the total optical output power with the heating issues remaining. Thus, the method proposed in this work provides an alternative way to achieve the desired total output power simultaneously recycling the thermal heat and achieving thermal harvesting. More importantly, the proposed approach is more promising to address thermal issues in some specific situations, for example, Ribbon Filament LED, which has no additional space to add the external cooling architectures because all the LEDs are allocated along the filament.

CONCLUSION

To conclude, in this work, we propose and demonstrate a new design to address the challenge in thermal heat issues, as supported by experiments, by recycling the thermal heat. The elevated temperature is found to be beneficial due to enhanced carrier concentrations and Energy recycling when the applied voltage is lower than the photon voltage. We present experimental results emphasizing the superior edge of the proposed configuration, in which with the varied biases applied to two LEDs, the thermal heat is exchanged and absorbed by the carriers thus the improved efficiency of the whole system through Energy recycling and thermal harvesting is achieved. Furthermore, owing to heat transmission the high-biased LED succeeds in reducing the device temperature and alleviating the thermal droop. Such a superior edge of the studied approach may become pronounced when exploited to the ribbon LED lamp, in which the space for designing and allocating the chips is limited and the LEDs arrangement is critical in the point of thermal management. Due to the advantages of the proposed setup, this method can act as an extremely useful intermediate research prototype to design the high-efficient LED arrays and achieve better energy recycling and thermal control, especially for mini- and micro-LEDs. Lastly, these findings in this work further support the possibility to remove the heat sink.

DATA AVAILABILITY STATEMENT

The original contributions presented in the study are included in the article/Supplementary Material, further inquiries can be directed to the corresponding authors.

AUTHOR CONTRIBUTIONS

SL and YZ contribute to this work equally. All authors reviewed the paper.

FUNDING

This work is supported by the Guangdong Basic and Applied Basic Research Foundation (Grant No. 2020B1515020032, 2020B1515120022), the National Natural Science Foundation of China (Grant No. 62074060), the Guangdong Science and Technology Plan (Grant No. 2019B040403003) and the Pearl River S&T Nova Program of Guangzhou (Grant No. 201906010058).

REFERENCES

1. Pimputkar S, Speck JS, DenBaars SP, and Nakamura S. Prospects for LED Lighting. *Nat Photon* (2009) 3:180–2. doi:10.1038/nphoton.2009.32
2. Khan A, Balakrishnan K, and Katona T. Ultraviolet Light-Emitting Diodes Based on Group Three Nitrides. *Nat Photon* (2008) 2:77–84. doi:10.1038/nphoton.2007.293
3. Tian S, Sui F, He K, Cheng G, Ge Y, Ning D, et al. Co-Axial Silicon/Perovskite Heterojunction Arrays for High-Performance Direct-Conversion Pixelated X-ray Detectors. *Nano Energy* (2020) 78:105335. doi:10.1016/j.nanoen.2020.105335
4. Chen M, Wang Z, Ge X, Wang Z, Fujisawa K, Xia J, et al. Controlled Fragmentation of Single-Atom-Thick Polycrystalline Graphene. *Matter* (2020) 2:666–79. doi:10.1016/j.matt.2019.11.004
5. Nakamura S, Mukai T, and Senoh M. Candela-Class High-Brightness InGaN/AlGaN Double-Heterostructure Blue-Light-Emitting Diodes. *Appl Phys Lett* (1994) 64:1687–9. doi:10.1063/1.111832
6. Zhang Y, Lu S, Qiu Y, Wu J, Zhang M, and Luo D. Experimental and Modeling Investigations of Miniaturization in InGaN/GaN Light-Emitting Diodes and Performance Enhancement by Micro-Wall Architecture. *Front Chem* (2021) 8: 8. doi:10.3389/fchem.2020.630050
7. Tanaka S, Zhao Y, Koslow I, Pan C-C, Chen H-T, Sonoda J, et al. Droop Improvement in High Current Range on PSS-LEDs. *Electron Lett* (2011) 47: 335–6. doi:10.1049/el.2010.3306
8. Ponce FA, and Bour DP. Nitride-Based Semiconductors for Blue and Green Light-Emitting Devices. *Nature* (1997) 386:351–9. doi:10.1038/386351a0
9. Kobayashi Y, Kumakura K, Akasaka T, and Makimoto T. Layered Boron Nitride as a Release Layer for Mechanical Transfer of GaN-Based Devices. *Nature* (2012) 484:223–7. doi:10.1038/nature10970
10. Lu S, Zhang Y, Zhang Z-H, Tsai PC, Zhang X, Tan ST, et al. Strain-Reduced Micro-LEDs Grown Directly Using Partitioned Growth. *Front Chem* (2021) 9: 9. doi:10.3389/fchem.2021.639023
11. Liu L, Yang J, Ling M, Zhong J, Teng D, and Wang G. Aggravated Efficiency Droop in Vertical-Structured Gallium Nitride Light-Emitting Diodes Induced by High Temperature Aging. *J Appl Phys* (2013) 113:083105. doi:10.1063/1.4790594
12. Choi S, Kim HJ, Kim S-S, Liu J, Kim J, Ryou J-H, et al. Improvement of Peak Quantum Efficiency and Efficiency Droop in III-Nitride Visible Light-Emitting Diodes With an InAlN Electron-Blocking Layer. *Appl Phys Lett* (2010) 96:221105. doi:10.1063/1.3441373
13. David A, and Gardner NF. Droop in III-Nitrides: Comparison of Bulk and Injection Contributions. *Appl Phys Lett* (2010) 97:193508. doi:10.1063/1.3515851
14. Ryu H-Y, Shin D-S, and Shim J-I. Analysis of Efficiency Droop in Nitride Light-Emitting Diodes by the Reduced Effective Volume of InGaN Active Material. *Appl Phys Lett* (2012) 100:131109. doi:10.1063/1.3698113
15. Vaxenburg R, Lifshitz E, and Efros AL. Suppression of Auger-Stimulated Efficiency Droop in Nitride-Based Light Emitting Diodes. *Appl Phys Lett* (2013) 102:031120. doi:10.1063/1.4789364
16. Jung E, Hwang G, Chung J, Kwon O, Han J, Moon Y-T, et al. Investigating the Origin of Efficiency Droop by Profiling the Temperature across the Multi-Quantum Well of an Operating Light-Emitting Diode. *Appl Phys Lett* (2015) 106:041114. doi:10.1063/1.4907177

17. Meneghini M, De Santi C, Tibaldi A, Vallone M, Bertazzi F, Meneghesso G, et al. Thermal Droop in III-Nitride Based Light-Emitting Diodes: Physical Origin and Perspectives. *J Appl Phys* (2020) 127:211102. doi:10.1063/5.0005874
18. Lu S, Liu W, Zhang Z-H, Tan ST, Ju Z, Ji Y, et al. Low Thermal-Mass LEDs: Size Effect and Limits. *Opt Express* (2014) 22:32200–7. doi:10.1364/oe.22.032200
19. Han N, Viet Cuong T, Han M, Deul Ryu B, Chandramohan S, Bae Park J, et al. Improved Heat Dissipation in Gallium Nitride Light-Emitting Diodes With Embedded Graphene Oxide Pattern. *Nat Commun* (2013) 4:1452. doi:10.1038/ncomms2448
20. Liou B-H, Chen C-M, Horng R-H, Chiang Y-C, and Wuu D-S. Improvement of Thermal Management of High-Power GaN-Based Light-Emitting Diodes. *Microelectronics Reliability* (2012) 52:861–5. doi:10.1016/j.microrel.2011.04.002
21. Horng RH, Chiang CC, Hsiao HY, Zheng X, Wuu DS, and Lin HI. Improved Thermal Management of GaN/Sapphire Light-Emitting Diodes Embedded in Reflective Heat Spreaders. *Appl Phys Lett* (2008) 93:111907. doi:10.1063/1.2983740
22. He W, Zhang G, Zhang X, Ji J, Li G, and Zhao X. Recent Development and Application of Thermoelectric Generator and Cooler. *Appl Energ* (2015) 143: 1–25. doi:10.1016/j.apenergy.2014.12.075
23. Lu S, Zhang Y, Zhang Z-H, Zhu B, Zheng H, Tan ST, et al. High-Performance Triangular Miniaturized-LEDs for High Current and Power Density Applications. *ACS Photon* (2021) 8:2304–10. doi:10.1021/acsphotonics.1c00430
24. Tang B, Miao J, Liu Y, Wan H, Li N, Zhou S, et al. Enhanced Light Extraction of Flip-Chip Mini-LEDs with Prism-Structured Sidewall. *Nanomaterials* (2019) 9:319. doi:10.3390/nano9030319
25. Son KR, Lee TH, Lee BR, Im HS, and Kim TG. Nitride-Based Microlight-Emitting Diodes Using AlN Thin-Film Electrodes With Nanoscale Indium/Tin Conducting Filaments. *Small* (2018) 14:1801032. doi:10.1002/smll.201801032
26. Park S-I, Xiong Y, Kim R-H, Elvikis P, Meitl M, Kim D-H, et al. Printed Assemblies of Inorganic Light-Emitting Diodes for Deformable and Semitransparent Displays. *Science* (2009) 325:977–81. doi:10.1126/science.1175690
27. Zhang K, Liu Y, Kwok H-s., and Liu Z. Investigation of Electrical Properties and Reliability of GaN-Based Micro-LEDs. *Nanomaterials* (2020) 10:689. doi:10.3390/nano10040689
28. Wu T, Sher C-W, Lin Y, Lee C-F, Liang S, Lu Y, et al. Mini-LED and Micro-LED: Promising Candidates for the Next Generation Display Technology. *Appl Sci* (2018) 8:1557. doi:10.3390/app8091557
29. Lin JY, and Jiang HX. Development of MicroLED. *Appl Phys Lett* (2020) 116: 100502. doi:10.1063/1.5145201
30. Kang C-M, Kong D-J, Shim J-P, Kim S, Choi S-B, Lee J-Y, et al. Fabrication of a Vertically-Stacked Passive-Matrix Micro-LED Array Structure for a Dual Color Display. *Opt Express* (2017) 25:2489–95. doi:10.1364/oe.25.002489
31. Huang Y, Hsiang E-L, Deng M-Y, and Wu S-T. Mini-LED, Micro-LED and OLED Displays: Present Status and Future Perspectives. *Light Sci Appl* (2020) 9:105. doi:10.1038/s41377-020-0341-9
32. Dousmanis GC, Mueller CW, Nelson H, and Petzinger KG. Evidence of Refrigerating Action by Means of Photon Emission in Semiconductor Diodes. *Phys Rev* (1964) 133:A316–A318. doi:10.1103/physrev.133.a316
33. Piprek J, and Li Z-M. Electroluminescent Cooling Mechanism in InGaN/GaN Light-Emitting Diodes. *Opt Quant Electron* (2016) 48:472. doi:10.1007/s11082-016-0729-1
34. Hurni CA, David A, Cich MJ, Aldaz RI, Ellis B, Huang K, et al. Bulk GaN Flip-Chip Violet Light-Emitting Diodes With Optimized Efficiency for High-Power Operation. *Appl Phys Lett* (2015) 106:031101. doi:10.1063/1.4905873
35. Xue J, Zhao Y, Oh S-H, Herrington WF, Speck JS, DenBaars SP, et al. Thermally Enhanced Blue Light-Emitting Diode. *Appl Phys Lett* (2015) 107:121109. doi:10.1063/1.4931365
36. Sadi T, Radevici I, and Oksanen J. Thermophotonic Cooling With Light-Emitting Diodes. *Nat Photon* (2020) 14:205–14. doi:10.1038/s41566-020-0600-6
37. Santhanam P, Gray DJ, and Ram RJ. Thermoelectrically Pumped Light-Emitting Diodes Operating Above Unity Efficiency. *Phys Rev Lett* (2012) 108:097403. doi:10.1103/PhysRevLett.108.097403
38. Li N, Han K, Spratt W, Bedell S, Ott J, Hopstaken M, et al. Ultra-low-Power Sub-Photon-Voltage High-Efficiency Light-Emitting Diodes. *Nat Photon* (2019) 13:588–92. doi:10.1038/s41566-019-0463-x
39. Radevici I, Tiira J, Sadi T, Ranta S, Tukiainen A, Guina M, et al. Thermophotonic Cooling in GaAs Based Light Emitters. *Appl Phys Lett* (2019) 114:051101. doi:10.1063/1.5064786
40. Sadi T, Radevici I, Kivisaari P, and Oksanen J. Electroluminescent Cooling in III-V Intracavity Diodes: Practical Requirements. *IEEE Trans Electron Devices* (2019) 66:963–8. doi:10.1109/TED.2018.2885267
41. Kuritzky LY, Weisbuch C, and Speck JS. Prospects for 100% Wall-Plug Efficient III-Nitride LEDs. *Opt Express* (2018) 26:16600–8. doi:10.1364/OE.26.016600
42. Wang T, Nakagawa D, Wang J, Sugahara T, and Sakai S. Photoluminescence Investigation of InGaN/GaN Single Quantum Well and Multiple Quantum wells. *Appl Phys Lett* (1998) 73:3571–3. doi:10.1063/1.122810
43. Zhang Z-H, Kyaw Z, Liu W, Ji Y, Wang L, Tan ST, et al. A Hole Modulator for InGaN/GaN Light-Emitting Diodes. *Appl Phys Lett* (2015) 106:063501. doi:10.1063/1.4908118
44. Ju ZG, Liu W, Zhang Z-H, Tan ST, Ji Y, Kyaw Z, et al. Advantages of the Blue InGaN/GaN Light-Emitting Diodes With an AlGaN/GaN/AlGaN Quantum Well Structured Electron Blocking Layer. *ACS Photon* (2014) 1:377–81. doi:10.1021/ph500001e
45. Zhang YP, Zhang Z-H, Liu W, Tan ST, Ju ZG, Zhang XL, et al. Nonradiative Recombination - Critical in Choosing Quantum Well Number for InGaN/GaN Light-Emitting Diodes. *Opt Express* (2015) 23:A34–A42. doi:10.1364/oe.23.000a34
46. Han D-P, Zheng D-G, Oh C-H, Kim H, Shim J-I, Shin D-S, et al. Nonradiative Recombination Mechanisms in InGaN/GaN-Based Light-Emitting Diodes Investigated by Temperature-Dependent Measurements. *Appl Phys Lett* (2014) 104:151108. doi:10.1063/1.4871870
47. Hossain MI, Itokazu Y, Kuwaba S, Kamata N, and Hirayama H. Temperature Dependence of Nonradiative Recombination Processes in UV-B AlGaN Quantum Well Revealed by below-gap Excitation Light. *Opt Mater* (2020) 105:109878. doi:10.1016/j.optmat.2020.109878
48. De Santi C, Meneghini M, Monti D, Glaab J, Guttmann M, Rass J, et al. Recombination Mechanisms and thermal Droop in AlGaN-Based UV-B LEDs. *Photon Res* (2017) 5:A44–A51. doi:10.1364/prj.5.000a44
49. Schubert EF. *Light-Emitting Diodes*. New York: Cambridge University Press (2006).
50. Cho Y-H, Gainer GH, Fischer AJ, Song JJ, Keller S, Mishra UK, et al. "S-Shaped" Temperature-Dependent Emission Shift and Carrier Dynamics in InGaN/GaN Multiple Quantum wells. *Appl Phys Lett* (1998) 73:1370–2. doi:10.1063/1.122164
51. Yan WS, Zhang R, Xiu XQ, Xie ZL, Han P, Jiang RL, et al. Temperature Dependence of the Pyroelectric Coefficient and the Spontaneous Polarization of AlN. *Appl Phys Lett* (2007) 90:212102. doi:10.1063/1.2741600
52. Meyaard DS, Shan Q, Cho J, Fred Schubert E, Han S-H, Kim M-H, et al. Temperature Dependent Efficiency Droop in GaInN Light-Emitting Diodes With Different Current Densities. *Appl Phys Lett* (2012) 100:081106. doi:10.1063/1.3688041
53. Dai Q, Shan Q, Cho J, Schubert EF, Crawford MH, Koleske DD, et al. On the Symmetry of Efficiency-Versus-Carrier-Concentration Curves in GaInN/GaN Light-Emitting Diodes and Relation to Droop-Causing Mechanisms. *Appl Phys Lett* (2011) 98:033506. doi:10.1063/1.3544584

Conflict of Interest: The authors declare that the research was conducted in the absence of any commercial or financial relationships that could be construed as a potential conflict of interest.

frontiers in Physics

ORIGINAL RESEARCH
published: 04 October 2021
doi: 10.3389/fphy.2021.737205

Multi-Chromophore Dyes for Improving Light Stability of Electro-Fluidic Displays

Yong Deng[1], Dechao Ye[1], Yuanyuan Guo[2], Guofu Zhou[1,2] and Hongwei Jiang[2]*

[1]Academy of Shenzhen Guohua Optoelectronics, Shenzhen, China, [2]South China Academy of Advanced Optoelectronics, South China Normal University, Guangzhou, China

Electro-fluidic display (EFD) is a new reflective display based on electrowetting phenomenon which is applied to the outdoor billboard. Organic dyes are the most important materials for the color gamut and reliability of the EFD devices, which are always synthesized based on mono-chromophore dye in previous work. In this paper, we report our research on azopyrazolone as the chromophore to construct a polychromic macromolecular dye system. The light stability and photo-electric properties of these new dyes are researched detailed. It is found that the light stability of multi-chromophore dyes and backflow properties are much better than corresponding mono-chromophore dye.

Keywords: colored oil, photo-stability, azo pyrazolone dyes, electro-fluidic display, multi-chromosome dyes

Edited by:
Feng Chi,
University of Electronic Science and Technology of China, China

Reviewed by:
Hui Li,
Shenzhen University, China
Jingjing Yang,
Nanjing Xiaozhuang University, China

****Correspondence:***
Hongwei Jiang
hongwei.jiang0822@gmail.com

Specialty section:
This article was submitted to Optics and Photonics, a section of the journal Frontiers in Physics

Received: *06 July 2021*
Accepted: *21 September 2021*
Published: *04 October 2021*

Citation:
Deng Y, Ye D, Guo Y, Zhou G and Jiang H (2021) Multi-Chromophore Dyes for Improving Light Stability of Electro-Fluidic Displays. Front. Phys. 9:737205. doi: 10.3389/fphy.2021.737205

INTRODUCTION

Recently, electro-fluidic display as an emerging display technology has received widespread attention [1–4]. It has many advantages such as fast response time and full-color compared to electrophoretic display [5–7]. In electro-fluidic devices, transparent polar liquids play the role of changing wettability on solid surfaces to realize various applications. The contact angle of polar liquid on solid surface is determined by Young's equation as shown in **Eq. 1**.

$$\cos\theta_0 = \left(\gamma_{sg} - \gamma_{sl}\right)/\gamma_{\mathrm{lg}} \tag{1}$$

where θ_0 is the initial contact angle of liquid on solid, γ_{sg} is surface tension of solid-gas, γ_{sl} is surface tension of solid-liquid, while γ_{lg} is surface tension of liquid-gas. θ_0 is a constant, which only depends on the physical properties of liquid and solid.

When a voltage is applied across the polar liquid and solid, the contact angle of polar liquid on solid surface will be changed, and it obeys Young-Lippmann equation, as shown in **Eq. 2**.

$$\cos\theta_V = \cos\theta_0 + \varepsilon_0\varepsilon_r V^2/2d\cdot\gamma_{\mathrm{lg}} \tag{2}$$

where θ_V is contact angle with a voltage applied, ε_0 is dielectric constant in vacuum, ε_r is the effective dielectric constant of dielectric layer, V is electromotive force applied between solid surface and polar liquid, d is the thickness of dielectric layer.

Colored oil, another critical material in electrowetting display, is not miscible with polar liquids. The movement of polar liquid promotes the contraction and spread of ink to achieve the display purpose. An unbalance force ΔF can be formed in the polar liquid with a voltage applied, and the phenomenon is that the liquid has an advancing angle and a receding angle. The unbalance force ΔF is the initial force that drives the movement of polar liquid, and its magnitude of force follows **Eq. 3**.

$$\Delta F = \gamma(\theta_1 - \theta_2) = \frac{1}{2}CV^2 = \frac{1}{2}\frac{\varepsilon_r\varepsilon_0 A}{d}V^2 \qquad (3)$$

Colored oils are so important in electrowetting display that lots of special dyes have been disclosed in previous research, such as the designation of anthraquinone dyes [8, 9], azo dyes [10–14], dipyrrole methane metal dyes [15], and pigment dispersion [16, 17]. However, all the dyes are mono-chromophore structure, which cannot avoid the backflow caused by dye's polarization.

The tendency of oil to flow back into pixel at a constant voltage is called "backflow". The reduction of oil contraction affects the pixel aperture for "backflow" oil, which has an impact on the power consumption of the display. Since a static reading mode is operated for an EFD display, low "backflow" oil will lead to the decrease of refresh rate for display. Thus, the power consumption can be reduced because of its scaling with the refresh rate. Studies have shown that the addition of polar dye molecules has a negative effect on ink reflow [18, 19]. Due to their polarities, the dye molecules are oriented under an external electric field, and the affinity between the oil and the hydrophobic layer increases. Polarized dye molecules also tend to cause external charges and penetrate at the three-phase contact line of the ink-water-insulation layer, which eventually caused the electrostatic force F.

Moreover, a large number of experiments have shown that the light stability of dye molecules is depended on their molecular structure. The greater aggregation is, the better the light stability of dyes have. When the same amount of dye molecular exposed to air, moisture and sunlight, the smaller surface area of the molecule is, the lower probability of dye molecule being oxidized by light. Conversely, when the dye is dissolved in a mono-disperse state, the surface area of the molecule is much higher than aggregation state, thus the chance of photo-oxidation or photo-reduction reaction is great. G. Baxter research shows that when the dye molecules are present in a highly disperse state, the photo-fading reaction is an apparent first-order reaction, while the photo-fading reaction of the dye molecules in the aggregation state is an apparent 0-order reaction [20]. It was also found that water-insoluble dyes have stronger internal molecular forces in the aggregation state, which makes it easier to transfer energy, and connect dye molecules through bridges to increase the degree of dye aggregation and reduce the overall molecular weight.

In this paper, azopyrazolone dye is used as the chromophoric matrix to construct a multi-chromophore macromolecular dye system, using binding effect of the bridge group in space to reduce the dipole moment of the entire molecule, thereby reducing the backflow effect of oils under external electric field. The polychromatic azopyrazolone-type molecules have an increased degree of chromophore aggregation, which may strengthen the chromophore's bridge-based molecular skeleton energy transfer channel, induction effect, and covalent bond action. Therefore, the design of this type of dye has high solubility, absorption coefficient and light stability.

EXPERIMENTAL

Materials

Chemicals are purchased analytically pure and used without further purification. Indium Tin Oxide, SU-8 3,005 photoresist, AF Teflon® 1,600X were purchased and used in industrial grade.

Electro-Fluidic Display Oil Formulation and Device Fabrication

Dyes and solvents were calculated and weighted in a cell, dissolved, and filtrated with a 0.2 μm filtrator. The filtration was collected as EFD oil and used to formulate EFD device followed by our previous process [21].

Dye Synthesis and Characterization

The structures of three designed dyes were shown in **Figure 1**. D-1: 1.27 g (121 g/mol, 0.01 mol) 4-aminophenylethane was dissolved in 20 ml water in a three-necked flask with agitation, and the solution was heated to 80°C until it dissolved completely. Then, hydrochloric acid (4.2 ml, 12 mol/L) was added dropwisely and the solution was quickly cooled down to 0–5°C. Then 1.04 g of sodium nitrite (1.5 times, 69 g/mol) was added at one time, the solution was continuously stirred for 2 h. The temperature of the reaction system was kept at 0–5°C. The Ehrlich reagent was used to detect the end of the diazotization reaction. After that, a certain amount of urea is added to remove unreacted sodium nitrite. 4.56 g (294 g/mol, 0.02 mol) of 3- (1-ethylpentyl) -1- (1-ethylhexyl) -2-pyrazolin-5-ol and sodium carbonate were solute in ethanol. The diazo salt solution prepared above was added into the solution dropwisely in 2 h. After that, the solution was poured into 100 ml water, and 30 ml ethyl acetate and petroleum ether solution (1:10, v/v) was used to extract the yellow dye. The organic layer was collected and evaporated to get 3.51 g crude product D-1. The crude D-1 was purified by flash chromatography on silica gel (eluting agent: petroleum ether and ethyl acetate). Characterization: D-1; yield: 82.9%; λ (max) = 420 nm (in decane); ε = 11,730 L mol^{-1}·cm^{-1}. IR (KBr, cm^{-1}): 3,071.2(Ar-H); 2,963.1(-CH$_3$), 2,928.1(-CH$_2$-), 2,857.2(-CH$_3$); 1,642.2(-C=O); 1,581.8(Ar); 1,551.2(Ar-H), 1,524.8(Ar),1,459.9(-CH-),1,378.2(-CH$_3$), 1,254.1(C-N-C); ^{1}H NMR (400 MHz, CDCl$_3$): 13.796(s, 1H), 8.442(s, 1H), 7.639(m, 6H), 7.610(m, 2H), 7.232(m, 2H), 7.256(m, 2H), 4.580(m, 2H), 3.739(m, 2H), 2.698–2.559(m, 1H), 1.550–1.521(m, 4H), 1.289–1.233(m,12H), 0.899–0.7599(m,12H); ^{13}C NMR (400 MHz, CDCl$_3$): 182.11, 146.560, 134.570, 131.840, 126.030, 123.660, 109.670, 45.990, 39.470, 31.280, 29.040, 24.530, 23.030, 14.120, 10.990; MS (MALDI-TOF) (DIF) M/Z (%): 427.3.

Intermediate: 1.27 g (137 g/mol, 0.01 mol) 4-aminophenethyl alcohol was dissolved in 20 ml water in a three-necked flask with agitation, and the solution was heated to 80°C until it dissolved completely. Then, hydrochloric acid (4.2 ml, 12 mol/L) was added dropwisely and the solution was quickly cooled down to 0–5°C. 1.04 g (0.015 mol, 69 g/mol) of sodium nitrite was added at one time, the reaction was last for 2 h. The temperature of the reaction system was kept at 0–5°C. The Ehrlich reagent was used to detect the end of the diazotization reaction. A certain amount of urea is added to remove unreacted sodium nitrite. 4.56 g (294 g/mol, 0.02 mol) of 3- (1-ethylpentyl) -1- (1-ethylhexyl) -2-pyrazolin-5-ol and sodium carbonate were solute in ethanol. The diazo salt

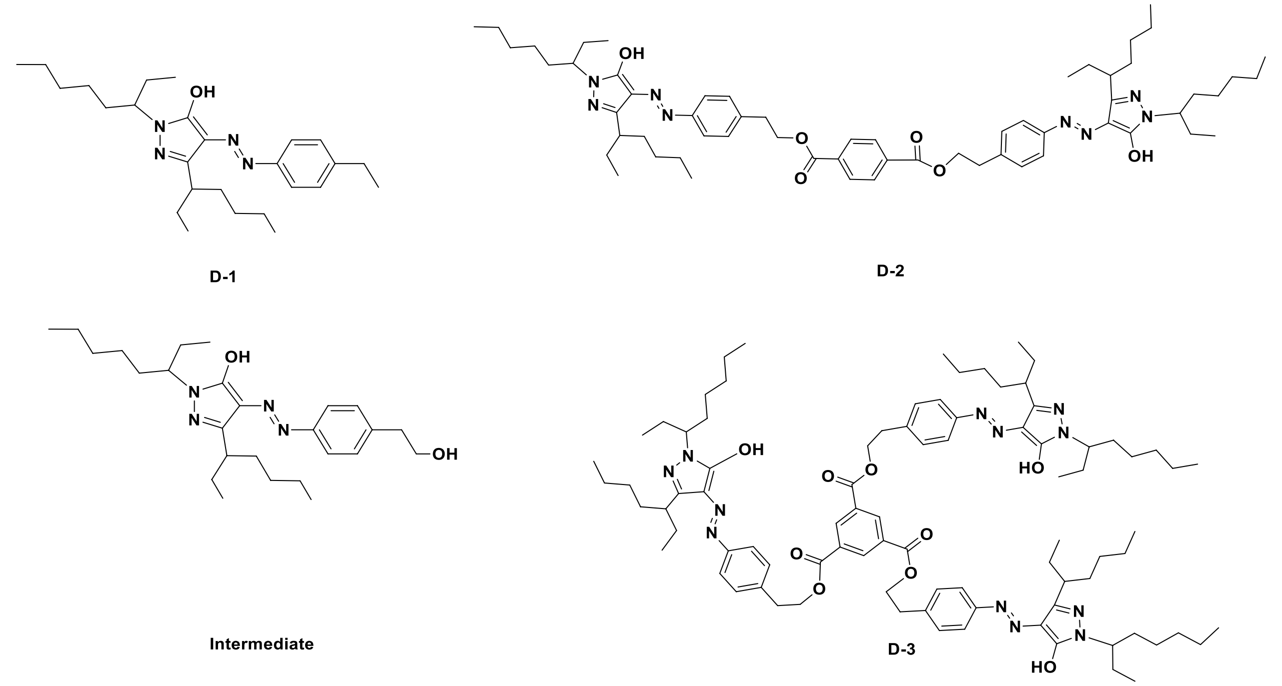

FIGURE 1 | Molecular structures of the Intermediate and three synthesized dyes.

prepared above was added into the solution dropwisely in 2 h. After that, the solution was poured into 100 ml water, and 30 ml ethyl acetate and petroleum ether solution (1:10, v/v) was used to extract the yellow dye. The organic layer was collected and evaporated to get 3.60 g crude product. The crude Intermediate was purified by flash chromatography on silica gel (eluting agent: petroleum ether and ethyl acetate); yield: 81.9%; λ (max) = 420 nm (in decane); IR (KBr, cm^{-1}): 3,061.3 (Ar-H), 2,951.3(-CH_3), 2,921.1(-CH_2–), 2,880.1(-CH_3); 1,642.9(-C=O), 1,582.8(Ar); 1,555.2(Ar-H), 1,521.2(Ar); 1,458.9 (-CH-); 1,379.1(-CH_3); 1,257.3 (C-N-C); 817.8. ^{1}H NMR (400 MHz, $CDCl_3$): 13.781(s, 1H), 8.421(s, 1H), 7.76(m, 6H), 7.622(m, 2H), 7.262(m, 2H), 7.267(m, 2H), 4.555(m, 2H), 3.555(m, 2H), 2.670–2.551(m, 1H), 1.548–1.526(m, 4H), 1.283–1.245(m, 12H), 0.891–0.761(m, 12H); ^{13}C NMR (400 MHz, $CDCl_3$): 190.090, 144.460, 134.480, 132.440, 127.480, 124.640, 110.140, 44.490, 38.470, 32.480, 29.920, 24.620, 22.520, 15.230, 11.890; MS (MALDI-TOF) (DIF)M/Z (%): 443.3.

D-2: 0.58 g Intermediate was dissolved in 20 ml n-decane, then 0.1 g (0.30 mmol, 234 g/mol) 1,4-phthaloyl chloride and 4.2 ml (91 g/mol, 0.2 mol) triethylamine was added dropwisely into the reaction solution. The temperature was raised to 50°C. TLC was used to monitor the termination of reaction. After the reaction was completed, the solution was cooled down, and poured into 100 ml water. 50 ml petroleum ether was used to extract the product three times, and the oil layers were collected and rotary evaporated. Then the crude product D-2 was column purified with 1: 120 of n-hexane and petroleum ether mixture as eluent. Compound D-2 was obtained as yellow dye with yield of 82.0%. λ (max) = 420 nm (in decane); ε = 16,119 L mol^{-1} cm^{-1}. IR (KBr, cm^{-1}): 3,061.2(Ar-H), 2,962.5(-CH_3), 2,921.5(-CH_2–), 2,859.5(-CH_3), 1,645.3(-C=O), 1,581.3(Ar), 1,555.1(Ar), 1,521.2(Ar), 1,458.9(-CH-), 1,378.2(-CH_3), 1,257.8(C-N-C); ^{1}H NMR (400 MHz, $CDCl_3$): 12.998 (s, 2H)8.420(s, 2H), 7.389(m, 3H), 7.253 (m, 2H), 4.590(m, 2H), 3.541(m, 2H), 2.669–2.551(m, 2H), 1.536–1.518(m, 4H), 1.287–1.253(m, 24H), 0.901–0.753(m, 24H). ^{13}C NMR (400 MHz, $CDCl_3$): 181.110, 145.560, 139.130, 134.370, 131.240, 126.230, 123.260, 114.220, 109.620, 45.920, 39.420, 31.220, 29.030, 24.230, 23.230, 14.130, 10.890; MS (MALDI-TOF) (DIF)M/Z (%): 1,015.8.

D-3: 0.58 g Intermediate was dissolved in n-decane, 0.1 g (0.30 mmol, 234 g/mol) 1,3,5-trisyl chloride and 4.2 ml (91 g/mol, 0.2 mol) triethylamine was added dropwisely in the reaction solution. The temperature was raised to 50°C. TLC was used to monitor the termination of reaction. After the reaction was completed, the solution was cooled down, and poured into 100 ml water. 50 ml petroleum ether was used to extract the product three times, and the oil layers were collected and rotary evaporated. Then the crude product D-3 was column purified with 1: 120 of n-hexane and petroleum ether mixture as eluent. D-3 was obtained as yellow dye with yield of 85.0%. λ (max) = 420 nm (in decane); ε = 49,710 L mol^{-1} cm^{-1}. IR (KBr, cm^{-1}): 3,062.7(Ar-H), 2,962.7(-CH_3), 2,922.4(-CH_2-), 2,882.3(-CH_3), 1,642.7(-C=O), 1,582.7(Ar); 1,552.1(Ar); 1,523.9(Ar); 1,453.8(-CH-); 1,379.2(-CH3); 1,257.2(C-N-C); 816.7. ^{1}H NMR (400 MHz, $CDCl_3$): 13.555 (s, 3H)8.834(s,3H), 7.349–7.332(m, 12H), 4.581–4.573(m, 6H), 3.715–3.684(m, 3H), 3.143–3.137(m, 6H), 2.608–2.577(m, 3H), 1.70(m, 6H), 1.541–1.519(m, 12H), 1.519(m, 6H), 1.371–1.248(m, 33H), 0.891–0.879(m, 27H). ^{13}C NMR (400 MHz, $CDCl_3$): 181.110, 146.460, 133.570, 132.840,

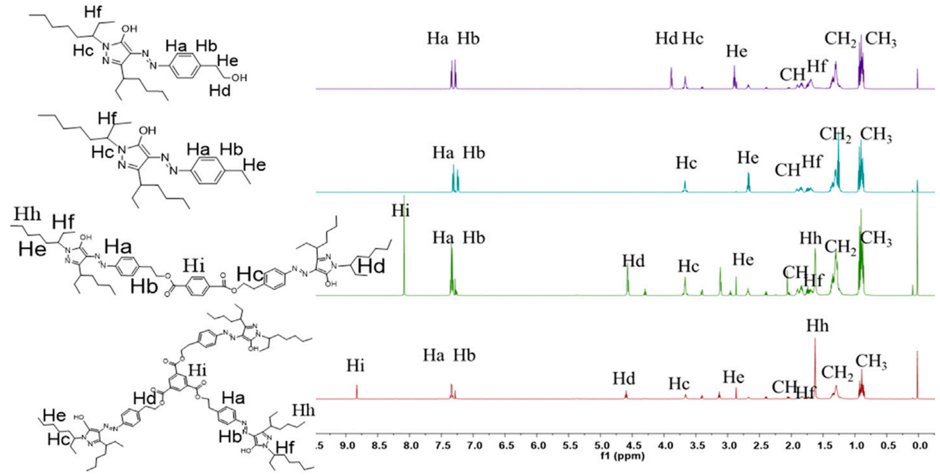

FIGURE 2 | ^{1}H NMR spectra of three synthesized dyes and Intermediate.

125.030, 123.560, 114.590, 109.570, 45.590, 39.450, 31.250, 29.050, 24.550, 23.050, 14.150, 10.590; MS (MALDI-TOF) (DIF)M/Z (%): 1,483.5.

RESULTS AND DISCUSSION

The ^{1}H NMR spectra for the target molecules recorded in $CDCl_3$ are shown in **Figure 2**. The structures of dyes were confirmed by the presence of four distinct downfield signals characteristic of the aromatic rings. For D-1 and Intermediate, the structure of pyrazoline ring was confirmed by the presence of four distinct downfield signals ("Ha", "Hb"). The "Ha" and "Hb" protons of D-1 and Intermediate exhibited two doublets between 7.27 ppm and 7.58 ppm. For the substituents in the N-position, these two dyes displayed one common multiple peak "Hc" between 3.50 and 4.00 ppm, corresponding to the methene protons adjacent to the imide group. The "Hd" protons appeared as a singlet between 3.88 and 4.00 ppm. For the other pyrazolone dyes D-2/3, the "Ha" and "Hb" protons of D-2/3 exhibited two doublets between 7.50 ppm and 7.25 ppm. The "Hi", protons of D-2 exhibited one singlet at 8.23 ppm. The "Hi", protons of D-3 exhibited one singlet at 8.95 ppm. Two dyes: D-2/3, displayed one common multiple peak "Hc" and "Hd" at 4.60 and 3.78 ppm corresponding to the methene protons adjacent to the imide group and O atom. Moreover, the common multiple peak "Hf" of those four molecules represented the protons on the methyl group, and the "CH" protons existed between 0.78 and 0.92 equivalent to the number of protons which were obtained. The chemical values confirmed the structural correctness of the four molecules.

Absorption Properties of Dyes

As can be seen in **Figure 3**, the uv-visible absorption spectra and data of all the dyes were recorded in decane. It is found that the maximum wavelength numbers ($\lambda_{\max}$) of three dyes D-1/3 are all at 420 nm, showing a same color of yellow. The maximum wavelengths are independent with the number of chromophoric matrix. The molar extinction coefficients of the three dyes are 11,730, 38,470 and 49,710 L $mol^{-1}\cdot cm^{-1}$ for D-1, D-2 and D-3, respectively. And we can see from **Figure 3B,** as the number of chromophore increase, the molar extinction coefficient of the dyes increase.

Electrowetting Properties

The contact angle of DI water droplet on AF (amorphous fluoropolymers) surface in different ambient oil was characterized by varying the applied voltage between the Pt electrode and the substrate electrode in the range of −40 to 40 V at a ramp speed of 1V/1s to demonstrate the potential of EW-based tensiometry. The initial contact angle of DI-water droplet on the AF surface was at ~145° in D-1 oil. The contact angle gradually decreased from ~145° to ~105° as the applied voltage was changed from 0 to ±40 V. The initial contact angle of DI-water droplet on AF surface was at ~154° in D-2 oil. The contact angle gradually decreased from ~154° to ~113° as the same applied voltage change. The initial contact angle of DI-water droplet on AF surface was at ~156° in D-3 oil. The contact angle gradually decreased from ~156° to ~123°. The data shown in **Figure 4** are collected over two cycles, during which the voltage is slowly ramped up and down. The dc results conclusively showed that a strong and reversible electrowetting response can be achieved in the three different kinds of oil.

Backflow Effect of Oils

Synthesized dyes were designed to analyze the effect of dye molecular structure on electrowetting backflow effect. As D-2 has low solubility in decane, only D-1 and D-3 were tested in devices. According to the experimental data shown in **Figure 5**, the backflow time of D-1 device is 150 s, and the backflow time of D-3 device is 250 s. Comparing the backflow time of the D-1 and D-3 devices, it can be clearly seen that D-3 device has longer backflow time, which can be attributed to the smaller dipole moment of D-3. As the arrangement direction of three chromophores in D-3 is non-uniformity, thus the dipole

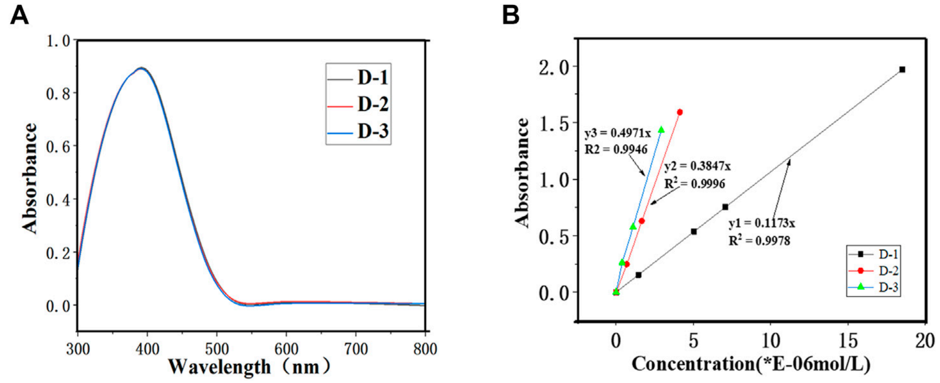

FIGURE 3 | (A) UV-visible absorption spectrum of three dyes **(B)** Working curve of three dyes.

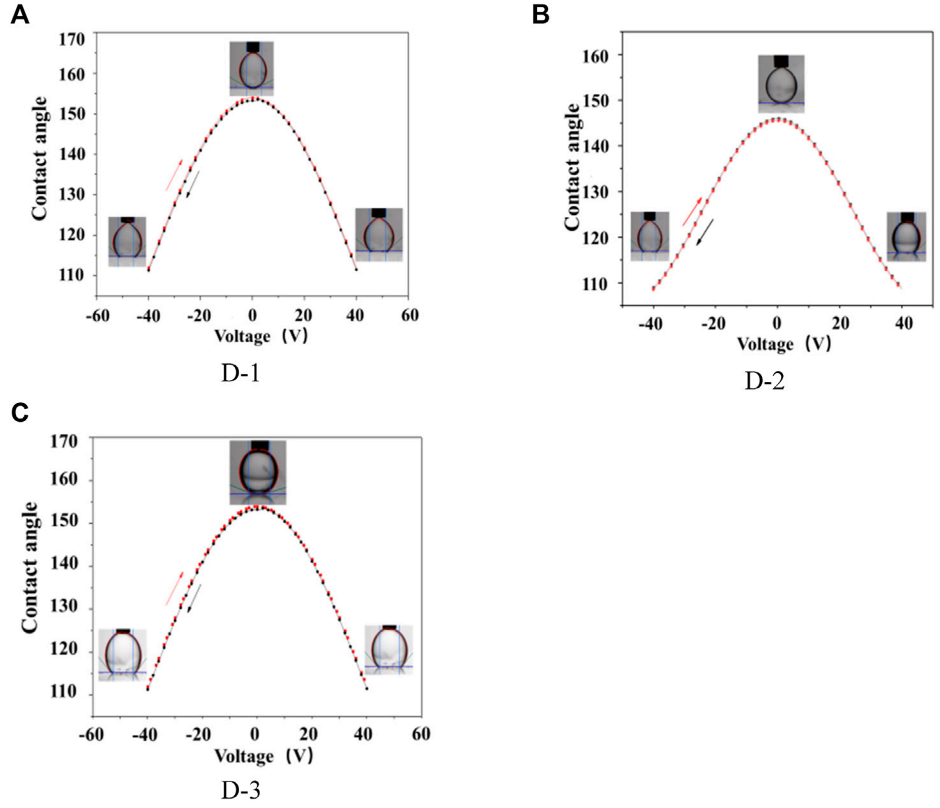

FIGURE 4 | Contact angle of water in oils on AF layer as a function of DC voltage. **(A)** D-1; **(B)**: D-2; **(C)**: D-3; Solvent: decane.

moment of whole dye D-3 will be partially or completely cancelled out.

Photoelectric Response Properties of Dyes

The photoelectric response properties of D-1/3 dyes were demonstrated by measuring the capacitance of the EFD cell under different voltage. The results could be seen in **Figure 6**. As the voltage raise from 0 to 40 V, we can see that the capacitance of the cell has an abrupt change point at 26 V, showing that the oil begins to break up and shrink at 26 V, which is called the threshold voltage. When the voltage decreased from 40 to 0 V, we can see that the capacitance of the cell decreased gradually as expected, which didn’t suffer an abrupt change. The CA hesterisis and existing of oil film rupture corresponded threshold voltage caused the asymmetry of the C–V curves in ON and OFF process. D-3

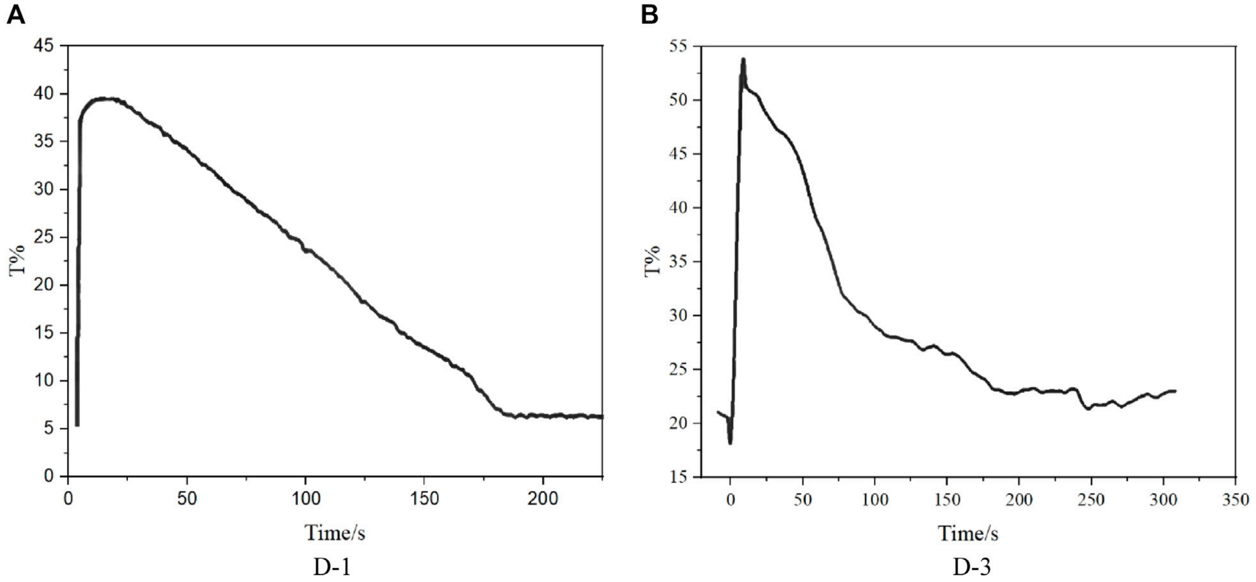

FIGURE 5 | Backflow time of electrowetting display devices formulated by Dyes D-1/3. **(A)**: D-1; **(B)**: D-3.

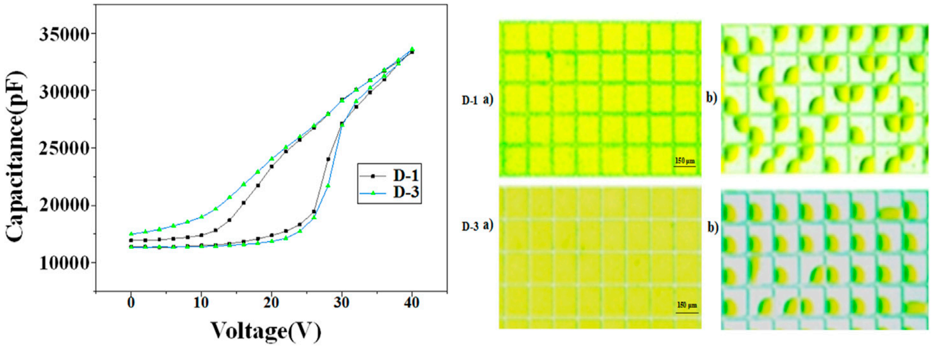

FIGURE 6 | Photoelectric response properties of dyes D-1/3.

has more smoothly curve when the voltage decrease, that's because D-3 has lower electric susceptibiltiy than D-1, the retracted oil drop is more stable at certain voltage. The photos of EFD device at ON and OFF states were recorded, and the aperture ratios were calculated in photoshop software. The aperture ratio of D-1 and D-3 could reach as high as 68.5 and 75% respectively.

Light-Stability Research of Dyes

As researched by G. Baxter and Shufen Zhang, the dye molecules under aggregation state have stronger internal molecular force, which makes it easier to transfer energy, thus the aggregation have much better light stability. The light stability comparison of multi-chromophore dye and corresponding mono-chromophore dye were researched. The test was carried under accelerated xenon lamp for 100 h at 45°C, which can translate to several years of normal conditions [22].

The color coordinates of colored EFD cell formulated by D-1 and D-3 were tested, the results were showed in (x, y) in CIE1931 color space. The color deviation ΔE were calculated from the deviation of l, a, b value. The results could be seen in **Figure 7** and **Table 1**. For D-1, as the irradiation time increased, color coordinates (x, y) of EFD panel were changed. The color coordinate x increased from 0.426 to 0.440, while the color coordinate y increased from 0.416 to 0.432, showing that the color changed from bright yellow to light yellow. The ΔE of D-1 was found to be as high as 2.680 after 100 h of irradiation. For the D-3, the color coordinate x increased from 0.464 to 0.466, while the color coordinate y did not change. The ΔE of D-3 was 1.200, showing a very

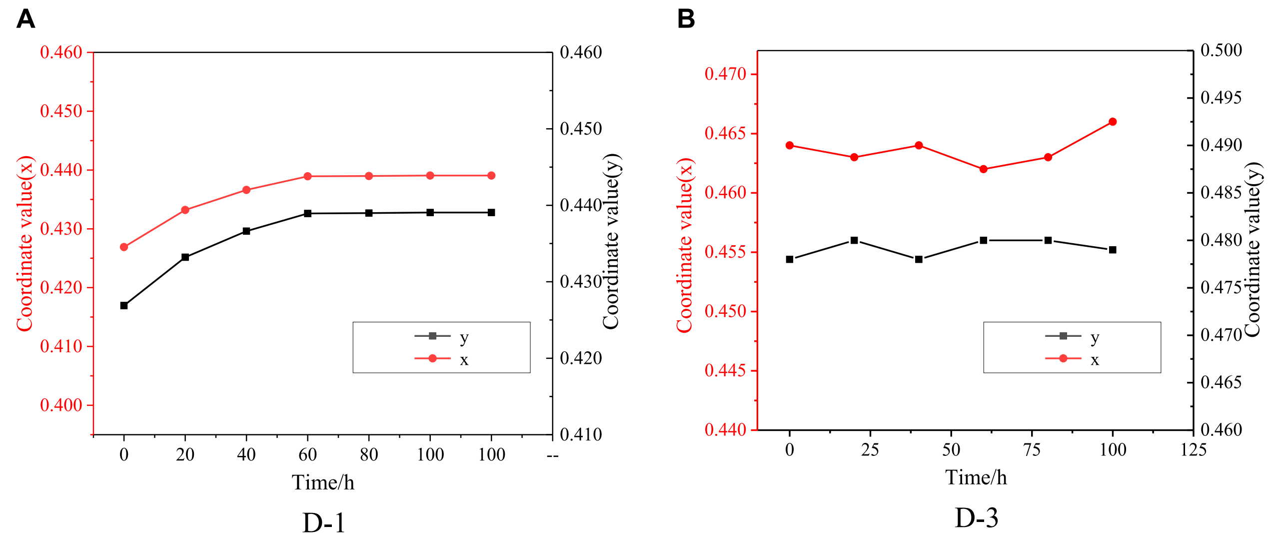

FIGURE 7 | Variation of color coordinates (x, y) of oils in CIE1931 color space (Irradiation condition: 0.55 W/m^2 (340 nm); Temperature 45°C); **(A)**: D-1; **(B)**: D-3.

TABLE 1 | Color change (ΔE) of two formulated dyes before and after accelerated irradiation.

Dye	Before irradiation			After irradiation			ΔE
	L	A	b	L	A	b	
D-1	246.500	−8.720	182.640	244.030	−7.680	182.670	2.680
D-3	239.400	14.000	210.500	238.300	14.400	210.300	1.200

(Irradiation condition: 0.55 W/m^2 (340 nm); Irradiation time: 100 h; Temperature 45°C).

small color change which can hardly be distinguished by the naked eye after 100 h irradiation. These performances are highly relevant to their structure stability.

CONCLUSION

In summary, we have constructed a multi-chromophore macromolecular dye system and synthesized three EFD oil materials based on azo pyrazolone dyes. The absorption, electrical-optical response, and light-stability of these dyes were researched in detail. The three-chromophore dye D-3 has higher aggregation and lower polarity than mono-chromophore dye D-1, thus it has low backflow effect and good light-stability. The research showed that low polarity and high degree of dye aggregation can highly increase the light-stability property and decrease the backflow of EFD oil.

DATA AVAILABILITY STATEMENT

The original contributions presented in the study are included in the article/Supplementary Material, further inquiries can be directed to the corresponding author.

AUTHOR CONTRIBUTIONS

HJ and YD conceived the idea; YD conducted the analyses; HJ, DY, YG, and GZ provided the data; all authors contributed to the writing and revisions.

FUNDING

This work was supported by National Natural Science Foundation of China (22,008,156), Program for Guangdong Innovative and Enterpreneurial Teams (No. 2019BT02C241), Science and Technology Program of Guangzhou (No. 2019050001, No. 201904020007), Program for Chang Jiang Scholars and Innovative Research Teams in Universities (No. IRT_17R40), National Natural Science Foundation of Guangdong, China (2018A0303130059), Guangdong Provincial Key Laboratory of Optical Information Materials and Technology (Grant No. 2017B030301007), Guangzhou Key Laboratory of Electronic Paper Displays Materials and Devices (201,705,030,007), MOE International Laboratory for Optical Information Technologies and the 111 Project.

REFERENCES

1. Hayes RA, and Feenstra BJ. Video-speed Electronic Paper Based on Electrowetting. *Nature* (2003) 425(6956):383–5. doi:10.1038/nature01988
2. Tang B, Groenewold J, Zhou M, Hayes RA, and Zhou G. Interfacial Electrofluidics in Confined Systems. *Sci Rep* (2016) 6(1):26593. doi:10.1038/srep26593
3. Berge B, and Peseux J. Variable Focal Lens Controlled by an External Voltage: An Application of Electrowetting. *The Eur Phys J E.* (2000) 3(2):159–63. doi:10.1007/s101890070029
4. Riahi M, Brakke KA, Alizadeh E, and Shahroosvand H. Fabrication and Characterization of an Electrowetting Display Based on the Wetting-Dewetting in a Cubic Structure. *Optik* (2016) 127(5):2703–7. doi:10.1016/j.ijleo.2015.11.205

5. Sung Kwon Cho SK, Hyejin Moon H, and Chang-Jin Kim CJ. Creating, Transporting, Cutting, and Merging Liquid Droplets by Electrowetting-Based Actuation for Digital Microfluidic Circuits. *J Microelectromech Syst* (2003) 12(1):70–80. doi:10.1109/JMEMS.2002.807467
6. Heikenfeld J, Smith N, Dhindsa M, Zhou K, Kilaru M, Hou L, et al. Recent Progress in Arrayed Electrowetting Optics. *Opt Photon News* (2009) 20(1):20. doi:10.1364/OPN.20.1.000020
7. Heikenfeld J, Zhou K, Kreit E, Raj B, Yang S, Sun B, et al. Electrofluidic Displays Using Young-Laplace Transposition of Brilliant Pigment Dispersions. *Nat Photon* (2009) 3(5):292–6. doi:10.1038/nphoton.2009.68
8. Van DW, and Hayes RA. *Electrowetting Elements*. U.S. Patent 8980141 (2011).
9. Ishida M, Shiga Y, Takeda U, and Kadowaki M. *Ink Containing Anthraquinone Based Dye, Dye Used in the Ink, and Display*. U.S. Patent 8999050 (2013).
10. Shiga Y, Takeda U, Ichinosawa S, and Ishida M. *Ink Containing Heterocyclic Azo Dye, and Dye for Use in Said Ink*. U.S. Patent 8747537 (2014).
11. Shiga Y, and Ishida M. *Pyrazole Disazo Dye and Ink Containing the Dye*. U.S. Patent 8143382 (2012).
12. Chiang Y, and Chao Y. Synthesis of Dis-Azo Black Dyes for Electrowetting Displays. *Mater Sci Eng B* (2012) 177(18):1672–7. doi:10.1016/j.mseb.2012.08.011
13. Farrand LD, Smith N, Corbett A, and Merck Patent GmbH L, A. *Electrowetting Fluids*. U.S. Patent 20150355456 A1 (2015).
14. Chiang Y-F, and Chao Y-C. Synthesis and Application of Oil-Soluble Red Dyes Derived from P-N-Alkyl Aniline. *Msa* (2014) 05(8):485–90. doi:10.4236/msa.2014.58052
15. Kato T, Higuchi S, Fukushige Y, Jimbo Y, and Sasaki D. *Colored Composition for Electrowetting Display, Image Display Structure, and Electrowetting Display Device*. U.S. Patent 9494789 (2014).
16. Lee PTC, Chiu C-W, Chang L-Y, Chou P-Y, Lee T-M, Chang T-Y, et al. Tailoring Pigment Dispersants with Polyisobutylene Twin-Tail Structures for Electrowetting Display Application. *ACS Appl Mater Inter* (2014) 6(16):14345–52. doi:10.1021/am503599k
17. Lee PTC, Chiu C-W, Lee T-M, Chang T-Y, Wu M-T, Cheng W-Y, et al. First Fabrication of Electrowetting Display by Using Pigment-In-Oil Driving Pixels. *ACS Appl Mater Inter* (2013) 5(13):5914–20. doi:10.1021/am401840b
18. Beni G, and Tenan MA. Dynamics of Electrowetting Displays. *J Appl Phys* (1981) 52(10):6011–5. doi:10.1063/1.329822
19. Deng Y, Jiang H, Ye D, Zhou R, Li H, Tang B, et al. Synthesis and Application of an Alkylated Pyrazole-Based Azo Dye for Electrofluidic Display. *Jnl Soc Info Display* (2018) 26(6):369–75. doi:10.1002/jsid.668
20. Baxter G, Giles CH, and Lewington WJ. Relation between Physical State and Rate of Fading of Dyes. *J Soc Dyers Colourists* (1957) 73(8):386–92. doi:10.1111/j.1478-4408.1957.tb02210.x
21. Deng Y, Li S, Ye D, Jiang H, Tang B, and Zhou G. Synthesis and a Photo-Stability Study of Organic Dyes for Electro-Fluidic Display. *Micromachines* (2020) 11(1):81. doi:10.3390/mi11010081
22. Van DW, Melanie M, Massard R, and Hayes RA. *Improvements in Relation to Electrowetting Elements*. U.S. Patent WO2010031860 A2 (2010).

Conflict of Interest: The authors declare that the research was conducted in the absence of any commercial or financial relationships that could be construed as a potential conflict of interest.

ORIGINAL RESEARCH
published: 01 November 2021
doi: 10.3389/fphy.2021.755081

Ultrafast Laser Modulation of Local Magnetization Orientation in Perpendicularly Exchange-Coupled Bilayer

Zhikun Xie[1†], Jielin Zhou[1†], Yuanhai Cai[1], Jipei Chen[1,2*], Wei Zhang[1,2], Jun Peng[1] and Zhifeng Chen[1,2*]

[1]School of Physics and Materials Science, Guangzhou University, Guangzhou, China, [2]Research Center for Advanced Information Materials (CAIM), Guangzhou University, Guangzhou, China

Edited by:
Feng Chi,
University of Electronic Science and Technology of China, China

Reviewed by:
Yanxiong Du,
South China Normal University, China
Lihua Teng,
Qingdao University of Science and Technology, China

***Correspondence:**
Zhifeng Chen
chenzf@gzhu.edu.cn
Jipei Chen
chenjp@gzhu.edu.cn

†These authors have contributed equally to this work

Specialty section:
This article was submitted to Optics and Photonics, a section of the journal Frontiers in Physics

Received: 07 August 2021
Accepted: 10 September 2021
Published: 01 November 2021

Citation:
Xie Z, Zhou J, Cai Y, Chen J, Zhang W, Peng J and Chen Z (2021) Ultrafast Laser Modulation of Local Magnetization Orientation in Perpendicularly Exchange-Coupled Bilayer. Front. Phys. 9:755081. doi: 10.3389/fphy.2021.755081

Laser-induced magnetization dynamics in a perpendicularly exchange-coupled TbFeCo/GdFeCo bilayer film are studied by using pump-probe magneto-optical Kerr spectroscopy. An ultrafast modulation effect on local magnetization orientation is observed. Such ultrafast magnetization reorientation in the GdFeCo layer is revealed to be triggered by the femtosecond laser pulse and driven by the effective exchange field. These processes occur within a timescale of hundreds of picoseconds, in which the field- and fluence-dependent dynamical behaviors are demonstrated. In addition, an atomistic Heisenberg model is proposed for studying the laser-induced magnetization dynamics by using micromagnetic simulation. The simulated results agree with the experimental phenomena and further reveal the underlying mechanism. These results show an approach for ultrafast manipulation of the local magnetization orientation in perpendicularly exchange-coupled structures.

Keywords: magnetization dynamics, exchange coupling, time-resolved magneto-optical Kerr spectroscopy, magnetization reorientation, femtosecond laser, micromagnetic simulation

1 INTRODUCTION

Exchange-coupled composites (ECCs) have attracted much interest due to their designable magnetic properties from combining individual material with different properties [1, 2] and also potential applications in magnetic recording [3, 4], magnetic sensors [5, 6] and magnonic devices [7, 8]. In particular, many research works focused on the perpendicular ECCs which have high thermal stability, reduced switching field, and thus excellent applied potential for ultrahigh-density magnetic recording [9–11]. On the other hand, laser-induced magnetization dynamics in magnetic system is also an active field. Introduction of the ultrashort laser pulses can lead to infusive effects, such as further reduce coercivity and remarkably accelerate magnetization reversal for magnetic recording [12–15]. Therefore, studying laser-induced or -modulated ultrafast magnetization dynamics in perpendicular ECCs is demanded for developing related applications.

Amorphous ferrimagnetic rare earth-transition metal (RE-TM) alloy films, such as GdFeCo and TbFeCo, are one kind of the most-concerned materials for ultrafast magnetic applications [16–18]. Typically, GdFeCo and TbFeCo can be used as the free and pinning layers, respectively, in perpendicular ECCs due to their dissimilar spin-orbit coupling and perpendicular magnetic anisotropy (PMA) [2, 19]. RE-TM ECCs have attracted attentions also due to their applied

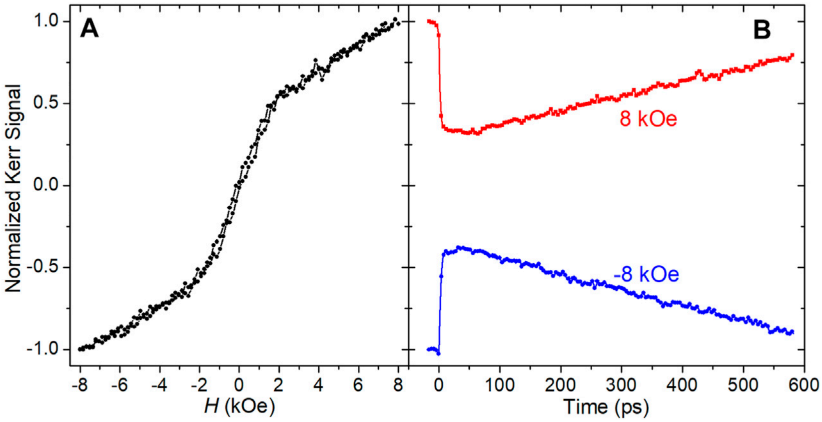

FIGURE 1 | (A) Normalized polar Kerr hysteresis loop of the GdFeCo layer. **(B)** Laser-induced magnetization dynamics measured under *H* = ±8 kOe and pump fluence of 9.8 mJ/cm^2. The Kerr signal is normalized to the static Kerr value at *H* = ±8 kOe.

potential in magnetic super resolution (MSR) for magneto-optical readout [20–22], but observation of the related dynamical process has not been reported.

In this paper, we investigate the laser-induced magnetization dynamics in a perpendicularly exchange-coupled TbFeCo/GdFeCo bilayer film by using pump-probe magneto-optical polar Kerr spectroscopy. We observe an ultrafast modulation effect on local magnetization orientation in the GdFeCo layer which is triggered by the femtosecond laser pulse and driven by the effective exchange field, and also first demonstrate the dynamics. In addition, an atomistic Heisenberg model is proposed for studying these laser-induced magnetization dynamics by using micromagnetic simulation.

2 EXPERIMENT

The sample studied here is a TbFeCo(40 nm)/GdFeCo(50 nm) coupled bilayer film prepared on a glass substrate by magnetron sputtering. The TbFeCo layer with high PMA has a strong coercivity (H_c) of ~7 kOe, while the GdFeCo layer has weak magnetocrystalline anisotropy and hence possesses in-plane magnetization.

The laser-induced magnetization dynamics are measured by using a time-resolved pump-probe magneto-optical Kerr configuration. Linearly polarized laser pulse train with a central wavelength of 800 nm, a duration of 100 fs, and a repetition rate of 1 kHz is generated from a Ti:sapphire regenerative amplifier and split into the pump and probe beams. Both the two beams are almost incident normally on the surface of GdFeCo layer with a pulse fluence ratio of pump to probe larger than 30. The focused spot diameter of the pump beam is ~150 μm, while the probe spot located at the center of the pump spot is set to be nearly a half smaller to decrease the temperature gradient within the probed area. The probe beam reflected from the sample is divided into two orthogonally polarized components by a Glan prism to measure the polar Kerr rotation by using a differential detector combined with a lock-in amplifier. A variable magnetic field generated by an electromagnet is applied perpendicularly to the sample plane. All measurements are performed at room temperature.

3 RESULTS AND DISCUSSION

Considering the light penetration depth, the polar Kerr signal in our experiment mainly comes from the out-of-plane magnetization component in the upper half part of GdFeCo layer. Note that for RE-TM materials, the Kerr signal probed at 800 nm is contributed from the magnetic moment of TM atoms [18], namely FeCo atoms here. As shown in **Figure 1A**, the out-of-plane polar Kerr hysteresis loop presents the hard-axis hysteresis of GdFeCo layer. Due to the competition between the demagnetizing field and the effective bias field from exchange coupling [2, 10], a nonuniform magnetization distribution is formed in the GdFeCo layer. The slight hysteresis under small external field just presents the different magnetization states of GdFeCo layer originated from the opposite saturation states of TbFeCo layer.

Figure 1B shows the laser-induced magnetization dynamics measured under pump fluence of 9.8 mJ/cm^2 and external field (H) of ±8 kOe which is larger than H_c of TbFeCo layer. Only ultrafast demagnetization and magnetization recovery can be observed in the dynamical process. The magnetization recovery time is ~460 ps, showing a slow heat-diffusion process.

Next, field-dependent magnetization dynamics are measured. Anomalous dynamical phenomena are observed in a range of small field. In **Figure 2A**, it seems that the trace for H = 1.6 kOe still only presents the typical dynamical processes of ultrafast demagnetization and magnetization recovery. However, the decay curves for −800 Oe, −320 Oe, and 0 Oe all cross their initial magnetization states. With decreasing H, the crossing amplitude increases, while the crossing time decreases from 462 to 176 ps. In the case of 0 Oe (without external field applied), the crossing amplitude seems even larger than the demagnetization amplitude. This anomalous behavior could not be attributed to the magnetization precession, a strong evidence is that the crossing time increases with increasing H, whereas the time period of magnetization precession should decrease with increasing H [23]. Then, what does it originate from?

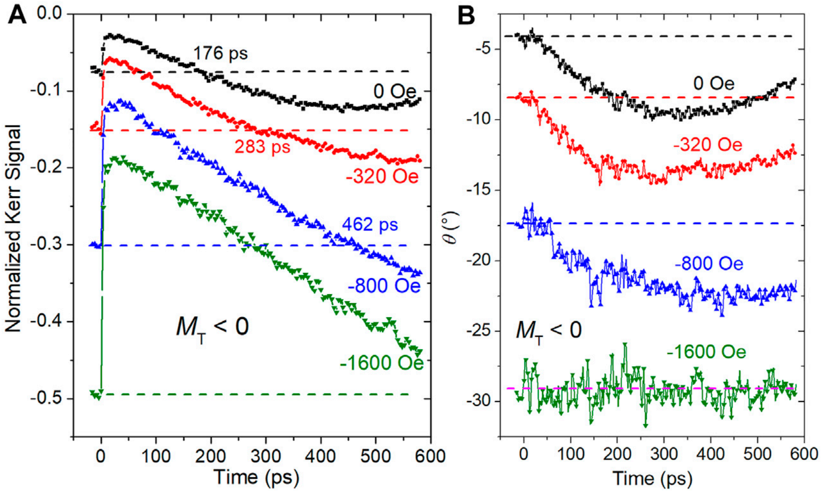

FIGURE 2 | (A) Laser-induced magnetization dynamics measured under different external field and a constant pump fluence of 9.8 mJ/cm^2. **(B)** Average magnetization orientation angle θ as functions of delay time. The dashed lines in both **(A)** and **(B)** denote the initial state before excitation. The sign of M_T shows the saturated state of the TbFeCo magnetization.

As mentioned above, because of the limited light penetration depth, direct laser excitation on the TbFeCo layer can be neglected. The femtosecond laser pulse mainly decreases the transient magnetization of GdFeCo layer, and simultaneously reduce the demagnetizing energy (E_d) and the exchange energy (E_A) [10]. These would change the equilibrium distribution of the magnetization orientation in GdFeCo layer, leading to the transient magnetization reorientation. Mostly in RE-TM layer, the reduction of E_d is more obvious, so the magnetization reorientation is expected to toward the orientation of TbFeCo magnetization driven by the exchange field. Note that along the vertical direction, the demagnetizing field in GdFeCo layer is nonuniform, the vertical diffusion of laser heating should increase the transient influence on demagnetizing field, and thus further singularize the role of exchange field. Especially, if the transient temperature is around the magnetization compensation point [16], a remarkable reduction of E_d should also significantly enhance this effect. Moreover, with H increased, the role of exchange field in the total effective field become minor, and thus the magnetization reorientation effect would be gradually submerged by the magnetization recovery, leading to smaller crossing amplitude and shorter crossing time.

Time dependence of the magnetization orientation can be estimated *via* the relation $M_z(t) = |\boldsymbol{M}(t)| \sin\theta(t)$, where $M_z(t)$ is the projection of magnetization on z axis (out-of-plane component) and θ is the angle between magnetization orientation and the sample plane. $|\boldsymbol{M}(t)|$ is the magnitude of magnetization which is dependent on the transient temperature and can be approximately obtained from the dynamic trace measured under $H = \pm 8$ kOe as shown in **Figure 1B** [15]. **Figure 2B** shows θ as functions of the delay time extracted from **Figure 2A**. Here we can clearly see an ultrafast modulation effect on the local magnetization orientation in GdFeCo layer. Note that those are only the average results of the nonuniform magnetization distribution in the probe depth. Such modulation effect of θ can be only observed under relatively small field ($H < \sim 1$ kOe). The max change of θ is ~6.1° and occurs at ~300 ps after laser excitation without external field applied. Evidently, recovery of θ originates from the recovery of E_d and E_A.

To further demonstrate the role of exchange field in the dynamics, we compare the transient traces measured with opposite saturated magnetization states of the TbFeCo layer (denoted by the sign of M_T) and opposite directions of H, respectively, as shown in **Figure 3A**. As expected, opposite M_T results in opposite direction of magnetization reorientation, even with the same condition of external field and laser fluence. This is also another strong evidence for excluding the magnetization precession as the origin of the observed dynamical phenomena. It is clear that the initial state of magnetization in the probed area is dominated by H, while the direction of magnetization reorientation is controlled by M_T, implying that just the exchange field drives the magnetization reorientation after laser excitation. This result agrees with that of the steady measurements for MSR [20], but here we first reveal the dynamics and related timescale.

Figure 3B shows the dynamics measured under the same H and M_T but different laser fluence. The higher fluence not only leads to a more remarkable demagnetization, but also a larger crossing amplitude and a shorter crossing time, showing that increase of the laser excitation energy can accelerate the magnetization reorientation. This result further demonstrates the laser modulation effect of the local magnetization orientation.

4 MICROMAGNETIC SIMULATION

In order to further understand the mechanism of above experimental phenomena, we construct an atomistic

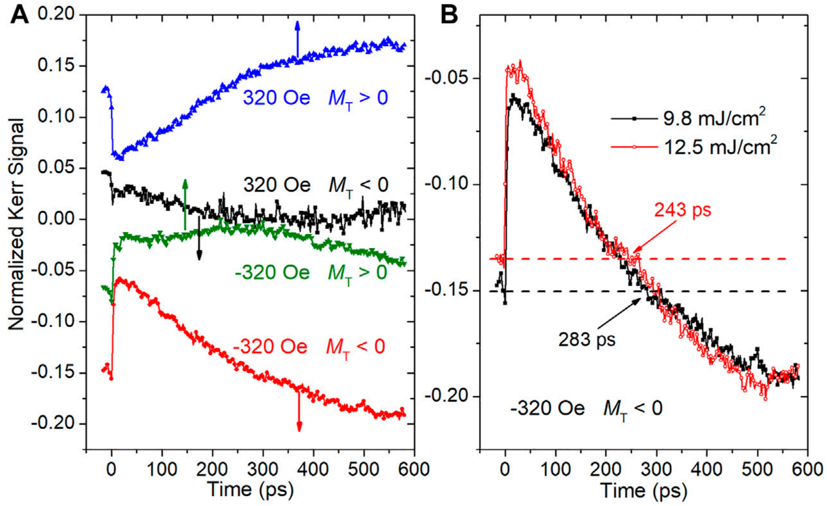

FIGURE 3 | (A) Laser-induced magnetization dynamics depended on the directions of exchange bias field and external field. The sign of M_T shows the saturated state of the TbFeCo magnetization which reflects the direction of exchange bias field. The arrows denote the direction of magnetization reorientation. **(B)** Comparison of magnetization dynamics measured under different excitation fluence.

Heisenberg model for describing the magnetic states of FeCo atoms in GdFeCo layer of the sample, which comprises of nearest ferromagnetic exchange interaction (J), anisotropy (A), and effective magnetic field (B_z) terms [24, 25]:

$$\mathcal{H} = -J\sum_{i,j} \boldsymbol{m}_i \cdot \boldsymbol{m}_j - A\sum_i \left(m_{i,x}^2 + m_{i,y}^2\right) - \boldsymbol{B}_z \cdot \sum_i \boldsymbol{m}_i, \qquad (1)$$

where the magnetic moments are imposed on a two-dimensional square lattice with periodic boundary conditions, with $\boldsymbol{m}_i = (m_{i,x}, m_{i,y}, m_{i,z})$ denoting the magnetic moment at site i in the xy-plane. We consider an easy-plane magnetic anisotropy ($A > 0$) in the GdFeCo layer as revealed by the experimental observation. In phenomenological sense, such an easy-plane anisotropy naturally arises from the strong magnetic dipolar interactions (demagnetization energy) in the system. The inter-layer exchange coupling can be parameterized by an exchange bias field acting on the FeCo atoms in the GdFeCo layer, which orients towards the same direction with that of M_T. For simplicity, the exchange bias field here is included into the external magnetic field as an effective magnetic field $\boldsymbol{B}_z = B_z \boldsymbol{e}_z$ normal to the xy-plane.

In the simulations, we first study the temperature dependences of equilibrium magnetic properties of GdFeCo layer using the Langevin Landau-Lifshitz-Gilbert stochastic equation [24, 25] (see *Simulation methods* in the **Supplementary Information**). The temperature-dependent behaviors are monitored by evaluating the thermal-averaged magnetization $<M>$ and magnetization components $<M_z>$ along the z-axis, which are defined as $<M> = \frac{1}{N^2} < (\sum_i S_{i,x})^2 + (\sum_i S_{i,y})^2 + (\sum_i S_{i,z})^2 >$ and $<M_z> = \frac{1}{N} < \sum_i S_{i,z} >$, where $\boldsymbol{S}_i = (S_{i,x}, S_{i,y}, S_{i,z})$ denotes a classical Heisenberg spin with unit length at site i, N is the number of spins, and <…> refers to the thermal average for the equilibrium states at a given temperature T. The simulated results in **Figure 4A** show that the magnetization $<M>$ decreases from 1.0 at $T = 0$ to ~0.0 at high temperature with T increases, corresponding to the transition from ferromagnetic state at low T to paramagnetic state at high T. In addition, the reduced $<M_z> - T$ curve exhibits that $|<M_z>|$ rises smoothly when $T < T_\mathrm{c}$ and drops down when $T > T_\mathrm{c}$ with T increases. This indicates that the out-of-plane reorientation of magnetization occurs with increasing temperature when $T < T_\mathrm{c}$ [26–28], and just agrees with the experimental results.

To proceed, we simulate the laser-induced ultrafast magnetization dynamics by employing the Landau–Lifshitz–Bloch (LLB) equation [29–32], in which the temperature of atomic spins are determined by using the three-temperature model [33–35] (see *Simulation methods* in the **Supplementary Information**). In this scheme, the system is first relaxed by solving the LLB equation under the effective magnetic field B_z for reaching the equilibrium state. Then we carefully tracked the dynamics of out-of-plane components of magnetization ($M_z = \frac{1}{N}\sum_i m_{i,z}$) from the initial equilibrium state after the laser excitation.

Figure 4B presents the evolutions of M_z as functions of time, and one can see that a sharp demagnetization occurs after excitation of laser-pulse heating. Subsequently, M_z gradually recovers to its equilibrium state. In this process, the intriguing behavior of magnetization reorientation appears and consists with our experimental observation.

In our experiments, M_z shows a slow recovery with complete recovery time larger than 600 ps. In this sense, one may understand the M_z dynamic behaviors from the equilibrated temperature-dependence of $<M_z>$ in

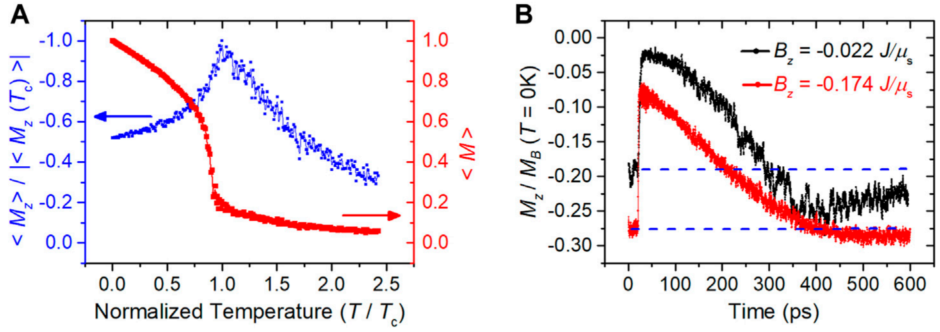

FIGURE 4 | (A) Simulated thermal-averaged out-of-plane magnetization component $< M_z >$ and magnetization $< M >$ of equilibrium states as functions of temperature T, under $B_z = -0.174\, J/\mu_S$ (μ_S is the atomistic magnetic moment). Here $< M_z >$ is normalized in the unit of $|< M_z\ (T_c) >|$, with $< M_z\ (T_c) >$ representing the out-of-plane magnetization at Curie temperature T_c. **(B)** Simulated laser-induced dynamics of out-of-plane magnetization component M_z under different effective magnetic field B_z. Here M_z is scaled in the reduced unit of M_B (T = 0 K), which denotes the magnetization under magnetic field B_z and temperature T = 0 K. The initial values of M_z before excitation are marked by the blue dashed lines.

Figure 4A, considering that the system becomes quasi-equilibrium states in the process of magnetization recovery. Thus, the orientation of spins gradually tends to the quasi-equilibrium direction depended on transient temperature, leading to M_z crossing its initial state. With the subsequent recovery of transient temperature, M_z gradually recovers to the equilibrium state. Note that the crossing amplitude decreases and the crossing time increases with increasing $|B_z|$, agreeing well with the experimental observations in **Figure 2A**.

5 CONCLUSION

In summary, the laser-induced magnetization dynamics and the ultrafast modulation effect on local magnetization orientation in a perpendicularly coupled TbFeCo/GdFeCo film are studied by using time-resolved magneto-optical Kerr spectroscopy. The magnetization reorientation in the GdFeCo layer is triggered by the femtosecond laser pulse and driven by the effective exchange field. These processes occur within a timescale of hundreds of ps. We discuss the field- and fluence-dependent dynamical behaviors, and propose an atomistic Heisenberg model to study the dynamics by using micromagnetic simulation. The simulation agrees with the experimental phenomena and further reveals the underlying mechanism. These results show an approach for ultrafast manipulation to the local magnetization orientation in perpendicularly exchange-coupled structures *via* changing exchange bias state and laser fluence.

DATA AVAILABILITY STATEMENT

The original contributions presented in the study are included in the article/**Supplementary Material**, further inquiries can be directed to the corresponding authors.

AUTHOR CONTRIBUTIONS

ZX and ZC designed the experiment, set up the configuration and carried out the measurement. JZ, YC, and JP contributed to the experiment. JZ and ZC finished the data analysis with supports from WZ. JC constructed the model and performed the computations. ZX, JC, and ZC prepared the manuscript. All authors commented on the manuscript.

FUNDING

This work was partially supported by the National Natural Science Foundation of China under Grant Nos. 11204044, 11604059, and 21903017; the Natural Science Foundation of Guangdong Province under Grant Nos. 2020A1515010411, 2019A1515010783, and 2017A030313020; and the Key Research Project of Guangzhou University under Grant No. YK2020003.

SUPPLEMENTARY MATERIAL

The Supplementary Material for this article can be found online at: https://www.frontiersin.org/articles/10.3389/fphy.2021.755081/full#supplementary-material

REFERENCES

1. Blanco-Roldán C, Quirós C, Sorrentino A, Hierro-Rodríguez A, Álvarez-Prado LM, Valcárcel R, et al. Nanoscale Imaging of Buried Topological Defects with Quantitative X-ray Magnetic Microscopy. *Nat Commun* (2015) 6:8196. doi:10.1038/ncomms9196
2. Wang K, Wang Y, Ling F, and Xu Z. Perpendicular Exchange Coupling Effects in Ferrimagnetic TbFeCo/GdFeCo Hard/soft Structures. *J Magnetism Magn Mater* (2018) 452:153–6. doi:10.1016/j.jmmm.2017.12.061
3. Wang J-P, Shen WK, Bai JM, Victora RH, Judy JH, and Song WL. Composite Media (dynamic tilted media) for Magnetic Recording. *Appl Phys Lett* (2005) 86:142504. doi:10.1063/1.1896431
4. Xu Z, Zhou SM, Ge JJ, Du J, and Sun L. Magnetization reversal mechanism of perpendicularly exchange-coupled composite $L1_0$-FePt/CoCrPt bilayers. *J Appl Phys* (2009) 105:123903. doi:10.1063/1.3148300
5. Radu F, Abrudan R, Radu I, Schmitz D, and Zabel H. Perpendicular Exchange Bias in Ferrimagnetic Spin Valves. *Nat Commun* (2012) 3:715. doi:10.1038/ncomms1728
6. Hebler B, Reinhardt P, Katona GL, Hellwig O, and Albrecht M. Double Exchange Bias in Ferrimagnetic Heterostructures. *Phys Rev B* (2017) 95: 104410. doi:10.1103/PhysRevB.95.104410
7. Zhang Z, Cui B, Wang G, Ma B, Jin QY, and Liu Y. Ultrafast Laser-induced Magnetization Precession Dynamics in FePt/CoFe Exchange-coupled Films. *Appl Phys Lett* (2010) 97:172508. doi:10.1063/1.3510473
8. Li S-F, He P, Cheng C-Y, Zhou S-M, and Lai T-S. Spin-Wave Modes in Exchange-Coupled FePt/FeNi Bilayer Films. *Chin Phys. Lett.* (2014) 31: 017502. doi:10.1088/0256-307X/31/1/017502
9. Makarov D, Lee J, Brombacher C, Schubert C, Fuger M, Suess D, et al. Perpendicular FePt-based Exchange-coupled Composite Media. *Appl Phys Lett* (2010) 96:062501. doi:10.1063/1.3309417
10. Chen Z, Li S, and Lai T. Laser-induced transient strengthening of coupling in $L1_0$-FePt/FeNi exchange-spring film. *J Phys D: Appl Phys* (2015) 48:145002. doi:10.1088/0022-3727/48/14/145002
11. Li ZW, Jiao JY, Luo Z, Ma TY, Qiao L, Wang Y, et al. Microstructure and Magnetic Properties of Exchange-Coupled $Co_{72}Pt_{28}$/Pt/$Co_{81}Ir_{19}$ Composite Media for Perpendicular Magnetic Recording. *J Supercond Nov Magn* (2019) 32:2229–33. doi:10.1007/s10948-018-4953-8
12. Xu C, Chen Z, Chen D, Zhou S, and Lai T. Origin of Anomalous Hysteresis Loops Induced by Femtosecond Laser Pulses in GdFeCo Amorphous Films. *Appl Phys Lett* (2010) 96:092514. doi:10.1063/1.3339878
13. Vahaplar K, Kalashnikova AM, Kimel AV, Hinzke D, Nowak U, Chantrell R, et al. Ultrafast Path for Optical Magnetization Reversal *via* a Strongly Nonequilibrium State. *Phys Rev Lett* (2009) 103:117201. doi:10.1103/PhysRevLett.103.117201
14. Stanciu CD, Tsukamoto A, Kimel AV, Hansteen F, Kirilyuk A, Itoh A, et al. Subpicosecond Magnetization Reversal across Ferrimagnetic Compensation Points. *Phys Rev Lett* (2007) 99:217204. doi:10.1103/PhysRevLett.99.217204
15. Chen Z, Gao R, Wang Z, Xu C, Chen D, and Lai T. Field-dependent Ultrafast Dynamics and Mechanism of Magnetization Reversal Across Ferrimagnetic Compensation Points in GdFeCo Amorphous Alloy Films. *J Appl Phys* (2010) 108:023902. doi:10.1063/1.3462429
16. Stanciu CD, Kimel AV, Hansteen F, Tsukamoto A, Itoh A, Kirilyuk A, et al. Ultrafast spin dynamics across compensation points in ferrimagnetic GdFeCo: The role of angular momentum compensation. *Phys Rev B* (2006) 73:220402. doi:10.1103/PhysRevB.73.220402
17. Ogasawara T, Iwata N, Murakami Y, Okamoto H, and Tokura Y. Submicron-scale Spatial Feature of Ultrafast Photoinduced Magnetization Reversal in TbFeCo Thin Film. *Appl Phys Lett* (2009) 94:162507. doi:10.1063/1.3123256
18. Chen Z, Li S, Zhou S, and Lai T. Ultrafast dynamics of 4f electron spins in TbFeCo film driven by inter-atomic 3d-5d-4f exchange coupling. *New J Phys* (2019) 21:123007. doi:10.1088/1367-2630/ab5aa4
19. Ye L-X, Lee C-M, Lai J-H, Canizo-Cabrera A, Chen W-J, and Wu Th. Magnetic Properties of MgO-based RE-TM Perpendicular Magnetic Tunnel Junctions. *J Magnetism Magn Mater* (2010) 322:L9–L11. doi:10.1016/j.jmmm.2009.11.021
20. Peng C, and Mansuripur M. Noise and Coupling in Magnetic Super-resolution Media for Magneto-optical Readout. *J Appl Phys* (1999) 85:6323–30. doi:10.1063/1.370133
21. Wang XY, Zhang YP, Li ZY, Shen DF, and Gan FX. Temperature-Induced Magnetization Reorientation in GdFeCo/TbFeCo Exchange-Coupled Double Layer Films. *Chin Phys Lett* (2003) 20:1359–61. doi:10.3321/j.issn:0256-307X.2003.08.052
22. Tani M. Domain Expansion Readout for Magnetic Amplifying Magneto-Optical System. *J Magn Soc Jpn* (2008) 32:43–9. doi:10.3379/msjmag.32.43
23. Chen Z, Yi M, Chen M, Li S, Zhou S, and Lai T. Spin Waves and Small Intrinsic Damping in an in-plane Magnetized FePt Film. *Appl Phys Lett* (2012) 101: 222402. doi:10.1063/1.4768787
24. Ostler TA, Barker J, Evans RFL, Chantrell RW, Atxitia U, Chubykalo-Fesenko O, et al. Ultrafast Heating as a Sufficient Stimulus for Magnetization Reversal in a Ferrimagnet. *Nat Commun* (2012) 3:6. doi:10.1038/ncomms1666
25. Radu I, Vahaplar K, Stamm C, Kachel T, Pontius N, Dürr HA, et al. Transient Ferromagnetic-like State Mediating Ultrafast Reversal of Antiferromagnetically Coupled Spins. *Nature* (2011) 472:205–8. doi:10.1038/nature09901
26. MacIsaac AB, De'Bell K, and Whitehead JP. Simulation of the Reorientation Transition in Ultrathin Magnetic Films with Striped and Tetragonal Phases. *Phys Rev Lett* (1998) 80:616–9. doi:10.1103/PhysRevLett.80.616
27. De'Bell K, MacIsaac AB, and Whitehead JP. Dipolar Effects in Magnetic Thin Films and Quasi-two-dimensional Systems. *Rev Mod Phys* (2000) 72:225–57. doi:10.1103/RevModPhys.72.225
28. Chen JP, Wang ZQ, Gong JJ, Qin MH, Zeng M, Gao XS, et al. Stripe-vortex Transitions in Ultrathin Magnetic Nanostructures. *J Appl Phys* (2013) 113: 054312. doi:10.1063/1.4790483
29. Evans RFL, Hinzke D, Atxitia U, Nowak U, Chantrell RW, and Chubykalo-Fesenko O. Stochastic Form of the Landau-Lifshitz-Bloch Equation. *Phys Rev B* (2012) 85:9. doi:10.1103/PhysRevB.85.014433
30. Vogler C, Abert C, Bruckner F, and Suess D. Landau-Lifshitz-Bloch Equation for Exchange-Coupled Grains. *Phys Rev B* (2014) 90:10. doi:10.1103/PhysRevB.90.214431
31. Mendil J, Nieves P, Chubykalo-Fesenko O, Walowski J, Santos T, Pisana S, et al. Resolving the Role of Femtosecond Heated Electrons in Ultrafast Spin Dynamics. *Sci Rep* (2014) 4:7. doi:10.1038/srep03980
32. Kazantseva N, Hinzke D, Nowak U, Chantrell RW, Atxitia U, and Chubykalo-Fesenko O. Towards Multiscale Modeling of Magnetic Materials: Simulations of FePt. *Phys Rev B* (2008) 77:7. doi:10.1103/PhysRevB.77.184428
33. Beaurepaire E, Merle J-C, Daunois A, and Bigot J-Y. Ultrafast Spin Dynamics in Ferromagnetic Nickel. *Phys Rev Lett* (1996) 76:4250–3. doi:10.1103/PhysRevLett.76.4250
34. Kim J-W, Vomir M, and Bigot J-Y. Ultrafast Magnetoacoustics in Nickel Films. *Phys Rev Lett* (2012) 109:5. doi:10.1103/PhysRevLett.109.166601
35. Zhang G, Hübner W, Beaurepaire E, and Bigot J-Y. Laser-induced Ultrafast Demagnetization: Femtomagnetism, a New Frontier?. In: B Hillebrands and K Ounadjela, editors. *Spin Dynamics in Confined Magnetic Structures I*. Berlin: Springer-Verlag Berlin (2002). p. 245–89. doi:10.1007/3-540-40907-6_8

Conflict of Interest: The authors declare that the research was conducted in the absence of any commercial or financial relationships that could be construed as a potential conflict of interest.

Advantages of publishing in Frontiers

OPEN ACCESS
Articles are free to read
for greatest visibility
and readership

FAST PUBLICATION
Around 90 days
from submission
to decision

HIGH QUALITY PEER-REVIEW
Rigorous, collaborative,
and constructive
peer-review

TRANSPARENT PEER-REVIEW
Editors and reviewers
acknowledged by name
on published articles

Frontiers
Avenue du Tribunal-Fédéral 34
1005 Lausanne | Switzerland

Visit us: www.frontiersin.org
Contact us: frontiersin.org/about/contact

REPRODUCIBILITY OF RESEARCH
Support open data
and methods to enhance
research reproducibility

DIGITAL PUBLISHING
Articles designed
for optimal readership
across devices

FOLLOW US
@frontiersin

IMPACT METRICS
Advanced article metrics
track visibility across
digital media

EXTENSIVE PROMOTION
Marketing
and promotion
of impactful research

LOOP RESEARCH NETWORK
Our network
increases your
article's readership